Computational Fluid and Solid Mechanics

S. Gopalakrishnan
A. Chakraborty · D. Roy Mahapatra

Spectral Finite Element Method

Wave Propagation, Diagnostics and Control in Anisotropic and Inhomogeneous Structures

Springer

Computational Fluid and Solid Mechanics

Series Editor:

Advisors:

Available Volumes

D. Chapelle, K.J. Bathe
The Finite Element Analysis of Shells – Fundamentals
2003

D. Drikakis, W. Rider
High-Resolution Methods for Incompressible and Low-Speed Flows
2005

M. Kojic, K.J. Bathe
Inelastic Analysis of Solids and Structures
2005

E.N. Dvorkin, M.B. Goldschmit
Nonlinear Continua
2005

B.Q. Li
Discontinuous Finite Elements in Fluid Dynamics and Heat Transfer
2006

J. Iannelli
Characteristics Finite Element Methods in Computational Fluid Dynamics
2006

S. Gopalakrishnan, A. Chakraborty, D. Roy Mahapatra
Spectral Finite Element Method
2007

S. Gopalakrishnan • A. Chakraborty
D. Roy Mahapatra

Spectral Finite Element Method

Wave Propagation, Diagnostics and Control in Anisotropic and Inhomogeneous Structures

Springer

Authors

S. Gopalakrishnan, PhD
Department of Aerospace Engineering
Indian Institute of Science
C.V Raman Avenue
Bangalore 560 012
India

A. Chakraborty, PhD
General Motors India
Units 1–8, 3rd Floor, Creator Building
Whitefield Road
Bangalore 560 066
India

D. Roy Mahapatra, PhD
Department of Aerospace Engineering
Indian Institute of Science
C.V Raman Avenue
Bangalore 560 012
India

ISBN 978-1-84628-355-0 e-ISBN 978-1-84628-356-7

DOI 10.1007/978-1-84628-356-7

Computational Fluid and Solid Mechanics Series ISSN 1860-482X

British Library Cataloguing in Publication Data
A catalogue record for this book is available from the British Library

Library of Congress Control Number: 2007938275

Cover design: deblik, Berlin, Germany

Printed on acid-free paper

9 8 7 6 5 4 3 2 1

springer.com

To our parents and wives

Preface

Wave propagation is an exciting field having applications cutting across many disciplines. In the field of structural engineering and smart structures, wave propagation based tools have found increasing applications especially in the area of structural health monitoring and active control of vibrations and noise. In addition, there has been tremendous progress in the area of material science, wherein a new class of structural materials is designed to meet the particular application. In most cases, these materials are not isotropic as in metallic structures. They are either anisotropic (as in the case of laminated composite structures) or inhomogeneous (as in the case of functionally graded materials). Analysis of these structures is many orders more complex than that of isotropic structures. For many scientists/engineers, a clear difference between structural dynamics and wave propagation is not evident. Traditionally, a structural designer will not be interested in the behavior of structures beyond certain frequencies, which are essentially at the lower end of the frequency scale. For such situations, available general purpose finite element code will satisfy the designer's requirement. However, currently, structures are required to be designed to sustain very complex and harsh loading environments. These loadings are essentially multi-modal phenomena and their analysis falls under the domain of wave propagation rather than structural dynamics. Evaluation of the structural integrity of anisotropic and inhomogeneous structures subjected to such loadings is a complex process. The currently available analysis tools are highly inadequate to handle the modeling of these structures. In this book, we present a technique called the "Spectral Finite Element Method", which we believe will address some of the shortcomings of the existing analysis tools.

Although the spectral finite element method has been in existence for a long time under the name of the dynamic stiffness method, its use was limited to simple vibration studies. It is only in recent times that the potential of this method to handle a wide range of applications has been realized. This is evident from the increasing number of publications in the archival literature. However, we believe that its impact has reached only a small subset

of scientists/engineers working in these areas due to the non-availability of a good textbook. The main aim of this book is to reach out to those analysts/engineers working in new and cutting edge areas to not only highlight the power of this method, but also to serve as a good reference book for specialists.

The spectral finite element method is essentially a finite element method in the frequency domain. In essence, the beauty of the method lies in the fact that one can easily convert a finite element code to a spectral element code without much difficulty. In addition, it uses spectral analysis as a basic tool for element formulation. That is, in the process of element formulation, one can deeply understand the physics behind wave propagation in complex media and its interaction with various boundaries. Frequency domain formulation enables easy and straightforward solution of inverse problems. Hence, the spectral element method can be used as a tool to post-process experimental data.

The book mainly addresses the wave behavior in composites and inhomogeneous media in addition to its application to structural health monitoring and active vibration and wave control. The book introduces new methods for the solution of wavenumbers for propagation in composites and inhomogeneous waveguides. For structural health monitoring, waveguide models for different types of damage are developed. The reader is also introduced to various damage detection schemes that blend well with the spectral element method. Towards the end of the book, a chapter on the use of the spectral element method for active control application is presented.

A step by step modular approach is adopted here in writing this book. A number of numerical results are presented to not only emphasize the efficiency and numerical superiority of the method, but also to bring out the physics of the problem. The reader may notice that in most cases only one element is sufficient for solution of certain problems, where thousands of finite elements are required. The material presented in this book can serve as a graduate level textbook on wave propagation in structures. A separate graduate level course on the spectral finite element method can be developed using this book. This book is written assuming that the reader has only an elementary background in the theory of elasticity, strength of materials, linear algebra and methods for solving ordinary and partial differential equations.

We would like to thank many of the graduate students who have contributed directly or indirectly towards the development of the book. We would particularly thank A. Nag, D. Srikanth, A. Garg and A. Singhal for their contributions.

Bangalore, India
October, 2007

S. Gopalakrishnan
A. Chakraborty
D. RoyMahapatra

Contents

1

Introduction

Dynamic analysis in structural engineering falls into two different classes, one involving low frequency loading and the other involving high frequency loading. Low frequency problems are categorized as ***Structural Dynamics*** problems while those involving high frequency loading fall into the category of ***Wave Propagation*** problems. In structural dynamics problems, the frequency content of the dynamic load is of the order of a few hundred hertz (Hz) and the designer will be mostly interested in the long-term (or steady-state) effects of the dynamic load on the structures. Hence, the first few normal modes and natural frequencies are sufficient to assess the performance of the structure. The phase information of the response is not critical here. Most of the dynamic problems in structures will fall into this category. On the other hand, for wave propagation problems, the frequency content of the input loading is very high (of the order of kilohertz (kHz) or higher) and hence, short-term effects (transient response) become very critical. Further, many higher order modes will participate in amplifying the dynamic response. Impact and blast-type of loading fall into this category. The multi-modal nature of wave propagation makes one parameter very important, and that is the phase information.

1.1 Solution Methods for Wave Propagation Problems

Dynamic analyses are traditionally performed using the conventional Finite Element Method (FEM). For wave propagation problems wherein the frequency content of the input is very high, many higher order vibrational modes participate in the motion. At these higher frequencies, the wavelengths are very small and hence to capture these modes effectively, FE meshes need to be very fine. This is due to the requirement that the element sizes should be of the same order as the wavelength of the signal. For larger mesh sizes, the element edges will act like a free boundary and start reflecting the initial

responses from these element edges. A fine mesh, although ensuring accurate distribution of the inertia, also increases the computation cost enormously.

FE solutions in dynamics are obtained by two different methods [1]; the modal method and the time marching scheme. Modal methods cannot be applied to multi-modal problems such as those involving wave propagation analysis. This is because, unlike structural dynamics problems, here we need to determine the natural frequencies and the mode shapes of both the low and high frequency modes. It is well known that the extraction of the eigenvalues is computationally the most expensive problem in mechanics. Hence, modal methods are not suited to wave propagation problems. Alternatively we can use various time marching schemes under the FE environment. In this method, analysis is performed over a small time step, which is a fraction of the total time for which the response histories are required. For some time marching schemes, a constraint is placed on the time step, and this, coupled with very large mesh sizes, makes the solution of wave propagation problems (under the FE environment) computationally prohibitive. Hence, we need alternative methods of solution.

Numerical methods such as FEM are based on some assumed solutions to the field variable (say displacement). This assumed solution for wave propagation problems gives large system sizes due to its inability to approximate the mass distribution accurately. Hence, we need to look for a method that approximates the mass accurately. This can happen only when the assumed solution satisfies the governing wave equations as closely as possible. If one is interested in solving the governing wave equation in the time domain, it is very difficult to assume a solution that satisfies the governing wave equation. Instead, one can ignore the inertial part of the wave equation, and solve the static part of the equation exactly and use this solution to obtain the stiffness and mass matrices. This procedure will ensure that the stiffness distribution is nearly exact while the mass distribution is still approximate. Elements developed by this method are called the ***Super Convergent Finite Element (SCFE)***, which are formulated for higher order rods, beams, box-beams and inhomogeneous beams [2, 3, 4, 5, 6]. According to Reference [7], the error introduced by approximating stiffness is much higher than the approximate mass distribution. Hence, one can expect SCFE to give a smaller system size for wave propagation problems than conventional FEM.

Alternatively, one can transform the governing wave equation to the frequency domain and try to solve it exactly. This is a far easier option since transformation to the frequency domain removes the time variable from the governing equation and introduces frequency as a parameter. For 1-D systems, the transform method reduces a governing partial differential equation(s) to a set of ordinary differential equation(s), which are easier to solve than the original wave equation in the time domain. There are different transforms that one can use for this purpose, namely the *Laplace Transform*, the *Fourier Transform* and the *Wavelet Transform*. In this method first the wave equation is transformed into the frequency domain using appropriate forward transforms.

The governing equation in the transformed domain is then solved exactly or almost exactly and the results are post-processed to get all the relevant parameters in the frequency domain. The time domain solutions are then obtained by taking an inverse transform on the frequency domain solutions. Two aspects are very clear from the above discussion: (1) transform methods will yield solutions both in the time and the frequency domain; (2) one requires an efficient way of obtaining inverse transforms, either analytically or numerically, to obtain time domain solutions. If we look at the various available transforms, obtaining inverse Laplace transforms is not straightforward in most cases and this has limited its scope in the analysis of wave propagation problems. On the other hand, numerical versions of forward and inverse transforms are available for both the Fourier and Wavelet Transforms. The Fourier Transform uses the *Fast Fourier Transform* (FFT) numerical algorithm, while in the case of the Wavelet Transform, the Daubechies wavelet basis is commonly used for approximation in time. However, the Fourier transform is the most extensively used transform method for the solution of wave propagation problems due to its numerical superiority and the ease of implementation of the FFT algorithm. The ***Spectral Finite Element Method*** (SFEM) is a numerical method evolved from the Fourier Transform based method. More details on the solution schemes are given in Section 3.4.

There are certain advantages that a transform method can offer over conventional FEM. Unlike the direct problem, wherein one determines the response to the given input, inverse problems deal with determining the input history using the measured responses or determining the system as a whole from the known input and output. These problems are called force (or source) identification problems and system identification problems, respectively. Using a transform method such as SFEM, one can perform inverse problems in a simple and straightforward manner. This is made possible due to an algebraic relationship between the output and the input through the system transfer function (frequency response function). In other words, the transform methods can give responses in both the time and frequency domain using a single analysis.

The SFEM was initially conceived by Narayan and Beskos [8]. This was later popularized by Doyle and co-workers [9]. In recent years, there has been an increasing number of papers on this method in the archival literature for various structural applications. Although its application to metallic structures is well documented, its application to the study of wave propagation in anisotropic and inhomogeneous structures is not well reported in the literature. Unlike metallic structures, the wave behavior in anisotropic and inhomogeneous structures is quite complex due to the presence of both stiffness and inertial coupling. These couplings sometimes give rise to newer set of waves. In addition, the SFEM has potential for use in the application of ***Structural Health Monitoring***(SHM) and ***Active Wave Control*** (AWC), since both these problems involve loading having a very high frequency content. Hence, the main objective of this book is to bring out the essential wave characteris-

tics in these complex structures and show how SHM and AWC problems can be effectively handled in the SFEM environment.

Studies involving the monitoring, detection and arrest of the growth of flaws such as cracks constitute what is universally termed Structural Health Monitoring (SHM). SHM is a type of inverse problem, wherein the presence of damage needs to be detected from the known input and the measured output. It is well known that the most common method of detecting damage is through modal methods [10], wherein one can look at the changes in the natural frequencies of the structure before and after the damage to assess/confirm the presence of damage. In laminated composites, the most common form of failure is the delamination of the plies. At the onset of the damage, the stiffness of the structure reduces, but this reduction is negligible for very small size damage. Hence, modal methods will show negligible change in the lower energy modes and higher modes may become slightly perturbed. The computational cost of determining the higher modes limits the use of modal methods for SHM of composite structures. In summary, small size damage affects only the higher order modes leaving the lower modes unchanged. This effectively means that to assess the presence of small size damage, one needs a mathematical model that can capture the high frequency response of the damaged structure with small problem sizes. In other words, we need a wave propagation based diagnostic tool for SHM studies. This is one of the fundamental goals of on-line SHM, and the SFEM is an ideal candidate for this kind of analysis.

The main requirements for on-line SHM are the following:

- Mathematical models to represent various types of damage. Some of the common types of damage in laminated composites are delamination (both single and multiple), fibre breakage, and surface breaking cracks. Also, models are required for aging composite structures with degraded properties. One can easily model all types of damage using the conventional FEM using 2-D or 3-D elements. The singularity near the flaw tip requires fine mesh discretization. In addition, the high frequency loading requirement for SHM studies further increases the mesh density. These obviously increase the time for solution, defeating the very purpose of on-line SHM. In this book, we describe simplified but accurate spectral element models for various types of damage for its use in SHM studies.
- Accurate damage detection algorithms that blend with the mathematical model used to represent the damage. The success of a damage detection algorithm depends on the quality of the measured responses. Often these responses may be incomplete and in most cases they are corrupted by the presence of high frequency noise. The main requirement is that these damage detection algorithms should be able to predict the presence of damage in an uncertain environment.
- Robust sensors and their placement. The sensitivity of the sensor is an extremely important parameter that determines the quality of the measured

response. The sensitivity depends on the type of sensor and its placement with respect to the damage location. Smart sensors made from *Piezoceramics* (say lead-zirconate-titanate (PZT) or Polyvinylidene Difluoride (PVDF)) are extremely popular for SHM applications. Sensors made from magnetostrictive materials (say TERFENOL-D) are also quite popular due to their large free strain property. Surface Acoustic Wave (SAW) and Bulk Acoustic Wave (BAW) devices also find usage in SHM applications. The placement of the sensors is critical for accurate damage estimation. Normally, sensors are placed in regions of high stress, which are likely locations for damage initiation. However, these locations are difficult to determine *a priori*. Hence, the damage detection algorithm must be able to predict the location of the damage from the far field responses.

Active wave control is yet another application that deals with inputs that have high frequency content. Hence, SFEM is again a suitable candidate for such applications. Vibration reduction in a structure can normally be achieved passively by identifying the resonant conditions and suitably modifying the geometry of the structure such that the natural frequency of the system is far away from the driving frequency of the system. Alternatively, one can do a detailed analysis and identify the regions in a structure having high vibration levels and design suitable damping mechanisms to alleviate vibrations. However, design constraints may not allow any modification to the existing structure. These exercises can be undertaken only when the frequency content of the exciting force is small and when it is desired to reduce the modal amplitudes of the first few modes. Alternatively, one can design a feed back control system, for which an interrogating signal triggered at a certain frequency is required. This signal can be generated using smart actuators made from materials such as PZT, TERFENOL-D *et al.* However, the design of the control system poses a big problem if the problem sizes are large, as in the case of conventional FEM. In such cases, one has resort to reduced-order models for a given FE discretization. The fundamental requirement of any reduced-order model is that the high energy mode that requires suppression should be retained in the reduced model. This is a very difficult problem and requires an experienced analyst to choose the appropriate degrees of freedom to be retained in the reduced-order model. If the problem is a multi-modal one where all the higher modes also have significant energy, the FE discretization is also enormously large and hence to design a feedback control system for such problems, a reduced-order model of the structure is an absolute necessity. Again here, the choice of appropriate degrees of freedom to be included in the reduced-order model is more difficult than the earlier case. The SFEM, due to its inherent property of retaining all modal information within its small size, can effectively be used in multi-modal wave control. The SFEM does not require any reduced-order modelling and it can be used effectively with smart actuators for control applications.

1.2 Fourier Analysis

The heart of SFEM lies in the synthesis of waves using the Fourier transform. A time signal can be represented in the Fourier (frequency) domain in three possible ways, namely the *Continuous Fourier Transform*(CFT), the *Fourier Series* (FS) and the *Discrete Fourier Transform* (DFT). In this section, only brief definitions of the above transforms are given. The reader is encouraged to refer to [9] for more details.

1.2.1 Continuous Fourier Transforms

Consider any time signal $F(t)$. The inverse and the forward CFTs, normally referred to as the transform pair, are given by

$$F(t) = \frac{1}{2\pi} \int_{-\infty}^{\infty} \hat{F}(\omega) e^{j\omega t} d\omega, \quad \hat{F}(\omega) = \int_{-\infty}^{\infty} F(t) e^{-j\omega t} dt\,, \tag{1.1}$$

where $\hat{F}(\omega)$ is the CFT of the time signal, ω is the angular frequency and j ($j^2 = -1$) is the complex number. $\hat{F}(\omega)$ is necessarily complex and a plot of the amplitude of this function against frequency will give the frequency content of the time signal. As an example, consider a rectangular time signal of pulse width d. Mathematically, this function can be represented as

$$\begin{aligned} F(t) &= F_0 \qquad -d/2 \le t \le d/2 \\ &= 0 \qquad \text{otherwise}\,. \end{aligned} \tag{1.2}$$

This time signal is symmetrical about the origin. If this expression is substituted in Equation (1.1), we get

$$\hat{F}(\omega) = F_0 d \left\{ \frac{\sin(\omega d/2)}{\omega d/2} \right\}. \tag{1.3}$$

The CFT for this function is real only and symmetric about $\omega = 0$. The term inside the curly brace is called the *sinc* function. Also, the value of the CFT at $\omega = 0$ is equal to the area under the time signal.

Now the pulse is allowed to propagate in the time domain by an amount t_0 seconds. Mathematically such a signal can be written as

$$\begin{aligned} F(t) &= F_0 \qquad t_0 \le t \le t_0 + d \\ &= 0 \qquad \text{otherwise.} \end{aligned} \tag{1.4}$$

Substituting the above function in Equation (1.1) and integrating, we get

$$\hat{F}(\omega) = F_0 d \left\{ \frac{\sin(\omega d/2)}{\omega d/2} \right\} e^{-j\omega(t_0 + d/2)}\,. \tag{1.5}$$

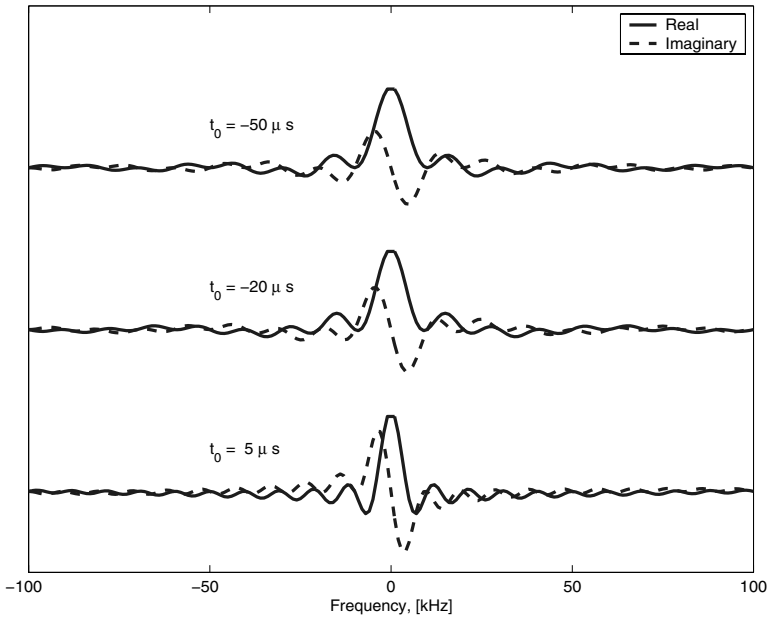

Fig. 1.1. Continuous Fourier transforms for various pulse width

The above CFT has both real and imaginary parts. These are also plotted in Figure 1.1. From Equations (1.3) and (1.5), we see that the magnitude of both these transforms are the same, however, the second transform has phase information built into it. Further, we see that the propagation of the signal in the time domain is associated with the change of phase in the frequency domain. Wave propagation problems are always associated with phase changes, which occur as the signal propagates. Based on the CFT, one can also determine the spread of the signal in both the time and frequency domain. For this, one has to look at the frequencies at which the CFT is zero. This occurs when

$$\sin\left(\frac{\omega_n d}{2}\right) = 0, \quad \text{or } \frac{\omega_n d}{2} = n\pi\,, \quad \text{or} \quad \omega_n = \frac{2n\pi}{d}\,,$$

$$\omega_2 - \omega_1 = \Delta\omega = \frac{4\pi}{d}\,.$$

That is, if the spread of the signal in the time domain is d then the spread in the frequency domain is $\Delta\omega = 4\pi/d$. Here, $\Delta\omega$ represents the frequency bandwidth. Hence, a Dirac delta function, which has infinitesimal width in the time domain, will have infinite bandwidth in the frequency domain. This aspect has greater implications in choosing the mesh sizes, when one resorts to FEM to solve the wave propagation problem. Following are some of the properties of the CFT:

- **Linearity:** Consider two time functions $F_1(t)$ and $F_2(t)$. The CFTs of these functions are given by $\hat{F_1}(\omega)$ and $\hat{F_2}(\omega)$, then the Fourier transform of the combined function is $F_1(t)+F_2(t) \Leftrightarrow \hat{F_1}(\omega)+\hat{F_2}(\omega)$. Here, the symbol $\Leftrightarrow$ is used to denote the CFT of a time signal. **Implications for wave propagation:** Here, $F_1(t)$ and $F_2(t)$ can be thought of as the incident and the reflected waves, respectively. The linearity property states that the combined transform of the incident and the reflected waves are equal to the individual transform of these obtained separately.
- **Scaling:** If a time signal is multiplied by a factor k to become $F(kt)$, the CFT of this time signal is given by $F(kt) \Leftrightarrow 1/k\hat{F}\,(\omega/k)$ **Implications for wave propagation:** Time domain compression is frequency domain expansion. This property fixes the frequency bandwidth of the given time signal.
- **Time shifting:** If a given time signal $F(t)$ is shifted by an amount t_s to become $F(t-t_s)$, the CFT of the shifted signal is given by $F(t-t_s) \Leftrightarrow \hat{F}(\omega)e^{-j\omega t}$. **Implications for wave propagation:** Propagation in the time domain is accompanied by phase changes in the frequency domain.
- **CFT is always complex:** Any given time function $F(t)$ can be split up into symmetric and anti-symmetric functions $F_s(t)$ and $F_a(t)$. Further, using the property of the linearity of the CFT, we can show that $F_s(t) = Real(\hat{F}(\omega))$ and $F_a(t) = jImag(\hat{F}(\omega))$. **Implications for wave propagation:** Since the time signals encountered in wave mechanics is neither symmetric (even) nor anti-symmetric in nature, the CFT is necessarily complex in nature. Hence, wave propagation problems are always associated with phase changes.
- **Symmetric property of the CFT:** Since the CFT of a time signal $F(t)$ is complex, it can be split into real and imaginary parts as $\hat{F}(\omega) = \hat{F_R}(\omega) + j\hat{F_R}I(\omega)$. Substituting this into the first part of Equation (1.1) and expanding the complex exponential in terms of the sine and cosine functions, we can write real and imaginary parts of the transform as

$$\hat{F}_R = \int_{-\infty}^{\infty} F(t)\cos(\omega t)dt, \quad \hat{F}_I = \int_{-\infty}^{\infty} F(t)\sin(\omega t)dt\,.$$

  The first integral is an even function and the second is an odd function, that is $\hat{F_R}(\omega) = \hat{F_R}(-\omega)$, and $\hat{F_I}(\omega) = -\hat{F_I}(-\omega)$. Now, if we consider the CFT about a point $\omega = 0$(origin), the transform on the right of the origin can be written as $\hat{F}(\omega) = \hat{F_R}(\omega) + j\hat{F_I}(\omega)$. Similarly, the transform to the left of the origin can be written as $\hat{F}(-\omega) = \hat{F_R}(-\omega)+j\hat{F_I}(-\omega) = \hat{F_R}(\omega) - j\hat{F_I}(\omega) = \hat{F}^*(\omega)$, which is the complex conjugate of the transform on the right side of the origin. The frequency point about which this happens is called the Nyquist frequency. **Implications for wave propagation:** The Nyquist frequency is an important parameter in wave propagation analysis, especially in the context of using the FFT (to be introduced later), since the analysis will be performed only up to this frequency.

- **Convolution:** This is a property relating to the product of two time signals $F_1(t)$ and $F_2(t)$. The CFT of the product of these two functions can be written as

$$\hat{F}_{12}(\omega) = \int_{-\infty}^{\infty} F_1(t)F_2(t)e^{-j\omega t}dt\,.$$

Substituting Equation (1.1) for both these functions in the above equation, we can write

$$\hat{F}_{12}(\omega) = \int_{-\infty}^{\infty} \hat{F}_1(\bar{\omega}) \int_{-\infty}^{\infty} F_2(t)e^{-j(\omega-\bar{\omega})t}dtd\bar{\omega} = \int_{-\infty}^{\infty} \hat{F}_1(\bar{\omega})\hat{F}_2(\omega-\bar{\omega})d\bar{\omega}$$

or

$$F_1(t)F_2(t) \Leftrightarrow \int_{-\infty}^{\infty} \hat{F}_1(\bar{\omega})\hat{F}_2(\omega-\bar{\omega})d\bar{\omega}\,.$$

The above form of CFT is called the convolution. Conversely, we can also write

$$\hat{F}_1(\omega)\hat{F}_2(\omega) \Leftrightarrow \int_{-\infty}^{\infty} F_1(\tau)F_2(t-\tau)d\tau\,.$$

Implication for wave propagation: The first property, using the product of two time domain signals, has its use in understanding signal processing aspects. For example, a truncated signal in the time domain is equal to the product of the original signal and the truncated signal. The second (or the converse) property is of great importance in wave propagation analysis. That is, all the responses (outputs) of a mechanical waveguide to applied loadings can be represented as the frequency domain product of the input and the system transfer function. Thus the time responses are obtained by convolving the transfer functions with the load spectrum.

1.2.2 Fourier Series

Both the forward and the inverse CFT require mathematical description of the time signal as well as their integration. In most cases, the time signals are point data acquired during experimentation. Hence, what we require is the numerical representation for the transform pair (Equation (1.1)), which is called the Discrete Fourier Transform (DFT). The DFT is introduced in detail in the next subsection. The Fourier Series (FS) is in between the CFT and the DFT, wherein the inverse transform is represented by a series, while the forward transform is still in the integral form as in CFT. That is, one still needs the mathematical description of the time signal to obtain the transforms.

The FS of a given time signal can be represented as

$$F(t) = \frac{a_0}{2} + \sum_{n=1}^{\infty} \left[a_n \cos\left(2\pi n \frac{t}{T}\right) + b_n \sin\left(2\pi n \frac{t}{T}\right) \right] \tag{1.6}$$

where $(n = 0, 1, 2, \ldots)$

$$a_n = \frac{2}{T} \int_0^T F(t) \cos\left(\frac{2\pi n t}{T}\right) dt, \quad b_n = \frac{2}{T} \int_0^T F(t) \sin\left(\frac{2\pi n t}{T}\right) dt. \tag{1.7}$$

Equation (1.6) corresponds to the inverse transform of the CFT, while Equation (1.7) corresponds to the forward transforms of the CFT. Here T is the period of the time signal, *i.e.,* the discrete representation of a continuous time signal $F(t)$, introduces periodicity of the time signal. The FS given in Equation (1.6) can also be written in terms of complex exponentials, which can give one-to-one comparison with CFT. That is, Equations (1.6) and (1.7) can be rewritten as

$$\begin{aligned} F(t) &= \tfrac{1}{2} \sum_{-\infty}^{\infty} (a_n - b_n) e^{j\omega_n t} = \sum_{-\infty}^{\infty} \hat{F}_n e^{j\omega_n t}, \quad n = 0, \pm 1, \pm 2, \ldots \\ \hat{F}_n &= \tfrac{1}{2}(a_n - b_n) = \tfrac{1}{T} \int_0^T F(t) e^{-j\omega_n t} dt, \;, \;\; \omega_n = \tfrac{2\pi n}{T}. \end{aligned} \tag{1.8}$$

Because of enforced periodicity, the signal repeats itself after every T seconds. Hence, we can define the fundamental frequency either in radians per second (ω_0) or Hz $(f_0 = \omega_0/2\pi = 1/T)$. We can now express the time signal in terms of the fundamental frequency as

$$F(t) = \sum_{-\infty}^{\infty} \hat{F}_n e^{j2\pi n f_0 t} = \sum_{-\infty}^{\infty} \hat{F}_n e^{jn\omega_0 t}. \tag{1.9}$$

From Equation (1.9), it is clear that, unlike in CFT, the transform given by FS is discrete in frequency. To understand the behavior of FS as opposed to the CFT, the same rectangular time signal used earlier is again considered here. The FS coefficients (or transform) are obtained by substituting the time signal variation in Equation (1.8). This is given by

$$\hat{F}_n = \frac{F_0}{T} \left[\frac{\sin(n\pi d/T)}{(n\pi d/T)} \right] e^{-j(t_0 + d/2)2\pi n/T}. \tag{1.10}$$

The plot of the transform amplitude obtained from the CFT and the FS are shown in Figure 1.2. The figure shows that the values of the transform obtained by FS at discrete frequencies fall exactly on the transform obtained by CFT. The figure also shows the transform values for different time periods T. We see from the figure that the larger the time period, the closer are the frequency spacings. Hence, if the period tends to infinity, the transform obtained by FS will be exactly equal to the transform obtained by CFT.

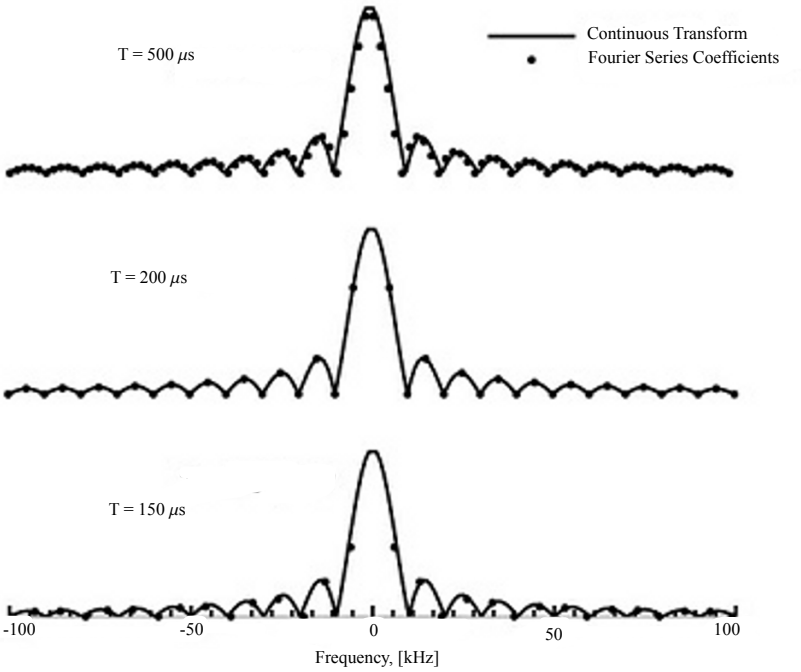

Fig. 1.2. Comparison of Fourier series with Continuous Fourier Transforms

1.2.3 Discrete Fourier Transform

The Discrete Fourier transform (DFT) is an alternative way of mathematically representing the CFT in terms of summations. Here, both the forward and inverse CFT given in Equation (1.1) are represented by summations. This will completely do away with all complex integration involved in the computation of CFT. In addition, it is not necessary to represent the time signals mathematically and the great advantage of this is that one can use the time data obtained from experiment. Numerical implementation of the DFT is done using the famous FFT algorithm.

We begin here with Equation (1.8), which is the FS representation of the time signal. The main objective here is to replace the integral involved in the computation of the Fourier coefficients by summation. For this, the plot of time signal shown in Figure 1.3 is considered.

The time signal is divided into M piecewise constant rectangles, whose height is given by F_m, and the width of these rectangles is equal to $\Delta T = T/M$. We derived earlier that the continuous transform of a rectangle is a *sinc* function. By rectangular idealization of the signal, the DFT of the signal will be the summation of M *sinc* functions of pulse width ΔT and hence the second integral in Equation (1.8) can now be written as

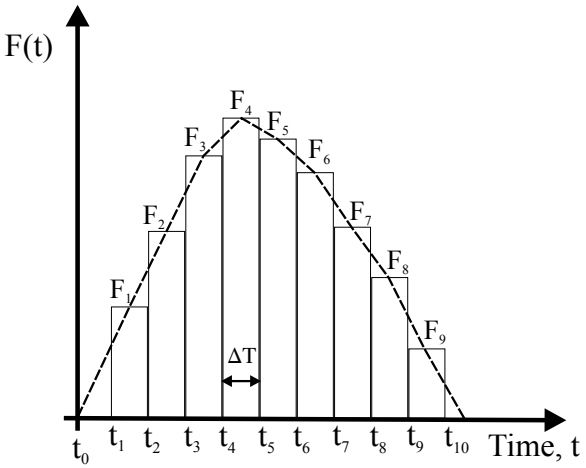

Fig. 1.3. Time signal discretization for DFT

$$\hat{F}_n = \Delta T \left[\frac{\sin(\omega_n \Delta T/2)}{(\omega_n \Delta T/2)} \right] \sum_{m=0}^{M} F_m e^{-j\omega_n t_m} \tag{1.11}$$

Let us now look at the *sinc* function in Equation (1.11). Its value depends on the width of the rectangle ΔT. That is, as the width of the rectangle becomes smaller, the term inside the bracket of Equation (1.11) tends to unity value. This will happen for all values of $n < M$. It can easily be shown that for values of $n \geq M$, the values of the transform is approximately equal to zero. Hence, the DFT transform pairs can now be written as

$$\begin{aligned} F_m &= F(t_m) = \tfrac{1}{T} \sum_{n=0}^{N-1} \hat{F}_m e^{j\omega_n t_m} = \tfrac{1}{T} \sum_{n=0}^{N-1} \hat{F}_m e^{j2\pi nm/N} \\ \hat{F}_n &= \hat{F}(\omega_n) = \Delta T \sum_{n=0}^{N-1} F_m e^{-j\omega_n t_m} = \Delta T \sum_{n=0}^{N-1} F_m e^{-j2\pi nm/N} \end{aligned} \tag{1.12}$$

Here, both m and n range from 0 to N−1.

The periodicity of the time signal is necessary for DFT as we begin from the FS representation of the time signal. Now, we can probe a little further to see whether the signal has any periodicity in the frequency domain. For this, we can look at the summation term in Equation (1.11). Hypothetically, let us assume $n > M$. Hence, we can write $n = M + \bar{n}$. Then, the exponential term in the equation becomes

$$e^{-j\omega_n t_m} = e^{-jn\omega_0 t_m} = e^{-jM\omega_0 t_m} e^{-j\bar{n}\omega_0 t_m} = e^{-j2\pi m} e^{-j\bar{n}\omega_0 t_m} = e^{-j\bar{n}\omega_0 t_m} .$$

Hence, the summation term in Equation (1.11) becomes

$$\Delta T \sum_{m=0}^{M-1} F_m e^{-j\bar{n}\omega_0 t_m} .$$

This term shows that the above summation has the same value when $n = \bar{n}$. For example, if $M = 6$, then the value of the summation for $n = 9, 11, 17$ is same as the value for $n = 3$, 5, and 11 respectively. Two aspects are very clear from this analysis. First, $n > M$ is not important, and second, there is forced periodicity in both the time and frequency domain in using DFT. This periodicity occurs about a frequency where the transform goes to zero. This frequency can be obtained if one looks at the *sinc* function given in Equation (1.11). That is, the argument of the *sinc* function is given by

$$\frac{\omega_n \Delta T}{2} = \pi n \Delta T = \frac{\pi n}{M}$$

where, we have used the relation $\Delta T = T/M$.

Here, we see that the *sinc* function goes to zero when $n = M$. It is at this value of n that the periodicity is enforced and the frequency corresponding to this value is called the *Nyquist* frequency. As mentioned earlier, this happens due to the time signal being real only and the transform beyond the Nyquist frequency is the complex conjugate of the transform before this frequency. Thus, N real points are transformed to $N/2$ complex points. Knowing the sampling rate ΔT, we can compute the Nyquist frequency from the expression

$$f_{Nyquist} = \frac{1}{2\Delta T} . \tag{1.13}$$

There are a number of issues in the numerical implementation of the DFT, which are not discussed here. However, the reader is encouraged to consult Reference [9] to get more information on these aspects. In all the wave propagation examples given in this textbook, the FFT is used to transform the signal back and forth from the time and frequency domains and vice versa. In order to see the difference in different transform representation, the same rectangular pulse is again used here. There are two parameters on which the accuracy of the transforms obtained by the DFT depends, namely the sampling rate ΔT and the time window parameter N. Figures 1.4 and 1.5 show the transform obtained for various sampling rates ΔT and time window parameter N. From the figures, we can clearly see the periodicity about the Nyquist frequency. For a given time window N, the figure shows that the frequency spacing increases with decreasing sampling rate. Also, the Nyquist frequency shifts to a higher value. Next, for a given sampling rate ΔT, the time window is varied through the parameter N. In this case, the Nyquist frequency does not change. However, for larger N, the frequency spacing becomes smaller and hence we get denser frequency distribution.

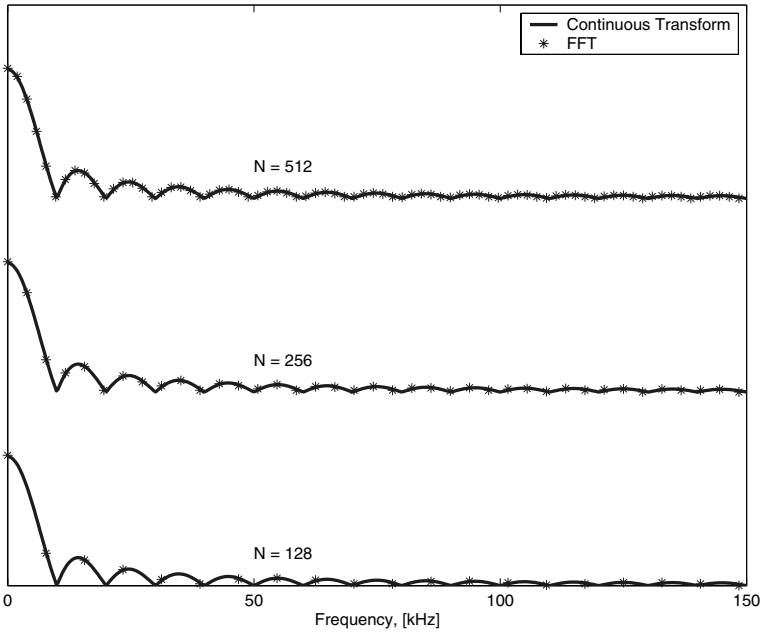

Fig. 1.4. Comparison of FFT and continuous transform for a sampling rate $\Delta T = 1\mu s$

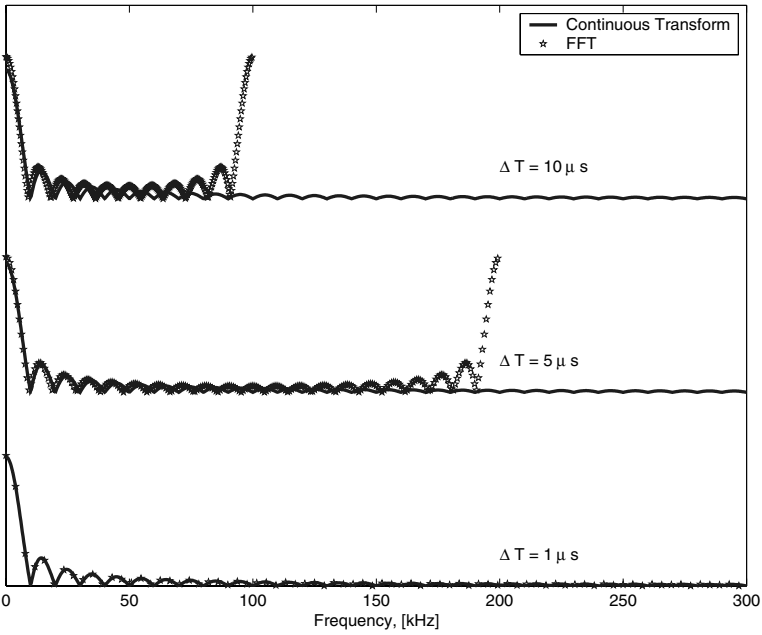

Fig. 1.5. Comparison of FFT and continuous transform for different sampling rates

1.3 Spectral Analysis

SFEM uses spectral analysis to obtain the local wave behavior for different waveguides and hence the wave characteristics, namely the *Spectrum* and the *Dispersion* relation. These local characteristics are synthesized to get the global wave behavior. Spectral analysis uses DFT to represent a field variable (say displacement) as a finite series involving a set of coefficients, which requires to be determined based on the boundary conditions of the problem. Spectral analysis enables the determination of two important wave parameters, namely the *wavenumbers* and the *group speeds*. These parameters are not only required for spectral element formulation, but also to understand the wave mechanics in a given waveguide. These parameters enable us to know whether the wave mode is a propagating mode or a damping mode or a combination of these two (propagation as well as wave amplitude attenuation). If the wave is propagating, the wavenumber expression will let us know whether it is *non-dispersive* (that is, the wave retains its shape as it propagates) or *dispersive* (when the wave changes its shape as it propagates). In this section, for the sake of completeness, we give a brief outline of spectral analysis for second- and fourth-order systems. More details can be found in Reference [9].

The starting point of spectral analysis is the governing differential equation. Consider a second-order partial differential equation given by

$$a\frac{\partial^2 u}{\partial x^2} + b\frac{\partial u}{\partial x} = c\frac{\partial^2 u}{\partial t^2} \tag{1.14}$$

where, *a, b, c* are known constants and $u(x,t)$ is the field variable, x is the spatial variable and t is the temporal variable. We first approximate or transform the above partial differential equation (PDE) to the frequency domain using DFT, which is given by

$$u(x,t) = \sum_{n=0}^{N-1} \hat{u}_n(x,\omega_n)e^{j\omega_n t} \tag{1.15}$$

where, ω_n is the circular frequency and N is the total number of frequency points used in the approximation. Here $\hat{u}$ is the frequency-dependent Fourier transform of the field variable. Substituting Equation (1.15) into Equation (1.14), we get

$$a\frac{d^2\hat{u}_n}{dx^2} + b\frac{d\hat{u}_n}{dx} + c\omega_n^2\hat{u}_n = 0\,, n = 0,\ldots,N-1\,. \tag{1.16}$$

From the above equation, we see that a partial differential equation is reduced to a set of ordinary differential equation (ODE) with the time variation removed and instead, the frequency introduced as a parameter. The summation is omitted in the above equation for brevity. Equation (1.16) is a constant coefficient ODE, which has a solution of the type $\hat{u}_n(x,\omega) = A_n e^{jkx}$, where A_n

is some unknown constant and k is called the *wavenumber*. Substituting the above solution in Equation (1.16), we get the following characteristic equation to determine k

$$(k^2 - \frac{bj}{a}k + \frac{c\omega_n^2}{a})A_n = 0\,. \tag{1.17}$$

The above equation is quadratic in k and has two roots corresponding to the two modes of wave propagation. These two modes correspond to the incident and reflected waves. If the wavenumbers are real, then the wave modes are called *propagating modes*. On the other hand, if the wavenumbers are complex, then the wave modes damp out the responses and hence they are called *evanescent modes*. These are given by

$$k_{1,2} = \frac{bj}{2a} \pm \sqrt{\frac{-b^2}{4a^2} + \frac{c\omega_n^2}{a}}\,. \tag{1.18}$$

Equation (1.18) is the generalized expression for the determination of the wavenumbers. Different wave behavior is possible depending upon the values of $a, b,$ and c. The behavior also depends on the numerical value of the radical $\sqrt{c\omega_n^2/a - b^2/4a^2}$. Let us consider a simple case of $b = 0$. The two wavenumbers are given by

$$k_1 = \omega_n \frac{c}{a}, \qquad k_2 = -\omega_n \frac{c}{a}\,. \tag{1.19}$$

From the above expression, we find that the wavenumbers are real and hence they are propagating modes. The wavenumbers are linear functions of frequency ω. At this point, we would like to introduce two important wave parameters that will determine the wave characteristics, namely the ***phase speed*** C_p and ***group Speed*** C_g. They are defined as

$$C_p = \frac{\omega_n}{Real(k)}, \qquad C_g = \frac{d\omega_n}{dk}\,. \tag{1.20}$$

For the wavenumbers given in Equation (1.19), the speeds are given by

$$C_p = C_g = \frac{a}{c}\,. \tag{1.21}$$

We find that both group and phase speed are constant and equal. Hence, when wavenumbers vary linearly with frequency ω and phase speed and group speed are constant and equal, then the wave, as it propagates, retains its shape. Such waves are called ***Non-dispersive waves***. Longitudinal waves in elementary rods are of this type. If the wavenumber varies in a non-linear manner with respect to the frequency, the phase and group speeds will not be constant but will be functions of frequency ω. That is, each frequency component travels with different speed and as a result, the wave changes its shape as it propagates. Such waves are called ***dispersive waves***.

Next, let us again consider Equation (1.18) with all the constants nonzero. The wavenumber no longer varies linearly with the frequency. Hence, one can expect dispersive behavior of the waves and the level of dispersion will depend upon the numerical value of the radical. We will investigate this aspect in a little more detail. There can be the following three situations:

1. $b^2/4a^2 > c\omega_n^2/a$
2. $b^2/4a^2 < c\omega_n^2/a$ and
3. $b^2/4a^2 = c\omega_n^2/a$

Let us now consider Case 1. When $(b^2)/(4a^2) > (c\omega_n^2)/(a)$, then the radical will be a complex number and hence all the wavenumbers will be complex, implying that the wave modes are not propagating and they would damp out rapidly. For Case 2, where $(b^2)/(4a^2) < (c\omega_n^2)/(a)$, the value of the radical will be positive and real and hence the wavenumber will have both real and imaginary parts, *i.e.*,, takes the form $k = p + jq$. Hence, waves having this feature will attenuate as they propagate. The phase and group speeds for this case are given by

$$C_p = \frac{\omega_n}{k} = \frac{\omega_n}{\sqrt{c\omega_n^2/a - b^2/4a^2}}\,, \tag{1.22}$$

$$C_g = \frac{d\omega_n}{dk} = \frac{a\sqrt{c\omega_n^2/a - b^2/4a^2}}{c\omega_n}\,. \tag{1.23}$$

It is quite obvious that these are not the same and hence the waves could be dispersive in nature. One can get back the non-dispersive solution by substituting $b = 0$ in Equation (1.23). Now, let us see Case 3 where the value of the radical will be zero and hence the wavenumber is purely imaginary indicating that the wave mode is a damping mode. The interesting point here is to find the frequency of transition at which the propagating mode becomes evanescent or a damping mode. This can be obtained by equating the radical to zero. Thus the transition frequency ω_t is given by

$$\omega_t = \frac{b}{2\sqrt{ac}}\,.$$

Once the wavenumbers are determined, the solution to the governing wave equation (Equation (1.16)) in the frequency domain can be written as (for $b = 0$)

$$\hat{u_n}(x, \omega_n) = A_n e^{-jk_n x} + B_n e^{jk_n x}, \qquad k_n = \omega_n \sqrt{\frac{c}{a}}\,. \tag{1.24}$$

In the above equation A_n represents the incident wave coefficient while B_n represents the reflected wave coefficient. Solution of the governing equation in the frequency domain is the starting point for the SFEM.

It is clearly seen how the values of the constants in the governing differential equation play an important part in dictating the type of wave propagation

in a given medium. Now let us consider a fourth-order system and study the wave behavior in such systems. Consider the following governing partial differential equation of motion:

$$A\frac{\partial^4 w}{\partial x^4} + Bw + C\frac{\partial^2 w}{\partial t^2} = 0\,. \tag{1.25}$$

Here w is the field variable, and A, B, C are known constants. The above equation is similar to the equation of motion of a beam on elastic foundations. Let us now assume the spectral form of solution to the field variable, which is given by

$$w(x,t) = \sum_{n=0}^{N} \hat{w_n}(x,\omega_n)e^{j\omega_n t}\,. \tag{1.26}$$

Using Equation(1.26) in Equation(1.25), the PDE is transformed to an ODE as

$$A\frac{d^4\hat{w_n}}{dx^4} - (C\omega_n^2 - B)\hat{w_n} = 0\,. \tag{1.27}$$

Again, this equation is an ODE with constant coefficients and it will have solutions of the form $\hat{w}_n = P_n e^{jkx}$. Using this solution in Equation (1.27), we get the characteristic equation for the solution of the wavenumber, which is given by

$$k^4 - \beta^4 = 0, \qquad \beta^4 = \left(\frac{C}{A}\omega_n^2 - \frac{B}{A}\right)\,. \tag{1.28}$$

The above is a fourth-order equation corresponding to four wave modes, two of which are for the incident wave and the other two are for the reflected wave. Also, the type of wave is dependent upon the numerical value of $C\omega_n^2/A - B/A$. Let us now assume that $C\omega_n^2/A > B/A$. For this case, the solution of Equation (1.28) will give the following wavenumbers:

$$k_1 = \beta, \qquad k_2 = -\beta, \qquad k_3 = j\beta, \qquad k_4 = -j\beta \tag{1.29}$$

In the above equation, k_1 and k_2 are the propagating modes while k_3 and k_4 are the damping or evanescent modes. From the above equations, we find that the wavenumbers are non-linear functions of the frequency and hence the waves are expected to be highly dispersive in nature. Also, using the above expression, we can find the phase and group speeds for the propagating modes using Equations (1.20) and (1.21), respectively.

Next, consider the case when $C\omega_n^2/A < B/A$. For this case, the characteristic equation and hence the wavenumbers are given by

$$k^4 + \beta^4 = 0 \tag{1.30}$$

$$k_1 = \left[\frac{1}{\sqrt{2}} + j\frac{1}{\sqrt{2}}\right]\beta, \qquad k_2 = -\left[\frac{1}{\sqrt{2}} + j\frac{1}{\sqrt{2}}\right]\beta\,, \tag{1.31}$$

$$k_3 = \left[-\frac{1}{\sqrt{2}} + j\frac{1}{\sqrt{2}}\right]\beta, \qquad k_4 = -\left[-\frac{1}{\sqrt{2}} + j\frac{1}{\sqrt{2}}\right]\beta\,. \tag{1.32}$$

From the above equation, we see that the change of sign of $C\omega_n^2/A - B/A$ has caused completely changed wave behavior. We find that all the wavenumbers have both real and the imaginary parts and hence all the modes are propagating as well as attenuating. Also the initial evanescent mode, after a certain frequency, becomes a propagating mode, giving a completely different wave behavior. The frequency at which this transition takes place is called the ***cut-off frequency***. The expression for the cut-off frequency can be obtained if we equate $C\omega_n^2/A - B/A$ to zero, giving $\omega_{cut-off} = \sqrt{B/C}$. We can see that when $B = 0$, the cut-off frequency vanishes and the wave behavior is similar to the first case, *i.e.,* it will have two propagating and two damping modes. In all cases, the waves will be highly dispersive in nature.

The solution of the fourth-order governing equation in the frequency domain (Equation (1.27)) can be written as

$$\hat{w_n}(x, \omega_n) = A_n e^{-j\beta x} + B_n e^{-\beta x} + C_n e^{j\beta x} + D e^{\beta x} \,. \tag{1.33}$$

As in the previous case, A_n and B_n are the incident wave coefficients and C_n and D_n are the reflected wave coefficients. These can be determined based on the boundary conditions of the problem.

From the above discussion, we see that spectral analysis gives us a deep insight into the wave mechanics of a system defined by its governing differential equation. The direct output of spectral analysis are the ***spectrum relation***, which is a plot of the wavenumber variation with frequency, and ***dispersion relations***, which is a plot of the phase speed against frequency. These relations are absolutely necessary for the spectral finite element formulation. The spectral analysis procedure outlined here will be used extensively throughout the textbook for characterization of waves in anisotropic and inhomogeneous media.

1.4 What is the Spectral Element Method?

The spectral element method is essentially a finite element method formulated in the frequency domain. However, their methods of implementation are quite different. The basic differences between SFEM and FEM are highlighted in the following paragraph.

FEM is based on an assumed polynomial for displacements. These assumed displacement polynomials are forced to satisfy the weak form of the governing differential equation, which would yield two different matrices, namely the stiffness matrix and the mass matrix. These elemental matrices are assembled to obtain global stiffness and mass matrices. The assembly process ensures equilibrium of forces between adjacent elements. This procedure will give the discretized form of the governing equation, given by $[M]\{\ddot{u}\} + [C]\{\dot{u}\} + [K]\{u\} = \{F(t)\}$, where $[M]$ and $[K]$ are the global mass and stiffness matrix and $\{\ddot{u}\}$, $\{\dot{u}\}$ and $\{u\}$ are the acceleration, velocity and

displacement vector, respectively. Matrix $[C]$ is the damping matrix, which is normally obtained from the stiffness and mass matrix as $[C] = \alpha[K] + \beta[M]$, where α and β are the stiffness and the mass proportional factors, and the damping scheme is called the proportional damping scheme. As mentioned earlier, the mode superposition method of solution cannot be used for wave propagation analysis. The preferred solution method is the time marching scheme, where two different strategies are available, namely the ***explicit methods*** and the ***implicit methods***. For wave propagation and highly transient dynamics problems, explicit methods are normally preferred. In the time marching scheme, the solution process takes place over a small time step ΔT. The solution of the dynamic equations will give displacement, velocity and acceleration histories. The solution process is repeated for N time steps until the total time $T = N\Delta T$ is reached. The solution time is directly proportional to the number of degrees of freedom in the model, which is usually very high for wave propagation problems.

SFEM on the other hand uses in most cases the exact solution to the wave equation as its interpolating function. For example, for second- and fourth-order governing equations, these were given in the last section as Equations (1.24) and (1.33). One can see, unlike the polynomials in the case of FEM, here, we need to deal with complex exponentials as the interpolating functions. The exact solution will have wave coefficients corresponding to the incident and reflected wave components. If one wants to model an infinite domain, then the reflected components can be dropped from the interpolating functions. This gives what is called the *throw-off elements*. This is a great advantage that SFEM has over FEM. Using the interpolating functions for the displacement, the dynamic element stiffness matrix is formulated. One can formulate this stiffness matrix as in the case of conventional FEM, using the weak form of the governing equations. This approach will involve complex integration. Alternatively, one can formulate the dynamic stiffness matrix using stress or force resultant expressions. This method is normally suitable since it does not involve complex integration. The basic steps involved in the analysis using SFEM are as follows. First, the given forcing function is transformed to the frequency domain using the forward FFT. In doing so, we need to choose the time sampling rate and number of FFT points to decide on the analysis time window. Care should be taken to see that the chosen window is good enough to avoid what are called *wraparound* problems [9]. The FFT output will yield the frequency, the real and imaginary part of the forcing function, which are stored separately. Over a big frequency loop, the element dynamic stiffness matrix is generated, assembled and solved as in the case of conventional FEM. However, these operations have to be performed at each sampled frequency. This does not pose a major computational hurdle since the problem sizes are many orders smaller than conventional FEM. The solution process is first performed for a unit impulse, which directly yields the *Frequency Response Function*(FRF). The FRF is then convolved with the load to get the

required output in the frequency domain. This output is then transformed to the time domain using the inverse FFT.

There are many advantages that SFEM gives over conventional FEM. The SFEM can give results in both the time and frequency domain in a single analysis. Obtaining the FRF is a big advantage of the SFEM. This enables one to solve inverse problems such as the force or the system identification problems in a straightforward manner. Since many damping properties are frequency dependent, damping in structures can be treated more realistically. Visco-elastic analysis can be performed without much alteration of the spectral element code. Since the approach gives the FRF first, responses to different loading can be obtained using a single analysis. In summary, SFEM is a method in which the FFT algorithm is an essential part and gives problem sizes many orders smaller than conventional FEM. SFEM for isotropic waveguides are already dealt with in Reference [9]. In this book, we address the formulation of spectral elements for anisotropic and inhomogeneous waveguides and also show how SFEM can be used to study wave scattering in the presence of flaws and hence show how it can be applied to SHM problems. As mentioned before, due to the exact nature of the dynamic stiffness matrix, SFEM can be directly used in control-related applications without resorting to model order reductions.

1.5 Outline and Scope of Book

The entire book is organized into 11 chapters. In Chapter 2, we first present a brief introduction to laminated composite and inhomogeneous structures. In particular, the homogenization of the constitutive model for composites and functionally graded material structures are addressed. We also introduce smart materials, their integration with composites and their constitutive model. In Chapter 3, all the necessary tools required for spectral element formulation are given. In this chapter we outline the general spectral element formulation and the available approaches to obtain the wavenumber and the wave amplitudes. Also a brief outline of the spectral element formulation for isotropic waveguides is given. In Chapter 4, element formulation for 1-D homogeneous, laminated composite structures is given. Both elementary and higher order spectral elements are formulated. This chapter describes how special damping schemes can be handled within the spectral element environment. A novel spectral element to model a composite tube is also presented.

Chapter 5 addresses wave propagation in 1-D inhomogeneous waveguides. As in Chapter 4, spectral element formulations for both elementary and higher order waveguides are provided. Inhomogeneity in both the depth-wise and length-wise directions is considered. A number of numerical examples are presented to bring out the essential features of wave propagation. In Chapter 6, wave propagation in homogeneous 2-D laminated composite structures is addressed. This chapter shows how to use SFEM to study Lamb wave propaga-

tion in laminated composite. In Chapter 7, wave propagation in 2-D inhomogeneous structures is discussed along with the development of a series of spectral elements to handle mechanical, thermal and coupled thermo-mechanical loading. A number of numerical examples are also provided to highlight the effect of inhomogeneity on wave behavior.

The last four chapters deal with the applications of the developed spectral finite elements. In Chapter 8, SFEM is used to solve inverse problems such as force history identification and material parameters estimation. Chapter 9 and 10 deal with the applications of SFEM to structural health monitoring. In Chapter 9, various spectral element based damage models for different failure modes, such as single and the multiple delaminations, fiber breakage, surface breaking cracks and degraded regions, are presented. Examples are provided to highlight the nature of wave scattering across a crack front. In Chapter 10, various damage diagnostic techniques that blend with SFEM are presented. The final chapter deals with the application of SFEM to active control of waves. A new numerical model for control called the Active Spectral Element Model (ASEM) is introduced for this purpose. A case study showing how the model can be used to control cabin noise in a helicopter is discussed.

2

Introduction to the Theory of Anisotropic and Inhomogeneous Materials

In this chapter, a very brief introduction to composite materials, the evaluation of material properties and their homogenization techniques are given. Also, a brief introduction is given to smart composites and the basic constitutive models for composites, where a few standard smart materials can be embedded. Towards the end of the chapter a brief description of how to obtain constitutive models for inhomogeneous materials, such as functionally graded materials, is presented.

2.1 Introduction to Composite Materials

As the name suggests, composite materials are obtained by combining two or more materials at the macroscale to obtain a useful structural material. Although these materials at the microscopic scale can be inhomogeneous, they can be considered homogeneous at the macroscopic level. These materials possess the qualities of each of the constituents and the choice of constituents depends on the application for which these materials are required. These materials are normally preferred due to their light weight, high strength, and high corrosion resistance properties. The two normal constituents of a composite material are the *Fiber* and the *Matrix*. Depending upon how they are bound together, different types of composite materials can be obtained. Owing to the difference in the constitutive behavior of these two constituent materials, the constitutive model of the compound material is normally anisotropic. Composites can be classified into three different categories, namely ***fibrous composites***, ***particulate composites*** and ***laminated composites***.

The fibrous composites consist of fibers or whiskers dispersed in a matrix to form a structural element. The fibers are normally expected to take all the load and all the fibers in the structural element are bound together by the matrix. In addition to binding, the matrix helps in stress transfer and also to protect the fibers from harmful environmental effects. The matrix material normally has low stiffness, density and strength compared to the fibers. Some

of the commonly used fibers are made of carbon, graphite, boron, E-glass *etc.* while the most commonly used matrix material is epoxy, which is essentially a polymer material.

The particulate composite consists of particles of one or more materials suspended in a matrix of a different material. The particles and the matrix can be metallic or non-metallic. Concrete is a very good example of a particulate composite wherein the sand and the granite are bound by a matrix material (cement). Here the particles are non-metallic. Use of mica in glass is yet another example of a particulate composite, which is used extensively as an insulating material in electrical applications. For spacecraft, rocket propellents are used extensively as a fuel. These propellents consist of aluminum powder and perchlorate oxidizers mixed in an organic binder. The normal binder material is polyurethene. This is an example of metallic particles in a non-metallic composite.

For structural applications, the above two forms of composite are seldom used; here the common type is the laminated composite. Hence an entire section is devoted to this form of composite.

2.2 Theory of Laminated Composites

Laminated composites have found extensive use as aircraft structural materials due to their high strength to weight and stiffness to weight ratios. Their popularity stems from the fact that they are extremely light-weight and the laminate construction enables the designer to tailor the strength of the structure in any required direction depending upon the loading directions to which the structure is subjected. In addition to aircraft structures, they have found their way into many automobile and building structures. Apart from having better strength, stiffness and lower weight properties, they have better corrosion resistance, thermal and acoustic insulation properties than metallic structures.

The laminated composite structure consists of many laminas (plies) stacked together to form the structure. The number of plies or laminas depends on the strength that the structure is required to sustain. Each lamina contains fibers oriented in the direction where the maximum strength is required. These fibers are bound together by a matrix material. The laminated composite structure derives its strength from the fibers. The commonly used fibers are made of carbon, glass, Kevler and boron. The most commonly used matrix material is epoxy resin. These materials are orthotropic at the lamina level while at the laminate level, they exhibit highly anisotropic properties. The anisotropic behavior results in stiffness coupling, such as bending axial shear coupling in beams and plates, bending axial torsion coupling in aircraft thin-walled structures, *etc.* These coupling effects make the analysis of laminated composite structures very complex.

2.2.1 Micromechanical Analysis of a Lamina

A lamina is a basic element of a laminated composite structure, constructed from fibers that are bound together by the matrix resin. The strength of the lamina, and hence the laminate, depends on the type of fiber, their orientation and also the volume fraction of fiber in relation to the overall volume of lamina. Since the lamina is a heterogeneous mixture of fibers dispersed in a matrix, determination of the material properties of the lamina, which is assumed to be orthotropic in character, is a very involved process. The method used in the determination of lamina material properties is micromechanical analysis. According to Jones [11], micromechanics is the study of composite material behavior, wherein the interaction of the constituent materials is examined in detail as part of the definition of the behavior of the heterogeneous composite material.

Hence, the objective of micromechanics is to determine the elastic moduli of a composite material in terms of the elastic moduli of the constituent materials, namely the fibers and the matrix. Thus, the property of a lamina can be expressed as

$$Q_{ij} = Q_{ij}(E_f, E_m, \nu_f, \nu_m, V_f, V_m)\,, \tag{2.1}$$

where E, ν and V are the elastic moduli, Poisson's ratio and the volume fraction respectively, and f and m subscripts denote the fiber and the matrix, respectively. The volume fraction of fiber is determined from the expression: V_f = (volume of fiber)/(total volume of lamina) and $V_m = 1 - V_f$.

There are two basic approaches for the determination of material properties of the lamina. They can be grouped under the following heads: (1) the strength of materials approach and (2) the theory of elasticity approach. The first method gives an experimental way of determining the elastic moduli. The second method gives upper and lower bounds on the elastic moduli and not their actual values. In fact, there are many papers available in the literature that deal with the theory of elasticity approach to determine the elastic moduli of a composite. In this section, only the first method is presented. There are many classic textbooks on composites such as Jones [11] and Tsai [12] that cover this in detail.

2.2.2 Strength of Materials Approach to Determination of Elastic Moduli

The material properties of a lamina are determined by making some assumptions concerning the behavior of its constituents. The fundamental assumption is that the fiber is the strong constituent of a composite lamina and hence is the main load bearing member, and the matrix is weak and its main function is to protect the fibers from severe environmental effects. Also, the strains in the matrix and the fiber are assumed to be the same. Hence, a plane section before the application of bending stress remains plane after bending. In the

present analysis, we consider a unidirectional, orthotropic composite lamina to derive expressions for the elastic moduli. In doing so, we limit our analysis to a small volume element, small enough to show the microscopic structural details, yet large enough to represent the overall behavior of the composite lamina. Such a volume is called the representative volume (RV). A simple RV is a fiber surrounded by matrix as shown in Figure 2.1.

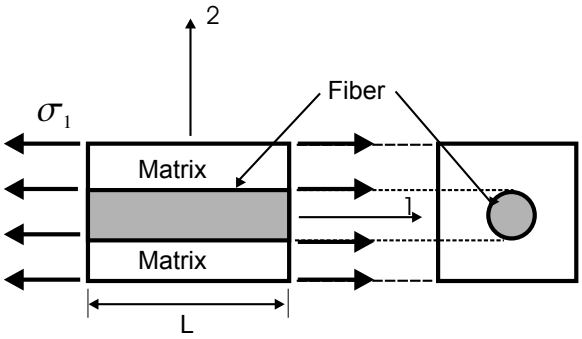

Fig. 2.1. RV for the determination of longitudinal material properties

First, the procedure for determining the elastic modulus E_1 is given. In Figure 2.1, the strain in the 1-direction is given by $\epsilon_1 = \Delta L/L$, where this strain is felt both by the matrix and the fiber, according to our basic assumption. The corresponding stresses in the fiber and the matrix are given by

$$\sigma_f = E_f \epsilon_1 \,, \quad \sigma_m = E_m \epsilon_1 \,. \tag{2.2}$$

Here E_f and E_m are the elastic modulus of the fiber and the matrix respectively. The cross-sectional area A of the RV is made up of the area of the fiber A_f and the area of the matrix A_m. If the total stress acting on the cross-section of the RV is σ_1, then the total load acting on the cross-section is

$$P = \sigma_1 A = E_1 \epsilon_1 A = \sigma_f A_f + \sigma_m A_m \,. \tag{2.3}$$

From the above expression, we can write the elastic moduli in the 1-direction as

$$E_1 = E_f \frac{A_f}{A} + E_m \frac{A_m}{A} \,. \tag{2.4}$$

The volume fraction of the fiber and the matrix can be expressed in terms of areas of the fiber and the matrix as

$$V_f = A_f/A \,, \quad V_m = A_m/A \,. \tag{2.5}$$

Using Equation (2.5) in Equation (2.4), we can write the modulus in the 1-direction as

$$E_1 = E_f V_f + E_m V_m \,. \tag{2.6}$$

Equation 2.6 is the well known rule of mixtures for obtaining the equivalent modulus of the lamina in the direction of the fibers.

The equivalent modulus E_2 of the lamina is determined by subjecting the RV to a stress σ_2 perpendicular to the direction of the fiber as shown in Figure 2.2. This stress is assumed to be the same in both the matrix and the fiber.

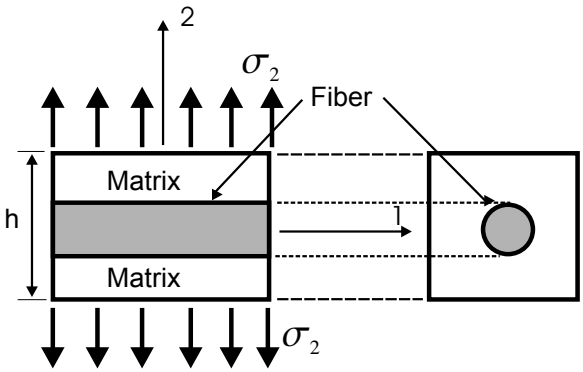

Fig. 2.2. RV for determination of transverse material property

The strains in the fiber and matrix due to this stress are given by

$$\epsilon_f = \sigma_2 / E_f \,, \quad \epsilon_m = \sigma_2 / E_m \,. \tag{2.7}$$

If h is the depth of the RV (see Figure 2.2), then this total strain ϵ_2 is distributed as a function of the volume fraction as

$$\epsilon_2 h = (V_f \epsilon_f + V_m \epsilon_m) h \,. \tag{2.8}$$

Substituting Equation (2.7) in Equation (2.8), we get

$$\epsilon_2 = V_f \frac{\sigma_2}{E_f} + V_m \frac{\sigma_2}{E_m} \,. \tag{2.9}$$

However, we have

$$\sigma_2 = E_2 \epsilon_2 = E_2 \left(V_f \frac{\sigma_2}{E_f} + V_m \frac{\sigma_2}{E_m} \right) \,. \tag{2.10}$$

From the above relation, the equivalent modulus in the transverse direction is given by

$$E_2 = \frac{E_f E_m}{V_f E_m + V_m E_f} \,. \tag{2.11}$$

The major Poissons ratio ν_{12} is determined as follows. If the RV of width W and depth h is loaded in the direction of the fiber, then both strains ϵ_1 and ϵ_2 will be induced in the 1 and 2 directions. The total transverse deformation δ_h is the sum of the transverse deformation in the matrix and the fiber and is given by

$$\delta_h = \delta_{hf} + \delta_{hm} \,. \tag{2.12}$$

The major Poissons ratio is also defined as the ratio of the transverse strain to the longitudinal strain and expressed as

$$\nu_{12} = -\epsilon_2/\epsilon_1 \,. \tag{2.13}$$

The total transverse deformation can also be expressed in terms of the depth h as

$$\delta_h = -h\epsilon_2 = h\nu_{12}\epsilon_1 \,. \tag{2.14}$$

Following the procedure adopted for the determination of the transverse modulus, the transverse displacement in the matrix and the fiber can be expressed in terms of its respective volume fraction and the Poissons ratio as

$$\delta_{hf} = hV_f\nu_f\epsilon_1 \,, \delta_{hm} = hV_m\nu_m\epsilon_1 \,. \tag{2.15}$$

Using Equations (2.14) and (2.15) in Equation (2.12), we can write the expression for the major Poissons ratio as

$$\nu_{12} = \nu_f V_f + \nu_m V_m \,. \tag{2.16}$$

By adopting a similar procedure to that used in the determination of the transverse modulus, we can write the shear modulus in terms of the constituent properties as

$$G_{12} = \frac{G_f G_m}{V_f G_m + V_m G_f} \,. \tag{2.17}$$

The next important property of the composite that requires determination is the density. For this, we begin with the total mass of the lamina, which is the sum of the masses of the fiber and the matrix. That is, the total mass M can be expressed in terms of the densities (ρ_f and ρ_m) and the volume fractions (V_f and V_m) as

$$M = M_f + M_m = \rho_f V_f + \rho_m V_m \,. \tag{2.18}$$

The density of the composite can then be expressed as

$$\rho = \frac{M}{V} = \frac{\rho_f V_f + \rho_m V_m}{V} \,. \tag{2.19}$$

Once the properties of the lamina are determined, then one can proceed to a macromechanical analysis of the lamina to characterize the constitutive model of the laminate.

2.2.3 Stress–Strain Relations for a Lamina

Determination of the overall constitutive model for a lamina of a laminated composite constitutes the macromechanical study of composites. Unlike the micromechanical study, where the composite is treated as a heterogeneous mixture, here the composite is presumed to be homogeneous and the effects of the constituent materials are accounted for only as an averaged apparent property of the composite. The following are the basic assumptions used in deriving the constitutive relations:

- The composite material is assumed to behave in a linear (elastic) manner. That is, Hookes law and the principle of superposition are valid.
- At the lamina level, the composite material is assumed to be homogeneous and orthotropic. Hence the material has two planes of symmetry, one coinciding with the fiber direction and the other perpendicular to the fiber direction.
- The state of the stress in a lamina is predominantly plane stress

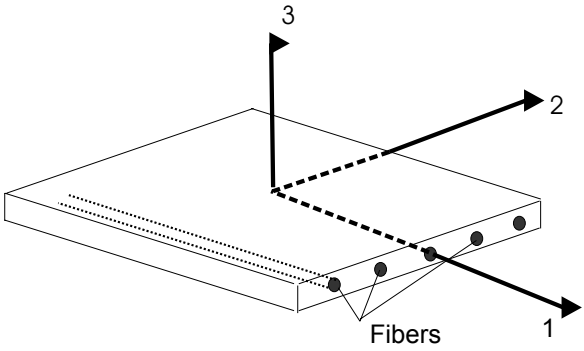

Fig. 2.3. Principal axes of a lamina

Consider the lamina shown in Figure 2.3 with its principal axes, which we denote the 1-2-3 axes. That is, axis 1 corresponds to the direction of the fiber and axis 2 is the axis transverse to the fiber. The lamina is assumed to be in a 3-D state of stress with six stress components given by $\{\sigma_{11}, \sigma_{22}, \sigma_{33}, \tau_{23}, \tau_{13}, \tau_{12}\}$. For an orthotropic material in the 3-D state of stress, nine engineering constants require to be determined. The macromechanical analysis will begin from here. The stress–strain relationship for an orthotropic material is given by [11]

$$\begin{Bmatrix} \epsilon_{11} \\ \epsilon_{22} \\ \epsilon_{33} \\ \gamma_{23} \\ \gamma_{13} \\ \gamma_{12} \end{Bmatrix} = \begin{bmatrix} S_{11} & S_{12} & S_{13} & 0 & 0 & 0 \\ S_{12} & S_{22} & S_{23} & 0 & 0 & 0 \\ S_{13} & S_{23} & S_{33} & 0 & 0 & 0 \\ 0 & 0 & 0 & S_{44} & 0 & 0 \\ 0 & 0 & 0 & 0 & S_{55} & 0 \\ 0 & 0 & 0 & 0 & 0 & S_{66} \end{bmatrix} \begin{Bmatrix} \sigma_{11} \\ \sigma_{22} \\ \sigma_{33} \\ \tau_{23} \\ \tau_{13} \\ \tau_{12} \end{Bmatrix} . \tag{2.20}$$

Here, S_{ij} are the material compliances. Their relationship with the engineering constants is given in Reference [11]. ν_{ij} is Poissons ratio for the transverse strain in the jth direction when the stress is applied in the ith direction, and is given by

$$\nu_{ij} = -\epsilon_{jj}/\epsilon ii \, . \tag{2.21}$$

The above condition is for $\sigma_{jj} = \sigma$ and all other stresses equal to zero. Since the stiffness coefficients $Q_{ij} = Q_{ji}$, it follows that the compliance matrix is also symmetrical, that is, $S_{ij} = S_{ji}$. This condition enforces the following relationship among Poissons ratio:

$$\frac{\nu_{ij}}{E_i} = \frac{\nu_{ji}}{E_j} \, . \tag{2.22}$$

Hence, for a lamina under a 3-D state of stress, only three Poissons ratios namely ν_{12}, ν_{23} and ν_{31}, are required to be determined. Other Poissons ratio can be obtained from Equation (2.22).

For most of our analysis, we assume the condition of plane stress. Here, we derive the equations assuming that conditions of plane stress exist in the $1-2$ plane (see Figure 2.3). However, if one has to do an analysis of a laminated composite beam, which is essentially a 1-D member, the condition of plane stress will exist in the $1-3$ plane and a similar procedure could be followed.

For the plane stress condition in the 1-2 plane, we set the following stresses equal to zero in Equation (2.20), $\sigma_{33} = \tau_{23} = \tau_{13} = 0$. The resulting constitutive model under plane stress conditions can be written as

$$\begin{Bmatrix} \epsilon_{11} \\ \epsilon_{22} \\ \gamma_{12} \end{Bmatrix} = \begin{bmatrix} 1/E_1 & -\nu_{12}/E_1 & 0 \\ -\nu_{21}/E_2 & 1/E_2 & 0 \\ 0 & 0 & 1/G_{12} \end{bmatrix} \begin{Bmatrix} \sigma_{11} \\ \sigma_{22} \\ \tau_{12} \end{Bmatrix} . \tag{2.23}$$

Note that the strain ϵ_{33} also exists, which can be obtained from the third constitutive equation

$$\epsilon_{33} = S_{13}\sigma_{11} + S_{23}\sigma_{22} \, . \tag{2.24}$$

This equation indicates that Poissons ratios ν_{13} and ν_{23} should also exist. Inverting Equation (2.23), we can express the stresses in terms of the strains:

$$\begin{Bmatrix} \sigma_{11} \\ \sigma_{22} \\ \tau_{12} \end{Bmatrix} = \begin{bmatrix} Q_{11} & Q_{12} & 0 \\ Q_{12} & Q_{22} & 0 \\ 0 & 0 & Q_{66} \end{bmatrix} \begin{Bmatrix} \epsilon_{11} \\ \epsilon_{22} \\ \gamma_{12} \end{Bmatrix} , \tag{2.25}$$

where Q_{ij} are the reduced stiffness coefficients, which can be expressed in terms of the elastic constants as

$$Q_{11} = \frac{E_1}{1 - \nu_{12}\nu_{21}}\,,\; Q_{12} = \nu_{21}Q_{11}\,,\; Q_{22} = \frac{E_2}{1 - \nu_{12}\nu_{21}}\,, Q_{66} = G_{12}\,. \quad (2.26)$$

2.2.4 Stress–Strain Relation for a Lamina with Arbitrary Orientation of Fibers

In most cases, the orientation of the global axes, which we call the $x - y$ axes and are geometrically natural for the solution of the problem, do not coincide with the lamina principle axes, which we have already designated as 1–2 axes. The lamina principal axes and the global axes are shown in Figure 2.4. A small element in the lamina of area dA is taken and the free body diagram (FBD) is shown in Figure 2.5.

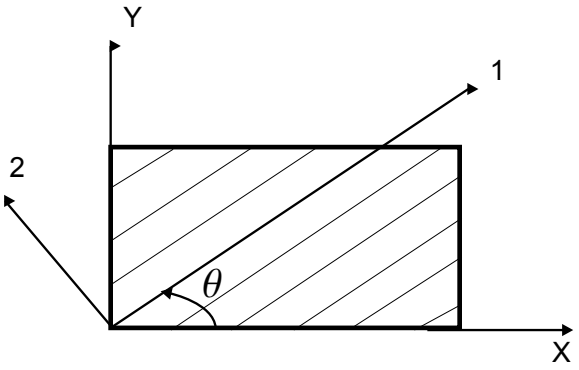

Fig. 2.4. Principal material axes of a lamina and the global $x - y$ axes

Consider the free body A. Summing all the forces in the 1-axis direction, we get

$$\begin{aligned}\sigma_{11}dA &- \sigma_{xx}(\cos\theta dA)(\cos\theta) - \sigma_{yy}(\sin\theta dA)(\sin\theta)\\ &- \tau_{xy}(\sin\theta dA)(\cos\theta) - \tau_{xy}(\cos\theta dA)(\sin\theta) = 0\,. \end{aligned} \quad (2.27)$$

On simplification, the above equation can be written as

$$\sigma_{11} = \sigma_{xx}\cos^2\theta + \sigma_{yy}\sin^2\theta + 2\tau_{xy}\sin\theta\cos\theta\,. \quad (2.28)$$

Similarly, by summing all the forces along the 2-axis (free body A), we get

$$\begin{aligned}\tau_{12}dA &- \sigma_{xx}(\cos\theta dA)(\sin\theta) - \sigma_{yy}(\sin\theta dA)(\cos\theta)\\ &- \tau_{xy}(\sin\theta dA)(\sin\theta) - \tau_{xy}(\cos\theta dA)(\cos\theta) = 0\,. \end{aligned} \quad (2.29)$$

Simplifying the above equation, we get

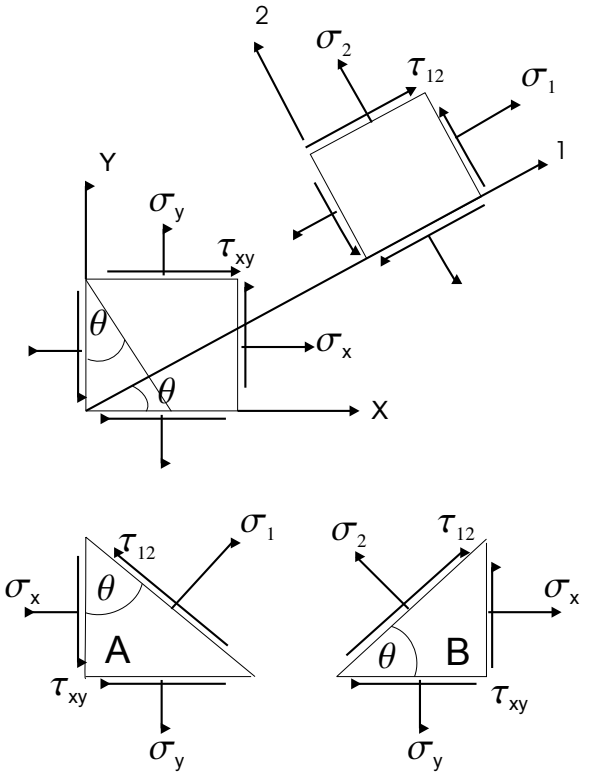

Fig. 2.5. Lamina and laminate coordinate system and FBD of a stressed element

$$\tau_{12} = -\sigma_{xx} \sin\theta \cos\theta + \sigma_{yy} \sin\theta \cos\theta + \tau_{xy}(\cos^2\theta - \sin^2\theta)\,. \tag{2.30}$$

Following the same procedure and summing all the forces in the 2-direction in the free body B, we can write

$$\sigma_{22} = \sigma_{xx} \sin^2\theta + \sigma_{yy} \cos^2\theta - 2\tau_{xy} \sin\theta \cos\theta\,. \tag{2.31}$$

Equations (2.28), (2.31) and (2.30) can be written in matrix form as

$$\begin{Bmatrix} \sigma_{11} \\ \sigma_{22} \\ \tau_{12} \end{Bmatrix} = \begin{bmatrix} C^2 & S^2 & 2CS \\ S^2 & C^2 & -2CS \\ -CS & CS & (C^2 - S^2) \end{bmatrix} \begin{Bmatrix} \sigma_{xx} \\ \sigma_{yy} \\ \tau_{xy} \end{Bmatrix},\ C = \cos\theta\,,\ S = \sin\theta \tag{2.32}$$

or

$$\{\sigma\}_{1-2} = [T]\{\sigma\}_{x-y}\,.$$

In a similar manner, the strains at the 1–2 axis, can be transformed to the x–y axis by a similar transformation. Note that to have the same transformation, the shear strains are divided by 2. They can be written as

$$\begin{Bmatrix} \epsilon_{11} \\ \epsilon_{22} \\ \frac{\gamma_{12}}{2} \end{Bmatrix} = \begin{bmatrix} C^2 & S^2 & 2CS \\ S^2 & C^2 & -2CS \\ -CS & CS & (C^2 - S^2) \end{bmatrix} \begin{Bmatrix} \epsilon_{xx} \\ \epsilon_{yy} \\ \frac{\gamma_{xy}}{2} \end{Bmatrix} \text{ or } \{\bar{\epsilon}\}_{1-2} = [T]\{\bar{\epsilon}\}_{x-y} . \quad (2.33)$$

Inverting Equations (2.32) and (2.33), we can express the stresses and strains in global coordinates as

$$\begin{Bmatrix} \sigma_{xx} \\ \sigma_{yy} \\ \tau_{xy} \end{Bmatrix} = \begin{bmatrix} C^2 & S^2 & -2CS \\ S^2 & C^2 & 2CS \\ CS & -CS & (C^2 - S^2) \end{bmatrix} \begin{Bmatrix} \sigma_{11} \\ \sigma_{22} \\ \tau_{12} \end{Bmatrix} , \{\sigma\}_{x-y} = [T]^{-1}\{\sigma\}_{1-2} . \quad (2.34)$$

$$\begin{Bmatrix} \epsilon_{xx} \\ \epsilon_{yy} \\ \frac{\gamma_{xy}}{2} \end{Bmatrix} = \begin{bmatrix} C^2 & S^2 & -2CS \\ S^2 & C^2 & 2CS \\ CS & -CS & (C^2 - S^2) \end{bmatrix} \begin{Bmatrix} \epsilon_{11} \\ \epsilon_{22} \\ \frac{\gamma_{12}}{2} \end{Bmatrix} , \textit{ or, } \{\bar{\epsilon}\}_{x-y} = [T]^{-1}\{\bar{\epsilon}\}_{1-2} . \quad (2.35)$$

Actual strain vectors in both 1–2 and x–y axes $\{\epsilon\}_{1-2}$ and $\{\epsilon\}_{x-y}$ are related to $\{\bar{\epsilon}\}_{1-2}$ and $\{\bar{\epsilon}\}_{x-y}$ through a transformation matrix as

$$\begin{Bmatrix} \epsilon_{11} \\ \epsilon_{22} \\ \gamma_{12} \end{Bmatrix} = \begin{bmatrix} 1 & 0 & 0 \\ 0 & 1 & 0 \\ 0 & 0 & 2 \end{bmatrix} \begin{Bmatrix} \bar{\epsilon}_{11} \\ \bar{\epsilon}_{22} \\ \frac{\bar{\gamma}_{12}}{2} \end{Bmatrix} \text{ and } \begin{Bmatrix} \epsilon_{xx} \\ \epsilon_{yy} \\ \gamma_{xy} \end{Bmatrix} = \begin{bmatrix} 1 & 0 & 0 \\ 0 & 1 & 0 \\ 0 & 0 & 2 \end{bmatrix} \begin{Bmatrix} \bar{\epsilon}_{xx} \\ \bar{\epsilon}_{yy} \\ \frac{\bar{\gamma}_{xy}}{2} \end{Bmatrix} , \quad (2.36)$$

$$\{\epsilon\}_{1-2} = [R]\{\bar{\epsilon}\}_{1-2} , \{\epsilon\}_{x-y} = [R]\{\bar{\epsilon}\}_{x-y} .$$

Now the constitutive equation of a lamina in its principal directions (Equation (2.25)) can be written as

$$\{\sigma\}_{1-2} = [Q]\{\epsilon\}_{1-2} . \quad (2.37)$$

Substituting Equations (2.32), (2.33) and (2.36) in Equation (2.37), we get

$$[T]\{\sigma\}_{x-y} = [Q][R]\{\bar{\epsilon}\}_{1-2} = [Q][R][T]\{\bar{\epsilon}\}_{x-y} = [Q][R][T][R]^{-1}\{\epsilon\}_{x-y} . \quad (2.38)$$

Hence the constitutive relation in the global x–y axes can now be written as

$$\{\sigma\}_{x-y} = [\bar{Q}]\{\epsilon\}_{x-y} = [T]^{-1}[Q][R][T][R]^{-1}\{\epsilon\}_{x-y} . \quad (2.39)$$

Here the matrix $[\bar{Q}]$ is fully populated. Hence, although the lamina in its own principal direction is orthotropic, in the transformed coordinate, it represents complete anisotropic behavior, that is the normal stresses are coupled to the shear strains and vice versa. The elements of $[\bar{Q}]$ are given by

$$\begin{aligned}
\bar{Q}_{11} &= Q_{11}C^4 + 2(Q_{12} + 2Q_{66})S^2C^2 + Q_{22}S^4 , \\
\bar{Q}_{12} &= (Q_{11} + Q_{22} - 4Q_{66})S^2C^2 + Q_{12}(S^4 + C^4) , \\
\bar{Q}_{16} &= (Q_{11} - Q_{12} - 2Q_{66})SC^3 + (Q_{12} - Q_{22} + 2Q_{66})S^3C , \\
\bar{Q}_{22} &= Q_{11}S^4 + 2(Q_{12} + 2Q_{66})S^2C^2 + Q_{22}C^4 , \\
\bar{Q}_{26} &= (Q_{11} - Q_{12} - 2Q_{66})S^3C + (Q_{12} - Q_{22} + 2Q_{66})SC^3 , \\
\bar{Q}_{66} &= (Q_{11} + Q_{22} - 2Q_{12} - 2Q_{66})S^2C^2 + Q_{66}(S^4 + C^4) ,
\end{aligned} \quad (2.40)$$

which gives the constitutive equation of a lamina under plane stress in the 1–2 plane.

2.3 Introduction to Smart Composites

Laminated composites provide numerous opportunities to tailor the strength in the required direction and enable placement of embedded sensors and actuators at any critical location to monitor the performance of the structure. This facility is not available in conventional metallic structures. Since many smart materials are available in thin-film or powder form, embedding them in a laminated composite structure does not pose any serious problem. Those composites that have an embedded smart material patch are called smart composite structures. Figure 2.6 shows how a piezoelectric material can be embedded in a laminated composite.

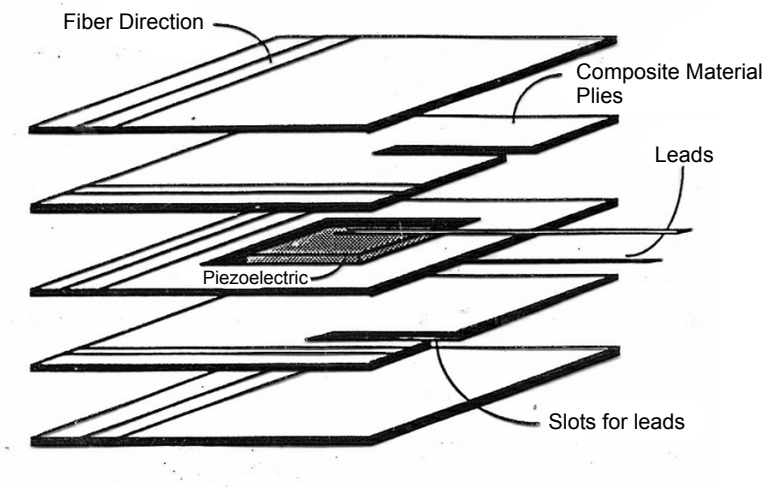

Fig. 2.6. Construction of a smart composite

Modeling systems with structures having embedded smart sensors and actuators is very similar to modeling conventional composite structures, wherein numerical techniques such as FEM or spectral techniques can be used. However, the modeling has to take care of the additional complexities arising due to the material properties of the smart materials. These are reflected in the constitutive law in the form of electromechanical coupling as in the case of piezo-ceramic or poly-vinylidine di-fluoride (PVDF) sensors or magneto-mechanical coupling as in the case of magnetostrictive sensors/actuators such as TERFENOL-D. From the modeling point of view, these complexities lead to additional matrices in the FEM/SFEM approach.

Piezoelectric or magnetostrictive materials have two constitutive laws, one of which is used for sensing and the other for actuation applications. For 2-D problems, the constitutive model for piezoelectric material is of the form

$$\begin{aligned}\{\sigma\}_{3x1} &= [Q]^{(E)}_{3x3}\{\varepsilon\}_{3x1} - [e]_{3x2}\{E\}_{2x1} \\ \{D\}_{2x1} &= [e]^{T}_{2x3}\{\varepsilon\}_{3x1} + [\mu]^{(\sigma)}_{2x2}\{E\}_{2x1}\end{aligned} \tag{2.41}$$

The first part of this constitutive law is called the actuation law, while the second is called the sensing law. Here, $\{\sigma\}^T = \left\{ \sigma_{xx}\ \sigma_{yy}\ \tau_{xy} \right\}$ is the stress vector, $\{\varepsilon\}^T = \left\{ \varepsilon_{xx}\ \varepsilon_{yy}\ \gamma_{xy} \right\}$ is the strain vector, $[e]$ is the matrix of piezoelectric coefficients of size 3×2, which has units of N/V-mm, $\{E\}^T = \left\{ E_x\ E_y \right\} = \left\{ V_x/t\ V_y/t \right\}$ is the applied field in the two coordinate directions. It has units of V/mm. $[\mu]$ is the permittivity matrix of size 2×2, measured at constant stress and has units of N/V/V and $\{D\}^T = \left\{ D_x\ D_y \right\}$ is the vector of electric displacement in the two coordinate directions. This has units of N/V-mm. $[Q]$ is the mechanical constitutive matrix measure at constant electric field. Normally, Equation (2.41) is written in the form

$$\{\varepsilon\} = [S]\{\sigma\} + [d]\{E\}\,. \tag{2.42}$$

In the above expression, $[S]$ is the compliance matrix, which is the inverse of the mechanical material matrix $[Q]$ and $[d] = [Q]^{-1}[e]$ is the electromechanical coupling matrix, where the elements of this matrix have units mm/V and are direction dependent. In most analyses, it will be assumed that the mechanical properties will change very little with the change in the electric field and as a result, the actuation law (Equation (2.41) can be assumed to behave linearly with the electric field, while the sensing law (Equation (2.41))) can be assumed to behave linearly with the stress. This assumption considerably simplifies the analysis process.

The first part of Equation (2.41) represents the stresses developed due to a mechanical load, while the second part of the same equation gives the stresses due to a voltage input. From these equations, it is clear that the structure will be stressed due to the application of an electric field even in the absence of mechanical load. Alternatively, when the mechanical structure is loaded, it generates an electric field even in the absence of an applied electric field. In other words, the above constitutive law demonstrates the electromechanical coupling, which can be exploited for a variety of structural applications such as vibration control, noise control, shape control or structural health monitoring. Actuation using piezoelectric materials can be demonstrated using a plate of length L, width W and thickness t. Thin piezoelectric electrodes are placed on the top and bottom surface of the plate as shown in Figure 2.7. Such a plate is called a bimorph plate. When a voltage is passed between the electrodes as shown in the figure (which is normally referred to as the poling direction), deformation in the length, width and thickness directions is given by

$$\delta L = d_{31}E_1 L = \frac{d_{31}VL}{t}, \quad \delta W = d_{31}E_2 W = \frac{d_{31}VW}{t}, \quad \delta t = d_{33}V\,. \tag{2.43}$$

Here, d_{31} and d_{33} are the electromechanical coupling coefficients in the directions 1 and 3 respectively. Conversely, if a force F is applied in any of

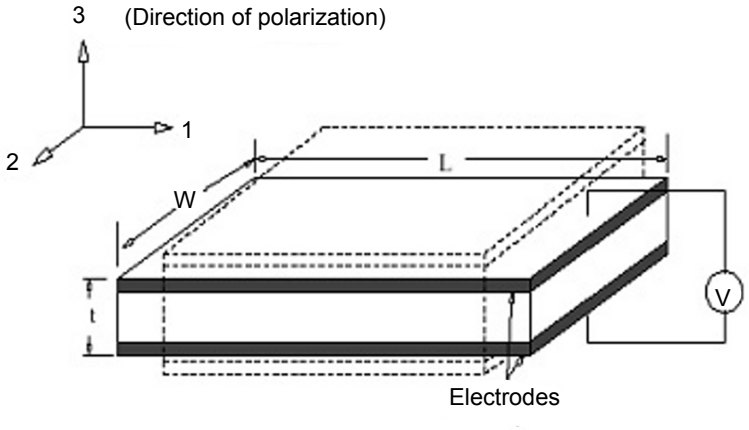

Fig. 2.7. Illustration of actuation effect in a piezoelectric plate

the length, width or thickness directions, the voltage V developed across the electrodes in the thickness direction is given by

$$V = \frac{d_{31}F}{\mu L} \quad \text{or}\, V = \frac{d_{31}F}{\mu W} \quad \text{or}\, V = \frac{d_{33}F}{\mu LW}\,. \tag{2.44}$$

Here μ is the dielectric permitivity of the material. The reversibility between strain and voltage makes piezoelectric materials ideal for both sensing and actuation.

There are different types of piezoelectric material that are used for many structural applications. The most commonly used material is PZT (lead zirconate titanate) material, which is extensively used as bulk actuator material as it has a high electromechanical coupling factor. On the other hand, due to the low electromechanical coupling factor, piezo-polymers (PVDF) are used only as sensor material. More recently, a new form of materials called piezo-fiber composite (PFC) has been found to be a very effective actuator material for use in vibration/noise control applications.

The constitutive laws (both actuation and sensing) for a magnetostrictive material such as TERFENOL-D are much more complex than those for piezoelectric materials. They are highly non-linear in behavior although they have a similar form to the piezoelectric material, which is given by

$$\{\varepsilon\} = [S]^{(H)}\{\sigma\} + [d]^T\{H\}\,, \tag{2.45}$$

$$\{B\} = \{d\}\{\sigma\} + [\mu]^{(\sigma)}\{H\}\,. \tag{2.46}$$

Here, $[S]$ is the compliance matrix measured at a constant magnetic field H, d is the magneto-mechanical coupling matrix, the elements of which have units of m/A, B is the vector of magnetic flux density in the two coordinate directions. It has units tesla, equal to weber/m^3. H is the magnetic field

intensity vector in the two coordinate directions and has unit oersted, equal to A/m. It is related to the AC current ($I(t)$) through the relation $H = nI$, where n is the number of turns in the actuator. $[\mu]$ is the matrix of magnetic permeability measured at constant stress and has units of weber/A-m. As in the case of piezoelectric material, the first equation (Equation (2.46)) is the actuation constitutive law, while the second equation is the sensing law. The stress strain relations are different for different magnetic field intensities. The strain is proportional to stress only for small H. For higher magnetic field intensities, both sensing and actuator equations require to be simultaneously solved to arrive at the correct stress–strain relation. This is because changes in the magnetic field cause changes in the stress, which in turn changes the magnetic permeability. Hence, the characterization of the material properties of TERFENOL-D is more difficult than for piezoelectric material.

In Chapter 11, we deal with the modeling of smart composites where we will use these constitutive models extensively. However, only linear behavior is assumed for most examples reported in this book. The constitutive model for smart composites is obtained in a similar manner to that for laminated composites, where the smart patches are also considered as a lamina to obtain the averaged properties.

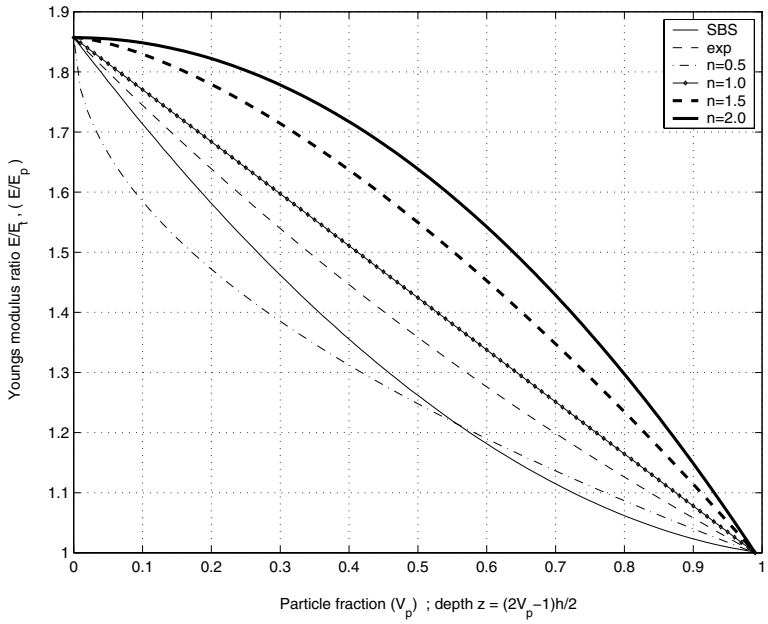

Fig. 2.8. Variation of Young's modulus for different models

2.4 Modeling Inhomogeneous Materials

Several analytical and computational models are available in the literature (see References [13] and [14]) that discuss the issue of finding suitable functions for approximating the modulus variation in an inhomogeneous material. There are several criteria for selecting them. They are desired to be continuous, simple and should have the ability to exhibit curvature, both "concave upward" and "concave downward" [14]. Here, two types of variations are considered, which generally cover all the existing analytical models. The exponential law, which is more common in fracture studies of functionally graded materials (FGM) (see References [15] and [16]), and does not show curvature in both directions, is given by

$$\mathcal{P}(z) = \mathcal{P}_t \ \exp(-\delta(1 - 2z/h)) \,, \qquad \delta = \frac{1}{2} \log\left(\frac{\mathcal{P}_t}{\mathcal{P}_b}\right) \,. \tag{2.47}$$

The power law, for commonly adopted Voight-type estimates [14], having all the desired properties and introduced by Wakashima *et al.* [17], is given by

$$\mathcal{P}(z) = (\mathcal{P}_t - \mathcal{P}_b)\left(\frac{z}{h} + \frac{1}{2}\right)^n \ + \ \mathcal{P}_b \,, \tag{2.48}$$

where $\mathcal{P}(z)$ denotes a typical material property (E, G, α, ϱ). $\mathcal{P}_t$ and $\mathcal{P}_b$ denote values of the variables at the topmost and bottommost layer of the structure, respectively, and n is a parameter, the magnitude of which determines the curvature. The working range of n is taken as $1/3$ to 3, as any value outside this range will produce an inhomogeneous material having too much of one phase (see [18]).

Another way of estimating material properties is by the rule-of-mixtures, which is generally employed for composite materials. A summary of this method can be found in References [11] and [12]. The concept of equivalent homogeneity results in different methods, namely, the composite sphere model, the three phase model, the composite cylinder model and the self-consistent scheme [19]. The composite sphere and cylinder models can be further improved by the step-by-step (SBS) method as given in Reference [20]. The method given for the particle reinforced composite material is best suited for use in the present context. The details are omitted here. In short, inhomogeneous materials such as FGM can be treated as a matrix particle mixture of different particle volume fractions, which vary smoothly vary throughout the depth of the structure. The two different materials at the top and bottom of the beam play the role of matrix and particle.

These different models for material property variations are compared in Figure 2.8, where the variation of the Young's modulus throughout the depth is plotted. Top and bottom materials (particle and matrix, respectively for the SBS method) are taken as steel and ceramic with a Young's modulus ratio of 1.857. The figure clearly shows the different trends of distribution

for different models. In the SBS method, "constant area composition" is used and the particle volume fraction V_{p1}, is taken as 0.001. Since, the SBS method predicts only the elastic and thermal properties, in calculations the inertial properties are evaluated using the power law model with a suitable value for the exponent n.

In this chapter, we have presented a detailed introduction to the constitutive laws of fiber reinforced composite laminate and a brief description of the theory of smart composite. More detailed discussions on smart composite will be given in Chapter 11. Further, the popular choices of the functional form of material property variations for inhomogeneous materials are also provided.

3

Idealization of Wave Propagation and Solution Techniques

In this chapter, all the necessary tools required for the spectral element formulation are derived. The most important of these is the determination of wavenumbers and wave amplitudes. An nth-order differential equation will yield an nth-order characteristic equation for the wavenumbers, which are normally difficult to solve. Here, we adopt some traditional techniques based on the theory of linear algebra to solve for wavenumbers and wave amplitudes. This chapter also describes the general spectral finite element formulation procedure, which is applied to form elements for isotropic waveguides.

3.1 General Form of the Wave Equations

Throughout the book, small letters with bold face are used to represent vectors and capital letters with bold face are used to represent matrices. The general form of the linear wave equation is given by

$$u_{tt} = \sum_{\alpha,\beta} u_{\alpha\beta}\,, \tag{3.1}$$

where the summation is over all possible combinations of α and β.

The wave equation in the structural mechanics context is the conservation of momentum (dynamic equilibrium) equation

$$\nabla \cdot \mathbf{T} = \rho \ddot{\mathbf{u}}\,, \tag{3.2}$$

where $\mathbf{T}$ is the stress measure at any point in the body, which is in general a non-linear function of the displacement vector $\mathbf{u} = \{u_x, u_y, u_z\}$, (the wave). A non-linear relation between $\mathbf{T}$ and $\mathbf{u}$ results in a non-linear wave equation, which will not be covered in the present discussion. Instead, it will be assumed that there exists a linear relationship between $\mathbf{T}$ and the strain (*i.e.* the displacement gradient), either in the time domain (linear elastic material) or in the frequency domain (visco-elastic material). However, the linear

coefficient (of the constitutive relation) can be direction (anisotropy) and/or position (inhomogeneity) dependent. In both cases, the response of homogeneous isotropic materials can be retrieved easily from these general material models.

3.2 Characteristics of Waves in Anisotropic Media

An important characteristic that separates waves in anisotropic media from its isotropic media counterpart is the direction of energy flow (i.e. group velocity) [21]. For isotropic material, the incident and reflected waves are purely longitudinal (P) or shear (S). In two-dimensional (2-D) media, for example, if the wave vector is given by $\mathbf{k} = (k_x, k_y)$, the direction cosines of the normal to the wavefront would be (k_x, k_y) and $(-k_y, k_x)$ for P and S wave, respectively. However, the situation is much more complex in the anisotropic case, where the wave directions are material property dependent and they can no longer be thought of as purely P or S waves. They are called the quasi-P wave and the quasi-S wave (vertical, QSV or horizontal, QSH). In this case, the three waves (in three Cartesian coordinate directions) are coupled, and in order to identify them, one needs to solve a sixth-order characteristic polynomial equation. Thus, the simplified analysis for the isotropic case based on the Helmholtz decomposition (possible by virtue of uncoupled P and S motions), is not practical in the anisotropic case. The wave velocity and direction in anisotropic material can be obtained from the governing equation and the plane wave assumption. The governing equation for a general homogeneous anisotropic media is

$$\frac{\partial \sigma_{ik}}{\partial x_k} = \rho \ddot{u}_i \,, \quad \sigma_{ik} = C_{ik\ell m} \epsilon_{\ell m} \,, \tag{3.3}$$

where the constitutive matrix $C_{ik\ell m}$ is symmetric with respect to ℓ and m. For the plane wave assumption, the displacement field is given by

$$u_i = A \alpha_i e^{jk(n_m x_m - ct)} \,, \tag{3.4}$$

where n_m are the direction cosines of the normal to the wavefront and α_i are the direction cosines of particle displacement. Substitution of the assumed form in the governing equation results in an eigenvalue problem for the phase velocity c as

$$(\Gamma_{im} - \rho c^2 \delta_{im}) \alpha_m = 0 \,, \quad \Gamma_{im} = C_{ik\ell m} n_k n_\ell \,, \tag{3.5}$$

where Γ_{im} is called the Christoffel symbol. Solving Equation (3.5), the wave phase velocity and the wave directions are obtained. From the previous discussion, it can be said that for a general anisotropic media, $\alpha \times \mathbf{n}$ and $\alpha \cdot \mathbf{n}$ are never zero.

3.3 General Form of Inhomogeneous Wave Equations

Compared to the wave propagation in anisotropic media, the waves in inhomogeneous media have totally different characteristics. Typically, the wave motion in the direction of the inhomogeneity is characterized by a reduction in the amplitude of the wave while it is propagating (see [22], [23]). A wave of this type is called an *inhomogeneous wave*. The homogeneous plane wave has the form (a variation of Equation (3.4))

$$f = \Phi(\omega)e^{j(k_x x + k_y y + k_z z - \omega t)} = \Phi(\omega)e^{j(\mathbf{k}\cdot\mathbf{r} - \omega t)}\,, \tag{3.6}$$

where $\Phi(\omega)$ is the wave amplitude (real) and $\mathbf{k}$ is the wave vector (real). This form describes the wave propagation phenomena in homogeneous, linear and non-dissipative solids. The inhomogeneous wave is described by the above form with complex Φ and $\mathbf{k}$ (see [24]).

These waves were initially observed in media with inbuilt dissipative properties (like the visco-elastic materials). However, inhomogeneous materials can also be carriers of this kind of wave, when the inhomogeneity is in the direction of wave propagation. These waves successfully describe the wave modes, and their dispersive character, whereby the propagation speed, attenuation constant and pertinent angles are, in general, dependent on the frequency (see [25], [26] and [27]). It is known that the time harmonic waves in dissipative media have a complex valued wavenumber. However, it is less well known that there can be waves with a complex valued wave vector, with real and imaginary parts $\mathbf{k}_1$ and $\mathbf{k}_2$ not necessarily parallel. Thus, more precisely, inhomogeneous waves ([28]) are waves where the wave vector $\mathbf{k}$ is complex valued ($\mathbf{k} = \mathbf{k}_1 + j\mathbf{k}_2$), and $\mathbf{k}_1$ and $\mathbf{k}_2$ are not parallel. Thus the general form becomes

$$\begin{aligned} f &= \Phi(\omega)e^{j(k_{1x}x + k_{1y}y + k_{1z}z - \omega t) - (k_{2x}x + k_{2y}y + k_{2z}z)} \\ &= \Phi(\omega)e^{j(\mathbf{k}_1\cdot\mathbf{r} - \omega t) - \mathbf{k_2}\cdot\mathbf{r}}\,, \end{aligned} \tag{3.7}$$

which describes a plane wave of varying amplitude [29]. It can be shown that $\mathbf{k}_1 \cdot \mathbf{k}_2 = 0$, which indicates that this wave propagates in the direction given by the vector $\mathbf{k}_1$, and its amplitude decreases in the perpendicular direction.

3.4 Basic Properties and Solution Techniques

This section can be thought of as an extension to Section 1.1. Other than the FEM, the two most powerful methods of solving linear second-order partial differential equations are (1) the method of separation of variables and (2) the method of integral transform. The first method is widely used to find natural vibration modes (or standing waves), which are again solutions of the wave equation with homogeneous boundary conditions.

The method of integral transform is more generally applicable, although it has some serious drawbacks. The method presumes the existence of a special integral transform (forward and inverse), which forms the backbone of the technique. Successful application of the method depends upon successful choice of the integral transform. Commonly used transforms are Fourier, Fourier sine and Fourier cosin whereas other transforms, like Laplace, Hankel, Melin and Radon transforms also find suitable applications. For a variable $u(x_1, x_2, \ldots, x_n)$ the transformation of the first independent variable will yield

$$\bar{u}(\xi, x_2, \ldots, x_n) = \int_{\alpha}^{\beta} u(x_1, x_2, \ldots, x_n) K(\xi, x_1) dx_1 \,, \tag{3.8}$$

where $K(\xi, x_1)$ is called the kernel. For certain kernels, it is possible to have an inversion relation (and the solution):

$$u(x_1, x_2, \ldots, x_n) = \int_{\gamma}^{\delta} \bar{u}(\xi, x_2, \ldots, x_n) H(\xi, x_1) d\xi \,. \tag{3.9}$$

The kernels K and H are generally of similar form (identical for the sine and cosine transform). However, for all commonly used transformations, the domains of integration (defined by α, β, γ and δ) extend to infinity. Thus, the physical domain also has to be extended to infinity for valid application of integral transforms. Thus, integral transform based solution techniques work perfectly for those variables for which no boundary conditions are specified, *i.e.* for boundary value problems the method is inadequate. For one-dimensional structural problems (rod, truss or beam), for example, the integral transform is used for the time variable only and the method works perfectly for all kinds of boundary conditions, although initial conditions like displacement or velocity cannot be accommodated. However, the advantage of these methods is the availability of closed form solutions.

The most popular and efficient method of solving initial-boundary value problems that exists today is the finite element method, which belongs to the class "the method of weighted residual". Although FEM does not guarantee a closed form solution, it is applicable to all types of problems. Another advantage is that it can exploit the exact solution of relatively simple structures to solve problems for which it is difficult to obtain closed form solutions.

The spectral finite element method is based on the method of integral transform and thus delivers closed form solutions. However, the method is structured to have a stiffness matrix (dynamic) like the regular FEM, which increases its applicability and provides generality, which has so far been enjoyed only by FEM.

3.5 Spectral Finite Element Discretization

The history of the study of wave propagation dates back several centuries. An account of these developments can be found in [30]. However, analysis of wave

propagation by SFEM is a relatively new approach. The SFEM is based on the method of integral transform [31], in particular, Fourier transform. Application of the continuous Fourier transform (CFT) to the solution of wave propagation problems is quite standard as can be judged by early work [32]. The analysis involves performing an inverse transform (reconstructing the signal), which is very difficult to do in an exact analytical manner. Consequently, many approximate and asymptotic schemes have been developed. These are quite adequate for studying the far-field behavior, *e.g.* for seismological studies. However, for structural wave propagation, these schemes are not sufficient because of heavy loss of information caused by the reflection of the interacting stress waves at numerous boundaries. Further, analytical transforms are feasible only if the functions to be transformed are relatively simple - which is not the case for most practical problems. Thus, the absence of a suitable inversion technique arrested the growth of CFT based methods and paved the way for the discrete fourier transform (DFT), which is an approximation of the integral involved in CFT. However, the application of the discrete Fourier series was quite limited, with some early exceptions being References [33], [34], and [35]. The reason behind this is the absence of suitable forward and inverse transform schemes, which are required for processing all general inputs and outputs. These were explained in detail in Section 1.2.

Thus, the SFEM had to wait for the re-invention (it was known to K.F. Gauss in 1805, [36]) and publication of a FFT algorithm, popularly known as the Cooley Tukey algorithm [37], which revolutionized signal processing. The SFEM, conceived by Doyle [9], is a DFT based analysis of wave propagation, where the DFT is performed by a FFT algorithm. The unknown variable (can be scalar or vector), a function of space and time, is approximated as

$$\mathbf{u}(x,y,z,t) = \sum_{n=0}^{N-1} \hat{\mathbf{u}}(x,y,z,\omega_n) e^{-j\omega_n t}\,, \quad j^2 = -1\,, \tag{3.10}$$

where N is the number of FFT points. ω_n is the discrete circular frequency, which is related to the time window T by

$$\omega_n = n\Delta\omega = \frac{n\omega_f}{N} = \frac{n}{N\Delta t} = \frac{n}{T}\,, \tag{3.11}$$

where Δt is the rate of time sampling and ω_f is the highest frequency captured by Δt. The frequency content of the load decides N and consideration of the wrap-around problem or aliasing problem decides $\Delta\omega$. More details on the associated problems are given in Reference [9].

Representation of the unknown variable in Equation (3.10), removes one dimension from the system, *i.e.,* the time t and frequency enters as a parameter. If the structure is a 1-D idealization, then the governing partial differential equation (PDE) reduces to an ordinary differential equation (ODE). The ODE has constant coefficients for isotropic and anisotropic homogeneous materials and for inhomogeneous material graded in the normal direction of wave propagation. Variable coefficients arise for inhomogeneity in the direction of wave

propagation. For a constant coefficient ODE, the exact solution can be found for any order of the equation. SFEM employs this exact solution as an interpolating function for element formulation. The constants of integration are made to satisfy the boundary conditions in the frequency domain (FD) and thus all the requirements are satisfied at each discrete frequency, ω_n. Using the inverse-FFT (IFFT), the time domain data are obtained.

However, there is more to SFEM than just solving PDEs in FD using FFT. As the name suggests, the method has a resemblance to the FEM. As is done in FEM, in SFEM, the Rayleigh–Ritz method is employed in FD to obtain the structural stiffness matrix, known as the dynamic stiffness matrix $\hat{\mathbf{K}}_n$. The matrix vector equation (much like the FEM) that is solved at each frequency ω_n is

$$\hat{\mathbf{K}}_n \hat{\mathbf{u}}_n = \hat{\mathbf{f}}_n \,, \tag{3.12}$$

where $\hat{\mathbf{u}}_n$ and $\hat{\mathbf{f}}_n$ are the vectors of unknown variables (displacements) and known forces, respectively, at frequency ω_n. The dynamic stiffness matrix can also be obtained using regular FEM by taking the Fourier transform of the governing equation, using the stiffness $\mathbf{K}$ and the consistent mass matrix $\mathbf{M}$ as

$$\hat{\mathbf{K}}_n = \mathbf{K} - \omega_n^2 \mathbf{M} \,, \tag{3.13}$$

where n in the suffix indicates the formation at ω_n. However, $\hat{\mathbf{K}}_n$ in SFEM is obtained using the exact solution, whereas $\hat{\mathbf{K}}_n$ from FEM is just an approximation. The $\hat{\mathbf{K}}_n$ in FEM approaches the $\hat{\mathbf{K}}_n$ from SFEM in the limiting process of taking the number of FEs to infinity. Further, the matrix–vector structure of the SFEM gives the flexibility of FE modeling, where large structures can be assembled in terms of many small spectral finite element (SFE) waveguides. The assemblage and imposition of boundary condition in SFEM is the same as is done in FEM, which makes the method more attractive to the FEM community. Moreover, the Ritz method enables the use of regular SFE for irregular structures, much like FEM with higher level discretization, although the number of SFEs is still much lower compared to FE requirements. Another advantage is the augmentation of SFE and FE, which enables the modeling of structures with discontinuities, like cracks or inclusions.

In comparison, the formulation of SFEs for 2-D structural waveguide poses extra complexity. The reduced equation in the FD is no longer an ODE (but a PDE or system of PDEs of two space variables). This PDE is not readily solvable and another transform is necessary to reduce the equation to one spatial dimension and we move to the frequency–wavenumber domain (FWD). Thus, the unknown variable is further decomposed, normally using a Fourier series (FS) representation as

$$\hat{\mathbf{u}}(x, y, \omega_n) = \sum_{m=0}^{M-1} \tilde{\mathbf{u}}(x, \eta_m, \omega_n) \begin{Bmatrix} \sin(\eta_m y) \\ \cos(\eta_m y) \end{Bmatrix} , \tag{3.14}$$

where M is the number of FS points. η_m is the discrete wavenumber related to the spatial window Y by

$$\eta_m = m\Delta\eta = \frac{m\eta_f}{M} = \frac{m}{M\Delta y} = \frac{m}{Y}\,, \tag{3.15}$$

where Δy is the spatial sampling rate and η_f is the highest wavenumber captured by Δy. The spatial variation of the load determines M. Using this representation, the governing equation becomes an ODE (in x) and again can be solved exactly for some cases. This exact solution is again used as the interpolating function for the unknown. Thus, for each frequency ω_n and wavenumber η_m the dynamic stiffness matrix is formed and assembled and the unknown variable is solved for its FWD amplitude $\tilde{\mathbf{u}}_{n,m}$ as

$$\tilde{\mathbf{K}}_{n,m}\tilde{\mathbf{u}}_{n,m} = \tilde{\mathbf{f}}_{n,m}\,, \tag{3.16}$$

where $\tilde{\mathbf{f}}_{n,m}$ is the FWD amplitude of applied load. From $\tilde{\mathbf{u}}_{n,m} = \tilde{\mathbf{u}}(x, \eta_m, \omega_n)$, $\hat{\mathbf{u}}(x, y, \omega_n)$ is recovered by the FS and $\mathbf{u}(x, y, t)$ is recovered by the IFFT algorithm.

To obtain the exact solution of the ODE in FD (for 1-D analysis) or FWD (for 2-D analysis), it is assumed that the solution of $\hat{\mathbf{u}}(x, \omega_n)$ or $\tilde{\mathbf{u}}(x, \eta_m, \omega_n)$ is in the form $u_\circ e^{-jkx}$, where $\mathbf{u}_\circ$ is an unknown constant (possibly vector) and k is the wavenumber (unknown) in the direction of propagation, say, x direction. This assumption is valid for a constant coefficient ODE or system of ODEs only. However, it will be seen later that the above assumption may sometimes yield good approximate solutions even for variable coefficient equations. Substitution of the solution in the reduced ODE results in a single homogeneous linear algebraic equation for $\mathbf{u}_\circ$ (in the case of a single ODE) or a system of linear homogeneous algebraic equations for $\mathbf{u}_\circ$ (for a system of ODEs) as

$$[\mathbf{W}(k, \omega_n, \eta_m)]\mathbf{u}_\circ = 0\,, \quad \mathbf{W} \in \mathbf{C}^{N_v \times N_v}\,, \mathbf{u}_\circ \in \mathbf{C}^{N_v \times 1}\,. \tag{3.17}$$

$\mathbf{W}$ is called the wave matrix, which is of the order $N_v \times N_v$, where N_v is the number of independent variables. For a non-trivial solution of $\mathbf{u}_\circ$, the wave matrix must be singular, *i.e.,* its determinant must be zero. This condition generates the required equation for the solution of wavenumber k, which will be a polynomial in k, called the spectrum relation. Wavenumbers essentially determine the type of wave, *i.e.,* dispersive or non-dispersive.

If there are N_k roots of the polynomial equation then the complete solution is

$$\hat{\mathbf{u}}(x, \omega_n) \text{ or } \tilde{\mathbf{u}}(x, \eta_m, \omega_n) = \sum_{i=1}^{N_k} \mathbf{u}_{\circ,i} \exp\left(-jk_i x\right), \tag{3.18}$$

where k_i is the ith wavenumber and $\mathbf{u}_{\circ,i}$ is the ith coefficient vector, called the wave amplitude vector. Thus at the heart of the SFE formulation is the computation of wavenumber k and $\mathbf{u}_{\circ,i}$, whose efficient implementation determines the efficiency of the SFEM.

3.6 Efficient Computation of the Wavenumber and Wave Amplitude

The constitutive relation and the displacement field in an anisotropic material give rise to both stiffness and inertial coupling, which poses great difficulty in analysis and hence, in the development of SFE. The main difficulty is in the wavenumber computation (where the order of the polynomial is increased) and in the wave amplitude vector $\mathbf{u}_{\circ,i}$ computation (where the order of the wave matrix is increased). The conventional method of wavenumber and coefficient computation (see [9]) is not adequate to tackle this kind of situation and there is a need to improve the existing formalism. The development towards this end started with the elementary composite beam [38], which needs a sixth-order polynomial (emanated from the determinant of a 2×2 wave matrix) to be solved for wavenumber computation. The wavenumbers were computed numerically, where the Newton–Raphson (NR) method was used to find the single real root. The rest of the roots were expressed in terms of this real wavenumber. The coefficient vectors were evaluated analytically. The situation became a little complicated in the first-order shear deformable beam [39], where the wave matrix had a size of 3×3, although the spectrum relation was still a sixth-order polynomial. As was done before, the spectrum relation was solved numerically (by tracking the real root first using the NR algorithm) and wave amplitude vectors were evaluated analytically. It must be noted that computation of the wave amplitude vectors required solution of a system of matrices of size $N_v - 1 \times N_v - 1$. The situation became too difficult to handle in the 3-D beam model and uniform tube model, where $N_v = 6$. Thus, the 6×6 wave matrix generated a 12th-order polynomial, which was required to be solved at each frequency domain. The strategy applied in these works was called a subspace averaging scheme, where wavenumbers of the partially decoupled problems were computed first, *e.g.,* axial–flexure, axial–torsion and torsion–bending cases. These are essentially represented by the submatrices of the original wave matrix. Trial roots were obtained by averaging the computed wavenumbers contributing in the appropriate modes. Thus, the wavenumbers were computed in a somewhat ad hoc basis and they were approximate in nature. For computation of the wave amplitude vectors (12 in number), a 5×5 matrix–vector equation needs to be solved each time, which, this time, was performed numerically. It must be noted that in this matrix–vector equation, the row space (or column space) of the matrix must be 5, for the solutions to be unique. However, it is difficult to ascertain that the chosen rows (or columns) are linearly independent and in the absence of a robust wavenumber solver, the situation becomes worse. This discussion reveals that the current status of the SFE formulation demands

1. A robust, generally applicable and accurate wavenumber solving algorithm, which will be applicable to all models, irrespective of the number of variables, N_v. Further, the solver must be efficient, since the job is to be performed at each frequency step.

2. A robust, accurate and efficient numerical scheme for computing the wave amplitude vectors for a given value of the wavenumber.

It does not take long to identify that the matrix in Equation (3.17) is a polynomial over k and the problem of finding wavenumber k and wave amplitude $\mathbf{u}_\circ$ is a standard polynomial eigenvalue problem (PEP) of finding nonzero $\mathbf{v}$ and k such that

$$\mathbf{W}(k)\mathbf{v} = (\sum_{i=0}^{p} k^i \mathbf{A}_i)\mathbf{v} = 0\,, \mathbf{A}_i \in \mathbb{C}^{N_v \times N_v}\,, \mathbf{v} \in \mathbb{C}^{N_v \times 1}\,, \tag{3.19}$$

where p is the order of the PEP. Each $\mathbf{A}_i$ depends upon the material properties, frequency and wavenumber (in 2-D). Two different strategies are given here to solve the PEP.

3.6.1 Method 1: The Companion Matrix and the SVD Technique

In the first method, it is noted that the desired eigenvalues are the latent roots, which satisfy the condition $det(\mathbf{W}(k)) = 0$ [40]. Further, if k_i is any such root, then there is at least one non-trivial solution for $\mathbf{v}$, which is known as the latent eigenvector. To find the latent root, the determinant is expanded in a polynomial of k, $p(k)$, and solved by the companion matrix method. In this method, the companion matrix $L(p)$, corresponding to $p(k)$ is formed, which is defined as

$$L(p) = \begin{bmatrix} 0 & 1 & 0 & \cdots & 0 \\ 0 & 0 & 1 & & . \\ \vdots & \vdots & \vdots & \ddots & \vdots \\ 0 & 0 & & 0 & 1 \\ -\alpha_m & -\alpha_{m-1} & \cdots & -\alpha_2 & -\alpha_1 \end{bmatrix}, \tag{3.20}$$

where $p(\lambda)$ is given by

$$p(\lambda) = \lambda^m + \alpha_1 \lambda^{m-1} + \cdots + \alpha_m\,. \tag{3.21}$$

One of the many important properties of the companion matrix is that the characteristic polynomial of $L(p)$ is $p(k)$ itself [41]. Thus, eigenvalues of $L(p)$ are the roots of $p(k)$, which are obtained readily using any standard subroutine, *e.g.,* LAPACK (xGEEV group).

Once the eigenvalues are obtained they can be used to obtain the eigenvectors. To do so, it is to be noted that the eigenvectors are the elements of the null space of $\mathbf{W}(k)$ and the eigenvalues make this null space non-trivial by rendering $\mathbf{W}(k)$ singular. Hence, computation of the eigenvectors is equivalent to computation of the null space of a matrix. To this end, the singular value decomposition (SVD) method is most effective. Any matrix $\mathbf{A} \in \mathbb{C}^{m \times n}$ can be decomposed in terms of unitary matrices $\mathbf{U}$ and $\mathbf{V}$ and diagonal matrix $\mathbf{S}$

as $\mathbf{A} = \mathbf{USV}^H$, where H in the superscript denotes the Hermitian conjugate [42]. $\mathbf{S}$ is the matrix of singular values. For singular matrices, one or more of the singular values will be zero and the required property of the unitary matrix $\mathbf{V}$ is that the columns of $\mathbf{V}$ that correspond to zero singular values (zero diagonal elements of $\mathbf{S}$) are the elements of the null space of $\mathbf{A}$. The SVD again can be performed by any standard subroutine (e.g. xGESVD group of LAPACK).

3.6.2 Method 2: Linearization of PEP

In this method the PEP is linearized as

$$\mathbf{A}z = \lambda \mathbf{B}z\,, \quad \mathbf{A}, \mathbf{B} \in \mathbb{C}^{pN_v \times pN_v} \tag{3.22}$$

where

$$\mathbf{A} = \begin{bmatrix} 0 & \mathbf{I} & 0 & \cdots & 0 \\ 0 & 0 & \mathbf{I} & \cdots & 0 \\ \vdots & \vdots & \ddots & \ddots & \vdots \\ \vdots & \vdots & \ddots & \ddots & \mathbf{I} \\ -\mathbf{A}_0 & -\mathbf{A}_1 & \mathbf{A}_2 & \cdots & -\mathbf{A}_{p-1} \end{bmatrix}, \mathbf{B} = \begin{bmatrix} \mathbf{I} & & & & \\ & \mathbf{I} & & & \\ & & \ddots & & \\ & & & \mathbf{I} & \\ & & & & -\mathbf{A}_p \end{bmatrix}, \tag{3.23}$$

and the relation between x and z is given by $z = (x^T, \lambda x^T, \ldots, \lambda^{p-1} x^T)^T$. $\mathbf{B}^{-1}\mathbf{A}$ is a block companion matrix of the PEP. The generalized eigenvalue problem of Equation (3.22) can be solved by the QZ algorithm, the iterative method, the Jacobi–Davidson method or the rational Krylov method. Each one of these has its own advantages and deficiencies, however, the QZ algorithm is the most powerful method for small to moderate sized problems, and is employed in the subroutines available in LAPACK (xGGEV and xGGES group).

In both of these methods, an eigenvalue solver is employed, where for the QZ algorithm the cost of computation is $\sim 30n^3$ and an extra $\sim 16n^3$ for eigenvector computation (n is the order of the matrix). Since, the order of the companion matrix in the second method is three times that of the first method, the cost is 27 times more, which is significant as this computation is to be performed $N \times M$ times.

The PEP admits $N_v \times p$ eigenvalues and p eigenvectors. If both $\mathbf{A}_0$ and $\mathbf{A}_p$ are singular the problem is potentially ill-posed. Theoretically, the solutions might not exist or might not be unique. Computationally, the computed solutions may be inaccurate. If one, but not both, $\mathbf{A}_0$ and $\mathbf{A}_p$ is singular, the problem is well posed, but some of the eigenvalues may be zero or infinite, and caution should be exercised in rejecting those roots.

There are advantages and disadvantages of both methods. In the first method, the determinant of the wave matrix needs to be formed, which for large N_v is too difficult to obtain. In this case, resorting to the second method

is advantageous as it obviates the necessity for obtaining the lengthy expressions for α_i in Equation (3.21). However, in the second method, there is no control over the eigenvalues, as we might be interested sometimes in separating the forward propagating wavenumbers (for the formulation of throw-off elements). In this case, the first method is the only option.

The existing 2-D SFE formulation has its own share of shortcomings. The layer elements of Rizzi [43] were formed using Helmholtz decomposition of the displacement field, which generates two independent Helmholtz equations. After obtaining the FWD solutions of the Helmholtz potentials, the FWD representations of the displacement field were obtained by expressing them in terms of the potentials. However, for anisotropic materials there is no guarantee that these potentials will exist and thus a general approach in terms of direct solution for the displacement field is necessary. These are discussed in great detail in Chapter 6. Next, we will use this procedure to demonstrate the formulation of SFEs for isotropic 1-D waveguides.

3.7 Spectral Element Formulation for Isotropic Material

In this section, spectral elements are formulated for isotropic homogeneous one-dimensional structures using the previously described methods.

3.7.1 Spectral Element for Rods

The homogeneous form of the governing equation for an isotropic homogeneous rod (with density ρ and modulus E) is

$$\frac{\partial^2 u}{\partial t^2} = c^2 \frac{\partial^2 u}{\partial x^2}\,, \tag{3.24}$$

where $u = u(x,t)$ is the axial displacement and $c^2 = E/\rho$ is the square of the wave speed in the material. The governing equation is supplemented by the force (natural) boundary condition

$$F(x,t) = AE\frac{\partial u}{\partial x}\,, \tag{3.25}$$

where A is the cross-sectional area of the rod and $F(x,t)$ is the axial force. The displacement (essential) boundary condition is the specification of the displacement u at any value of x. It should be noted that only homogeneous initial conditions can be tackled with the present method, *i.e.* initial displacement and velocity are zero.

Assuming a solution of the form

$$u(x,t) = \sum_{n=1}^{N} \hat{u}(x,\omega_n) e^{-j\omega_n t}\,, \tag{3.26}$$

time dependency is replaced by parameter ω_n. The summation is carried out up to the Nyquist frequency, ω_N. Substituting solution (3.26) in (3.24), the reduced governing ordinary differential equation becomes

$$c^2 \frac{d^2\hat{u}}{dx^2} + \omega_n^2 \hat{u} = 0\,, \tag{3.27}$$

whose solution is of the form $u_\circ e^{-jkx}$. On substitution in Equation (3.27) the discretized form of the governing equation becomes

$$(-c^2k^2 + \omega_n^2)u_\circ = 0\,, \tag{3.28}$$

which is the PEP for this model. As the equation suggests, $N_v = 1$ and $p = 1$ in this case. The wavenumber can be computed trivially in this case as $k_n = \pm\omega_n/c$ and for both values, wave amplitude can be taken as 1. Thus, the complete solution is

$$\hat{u}(x, \omega_n) = C_1 e^{-jk_n x} + C_2 e^{+jk_n x}\,, \tag{3.29}$$

where C_1 and C_2 are coefficients to be determined. These coefficients are dependent on the displacement and/or force boundary conditions.

Considering an element of length L, with nodes at $x = x_1$ and $x = x_2$, ($|x_1 - x_2| = L$), the unknown constants can be expressed in terms of the nodal displacements $\hat{u}_1 = \hat{u}(x_1, \omega_n)$ and $\hat{u}_2 = \hat{u}(x_2, \omega_n)$ as

$$\begin{Bmatrix} \hat{u}_1 \\ \hat{u}_2 \end{Bmatrix} = \begin{bmatrix} e^{-jk_n x_1} & e^{+jk_n x_1} \\ e^{-jk_n x_2} & e^{+jk_n x_2} \end{bmatrix} \begin{Bmatrix} C_1 \\ C_2 \end{Bmatrix}\,, \tag{3.30}$$

where the matrix involved is represented as $\mathbf{T}_1$.

Similarly, the force in the frequency domain, $\hat{F}(x, \omega_n)$ can be evaluated at x_1 and x_2 where the nodal forces are

$$\hat{F}_1 = -\hat{F}(x_1, \omega_n)\,, \hat{F}_2 = +\hat{F}(x_2, \omega_n)\,. \tag{3.31}$$

These forces are related to the unknown constants by

$$\begin{Bmatrix} \hat{F}_1 \\ \hat{F}_2 \end{Bmatrix} = AE(jk_n) \begin{bmatrix} e^{-jk_n x_1} & -e^{+jk_n x_1} \\ -e^{-jk_n x_2} & e^{+jk_n x_2} \end{bmatrix} \begin{Bmatrix} C_1 \\ C_2 \end{Bmatrix}\,, \tag{3.32}$$

where the matrix involved is represented as $\mathbf{T}_2$. Thus, the nodal forces are related to the nodal displacements by

$$\begin{Bmatrix} \hat{F}_1 \\ \hat{F}_2 \end{Bmatrix} = \mathbf{T}_2 {\mathbf{T}_1}^{-1} \begin{Bmatrix} \hat{u}_1 \\ \hat{u}_2 \end{Bmatrix}\,, \tag{3.33}$$

Hence, the dynamic stiffness matrix (DSM) for the rod at frequency ω_n is $\mathbf{D}_{SFEM} = \mathbf{T}_2 {\mathbf{T}_1}^{-1}$. In comparison, the DSM for conventional FEM will be $\mathbf{D}_{FEM} = \mathbf{K} - {\omega_n}^2\mathbf{M}$, where $\mathbf{K}$ and $\mathbf{M}$ are the stiffness and mass matrices, respectively. If these two DSMs are compared, it is found that in the limit of infinitely many finite elements $\mathbf{D}_{FEM} \to \mathbf{D}_{SFEM}$ [9].

3.7.2 Spectral Element for Beams

According to the first-order shear deformation (Timoshenko beam) theory, the governing equations are

$$\begin{aligned} GA\frac{\partial}{\partial x}\left[\frac{\partial w}{\partial x}-\phi\right] &= \rho A\ddot{w}\,, \\ EI\frac{\partial^2\phi}{\partial x^2}+GA\left[\frac{\partial w}{\partial x}-\phi\right] &= \rho I\ddot{\phi}\,, \end{aligned} \tag{3.34}$$

where $w(x,t)$ and $\phi(x,t)$ are the transverse displacement and rotation of the mid-plane of the beam, G is the shear modulus and I is the moment of inertia of the cross-section of the beam. These equations are supplemented by the boundary conditions

$$\text{specify } w \text{ or } V = GA\left[\frac{\partial w}{\partial x}-\phi\right] \quad \text{and} \quad \text{specify } \phi \text{ or } M = EI\frac{\partial \phi}{\partial x}\,, \tag{3.35}$$

where V is the shear force and M is the bending moment. Assuming a solution of the form

$$w(x,t) = w_\circ e^{j(kx-\omega_n t)}\,, \phi = \phi_\circ e^{j(kx-\omega_n t)}\,, \tag{3.36}$$

and substituting them back in Equation (3.34), the PEP becomes

$$\left\{ k^2 \underbrace{\begin{bmatrix} GA & 0 \\ 0 & EI \end{bmatrix}}_{\mathbf{A}_2} + k \underbrace{\begin{bmatrix} 0 & -jGA \\ jGA & 0 \end{bmatrix}}_{\mathbf{A}_1} + \underbrace{\begin{bmatrix} -\rho A{\omega_n}^2 & 0 \\ 0 & GA-\rho I{\omega_n}^2 \end{bmatrix}}_{\mathbf{A}_\circ} \right\} \begin{Bmatrix} w_\circ \\ \phi_\circ \end{Bmatrix} = 0\,, \tag{3.37}$$

where the unknowns are k, $w_\circ$ and $\phi_\circ$. Thus, in this case, the order of the matrix polynomial p is 2 and $N_v = 2$. Thus, there are four eigenvalues (k) and eigenvectors ($\{w_\circ\ \phi_\circ\}$). The determinant of the matrix polynomial suggests that the roots are complex conjugate. Solving by any of the methods outlined previously, the eigenvectors are arranged in a matrix $\mathbf{R}$, so that

$$\left\{ {k_p}^2\mathbf{A}_2 + k_p\mathbf{A}_1 + \mathbf{A}_\circ \right\} \begin{Bmatrix} R_{1p} \\ R_{2p} \end{Bmatrix} = 0\,. \tag{3.38}$$

The complete solution at frequency ω_n is now written as

$$\begin{Bmatrix} \hat{w}(x,\omega_n) \\ \hat{\phi}(x,\omega_n) \end{Bmatrix} = \sum_{m=1}^{4} C_m \begin{Bmatrix} R_{1m} \\ R_{2m} \end{Bmatrix} e^{-jk_m x}\,, \tag{3.39}$$

where C_m are the unknown coefficients to be determined from the boundary conditions. Evaluating Equation (3.39) at the nodes, $x = x_1$ and $x = x_2$, the $\mathbf{T}_1$ matrix is formed as

$$\mathbf{T}_1 = \begin{bmatrix} R_{11}e^{-jk_1x_1} & R_{12}e^{-jk_2x_1} & R_{13}e^{-jk_3x_1} & R_{14}e^{-jk_4x_1} \\ R_{21}e^{-jk_1x_1} & R_{22}e^{-jk_2x_1} & R_{23}e^{-jk_3x_1} & R_{24}e^{-jk_4x_1} \\ R_{11}e^{-jk_1x_2} & R_{12}e^{-jk_2x_2} & R_{13}e^{-jk_3x_2} & R_{14}e^{-jk_4x_2} \\ R_{21}e^{-jk_1x_2} & R_{22}e^{-jk_2x_2} & R_{23}e^{-jk_3x_2} & R_{24}e^{-jk_4x_2} \end{bmatrix} . \tag{3.40}$$

Similarly, the forces and moments are evaluated at the nodes as

$$\hat{V}_1 = -V(x_1)\,, \hat{V}_2 = +V(x_2)\,, \hat{M}_1 = -M(x_1)\,, \hat{M}_2 = +M(x_2)\,, \tag{3.41}$$

which can be expressed in terms of C_m by the $\mathbf{T}_2$ matrix where

$$\begin{aligned} T_2(1,m) &= -GA(-jk_mR(1,m) - R(2,m)) \\ T_2(2,m) &= -EI(-jk_m)R(2,m) \\ T_2(3,m) &= +GA(-jk_mR(1,m) - R(2,m)) \\ T_2(4,m) &= +EI(-jk_m)R(2,m)\,. \end{aligned} \tag{3.42}$$

Once these two matrices are obtained, $\mathbf{D}_{SFEM}$ is formed as $\mathbf{T}_2{\mathbf{T}_1}^{-1}$.

In this chapter, the various solution techniques for wave propagation problems are highlighted. The general framework of SFEM is presented in detail, which is applicable to both 1-D and 2-D waveguides. Methods for obtaining the wavenumbers and wave amplitudes are presented, which are then utilized to derive SFE for isotropic waveguides. The procedure forms the basis for all subsequent element formulation discussed in this book.

4

Wave Propagation in One-dimensional Anisotropic Structures

In this section, first, wave propagation in elementary laminated composite beams is discussed. The main objective is to bring out the effect of stiffness and inertial coupling on the overall wave response behavior. Next, the same is discussed for higher order composite beams. Here, the effect of lateral contraction is also introduced. The method of treating various damping schemes is addressed. The last part of this chapter deals with the spectral element formulation of layered composite tube. A number of numerical examples are provided to highlight the wave behavior. For many examples, comparisons of spectral solutions with regular FEM are provided.

4.1 Wave Propagation in Laminated Composite Thin Rods and Beams

The effect of impact on laminated composite structures is a crucial issue, which researchers have tried to address with increasing emphasis. The main reason is that the way these laminated fiber reinforced structures are constructed contributes to high ratios of longitudinal to lateral elastic moduli, and in addition, they have significant layer-wise anisotropy due to ply orientations. One of the critical aspects is that the steep and discontinuous bending stress gradient at the ply interfaces may cause eventual delamination or de-bonding of the layers, thus putting the structural integrity in question. Starting from manufacturing, and throughout their design life, these structures are vulnerable to highly transient loading such as tool drop and other kinds of impact. These loadings have very small duration (μs range). Hence, the energy of the system is confined over a large frequency band, exciting all higher order modes. Other than local damage, these disturbances generate stress waves that propagate through the structure. Also, an initial compressive pulse can develop tensile stresses due to the effects of local inhomogeneity [44]. The incident stress waves interact with the joints and boundaries and give rise to totally different types of waves. In addition, the responses become even more complicated if

there is cross-sectional asymmetry due to composite ply stacking, which gives rise to axial–flexural coupling. Therefore, an efficient computational tool becomes necessary to study the effect of ply orientation on the dynamic response and the effect of the exciting frequency range on the propagation of coupled axial–flexural waves. SFEs are aimed towards this study.

The layer-wise construction of fiber reinforced composite beam has the great advantage of allowing the embedding of different functional materials, such as piezoelectric ceramic, relaxor and anti-ferroelectric thin films, magnetostrictive plate strips and particle layers mixed with matrix [45], [46]. Such configurations necessarily lead to cross-sectional asymmetry. The axial–flexural coupling due to asymmetric construction across the thickness of the beam or discontinuities in some layers, may give rise to additional progressive waves, which are unlikely in a beam made up of homogeneous material. There are very few reports available that consider the axial–flexural coupling in the dynamics of laminated beams.

For laminated composite beams, it has been well established that shear deformation and rotary inertia play a key role in the prediction of responses. In this regard, Kant and Marur [47] have shown the effects of shear deformation introduced by higher order refined theory on the transient response of laminated composite beams. However, these effects are dependent on length-to-depth ratio (L/h) of the beam. As seen in the work of Chandrashekhara *et al.*, [48], first-order shear deformation theory (FSDT) including rotary inertia, and Euler–Bernoulli theory (EBT) produce identical results for a slender beam ($L/h > 100$). In addition, Bhimaraddi [49] has derived one perturbation solution, which shows that the error in the first natural frequency predicted by EBT for cross-ply beams with $L/h > 20$ is well within 5% compared to that predicted by parabolic shear deformation (PSD) theory. In this chapter, first the spectral element is derived, based on EBT with rotary inertia neglected. The wave propagation analysis of thick beams and connected members are presented in Section 4.6.

4.1.1 Governing Equations and PEP

Considering EBT for a general laminated composite thin beam, the axial and transverse displacement field can be expressed as

$$u(x,y,z,t) = u^o(x,t) - zw(x,t)_{,x} \ , \qquad w(x,y,z,t) = w(x,t) \ , \tag{4.1}$$

where u^o and w are the axial and transverse displacement of the reference plane, respectively (as shown in Figure 4.1) and z is measured from the reference plane. The layer-wise constitutive law is defined as

$$\sigma_{xx} = \bar{Q}_{11}\epsilon_{xx} \ , \tag{4.2}$$

where σ_{xx} and ϵ_{xx} are the stress and strain in the X direction. The expression for $\bar{Q}_{11}$ as a function of ply fiber angle θ is given by

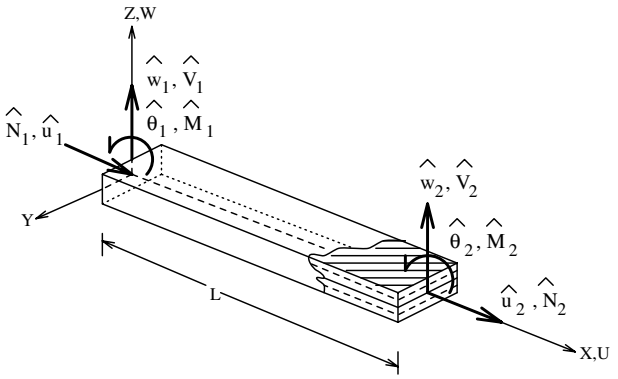

Fig. 4.1. Coordinate system and degrees of freedom for the spectral element

$$\bar{Q}_{11} = Q_{11}cos^4\theta + Q_{22}sin^4\theta + 2\left(Q_{12} + 2Q_{66}sin^2\theta cos^2\theta\right) \ , \tag{4.3}$$

where Q_{ij} are the orthotropic elastic coefficients for the individual composite ply and can be found in [50]. The strain energy and the kinetic energy are defined as

$$S = \frac{1}{2}\int \sigma_{xx}\epsilon_{xx}d\upsilon \ , \qquad \Gamma = \frac{1}{2}\int \rho(\dot{u^o}^2 + \dot{w}^2)d\upsilon \ , \tag{4.4}$$

where $\dot{(\ )}$ denotes derivative with respect to time and ρ is the layer-wise density.

Applying Hamilton's principle, the governing differential equations are obtained, and can be expressed as

$$\rho A\ddot{u^o} - A_{11}u^o{}_{,xx} + B_{11}w_{,xxx} = 0 \ , \tag{4.5}$$

$$\rho A\ddot{w} - B_{11}u^o{}_{,xxx} + D_{11}w_{,xxxx} = 0 \tag{4.6}$$

and the force boundary conditions are obtained as

$$A_{11}u^o{}_{,x} - B_{11}w_{,xx} = N_x \ , \tag{4.7}$$

$$B_{11}u^o{}_{,xx} - D_{11}w_{,xxx} = V_x \ , \tag{4.8}$$

$$-B_{11}u^o{}_{,x} + D_{11}w_{,xx} = M_x \ , \tag{4.9}$$

where

$$[A_{11}, B_{11}, D_{11}] = \int_{-h/2}^{+h/2} \bar{Q}_{11}\left[1, z, z^2\right] b\, dz \ , \tag{4.10}$$

h is the depth of the beam, b is the layer width and A is the cross-sectional area of the beam. N_x, V_x and M_x are the axial force, shear force and bending moment, respectively. The governing differential Equations (4.5) and (4.6)

represent a system of coupled linear PDEs, which by virtue of the assumed displacement field

$$u^o(x,t) = \sum_{n=1}^{N} \hat{u}(x,\omega_n) e^{i\omega_n t} = \sum_{n=1}^{N} \left(\tilde{u}_p e^{-ik_p x}\right) e^{i\omega_n t} \,, \tag{4.11}$$

$$w(x,t) = \sum_{n=1}^{N} \hat{w}(x,\omega_n) e^{i\omega_n t} = \sum_{n=1}^{N} \left(\tilde{w}_p e^{-ik_p x}\right) e^{i\omega_n t} \,, \tag{4.12}$$

becomes a PEP as

$$\begin{aligned} &\big(k_p^4 \begin{bmatrix} 0 & 0 \\ 0 & D_{11} \end{bmatrix} + k_p^3 \begin{bmatrix} 0 & -jB_{11} \\ jB_{11} & 0 \end{bmatrix} \\ &+k_p^2 \begin{bmatrix} A_{11} & 0 \\ 0 & 0 \end{bmatrix} + \begin{bmatrix} -\rho A\omega^2 & 0 \\ 0 & -\rho A\omega^2 \end{bmatrix} \big) \begin{Bmatrix} \tilde{u}_p \\ \tilde{w}_p \end{Bmatrix} = \begin{Bmatrix} 0 \\ 0 \end{Bmatrix} \end{aligned} \tag{4.13}$$

where the determinant of the matrix gives the required spectrum and dispersion relation. Once the solutions k_p and the pairs $\{\tilde{u}_p, \tilde{w}_p\}$ are obtained for each p the explicit form of the solution is

$$\begin{Bmatrix} \hat{u}(x,\omega_n) \\ \hat{w}(x,\omega_n) \end{Bmatrix} = \sum_{m=1}^{6} C_m \begin{Bmatrix} R_{1m} \\ R_{2m} \end{Bmatrix} e^{-jk_m x} \,. \tag{4.14}$$

4.1.2 Spectrum and Dispersion Relations

The main objective here is to bring out the effect of coupling on wave behavior. The maximum axial–flexural coupling that one gets from such natural ply-stacking (other than the inclusion of any other materials in the form of thin films, fibers or particle layers) is when the cross-plies and 0^o plies are stacked in separate groups. A generalization of the effect of axial–flexural coupling gives some valuable insights, when the spectrum relation (Figure 4.2) and dispersion relation (Figure 4.3) are studied. AS/3501-6 graphite–epoxy plies (thickness of each layer 1.0 mm) with three stacking sequences $[0_{10}]$ ($r = B_{11}^2/(A_{11}D_{11}) = 0.0$), $[0_5/30_2/60_3]$ ($r = 0.312$) and $[0_5/90_5]$ ($r = 0.574$) are considered. In Figure 4.2, it can be observed that, corresponding to axial mode (Mode 1) and flexural modes (Mode 2 and 3), the wavenumbers increase in magnitude for increasing coupling. However, this increase in Mode 2 (propagating component) is more than that in Mode 3 (evanescent component). Figure 4.3 also shows the variation of group speed $C_g = d\omega/dk_j$ normalized with the parameter $C_o = \sqrt{E/\rho}$ (speed in aluminum). From these plots, it is clear that the axial speed is reduced by more than 26% due to the presence of asymmetry arising from cross-ply stacking in groups. Also at around 50 kHz, the flexural speed of propagation is reduced by 42% for maximum coupling.

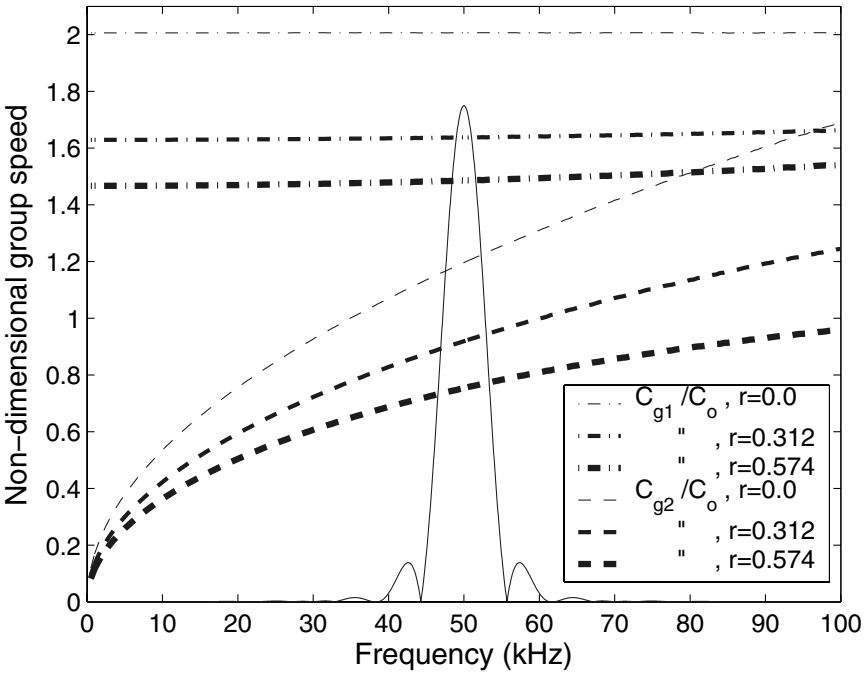

Fig. 4.2. Spectrum relation for various axial–flexural couplings — frequency amplitude spectrum of a modulated sinusoidal pulse

4.2 Spectral Element Formulation

As mentioned in the earlier chapters, two special cases arise in the dynamics of connected beams. One is the finite length beam that is connected at both ends. The other is when the member extends to infinity. This will be referred to as a single node or throw-off element. The behavior of these are fundamentally different and so will be treated separately. Since the elements will be derived in the frequency domain, all the conventional nodal measures such as nodal displacement, strain, stress, force, *etc.*, will correspond to their frequency domain counterparts, *i.e.,* spectral amplitudes.

4.2.1 Finite Length Element

A 2-node finite element of length L with nodal displacements and forces as shown in Figure 4.1 is considered. Using the explicit expression for displacement field given by Equation (4.14), the element nodal displacement vector $\hat{\mathbf{u}}^{\mathrm{e}}$ with entries $\hat{u}_1 = \hat{u}(0,\omega_n)$, $\hat{w}_1 = \hat{w}(0,\omega_n)$, $\hat{\theta}_1 = \hat{w}_{,x}(0,\omega_n)$, $\hat{u}_2 = \hat{u}(L,\omega_n)$, $\hat{w}_2 = \hat{w}(L,\omega_n)$ and $\hat{\theta}_2 = \hat{w}_{,x}(L,\omega_n)$ is expressed in terms of the wave coefficient vector $\tilde{\mathbf{u}}$ with entries $\tilde{u}_j$, $\tilde{w}_j$ as

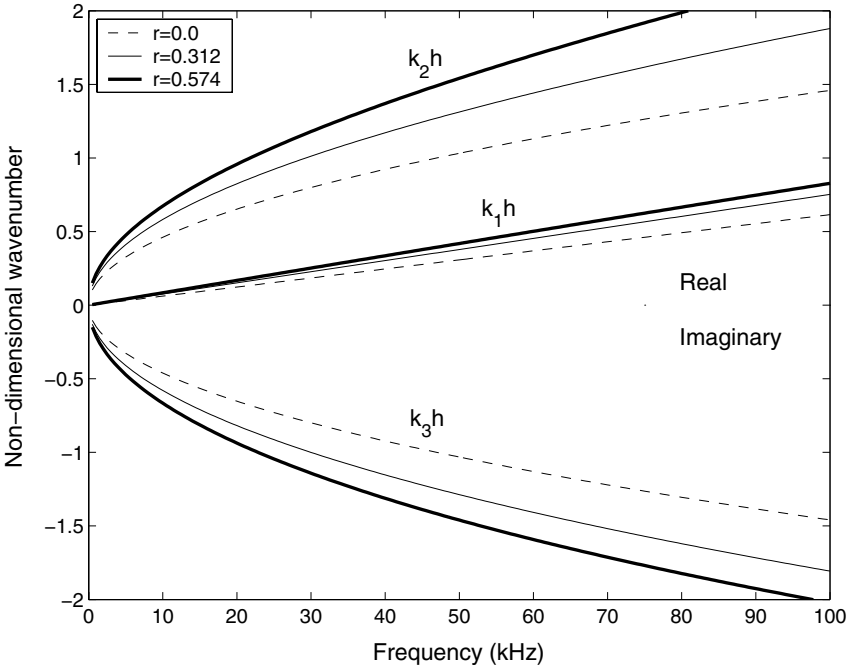

Fig. 4.3. Dispersion relation for various axial–flexural couplings

$$\hat{\mathbf{u}}^{\mathrm{e}} = \hat{\mathbf{T}}_{\mathbf{1}}\tilde{\mathbf{u}} \,, \tag{4.15}$$

where $\hat{\mathbf{u}}^{\mathrm{e}} = \{\hat{u}_1\ \hat{w}_1\ \hat{\theta}_1\ \hat{u}_2\ \hat{w}_2\ \hat{\theta}_2\}^T$ and $\tilde{\mathbf{u}} = \{\tilde{u}_1\ \tilde{u}_2\ \tilde{w}_3\ \tilde{w}_4\ \tilde{w}_5\ \tilde{w}_6\}^T$. $\hat{\mathbf{T}}_{\mathbf{1}}$ is a 6×6 non-symmetric, non-singular matrix, which is a function of frequency, material properties and dimensions of the element. This matrix represents the local wave characteristic of the displacements.

Next, using the expressions for force boundary condition from Equations (4.7–4.9), the nodal forces are related to the wave coefficients $\tilde{u}_j$ and $\tilde{w}_j$ through the following force boundary equations:

$$\begin{aligned} &\hat{N}_1 = -\hat{N}_x(0,\omega_n)\,, \qquad \hat{V}_1 = -\hat{V}_x(0,\omega_n)\,, \qquad \hat{M}_1 = -\hat{M}_x(0,\omega_n)\,, \\ &\hat{N}_1 = \hat{N}_x(L,\omega_n)\,, \qquad \hat{V}_1 = \hat{V}_x(L,\omega_n)\,, \qquad \hat{M}_1 = \hat{M}_x(L,\omega_n)\,. \end{aligned} \tag{4.16}$$

In matrix notation, this can be written as

$$\hat{\mathbf{f}}^{\mathrm{e}} = \hat{\mathbf{T}}_{\mathbf{2}}\tilde{\mathbf{u}} \,, \tag{4.17}$$

where the element nodal force vector $\hat{\mathbf{f}} = \{\hat{N}_1\ \hat{V}_1\ \hat{M}_1\ \hat{N}_2\ \hat{V}_2\ \hat{M}_2\}^T$. The matrix $\hat{\mathbf{T}}_{\mathbf{2}}$ has properties that are similar to $\hat{\mathbf{T}}_{\mathbf{1}}$, and it represents the local wave characteristic of forces. Combining Equations (4.15) and (4.17), the equilibrium equation is obtained as

$$\hat{\mathbf{f}}^{\mathrm{e}} = \hat{\mathbf{T}}_{\mathbf{2}}\hat{\mathbf{T}}_{\mathbf{1}}^{-1}\hat{\mathbf{u}}^{\mathrm{e}} = \hat{\mathbf{K}}^{\mathrm{e}}\hat{\mathbf{u}}^{\mathrm{e}} \,, \tag{4.18}$$

where $\hat{\mathbf{K}}^{\mathrm{e}}$ is the symmetric dynamic stiffness matrix for an unsymmetric composite beam element as a complex function of frequency.

4.2.2 Throw-off Element

Unlike the conventional finite element, here we derive a special case when the beam is very long, and application of any transient load at any location causes no secondary disturbances other than incident waves departing that location. This simulates a condition wherein the boundaries are at such a distance that the effect of reflected waves becomes negligible due to attenuation throughout their long traversal, and do not reach the location under consideration within the time of observation. In other words, a throw-off element is a non-resonant single node element that acts as a conduit to allow the propagation of trapped energy out of the system. Considering only the incident part of the displacement field given by Equation (4.14), the field variables for the throw-off element can be written as

$$\begin{Bmatrix} \hat{u}(x,\omega_n) \\ \hat{w}(x,\omega_n) \end{Bmatrix} = \begin{bmatrix} R_{11} & R_{13} & R_{15} \\ R_{21} & R_{23} & R_{25} \end{bmatrix} \begin{Bmatrix} \tilde{u}_1 e^{-ik_1 x} \\ \tilde{w}_3 e^{-ik_2 x} \\ \tilde{w}_5 e^{-ik_3 x} \end{Bmatrix} . \tag{4.19}$$

Using the same procedure as followed in the case of finite length element formulation in the previous subsection, a 3×3 symmetric dynamic stiffness matrix $\hat{\mathbf{K}}^{\mathrm{e}}$ as a complex function of frequency can be derived. An important property of the dynamic stiffness matrix is that the elements are always complex.

4.3 Numerical Results and Discussions

4.3.1 Impact on a Cantilever Beam

In order to study the quality of the response obtained from the SFE, the results are compared with the time domain FE results. For this purpose, a finite element model is employed where the element has the following mid-plane displacement field:

$$u^o(x,t) = C_1 + C_2 x \,, \qquad w(x,t) = C_3 + C_4 x + C_5 x^2 + C_6 x^3 \,, \tag{4.20}$$

which exactly satisfies the static part of the governing differential equations.

A cantilever beam as shown in Figure 4.4 is considered with length $L = 1.0$ m, width $b = 0.01$ m, depth $h = 0.01$ m, and made up of AS/3501-6 graphite–epoxy, having properties $E_1 = 144.48$ GPa, $E_2 = 9.632$ GPa, $G_{12} = 4.128$ GPa, $\nu_{12} = 0.3$, $\rho = 1389$ kg/m^3. The ply-stacking sequence used is $[0_5/90_5]$,

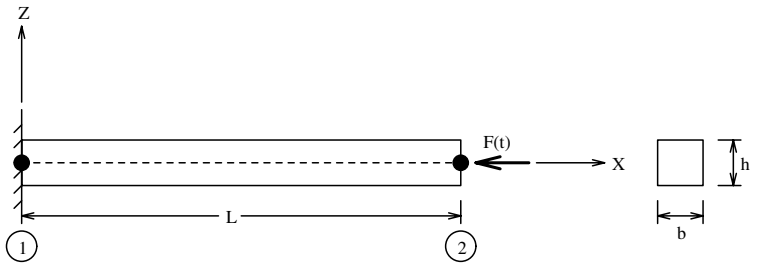

Fig. 4.4. A AS/3501-6 graphite–epoxy $[0_5/90_5]$ composite cantilever beam with an impact load at the tip

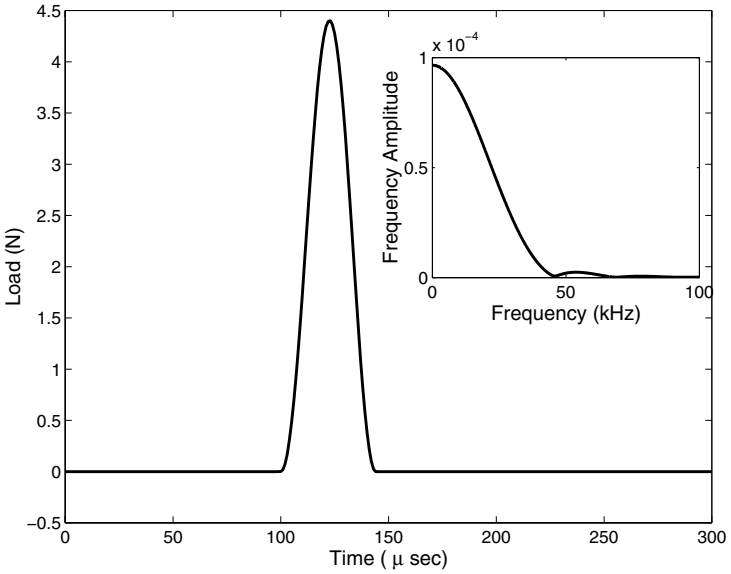

Fig. 4.5. Impact load history. Frequency spectrum of the load is shown in the inset

which gives a coupling factor $r = 0.574$. An impact load of 4.4 N and $50\,\mu$s duration shown in Figure 4.5 is considered. The figure shows that the load has a very high frequency content of about 50 kHz.

This impact load is first applied at the cantilever tip in the axial direction. In SFEM, the whole beam is considered as a single element, whereas in FEM, the domain is modeled with 1000 elements (overall system size 3000×6 where 6 is the bandwidth of the stiffness and mass matrix). The Newmark time integration scheme with a time step of $1\,\mu$s is adopted. Figure 4.6 shows a comparison of the axial tip velocities obtained from the SFEM and FEM. Next, the beam is impacted in the transverse direction at the tip and Figure 4.7 shows a comparison of the transverse tip velocities. For both cases, the plots show good agreement. From Figure 4.6, it is clear that the axial wave

propagates non-dispersively, while the flexural wave (shown in Figure 4.7) is dispersive. Figure 4.7 also shows that the response obtained by SFEM is slightly on the higher side. This may be attributed to the different damping schemes employed by SFEM and FEM. This aspect is studied in more detail in the next section.

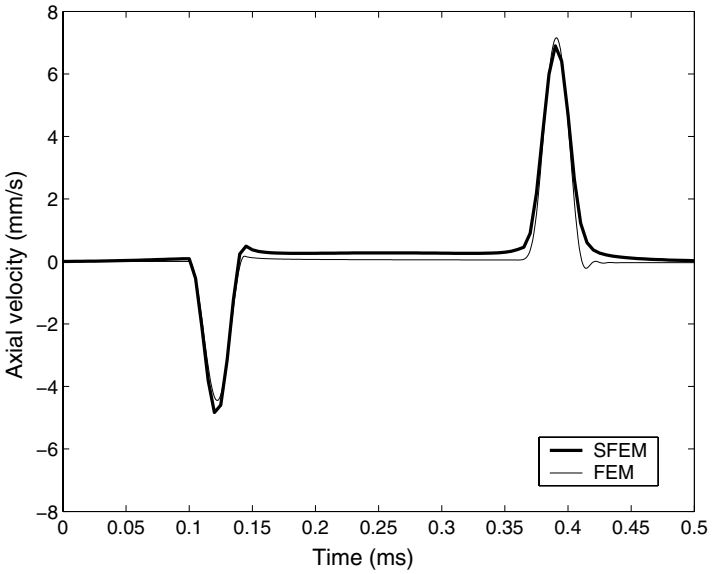

Fig. 4.6. Axial response at the cantilever tip due to axial tip load

4.3.2 Effect of the Axial–Flexural Coupling

One of the characteristics of an asymmetric composite beam is the presence of axial–flexural coupling. That is, an incident axial wave will give rise to a flexural wave and vice versa. The aim of the following example is to capture this behavior. In order to see this, it is required that the waves travel non-dispersively. Hence, for this purpose, a sinusoidally modulated pulse is allowed to propagate through an infinite beam shown in Figure 4.8.

The pulse is modulated at 50 kHz frequency. The frequency amplitude of this pulse has been plotted with firm line in Figure 4.2. From this figure, we see that this modulated pulse contributes zero energy at all frequencies except over the narrow frequency band centered at 50 kHz, at which the pulse is modulated. This center frequency is called the modulation frequency. Since the group speed and phase speed are functions of frequency, only the modulation frequency governs the propagation characteristics. This property of the pulse makes it almost non-dispersive even in a dispersive medium. The

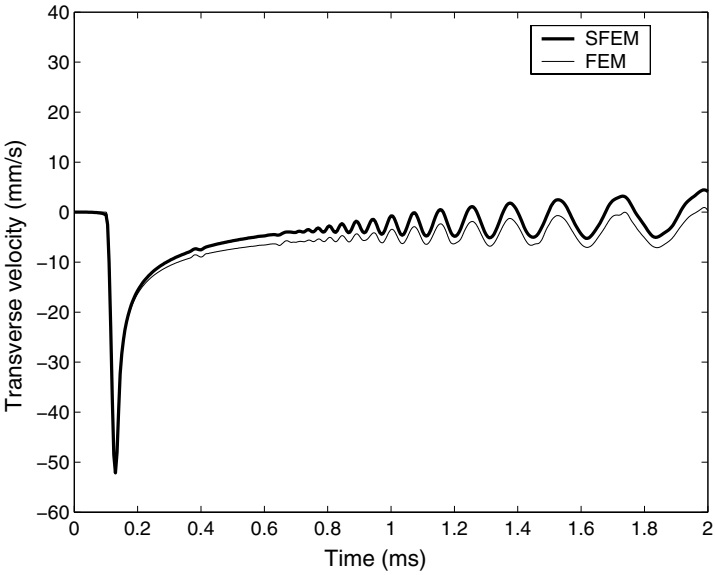

Fig. 4.7. Transverse response at the cantilever tip due to transverse tip load

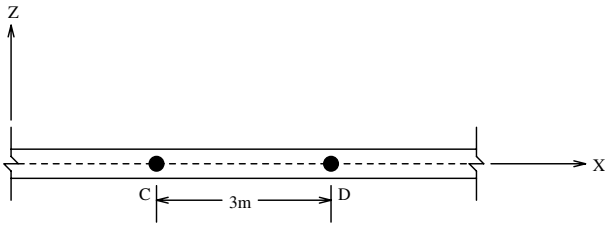

Fig. 4.8. AS/3501-6 graphite–epoxy beam with infinite span

infinite beam is modeled using two throw-off elements and one finite length element. Three ply-stacking sequences having coupling parameters $r = 0.0$, 0.312 and 0.574 (as used in Section 4.1.2) are considered. The modulated pulse is first applied in the axial direction at C. The axial and transverse velocity histories obtained at D, which is 3.0 m away from the application of load are shown in Figures 4.9(a) and 4.9(b), respectively. In Figure 4.9(a), the time shifts in the predominant axial mode response for increasing values of r can be attributed to the reduction in the axial group speed (C_{g_1} in Figure 4.2). Also, for $r = 0.574$, the effect of flexural mode induced in the axial response is clearly visible around 1.0 ms. The time of occurrence of this additional mode corresponds to the flexural group speed (C_{g_2}) in Figure 4.2 at 50 kHz, which is the modulation frequency of the applied load. Similarly, in Figure 4.9(b), the increasing effect of both the modes induced in the flexural response is visible for increasing values of r, and their times of occurrence

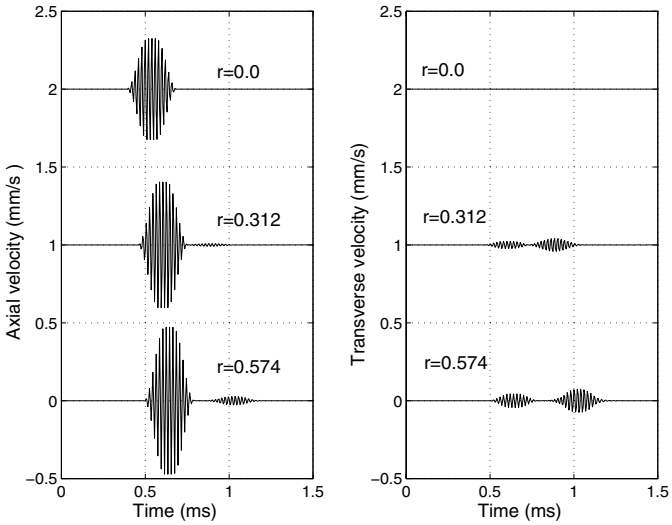

Fig. 4.9. (a) Axial response and (b) transverse response at D due to axial modulated pulse applied on the infinite beam at C

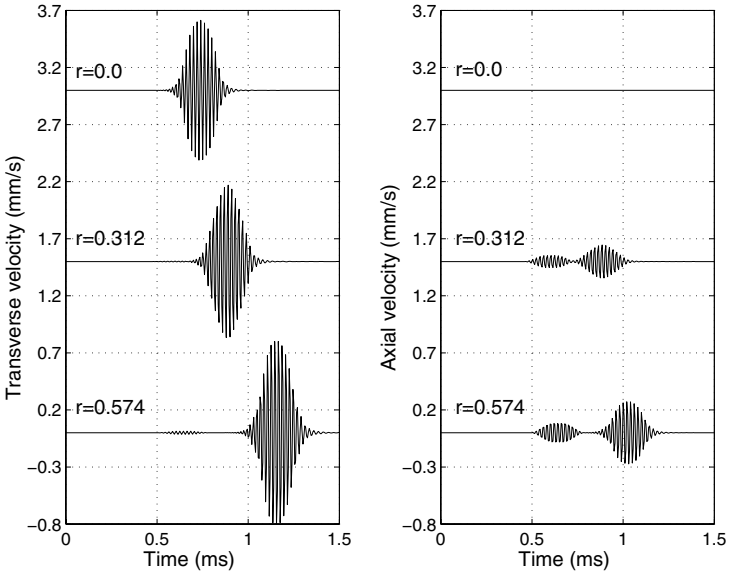

Fig. 4.10. (a) Transverse response and (b) axial response at D due to transverse modulated pulse applied on the infinite beam at C

resemble those in Figure 4.9(a). Next, the same modulated pulse is applied in the transverse direction on the infinite beam at C. The transverse and axial velocity histories at D are plotted in Figure 4.10(a) and 4.10(b), respectively. In Figure 4.10(a), it can be observed that the effect of the axial mode induced in the transverse response is of negligible order. Here, the time shifts in the flexural mode response for increasing values of r are greater than those in the axial mode response due to axial loading, as shown in Figure 4.9(a), which correlates the fact that for the chosen modulation frequency (50 kHz), the percentage reduction of flexural group speed (C_{g_2}) is nearly 10% more than that of axial group speed, as revealed from Figure 4.2. From Figure 4.10(b), for maximum value of coupling, two propagating pulses can be seen clearly. The first is due to the axial mode and the second is due to the flexural mode. It is seen that the magnitude of the flexural mode is slightly higher than that of the axial mode. A general trend observed from this example is that there is an increase in the magnitude of the responses for increasing values of r, and this is attributed to the reduction in the strength of the structure with more off-axis ply orientations. Hence, by using SFEM, the presence of the two simultaneously propagating spectram due to asymmetric ply orientations becomes tractable in both quantitative as well as qualitative forms.

4.3.3 Wave Transmission and Scattering Through an Angle-joint

Often in practice, we come across planar frame structures with complex geometry. Such structures are often used for space applications such as solar panels, antennas *etc.*, wherein a number of skeletal members are connected by rigid or flexible joints, thereby creating a complex structural network. The proposed SFEM can account for such situation with relative ease. In this example, we consider a rigid angle-joint with three composite members (Figure 4.11) to analyze the nature of reflected and transmitted waves through the joint. In particular, it will be interesting to observe how the dynamics of the system change with the change in joint angle. In addition, it is also important to know the effect of axial–flexural coupling on the overall response. The SFEM model has 0.5 m long segments on both sides of the joint along the x-axis, which are modeled with two finite length spectral elements. The rest of the semi-infinite segments are modeled with three throw-off elements. In FEM, these three semi-infinite segments are modeled with 950 elements each, while the segment AB is modeled with 100 elements. The length of each element is 1.0 cm. This gives an overall system size of 8994×9 in banded form.

Each member connected to the joint is made up of AS/3501-6 graphite–epoxy, as considered in the previous cases, and with ply-stacking sequence $[0_5/45_5]$. Here, the coupling factor $r = 0.213$. First of all, to validate the accuracy of the response obtained from SFEM, an impact load as considered earlier (Figure 4.5) is applied axially at A for joint angle $\phi = 30^o$. The axial velocity history at the same point A, is computed and compared with the FEM result, which is shown in Figure 4.12(a). Similarly, the same load is applied

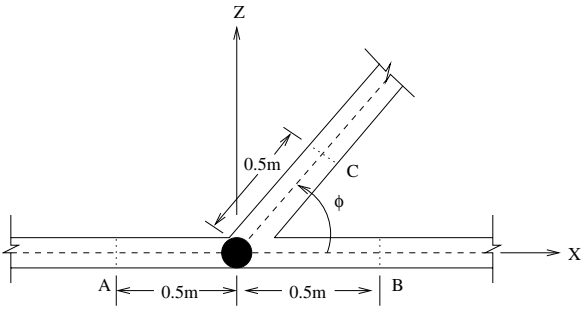

Fig. 4.11. Rigid angle-joint with AS/3501-6 graphite–epoxy composite members

transversely at A. The axial velocity history at the same point A is computed, and also compared with the FEM result, which is shown in Figure 4.12(b). In the above two cases, both results show good agreement.

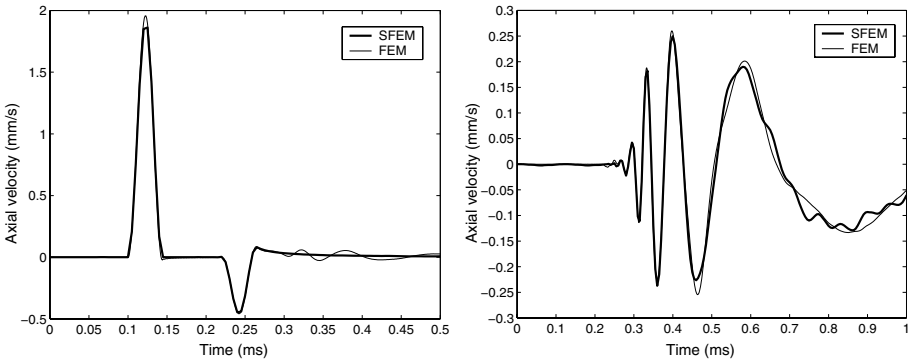

(a) (b)

Fig. 4.12. (a) Comparison of axial response at A, due to axial impact load applied at A. (b) Comparison of axial response at A, due to transverse impact load applied at A

To study the effect of axial–flexural coupling on the dynamic response, the same rigid joint (Figure 4.11) with an axial loading at point A, is considered as in the previous case. The angle of the rigid joint ϕ is taken as 45^o. The non-dimensional coupling parameter r is varied by using different ply-stacking sequences as taken before. In Figure 4.13(a), the axial velocity (normalized with $P_{max}c_L/A_{11}$) response at A and B (both are at the same distance of 0.5 m from the joint) is plotted. The figure shows that the reflected axial response at A, as well as the transmitted axial response at B, occur at the same time for a particular value of r. However, due to the decrease in the values of A_{11}, for increasing values of r, the axial speed of propagation decreases. As a result,

both responses occur at a later stage. A separation of 0.24 ms can be seen between responses due to unsymmetric cross-ply and the symmetric 0^o ply configurations. Also, an increasing level of dispersiveness becomes dominant after the initial peak, which can be considered as a contribution from Mode 2 and Mode 3, as discussed earlier. Figure 4.13(b) shows the plot of transverse velocity (normalized with $P_{max}c_L h^2/D_{11}$) response at A and B. Other than a similar time lag in the arrival of reflected and transmitted responses as observed in the case of axial propagation, the smoothness in the response curves disappears and their transient nature becomes significant for increasing values of r.

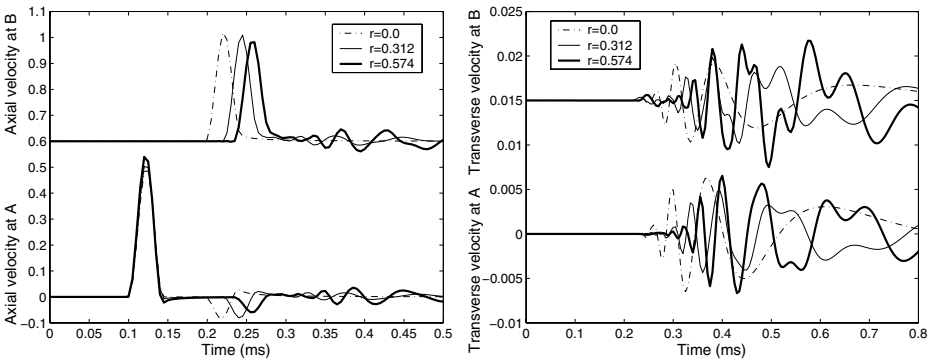

(a) (b)

Fig. 4.13. (a) Normalized axial velocity history and (b) normalized transverse velocity history at A and B (Figure 4.11), showing the reflection and transmission response through the rigid joint ($\phi = 45^o$) due to an axial impact load at A

These examples have shown the ease with which SFEM allows handling of the dynamics of complicated networks of connected beams. Unlike the conventional FE formulation, however, the length of the spectral element is not a limiting factor; each element is formulated exactly, irrespective of its length. This leads to a substantial reduction in the number of equations that are to be solved. The work presented in this section has mainly dealt with the behavior of elementary asymmetric composite beams, without the effects of shear deformation and rotary inertia. For this reason, the numerical investigation has been restricted to slender beams and frames with asymmetry. This is basically to avoid any appreciable deviation from the actual structural response.

It is seen from the numerical investigation that the main effect of asymmetric ply orientation is alteration of the spectrum and dispersion relations. It is found that the longitudinal wave mode (Mode 1) is least affected by asymmetry. However, the flexural wave modes (Mode 2 and 3) are most affected. That is, the flexural wave speed is greatly reduced (about 20%) due to asymmetry. The numerical studies have also shown that the results from the formulated

spectral element agree well with the established FEM. This study, through SFEM, has clearly brought out the changes that an asymmetric ply configuration can introduce to alter the dynamics of multiply connected composite beams.

Another big advantage of SFEM is that the solution has very little storage requirement compared to conventional FEM. In the actual computation of the angle joint, it has been found that the storage requirement for the formation of the matrices is approximately 2.05 KB for SFEM in contrast to 1.5MB for FEM. In the next section, higher order formulations to deal with coupled wave propagation in composite beams are developed.

4.4 Wave Propagation in Laminated Composite Thick Beams: Poisson's Contraction and Shear Deformation Models

In the last section we demonstrated the versatility of the spectral element approach in capturing the essential features of wave propagation in elementary composite beams. Very small system sizes were used for modeling highly asymmetric ply stacking sequences subjected to a forcing function having high frequency content. In this section, we extend this approach to study the wave propagation behavior in thick composite beams based on first-order shear deformation theory (FSDT). Such a formulation for thick isotropic rod and beam is available in the literature [51]. It was shown there that higher order isotropic waveguides introduce a pair of additional propagating modes (called propagating shear wave modes) above a cut-off frequency. It is of interest to know how such higher order effects influence the behavior of thick composite beams with an asymmetric ply-stacking sequence, giving rise to axial–flexural shear coupling over a wide frequency range of excitation. The present section will be devoted to capturing this special feature. In addition, a generalization of the approach towards the development of SFEMs, such as treatment of damping, distributed loading *etc.*, which were not addressed in the previous section, will be dealt with in detail in this section.

For thick beams, FSDT was first introduced by Timoshenko [52] (see also [53]). However, FSDT when used with FE, has its own limitations such as shear locking. Hence, it becomes difficult to adopt FSDT for thick as well as thin beams unless proper locking alleviation schemes are employed. To capture the shear deformation more accurately, higher order beam theories (HSDT) [54], [55], [56], [50] have been reported. In the finite element context, these HSDTs need additional degrees of freedom at element nodes. In transient dynamic analysis, this is a drawback because the system size increases in multiples of the number of effective nodes. Therefore, in conventional time domain FE analysis, the question of priority among accuracy and computational effort becomes important. In addition to this, other complexities due

to the mechanics of the composite play a role. Due to the high ratios of elastic moduli, prediction of error while applying different beam theories is not straightforward. The studies reported in [49], [57], [3] show that for thick composite beam with strong asymmetry in the ply-stacking sequence, errors due to EBT become significant. Comparative studies using FSDT and HSDT in the presence of asymmetric ply-stacking configuration are not available in the reported development. Although, for moderately thick composite beams (L/h up to 20) with symmetric ply-stacking sequence, they match well with 2-D plane-stress FE analysis [3].

In this section, FSDT is used, which includes the contribution of stiffness and inertial coupling, to study the characteristic wave propagation in asymmetrically stacked laminated composite beams. One of the important characteristic features of higher order waveguides is the presence of cut-off frequencies due to inherent shear constraints. That is, the shear constraints convert the evanescent flexural mode into propagating shear mode beyond the cut-off frequency. The appearance of higher order Lamb wave modes above certain cut-off frequencies have been studied for metallic beams [58], [9], [2], and for laminated composite plates [59]. In this chapter, the contribution of the contractional mode along with the shear mode is studied for different types of structural composites. Expressions for the cut-off frequencies in the shear and contractional mode in the presence of an asymmetric ply-stacking sequence are also derived.

4.4.1 Wave Motion in a Thick Composite Beam

The displacement field for the axial and transverse motion based on FSDT and thickness contraction [2] is given by

$$u(x,y,z,t) = u^o(x,t) - z\phi(x,t)\ , \quad w(x,y,z,t) = w(x,t) + z\psi(x,t) \tag{4.21}$$

where u and w are, respectively, the axial and transverse displacements at a material point. u^o and w^o are the beam axial and transverse displacement of the reference plane. ϕ is the curvature-independent rotation of the beam cross-section about the Y-axis. $\psi = \varepsilon_{zz}$ is the contraction/elongation parallel to the Z-axis (shown in Figure 4.14). Following conventional notation [50], the constitutive model for an orthotropic laminated composite beam can be expressed as

$$\begin{Bmatrix} \sigma_{xx} \\ \sigma_{zz} \\ \tau_{xz} \end{Bmatrix} = \begin{bmatrix} \bar{Q}_{11} & \bar{Q}_{13} & 0 \\ \bar{Q}_{13} & \bar{Q}_{33} & 0 \\ 0 & 0 & \bar{Q}_{55} \end{bmatrix} \begin{Bmatrix} \varepsilon_{xx} \\ \varepsilon_{zz} \\ \gamma_{xz} \end{Bmatrix} . \tag{4.22}$$

Using Hamilton's principle and Equations (4.21) and (4.22), the governing wave equations can be obtained as

$$\delta u:\ I_0\ddot{u}^o - I_1\ddot{\phi} - A_{11}u^o{}_{,xx} + B_{11}\phi_{,xx} - A_{13}\psi_{,x} = 0\ , \tag{4.23}$$

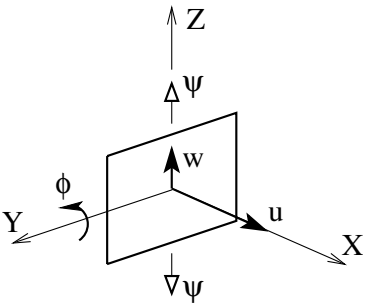

Fig. 4.14. Beam cross-section in the YZ plane and degrees of freedom

$$\delta\psi:\ I_2\ddot{\psi} + I_1\ddot{w} + A_{13}u^o{}_{,x} - B_{13}\phi_{,x} + A_{33}\psi - B_{55}\left(w_{,xx} - \phi_{,x}\right) - D_{55}\psi_{,xx} = 0\ , \tag{4.24}$$

$$\delta w:\ I_0\ddot{w} + I_1\ddot{\psi} - A_{55}\left(w_{,xx} - \phi_x\right) - B_{55}\psi_{,xx} = 0\ , \tag{4.25}$$

$$\delta\phi:\ I_2\ddot{\phi} - I_1\ddot{u}^o - A_{55}\left(w_{,x} - \phi\right) - B_{55}\psi_{,x} + B_{11}u^o{}_{,xx} - D_{11}\phi_{,xx} + B_{13}\psi_{,x} = 0\,. \tag{4.26}$$

The four associated force boundary conditions are

$$A_{11}u^\circ{}_{,x} - B_{11}\phi_{,x} + A_{13}\psi = N_x\ ,\ B_{55}\left(w_{,x} - \phi\right) + D_{55}\psi_{,x} = Q_x\ , \tag{4.27}$$

$$A_{55}\left(w_{,x} - \phi\right) + B_{55}\psi_{,x} = V_x\ ,\ -B_{11}u^\circ{}_{,x} + D_{11}\phi_{,x} - B_{13}\psi = M_x\ . \tag{4.28}$$

The stiffness coefficients which are functions of individual ply properties, ply orientation *etc.* and integrated over the beam cross-section, can be expressed as

$$\left[A_{ij}, B_{ij}, D_{ij}\right] = \sum_i \int_{z_i}^{z_{i+1}} \bar{Q}_{ij}\left[1, z, z^2\right] b dz\ , \tag{4.29}$$

which is a slightly generalized form of Equation (4.10). The coefficients associated with the inertial terms can be expressed as

$$\left[I_0, I_1, I_2\right] = \sum_i \int_{z_i}^{z_{i+1}} \rho\left[1, z, z^2\right] b dz\ . \tag{4.30}$$

In Equations (4.29) and (4.30), z_i and z_{i+1} are the Z-coordinate of bottom and top surfaces of the ith layer and b is the overall width of the beam. It can be noticed that for asymmetric ply stacking, all four modes; axial, flexural, shear and thickness contraction, are coupled with each other. This makes the problem cumbersome to solve accurately using an analytical approach for all boundary conditions. However, at this stage, different approximate methods can be used [57], which are computation intensive. Here we use the PEP technique to solve for the wavenumbers. Two cases are considered, one with thickness contraction mode and the other without.

4.4.2 Coupled Axial–Flexural Shear and Thickness Contractional Modes

For element formulation, a plane wave type solution is sought, where the displacement field, $\{\mathbf{u}\} = \{u^o\ ,\ \psi\ ,\ w\ ,\ \phi\}(x,t)$, can be written as

$$\{\mathbf{u}\} = \sum_{n=1}^{N} \{\tilde{u}\ ,\ \tilde{\psi}\ ,\ \tilde{w}\ ,\ \tilde{\phi}\}(x) e^{-j\omega_n t} = \sum_{n=1}^{N} \{\tilde{\mathbf{u}}(x)\} e^{-j\omega_n t}\,, \tag{4.31}$$

where ω_n is the circular frequency at the nth sampling point and N is the frequency index corresponding to the Nyquist frequency in FFT.

Substituting the assumed solution of the field variables in Equations (4.23)–(4.26), a set of ODEs is obtained for $\tilde{\mathbf{u}}(\mathbf{x})$. Since, the ODEs have constant coefficients, the solution is of the form $\{\tilde{\mathbf{u}}_\circ\} e^{-jkx}$, where k is the wavenumber and $\{\tilde{\mathbf{u}}_\circ\}$ is a vector of unknown constants, *i.e.*, $\{\tilde{\mathbf{u}}_\circ\} = \{u_\circ\ ,\ \psi_\circ\ ,\ w_\circ\ ,\ \phi_\circ\}$. Substituting the assumed form in the set of ODEs, a matrix–vector relation is obtained which gives the following characteristic equation

$$[W]\{\tilde{\mathbf{u}}_\circ\} = \mathbf{0}\,, \tag{4.32}$$

where $[W]$ is

$$\begin{bmatrix} A_{11}k^2 - I_\circ\omega_n^2 & jA_{13}k & 0 & I_1\omega_n^2 - B_{11}k^2 \\ -jA_{13}k & -k_I I_2\omega_n^2 + A_{33} + D_{55}k^2 & -I_1\omega_n^2 + B_{55}k^2 & -jB_{55}k + jB_{13}k \\ 0 & -I_1\omega_n^2 + B_{55}k^2 & A_{55}k^2 - I_\circ\omega_n^2 & -jA_{55}k \\ I_1\omega_n^2 - B_{11}k^2 & jB_{55}k - jB_{13}k & jA_{55}k & -I_2\omega_n^2 + D_{11}k^2 + A_{55} \end{bmatrix}. \tag{4.33}$$

According to the previous discussion, in this case, the order of the PEP, $p = 2$ and N_v (size of the $[W]$) is 4. Thus, there are eight eigenvalues altogether, which are the roots of the polynomial (called the spectrum relation) obtained from the singularity condition of $[W]$ as

$$Q_1 k^8 + Q_2 k^6 + Q_3 k^4 + Q_4 k^2 + Q_5 = 0\,. \tag{4.34}$$

The spectrum relation suggests that the roots can be written as $\pm k_1$, $\pm k_2$, $\pm k_3$ and $\pm k_4$.

Before solving this 8th-order characteristic equation (obtained by setting the determinant of the PEP equal to zero), one can obtain an overview of the number of propagating and evanescent modes as follows. By substituting $\omega_n = 0$ in the characteristic equation and solving for k_j, it can be shown that for the uncoupled case ($B_{ij} = 0$)

$$k(0)_{1,\cdots,6} = 0\,, \qquad k(0)_{7,8} = \pm\sqrt{\frac{A_{13}^2 - A_{11}A_{33}}{A_{55}D_{55}}}\,. \tag{4.35}$$

This implies that six zero roots starting at $\omega_n = 0$ correspond to the axial, flexural and shear modes, whereas the two nonzero roots must be the

wavenumbers associated with the contractional mode. Here, it is to be noted that $\sigma_{zz} = 0$ for EBT and FSDT and the orthotropic constitutive model with respect to the XY plane, whereas in the presence of thickness contraction, $\sigma_{zz} \neq 0$, which requires a plane-stress model in the XZ plane reduced from a 3-D constitutive model. This produces a slight difference in the values of A_{55} compared to that in FSDT. However, almost all the conventional fiber reinforced composites used as structural material have $Q_{11} > Q_{13}$, $Q_{33} > Q_{13}$, which implies that the nonzero roots in Equation (4.35) must be imaginary at and near $\omega_n = 0$. Therefore, we have two evanescent (one forward and one backward) components in the contractional mode in the low frequency regime. Next, by substituting $k_j = 0$ in Equation (4.34) and solving for ω_n, we get the cut-off frequencies as

$$\omega_{\text{cut-off}} = 0\ ,0\ ,0\ ,0\ ,\sqrt{\frac{A_{55}}{I_2(1-s_2^2)}}\ ,\sqrt{\frac{A_{33}}{I_2(1-s_2^2)}}\ . \tag{4.36}$$

This shows that initially there are two forward propagating modes (one axial, one flexural), two backward propagating modes (one axial and one flexural), two evanescent flexural modes (forward and backward) and two additional evanescent contractional modes (forward and backward) for $\omega_n > 0$. The shear mode starts propagating after the cut-off frequency corresponding to A_{55} in Equation (4.36). The contractional mode starts propagating later, since $A_{33} \geq A_{55}$.

In Figure 4.15, the wavenumber dispersion is plotted for AS/3501 graphite–epoxy and glass–epoxy $[0]_{10}$ composite beam with total thickness $h = 0.01$ m. Material properties are taken from [50]. Note that the graphite–epoxy has very high ratio E_{11}/G_{13} (≈ 20) and moderate stiffness $E_{11} \approx 144$ GPa. On the other hand, the glass–epoxy has very low ratio E_{11}/G_{13} (≈ 6) and very low stiffness $E_{11} \approx 54$ GPa. For both of these materials, the plot in Figure 4.15 shows that the propagating components before the cut-off frequency in contraction are similar to those in Figure 4.16(a) in the absence of the variable ψ. The latter is studied in more detail in Section 4.4.4. Also the wavenumber associated with the evanescent components in contractional mode before the cut-off frequency is much higher than that due to shear, and therefore decays rapidly. Hence, below the cut-off frequency in contraction (which is always much higher than shear cut-off since $A_{33} > A_{55}$ for a composite), change in the response due to addition of the contractional mode is negligible. Such behavior is different from that in metal, as the cut-off frequencies for shear and contractional modes in isotropic material are very close to each other. The behavior and the restriction of the isotropic beam waveguide model has been discussed in the context of a three-mode beam theory and Lamb wave modes in 2-D cross-section in [9]. To accommodate such higher order effects in the present asymmetric composite beam waveguide model, the following corrections can be imposed for high frequency applications.

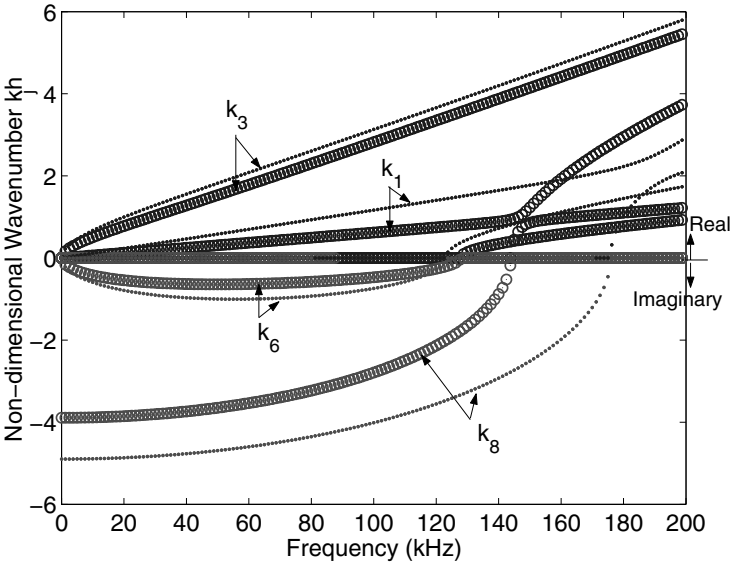

Fig. 4.15. Nature of wavenumber dispersion in axial (k_1), flexural (k_3), and shear (k_6) with cut-off and contraction (k_8) with cut-off; 'o', graphite–epoxy AS/3501 $[0]_{10}$ composite; **.....**, glass–epoxy $[0]_{10}$ composite; Total thickness $h = 0.01$ m

4.4.3 Correction Factors at High Frequency Limit

For applications where the beam cross-sectional configuration and the range of excitation frequency ω_{max} are such that

$$\omega_{max} > min\left(\sqrt{\frac{A_{33}}{I_2(1-s_2^2)}}, \quad \sqrt{\frac{A_{55}}{I_2(1-s_2^2)}}\right) , \tag{4.37}$$

four correction factors K_1, K_2, K_3 and K_4 can be introduced as $A_{55} \rightarrow K_1 A_{55}$, $D_{55} \rightarrow K_2 D_{55}$, $I_2 \rightarrow K_3 I_2$ and $A_{33} \rightarrow K_4 A_{33}$. The idea is to estimate these factors by having an upper bound on the cut-off frequencies from appropriate Lamb wave modes and by adjusting the propagating wavenumbers from those of the Lamb wave modes at high frequencies. Now, what appears as a contrast between the pairs of longitudinal, flexural, shear and contractional modes as shown in Figure 4.15 with the propagation of the first three pairs of symmetric Lamb wave modes and the first three pairs of antisymmetric Lamb wave modes in actual 2-D cross-section (the YZ plane in Figure 4.14) is as follows. At low frequencies, the pair of propagating longitudinal modes are identical to the first pair of propagating symmetric Lamb wave modes. Also, at low frequencies, the pair of propagating flexural modes and the pair of evanescent shear modes are identical to the first pair of propagating antisymmetric Lamb

wave modes and second pair of evanescent antisymmetric Lamb wave modes, respectively. The rest of the symmetric and antisymmetric Lamb wave modes are evanescent, therefore the effect is highly localized and can be neglected. At high frequencies, the pair of propagating flexural modes and the pair of propagating shear modes are respectively given by

$$k_{3,4} \approx \pm\omega_n \sqrt{\frac{I_0}{K_1 A_{55}}}\,, \quad k_{5,6} \approx \pm\omega_n \sqrt{\frac{K_3 I_2}{D_{11}}}\,. \tag{4.38}$$

These forms differ slightly from the corresponding first and second pair of antisymmetric Lamb wave modes. The adjustable cut-off frequencies in shear and contraction are now

$$\omega_{cs} = \sqrt{\frac{K_1 A_{55}}{K_2 I_2 (1 - s_2^2)}}\,. \quad \omega_{cc} = \sqrt{\frac{A_{33}}{K_2 I_2 (1 - s_2^2)}}\,. \tag{4.39}$$

Note from Figure 4.15 the sudden diversion of the propagating longitudinal modes when they interact with the propagating contractional modes. After such interaction, at higher frequencies, the longitudinal modes and the contractional modes are respectively given by

$$k_{1,2} \approx \pm\omega_n \sqrt{\frac{K_3 I_2}{K_2 D_{55}}}\,, \quad k_{7,8} \approx \pm\omega_n \sqrt{\frac{I_0}{A_{33}}}\,, \tag{4.40}$$

which are not due to the interaction of second and third pairs of propagating symmetric Lamb wave modes, because they first become complex, just above the cut-off frequency and break down followed by the addition of the fourth pair at higher frequencies. This fourth pair of symmetric Lamb wave modes propagate with similar form to that in Equation 4.40 for $k_{7,8}$. Now, we denote the Rayleigh wave speeds c_R in the cross-sectional planes YZ. c_R is associated with the non-dispersive wave propagation along x due to impact at the top or bottom surface of the beam. However, for general ply stacking, one needs to compute c_R using a plane-stress model and appropriate averaging in the YZ plane. As a frequency approximation, we can write

$$|k_{1,2}| = \frac{\omega_n}{c_R}\,, \quad |k_{3,4}| = \frac{\omega_n}{c_R}\,, \quad \omega_{cs} \approx \frac{1}{2}\frac{2\pi}{h} c_s\,, \quad \omega_{cc} \approx \frac{2\pi}{h} c_s\,, \tag{4.41}$$

where $\pi c_s/h$ is the first non-zero cut-off frequency of the antisymmetric Lamb wave mode pair and $2\pi c_s/h$ is the first non-zero cut-off frequency of the symmetric Lamb wave mode pair. c_s is the shear wave speed, h is the depth of the beam cross-section. Substituting Equations (4.38)–(4.40) in Equation (4.41), we get

$$K_1 = \frac{c_R^2}{c_s^2}\,, \quad K_3 = \frac{h^2 I_0}{\pi^2 I_2 (1 - s_2^2)} \frac{c_R^2}{c_s^2}\,, \tag{4.42}$$

$$K_2 = \frac{h^2 I_0}{\pi^2 I_2 (1 - s_2^2) K_5} \frac{c_R^4}{c_s^4}\,, \quad K_4 = 4 \frac{A_{55}}{A_{33}} \frac{c_R^2}{c_s^2}\,. \tag{4.43}$$

In the case of isotropic materials, the above reduces to

$$K_5 = \frac{A_{55}I_2}{D_{55}I_0} = 1\ , \quad s_2 = 0\ , \quad \left.\frac{c_R^2}{c_s^2}\right|_{\nu=0.3} = 0.86\ , \quad \left.\frac{A_{55}}{A_{33}}\right|_{\nu=0.3} = 0.28\ , \tag{4.44}$$

and we recover the so called shear correction factors $K_1 = 0.86$, $K_3 = 1.216$ (discussed in [9], and also previously proposed in [53] as $K_1 = 5/6$, $K_3 = 1$) for a Timoshenko beam along with $K_2 = 0.89$ and $K_4 = 0.98$, which accommodate the second pair of antisymmetric Lamb wave modes (shear modes) and second pair of symmetric Lamb wave modes (contractional modes) within the high frequency limit given by the cut-off frequency of the next higher order Lamb wave mode. Hence, for asymmetric laminated composite, as long as the frequency content of the excitation is below the cut-off in contraction, the model of coupled axial flexural shear wave modes can be adjusted to obtain sufficient accuracy.

4.4.4 Coupled Axial–Flexural Shear Without the Thickness Contractional Modes

When the thickness contraction term ψ is neglected in the displacement field, and subsequently in the wave equations, the characteristic equation is a 6th-order polynomial in k. Again, the PEP framework is used to obtain the wavenumber and hence, the group speeds.

In Figure 4.16, the dispersion of wavenumbers corresponding to axial, flexural and shear modes are shown. An AS/3501-6 graphite–epoxy beam cross-section with depth $h = 0.01$ m is considered. Beside this, to study how the wave packets travel at different frequencies, the group speeds $C_g = Re[d\omega_n/dk_j]$ in the axial, flexural and shear modes are plotted in Figure 4.17, where $C_0 = \sqrt{A_{11}/I_0}$ is the constant phase speed in axial mode. From these two plots, only one cut-off frequency appears, above which the shear mode starts propagating, which is otherwise an evanescent component contributing to the flexural wave. Figure 4.17 shows that the higher the stiffness coupling (higher value of r) the higher the group speed of the shear wave above the cut-off frequency. At the same time, the group speed of the longitudinal wave drastically falls well before the cut-off frequency. The flexural mode remains least affected by both stiffness and mass coupling, and remains almost non-dispersive above the cut-off frequency.

The procedure for spectral element formulation is similar to the procedure followed for the elementary beam formulation.

Finite Length Element

The displacement field for the two-noded finite length element will have four forward moving and four backward moving (reflected) components. Hence, the

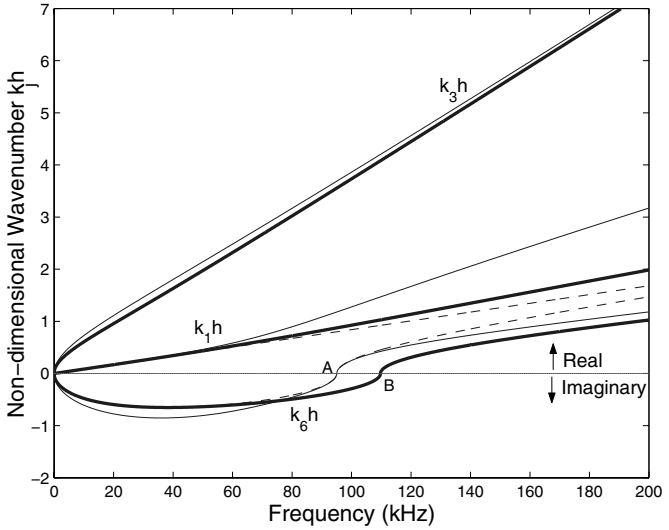

Fig. 4.16. Nature of wavenumber dispersion in axial, flexural and shear modes for different stiffness and material asymmetries; - - -, $r = 0.0$, $s2 = 0.0$; ——, $r = 0.757$, $s2 = 0.0$; ——, $r = 0.0$, $s2 = 0.5$. The locations of cut-off frequency are marked by A and B

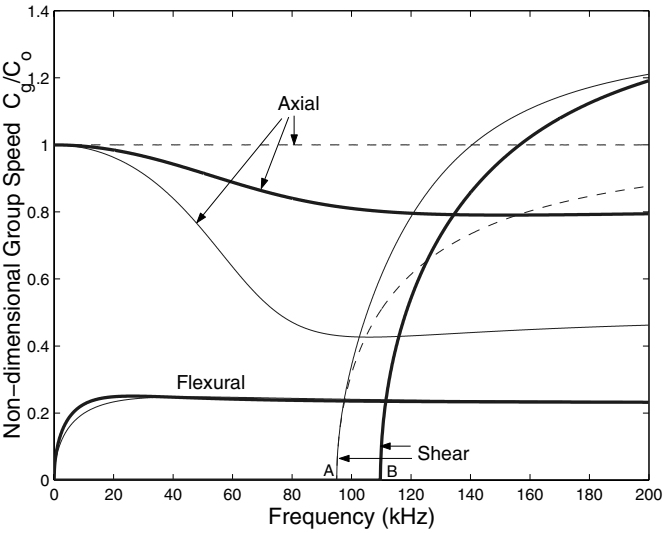

Fig. 4.17. Dispersion of group speeds in axial, flexural and shear modes for different stiffness and material asymmetries; - - -, $r = 0.0$, $s2 = 0.0$; ——, $r = 0.757$, $s2 = 0.0$; ——, $r = 0.0$, $s2 = 0.5$. The locations of cut-off frequency are marked by A and B

displacement field will contain eight constants. They need to be determined from eight boundary conditions coming from the two nodes. The displacement at any point x ($x \in [0, L]$) and at frequency ω_n becomes

$$\{\tilde{\mathbf{u}}\}_n = \begin{Bmatrix} \hat{u}(x,\omega_n) \\ \hat{\psi}(x,\omega_n) \\ \hat{w}(x,\omega_n) \\ \hat{\phi}(x,\omega_n) \end{Bmatrix} = \begin{bmatrix} R_{11} \ \dots \ R_{18} \\ R_{21} \ \dots \ R_{28} \\ R_{31} \ \dots \ R_{38} \\ R_{41} \ \dots \ R_{48} \end{bmatrix} \begin{bmatrix} e^{-jk_1x} & 0 & \dots & 0 \\ 0 & e^{-jk_2x} & \dots & 0 \\ \vdots & \ddots & \ddots & \vdots \\ 0 & \dots & \dots & e^{-jk_8x} \end{bmatrix} \{\mathbf{a}\}_n , \quad (4.45)$$

where ($k_{p+4} = -k_p , p = 1, \dots, 4$). The above equation in concise form can be written

$$\{\tilde{\mathbf{u}}\}_n = [R]_n [D(x)]_n \{\mathbf{a}\}_n, \quad (4.46)$$

where $[D(x)]_n$ is a diagonal matrix of size 8×8 whose ith element is e^{-jk_ix}. $[R]_n$ is the amplitude ratio matrix and is of size 4×8. This matrix needs to be known beforehand for subsequent element formulation. There are several ways to compute the elements of this matrix. In this formulation the SVD method, explained in Chapter 3, is followed, which is suitable for structural models with a large number of degrees of freedom (dof).

Here, $\mathbf{a_n}$ is a vector of eight unknown constants to be determined. These unknown constants are expressed in terms of the nodal displacements by evaluating Equation (4.45) at the two nodes, *i.e.,* at $x = 0$ and $x = L$. In doing so, we get

$$\{\hat{\mathbf{u}}\}_n = \begin{Bmatrix} \tilde{\mathbf{u}}_1 \\ \tilde{\mathbf{u}}_2 \end{Bmatrix}_n = \begin{bmatrix} R \\ R \end{bmatrix}_n \begin{bmatrix} D(0) \\ D(L) \end{bmatrix}_n \{\mathbf{a}\}_n = [T_1]_n \{\mathbf{a}\}_n , \quad (4.47)$$

where $\tilde{\mathbf{u}}_1$ and $\tilde{\mathbf{u}}_2$ are the nodal displacements of node 1 and node 2, respectively.

Using the force boundary conditions Equations (4.27) and (4.28), the force vector $\{\mathbf{f}\}_n = \{N_x \ , \ Q_x \ , \ V_x \ , \ M_x\}_n$ can be written in terms of the unknown constants $\{\mathbf{a}\}_\mathbf{n}$ as $\{\mathbf{f}\}_n = [P]_n \{\mathbf{a}\}_\mathbf{n}$. When the force vector is evaluated at node 1 and node 2, nodal force vector, $\{\hat{\mathbf{f}}\}_n$, is obtained and can be related to $\{\mathbf{a}\}_n$ by

$$\{\hat{\mathbf{f}}\}_n = \begin{Bmatrix} \tilde{\mathbf{f}}_1 \\ \tilde{\mathbf{f}}_2 \end{Bmatrix}_n = \begin{bmatrix} P(0) \\ P(L) \end{bmatrix}_n \{\mathbf{a}\}_n = [T_2]_n \{\mathbf{a}\}_n . \quad (4.48)$$

Equations (4.47) and (4.48) together yield the relation between the nodal force and the nodal displacement vector at frequency ω_n:

$$\{\hat{\mathbf{f}}\}_n = [T_2]_n [T_1]_n^{-1} \{\hat{\mathbf{u}}\}_n = [K]_n \{\hat{\mathbf{u}}\}_n , \quad (4.49)$$

where $[K]_n$ is the dynamic stiffness matrix at frequency ω_n of dimension 8×8. Explicit forms of the matrix $[T_1]$ and $[T_2]$ are given below.

$$T_1(1:4, 1:8) = R(1:4, 1:8) \quad (4.50)$$

$$T_1(l,m) = R(l-4,m)e^{-jk_mL}\,, \quad l = 5..8\,, m = 1,\ldots,8\,. \tag{4.51}$$

Similarly,

$$\begin{aligned}
T_2(1,i) &= j(A_{11}R(1,i) - B_{11}R(4,i))k_i - A_{13}R(2,i)\\
T_2(2,i) &= -B_{55}(-jR(3,i)k_i - R(4,i)) + jk_dD_{55}R(2,i)k_i\\
T_2(3,i) &= -A_{55}(-jR(3,i)k_i - R(4,i)) + jB_{55}R(2,i)k_i\\
T_2(4,i) &= -j(B_{11}R(1,i) - D_{11}R(4,i))k_i + B_{13}R(2,i)\\
T_2(5:8,i) &= -T_2(1:4,i)e^{-jk_iL}\,, \quad i = 1,\ldots,8\,.
\end{aligned} \tag{4.52}$$

Throw-off Element

For the infinite length element, only the forward propagating modes are considered. The displacement field (at frequency ω_n) becomes

$$\{\tilde{\mathbf{u}}\}_n = \sum_{m=1}^{4} R_n^m e^{-jk_{m_n}x}a_m^n = [R]_n[D(x)]_n\{\mathbf{a}\}_n\,, \tag{4.53}$$

where $[R]_n$ and $[D(x)]_n$ is now of size 4×4. The $\{\mathbf{a}\}_n$ is a vector of four unknown constants. Evaluating the above expression at node 1 ($x = 0$), the nodal displacements are related to these constants through the matrix $[T_1]$ as

$$\{\hat{\mathbf{u}}\}_n = \{\tilde{\mathbf{u}}_1\}_n = [R]_n[D(0)]_n\{\mathbf{a}\}_n = [T_1]_n\{\mathbf{a}\}_n\,, \tag{4.54}$$

where $[T_1]$ is now a matrix of dimension 4×4. Similarly, the nodal forces at node 1 can be related to the unknown constants

$$\{\hat{\mathbf{f}}\}_n = \{\tilde{\mathbf{f}}_1\}_n = [P(0)]_n\{\mathbf{a}\}_n = [T_2]_n\{\mathbf{a}\}_n\,. \tag{4.55}$$

Using Equations (4.54) and (4.55), nodal forces at node 1 are related to the nodal displacements at node 1

$$\{\hat{\mathbf{f}}\}_n = [T_2]_n[T_1]_n^{-1}\{\hat{\mathbf{u}}\}_n = [K]_n\{\hat{\mathbf{u}}\}_n\,, \tag{4.56}$$

where $[K]_n$ is the element dynamic stiffness matrix of dimension 4×4 at frequency ω_n. The matrices $[T_1] = R(1:4,1:4)$ and $[T_2](1:4,i)$ are the same as for the finite length element ($i = 1\ldots4$). As in the elementary case, the dynamic stiffness is complex.

4.4.5 Modeling Spatially Distributed Dynamic Loads

In the context of FSDT, under a distributed load $\hat{\mathbf{p}}(x,\omega_n) = \{\hat{p}_x,\ \hat{p}_z,\ \hat{p}_y\}^T$, where $\hat{p}_x$, $\hat{p}_z$ are the forces per unit length in the longitudinal and transverse directions and $\hat{p}_y$ is the distributed moment, the stationary principle in the frequency domain [60] is used to compute the consistent nodal load vector.

Here, we represent the product of spectral amplitudes of the conjugate quantities as an energy equivalent measure in the frequency domain. Such a frequency domain energy functional in the context of the virtual work principle is discussed in the work [60] and it is not the same as the frequency domain counterpart (in terms of convolution integral) of the time domain energy. Also, such a measure is different from the frequency domain power [61] and [45], which is defined as the product of the force vector and the conjugate of velocity vector. Here, we define the frequency domain strain energy, kinetic energy and external work, respectively, as

$$\hat{U}_S = \int \hat{\sigma}^T \hat{\varepsilon}\, d\Omega\ , \quad \hat{U}_I = -\int \omega_n^2 \rho \hat{\mathbf{u}}^T \hat{\mathbf{u}}\, d\Omega\ , \quad \hat{V} = -\int_0^L \hat{\mathbf{p}}^T \hat{\mathbf{u}}\, dx - \hat{\mathbf{f}}^{\mathrm{e}^T} \hat{\mathbf{u}}^{\mathrm{e}}\ . \tag{4.57}$$

At each sampling frequency ω_n, the continuous system reduces to a stationary system in Equation (4.57). Applying the principle of virtual work (PVW) to this stationary system as

$$\delta\left(\hat{U}_S + \hat{U}_I + \hat{V}\right) = 0 \tag{4.58}$$

and minimizing the total stationary potential $\hat{U} = \hat{U}_S + \hat{U}_I + \hat{V}$ with respect to the unknown displacement coordinate $\hat{u}^{\mathrm{e}}$, the equilibrium equation is obtained as

$$\left(\int \mathbf{B}^{\mathrm{e}^T} \bar{\mathbf{Q}} \mathbf{B}^{\mathrm{e}} d\Omega - \int \omega_n^2 \rho \aleph^{\mathrm{e}^T} \aleph^{\mathrm{e}} d\Omega\right) \hat{\mathbf{u}}^{\mathrm{e}} = \hat{\mathbf{f}}^{\mathrm{e}} + \int_0^L \aleph^{\mathrm{e}^T} \hat{\mathbf{p}}\, dx\ . \tag{4.59}$$

This minimization procedure is the same as the Ritz method [1] in the frequency domain, where the generic displacement field $\hat{u}(x, \omega_n)$ is represented using a Ritz function (same as the spectral element shape function) $\aleph(x, \omega_n)$ and unknown displacement coordinates $\hat{u}$ in Equation (4.45). Note that upon choosing $\hat{u}(x, \omega_n)$ as the Ritz function, the geometric boundary conditions are automatically satisfied. In addition, since $\hat{u}(x, \omega_n)$ is derived by satisfying the governing homogeneous wave equations exactly, it can be shown that the dynamic stiffness matrix obtained in Equation (4.59) is identical to the spectral element stiffness matrix $\hat{\mathbf{K}}^{\mathrm{e}}$ obtained in Equation (4.49), *i.e.,*

$$\frac{\partial^2 \hat{U}}{\partial \hat{u}_i^{\mathrm{e}} \partial \hat{u}_j^{\mathrm{e}}} = \hat{K}_{ij}^{\mathrm{e}} \quad \text{or} \quad \int \mathbf{B}^{\mathrm{e}^T} \bar{\mathbf{Q}} \mathbf{B}^{\mathrm{e}} d\Omega - \int \omega_n^2 \rho \aleph^{\mathrm{e}^T} \aleph^{\mathrm{e}} d\Omega = \hat{\mathbf{K}}^{\mathrm{e}}\ . \tag{4.60}$$

Here, $\hat{\mathbf{B}}^{\mathrm{e}}$ is the complex spectral element strain–displacement matrix given by

$$\mathbf{B}^{\mathrm{e}} = \begin{bmatrix} \frac{\partial}{\partial x} & 0 & -z\frac{\partial}{\partial x} \\ 0 & \frac{\partial}{\partial x} & -1 \end{bmatrix} \aleph^{\mathrm{e}}\ . \tag{4.61}$$

Using $\hat{\mathbf{K}}^{\mathrm{e}}$ from Equation (4.60) in Equation (4.59), the equilibrium equation can be solved, which includes the contribution of distributed load vector $\hat{\mathbf{p}}$ on

the spectral element nodes through a dynamically consistent exact nodal load vector given by

$$\hat{\mathbf{f}}_{\mathrm{d}}^{\mathrm{e}} = \int_0^L \aleph^{\mathrm{e}T} \hat{\mathbf{p}}\, dx\ . \tag{4.62}$$

For example, consider a spectral beam finite element subjected to distributed loading of the form $\mathbf{p}(x,t) = \mathbf{p_0}(t) + x\mathbf{p_1}(t)$. The spectral amplitude can be written as $\hat{\mathbf{p}}(x,\omega_n) = \hat{\mathbf{p}}_\mathbf{0} + x\hat{\mathbf{p}}_\mathbf{1}$. One can obtain expressions for the exact nodal force vector due to this loading using Equation (4.62). For example, the nodal force vector due to uncoupled axial dofs can be obtained as

$$\left\{ \begin{array}{c} \hat{f}_{1_{\mathrm{d}}} \\ \hat{f}_{4_{\mathrm{d}}} \end{array} \right\}^{\mathrm{e}} = \frac{i\left(1-e^{-ik_aL}\right)}{\left(1+e^{-ik_aL}\right)k_a} \left\{ \begin{array}{c} 1 \\ 1 \end{array} \right\} \hat{p}_0 + \left\{ \begin{array}{c} \dfrac{1}{k_a^2} - \dfrac{i2Le^{-ik_aL}}{\left(1-e^{-i2k_aL}\right)k_a} \\ \dfrac{iL\left(1+e^{-i2k_aL}\right)}{\left(1-e^{-i2k_aL}\right)k_a} - \dfrac{1}{k_a^2} \end{array} \right\} \hat{p}_1\ . \tag{4.63}$$

Similar expressions for the transverse and rotational dofs can also be obtained in closed form.

4.5 Modeling Damping Using Spectral Element

The damping effect is important for polymer based laminated composites. The viscosity of the polymer matrix along with interfacial defects and inclusions causes scattering and absorption of energy. As observed in the measured response, especially in NDT techniques, the idealistic and undamped models do not tally satisfactorily with what is measured. Hence, it is most often important to incorporate appropriate damping mechanisms. Damping mechanisms can be incorporated under the classifications of (1) proportional and (2) non-proportional models. Phenomenologically, the mechanisms can be distinguished as (1) viscous damping, (2) non-viscous damping. In the following subsections, incorporation of viscous air damping, dry friction and strain rate dependent damping as proportional damping mechanisms within the framework of SFEM are discussed.

4.5.1 Proportional Damping Through a Discretized Finite Element Model

In a finite element system, the damping matrix $\mathbf{C}$ is most often represented as a linear combination of the mass matrix $\mathbf{M}$ and stiffness matrix $\mathbf{K}$ and is known as *Rayleigh damping*. It is always advantageous to obtain such a system because classical normal modes are preserved so that efficient computation can be performed. To this end, as a generalization of linear damping by retaining classical normal modes, one can use the *Caughey series* expressed in terms of the power of $\mathbf{M}^{-1}\mathbf{K}$ as

$$\mathbf{C} = \mathbf{M} \sum_{j=0,\cdots} \alpha_j \left[\mathbf{M}^{-1}\mathbf{K}\right]^j \tag{4.64}$$

for systems with non-repeated roots [62]. A further generalization to construct $\mathbf{C}$ from classical normal mode synthesis [63] can be written as

$$\mathbf{C} = \mathbf{M} g_1\left(\mathbf{M}^{-1}\mathbf{K}, \mathbf{K}^{-1}\mathbf{M}\right) + \mathbf{K} g_2\left(\mathbf{M}^{-1}\mathbf{K}, \mathbf{K}^{-1}\mathbf{M}\right) \tag{4.65}$$

where g_1 and g_2 are frequency dependent functions and can be reduced to the constant *Rayleigh damping coefficients*. The above two equations show that identification of damping coefficient in a distributed flexible structure requires suitable measurements, which in most cases have their own limitations, such as the large number of sensor measurements and incomplete measurements over a broad frequency band. In many spectral analysis techniques (*e.g.,* [64]), eigenvalues, left and right eigenvectors are used to compute the spectral amplitude vector. Also, handling such a computation over a broad frequency band becomes computationally expensive. In contrast, the spectral element does not solve a quadratic eigenvalue problem [65]. Here, in SFEM, we have a much lower number of finite element nodes due to exact element dynamic stiffness. But, computation is done at each FFT sampling frequency point (typically $512 - 8192$) irrespective of eigenvalues, and the accuracy depends on the frequency window. Therefore, like modal analysis, normal mode synthesis is not an issue in SFEM. Now, we look at how the above linear damping model can be treated in SFEM.

Using Equation (4.47) for the spectral element shape function and Equation (4.61) for the strain–displacement matrix, a frequency dependent general mass matrix and stiffness matrix can be defined, respectively as

$$\hat{\mathbf{M}} = \int \rho \aleph^{\mathrm{e}T} \aleph^{\mathrm{e}} d\Omega \,, \quad \hat{\mathbf{K}} = \int \mathbf{B}^{\mathrm{e}T} \bar{\mathbf{Q}} \mathbf{B}^{\mathrm{e}} d\Omega \,. \tag{4.66}$$

Following Equation (4.65), a frequency dependent damping matrix can be identified as

$$\hat{\mathbf{C}}^{\mathrm{e}} = \hat{\mathbf{M}} \hat{g}_1(\omega_n) + \hat{\mathbf{K}} \hat{g}_2(\omega_n) \,. \tag{4.67}$$

The governing algebraic form including the effect of velocity proportional damping can now be written as

$$\left(\hat{\mathbf{K}}^{\mathrm{e}} + i\omega_n \hat{\mathbf{C}}^{\mathrm{e}}\right) \hat{\mathbf{u}}^{\mathrm{e}} = \hat{\mathbf{f}}^{\mathrm{e}} \,. \tag{4.68}$$

Here, the coefficients $\hat{g}_1$ and $\hat{g}_2$ are different from those in Equation (4.65) and need to be identified using broadband measurements having identical resolution in the FFT used in SFEM. However, in the context of *Rayleigh damping*, the same constant coefficients g_1 and g_2 used for modal analysis can also be used here.

Wave Propagation in Lightly Damped Structures

Here, we assume that a small proportional damping in Equation (4.67), perturbs the spectral amplitude of the undamped system as

$$\hat{\mathbf{u}}'^{\mathrm{e}} = \hat{\mathbf{u}}^{\mathrm{e}} + \Delta\hat{\mathbf{u}}^{\mathrm{e}} \, . \tag{4.69}$$

By substituting the above in Equation (4.68) and with the help of Equation (4.49), we get

$$\hat{\mathbf{K}}^{\mathrm{e}}\Delta\hat{\mathbf{u}}^{\mathrm{e}} + i\omega_n\hat{\mathbf{C}}^{\mathrm{e}}\hat{\mathbf{u}}^{\mathrm{e}} + i\omega_n\hat{\mathbf{C}}^{\mathrm{e}}\Delta\hat{\mathbf{u}}^{\mathrm{e}} = 0 \, . \tag{4.70}$$

Since, the damping is small, the above equation along with Equation (4.69) yields

$$\hat{\mathbf{u}}'^{\mathrm{e}} \approx \left(\mathbf{I} - i\omega_n\hat{\mathbf{K}}^{\mathrm{e}^{-1}}\hat{\mathbf{C}}^{\mathrm{e}}\right)\hat{\mathbf{u}}^{\mathrm{e}} \, . \tag{4.71}$$

While solving the spectral finite element system, very fine frequency sampling can be considered without compromising the computational cost. Therefore, Equation (4.71) will also hold for the analysis of a structure whose eigenfrequencies are not well separated. In a lightly damped wave propagation problem, the perturbation of the spectral amplitude by a complex quantity in Equation (4.71) states that the motion becomes asynchronous. That is, the motion of any two points is no longer in phase with each other. This is also shown in [66] and [67] using normal mode analysis, but they are based on the additional assumption that the eigenfrequencies are not dense and the perturbation on one of them does not cross over another.

4.5.2 Proportional Damping Through the Wave Equation

Here, first we consider a general damping model to include the combined effect of dry friction, viscous air damping and strain rate dependent damping (also called Kelvin–Voigt damping) in the wave motion. The wave equations in this case can be obtained using Hamilton's principle with generalized forcing terms. This leads to a form similar to the axial–flexural shear coupled equation of motion in FSDT, plus some additional terms as

$$\delta u^o : \; I_o\ddot{u}^o - I_1\ddot{\phi} - A_{11}u^o{}_{,xx} + B_{11}\phi_{,xx} + \eta_1 u^o + \eta_6\dot{u}^o + \left(\int \eta_4 dA\right)\dot{u}^o{}_{,x} = 0 \, , \tag{4.72}$$

$$\delta w : \; I_o\ddot{w} - A_{55}\left(w_{,xx} - \phi_{,x}\right) + \eta_2 w + \eta_5\dot{w} = 0 \, , \tag{4.73}$$

$$\delta\phi : \; I_1\ddot{u}^o - I_2\ddot{\phi} + A_{55}\left(w_{,x} - \phi\right) - B_{11}u^o{}_{,xx} + D_{11}\phi_{,xx} - \eta_3\phi + \left(\int \eta_6 z dA\right)\dot{u}^o{}_{,x} - \left(\int \eta_6 z^2 dA\right)\dot{\phi}_{,x} = 0 \tag{4.74}$$

where, η_1, η_2 and η_3 are the coefficient of dry friction in the longitudinal, transverse and rotational motions respectively. η_4 and η_5 are the viscous air

damping coefficients associated with the longitudinal and transverse velocity vectors respectively. η_6 is the coefficient associated with strain rate dependent damping $-\eta_6\dot{\varepsilon}_{xx}$ and has been studied in isotropic beams ([68], [69]). For simplicity, we assume η_4 and η_6 are constant for all the plies, irrespective of the stacking sequence. The characteristic polynomial in terms of wavenumbers k_j becomes

$$\text{Det}\left(\mathbf{F_1}(k_j) + \mathbf{F_2}(k_j)\right) = 0 \tag{4.75}$$

where, $\text{Det}(\mathbf{F_1}(k_j)) = 0$ is expanded as before to get the characteristic equation and the additional matrix $\mathbf{F_2}(k_j)$, which is diagonal, is given by

$$\mathbf{F_2}(k_j) = \begin{bmatrix} \eta_1 + i\omega_n\eta_4 + A_0\omega_n\eta_6 k_j & 0 & 0 \\ 0 & \eta_2 + i\omega_n\eta_5 & 0 \\ 0 & 0 & -\eta_3 - A_2\omega_n\eta_6 k_j \end{bmatrix}, \tag{4.76}$$

where $[A_0\ A_2] = \int [1\ z^2] dA$. Irrespective of small or large dissipation or friction, let us consider first the uncoupled ($B_{11} = 0$) solution for wavenumbers in axial mode given by

$$k_{1,2} = -\frac{\omega_n\eta_6 A_0}{2A_{11}} \pm \sqrt{\frac{1}{4}\left(\frac{\omega_n\eta_6 A_0}{A_{11}}\right)^2 + \frac{\omega_n^2 I_0}{A_{11}} - \left(\frac{\eta_1 + i\omega\eta_4}{A_{11}}\right)}\,. \tag{4.77}$$

Now imposing $k_j = 0$ in the above equation leads to a new cut-off frequency in the axial mode, which is given by

$$\omega_{\text{cut-off}} = \sqrt{\frac{\eta_1}{I_0}} \tag{4.78}$$

and is independent of η_4 and η_6. For the conventional stiff composite beam, such a cut-off frequency is unlikely since η_1, which is caused physically by the distributed horizontal spring effect, must reach the order of $\omega_n^2 I_0$. At low frequency, such a cut-off frequency may occur in polymer thin film (I_0 very small) and the primary in-plane wave may cease to propagate leaving only the evanescent waves. However, additional small propagating components will appear when $\eta_4 \neq 0$, $\eta_6 \neq 0$. In the absence of axial friction ($\eta_1 = 0$) and strain rate dependent damping ($\eta_6 = 0$), and under the assumption that the viscous damping η_4 is small, Equation (4.77) can be approximated as

$$k_{1,2} \approx \pm k_a \left[1 - i\frac{\eta_4}{2\omega_n I_0}\right] = \pm k_a \left[1 - i\eta(\omega_n)\right]\,. \tag{4.79}$$

In the case of isotropic rod, a similar formulation has been discussed in [9]. In the open literature, several studies related to damped wave propagation use a similar form $k(1 - i\eta)$ (shown in Equation (4.79)) as a simplification. It can be shown that in the presence of strain rate dependent damping $\eta_6 \neq 0$, any additional propagating wave can be blocked completely if the relation

$$\eta_4 = \eta_6 A_0 \sqrt{\frac{\eta_1}{A_{11}} - \frac{\omega_n^2 I_0}{A_{11}}} \tag{4.80}$$

holds for any tailored structural configuration. Next, let us consider the wavenumbers for uncoupled ($B_{11} = 0$) flexural motion given by

$$k_{3,\cdots,6} = \pm\sqrt{\frac{A_{55}}{2D_{11}}}\left[\alpha_0 \pm \sqrt{\alpha_0^2 + 4\frac{D_{11}}{A_{55}}\left(\frac{\omega_n^2 I_2}{A_{55}} - 1\right)\left(-\frac{\omega_n^2 I_0}{A_{55}} + \frac{i\omega_n \eta_5}{A_{55}}\right)}\right]^{1/2} \tag{4.81}$$

where

$$\alpha_0 = \frac{\omega_n^2}{A_{55}}\left(I_2 + I_0\frac{D_{11}}{A_{55}}\right) - \frac{i\omega_n \eta_5 D_{11}}{A_{55}^2}\ , \quad \eta_2 = 0\ , \quad \eta_3 = 0\ , \quad \eta_6 = 0\ . \tag{4.82}$$

Here, we consider $\eta_6 = 0$, which otherwise produces a complete 4th-order complex characteristic polynomial, for which the roots are to be computed numerically and is not discussed here. Now, by substituting $k_j = 0$ in Equation (4.81), it can be shown that the cut-off frequency in shear mode given in Equation (4.36) does not change due to the viscous damping terms. However, in the presence of transverse and rotational friction (η_2 and η_3), two cut-off frequencies can be observed.

In this section we focus on understanding the effect of viscous damping on the characteristic behavior. We estimate the percentage change in the relative group speed of the damped wave as

$$\%\Delta C_g = \frac{C_g' - C_g}{C_g} \times 100 \tag{4.83}$$

where the superscript $'$ is for a damped system. Subsequently, if one defines the change in wavenumber as

$$\Delta k_j = k_j' - k_j \tag{4.84}$$

then the amplitude of the damped wave coefficients $\tilde{u}_j'$ can be expressed in terms of the amplitude of the undamped wave coefficients $\tilde{u}_j$ as

$$|\tilde{u}_j'| = \psi_d^y |\tilde{u}_j|\ , \quad \psi_d = |e^{-i\Delta k_j/|k_j|}|\ , \quad y = |k_j| x\ , \tag{4.85}$$

i.e., the imaginary part of Δk_j, if negative, will contribute to the decay of the wave amplitude in the exponential power of the distance x. The real part of Δk_j will cause lead or lag in the phase depending upon the sign. ψ_d is the damping factor in the amplitude of the wave coefficient at a distance $x = 1/|k_j|$. For numerical illustration, cross-sectional properties are taken for the AS/3501 graphite–epoxy beam configuration considered earlier.

For a range of $\eta_4 = 10^{-2}$ to 10^5, $\%\Delta C_g$ and corresponding ψ_d in axial mode are plotted in Figure 4.18 and Figure 4.19 respectively. It can be observed that

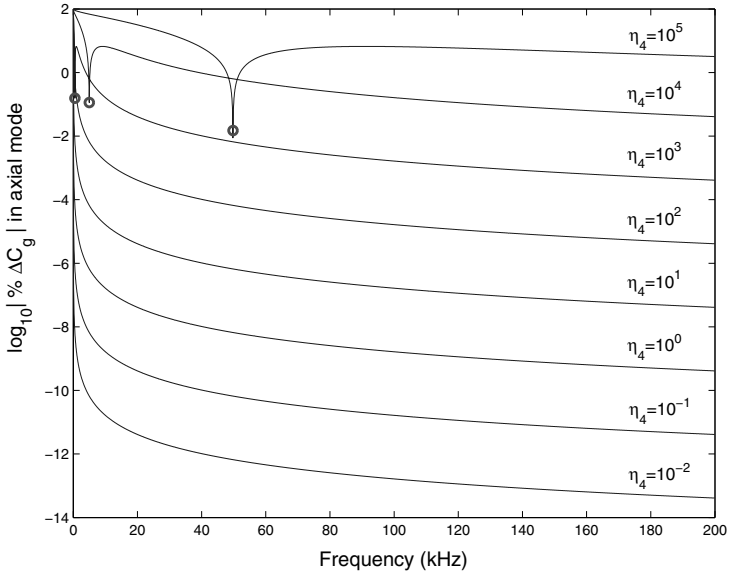

Fig. 4.18. Plot of percentage change in relative group speed $\%\Delta C_g$ in axial mode for different values of viscous damping coefficient η_4. For $\eta_4 \geq 10^3$, transition of negative to positive $\%\Delta C_g$ occurs at the mark 'o'. For lower damping, $\%\Delta C_g$ is positive

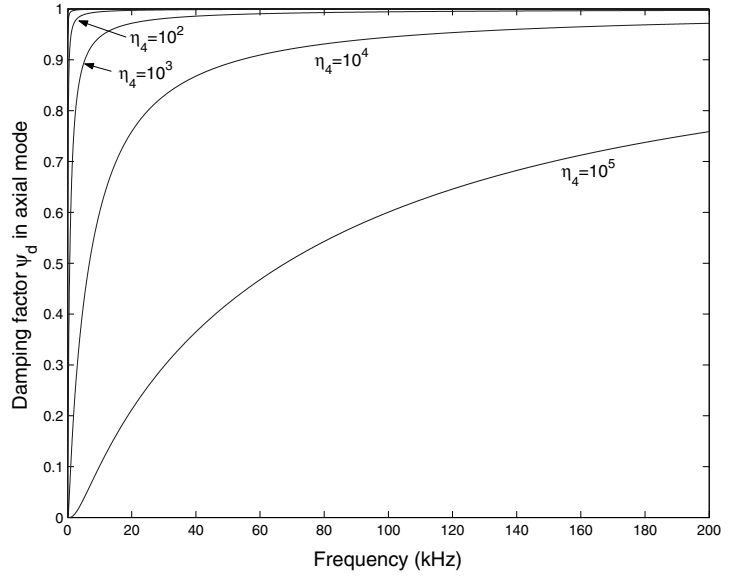

Fig. 4.19. Plot of damping factor ψ_d in the wave amplitude in axial mode for different values of viscous damping coefficient η_4

at low damping, the group speed of the damped wave compared to that of the undamped wave increases and the rate of increase linearly changes with the order of frequency. Increase in the group speed actually causes delocalization or deflation of the disturbance over x in the forward and backward directions. At $\eta_4 \geq 10^3$, the group speed of the damped wave starts decreasing relative to that of the undamped wave up to a certain frequency and then again starts increasing. This transition point shifts to higher frequency for higher damping. This shows that in the presence of very high damping, the group speed can tend to zero and hence most of the energy can cease to propagate, thus leaving only an insignificant amount of high frequency components. In Figure 4.19, it can be observed that in the low frequency region, ψ_d decreases rapidly, whereas in the high frequency region, it reaches a near constant value. Figure 4.16(a) shows that k_j increases at higher frequencies and hence decay of the wave amplitude at low frequency will occur at lesser distance compared to the distance required for the same amount of damping of wave amplitude at high frequency. Similar behavior can be observed for the damped flexural wave plotted in Figs. 4.20 and 4.21 and the shear wave plotted in Figs. 4.22 and 4.23.

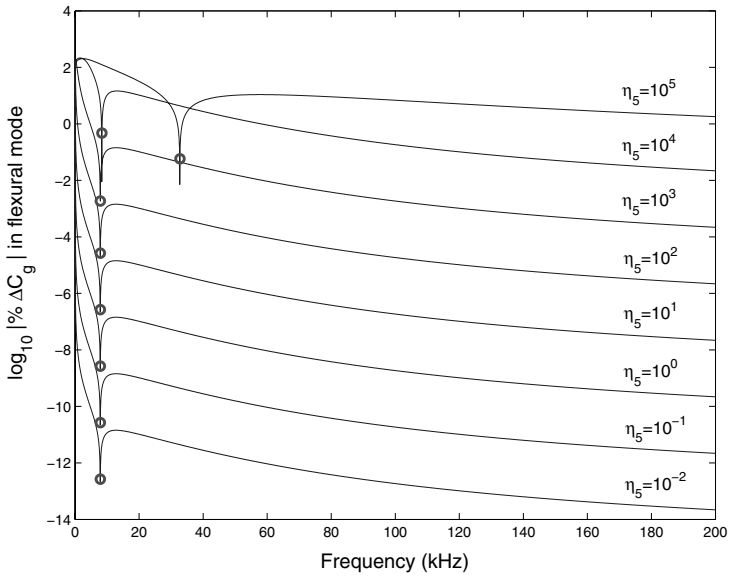

Fig. 4.20. Plot of percentage change in relative group speed $\%\Delta C_g$ in flexural mode for different values of viscous damping coefficient η_5. Transition of negative to positive $\%\Delta C_g$ occurs at the mark 'o'

Here, the transition frequency for percentage change in the relative group speed of the damped flexural wave remains the same at low and moderate

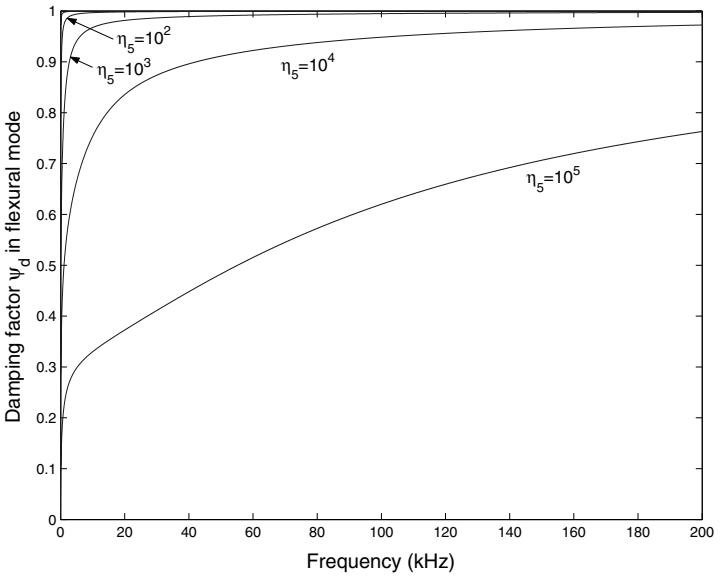

Fig. 4.21. Plot of damping factor ψ_d in the wave amplitude in flexural mode for different values of viscous damping coefficient η_5

damping, and is < 10 kHz. This tells us that the presence of even a small amount of damping (in the order of η_5 considered in the plots) may cause significant dissipation of energy since the energy propagates with group speed. In the shear wave, similar behavior (Figure 4.22) can be observed within 10 kHz just after the cut-off frequency. Also seen in Figure 4.24 is the wavenumber associated with the backward propagating wave in shear mode before the cut-off frequency. The corresponding group speed is positive and is shown in Figure 4.25. Similar relationships between wavenumber and group speed associated with the forward propagating shear wave can be established. The opposite sign of k_j and C_g in shear mode before the cut-off frequency can be attributed to the fact that in the presence of damping, energy can propagate in a direction opposite to the direction of the movement of individual wavefronts (that is the direction of phase velocity). This is analogous to the movement of a caterpillar [70]. Note that at very high damping, the shear energy does not increase much at frequencies less than the cut-off frequency (Figure 4.25), although the wavenumber and hence the phase speed increases (Figure 4.24).

4.6 Numerical Results and Discussions

In the following numerical examples, the effect of contractional mode is not included, but is discussed in great detail in the next chapter. Analysis is performed considering the system as undamped. In this section, first the validity

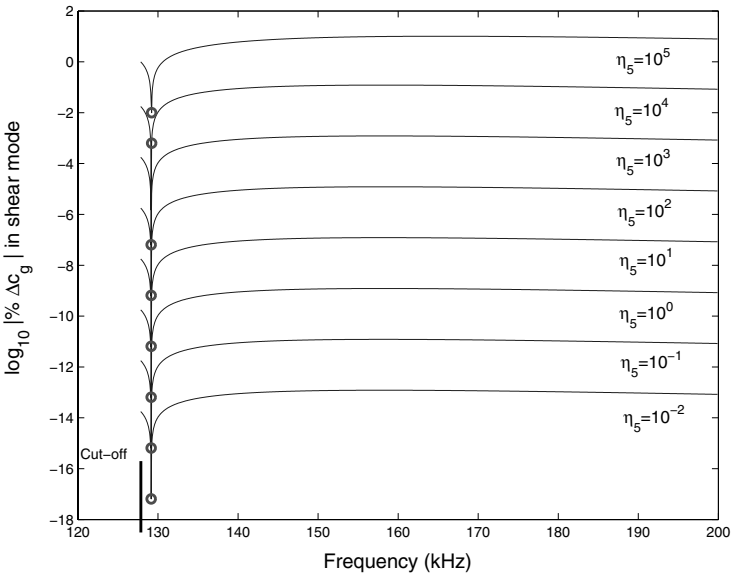

Fig. 4.22. Plot of percentage change in relative group speed $\%\Delta C_g$ in shear mode after cut-off for different values of viscous damping coefficient η_5. Transition of negative to positive nature of $\%\Delta C_g$ occurs at the mark 'o'.

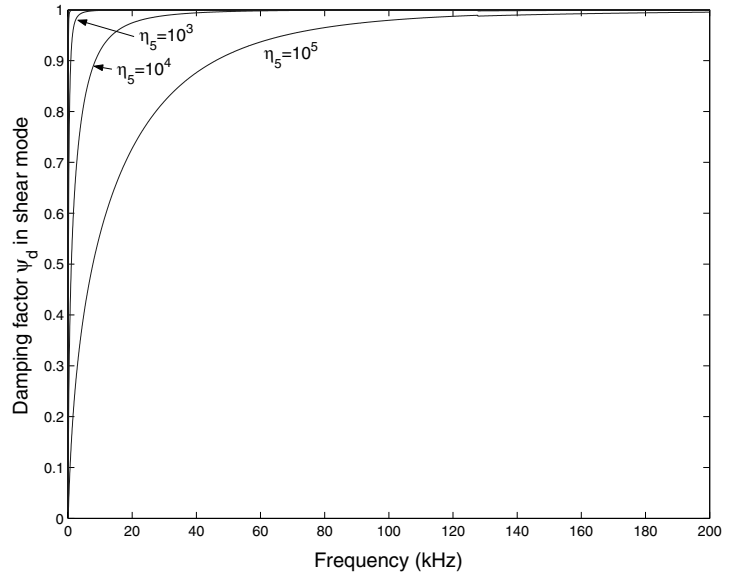

Fig. 4.23. Plot of damping factor ψ_d in the wave amplitude in the small propagating shear mode before cut-off and dominant shear mode after cut-off for different values of viscous damping coefficient η_5

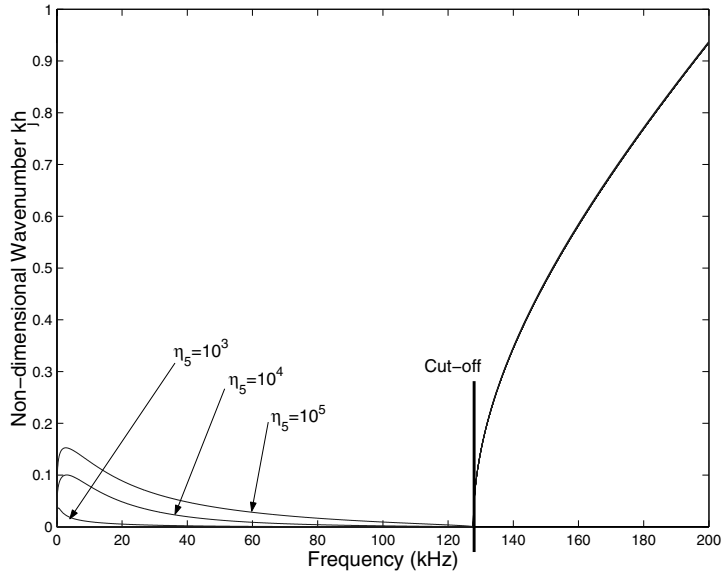

Fig. 4.24. Appearance of real negative wavenumber (the absolute value) associated with backward propagating wave in shear mode before cut-off due to different values of viscous damping coefficient η_5

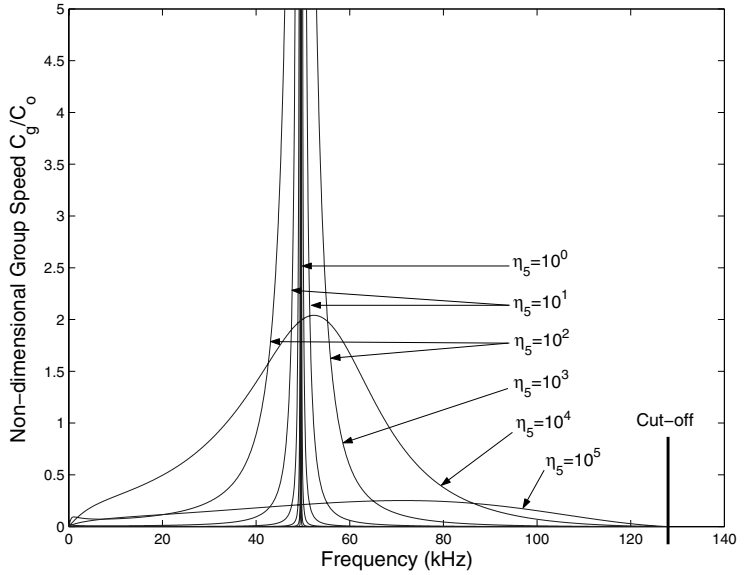

Fig. 4.25. Appearance of positive group speed (energy traveling forward) associated with backward propagating wave (Figure 4.24) in shear mode before cut-off due to different values of viscous damping coefficient η_5

of the formulated element is established in two different ways. In the first, the solutions are compared with standard FEM solutions. In this process, also the effect of axial–flexural shear coupling on the response as well as on the wave speeds are illustrated. Next, the existence of axial–flexural shear modes is shown. The time of occurrence of these modes with respect to wave speeds is confirmed from the dispersion plots. The last example will demonstrate the use of this element to handle composite ply-drops.

4.6.1 Comparison of Response with Standard FEM

Comparisons with the results based on a previously reported spectral element for EBT (Section 4.3), time domain refined finite element for FSDT [3] and 2-D plane stress FEM are presented in this section. The time domain refined finite element [3] uses a higher order polynomial displacement field, given by

$$u^o(x,t) = C_1 + C_2 x + C_3 x^2 \ , \quad w(x,t) = C_4 + C_5 x + C_6 x^2 + C_7 x^3 \ , \quad (4.86)$$

$$\phi(x,t) = C_8 + C_9 x + C_{10} x^2 \ , \quad (4.87)$$

which is based on the exact solution to the axial–flexural shear coupled static form of governing equation for the laminated composite beam. This FSDT (FEM) has an exact stiffness matrix, and approximate but consistent mass matrix. The 2D plane stress FEM used for the comparison is based on a constant strain triangular element. In the FSDT (FEM) as well as in the 2-D FEM, Newmark time integration is used. An AS/3501-6 graphite–epoxy composite cantilever beam of length $L = 1$ m, depth $h = 0.01$ m and width $b = 0.01$ m is considered. The same broadband pulse as in previous examples (Figure 4.5) is applied at the free end where the response is also measured. Stiffness coupling factor $r = 0.460$ ($[0^o]_{10}/[45^o]_{10}$) is considered. A single element is used in the present FSDT (SFEM) and also in EBT (SFEM) with 32768 FFT points ($\Delta\omega = 191.75$ rad/s). 2000 elements are used in FSDT (FEM) with time step $\Delta t = 0.1$ μs in the Newmark time integration. 4000 constant strain triangular elements are used in the 2-D FEM with same time step. In Figure 4.26, modulation of the axial response after reflection from the fixed boundary can be seen. The shape of the reflected pulse in the EBT (SFEM) shows the non-dispersiveness, whereas in the FSDT (FEM) and the FEM results, it is dispersive, a phenomenon that can be attributed to the combined effect of the shear and axial–flexural coupling. The initial history of SFEM matches well with the FEM result based on the FSDT. However, the peak amplitude of the reflected response is slightly smaller than that predicted by FEM. This may be attributed to an approximate mass distribution of the FE solution. In addition, the undamped nature of the response causes never-ending motion within the selected time window. Hence, we get distortion of the actual response during inverse FFT. To avoid this, a small amount of damping η is introduced to the wavenumbers as $k_j \rightarrow k_j(1 - i\eta)$, which cause the response amplitude to decay towards the end of the time window. In the

present case $\eta = 0.7 \times 10^{-2}$ has been used to remove the maximum amount of distortion. In the transverse response plotted in Figure 4.27, the onset of reflection is much earlier in EBT than in FSDT and the 2-D plane stress model. This is because of the combined effect of the higher flexural speed in EBT, which exists due to the infinite shear stiffness and the absence of rotary inertia in the EBT-based prediction. To minimize the effect of distortion in the time window, the same value of η as in the axial velocity history is used.

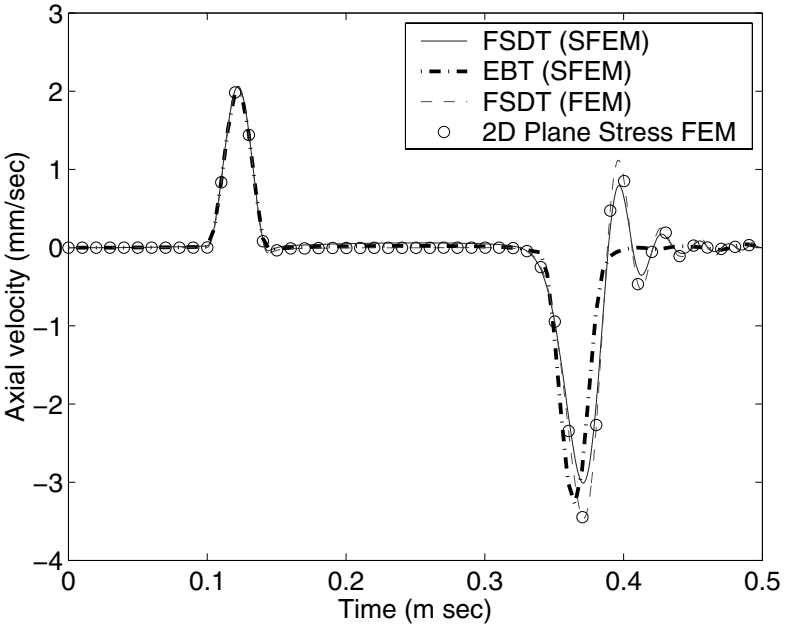

Fig. 4.26. Comparison of axial response of a cantilever beam with $[0]_{10}/[45^\circ]_{10}$ ply stacking and $L/h = 50$, predicted by SFEM and standard FEM

The reflected history predicted by FSDT (SFEM) has lower amplitude due to the introduction of the artificial damping. However, the two plots show that EBT-based prediction can be reliable enough, even for a moderately thick beam, to obtain the initial response. And in most damped systems, such an initial peak can be expected to cause structural failure. However, accurate estimation of wave reflection at the later stages of time has its own importance in identifying the localized effect in complex skeletal structures under impact loading. The SFEM developed is well suited to analyzing such aspects using the frequency response as well as the temporal response.

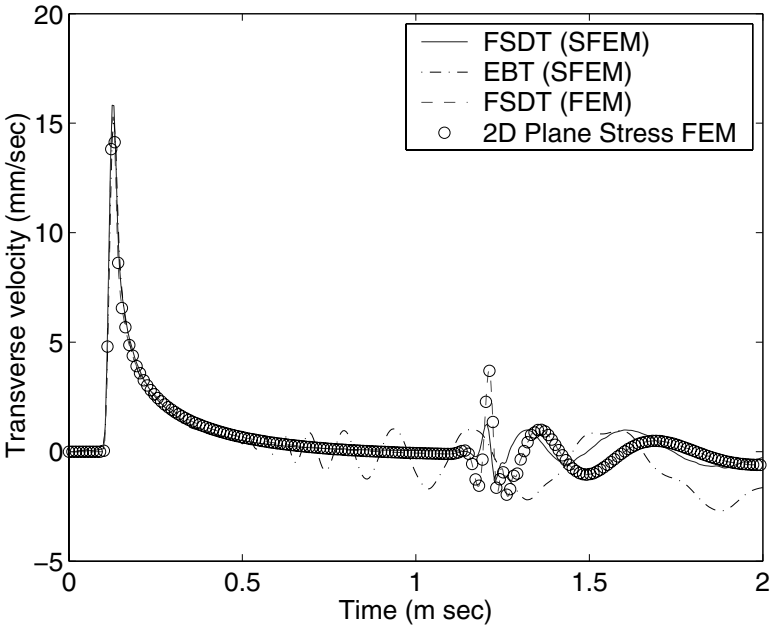

Fig. 4.27. Comparison of transverse response of a cantilever beam with $[0]_{10}/[45^o]_{10}$ ply stacking and $L/h = 50$ predicted by SFEM and standard FEM

4.6.2 Presence of Axial–Flexural Shear Coupling

To simulate the effect of stiffness coupling due to asymmetric ply stacking on the different wave modes, an infinite beam made of AS/3501-6 graphite–epoxy is considered as shown in Figure 4.28. A sinusoidal pulse modulated at

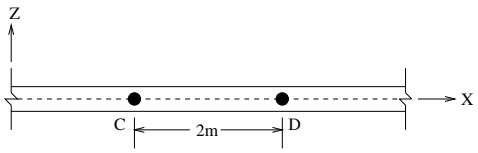

Fig. 4.28. An infinite beam to study the propagation of a modulated pulse in different wave modes

120 kHz is applied at C. One property of such a modulated pulse is that the pulse propagates non-dispersively even in a dispersive media. As a result, the shape of the pulse remains unaltered during propagation and hence is useful in the present context to study the occurrence of dispersive flexural and shear modes. The response is measured at point D, 2.0 m away from point C. Three

different ply stackings $[0^o]_5/[0^o]_5$, $[0^o]_5/[60^o]_5$ and $[0^o]_5/[90^o]_5$ are considered, which yield stiffness coupling factor $r = B_{11}^2/(A_{11}D_{11}) = 0.0$, 0.667 and 0.757 respectively. Figure 4.29 shows the axial and transverse response at D under axial loading at C. Figure 4.30 shows axial and transverse response at D under transverse loading at C. In the axial velocity plot in Figure 4.29, the

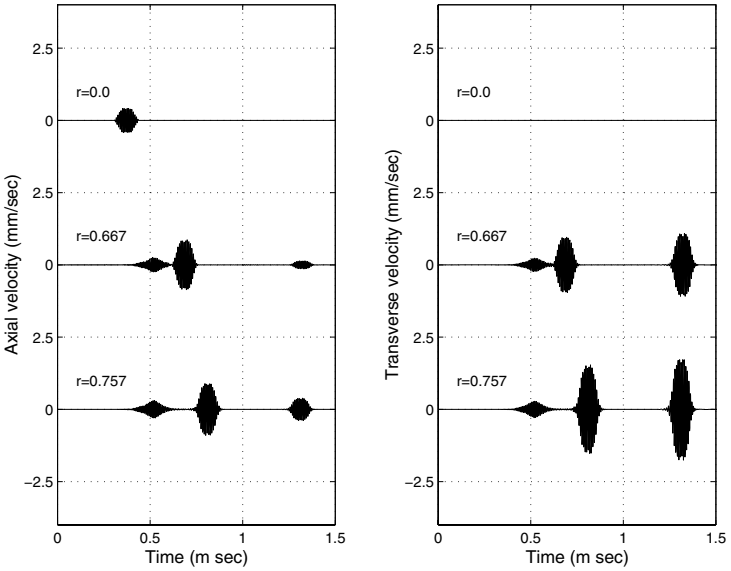

Fig. 4.29. Axial and transverse velocity history at D due to axial modulated pulse applied at C

bigger blobs in three cases are the dominant axial mode. Clearly, the speed of the longitudinal wave does not increase linearly with axial–flexural coupling (characterized by the parameter r). This resembles the non-dispersive nature of axial group speed in Figure 4.16(b). Here, it is noticed that the loading frequency is 120 kHz which is well above the shear cut-off frequency ($\approx$ 95 kHz) for all three ply configurations. Note from Equation (4.36) that the cut-off frequencies are functions of inertial coupling factor (s_2) only, not the stiffness coupling factor (r). However, it is clear from Figure 4.16(b) that along the frequency axis, for increasing coupling, the shear speed crosses over first the flexural and then the longitudinal wave speeds, and remains almost non-dispersive for $r = 0.667$ and 0.757. Due to this constant value and the almost non-dispersive nature of the shear speed, the initial small blobs in both responses ($r = 0.667$ and 0.757) evolve at the same time (0.5 ms). Similarly, the flexural mode appears at the same time (1.35 ms) for these two coupling factors, but with much lower speed. Similar inferences can also be drawn from Figure 4.30. These times of arrival for individual modes match exactly with

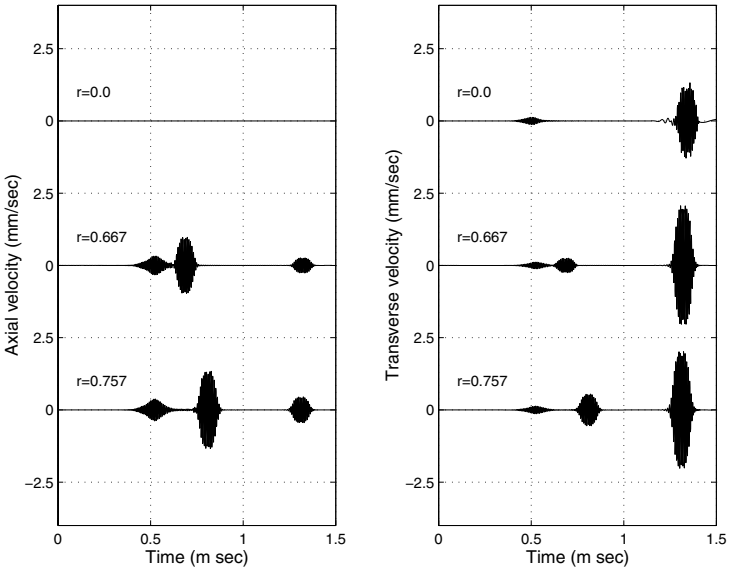

Fig. 4.30. Axial and transverse velocity history at D due to transverse modulated pulse applied at C

those computed numerically from the expression for the group speed C_g. In addition, this figure also shows the relative scale of magnitude of the shear mode (at 0.5 ms) in the transverse velocity history.

Laminated composite materials show a greater amount of damping than metals. Hence, for signal measurement purposes, it becomes important to shift a suitable distance away from the point of excitation where the travelling non-dispersive pulse (as used above or other solitary waveforms) in an individual mode can be detected. In the context of viscous damping (Equations (4.83)–(4.85)), an idealistic estimate can be obtained of the damped wave amplitude by ψ_d^y. For example, let us consider the type 3 wave (propagating flexural wave) (see Figure 4.16(a)). At the loading frequency 120 kHz, $k_3 \approx 4.5/h = 450\ \mathrm{m}^{-1}$ and for 1% damping, we get $\psi_d \approx 0.998$. Hence at a distance $x = 2$ m, the wave amplitude will be reduced to approximately $\psi_d^{k_3 x} \approx 0.165$ times the undamped wave amplitude. Arrival time remains the same since $\%\Delta C_g$ is of the order of $+10^{-13}$ (see Figure 4.20). Note that if the pulse was a low frequency one, typically below 10 kHz, nothing would have reached the measuring point. Therefore precise estimation of the optimal measurement point as well as the capacity of the sensors is crucial for application in such problems in NDT and micro-electro-mechanical systems (MEMS).

4.6.3 Parametric Studies on a Cantilever Beam

The response of the same cantilever beam considered above is studied here for different ply-stacking sequences. The same broadband pulse loading as shown in Figure 4.5 is applied at the cantilever tip. Axial velocity history under axial loading is plotted in Figure 4.31. For maximum possible stiffness coupling (due to $[0^o]/[90^o]$ plies in group) $r = 0.757$, peak axial velocity at the loading initiation is nearly 1.5 times greater than for the unidirectional ply configuration ($r = 0.0$). The locations of the reflected pulse change due to the variation of the group speed with r. Another interesting feature noticed is the dispersiveness of the reflected wave. This dispersion increases with increase in the coupling. In Figure 4.32, transverse velocity history under transverse loading is plotted, and shows increasing dispersion of the reflected waves for increasing stiffness coupling. For $[0^o]/[90^o]$ ply stacking ($r = 0.757$), the peak transverse velocity at the loading initiation increases by 20% compared to that for the unidirectional ply configuration.

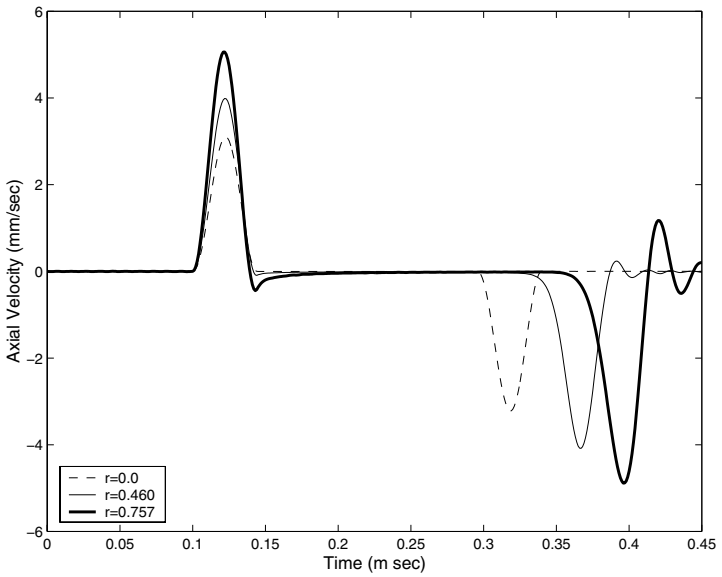

Fig. 4.31. Axial tip response of AS/3501-6 graphite–epoxy cantilever beam with different asymmetric ply-stacking configuration under axial loading at the tip

4.6.4 Response of a Beam with Ply-drops

Very often in composite structural components, a tapered profile is provided by ply-drops. Sometimes, such a configuration also becomes necessary to meet

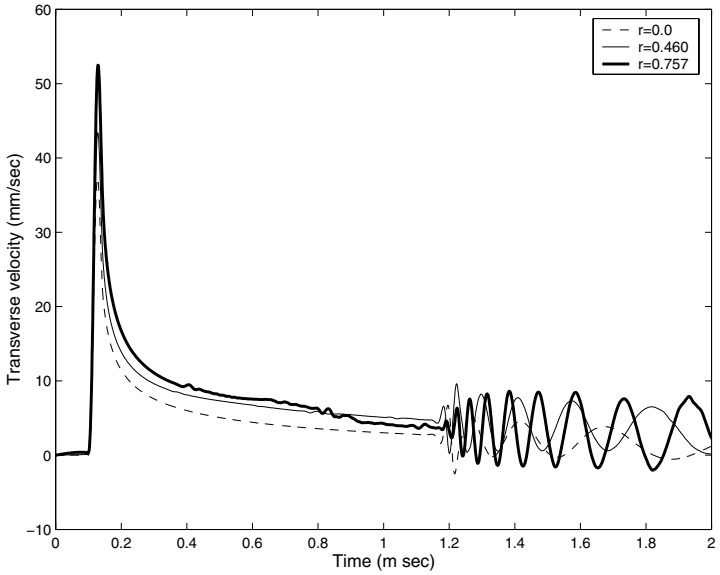

Fig. 4.32. Transverse tip response of AS/3501-6 graphite–epoxy cantilever beam with different asymmetric ply-stacking configuration under transverse loading at the tip

cost-effective design requirements. This can be achieved in the case of composite beams by reducing the number of plies along the longitudinal direction at appropriate locations. This example demonstrates the use of the developed SFEM to estimate the effects of ply-drops in a composite beam subjected to impact loading. Figure 4.33 shows the geometrical representation of an AS/3501-6 graphite epoxy cantilever beam with ply-drops for the purpose of numerical illustration. The beam has thickness 0.025 m at the root and 0.01 m at the tip. The broadband pulse loading of Figure 4.5 is applied at the free end and the response is measured at the same location.

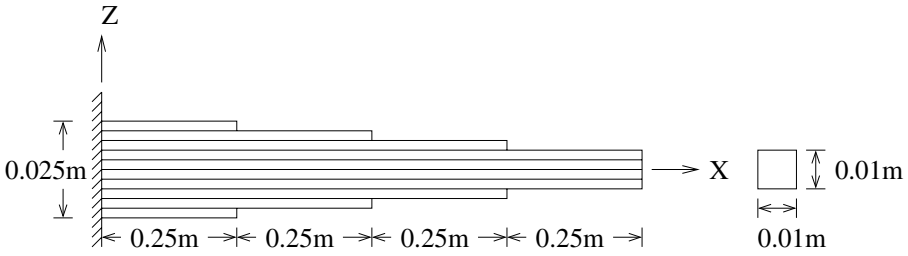

Fig. 4.33. Composite cantilever beam with ply-drops along the length

The axial velocity history at the free end under axial loading is shown in Figure 4.34. It can be observed from this plot that there are four reflected pulses occurring after the incident pulse. The first three are reflections from points where there is a change in thickness. Also, the magnitude of the velocity peaks changes with the change in stiffness across the discontinuity. For asymmetric ply stacking (for $[+45^o]/[-45^o]$ in group, $r = 0.460$), there is a significant delay in the arrival of the reflected pulses. Figure 4.35 shows the transverse velocity history at the free end under transverse loading. Presence of reflected pulses due to change of thickness along the beam can clearly be seen in this plot. It can also be observed that the reflection from the fixed boundary arrives at near 1.2 ms. Similar to the axial velocity history, even here the occurrence of the reflection is little delayed for $r = 0.460$. This can be attributed to the reduction in the axial as well as the flexural stiffness, which reduces the speed of propagation in both modes.

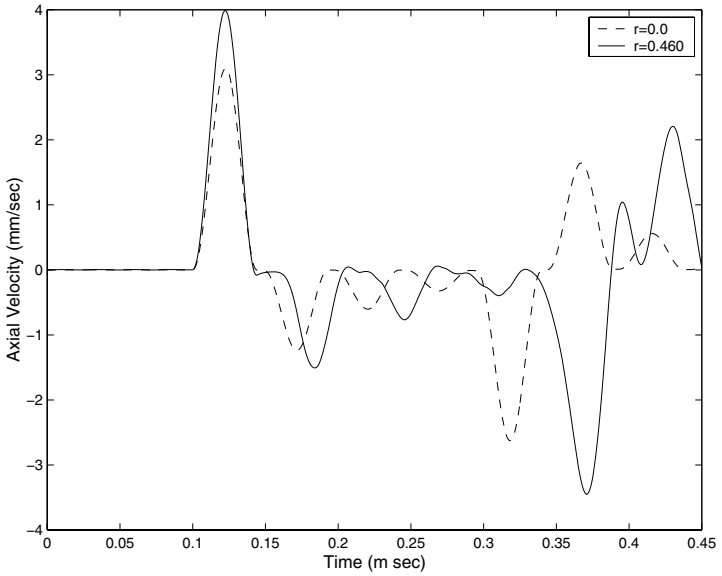

Fig. 4.34. Axial velocity history at the tip of cantilever beam with ply-drops under axial loading at the tip and for different ply stacking

In this section, SFEM for axial–flexural shear coupled wave propagation in thick laminated composite beams with arbitrary ply-stacking sequence is developed. The phase and group dispersion for different stiffness coupling and inertial coupling are studied over a broad frequency range. The range of validity of the first-order shear deformation is investigated in light of higher order thickness contractional wave modes and higher order Lamb wave modes. The study shows that the accuracy of the predicted response is restricted by

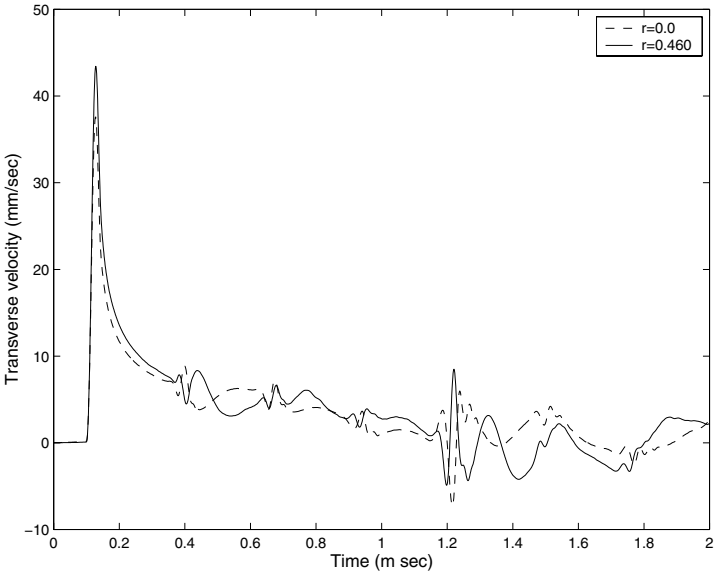

Fig. 4.35. Transverse velocity history at the tip of cantilever beam with ply-drops under transverse loading at the tip and for different ply stacking

the cut-off frequency of the higher order Lamb wave modes. Correction factors for the present model are derived based on the high frequency approximation of the Lamb wave modes in actual 2-D beam cross-section.

Next, linear damping models are formulated for the SFEM environment. Numerical studies of the effect of viscous damping on group speed and wave amplitude are performed. The results help us to explain situations, wherein the energy ceases to propagate under certain conditions. Also the plots reveal a caterpillar-like effect on the shear wave in the presence of viscous damping. Results from the developed SFEM based on FSDT are compared with SFEM based on EBT, with a time domain beam FE based on refined FSDT, and also with a 2D plane stress triangular FE model. However, window distortion, which is one inherent drawback of the Fourier transform, limits the accuracy of the predicted long duration response for undamped system. Some applications, such as wave propagation in composite beams with ply-drops, are also studied.

4.7 Layered Composite Thin-walled Tubes

In the previous section, wave propagation in connected composite waveguides of solid cross-section were studied in detail. In those studies, the complexity was gradually increased from elementary waveguide models to shear deformable waveguide models. In the present section, wave propagation in a slender cylindrical composite tubular structure is addressed. In such studies,

in addition to shear deformation, various other effects, such as cross-sectional ovalling, will come into play. The overall dynamics will be further complicated due to the coupling between various modes and this aspect will be studied in greater detail in this section.

Metallic tubular structures are used extensively in piping and skeletal components. There is an increasing usage of fiber-wound and laminated composite cylinders and tubes in automobiles, aircraft and spacecraft. Owing to their high strength, high stiffness and lightweight properties, graphite–epoxy composite strut tubes have been chosen for the International Space Station (ISS) Freedom [71]. Due to the high load carrying ability under pressurized conditions, such tubular beams are useful in inflatable space structures [72]. Significant research has been reported in the literature addressing issues related to vibration and noise transmission [73], impact dynamics, fatigue and damage in such structural components. In problems related to high frequency vibration, noise transmission and impact, many analytical and numerical methods based on wave motion have also been reported. The present section deals with the development of a spectral finite element for efficient analysis of broadband wave propagation in uniform composite tubes and connected skeletal structures. Also, special emphasis is given to model coupled wave propagation in such uniform tubular elements due to variation in the angle of laminated composite ply orientation and fiber winding.

Composite tubular structures can be modeled in two ways. (1) The general method is to use cylindrical shell kinematics. Various theories (*e.g.,* [74], [75], [76] and later [77], [78] and [79] for a composite shell) in this direction have been reported, which are based on the simpler and computationally tractable framework and observations of infinite order frequency spectral characteristics from 3-D analysis [80]. Xi *et al.* [81] used a 3-D elasticity solution and shell radial displacement from finite strip element analysis to develop a semi-analytical model to study the characteristic waves, their phase and group dispersion in a laminated composite cylindrical shell. (2) For a closed cylindrical shell, often it is useful to represent an equivalent thin-walled beam kinematics and this latter approximation based on non-axially symmetric first-order shear kinematics is used in the present work.

For uniform circular cylinders, singly curved shell kinematics is sufficient. For coupled wave propagation analysis, the displacement field in this case requires in-plane displacements, bi-directional bending and rotation about the shell normal. For a thick shell, transverse shear deformation becomes significant and 30% or higher error in deflection and natural frequencies may occur when the effect of such shear is neglected [82]. Considering first-order shear deformation in laminated anisotropic shells, finite element results and exact results for simply-supported boundary conditions have been reported in [83], [84], [85], [82]. In high frequency vibration analysis, it is essential to consider the waveband, and the representation of the entire modal group is important compared to the accuracy of one or two specific vibration modes. Therefore, analysis in the wavenumber space (k space) is found most suitable.

It was pointed out in [86] and [45] that the wave amplitudes for in-plane and flexural (circumferential) motions have significant scale difference. However, it has been shown that [87] in the presence of ring stiffeners, wave energy flow has stop bands, which are broadband and can be tuned to a required frequency band. It can be seen from the expression for the ring frequency [86] given by $\omega_R = (1/R)\sqrt{E/\rho(1-\nu^2)}$ (for flexural wave motion in cylindrical isotropic shell) that natural frequency increases as the radius of curvature R decreases. This tells us that for closed circular cylinders with short span and high thickness-to-radius ratio, the flexural vibrational modes transit from a low frequency to high frequency zone and fall in comparable scale with in-plane motion. In addition, the rotation about the shell normal causes overall torsional motion in such a tubular structure and interacts with the in-plane and flexural motion depending upon the geometrical parameter $\eta = h/R$, where $2h$ is the shell thickness. This length-scale interaction has significance for coupled wave propagation in laminated or fiber-wound composite tubular structures due to the wide range of tailorability. Further, for broadband wave propagation (waves with low as well as high group speeds for axial, flexural and torsional motion in a composite tube), a time scale $\tau = Rc_g^{-1}$ characterizes the dynamics, where $c_g(= d\omega/dk)$ is the group speed of a particular type of wave. Kaplunov *et al.* [88] discussed the wave motion in thin-walled elastic bodies considering the above scale effects.

Although there are many important applications of high frequency vibration and elastic wave propagation in composite thin-walled structures in rotorcraft, turbomachinery, piping and skeletal structures, efficient and automated modeling strategies and computational simulations need further development. In most cases, attempts to solve the problems in closed form become enormously complex. On the other hand, while using standard finite element methods, much care is needed to ensure appropriate mesh and solution schemes using a large number of cylindrical shell elements or thin-walled beam elements to capture higher order vibrational modes. Wang *et al.* [89] developed a theoretical solution for an orthotropic thick cylindrical shell under impact load based on the finite Hankel transform and Laplace transform and validated the results using an axisymmetric finite element model. Frequency domain based spectral analysis of wave motion in thin-walled bodies has been discussed in [9]. Also, structural acoustics of a complete cylindrical cavity has been studied here by solving the Helmholtz equation in cylindrical coordinates.

Several studies on free and forced vibration of composite thin-walled bodies have been reported. Song and Liberescu [90] modeled composite thin-walled closed-section beams considering non-classical effects such as primary and secondary warping. Rand [91] carried out closed-form analysis of thin-walled beams with arbitrary cross-sections and out-of-plane warping under static loading. Effects of bending twist coupling and extension bending coupling for different lamination angles have been investigated in the above work. The influence of similar coupling effects on the free vibration response of anisotropic

thin-walled closed-section beams have been reported in [92] and [93]. Ferrero *et al.* [94] studied uncoupled torsional motion in thin-walled composite beams with mid-plane symmetry. In this section, we consider coupling between axial, flexural and torsional wave modes in a first-order shear deformable composite tube in a general form, and present a computational strategy to deal with broadband wave propagation.

4.7.1 Linear Wave Motion in Composite Tube

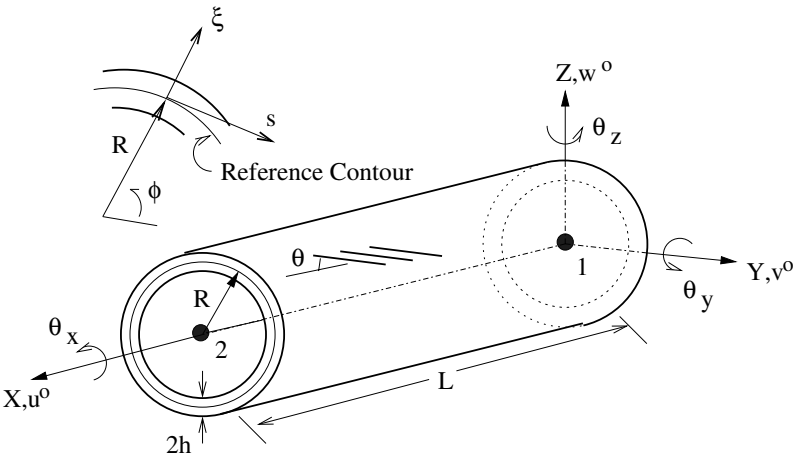

Fig. 4.36. Coordinate system and degrees of freedom in the spectral finite element for a uniform composite tube. Two finite element nodes are shown with solid circles

Considering the reference X-axis of the cylinder (Figure 4.36) as passing through the center of the annular cross-section, the displacement field can be written in terms of three primary displacements u^o, v^o and w^o and three cross-sectional rotations θ_x, θ_y and θ_z at the center as follows:

$$u(x,y,z,t) = u^o(x,t) + z\left[1 + \frac{\xi}{\sqrt{y^2+z^2}}\right]\theta_y(x,t) + y\left[1 - \frac{\xi}{\sqrt{y^2+z^2}}\right]\theta_z(x,t)\ , \tag{4.88}$$

$$v(x,y,z,t) = v^o(x,t) - z\theta_x(x,t)\ , \tag{4.89}$$

$$w(x,y,z,t) = w^o(x,t) + y\theta_x(x,t)\ , \tag{4.90}$$

where u, v and w are the longitudinal, lateral and transverse displacements, respectively, at a material point (x,y,z). θ_x, θ_y and θ_z are the torsional, transverse bending and lateral bending rotations. ξ is the radial distance of a material point measured from the mid-plane reference contour. We assume that any straight line representing the mean diameter of a circular lay-up remains

straight during deformation. This leads to the first-order shear flexibility of the annular cross-section. Such shear flexibility can be considered when an appropriate shear correction factor is introduced and will be discussed later. It is important to note that primary warping for a circular contour is zero and only secondary warping can occur, which can be derived from the formulations given by Song and Liberescu [90]. As seen in the expression for axial displacement field ($u(x, y, z, t)$) in Equation (4.88), the non-linear terms appear as the combined effect of bending and radial displacement (circumferential mode) of the reference contour, and is termed ovalling. Also note that in the above higher order cylindrical bending model, displacement continuity at the mid-plane contour is ensured. The bending rotations θ_y and θ_z are independent of the curvature and assumed constant throughout the cross-section as in the case of the Timoshenko beam model. Further details regarding similar higher order models for thin-walled closed section beams can be found in [92] and [90]. The global bending mode has multiplicity of two due to cross-sectional symmetry about the Y-axis and Z-axis. The circumferential modes consist of anti-symmetric and symmetric thickness stretching. Resonant wavenumbers for the anti-symmetric thickness stretching of a complete circular cylindrical shell simply-supported at the ends is $k = 2m\pi/S$, S being the arc-length [86]. Symmetric thickness stretching is a local higher order effect due to the Poisson's ratio and is of significance only for large $\eta = h/R$ and is not considered in the present thin-walled beam modeling. For uncoupled flexural motion of the cylindrical shell surface, the associated natural frequency is the same as the ring frequency.

The constitutive relation in the element coordinate system (X, Y, Z) is first expressed as

$$\begin{Bmatrix} \sigma_{xx} \\ \tau_{xz} \\ \tau_{xy} \end{Bmatrix} = \bar{\bar{\mathbf{Q}}} \begin{Bmatrix} \varepsilon_{xx} \\ \gamma_{xz} \\ \gamma_{xy} \end{Bmatrix} , \tag{4.91}$$

where

$$\bar{\bar{\mathbf{Q}}} = \begin{bmatrix} 1 & 0 & 0 \\ 0 & \sin\phi & \cos\phi \\ 0 & \cos\phi & -\sin\phi \end{bmatrix} \begin{bmatrix} \bar{Q}_{11} & 0 & \bar{Q}_{16} \\ 0 & \bar{Q}_{55} & 0 \\ \bar{Q}_{16} & 0 & \bar{Q}_{66} \end{bmatrix} \begin{bmatrix} 1 & 0 & 0 \\ 0 & \sin\phi & \cos\phi \\ 0 & \cos\phi & -\sin\phi \end{bmatrix} , \tag{4.92}$$

and ϕ is the polar angle of a material point in the cross-sectional plane YZ (shown in Figure 4.36). Expressions for the elements of the matrix $\bar{\mathbf{Q}}$ are obtained from the elasticity matrix $\mathbf{C}$ (given in [50]) for transversely orthotropic plies in the fiber-local coordinate system, then by rotating in the ply-local system (x, s, ξ) and then imposing plane-stress conditions on the thin-walled surface (radius of curvature R) as $\sigma_{\xi\xi} = 0$, $\tau_{s\xi} = 0$ and $\tau_{x\xi} = 0$ as discussed in [91]. This gives rise to the matrix $\bar{\mathbf{Q}}$, whose elements can be expressed as

$$\bar{Q}_{11} = Q_{11} - \frac{1}{\Delta} Q_{12} \left(Q_{13} Q_{23} - Q_{33} Q_{12} \right) + \frac{1}{\Delta} Q_{13} \left(Q_{22} Q_{13} - Q_{12} Q_{23} \right) , \tag{4.93}$$

$$\bar{Q}_{16} = Q_{16} + \frac{1}{\Delta} Q_{26} \left(Q_{12} Q_{33} - Q_{13} Q_{23} \right) \ , \quad \bar{Q}_{55} = Q_{55} - \frac{Q_{45}^2}{Q_{44}} \ , \tag{4.94}$$

$$\bar{Q}_{66} = Q_{66} + \frac{1}{\Delta} Q_{26} \left(Q_{26} Q_{33} - Q_{23} Q_{36} \right) \ , \quad \Delta = Q_{23}^2 - Q_{33} Q_{22} \tag{4.95}$$

and

$$\mathbf{Q} = \mathbf{\Gamma}^T \mathbf{C} \mathbf{\Gamma} \tag{4.96}$$

is the transformation of the elasticity matrix $\mathbf{C}$ from fiber-local coordinates to ply-local coordinates, where θ (shown in Figure 4.36) represents the fiber orientation in the ply-local coordinate system.

Shear moduli $\bar{Q}_{44}$, $\bar{Q}_{55}$ and $\bar{Q}_{66}$ are multiplied by a shear correction factor (K'), which can be computed from the expression proposed by [53]:

$$K' = \frac{6(1+\nu)(1+h'^2)^2}{(7+6\nu)(1+h'^2)^2 + (20+12\nu)h'^2} \ , \quad h' = \frac{R-h}{R+h} \ , \tag{4.97}$$

where $\nu = \nu_{23}, \nu_{13}$ and ν_{12} corresponding to $\bar{Q}_{44}$, $\bar{Q}_{55}$ and $\bar{Q}_{66}$ respectively. In the process of deriving the governing equations of motion and force boundary equations, we come across many higher order stiffness and mass coefficients, which in compact notation, are expressed, respectively, as

$$\mathbf{A}_{jl} = \int_0^{2\pi} \int_{R-h}^{R+h} \bar{\bar{Q}}_{jl} \mathbf{\Psi}^T \mathbf{\Psi} \, r \, dr \, d\phi \ , \qquad \mathbf{M} = \int_0^{2\pi} \int_{R-h}^{R+h} \rho \mathbf{\Psi}^T \mathbf{\Psi} \, r \, dr \, d\phi \ , \tag{4.98}$$

where

$$\mathbf{\Psi} = \left\{ 1 \ y \ z \ \bar{y} \ \bar{z} \ \bar{y}_{,y} \ \bar{y}_{,z} \ \bar{z}_{,y} \ \bar{z}_{,z} \right\} \ , \tag{4.99}$$

$$\bar{y} = yR \left(y^2 + z^2 \right)^{-1/2} \ , \qquad \bar{z} = z \left\{ 2 - R \left(y^2 + z^2 \right)^{-1/2} \right\} \ , \tag{4.100}$$

$$y = r \, \cos\phi \ , \qquad z = r \, \sin\phi \ , \quad r = R + \xi \ . \tag{4.101}$$

Note that in Equation (4.98), $\mathbf{A}_{jl}$ is a 9×9 matrix for each $\bar{\bar{Q}}_{jl}$, and hence, we shall use two additional subscripts after jl while expressing a single stiffness coefficient in the following derivations. The explicit forms of $\mathbf{A}_{jl}$ and $\mathbf{M}$ are given by

$$(\mathbf{A}_{jl}, \mathbf{M}) = \int_0^{2\pi} \int_{R-h}^{R+h} \left(\bar{\bar{Q}}_{jl}, \rho \right) \mathbf{\Upsilon} r dr d\phi \ , \tag{4.102}$$

where

$$\mathbf{\Upsilon} = \begin{bmatrix} 1 & y & z & \bar{y} & \bar{z} & \bar{y}_{,y} & \bar{y}_{,z} & \bar{z}_{,y} & \bar{z}_{,z} \\ & y^2 & yz & y\bar{y} & y\bar{z} & y\bar{y}_{,y} & y\bar{y}_{,z} & y\bar{z}_{,y} & y\bar{z}_{,z} \\ & & z^2 & z\bar{y} & z\bar{z} & z\bar{y}_{,y} & z\bar{y}_{,z} & z\bar{z}_{,y} & z\bar{z}_{,z} \\ & & & \bar{y}^2 & \bar{y}\bar{z} & \bar{y}\bar{y}_{,y} & \bar{y}\bar{y}_{,z} & \bar{y}\bar{z}_{,y} & \bar{y}\bar{z}_{,z} \\ & & & & \bar{z}^2 & \bar{z}\bar{y}_{,y} & \bar{z}\bar{y}_{,z} & \bar{z}\bar{z}_{,y} & \bar{z}\bar{z}_{,z} \\ & & & sym. & & \bar{y}_{,y}^2 & \bar{y}_{,y}\bar{y}_{,z} & \bar{y}_{,y}\bar{z}_{,y} & \bar{y}_{,y}\bar{z}_{,z} \\ & & & & & & \bar{y}_{,z}^2 & \bar{y}_{,z}\bar{z}_{,y} & \bar{y}_{,z}\bar{z}_{,z} \\ & & & & & & & \bar{z}_{,y}^2 & \bar{z}_{,y}\bar{z}_{,z} \\ & & & & & & & & \bar{z}_{,z}^2 \end{bmatrix}$$

and

$$\bar{\bar{Q}}_{11} = \bar{Q}_{11}\ , \quad \bar{\bar{Q}}_{15} = \bar{Q}_{16}\cos\phi\ , \quad \bar{\bar{Q}}_{16} = \bar{Q}_{16}\sin\phi\ ,$$
$$\bar{\bar{Q}}_{55} = \bar{Q}_{55}\sin^2\phi + \bar{Q}_{66}\cos^2\phi\ , \quad \bar{\bar{Q}}_{56} = \left(\bar{Q}_{55} - \bar{Q}_{66}\right)\sin\phi\cos\phi\ ,$$
$$\bar{\bar{Q}}_{66} = \bar{Q}_{66}sin^2\phi + \bar{Q}_{55}cos^2\phi\,.$$

Now, the six coupled wave equations derived using Hamilton's principle pertaining to six primary displacement variables, can be arranged as follows:

$$\begin{aligned}\delta u^o : 0 = {} & M_{11}\ddot{u}^o + M_{15}\ddot{\theta}_y + M_{14}\ddot{\theta}_z - A_{1111}u^o{}_{,xx} - A_{1611}v^o{}_{,xx} - A_{1511}w^o{}_{,xx} \\ & -(A_{1512} - A_{1613})\theta_{x,xx} - A_{1115}\theta_{y,xx} - A_{1114}\theta_{z,xx} - (A_{1519} + A_{1618})\theta_{y,x} \\ & -(A_{1517} + A_{1616})\theta_{z,x}\ ,\end{aligned} \tag{4.103}$$

$$\begin{aligned}\delta v^o : 0 = {} & M_{11}\ddot{v}^o - M_{13}\ddot{\theta}_x - A_{1611}u^o{}_{,xx} - A_{6611}v^o{}_{,xx} - A_{5611}w^o{}_{,xx} \\ & -(A_{5612} - A_{6613})\theta_{x,xx} - A_{1615}\theta_{y,xx} - A_{1614}\theta_{z,xx} - (A_{5619} + A_{6618})\theta_{y,x} \\ & -(A_{5617} + A_{6616})\theta_{z,x}\ ,\end{aligned} \tag{4.104}$$

$$\begin{aligned}\delta w^o : 0 = {} & M_{11}\ddot{w}^o + M_{12}\ddot{\theta}_x - A_{1511}u^o{}_{,xx} - A_{5611}v^o{}_{,xx} - A_{5511}w^o{}_{,xx} \\ & -(A_{5512} - A_{5613})\theta_{x,xx} - A_{1515}\theta_{y,xx} - A_{1514}\theta_{z,xx} - (A_{5519} + A_{5618})\theta_{y,x} \\ & -(A_{5517} + A_{5616})\theta_{z,x}\ ,\end{aligned} \tag{4.105}$$

$$\begin{aligned}\delta\theta_x : 0 = {} & (M_{22} + M_{33})\ddot{\theta}_x - M_{13}\ddot{v}^o + M_{12}\ddot{w}^o - (A_{1512} - A_{1613})u^o{}_{,xx} \\ & -(A_{5612} - A_{6613})v^o{}_{,xx} - (A_{5512} - A_{5613})w^o{}_{,xx} \\ & -(A_{5522} - 2A_{5623} + A_{6633})\theta_{x,xx} - (A_{1525} - A_{1635})\theta_{y,xx} \\ & -(A_{1524} - A_{1634})\theta_{z,xx} - (A_{5529} + A_{5628} - A_{5639} - A_{6638})\theta_{y,x} \\ & -(A_{5527} + A_{5626} - A_{5637} - A_{6636})\theta_{z,x}\ ,\end{aligned} \tag{4.106}$$

$$\begin{aligned}\delta\theta_y : 0 = {} & M_{55}\ddot{\theta}_y + M_{15}\ddot{u}^o + M_{45}\ddot{\theta}_z - A_{1115}u^o{}_{,xx} - A_{1615}v^o{}_{,xx} - A_{1515}w^o{}_{,xx} \\ & -(A_{1525} - A_{1635})\theta_{x,xx} - A_{1155}\theta_{y,xx} - A_{1145}\theta_{z,xx} + (A_{1519} + A_{1618})u^o{}_{,x} \\ & +(A_{5619} + A_{6618})v^o{}_{,x} + (A_{5519} + A_{5618})w^o{}_{,x} + (A_{5529} + A_{5628} - A_{5639} \\ & -A_{6638})\theta_{x,x} + (A_{1648} + A_{1549} - A_{1557} - A_{1656})\theta_{z,x} + (A_{5599} + 2A_{5689} \\ & +A_{6688})\theta_y + (A_{5579} + A_{5669} + A_{5678} + A_{6668})\theta_z\ ,\end{aligned} \tag{4.107}$$

$$\begin{aligned}\delta\theta_z : 0 = {} & M_{44}\ddot{\theta}_z + M_{14}\ddot{u}^o + M_{45}\ddot{\theta}_y - A_{1114}u^o{}_{,xx} - A_{1614}v^o{}_{,xx} - A_{1514}w^o{}_{,xx} \\ & -(A_{1524} - A_{1634})\theta_{x,xx} - A_{1145}\theta_{y,xx} - A_{1144}\theta_{z,xx} + (A_{1517} + A_{1616})u^o{}_{,x} \\ & +(A_{5617} + A_{6616})v^o{}_{,x} + (A_{5517} + A_{5616})w^o{}_{,x} + (A_{5527} + A_{5626} - A_{5637} \\ & -A_{6636})\theta_{x,x} + (A_{1557} + A_{1656} - A_{1549} - A_{1648})\theta_{y,x} + (A_{5579} + A_{5678} + A_{5669} \\ & +A_{6668})\theta_y + (A_{5577} + 2A_{5667} + A_{6666})\theta_z\ ,\end{aligned} \tag{4.108}$$

and the associated force boundary equations can be obtained as

$$\begin{aligned}& A_{1111}u^o{}_{,x} + A_{1611}v^o{}_{,x} + A_{1511}w^o{}_{,x} + (A_{1512} - A_{1613})\theta_{x,x} + A_{1115}\theta_{y,x} \\ & +A_{1114}\theta_{z,x} + (A_{1519} + A_{1618})\theta_y + (A_{1517} + A_{1616})\theta_z = N_x\ ,\end{aligned} \tag{4.109}$$

$$\begin{aligned}& A_{1611}u^o{}_{,x} + A_{6611}v^o{}_{,x} + A_{5611}w^o{}_{,x} + (A_{5612} - A_{6613})\theta_{x,x} + A_{1615}\theta_{y,x} \\ & +A_{1614}\theta_{z,x} + (A_{5619} + A_{6618})\theta_y + (A_{5617} + A_{6616})\theta_z = V_{xy}\ ,\end{aligned} \tag{4.110}$$

$$A_{1511}u^o{}_{,x} + A_{5611}v^o{}_{,x} + A_{5511}w^o{}_{,x} + (A_{5512} - A_{5613})\theta_{x,x} + A_{1515}\theta_{y,x} + A_{1514}\theta_{z,x} + (A_{5519} + A_{5618})\theta_y + (A_{5517} + A_{5616})\theta_z = V_{xz} \ , \tag{4.111}$$

$$(A_{1512} - A_{1613})u^o{}_{,x} + (A_{5612} - A_{6613})v^o{}_{,x} + (A_{5512} - A_{5613})w^o{}_{,x} + (A_{5522} - 2A_{5623} + A_{6633})\theta_{x,x} + (A_{1525} - A_{1635})\theta_{y,x} + (A_{1524} - A_{1634})\theta_{z,x} + (A_{5529} + A_{5628} - A_{5639} - A_{6638})\theta_y + (A_{5527} + A_{5626} - A_{5637} - A_{6636})\theta_z = M_x \ , \tag{4.112}$$

$$A_{1115}u^o{}_{,x} + A_{1615}v^o{}_{,x} + A_{1515}w^o{}_{,x} (A_{1525} - A_{1635})\theta_{x,x} + A_{1155}\theta_{y,x} + A_{1145}\theta_{z,x} + (A_{1559} + A_{1658})\theta_y + (A_{1557} + A_{1656})\theta_z = M_y \ , \tag{4.113}$$

$$A_{1114}u^o{}_{,x} + A_{1614}v^o{}_{,x} + A_{1514}w^o{}_{,x} + (A_{1524} - A_{1634})\theta_{x,x} + A_{1145}\theta_{y,x} + A_{1144}\theta_{z,x} + (A_{1549} + A_{1648})\theta_y + (A_{1547} + A_{1646})\theta_z = M_z \ . \tag{4.114}$$

We solve the wave Equations (4.103)–(4.108) exactly in the frequency domain. The solution for wavenumber and wave amplitudes are quite complex here and the PEP based method must be used. The PEP will result in a 12th order polynomial for k. The details are skipped here because of the complexity.

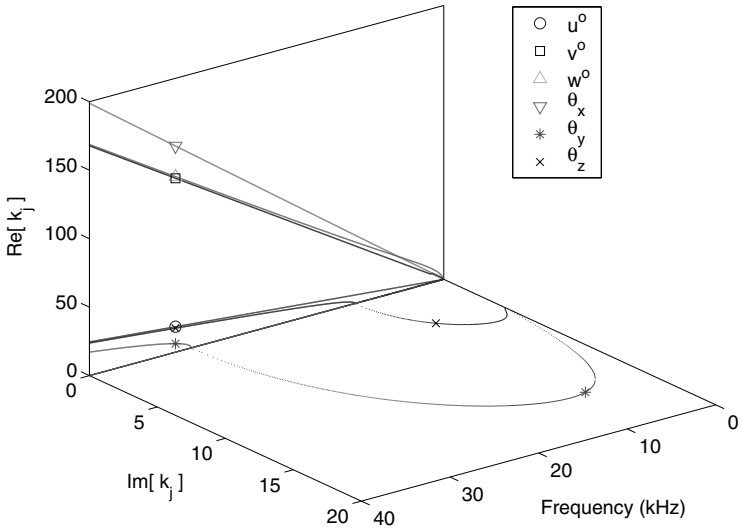

Fig. 4.37. Plot of wavenumbers k_j for an AS/3501-6 graphite–epoxy composite tubular cross-section with fiber angle $\theta = 0^o$, $h = 0.002\,m$, $\eta = h/R = 0.1$

Wavenumber dispersion curves are plotted in Figure 4.37 for an AS/3501-6 graphite–epoxy composite tubular cross-section with fiber angle $\theta = 0^o$, $h = 0.002$ m, $\eta = h/R = 0.1$. The material properties used are: elastic moduli $E_{11} = 144.48$ GPa, $E_{22} = 9.632$ GPa, $E_{33} = 9.412$ GPa, $G_{23} = 6.516$ GPa, $G_{13} = 7.457$ GPa, $G_{12} = 4.128$ GPa; Poisson's ratio: $\nu_{23} = 0.49$, $\nu_{13} = 0.3$, $\nu_{12} = 0.3$ and density $\rho = 1389.2$ kg/m^3. In Figure 4.37, only the positive

wavenumbers (forward propagating and evanescent modes) are plotted. Negative wavenumbers with the same amplitudes also exist and they represent backward propagating or evanescent modes. One order of scale difference between the wavenumbers associated with propagating axial, shear and propagating flexural, torsional modes can be seen. The plot also shows that at any material point, there will be additional propagating shear wave modes due to shear deformations γ_{xz} and γ_{xy} above the respective cut-off frequencies. The cut-off frequencies satisfy $\mathrm{Det}\mathbf{F}(0) = 0$. Below these cut-off frequencies, the shear waves are evanescent in nature.

4.8 Spectral Finite Element Model

The formulation of the finite length and throw-off elements are very similar to previous formulations and hence not given here. Each node in this tube element has six dof and the size of the stiffness matrix for a finite tube is 12×12 while that for the throw-off element is 6×6.

4.8.1 Short and Long Wavelength Limits for Thin Shell and Limitations of the Proposed Model

From the kinematic assumptions (Equations (4.88)–(4.90)) in the proposed higher order cylindrical bending model, it is clear that there are restrictions on using this model for wave propagation in very thin as well as very thick shells. Typically, for thin shells, one would expect the shell transverse motion to be the predominant one compared to that due to bending rotation of the shell cross-section. In thin cylindrical shells, therefore, the axisymmetric radial motion becomes important. On the other hand, in thick cylindrical shells, one would expect the propagation of higher order Lamb wave modes (first and higher symmetric stretching modes, and third and higher anti-symmetric modes) apart from the propagating longitudinal, flexural and shear wave modes. For thick cylindrical shells, therefore, the spectral band should be limited to below the cut-off frequencies of the higher order Lamb wave modes that are not included in the kinematics of the present model. The short and long wavelength limits for thin shells (based on Love's thin shell theory), beyond which significant deviation of the proposed model from the actual behavior may occur, are discussed below.

Let us consider a cylindrical thin shell segment as shown in Figure 4.38, where u, v and w are the longitudinal, tangential and radial displacements, respectively. By neglecting the effect of bending moment, transverse shear deformation and rotation of the shell normal, the thin shell kinematics [95] can be written as

$$\varepsilon_{xx} = u_{,x} \ , \quad \varepsilon_{\phi\phi} = \frac{1}{R}\left(w + v_{,\phi}\right) \ , \quad \gamma_{x\phi} = v_{,x} + \frac{1}{R}u_{,\phi} \ . \tag{4.115}$$

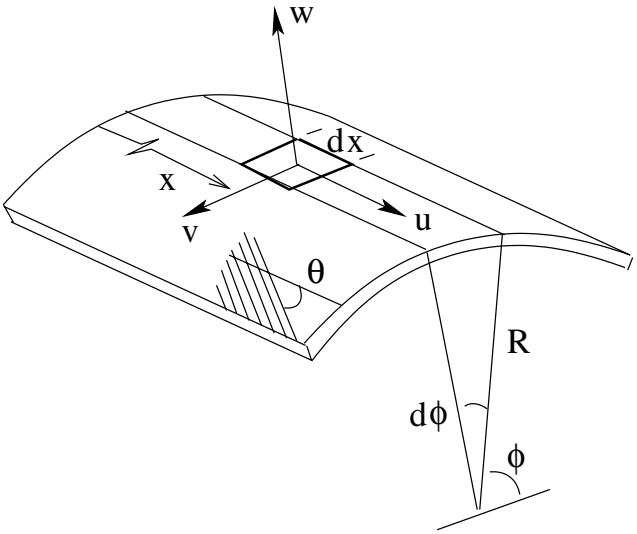

Fig. 4.38. Coordinate system and degrees of freedom for a laminated composite thin shell ($h << R$)

The orthotropic constitutive model in the ply-local coordinate system can be expressed as

$$\begin{Bmatrix} \sigma_{xx} \\ \sigma_{\phi\phi} \\ \tau_{x\phi} \end{Bmatrix} = \begin{bmatrix} \bar{Q}_{11} & \bar{Q}_{12} & \bar{Q}_{16} \\ \bar{Q}_{12} & \bar{Q}_{22} & \bar{Q}_{26} \\ \bar{Q}_{16} & \bar{Q}_{26} & \bar{Q}_{66} \end{bmatrix} \begin{Bmatrix} \varepsilon_{xx} \\ \varepsilon_{\phi\phi} \\ \gamma_{x\phi} \end{Bmatrix} . \tag{4.116}$$

Substituting Equations (4.115) and (4.116) in the energy components and applying Hamilton's principle, the coupled wave equations for the composite thin shell can be expressed as

$$\begin{aligned} -I_0\ddot{u} + \bar{A}_{11}u_{,xx} + \bar{A}_{12}\tfrac{1}{R}(w_{,x} + v_{,x\phi}) + \bar{A}_{26}\tfrac{1}{R^2}(w_{,\phi} + v_{,\phi\phi}) \\ + \bar{A}_{16}(\tfrac{2}{R}u_{,x\phi} + v_{,xx}) + \bar{A}_{66}\tfrac{1}{R}(v_{,x\phi} + \tfrac{1}{R}u_{,\phi\phi}) = 0 , \end{aligned} \tag{4.117}$$

$$\begin{aligned} -I_0\ddot{v} + \bar{A}_{12}\tfrac{1}{R}u_{,x\phi} + \bar{A}_{22}\tfrac{1}{R^2}(w_{,\phi} + v_{,\phi\phi}) + \bar{A}_{16}u_{,xx} \\ + \bar{A}_{26}\tfrac{1}{R}(w_{,x} + 2v_{,x\phi} + u_{,\phi\phi}) + \bar{A}_{66}(v_{,xx} + \tfrac{1}{R}u_{,x\phi}) = 0 , \end{aligned} \tag{4.118}$$

$$I_0\ddot{w} + \bar{A}_{12}\frac{1}{R}u_{,x} + \bar{A}_{22}\frac{1}{R^2}(w + v_{,\phi}) + \bar{A}_{26}\frac{1}{R}v_{,x} = 0 , \tag{4.119}$$

where

$$(\bar{A}_{jl}, I_0) = \int_{-h}^{+h} (\bar{Q}_{jl}, \rho)\, dz . \tag{4.120}$$

To obtain the characteristic equation, the spectral form of the displacement variable $\mathbf{u} = \{u\ , v\ , w\}^T$ in k-space can be assumed, which is

$$\mathbf{u} = \sum \hat{\mathbf{u}}(\phi) e^{-j(kx - \omega_n t)} , \tag{4.121}$$

where k is the wavenumber in the longitudinal direction. For displacement continuity of the circumferential motion, $\hat{\mathbf{u}}(\phi) = \hat{\mathbf{u}}(2\pi + \phi)$. Therefore, for circumferential wave propagation, we can write

$$\mathbf{u} = \sum \tilde{\mathbf{u}}(\phi) e^{-j(kx+\gamma\phi-\omega_n t)} \ , \tag{4.122}$$

where γ is the integer wavenumber in the tangential direction. Coupling between the longitudinal and tangential modes for different fiber angles θ (Figure 4.38) is preserved through the wave coefficient vector $\tilde{\mathbf{u}}$. Substituting Equation (4.122) in the thin shell wave Equations (4.117)–(4.119), the characteristic equation becomes

$$\mathrm{Det}\mathbf{G}(k,\gamma) = 0 \ . \tag{4.123}$$

Since our objective here is to determine restrictions of the proposed model as the shell becomes very thin $h << R$, the fundamental axisymmetric modes and pure tangential modes need to be studied at the limits of the short and long wavelengths.

The fundamental axisymmetric modes (longitudinal and radial) and vanishing tangential mode are recovered from Equation (4.123) by substituting $\eta = 0$ and solving for k. In this case, we get a fourth-order characteristic equation in k given by

$$ak^4 + bk^2 + c = 0 \ , \tag{4.124}$$

where

$$\begin{aligned} a = \omega_n^2 I_0(-\bar{A}_{11}\bar{A}_{66} + \bar{A}_{16}^2) + \tfrac{1}{R^2}\left(\bar{A}_{11}\bar{A}_{22}\bar{A}_{66} - \bar{A}_{11}\bar{A}_{26}^2 - \bar{A}_{16}^2\bar{A}_{22}\right. \\ \left. +2\bar{A}_{12}\bar{A}_{16}\bar{A}_{26} - \bar{A}_{12}^2\bar{A}_{66}\right) \ , \end{aligned} \tag{4.125}$$

$$b = \omega_n^4 I_0^2(A_{66} + A_{66}) - \omega_n^2 I_0 \frac{1}{R^2}\left(A_{11}A_{22} + A_{22}A_{66} - A_{12}^2 - A_{26}^2\right) \ , \tag{4.126}$$

$$c = -\omega_n^6 I_0^3 + \omega_n^2 I_0 \frac{1}{R^2} A_{22} \ . \tag{4.127}$$

In the short wavelength limit, $k \to \infty \Rightarrow a = 0$

$$\Rightarrow \omega_s = \omega_n = \left[\frac{(A_{11}A_{22} - A_{12}^2)A_{66} + 2A_{12}A_{16}A_{26} - A_{11}A_{26}^2 - A_{22}A_{16}^2}{R^2 I_0(A_{11}A_{66} - A_{16}^2)}\right]^{1/2} \tag{4.128}$$

is the frequency at which the wave dispersion has a singularity. That is, the cylinder experiences resonance at ω_s in the axisymmetric radial mode. In the long wavelength limit, $k \to 0 \Rightarrow c = 0$

$$\Rightarrow \omega_l = \omega_n = 0 \ , \frac{1}{R}\sqrt{\frac{A_{22}}{I_0}} \tag{4.129}$$

is the frequency after which the axisymmetric radial mode again starts propagating and is also the cut-off frequency for the axisymmetric wave propagating

in thin shell. For the isotropic case, this becomes $(1/R)\sqrt{E/\rho(1-\nu^2)}$ and is called the ring frequency, which was discussed in the introductory discussion. Also, for the isotropic case, ω_s becomes simply $(1/R)\sqrt{E/\rho}$ and smaller than the ring frequency. Hence, for isotropic as well as orthotropic materials, it can be said that the axisymmetric radial mode first becomes resonant at ω_s and cease to propagate and then again starts propagating at a little higher frequency, that is at ω_l. For $h = 2$ mm and $\eta = 0.1$ as considered in Figure 4.37, these limiting frequencies are $\omega_s = 20.954$ kHz and $\omega_l = 21.017$ kHz.

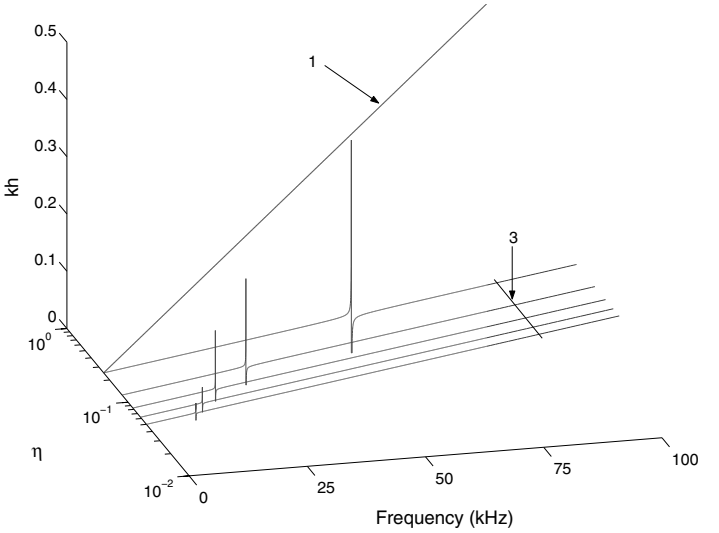

Fig. 4.39. Plot of wavenumbers in axisymmetric modes (1 - longitudinal, 3 - radial) for different $\eta(= h/R)$ (0.05 to 0.25) for $\theta = 0^o$ AS/3501-6 graphite–epoxy composite shell

Figure 4.39 shows the location of the singularity and cut-off in the axisymmetric radial mode (marked 3) in a graphite–epoxy composite shell with different $\eta(= h/R)$ and $\theta = 0$. The non-dispersive longitudinal modes (marked 1) remain unchanged for all values of η. Figure 4.40 shows the separation between the singularity (ω_s on the lower side along the frequency axis) and the cut-off frequency following the new propagation of the axisymmetric radial mode (ω_l on the higher side along the frequency axis). Therefore, to exclude the effect of the unaccounted radial mode (as in the case of the proposed new tubular element), the best comparable behavior of a cylindrical tube (when modeled as a beam) can be obtained for a certain range of η, such that the applied forcing frequency band falls below $\omega_s < \omega_l$. As a special case for certain orientation of the fibers, a second frequency band between ω_s and ω_l (Figure 4.40) can be obtained, within which the axisymmetric radial mode vanishes. This can be clearly seen from Figure 4.41, which shows that almost

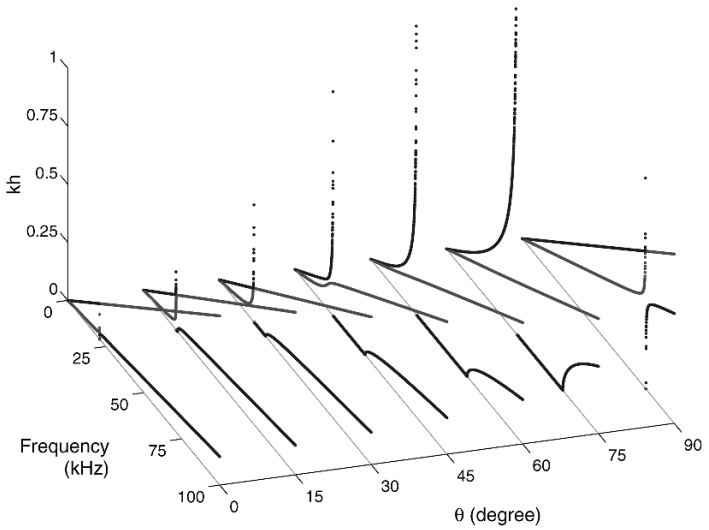

Fig. 4.40. Plot of wavenumbers in axisymmetric modes (1 - longitudinal, 3 - radial) for different fiber angles θ for $\eta = 0.1$ $h = 2$ mm AS/3501-6 graphite–epoxy composite shell

35 kHz bandwidth is available with vanishing axisymmetric radial mode for a tube cross-section having $\eta = 0.1$ and fiber angle $\theta = 60°$. This is the so called stop-band for the radial mode, which is an important design parameter for composite shells for controlling vibration and buckling. However, it should be noted that for the composite tube when designed to behave mainly as a thin-walled beam structure, the beam motion is less likely to be affected by the radial mode (as the motion of the beam axis remains unaltered), unless a circumferential normal pressure type loading is applied.

The fundamental cross-sectional warping mode consisting of coupled torsional radial motion is recovered by substituting $k = 0$ in Equation (4.123) and solving the fourth-order polynomial in γ given by

$$a'\gamma^4 + b'\gamma^2 + c' = 0 \,, \tag{4.130}$$

where

$$a' = -\omega_n^2 I_0 \frac{1}{R^4} A_{22} A_{66} + \omega_n^2 I_0 \frac{1}{R^3} A_{26}^2 \,, \tag{4.131}$$

$$b' = \omega_n^4 I_0^2 \frac{1}{R^2}(A_{22} + A_{66}) - \omega_n^2 I_0 \frac{1}{R^4} A_{22} A_{66} \,, \tag{4.132}$$

$$c' = -\omega_n^6 I_0^3 + \omega_n^4 I_0^2 \frac{1}{R^2} A_{22} \,. \tag{4.133}$$

In the short wavelength limit, $\gamma \to \infty \Rightarrow a' = 0$

$$\Rightarrow \omega_s = \omega_n = 0 \quad \text{or} \quad R = \frac{A_{22} A_{66}}{A_{66}^2} \to \infty \,, \tag{4.134}$$

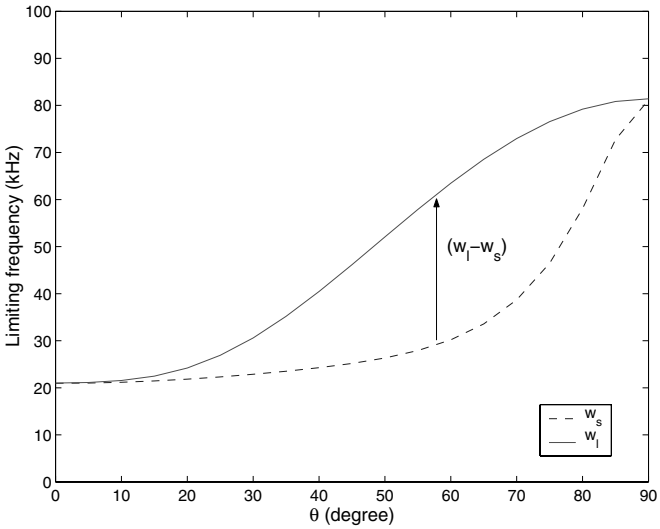

Fig. 4.41. Separation between the short and long wave limiting frequencies ($\omega_l - \omega_s$) for different fiber angles θ for $\eta = 0.1$, $h = 2$ mm AS/3501-6 graphite–epoxy composite shell

which shows that for a smaller radius cylindrical tube, the wavelength of the radial mode becomes longer and vanishes beyond the long wavelength limit ω_l, which is also the cut-off frequency for such propagation. This long wavelength limit is obtained for $\gamma \to 0 \Rightarrow c' \to 0$

$$\Rightarrow \omega_l = \omega_n = 0 \, , \frac{1}{R}\sqrt{\frac{A_{22}}{I_0}} \, , \tag{4.135}$$

which is the same as the cut-off frequency of the radial mode in the axisymmetric case (Equation (4.129)). Figure 4.43 shows the decreasing nature of γ (hence increasing wavelengths) for the tangential and the radial modes for increasing η. Also, the cut-off frequency of the radial modes shifts towards higher frequencies for increasing η (smaller radius for a given shell thickness). Figure 4.42 shows a similar shift in the cut-off frequency of the radial mode (as in the above case) for increasing fiber angles θ for $\eta = 0.1$. However, the tangential or torsional mode has a symmetry about $\theta = 45^o$ and is non-dispersive. Such cross-sectional warping is already present in the proposed model (see the kinematics), where propagation of the radial mode induced by torsional load is not restricted due to any additional kinematical assumptions.

The above analysis shows that the main limitation of the proposed tubular element while capturing the behavior of composite thin cylindrical shells, is that the axisymmetric radial mode induced by longitudinal load is absent in the element. Also, the circumferential normal pressure load on the cylindrical cross-section cannot be modeled. The best comparable thin shell

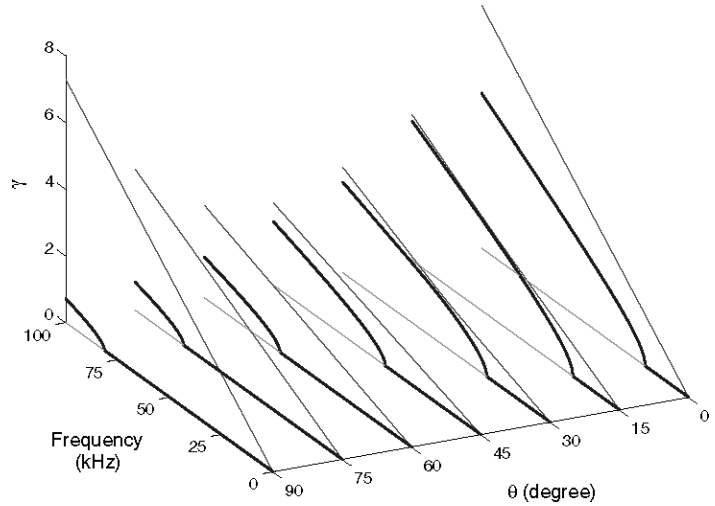

Fig. 4.42. Plot of wavenumbers in tangential-radial modes (2 - tangential, 3 - radial) for different fiber angles θ for $\eta = 0.1$ $h = 2$ mm AS/3501-6 graphite–epoxy composite shell. Only integer values of the wavenumbers γ are admissible

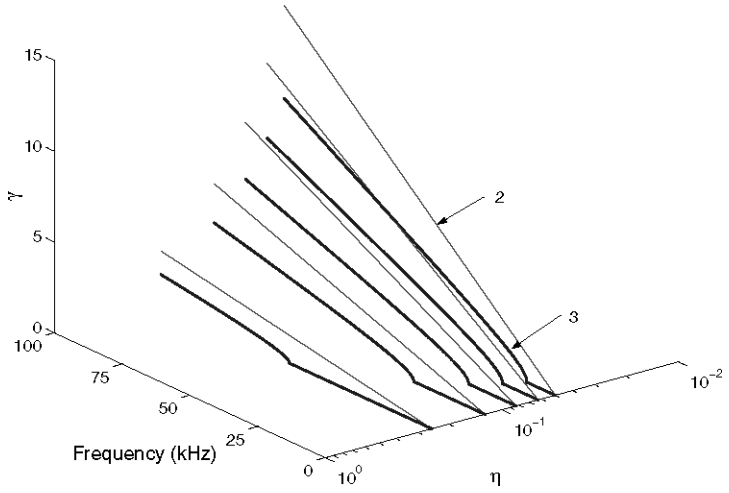

Fig. 4.43. Plot of wavenumbers in tangential-radial modes (2 - tangential, 3 - radial) for different $\eta(= h/R)$ (0.05 to 0.25) for $\theta = 0^{\circ}$ AS/3501-6 graphite–epoxy composite shell. Only integer values of the wavenumbers γ are admissible

behavior can be captured over a frequency band below the limiting frequency of short wavelength ω_s and over the stop-bands $(\omega_l - \omega_s)$ for specified values of $\eta(= h/R)$ and fiber angle θ for axisymmetric modes. On the higher side of η and smaller L/R, one needs to consider the effect of parabolic transverse shear stress variation across the shell thickness and vanishing normal stress at the shell surfaces in the kinematics, which are not included in the present model. Therefore, for accurate results, application of the present tubular element needs to be restricted to forcing frequency bandwidths below the lowest of the new cut-off frequencies of any of these unaccounted modes (*i.e.,* higher order anti-symmetric Lamb wave mode due to parabolic transverse shear, and symmetric Lamb wave mode due to vanishing normal stress at the shell surfaces). However, it can be seen that for both axisymmetric and torsional excitations in very thick cylindrical shell and rod [80], the lowest longitudinal and torsional modes remain non-dispersive and they are preserved in the present model. The studies on characteristic wave behavior reported in [81] for higher thickness and anisotropy can be adopted to determine the thickness limit for a particular application while using the present SFE.

4.8.2 Comparison with Analytical Solution

Although many theories based on potential functions as well as first-order and higher order shear deformable shell kinematics have been reported in the literature as discussed earlier, most of the wave propagation studies are focused on the analysis of the frequency spectrum and harmonic analysis in modal space and these are difficult to apply for transient dynamic analysis. For validation of the results from the present SFEM, which is highly suited to broadband and impact type loading on composite tubes, we consider the analytical solution for impact induced response of a semi-infinite membrane shell [95] for unidirectional ($\theta = 0^o$) composite. The kinematics is given in Equation (4.115). Additional approximations that can be made under longitudinal impact are $\frac{\partial}{\partial \phi}(\,) = 0$ and $v \to 0$. Starting with shear deformable kinematics also, the same approximation remains valid (except near structural boundaries across the span) under longitudinal impact, and the wave equations take the form

$$-I_0 \ddot{u} + A_{11} u_{,xx} + A_{12} \frac{1}{R} w_{,x} = 0 \,, \tag{4.136}$$

$$I_0 \ddot{w} + A_{12} \frac{1}{R} u_{,x} + A_{22} \frac{1}{R^2} w = 0 \,, \tag{4.137}$$

subjected to initial condition $\dot{u}(x, 0) = 0$ at $t = 0$, the boundary conditions $u = u(x, t)$ and $w = w(x, t)$ prescribed at a particular x or

$$-A_{11} u_{,x} - A_{12} \frac{1}{R} w = N_x \,, \tag{4.138}$$

where N_x is the applied longitudinal impact. Assuming the solution of the field variables $\mathbf{u}$ transformed into their time uncoupled Fourier coefficients (spectral amplitude) $\hat{\mathbf{u}}$ as done earlier, we can write

$$u = \sum_n \hat{u} e^{i\omega_n t} \ , \quad \hat{u} = \tilde{u}_1 e^{-j\bar{k}x} + \tilde{u}_2 e^{j\bar{k}x} \ , \tag{4.139}$$

$$w = \sum_n \hat{w} e^{i\omega_n t} \ , \quad \hat{w} = \tilde{w}_1 e^{-j\bar{k}x} + \tilde{w}_2 e^{j\bar{k}x} \ , \tag{4.140}$$

where the wavenumber

$$\bar{k} = \sqrt{\frac{\omega_n^2 I_0 \frac{1}{R^2} A_{22} - \omega_n^4 I_0^2}{\omega_n^2 I_0 A_{11} - (A_{11}A_{22} - A_{12}^2)\frac{1}{R^2}}} \tag{4.141}$$

is obtained by solving the characteristic equation derived from Equations (4.136) and (4.137). ω_n is the sampling frequency used for forward and inverse FFT and is the same as the sampling frequency of the impact loading spectrum $\hat{N}_x(\omega_n)$ (Figure (4.5)) used to excite the structure. Considering the free-end of the semi-infinite complete cylindrical membrane shell under impact load is at $x = L$ and the other end is at $x = -\infty$, the displacement spectrum $\hat{u}$ finally becomes

$$\hat{u} = \tilde{u}_1 e^{-j\bar{k}x} \ , \quad \tilde{u}_1 = \frac{\hat{N}_x/(2\pi R)}{(-j\bar{k}A_{11} + A_{12}\frac{1}{R}R_{21})e^{-j\bar{k}L}} \ , \tag{4.142}$$

where

$$R_{21} = \frac{-jA_{12}\frac{1}{R}\bar{k}}{-\omega^2 I_0 + A_{22}\frac{1}{R^2}} \ . \tag{4.143}$$

The short impulse type loading used for longitudinal impact is shown in Figure 4.5. The peak amplitude used in this case is 100 N, whereas, the time duration remains same as 50 μs. Fine discretization of the frequency spectrum with Nyquist point $N = 16384$ ($\Delta t = 1\,\mu$s) is made while the inverse FFT of the analytically computed velocity spectrum $j\omega_n\hat{u}$ (Equation (4.142)) is taken to obtain the velocity history at $x = L$. Graphite–epoxy unidirectional composite ($\theta = 0^o$) with material properties as considered earlier is used here. The velocity history from the analytical result is plotted in comparison with the velocity history from SFEM in Figure 4.44. It can be seen from the analytical result that the initial impact has produced a non-dispersive longitudinal wave coupled with radial motion after the initial incidence. Although the tube is semi-infinite along x, the almost stationary axisymmetric radial motion has a non-decaying effect, which has caused window distortion. This numerical problem inherent to the FFT is evident from the initial non-zero values in the analytical response before the initial incidence at around 100 μs (Figure 4.5). The non-dispersive nature of the longitudinal velocity after incidence, which is due to coupling with radial motion, could not be captured by the SFEM as the DOFs associated with axisymmetric radial motion are absent in the model. Also, the peak velocity estimate from SFEM is higher than that from the analytical result.

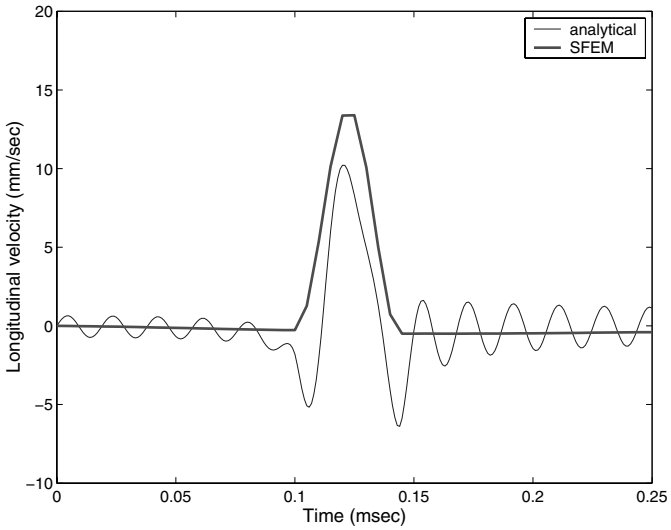

Fig. 4.44. Comparison of the mid-plane longitudinal velocity from SFEM and the analytical result at the free end of a semi-infinite graphite–epoxy unidirectional ($\theta = 0^o$) composite membrane shell ($h = 0.002$ m, $h/R = 0.1$) with a short pulse (Figure 4.5) applied in the longitudinal direction

4.9 Numerical Simulations

As discussed in the introduction, many solution methods and fundamental studies have been reported in the literature on wave propagation in cylindrical shells. Although few studies are on composite shells and thin-walled bodies, they focus on in-plane and flexural wave motions separately. In this section, numerical simulations are carried out considering a single cantilever graphite–epoxy tubular element.

4.9.1 Time Response Under Short Impulse Load and the Effect of Fiber Orientations

The short impulse load history used to excite the clamped–free graphite–epoxy composite tube at its free end is shown in Figure 4.5. The time duration is approximately $50\,\mu$s with peak amplitude of $100\,N$. Such a broadband load also encompasses the propagating shear wave modes (see Figure 4.37). The SFE is formulated considering an undamped system. However, in composite structures, damping is a common phenomenon. Different approaches to include the effect of proportional and non-proportional damping in SFEM have been proposed in the previous section and in [96]. In the following simulations, we assume a small amount of damping in the form $k_j \rightarrow k_j(1 - i\eta_d)$, where the damping coefficient (also called the loss factor) $\eta_d = 0.001$. Also,

improved numerical stability and reduced effect of frequency window distortion can be achieved by using such artificial damping in an undamped model when accurate time responses need to be post-processed.

First, we simulate the dynamic response of a clamped–free tube ($L = 1$ m, $L/R = 50$, $\eta = 0.1$, $\theta = 0^\circ$) by applying the above short pulse at the free end separately in global X and Z directions and a similar moment of 100 N-m about the X-axis.

For load applied in the X-direction, the deformed outer surface ($\xi = h$) geometry is snapped at $t = 0.5$ ms in Figure 4.45. One limitation of the model is clearly visible from this simulation; the absence of any axisymmetric surface undulations on the axially compressed rings. Such a small-scale effect can be obtained through general shell kinematics as discussed in Section 4.8.1. For three different sets of fiber angle, the axial displacement and the axial velocity histories at the point $(1, 0, R + h)$ on the free-end are shown, respectively, in Figure 4.46 and 4.47. After the initial incidence of the impact, repeated reflections from the clamped end of the tube can be seen in both responses. It is interesting to note that the $\theta = [0^o]_{10}/[90^o]_{10}$ configuration, which generates maximum thickness asymmetry along the local ξ direction, is less responsive than the $\theta = [+45^o]_{10}/[-45^o]_{10}$ configuration.

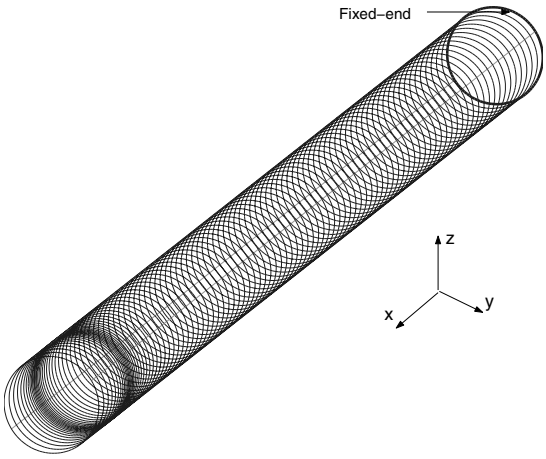

Fig. 4.45. Snap of the outer surface geometry at $t = 0.5$ msec for the graphite–epoxy composite clamped–free tube ($L = 1$ m, $L/R = 50$, $\eta = 0.1$ with $\theta = 0^\circ$ lay-up). A short pulse load (Figure 4.5) is applied uniformly at the free end along the X-direction. Scale-factor for displacement amplification is 1×10^8

For load applied in the Z-direction, the deformed outer surface ($\xi = h$) geometry is snapped at $t = 0.5$ ms in Figure 4.48. The effect of ovaling near the mid-length of the tube can be observed. For three different sets of fiber angle, the transverse displacement and transverse velocity histories at the

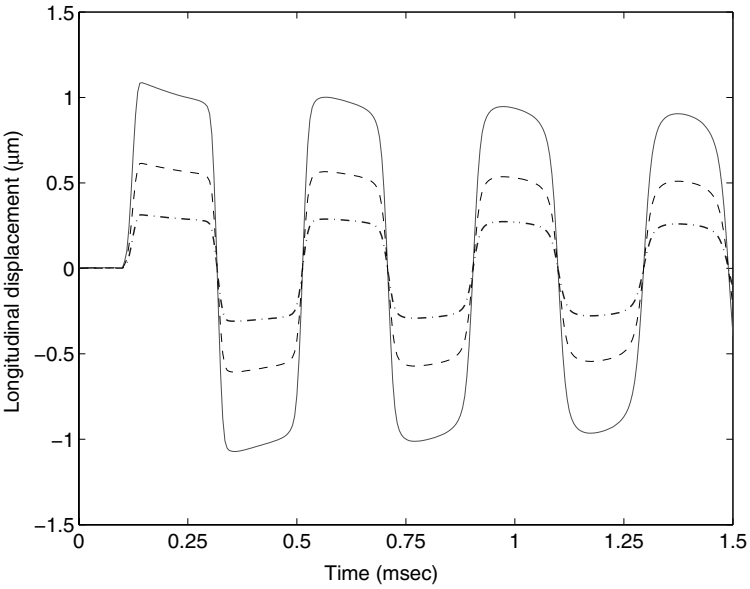

Fig. 4.46. Longitudinal displacement history $u(t)$ at a point on the outer top-surface ($y = 0$, $z = R + h$) at the free end ($x = 1$ m) of the cantilever composite tube for different fiber angles. -.-.- $\theta = [0^\circ]_{20}$; —— $\theta = [+45^\circ]_{10}/[-45^\circ]_{10}$; - - - $\theta = [0^\circ]_{10}/[90^\circ]_{10}$

point $(1, 0, R + h)$ on the free end are shown, respectively, in Figure 4.49 and 4.50. Unlike the axial responses shown earlier, here, the responses are dispersive. After the initial incidence of the impact, one reflection from the clamped end of the tube can be seen in both responses, which arrive at the measurement point at about $t = 1.4$ ms. Compared to the axial response, here the $\theta = [0^\circ]_{20}$ configuration generates the maximum transverse response. There are small distortions in the predicted responses before the incidence of impact (before $t = 50\,\mu$s), which are due to the frequency window wrap-around during inverse FFT and is inherent to any analysis in the transformed finite domain.

For torsional load applied about the X-axis, the deformed outer surface ($\xi = h$) geometry is snapped at $t = 0.5$ ms in Figure 4.51. It can be seen that the rings through which the torsional waves have propagated towards the clamped end have bulged almost axisymmetrically, which can be attributed to the combined effect of anti-symmetric thickness stretching and rotational inertia of the tube cross-section. For three different sets of fiber angle, lateral displacement and lateral velocity histories at the point $(1, 0, R+h)$ on the free end are shown, respectively, in Figures 4.52 and 4.53. Although the torsional waves are non-dispersive for $\theta = 0^o$ (see the dispersion curve in Figure 4.37), the lateral flexural waves are dispersive and finally, the combined effect (Equa-

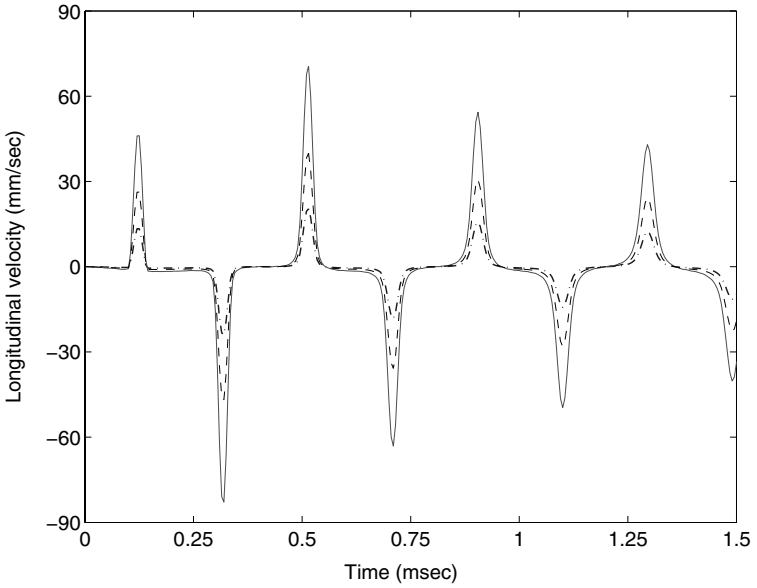

Fig. 4.47. Longitudinal velocity history $\dot{u}(t)$ at a point on the outer top-surface ($y = 0$, $z = R+h$) at the free end ($x = 1$ m) of the cantilever composite tube for different fiber angles. -.-.- $\theta = [0^\circ]_{20}$; —— $\theta = [+45^\circ]_{10}/[-45^\circ]_{10}$; - - - $\theta = [0^\circ]_{10}/[90^\circ]_{10}$

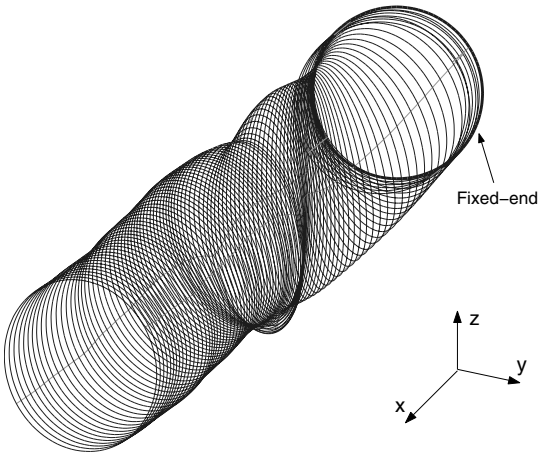

Fig. 4.48. Snap of the outer surface geometry at $t = 0.5$ msec for the graphite–epoxy composite clamped–free tube ($L = 1$ m, $L/R = 50$, $\eta = 0.1$ with $\theta = 0^o$ lay-up). A short pulse load (Figure 4.5) is applied uniformly at the free end along Z-direction. Scale-factor for displacement amplification is 1×10^7

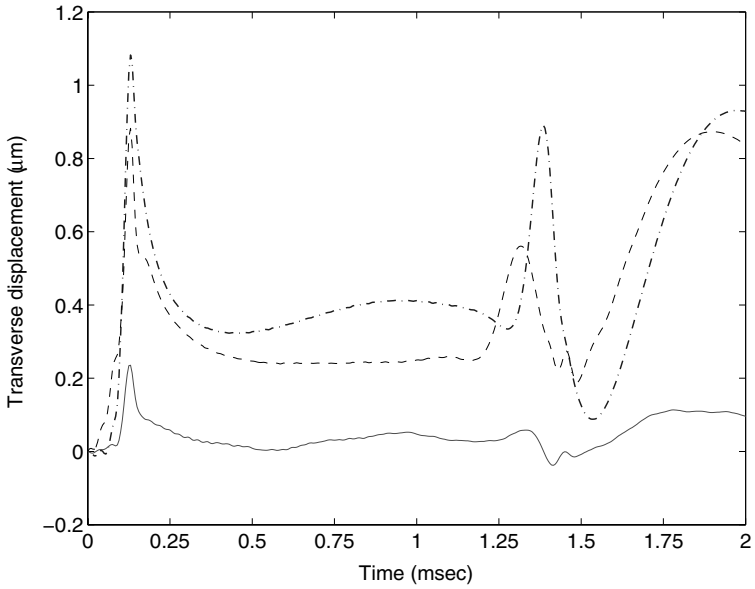

Fig. 4.49. Transverse displacement history $w(t)$ at a point on the outer top-surface ($y = 0$, $z = R+h$) at the free end ($x = 1$ m) of the cantilever composite tube for different fiber angles. -.-.- $\theta = [0°]_{20}$; ——$\theta = [+45°]_{10}/[-45°]_{10}$; - - - $\theta = [0°]_{10}/[90°]_{10}$

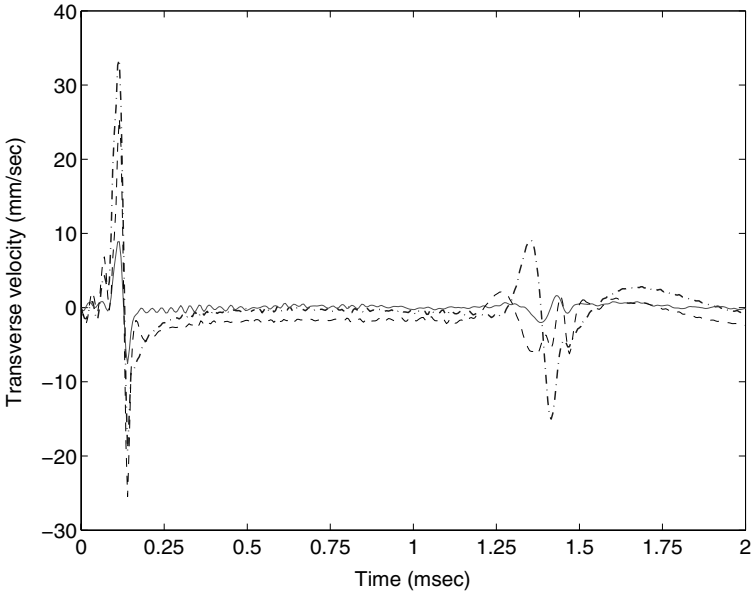

Fig. 4.50. Transverse velocity history $\dot{w}(t)$ at a point on the outer top-surface ($y = 0$, $z = R+h$) at the free end ($x = 1$ m) of the cantilever composite tube for different fiber angles. -.-.- $\theta = [0^o]_{20}$; —— $\theta = [+45^o]_{10}/[-45^o]_{10}$; - - - $\theta = [0^o]_{10}/[90^o]_{10}$

tion (4.89)) in the lateral motion on the outer top surface becomes attenuating in nature. For this reason, the incident peaks and the reflected peaks are visible only in the velocity history (Figure 4.53) that has dimensional similarity with the phase velocity of the dispersive waves. The displacement and the velocity histories corresponding to $\theta = [+45^\circ]_{10}/[-45^\circ]_{10}$ configuration are respectively 2 and 3 orders smaller than those from the two other configurations. As in the plots of transverse responses against transverse loading, even here we see small errors due to the window distortion in the initial responses (before $t = 50$ μs). However, these errors are within an acceptable range and do not alter the nature of the response significantly. Also, these errors can be eliminated by expanding the length of the frequency window with appropriate resolution.

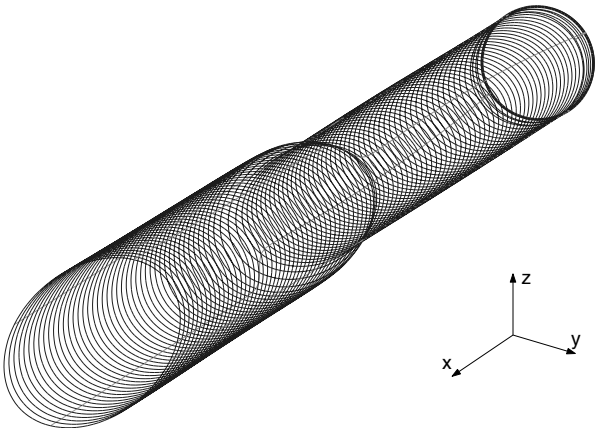

Fig. 4.51. Snap of the outer surface geometry at $t = 0.5$ msec for the graphite–epoxy composite clamped–free tube ($L = 1$ m, $L/R = 50$, $\eta = 0.1$ with $\theta = 0^o$ lay-up). A short pulsed torsional loading of peak amplitude $100\,N - m$ (similar to Figure 4.5) is applied uniformly at the free end about X-axis. Scale-factor for displacement amplification is 1×10^6

In this chapter, the dynamics of 1-D laminated composite waveguides of varying complexities are discussed. The numerical examples given in this chapter show the ease with which SFEM handles such complex problems. Advantages and limitations of various models relating to the approximations involved in the theory are explored in detail. The procedure for the evaluation of various correction factors associated with approximate theories are outlined in detail. The next logical step is to extend the SFEM to yet another class of difficult problems, namely the wave propagation analysis of inhomogeneous structures. This is addressed in the next chapter.

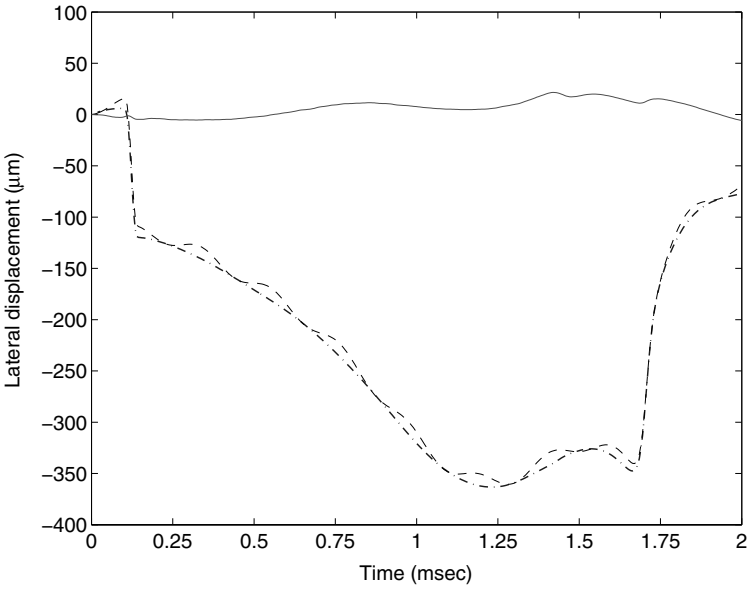

Fig. 4.52. Lateral displacement history $v(t)$ at a point on the top surface ($y = 0$, $z = R+h$) at the free end ($x = 1$ m) of the clamped–free composite tube for different fiber angles. -.-.- $\theta = [0°]_{20}$; —— $\theta = [+45°]_{10}/[-45°]_{10}$; - - - $\theta = [0°]_{10}/[90°]_{10}$

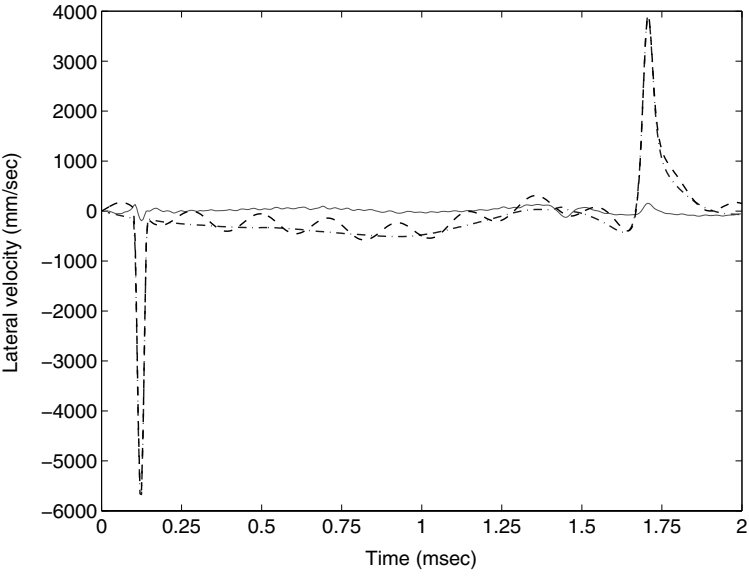

Fig. 4.53. Lateral velocity history $\dot{v}(t)$ at a point on the outer top surface ($y = 0$, $z = R+h$) at the free end ($x = 1$ m) of the clamped–free composite tube for different fiber angles. -.-.- $\theta = [0°]_{20}$; —— $\theta = [+45°]_{10}/[-45°]_{10}$; - - - $\theta = [0°]_{10}/[90°]_{10}$

5

Wave Propagation in One-dimensional Inhomogeneous Structures

It is now well-known that the homogeneous plane wave has the form $\mathbf{u} = \mathbf{A}e^{j(\mathbf{k}\cdot\mathbf{x}-\omega t)}$, where the wave amplitude $\mathbf{A}$ and the wave vector $\mathbf{k}$ are real. When $\mathbf{A}$ and $\mathbf{k}$ become complex numbers, as happens for the linear and dissipative (visco-elastic) system, $\mathbf{A}$ decreases with propagating distance and $\mathbf{u}$ is called an inhomogeneous wave [24]. Although the inhomogeneous wave is defined in a strict sense for two- or three-dimensional media, the definition can be extended to the one-dimensional situation.

Although it is known that a plane wave solution does not exist for heterogeneous media and only approximate methods can be employed for analysis, the present chapter discusses the possibility of an approximate plane wave solution with a complex wavenumber (wave vector in one dimension) for the wave propagating in the direction of inhomogeneity. This wave is called herein the inhomogeneous wave, whose behavior is similar to that of a wave propagating through visco-elastic material, although the inhomogeneous material (functionally graded material) considered in this chapter is linear elastic.

With the advent of FGM in several structural applications, it is essential to know their behavior under high frequency mechanical and thermal loading, to which they are frequently subjected. However, two different cases are considered; first, a wave propagating in the direction of gradation and second, propagation in the direction normal to the gradation. The first case gives rise to the inhomogeneous wave, where the wave amplitude decreases while propagating. This characteristic is missing in the second case, which we will refer to as the homogeneous wave case. The analysis procedure is the same as that normally done for anisotropic materials, except for one important difference. In FGM, asymmetric (about the reference plane) gradation in density may result in a first mass moment, which is absent from anisotropic materials. The literature is minimal on aspects of wave propagation analysis in one-dimensional heterogeneous waveguides.

In this chapter, the derivation and subsequent application of SFEs to 1-D FGM waveguides are presented. To establish the characteristics of the inhomogeneous wave, a simple inhomogeneous rod SFE is formulated. In the

absence of an exact solution, it is shown how approximate plane wave solutions can be obtained and approximate wavenumbers can be defined for inhomogeneous wave propagation through heterogeneous media. The principle of virtual work (weighted residual method) in the frequency domain is employed for SFE formulation. It is shown in [97] that approximate spectral elements can be formulated by using this principle for a structure with variable cross-section. The same procedure is applied here to derive an approximate SFE for length-wise graded waveguide. A new kind of idealization is introduced to get an approximate dispersion relation, which, when solved, results in a complex wavenumber that has non-trivial real and imaginary parts. Alternatively, as the governing equation for most of the inhomogeneous 1-D waveguides are devoid of any singularities, a series solution of the governing equation can be obtained and such a solution can be used to get new approximate spectral elements. This approach is followed in this chapter to derive a highly convergent spectral element. Thus, a series of approximate SFEs is formulated to analyse wave propagation in heterogeneous media.

The length-wise graded rod waveguide is further extended to a first-order shear flexible length-wise graded beam waveguide, where exponential variation of material properties are assumed. It is shown that for this kind of variation, an exact solution can be obtained for the one-parameter family of gradation and approximate solutions can be obtained for the two-parameter family of gradation.

In addition to these, another SFE is developed for beams with depth-wise gradation under FSDT with lateral contraction, already discussed in the previous chapter (Section 4.4.1). This beam can be reduced to FSDT under the limiting condition of negligible depth-wise variation of transverse displacement. Because of the high temperature environment in typical FGM applications, the effect of temperature is important and changes in material properties at elevated temperature should be taken into account. However, to avoid complications and to remain in the domain of linear analysis, the effect of temperature is introduced in the most simple fashion in the formulation of this SFE. Here, thermal stresses are introduced by solving the thermal equation separately to obtain the depth-wise temperature variation. This thermal field is then imposed as an externally applied distributed body and surface force along with the applied mechanical loading.

5.1 Length-wise Functionally Graded Rod

The governing differential equation for an inhomogeneous 1-D rod waveguide is derived as follows. A rod with different materials along the length and thickness, shown in Figure (5.1) is composed of essentially three types of materials. Material 1 and 2 are homogeneous (material properties do not vary with spatial coordinates), whereas the FGM has varying material properties in the X direction. Moreover, material properties of the FGM are those of

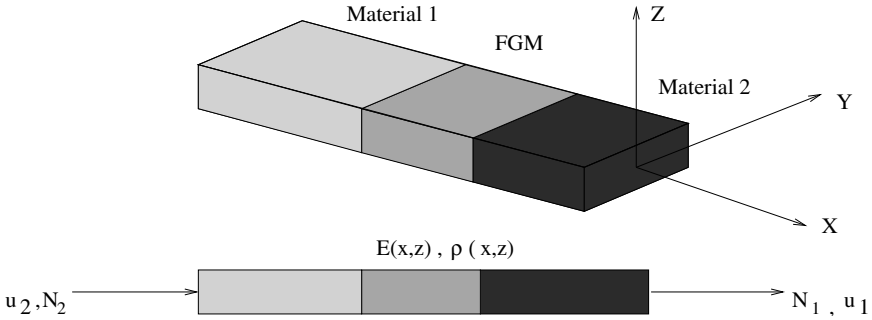

Fig. 5.1. Frequency domain finite element

material 1 at the left edge and those of material 2 at the right edge. As far as the spatial variation is concerned, the following expressions are assumed for Young's modulus E and density ρ,

$$E(x,z) = E_\circ f(x)g(z), \qquad \rho(x,z) = \rho_\circ s(x)t(z)\ , \tag{5.1}$$

where $E_\circ$ and $\rho_\circ$ are constant over the length and thickness of the rod. Since only longitudinal motion is considered, only the stress σ_{xx} and the longitudinal displacement u are involved. The stress is related to the displacement gradient by

$$\epsilon_{xx} = u_x, \qquad \sigma_{xx} = E(x,z)u_x\ , \tag{5.2}$$

where, as before, x as subscript denotes first derivative with respect to the spatial variable x. Applying Hamilton's principle , the governing partial differential equation for the FGM rod, in the absence of body force, is

$$(A_{11}f(x)u_x)_x = I_\circ s(x)\ddot{u}\ , \tag{5.3}$$

where, for simplicity, cross-sectional area A is assumed constant over the length, and dot over a variable denotes differentiation with respect to time. A_{11} and $I_\circ$ are depth-wise (z) integrated properties and are defined as

$$A_{11} = E_\circ \int_A g(z)\, dA, \qquad I_\circ = \rho_\circ \int_A t(z)\, dA\ . \tag{5.4}$$

The natural boundary condition, obtained from the variational principle, is

$$A_{11}f(x)u_x = F\ , \tag{5.5}$$

for the nodal points $x = 0$ and $x = L$, where F is the applied concentrated axial load at the boundary. Although, $g(z)$ and $t(z)$ introduced in Equation (5.1) can have arbitrary variations, in subsequent studies they are kept constant, *i.e.,* there is no depth-wise variation for E and ρ. The length-wise variation is described by $f(x)$ and $s(x)$, which, for polynomial variations, are described as:

$$f(x) = (1 + \alpha x)^n, \qquad s(x) = (1 + \beta x)^n \ , \tag{5.6}$$

and for exponential variation:

$$f(x) = e^{\alpha x}, \qquad s(x) = e^{\beta x} \ . \tag{5.7}$$

The easiest way to solve Equation (5.3) together with the boundary condition (5.5) is to apply the FE procedure. The details of FE development can be found in [98], [99]. However, the standard FE procedure can also be extended to the frequency domain, which generates approximate and exact SFEs.

Assuming a solution of the form, $u(x,t) = \sum_n \tilde{u}(x,\omega_n)e^{-j\omega_n t}$, Equation (5.3) then becomes

$$(A_{11} f(x)\tilde{u}_x)_x + I_\circ s(x)\omega_n^2 \tilde{u} = 0 \ , \tag{5.8}$$

for each value of ω_n. The equation is a classical example of the Sturm–Liouville (SL) boundary value problem or SL system whose generic form is

$$-d\big[p(x)dy/dx\big]/dx + q(x)y = \lambda r(x)y \ , \ p(x) > 0 \, , r(x) > 0 \ , \ x \in [a,b] \ . \tag{5.9}$$

The non-negative requirements for $p(x)$ and $r(x)$ are automatically satisfied for exponential variations laws (Equation (5.7)). For a linear variation, these requirements are satisfied by suitably choosing the values of α and β. The associated boundary conditions are

$$a_1 y(a) + a_2 p(x) y'(a) = 0 \, , \qquad b_1 y(b) + b_2 p(x) y'(b) = 0 \ . \tag{5.10}$$

For a cantilever rod problem, *e.g.,* $a_1 \, , b_2 = 1$, $a_2 = 0 \, , b_1 = 0$, the system is only satisfied for a discrete set of eigenvalues λ_j with $j = 0, 1, \ldots$, and corresponding eigenfunctions $y_j(x)$. The SL problem can be solved efficiently using the Prüfer transformation (see [100]), whose details can be found in [98] and are omitted here.

5.1.1 Development of Spectral Finite Elements

Introducing the homogeneous wavenumber $k_\circ$, Equation (5.8) becomes

$$f(x)\tilde{u}_{xx} + f'(x)\tilde{u}_x + k_\circ^2 s(x)\tilde{u} = 0, \qquad k_\circ^2 = I_\circ \omega^2 / A_{11} \ . \tag{5.11}$$

This equation in terms of the linear and exponential material variation laws takes the forms

$$\text{Linear } (n = 1) : (1 + \alpha x)\tilde{u}_{xx} + \alpha \tilde{u}_x + k_\circ^2 (1 + \beta x)\tilde{u} = 0 \ , \tag{5.12}$$

$$\text{Exponential} : \tilde{u}_{xx} + \alpha \tilde{u}_x + k_\circ^2 e^{\gamma x}\tilde{u} = 0, \qquad \gamma = \beta - \alpha \ . \tag{5.13}$$

There is no closed form solution for the polynomial variation, even in the particular case of $n = 1$ given by Equation (5.12), which is the only case in

the polynomial variation discussed further. Reference [101] gives this solution in terms of the solution of the degenerate hypergeometric equation, which is again another complicated series solution. For the exponentially varying material property (Equation (5.13)), the exact solution is also given in [101] and is expressed in terms of the Bessel function of fractional order. This solution gives no notion of wavenumber, which is essential for wave propagation studies and no conclusion can be drawn regarding the effect of inhomogeneity on the dispersion (dependence of wavenumber on frequency) relation. Hence, we develop an approximate propagating wave solution preserving the notion of wavenumber, which is expected to be easily implementable in generic finite element type matrix methodology giving the required accuracy when a sufficient number of elements is used. The basis for forming the matrix–vector equation in the frequency domain is the PVW (see Equation (4.58)) given by

$$\int_{\Omega} (\tilde{\sigma}_{kl}\delta\tilde{\epsilon}_{kl} - \rho\omega^2\tilde{u}_i\delta(\tilde{u}_i))\, d\Omega - \int_{\Omega} \tilde{f}_i\delta\tilde{u}_i)\, d\Omega - \int_{\Gamma} \tilde{t}_i\delta\tilde{u}_i)\, d\Gamma = 0\ , \qquad (5.14)$$

where $\tilde{u}$, $\tilde{\sigma}$ and $\tilde{\epsilon}$ are the frequency dependent displacement, stress and strains, ρ is the density and Ω and Γ denote the domain and boundary of the structure. In the present case, the PVW takes the form

$$\int_0^L A_{11}f(x)\tilde{u}_x\tilde{v}_x\, dx - \int_0^L I_\circ s(x)\omega^2\tilde{u}\tilde{v}\, dx - \overbrace{\Big[A_{11}f(x)(\tilde{u}_x)\tilde{v}\Big]_0^L}^{boundary\ terms} = 0\ , \qquad (5.15)$$

where $\tilde{v}$ is any arbitrary admissible weight function (virtual displacement) in the frequency domain.

Homogeneous Solution as an Interpolating Function

Since Equations (5.12) and (5.13) cannot be solved exactly, the nearest solution is taken as an interpolating function, namely the homogeneous rod solution

$$\tilde{u}(x,\omega) = Ae^{-jk_\circ x} + Be^{+jk_\circ x}\ . \qquad (5.16)$$

A and B are related to the nodal displacements $\tilde{u}_1$ and $\tilde{u}_2$ by

$$\left\{\begin{array}{c} A \\ B \end{array}\right\} = \frac{1}{\Delta}\left[\begin{array}{cc} -e^{+jk_\circ L} & 1 \\ e^{-jk_\circ L} & -1 \end{array}\right]\left\{\begin{array}{c} \tilde{u}_1 \\ \tilde{u}_2 \end{array}\right\}, \qquad \Delta = -e^{+jk_\circ L} + e^{-jk_\circ L}\ . \qquad (5.17)$$

Substituting Equations (5.17) and (5.16) into Equation (5.15), we obtain

$$\big\{[\mathbf{K}(\omega)] - \omega^{\mathbf{2}}[\mathbf{M}(\omega)]\big\}\{\hat{\mathbf{u}}\} = \{\hat{\mathbf{f}}\}\ , \qquad (5.18)$$

where $\{\hat{u}\}$ and $\{\hat{f}\}$ denote the nodal values of the displacement and axial force, respectively, at frequency ω. This equation is solved for different values

of ω and the IFFT gives the time domain history. The expressions for the dynamic stiffness matrix $[\mathbf{K}(\omega)] - \omega^2[\mathbf{M}(\omega)]$ for both linear and exponential material property variation are given below, and are obtained by using Equations (5.12) and (5.13) in Equation (5.15). In subsequent sections, elements with a linearly varying material property will be referred to as SEL1 (spectral element with linear material property variation) and the elements with exponentially varying material property will be referred to as SEE1. The elements of SEL1 (to be pre-multiplied by $[C]^T$ and post-multiplied by $[C]$, where $[C]$ is the matrix given in Equation (5.17) and $k = k_\circ$) are

$$\begin{aligned}
K_{SEL1}(1,1) &= (-1/4)j(2e^{(-2jkL)}A_{11}k^3 + \\
&\quad 2e^{(-2jkL)}A_{11}k^3\alpha L - je^{(-2jkL)}A_{11}k^2\alpha + \\
&\quad 2e^{(-2jkL)}I_o\omega^2 k + 2e^{(-2jkL)}I_o\omega^2\beta kL - \\
&\quad je^{(-2jkL)}I_o\omega^2\beta - 2A_{11}k^3 + jI_o\omega^2\beta + jA_{11}k^2\alpha - 2I_o\omega^2 k)/k^2 \ , \\
K_{SEL1}(1,2) &= A_{11}k^2L - I_o\omega^2 L + (1/2)A_{11}k^2\alpha L^2 - (1/2)I_o\omega^2\beta L^2 \ , \\
K_{SEL1}(2,2) &= (1/4)j(2e^{(2jkL)}A_{11}k^3 + \\
&\quad 2e^{(2jkL)}A_{11}k^3\alpha L + je^{(2jkL)}A_{11}k^2\alpha + \\
&\quad 2e^{(2jkL)}I_o\omega^2 k + 2e^{(2jkL)}I_o\omega^2\beta kL + \\
&\quad je^{(2jkL)}I_o\omega^2\beta - 2A_{11}k^3 - jI_o\omega^2\beta - jA_{11}k^2\alpha - 2I_o\omega^2 k)/k^2 \ .
\end{aligned}$$

The elements of SEE1 (to be pre-multiplied by $[C]^T$ and post-multiplied by $[C]$) are

$$\begin{aligned}
K_{SEE1}(1,1) &= -j(jI_o\omega^2 e^{(-L(2jk-\beta))}\alpha + 2I_o\omega^2 e^{(-L(2jk-\beta))}k + \\
&\quad jA_{11}k^2 e^{(-L(2jk-\alpha))}\beta + \\
&\quad 2A_{11}k^3 e^{(-L(2jk-\alpha))})/(j\beta + 2k)/(j\alpha + 2k) + \\
&\quad j(jI_o\omega^2\alpha + 2I_o\omega^2 k + jA_{11}k^2\beta + 2A_{11}k^3)/(j\beta + 2k)/(j\alpha + 2k) \ , \\
K_{SEE1}(1,2) &= -(-e^{(\alpha L)}A_{11}k^2\beta + e^{(\beta L)}I_o\omega^2\alpha)/\alpha/\beta - (A_{11}k^2\beta - I_o\omega^2\alpha)/\alpha/\beta \ , \\
K_{SEE1}(2,2) &= -j(jA_{11}k^2 e^{(L(2jk+\alpha))}\beta - 2A_{11}k^3 e^{(L(2jk+\alpha))} - 2I_o\omega^2 e^{(L(2jk+\beta))}k + \\
&\quad jI_o\omega^2 e^{(L(2jk+\beta))}\alpha)/(-2k + j\alpha)/(j\beta - 2k) + j(jA_{11}k^2\beta - 2A_{11}k^3 - \\
&\quad 2I_o\omega^2 k + jI_o\omega^2\alpha)/(-2k + j\alpha)/(j\beta - 2k) \ , \quad k = k_\circ .
\end{aligned}$$

Series Solution of Differential Equation

Alternatively, the series solution of the differential equation can be taken as interpolating function. The series solution for Equation (5.12) is

$$\begin{aligned}
\hat{u}(x) &= \hat{u}(0) + D\hat{u}(0)x + \big(-\alpha D\hat{u}(0)/2 - k_\circ^2\hat{u}(0)/2\big)x^2 + \\
&\quad \big(\alpha^2 D\hat{u}(0)/3 + \alpha k_\circ^2\hat{u}(0)/3 - k_\circ^2 D\hat{u}(0)/6 \\
&\quad -k_\circ^2\beta\hat{u}(0)/6\big)x^3 \ , \quad D\hat{u}(0) = \hat{u}_x|_{x=0} \ ,
\end{aligned} \tag{5.19}$$

which is the solution up to cubic order. Substituting $\hat{u}_1$ for $\hat{u}(0)$ and solving for $D\hat{u}(0)$ by evaluating $\hat{u}$ at $x = L$ and equating that to $\hat{u}_2$, $\hat{u}$ can be written in terms of nodal values as

$$\begin{aligned}
\hat{u}(x) &= \hat{u}_1 - \frac{\mathrm{p2}\,x}{\mathrm{p1}} + \left(\frac{1}{2}\frac{\alpha\,\mathrm{p2}}{\mathrm{p1}} - \frac{1}{2}\,{k_\circ}^2\,\hat{u}_1\right) x^2 \\
&+ \left(-\frac{1}{3}\frac{\alpha^2\,\mathrm{p2}}{\mathrm{p1}} + \frac{1}{3}\,\alpha\,{k_\circ}^2\,\hat{u}_1 + \frac{1}{6}\frac{{k_\circ}^2\,\mathrm{p2}}{\mathrm{p1}} - \frac{1}{6}\,{k_\circ}^2\,\beta\,\hat{u}_1\right) x^3 \\
\mathrm{p1} &= L - \frac{1}{2}\,L^2\,\alpha + \frac{1}{3}\,L^3\,\alpha^2 - \frac{1}{6}\,L^3\,{k_\circ}^2 \\
\mathrm{p2} &= \hat{u}_1 - \frac{1}{2}\,L^2\,{k_\circ}^2\,\hat{u}_1 + \frac{1}{3}\,L^3\,\alpha\,{k_\circ}^2\,\hat{u}_1 - \frac{1}{6}\,L^3\,{k_\circ}^2\,\beta\,\hat{u}_1 - \hat{u}_2\ .
\end{aligned}$$

This equation can be used to formulate another spectral element, which, although approximate, is expected to capture the essential wave propagation behavior when a sufficiently large number of elements is used. The dynamic stiffness matrix formulated from this interpolating function is given below, where k denotes $k_\circ$. This element will be further referred to as SEL2.

$$\begin{aligned}
K_{SEL2}(1,1) &= (-1/60)(40A_{11}\alpha^2k^2L^4 + 20\omega^2I_ok^2L^4 + 8\omega^2I_oL^5\beta k^2 + \\
&\quad 10\omega^2I_oL^5\beta\alpha^2 + 20\omega^2I_oL^3\beta - 100\omega^2I_oL^3\alpha - 28\omega^2I_oL^4\beta\alpha + \\
&\quad 32\omega^2I_oL^4\alpha^2 + 2\omega^2I_ok^4L^6 + 80A_{11}\alpha^2L^2 + \omega^2I_o\beta k^4L^7 - \\
&\quad 60A_{11}\alpha^3L^3 + 120A_{11}L\alpha - 6\omega^2I_oL^6\beta\alpha k^2 - 240A_{11} - \\
&\quad 14\omega^2I_oL^5\alpha k^2 - 10A_{11}\alpha k^4L^5 - 20A_{11}k^4L^4 + 80\omega^2I_oL^2)/ \\
&\quad L/(-2 + L\alpha)^2\ , \\
K_{SEL2}(1,2) &= (1/60L)(3\omega^2I_oL^5\alpha k^2 - 8\omega^2I_oL^4\alpha^2 - 40\omega^2I_oL^2 - 60A_{11}\alpha^3L^3 + \\
&\quad 40\omega^2I_oL^3\alpha - 5\omega^2I_oL^5\beta\alpha^2 - 20\omega^2I_oL^3\beta + 2\omega^2I_oL^6\beta\alpha k^2 + \\
&\quad 80A_{11}\alpha^2L^2 - 240A_{11} + 20A_{11}\alpha^2k^2L^4 + 22\omega^2I_oL^4\beta\alpha - \\
&\quad 10\omega^2I_ok^2L^4 - 6\omega^2I_oL^5\beta k^2 + 120A_{11}L\alpha)/(-2 + L\alpha)^2\ , \\
K_{SEL2}(2,2) &= (-1/30L)(6\omega^2I_oL^4\alpha^2 + 40\omega^2I_oL^2 - 30A_{11}\alpha^3L^3 + 40A_{11}\alpha^2L^2 - \\
&\quad 30\omega^2I_oL^3\alpha + 5\omega^2I_oL^5\beta\alpha^2 + 30\omega^2I_oL^3\beta - 120A_{11} + 60A_{11}L\alpha - \\
&\quad 24\omega^2I_oL^4\beta\alpha)/(-2 + L\alpha)^2\ .
\end{aligned}$$

Similarly, the equation for exponential material variation (Equation (5.13)) is solved, and the solution up to cubic order is given by

$$\begin{aligned}
\hat{u}(x) &= \hat{u}(0) + D\hat{u}(0)\,x + \left(-\frac{1}{2}\,\alpha\,D\hat{u}(0) - \frac{1}{2}\,ko^2\,\hat{u}(0)\right) x^2 \\
&+ \left(-\frac{1}{6}\,ko^2\,\beta\,\hat{u}(0) + \frac{1}{6}\,\alpha^2\,D\hat{u}(0) + \frac{1}{3}\,\alpha\,ko^2\,\hat{u}(0) - \frac{1}{6}\,ko^2\,D\hat{u}(0)\right) x^3\ .
\end{aligned}$$

Proceeding in a similar fashion and solving for nodal displacements u_1 and u_2, the solution becomes

$$\hat{u}(x) = \hat{u}_1 - \frac{\mathrm{p2}\, x}{\mathrm{p1}} + \left(\frac{1}{2} \frac{\alpha\, \mathrm{p2}}{\mathrm{p1}} - \frac{1}{2}\, ko^2\, \hat{u}_1 \right) x^2$$
$$+ \left(-\frac{1}{6}\, ko^2\, \beta\, \hat{u}_1 - \frac{1}{6} \frac{\alpha^2\, \mathrm{p2}}{\mathrm{p1}} + \frac{1}{3}\, \alpha\, ko^2\, \hat{u}_1 + \frac{1}{6} \frac{ko^2\, \mathrm{p2}}{\mathrm{p1}} \right) x^3 \,,$$
$$\mathrm{p1} = L - \frac{1}{2}\, L^2\, \alpha + \frac{1}{6}\, L^3\, \alpha^2 - \frac{1}{6}\, L^3\, ko^2 \,,$$
$$\mathrm{p2} = \hat{u}_1 - \frac{1}{2}\, L^2\, ko^2\, \hat{u}_1 - \frac{1}{6}\, L^3\, ko^2\, \beta\, \hat{u}_1 + \frac{1}{3}\, L^3\, \alpha\, ko^2\, \hat{u}_1 - \hat{u}_2 \,.$$

The spectral element can be formulated in the usual way and this element will be referred to as SEE2. The elements of the stiffness matrix are

$$\begin{aligned} K_{SEE2}(1,1) = {} & (24g\omega^2 I_o \alpha^3 k^2 L\beta - 8g\omega^2 I_o \alpha^5 L^2 \beta^2 - 16hA_{11}\beta^5 \alpha^3 L - \\ & 4\omega^2 I_o \alpha^4 L^2 \beta^3 + \omega^2 I_o \alpha^5 L^4 \beta^4 - 4\omega^2 I_o \alpha^3 L^3 k^2 \beta^3 + \\ & 2\omega^2 I_o \alpha^4 k^2 L^4 \beta^3 - 4\omega^2 I_o \alpha^4 L^3 \beta^4 + 4\omega^2 I_o \alpha^3 L^2 \beta^4 + \\ & 8\omega^2 I_o \alpha^3 \beta^3 L + 12g\omega^2 I_o \alpha^3 k^4 L^3 \beta + 48g\omega^2 I_o \alpha^4 k^2 L - \\ & 36g\omega^2 I_o \alpha^4 k^2 L^2 \beta - 8g\omega^2 I_o \alpha^3 k^2 L^2 \beta^2 - 8g\omega^2 I_o \alpha^3 \beta^2 + \\ & 24g\omega^2 I_o \alpha^5 \beta L - 2g\omega^2 I_o \alpha^3 k^4 L^4 \beta^2 - 24g\omega^2 I_o \alpha^3 k^4 L^2 + \\ & 8g\omega^2 I_o \alpha^4 k^2 L^3 \beta^2 - 24g\omega^2 I_o \alpha^4 \beta + 16g\omega^2 I_o \alpha^4 L \beta^2 - \\ & 24g\omega^2 I_o \alpha^5 + hA_{11}\beta^5 L^4 k^4 \alpha^2 - 4hA_{11}\beta^5 L^3 k^2 \alpha^3 - \\ & 24hA_{11}\beta^5 k^2 L\alpha + 4hA_{11}\beta^5 \alpha^4 L^2 + 16hA_{11}\beta^5 L^2 k^2 \alpha^2 + \\ & 8hA_{11}\beta^5 k^4 L^2 - 4hA_{11}\beta^5 L^3 k^4 \alpha + 20hA_{11}\beta^5 \alpha^2 - \\ & 20A_{11}\beta^5 \alpha^2 + 24\omega^2 I_o \alpha^5 + 4\omega^2 I_o \alpha^4 k^2 L^3 \beta^2 - \\ & 4\omega^2 I_o \alpha^5 L^2 \beta^2 - 24\omega^2 I_o \alpha^3 k^2 L\beta - 12\omega^2 I_o \alpha^4 k^2 L^2 \beta + \\ & 8\omega^2 I_o \alpha^4 L\beta^2 + 8\omega^2 I_o \alpha^3 \beta^2 + 24\omega^2 I_o \alpha^4 \beta - 48\omega^2 I_o \alpha^4 k^2 L + \\ & 24\omega^2 I_o \alpha^3 k^4 L^2 + 2\omega^2 I_o \alpha^3 k^4 L^4 \beta^2 + 12\omega^2 I_o \alpha^3 k^4 L^3 \beta - \\ & 16\omega^2 I_o \alpha^3 k^2 L^2 \beta^2 - 4A_{11}\beta^5 L^3 k^4 \alpha + 24A_{11}\beta^5 k^2 L\alpha - 8A_{11}\beta^5 k^4 L^2 - \\ & A_{11}\beta^5 L^4 k^4 \alpha^2 + 8A_{11}\beta^5 L^2 k^2 \alpha^2)/\alpha^3/L^2/(-2 + L\alpha)^2/\beta^5 \,, \end{aligned}$$

$$\begin{aligned} K_{SEE2}(1,2) = {} & -(4hA_{11}\beta^5 \alpha^3 L^2 - 12hA_{11}\beta^5 k^2 L + 20hA_{11}\beta^5 \alpha - 16hA_{11}\beta^5 \alpha^2 L + \\ & 8hA_{11}\beta^5 L^2 k^2 \alpha - 2hA_{11}\beta^5 L^3 k^2 \alpha^2 + 2g\omega^2 I_o \alpha^2 L^3 k^2 \beta^3 - \\ & 10g\omega^2 I_o \alpha^4 L^2 \beta^2 - 8g\omega^2 I_o \alpha^2 L^2 k^2 \beta^2 + 24\omega^2 I_o \alpha^4 + 12g\omega^2 I_o \alpha^2 k^2 L\beta - \\ & 18g\omega^2 I_o \alpha^3 L^2 k^2 \beta + 6g\omega^2 I_o \alpha^3 L^3 k^2 \beta^2 + 24g\omega^2 I_o \alpha^4 \beta L + \\ & 20g\omega^2 I_o \alpha^3 L\beta^2 - 24g\omega^2 I_o \alpha^3 \beta - 24g\omega^2 I_o \alpha^4 - 8g\omega^2 I_o \alpha^2 \beta^2 + \\ & 4g\omega^2 I_o \alpha^2 L\beta^3 - 6g\omega^2 I_o \alpha^3 L^2 \beta^3 + 2g\omega^2 I_o \alpha^4 L^3 \beta^3 - g\omega^2 I_o \alpha^3 L^4 k^2 \beta^3 + \\ & 24g\omega^2 I_o \alpha^3 k^2 L - 20A_{11}\beta^5 \alpha - 6\omega^2 I_o \alpha^3 L^2 k^2 \beta - 24\omega^2 I_o \alpha^3 k^2 L + \\ & 4\omega^2 I_o \alpha^3 L\beta^2 - 4\omega^2 I_o \alpha^2 L^2 k^2 \beta^2 + 24\omega^2 I_o \alpha^3 \beta + 4\omega^2 I_o \alpha^2 L\beta^3 - \\ & 2\omega^2 I_o \alpha^4 L^2 \beta^2 - 2\omega^2 I_o \alpha^3 L^2 \beta^3 + 12A_{11}\beta^5 k^2 L + 4A_{11}\beta^5 L^2 k^2 \alpha - \\ & 12\omega^2 I_o \alpha^2 k^2 L\beta + 8\omega^2 I_o \alpha^2 \beta^2)/\alpha^2/L^2/(-2 + L\alpha)^2/\beta^5 \,, \end{aligned}$$

$$K_{SEE2}(2,2) = -(-4g\omega^2 I_o \alpha^2 \beta^4 L^3 + 24g\omega^2 I_o \alpha^3 - 24g\omega^2 I_o \alpha^3 \beta L +$$

$$24g\omega^2 I_o\alpha^2\beta + 12g\omega^2 I_o\alpha^3\beta^2 L^2 - 4hA_{11}\beta^5\alpha^2 L^2 + 16hA_{11}\beta^5 L\alpha - 4g\omega^2 I_o\alpha^3\beta^3 L^3 - 24g\omega^2 I_o\alpha^2\beta^2 L + g\omega^2 I_o\alpha^3\beta^4 L^4 + 8g\omega^2 I_o\alpha\beta^2 + 12g\omega^2 I_o\alpha^2\beta^3 L^2 + 4g\omega^2 I_o\alpha\beta^4 L^2 - 8g\omega^2 I_o\alpha\beta^3 L - 20hA_{11}\beta^5 + 20A_{11}\beta^5 - 8\omega^2 I_o\alpha\beta^2 - 24\omega^2 I_o\alpha^2\beta - 24\omega^2 I_o\alpha^3)/\alpha/L^2/(-2+L\alpha)^2/\beta^5 ,$$

where $g = e^{\beta L}$, $h = e^{\alpha L}$ and $k = k_\circ$.

In addition to the above methods, Equation (5.13) is solvable in another approximate way incorporating a refinement of the homogeneous wavenumber. This is discussed in the next section.

Naive Wavenumber

The solution of a differential equation with constant coefficients can be written in the form e^{-jkx}. In the present case, the equation has a variable coefficient. We naively assume that the solution of Equation (5.13) still can be written as e^{-jkx} and try to find k. Substituting this assumed solution into Equation (5.13), the dispersion relation becomes

$$k^2 + jk\alpha = k_\circ^2 e^{\gamma x} . \tag{5.20}$$

The wavenumber k is a function of both x and frequency ω, and it is implicitly assumed that $\partial k/\partial x$ is negligible. We assume that the solution k has a real part a and an imaginary part b. Then the governing equations for a and b are

$$a^2 - b^2 - \alpha b = k_\circ^2 e^{\gamma x} , \qquad \alpha a + 2ab = 0 , \qquad a, b \in \mathbf{R} . \tag{5.21}$$

The solution can then be written as

$$k_{1,2} = \pm\Upsilon - j\alpha/2 , \qquad \Upsilon = \sqrt{|k_\circ^2 e^{\gamma x} - \alpha^2/4|} , \tag{5.22}$$

so that the solution of Equation (5.13) is

$$\tilde{u}(x) = e^{\alpha x/2}(Ae^{-j\Upsilon x} + Be^{+j\Upsilon x}) . \tag{5.23}$$

Following the same procedure as presented above, the dynamic stiffness matrix for this case can be formulated but the analytical integration will be too tedious. Thus, we make an approximation in the displacement by substituting x_c for x in Υ, where x_c is any constant value and can be taken as the center location of the element, *i.e.,* $L/2$. The wavenumber becomes constant and the standard procedure yields the dynamic stiffness matrix. With this approximation, for exponentially varying FGM, the axial wavenumber becomes

$$\breve{k} = k_\circ\sqrt{|(e^{\gamma x_c} - \alpha^2/4k_\circ^2)|} - j\alpha/2 , \tag{5.24}$$

that is, FGM supports an inhomogeneous wave (nonzero imaginary part). The element formulated using this solution is referred to as SEE3, where the

dynamic stiffness matrix (to be pre-multiplied by $[C]^T$ and post-multiplied by $[C]$), is

$$\begin{aligned}K_{SEE3}(1,1) = &(-I_o\omega^2 e^{(L(\beta-2jk+\alpha))}\alpha + (1/8)A_{11}e^{(2L(\alpha-jk))}\alpha^2\beta + \\ &jI_o\omega^2 e^{(L(\beta-2jk+\alpha))}k + (1/8)A_{11}e^{(2L(\alpha-jk))}\alpha^3 - \\ &(1/2)A_{11}e^{(2L(\alpha-jk))}k^2\beta + jA_{11}e^{(2L(\alpha-jk))}k^3 - \\ &3/2A_{11}e^{(2L(\alpha-jk))}k^2\alpha - 1/2jA_{11}e^{(2L(\alpha-jk))}k\alpha\beta - \\ &3/4jA_{11}e^{(2L(\alpha-jk))}k\alpha^2 + I_o\omega^2\alpha - 1/8A_{11}\alpha^2\beta - \\ &jI_o\omega^2 k - 1/8A_{11}\alpha^3 + 1/2A_{11}k^2\beta - jA_{11}k^3 + \\ &3/2A_{11}k^2\alpha + 1/2jA_{11}k\alpha\beta + 3/4jA_{11}k\alpha^2)/ \\ &(\beta\alpha - j\beta k - 3jk\alpha - 2k^2 + \alpha^2)\,,\end{aligned}$$

$$\begin{aligned}K_{SEE3}(1,2) = &(1/8)(-8I_o\omega^2\alpha e^{(L(\beta+\alpha))} + 4A_{11}e^{(2\alpha L)}k^2\beta + \\ &4A_{11}e^{(2\alpha L)}k^2\alpha + A_{11}e^{(2\alpha L)}\alpha^2\beta + \\ &A_{11}e^{(2\alpha L)}\alpha^3 + 8I_o\omega^2\alpha - 4A_{11}k^2\beta - \\ &4A_{11}k^2\alpha - A_{11}\alpha^2\beta - A_{11}\alpha^3)/(\beta+\alpha)/\alpha\,,\end{aligned}$$

$$\begin{aligned}K_{SEE3}(2,2) = &(-1/2A_{11}e^{(2L(\alpha+jk))}k^2\beta - I_o\omega^2 e^{(L(\beta+2jk+\alpha))}\alpha - \\ &jA_{11}e^{(2L(\alpha+jk))}k^3 - jI_o\omega^2 e^{(L(\beta+2jk+\alpha))}k - \\ &3/2A_{11}e^{(2L(\alpha+jk))}k^2\alpha + 1/2jA_{11}e^{(2L(\alpha+jk))}k\alpha\beta + \\ &3/4jA_{11}e^{(2L(\alpha+jk))}k\alpha^2 + 1/8A_{11}e^{(2L(\alpha+jk))}\alpha^2\beta + \\ &1/8A_{11}e^{(2L(\alpha+jk))}\alpha^3 + 1/2A_{11}k^2\beta + I_o\omega^2\alpha + \\ &jA_{11}k^3 + jI_o\omega^2 k + 3/2A_{11}k^2\alpha - 1/2jA_{11}k\alpha\beta - \\ &3/4jA_{11}k\alpha^2 - 1/8A_{11}\alpha^2\beta - 1/8A_{11}\alpha^3)/ \\ &(\beta\alpha + 3jk\alpha + \alpha^2 + j\beta k - 2k^2)\,,\end{aligned}$$

where $k = \breve{k}$.

In the following section, the elements and techniques developed so far for the analysis of inhomogeneous rod are studied, and the smoothing effect of graded materials is demonstrated for waves generated by high-frequency loading.

5.1.2 Smoothing of Reflected Pulse

When a structure has two dissimilar materials bonded together, reflection (and transmission) of waves occur at the interfaces. This happens due to the mismatch in modulus and density (impedance mismatch in acoustic terms). The reflected pulse can be as strong as the incident pulse, which again depends on the properties of the material encountered by the wave. This reflection is generated in addition to that from the physical boundary. Thus it may be desirable to eliminate these extra reflections, which otherwise, will cause

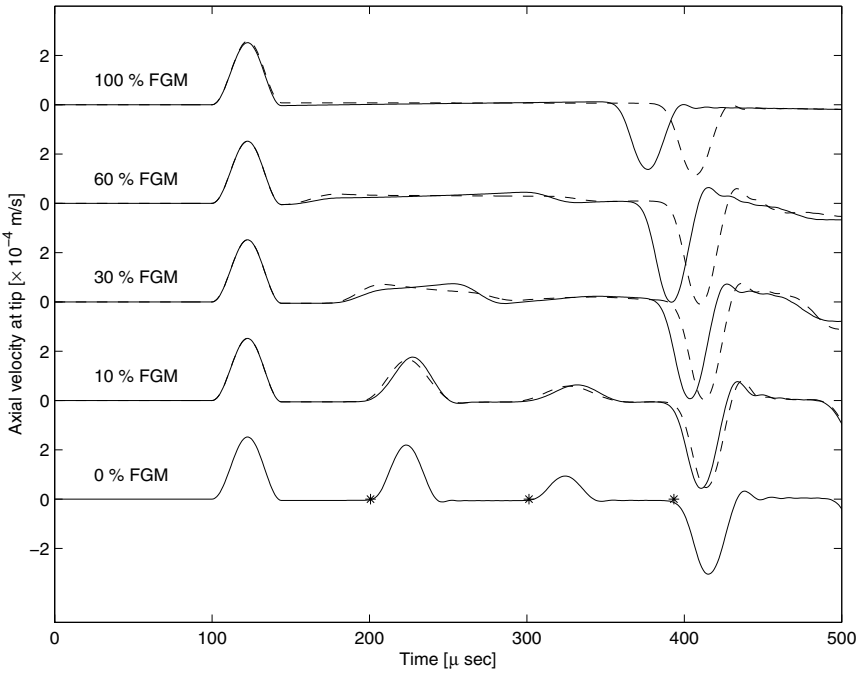

Fig. 5.2. Smoothing of reflected pulse in bimaterial rod : * denotes theoretical predictions, solid lines – exponential variation and dashed lines – linear variation

enhanced stresses in the structure. Graded materials can be used with great success in this situation. Instead of directly joining the two different materials, one graded material can be inserted at the material interface. In the graded material, properties vary smoothly from that of one material to another. Thus there cannot be any impedance mismatch as there is no jump in material properties. This advantage of graded materials is shown in this example.

A bi-material cantilever rod of aluminum ($E = 70$ GPa and ρ=2600 kg/m^3) and alumina ($E = 390$ GPa and ρ=3950 kg/m^3) with unit length and a cross-section of 0.01 m^2 is assumed. The unit pulse loading of Figure 5.3 is applied at the tip and the axial velocity response at the same point is measured. The FGM zone between the two materials is increased gradually from 0 to 100% of the rod length. The FGM is always placed in the center position of the rod and the other two materials are placed symmetrically, where in the fixed-end-side the material is aluminum and at the free-end-side the material is alumina. The response of the rod for various percentages of FGM is shown in Figure 5.2. The 0% FGM plot corresponds to the bi-material rod when no FGM is applied. The first peak corresponds to the load. The second and third peaks correspond to the reflection and re-reflection that occur in the alumina zone. Since the longitudinal wave speed in alumina is almost twice (1.915)

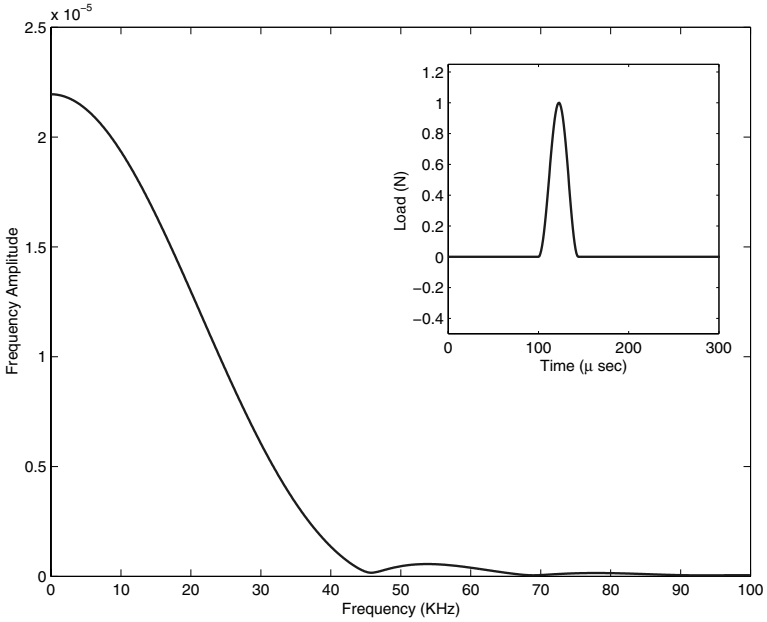

Fig. 5.3. Load applied at the tip (inset shows time history)

that of aluminum, the second reflection from the interface comes at the free end before the reflection from the fixed end arrives, which is the fourth peak with negative velocity. These observations can be put in a more concrete way if the arrival time is calculated in each case. Since the longitudinal velocity in alumina is $c_1 = 9.9365$ km/s (obtained from the formula $\sqrt{A_{11}/I_o}$), time taken by the incident pulse to travel 1.0 m (0.5 m forward and backward) is $1.0/c_1$ plus the initial padding of 100 μs, which amounts to 200.6 μs. This is the time of occurrence of the second peak. Similarly for the third peak, the required time is $2/c_1 + 100$ μs $= 301.28$ μs. Finally, as the longitudinal wave speed in aluminum is $c_2 = 5.1887$ km/s, the time taken by the incident pulse to reach the tip after being reflected from the fixed end is $1/c_1 + 1/c_2 + 100$ μs, *i.e.,* 393.36 μs. These values are marked with stars in the bi-material response, showing clearly the agreement between the theoretical prediction and the element behavior. It is also clearly seen in Figure (5.2) how the FGM gradually smooths the reflections occurring at the material boundary in the bi-material case. Both linear and exponential zones perform almost similarly in this reflection smoothing case. The full FGM configuration shows no reflection but the speeds are reduced as demonstrated by the uppermost curve. This is an expected result.

In summary, the governing wave equation with variable coefficients is solved approximately using several numerical techniques. The main objective is to find the solution of the elastodynamic equation governing the behavior

of a heterogeneous material. It is shown how an approximate plane wave solution can be obtained for inhomogeneous materials. It is also shown that, for an inhomogeneous material, the approximate wavenumber can be viewed as a complex number, where the imaginary part is responsible for wave amplitude attenuation. This approximation enables us to search for approximate spectral elements that solve the problem with small system sizes. Several such elements are formed and their superiority over the conventional time domain finite elements is demonstrated. It is shown that even the series solution of the governing equation can be used to construct spectral elements. The application of FGM in smoothing the reflected pulse that is generated at the bi-material interface is also demonstrated.

5.2 Depth-wise Functionally Graded Beam

In this section, SFEs are developed for both anisotropic and inhomogeneous beams for shear deformation with lateral contraction, which is also known as Herrmann–Mindlin theory (HMT). The effect of temperature is also considered in the formulation.

The displacement assumed for this theory is already given in Section 4.4.1. The linear strains in the presence of temperature field, obtained from Equation (4.21) are

$$\epsilon_{xx} = u_{,x} - z\phi_{,x} - \alpha(z)T(z)\,, \epsilon_{zz} = \psi - \alpha(z)T(z)\,, \gamma_{xz} = -\phi + w_{,x} + z\psi_{,x}\,, \tag{5.25}$$

where α and T are the depth-dependent coefficient of thermal expansion and temperature field. The non-zero stresses are related to these strains by

$$\{\sigma\} = \begin{Bmatrix} \sigma_{xx} \\ \sigma_{zz} \\ \tau_{xz} \end{Bmatrix} = \begin{bmatrix} \bar{Q}_{11}(z) & \bar{Q}_{13}(z) & 0 \\ \bar{Q}_{13}(z) & \bar{Q}_{33}(z) & 0 \\ 0 & 0 & \bar{Q}_{55}(z) \end{bmatrix} \begin{Bmatrix} \epsilon_{xx} \\ \epsilon_{zz} \\ \gamma_{xz} \end{Bmatrix} = [Q(z)]\{\epsilon\}\,, \tag{5.26}$$

where the $\bar{Q}_{ij}(z)$s are the depth-dependent elements of the constitutive matrix. For anisotropic homogeneous materials like fiber reinforced composites (FRC) they are constants and their expressions are given in the previous chapter in terms of ply-angle and composite properties (see also [50]). For inhomogeneous (but isotropic) materials $[\bar{Q}]$ becomes

$$\frac{E(z)}{1-\nu^2} \begin{bmatrix} 1 & \nu & 0 \\ \nu & 1 & 0 \\ 0 & 0 & (1-\nu)/2 \end{bmatrix}\,, \tag{5.27}$$

where $E(z)$ and ν are Young's modulus and Poisson's ratio. Here, Poisson's ratio is assumed constant. However, Young's modulus and α vary over the depth of the beam.

Following the regular procedure of Hamiltonian formulation, the four governing equations corresponding to four dof, u, ψ, w and ϕ are

$$I_\circ \ddot{u} - I_1 \ddot{\phi} - A_{11} u_{,xx} + B_{11} \phi_{,xx} - A_{13} \psi_{,x} = 0 \,, \tag{5.28}$$

$$K_I I_2 \ddot{\psi} + I_1 \ddot{w} + A_{31} u_{,x} - B_{31} \phi_{,x} + A_{33} \psi - B_{55} \left(w_{,xx} - \phi_{,x} \right) - K_d D_{55} \psi_{,xx} - L_T = 0 \,, \tag{5.29}$$

$$I_\circ \ddot{w} + I_1 \ddot{\psi} - A_{55} \left(w_{,xx} - \phi_x \right) - B_{55} \psi_{,xx} = 0 \,, \tag{5.30}$$

$$I_2 \ddot{\phi} - I_1 \ddot{u} - A_{55} \left(w_{,x} - \phi \right) - B_{55} \psi_{,x} + B_{11} u_{,xx} - D_{11} \phi_{,xx} + B_{13} \psi_{,x} = 0 \,, \tag{5.31}$$

and the four associated force boundary conditions are

$$A_{11} u_{,x} - B_{11} \phi_{,x} + A_{13} \psi - N_T = N_x \,, \; B_{55} \left(w_{,x} - \phi \right) + K_d D_{55} \psi_{,x} = Q_x \,, \tag{5.32}$$

$$A_{55} \left(w_{,x} - \phi \right) + B_{55} \psi_{,x} = V_x \,, \; - B_{11} u_{,x} + D_{11} \phi_{,x} - B_{13} \psi + M_T = M_x \,. \tag{5.33}$$

In the above equations, the stiffness coefficients and the mass moments integrated over the cross-section are defined in the same way as before (see Equations (4.29) and (4.30)). K_I and K_d are the correction factors introduced to compensate for the approximations introduced in the analysis [2]. Note that the governing equations and force boundary conditions are slightly different than the equations in Section 4.4.1, where the thermal effect was not considered.

The contributions from the temperature field come from the thermal forces N_T, M_T and L_T defined as

$$[N_T \,, \; M_T] = \int_{z_1}^{z_2} \alpha(z) \{ Q_{11}(z) + Q_{13}(z) \} [T(z) \,, \; z T(z)] \, b dz \,, \tag{5.34}$$

$$L_T = \int_{z_1}^{z_2} \alpha(z) \{ Q_{13}(z) + Q_{33}(z) \} T(z) \, b dz \,. \tag{5.35}$$

It is to be noted that the effect of the temperature field is limited to the force boundary conditions for the assumed displacement field of FSDT. However, in the present formulation, the Poisson's contraction results in a term in the governing equation (L_T), which will be treated as a body force.

Reduction to FSDT

The displacement field for FSDT is obtained by omitting the contractional dof ψ from the description of W as

$$U(x, y, z, t) = u^\circ(x, t) - z \phi(x, t) \,, \; W(x, y, z, t) = w^\circ(x, t) \,. \tag{5.36}$$

The resulting governing PDEs in terms of the three degrees of freedom (u°, w° and ϕ) are:

$$\delta u : \qquad I_\circ \ddot{u}^\circ - I_1 \ddot{\phi} - A_{11} u^\circ_{,xx} + B_{11} \phi_{,xx} = 0 \,, \tag{5.37}$$

$$\delta w^\circ : \qquad I_\circ \ddot{w}^\circ - A_{55} \left(w^\circ_{,xx} - \phi_x \right) = 0 \,, \tag{5.38}$$

$$\delta\phi : \quad I_2\ddot{\phi} - I_1\ddot{u}^{\circ} + B_{11}u^{\circ}{}_{,xx} - D_{11}\phi_{,xx} - A_{55}\left(w^{\circ}_{,x} - \phi\right) = 0 \ . \tag{5.39}$$

Associated force boundary conditions are

$$A_{11}u^{\circ}{}_{,x} - B_{11}\phi_{,x} - N_T = N_x \ , \tag{5.40}$$

$$A_{55}\left(w^{\circ}{}_{,x} - \phi\right) = V_x \ , \ -B_{11}u^{\circ}{}_{,x} + D_{11}\phi_{,x} + M_T = M_x \ , \tag{5.41}$$

where all the coefficients and mass moments are as defined before.

5.2.1 Spectral Finite Element Formulation

Following the same procedure as in Section 4.4.1, *i.e.,* substituting Equation (4.31) in the governing equations (without the thermal loading part), the same Equation (4.32) is obtained, which results in the 8th-order characteristic polynomial given in Equation (4.34). Variation of these roots with ω_n is discussed in the next section for a particular material distribution.

For the FSDT case, the wavematrix $\mathbf{W}$ is

$$[W] = \begin{bmatrix} A_{11}k^2 - I_{\circ}\omega_n^2 & 0 & -B_{11}k^2 + I_1\omega_n^2 \\ -B_{11}k^2 + I_1\omega_n^2 & jA_{55}k & D_{11}k^2 + A_{55} - I_2\omega_n^2 \\ 0 & A_{55}k^2 - I_{\circ}\omega_n^2 & -jA_{55}k \end{bmatrix} , \tag{5.42}$$

where all the integrated parameters are as defined before. Thus, in this case, $N_v = 3$ and $p = 2$, *i.e.,* there are six wavenumbers (eigenvalues).

The coefficients of the spectrum relation in both cases are real valued and frequency dependent although the roots can be complex for some values of ω_n. There are no closed form solutions of these roots and they must be found numerically, and are solved by the method of companion matrix . Once the variation of the wavenumbers with frequency is known, the variation of group speeds c_g^i, defined as $d\omega/d\Re(k_i)$ can be computed numerically, where $\Re$ denotes the real part of a complex number. In the following example, we take a beam structure and analyze it for its spectrum and dispersion relation and thereby draw several important conclusions.

5.2.2 The Spectrum and Dispersion Relation

The beam has 0.001 m width and 0.05 m depth. There are three layers in the beam. The top layer is made up of steel of 0.01 m thickness. The bottom layer is made up of ceramic of 0.031 m thickness. In between, there is an FGM layer of 0.009 m thickness, in which properties vary smoothly from that of steel to ceramic according to a power law, where the exponent n is set to 1.0. Material properties of steel are taken as $E = 210$ GPa, $\rho = 7800$ kg/m^3, while those of ceramic is $E = 390$ GPa and $\rho = 3950$ kg/m^3.

Figure 5.4 shows the spectrum relation of the beam with the material properties as stated before. To elicit the difference between the HMT and the FSDT, the spectrum relation for the same beam in terms of FSDT is

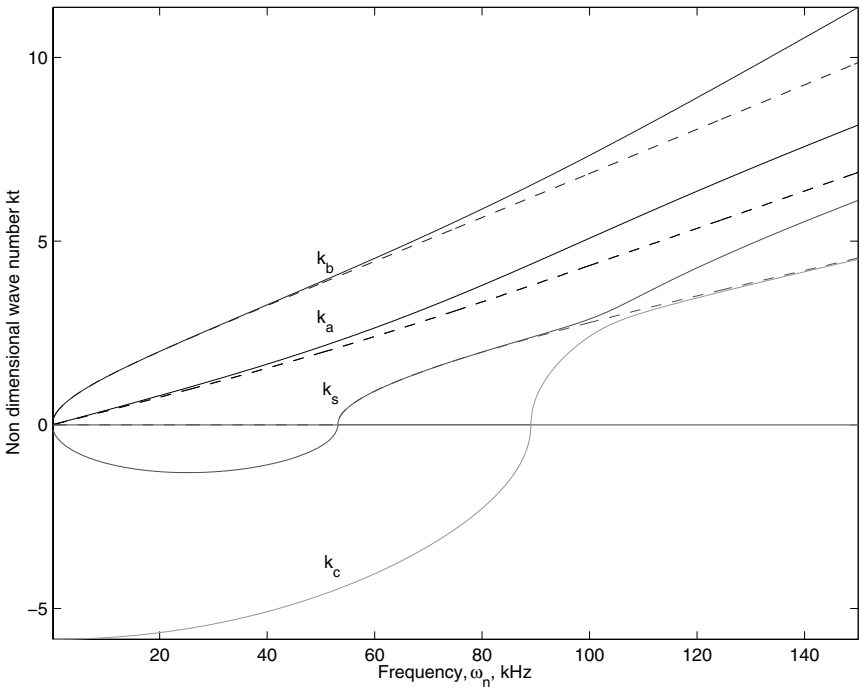

Fig. 5.4. Spectrum relation : solid line - HMT, dashed line FSDT, k_a, k_b, k_c and k_s denote axial, bending, contraction and shear wavenumber, respectively

plotted (in dashed lines) in the same figure. In the figure, k_a, k_b, k_s and k_c denote the axial, bending, shear and contraction wavenumbers , respectively. The wavenumbers plotted in the negative side of the ordinate denote the imaginary part of the wavenumbers. The frequencies at which the imaginary wavenumbers become real are called the cut-off frequencies, whose expressions were given earlier. More discussions on these frequencies are given in the next section. As is seen from the figure, the bending mode of FSDT matches the bending mode of HMT upto 40 kHz. There is always a difference in the axial modes of HMT and FSDT, which is more pronounced above 20 kHz. Although this difference is not clear in this figure for frequencies below 20 kHz, the dispersion relation (Figure 5.5) will reveal this feature clearly. In both axial and bending modes, the HMT predicts a higher gradient for the wavenumbers. The shear modes of the HMT and the FSDT match well upto 90 kHz. Above this frequency, the shear mode of FSDT overlaps the contraction mode of the HMT. However, the dispersion of these modes is quite different.

The dispersion relation of this beam model for both the HMT and the FSDT is plotted in Figure 5.5. The figure suggests that there is always a difference between the axial speeds predicted by the HMT and the FSDT. This difference is maximum near the second cut-off frequency and later decreases.

The bending speed predicted by the HMT and the FSDT is equal upto 20 kHz and beyond this frequency the difference between the two increases. The shear speeds are equal upto about 70 kHz but above this they behave quite differently. The shear speed predicted by the HMT dips and slowly regains a lower value than that of FSDT. This behavior can be attributed to the appearance of the contraction mode. The contraction speed at high frequencies matches the shear speed of the FSDT. It is important to note that there are propagating axial and bending modes for all frequencies, whereas, shear and contraction mode appear only when the frequency exceeds the respective cut-off frequencies.

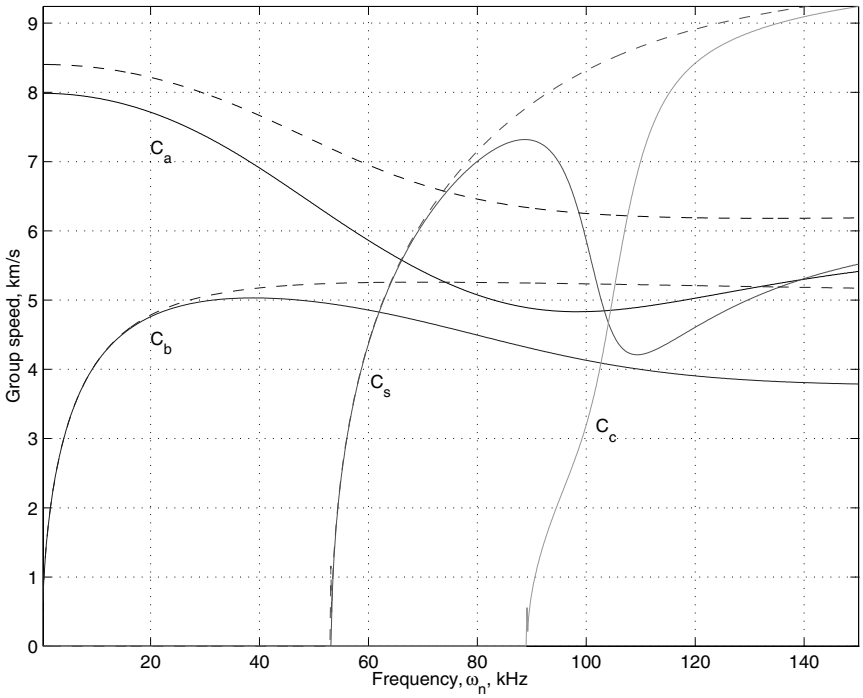

Fig. 5.5. Dispersion relation: solid line - HMT, dashed line FSDT, C_a, C_b, C_c and C_s denote axial, bending, contraction and shear group speeds, respectively

5.2.3 Effect of Gradation on the Cut-off Frequencies

Since the propagating modes appear only when the loading frequency exceeds the cut-off frequency, variation of the later with FGM parameters is important for response prediction. Explicit forms of the cut-off frequencies can be

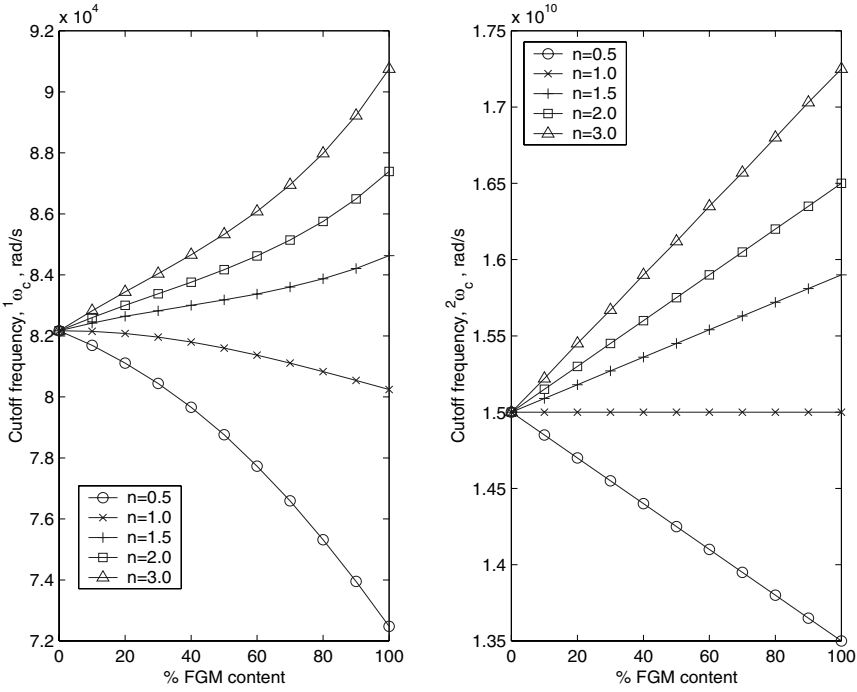

Fig. 5.6. Variation of the cut-off frequencies

obtained from the spectrum relation. Substituting $k = 0$ in the spectrum relation and solving for ω, the non-trivial roots are $\omega_{c1} = \sqrt{(I_\circ A_{55})/(I_\circ I_2 - I_1^2)}$ and $\omega_{c2} = \sqrt{(I_\circ A_{33})/(I_\circ I_2 - I_1^2)}$. These expressions for the beam geometry in the above example yield, $\omega_{c1} = 53.132$ and $\omega_{c2} = 89.087$ kHz, which are exactly the points from where the propagating shear and contraction mode are generated.

As the expressions for the cut-off frequencies suggest, they depend upon the FGM content of the beam (quantified by h_{fgm}/h, where h_{fgm} is the thickness of the FGM layer and h is the total beam thickness) and the gradation in the FGM layer (*i.e.,* n for power law variation Equation (2.48)). For the same beam, the thickness of the FGM layer is varied from 0% to 100% for a range of values of the parameter n. The variation is plotted in Figure 5.6. As is shown in the figure, ω_{c1} shows non-linear variation with FGM content, whereas, ω_{c2} shows linear variation. Both the frequencies decrease with FGM content when n is less than 1. When $n = 1$, ω_{c2} becomes independent of the FGM content, whereas, ω_{c1} decreases slowly. Although it is not shown here, ω_{c1} becomes independent of the FGM content for $n = 1.2$. For all values of n above 1, the cut-off frequencies increase monotonically with the FGM content. Hence, it is an added advantage of using FGM, where propagation of higher order

modes can be suppressed by increasing the FGM content, thereby increasing the range of validity of the FSDT.

Once we have the spectrum relation the SFE formulation can be started. As before, two types of elements can be formulated. One is the two-noded finite length element and the other is the one-noded infinite length element or the throw-off element. These elements have four dofs per node as is shown in Figure (4.1). The element formulation was given in the previous chapter, Section 4.4.4.

Stress Computation

The expressions for stress and strain can be found using Equation (4.45) and Equation (4.47) for the finite length element and similar expressions for the infinite length element. Using Equation (5.25) along with the previous equations, the strains at a point (x, z) of an element can be related to the nodal displacements of that element by

$$\begin{aligned}
\epsilon_{xx} &= \sum_{i=1}^{8} -jk_i e^{-jk_i x} \left[R_{1i} - zR_{4i}\right] [T_1]^{-1} \{\hat{u}\} - \alpha(z)T(z)\,, \\
\epsilon_{zz} &= \sum_{i=1}^{8} e^{-jk_i x} R_{2i} [T_1]^{-1} \{\hat{u}\} - \alpha(z)T(z)\,, \\
\gamma_{xz} &= \sum_{i=1}^{8} e^{-jk_i x} \left[-R_{4i} - jk_i R_{3i} - jzk_i R_{2i}\right] [T_1]^{-1} \{\hat{u}\}\,.
\end{aligned}$$

In matrix form, the above equation can be written

$$\{\epsilon\} = [B_1\, B_2\, \ldots\, B_8][D(x)][T_1]^{-1}\{\hat{u}\} - \{\epsilon\}_T\,, \tag{5.43}$$

where

$$B_i = \begin{bmatrix} -jk_i(R_{1i} - zR_{4i}) \\ R_{2i} \\ -R_{4i} - jk_i R_{3i} - jzk_i R_{2i} \end{bmatrix}, \tag{5.44}$$

and $\{\epsilon\}_T$ is the thermal (eigen) strain due to temperature whose elements are $-\alpha(z)T(z)\{1\ 1\ 0\}$. The stress–strain relation (using the $\bar{Q}$ matrix) can now be used to compute the stresses. Note that the above expressions are to be evaluated at each frequency ω_n.

Effect of the Temperature Field

As shown earlier, due to the temperature field, both body forces and nodal forces are generated. For the finite length element, the nodal force vector due to the temperature field is $\{\hat{\mathbf{f}}\}_T^n = \{N_T\ ,\ 0\ ,\ 0\ ,\ -M_T\ ,\ -N_T\ ,\ 0\ ,\ 0\ ,\ M_T\}$. The body force vector $\{\mathbf{b}\}$ is $\{0\ ,\ -L_T\ ,\ 0\ ,\ 0\}$ and the nodal force due to this

load can be obtained by applying the variational principle in the frequency domain (see [9]), which yields the load vector $\{\hat{\mathbf{f}}\}_{TB}^{n}$

$$\{\hat{\mathbf{f}}\}_{TB}^{n} = \int_0^L \int_{z_1}^{z_2} [N]_n^T \{\mathbf{b}\}\, b dz dx\,, \quad [N]_n = [R]_n [D(x)]_n [T_1]_n^{-1}\,, \tag{5.45}$$

where $[N]_n$ is the shape function matrix at frequency ω_n, which can be obtained by combining Equation (4.45) and Equation (4.47). The equilibrium equation at the nth frequency step becomes

$$\{\hat{\mathbf{f}}\}_n - \{\hat{\mathbf{f}}\}_T^n - \{\hat{\mathbf{f}}\}_{TB}^n = [K]_n \{\hat{\mathbf{u}}\}_n\,. \tag{5.46}$$

This body force term is absent in the FSDT-based SFE.

5.2.4 Computation of the Temperature Field

The problem of finding the temperature distribution through the thickness of the beam is solved independently and prior to the analysis of deformation due to mechanical loading. This is done by solving the one-dimensional heat conduction equation with prescribed boundary condition. The complexity of the problem increases because of the inhomogeneous structure of the beam. The thermal conductivity of the beam material is denoted by $k(z)$ at depth z and the governing equation of the temperature distribution is

$$d(k(z)dT/dz)/dz = 0\,, \quad T(z_1) = T_b\,, T(z_2) = T_t\,, \tag{5.47}$$

where T_t and T_b are the temperatures at the top and bottom layer of the beam. Integrating Equation (5.47) twice and satisfying the boundary condition we get the expression for the temperature at any depth as

$$T(z) = T_b + \int_{z_1}^{z} C_1/k(z)\, dz\,, \quad C_1 = (T_t - T_b)/\int_{z_1}^{z_2} 1/k(z)\, dz\,. \tag{5.48}$$

It is assumed that $k(z)$ varies according to the power law or exponential law given before. Once the temperature field is known, N_T, M_T and L_T can be computed using Equations (5.34) and (5.35).

5.3 Wave Propagation Analysis: Depth-wise Graded Beam (HMT)

In this section, numerical experiments are performed to demonstrate the accuracy and efficiency of the depth-wise graded SFE. First, the element is used to model an inhomogeneous beam subjected to mechanical loading only and the response is compared with other existing time domain FEs and SFEs. Next, the effect of the inhomogeneity on the contractional mode is studied. Also,

the variation of the stresses and their deviation from FSDT are studied in detail. Finally, the beam is subjected to a prescribed temperature field at the top and the bottom layer, along with a mechanical loading. The temperature distribution within the beam is computed first and subsequently the response of the beam for this thermo-mechanical loading is obtained.

5.3.1 Validation of the Formulated SFE

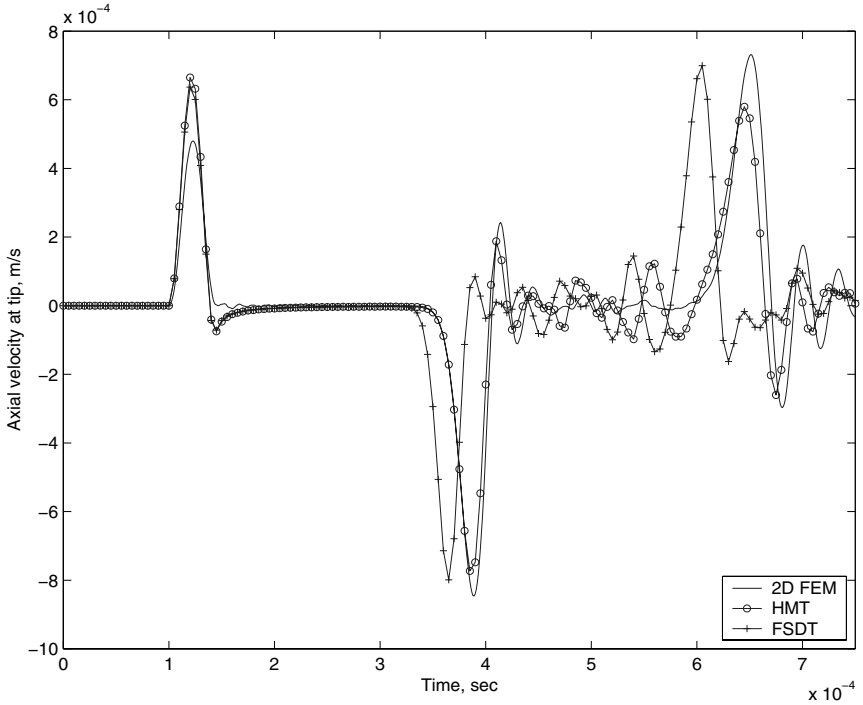

Fig. 5.7. Axial velocity at tip of the beam

The beam used earlier for analyzing the spectrum and dispersion relation is considered again and the cantilever boundary condition is imposed. The beam is subjected to an impact loading and its response is measured and compared with existing FEs and SFEs. Two types of load are considered, a broadband pulse loading and a modulated pulse loading. Further, two broadband pulses are used. The first one has relatively low frequency and is used to compare with 2-D FE analysis. Although this load does not excite the contraction mode of HMT, the frequency demands a very fine mesh in the FE analysis and any loading with higher frequency content will require a much

finer FE mesh and in turn a larger FE system size. Therefore, FE comparison is limited to this relatively low frequency loading. The second load has a higher frequency content so that all the modes are excited. A modulated pulse is used to segregate the propagating modes.

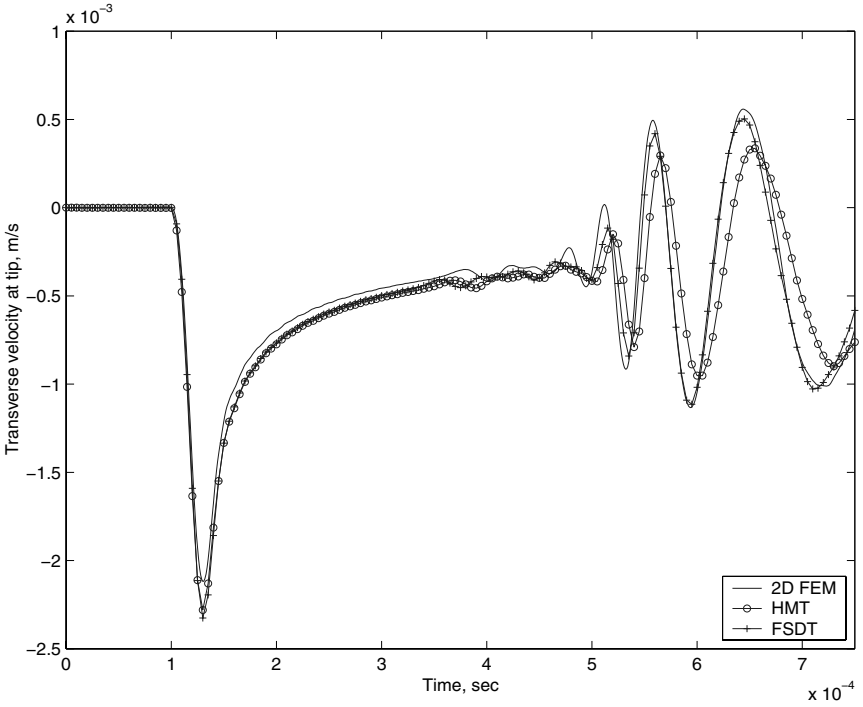

Fig. 5.8. Transverse velocity at tip of the beam

Response to Broadband Pulse

The pulse load with a comparatively smaller band is shown in Figure 5.3. As is seen in the figure, the load has a frequency content of around 46 kHz, which means (see the dispersion relation (Figure 5.5)) only the axial and bending modes will be excited. Hence, the beam will essentially behave like an elementary (Euler–Bernoulli) beam. The load is applied at the free end of the beam and velocity is measured at the same point. The same beam is also modeled with two-dimensional FEs for comparison. Two different types of 1-D SFE models are considered, the present element (HMT) and the Timoshenko beam model (FSDT) (Section 5.2). The 1-D spectral model consists of a single beam element, one end fixed, which results in a system matrix of size $[4\times4]$ for HMT and $[3\times3]$ for FSDT, which need to be inverted at each frequency step.

In comparison, the 2-D model of the beam consists of 400 triangular plane stress FEs, which results in a system size of $[500 \times 16]$, where 500 is the number of active dof and 16 is the half bandwidth. This large banded matrix needs to be inverted at each time step, where Newmark's time integration scheme with 1μs step size is adopted. Needless to say, the cost of the computation involved in the FE analysis is many orders higher than the cost of the SFE analysis.

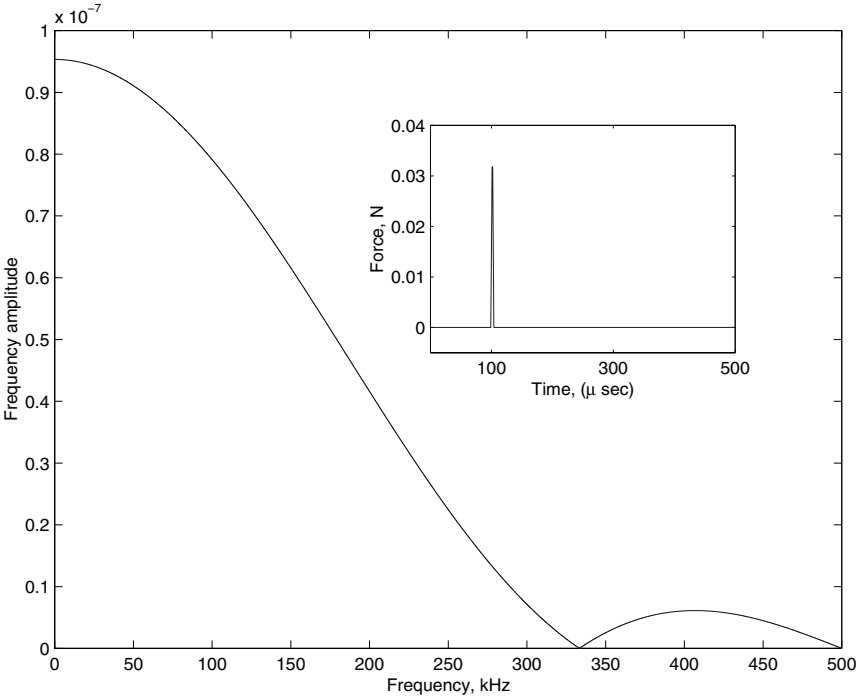

Fig. 5.9. High frequency load

To take care of the inhomogeneity in the FE model, material properties are first evaluated at the nodes by following a particular variation. Within each element, it is assumed that the material properties at any point can be described by the same shape functions that describe the displacements and the geometry. Hence, the material properties can be obtained for each Gauss point while the numerical integration is performed. The force input for spectral analysis is sampled at 1 μs time steps with 16384 FFT points.

First, the load is applied axially at the free end of the beam and the axial velocity (of the mid-depth of the FGM layer) at the same point is measured and plotted in Figure 5.7. In the figure, the peak at 0.1 ms is the incident part of the pulse. The wave then propagates towards the fixed end, is reflected at the boundary and moves towards the free end and appears at the tip at around

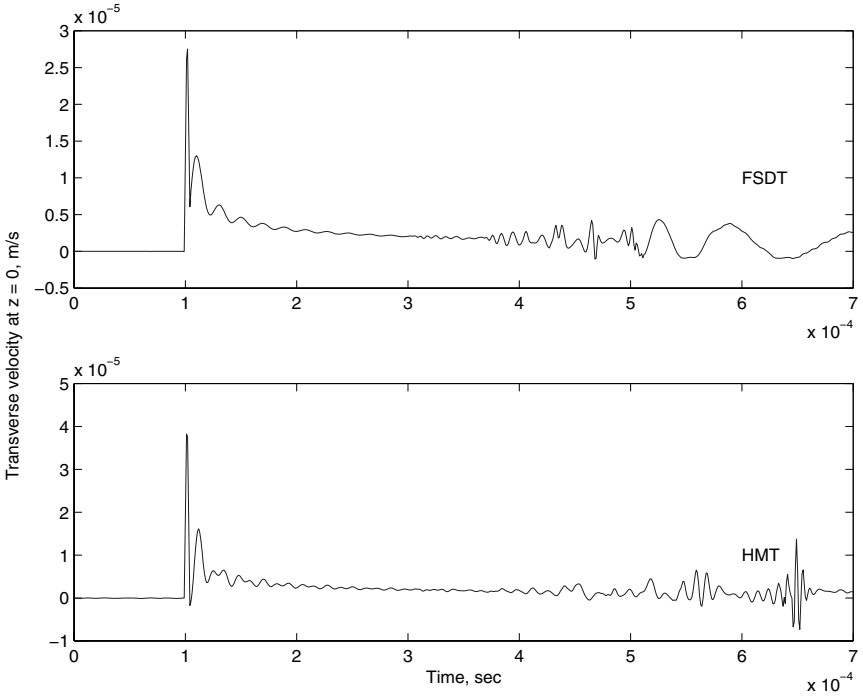

Fig. 5.10. Transverse velocity at the tip of the beam

0.3 ms. As is seen in the figure, 2-D FE and the present spectral element agree quite well, whereas, the FSDT SFE has differences in the occurrence of reflection from the boundary. This is expected, since, the dispersion relation suggests that the axial speed for FSDT is higher than that of HMT for all frequencies.

Next, the same load is applied in the transverse direction at the tip and the transverse velocity at the same point is measured, and plotted in Figure 5.8. It can be seen from the figure that all three responses agree quite well with each other. This is due to the fact that at low frequencies (below 40 kHz) there is very little or no difference in the bending speeds for the HMT and FSDT theory (see Figure 5.5). Figures 5.7 and 5.8 establish the accuracy and efficiency of the formulated SFE. They also demonstrate the need for higher order waveguides, especially at high frequencies. It is important to note that the response in Figure 5.8 is the history of $\dot{w}$, *i.e.,* $\dot{W}$ at $z = 0$. In the FSDT, $\dot{W}$ is the same at all points of the cross-section and equal to what is shown in Figure 5.8. For HMT, there can be variation in $\dot{W}$ over the depth of the beam and it can be markedly different from $\dot{w}$, specially for thicker cross-sections.

To have sufficient contribution from the contractional mode, the frequency content of the impact should extend beyond the second cut-off frequency, ω_{c2}. To this end, another pulse loading is considered, whose time and frequency

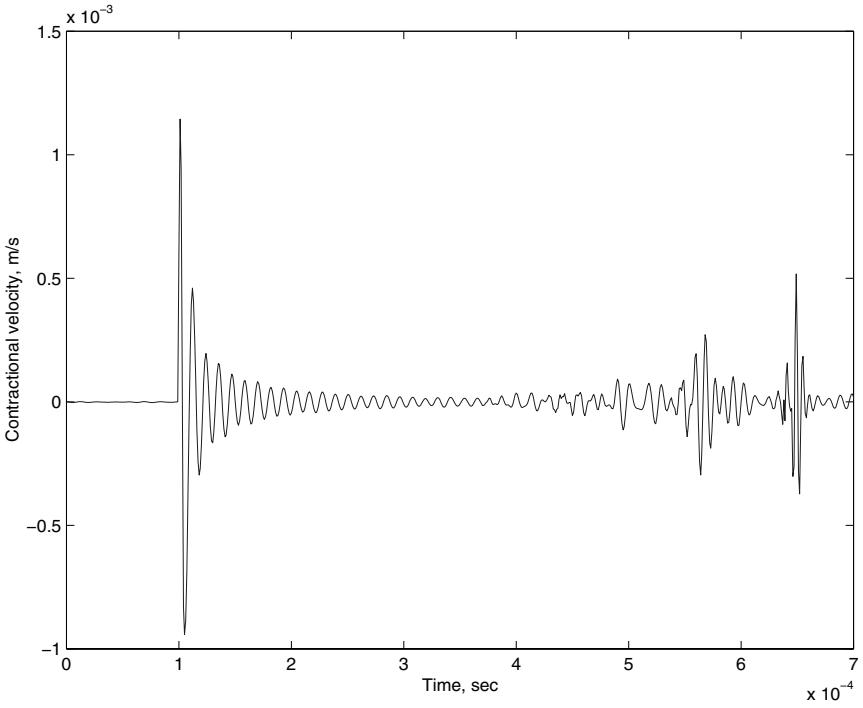

Fig. 5.11. Contractional velocity at the tip of the beam

domain representation is shown in Figure 5.9. This pulse has a very small duration (10 μs) and a frequency content of around 340 kHz, which is sufficient to force propagation of the contraction mode. This load is again applied at the tip of the cantilever beam in the Z direction and transverse velocity at the same point ($z = 0$) is measured, and plotted in Figure 5.10 along with the response from FSDT analysis. Comparing the two responses, it can be seen that there is considerable difference in the peak magnitude even though both velocities are measured at the reference plane ($z = 0$). The HMT predicts a peak velocity of about $4{\times}10^{-05}$ m/s, whereas, FSDT predicts peak velocity of less than $3{\times}10^{-05}$ m/s. This indicates that FSDT overestimates the stiffness of the beam. Further, there is a period shift in the FSDT response, marked by early appearance of the reflections from the boundary. In the FSDT response, the reflection appears at around 400 μs, whereas, in HMT, the bulk of the reflection arrives at around 550 μs. This difference is due to the higher bending speed at higher frequencies, as predicted by FSDT.

Coming to the contribution of the contractional mode, again we note that the maximum amplitude of $\dot{w}$ in Figure 5.10 (given by HMT) is 4.0×10^{-05} m/s. For the same load and the same beam, the contractional velocity $\dot{\psi}$ is plotted in Figure 5.11. As is seen in the figure, the contractional velocity

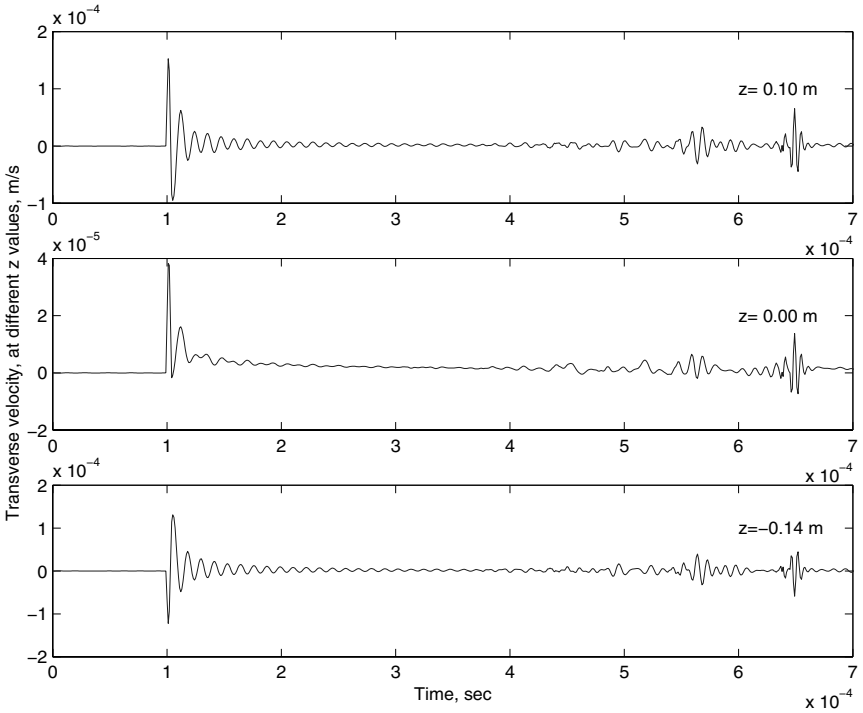

Fig. 5.12. Transverse velocity at the tip of the beam

shows high dispersiveness in the form of multiple oscillations. It shows reflections from the fixed end at around 550 μs, as found in the transverse velocity response. Further, contractional velocity has considerable magnitude over the initial part of the response and maximum amplitude of $\dot{\psi}$ is 1.2×10^{-03} s^{-1}, which is 30 times higher than $max|\dot{w}|$. Hence, considerable difference between the top and bottom layer velocities and the reference plane velocity can be expected. Figure 5.12 shows the variation of $\dot{W}$ at the top, bottom and reference plane. The figure shows that maximum $\dot{W}$ at the steel layer is 1.53 $\times 10^{-04}$ m/s, at the FGM layer is 0.38 $\times 10^{-04}$ m/s and at the ceramic layer is 1.3 $\times 10^{-04}$ m/s, *i.e.,* the difference in the peak velocity between the top and bottom layer is about 0.2×10^{-04} m/s, which is about 57% of the maximum reference plane velocity. Although predominant over only a very small domain, this differential nature is neglected by the FSDT.

5.3.2 Lamb Wave Propagation in FSDT and HMT Beams

The responses shown so far are superpositions of all the propagating/ evanescent modes. There are three propagating modes (axial, bending and shear) in FSDT, whereas, HMT has an additional contraction mode along with the

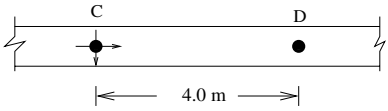

Fig. 5.13. Model for Lamb wave study

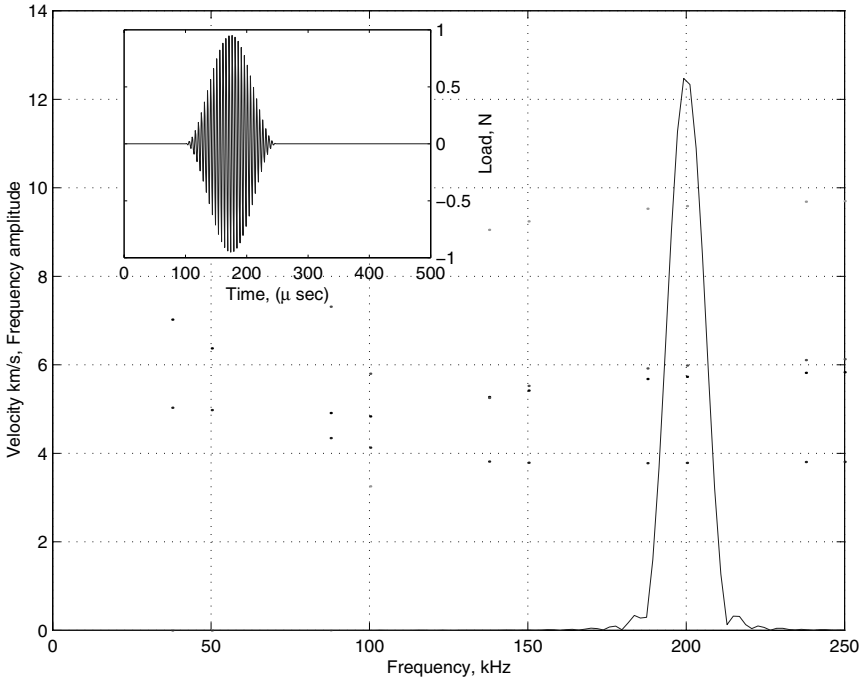

Fig. 5.14. Modulated pulse load applied to the beam

FSDT modes. These modes individually propagate with the group speeds shown in the dispersion relation. If one wants to study the principal components of the response (*i.e.,* the propagating modes) individually, then wideband pulse loading will not be useful due to the dependency of the speeds on the frequency. Instead, a modulated pulse (monochromatic) will force each individual mode to travel at its group (constant) speed. If the central frequency of the modulated pulse is so chosen that all propagating modes occur (this information can be obtained from the dispersion relation), then all these modes can be captured graphically if they are allowed to propagate for sufficient length.

Having this strategy in mind, a pulse load modulated at 200 kHz is applied to an infinite beam as shown in Figure 5.13. The beam is impacted at point C and the response is measured at point D, 4.0 m away from the impact site. The frequency domain representation of the load is shown in Figure 5.14. The

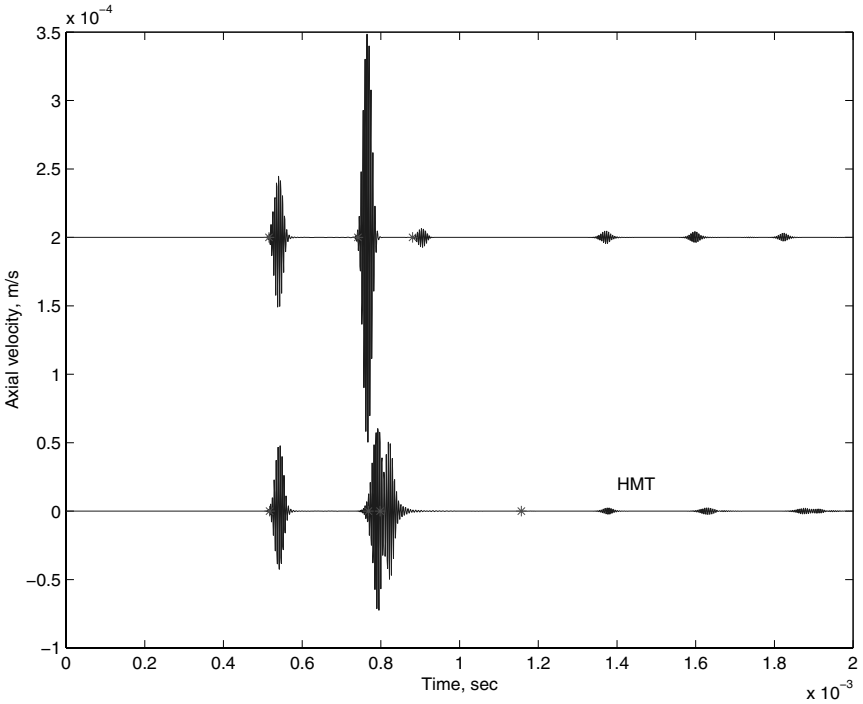

Fig. 5.15. Axial velocity history: the modes in order of appearance are contraction, shear, axial and bending with the FSDT response shifted for clarity

load has 150 μs duration, and is shown in the inset. The previous dispersion relation is also superposed in the same figure. As can be seen, all the modes propagate at this frequency. For HMT, the group speeds at this frequency are: $c_a = 5.73$ km/s, $c_b = 3.78$ km/s, $c_s = 5.98$ km/s and $c_c = 9.58$ km/s. For the given propagating distance, the time required for each mode to reach the point D will be as follows: $t_a = 0.798$ ms, $t_b = 1.157$ ms, $t_s = 0.768$ ms and $t_c = 0.517$ ms, where the subscripts after t denote the usual modes. Similarly, for the propagating waves described by FSDT: $c_a = 6.235$ km/s, $c_b = 5.125$ km/s and $c_s = 9.62$ km/s, which give $t_a = 0.742$ ms, $t_b = 0.880$ ms and $t_s = 0.516$ ms. These values will be compared with the time of arrival of the beam responses.

The load is first applied axially and the axial velocity at D is measured and plotted in Figure 5.15. The arrival times calculated earlier are also plotted with a star mark. As is seen there, the arrival of the different modes are predicted accurately by the dispersion relation for both FSDT and HMT. The propagating modes of FSDT are of considerable magnitude and can be identified easily, however, the bending response for HMT is very small compared to the other modes and cannot be detected easily. In any case, the bending

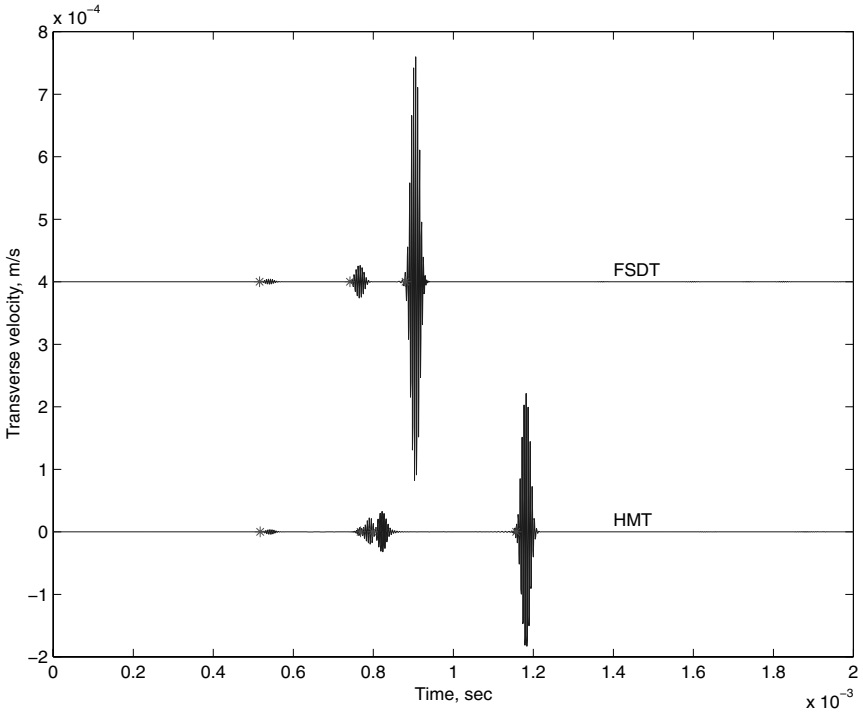

Fig. 5.16. Transverse velocity history: the modes in order of appearance are contraction, shear, axial and bending with the FSDT response shifted for clarity

response is not pre-dominant in axial motion. Next, the load is applied in the transverse direction and the transverse velocity (at the reference plane) at point D is measured and plotted in Figure 5.16. Here again, the arrival times are well predicted. In HMT response, the contraction mode has very small magnitude compared to the bending mode.

5.3.3 Effect of Gradation on Stress Waves

In this study, the justification for using the HMT over FSDT is given by comparing the stress wave responses. By virtue of the displacement field assumed at the beginning, HMT results normal stress σ_{zz}, which is zero in FSDT. This is one major drawback of FSDT, as will be shown in the later part of this section.

For this analysis, a deep beam is taken with slenderness ratio 5. The beam has a width of 0.001 m, length of 2.0 m and total depth of 0.4 m. The beam is made up of ceramic, steel (material properties as given before) and a FGM layer in between the ceramic and steel layer. The steel layer is 0.12 m thick and the ceramic layer is 0.2 m thick. The load of Figure 5.3 is applied at

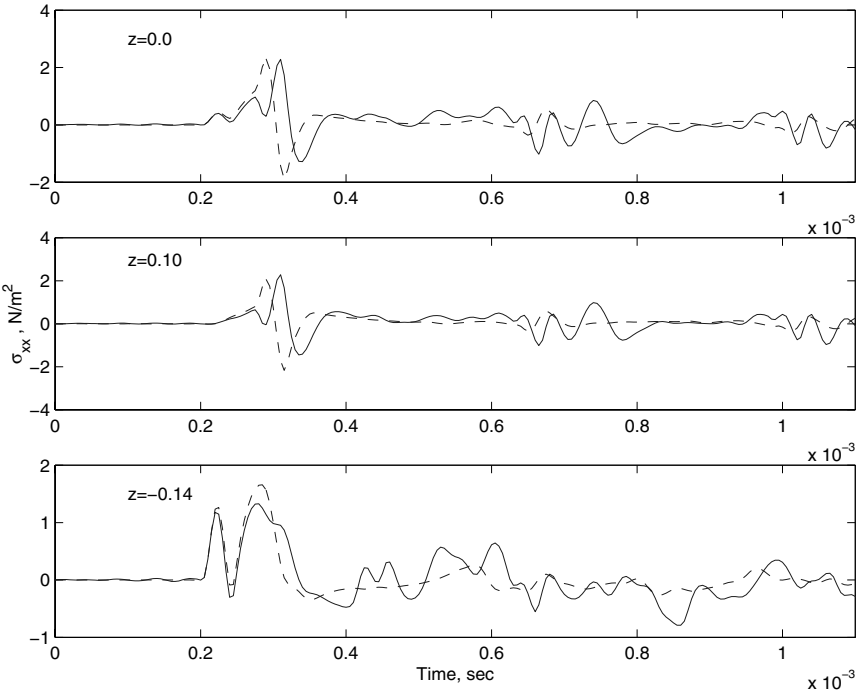

Fig. 5.17. Axial stress history in FGM ($z = 0.0$ m), ceramic ($z = -0.14$ m) and steel ($z = 0.10$ m) layer: solid line - HMT, dashed line - FSDT

the tip of the beam, first in the axial direction and then in the transverse direction. Stress histories are measured at the midpoint of the cantilever beam at three different z locations, $z = 0$, *i.e.,* midpoint of FGM layer, $z = 0.10$, *i.e.,* midpoint of the steel layer and $z = -0.14$, *i.e.,* midpoint of the ceramic layer, respectively. The beam is also analyzed for FSDT and the stresses are measured at the same locations and superposed over the HMT responses.

Axial stress is measured for the axial loading and the results are shown in Figure 5.17. As the figure suggests, the FGM and steel layer carry almost equal stresses, followed by the ceramic layer. The same trend is visible in the FSDT responses and in addition, the magnitude of the stresses predicted by the two theories are almost equal. However, for the metal and FGM layer, the FSDT results suffer period error, *i.e.,* the peak stresses occur at an early time instant compared to the HMT response. For the stress measured at the ceramic layer, this deviation is absent.

Next the normal and shear stresses are measured for a transverse tip load. Figure 5.18 shows the variation of the normal stress σ_{zz} at three points in the cross-section of the beam, for which there is no FSDT response to compare with. In this case, however, stress is maximum in the ceramic layer, followed

by the FGM layer and the metal layer is least stressed. This stress state within the beam is completely neglected in the FSDT.

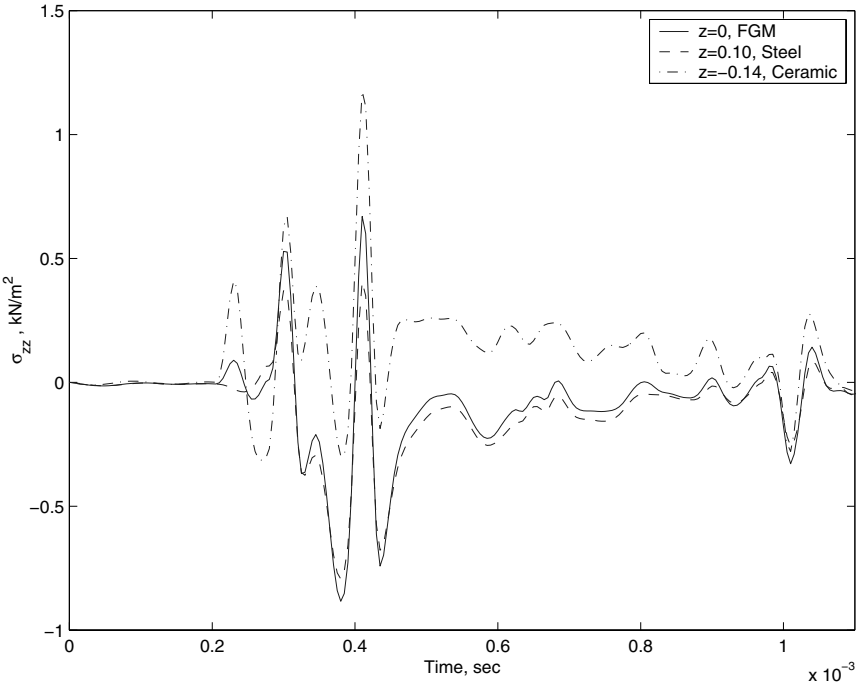

Fig. 5.18. Normal stress history

The shear stress (τ_{xz}) variation is plotted in Figure 5.19 for both HMT and FSDT. In this case, considerable difference can be observed in the peak magnitude for the FGM and ceramic layer, however, for the steel layer the difference is not so significant. The FSDT always predicts lower shear stress compared to that predicted by the HMT. Moreover, the difference can be noticed in the time of the occurrence of the stress peaks. This is due to the differences in the group speeds of the various modes.

This study shows that, the FSDT generates a stress field that suffers either magnitude error or period error in comparison to the HMT and fails to predict the normal stress in the thickness direction, which is quite significant. Thus, the stress state predicted by FSDT may not give the real picture of the dynamics of the beam and hence the prediction.

5.3.4 Coupled Thermoelastic Wave Propagation

In most practical applications of FGM, the structure is normally subjected to mechanical loading along with a specified temperature field. It was shown

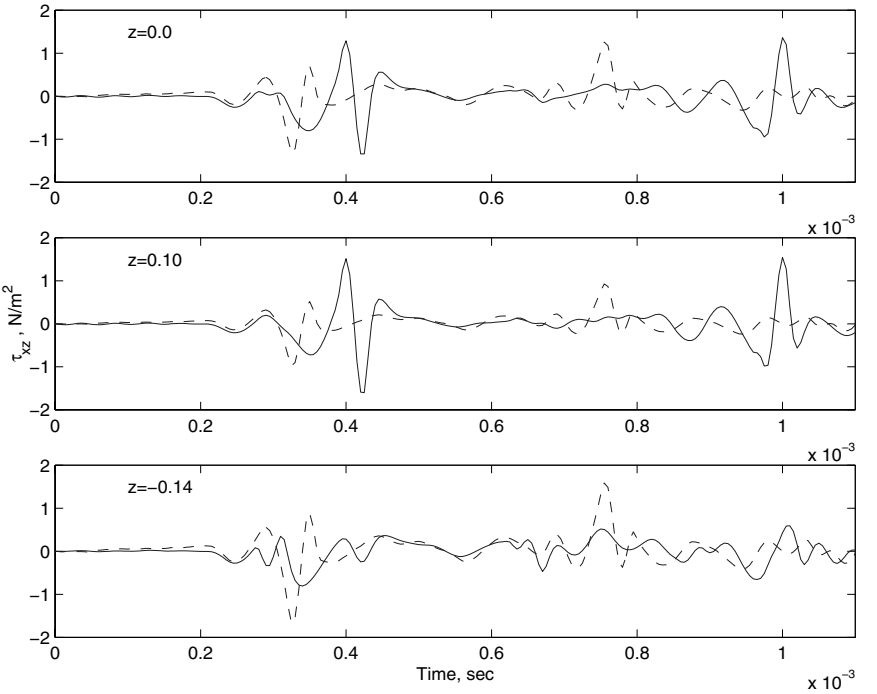

Fig. 5.19. Shear stress history in FGM ($z = 0.0$ m), steel ($z = 0.1$ m) and ceramic ($z = -0.14$ m) layer: solid line - HMT, dashed line - FSDT

in Section 5.2 that the specified temperature field induces body and surface (nodal) forces, which, although demands coupled thermo-mechanical analysis, can be analyzed separately from the mechanical loading. To this end, the configuration of the beam used in the verification study is taken along with the same material properties and boundary conditions. An axial and a transverse load of 1 kN magnitude are applied at the tip of a cantilever beam. The temperature is specified only on half of the beam. This applied temperature field is different at the ceramic (bottom) and metal (top) layer (see Figure 5.20a). Thermal expansion coefficients of steel and ceramic are taken as 14.0×10^{-6} and 7.0×10^{-6} °C^{-1}. Coefficient of thermal conductivity for steel and ceramic is taken as 20 and 1 W/m/°C. It is assumed that both the mechanical and thermal loading follow the same variation over time, which is given by Figure 5.3. The peak temperature rise ΔT_1 and ΔT_2 specified in this case are 5 and 10°C. Responses are compared between thermo-mechanical loading and mechanical loading, as predicted by HMT.

First, the thermal equation is solved independently to find the depth-wise variation within the beam. This known temperature field helps us to compute the thermal force resultants (with respect to x) N_T, M_T and L_T (see Equations (5.34) and (5.35)). As discussed in Section 5.2, the thermal field results in axial

load and moments at the nodes and a body force in the contractional mode, which in turn generates nodal forces in all dof. The structure is modeled with two SE as shown in Figure 5.20 and the temperature is specified in element 2.

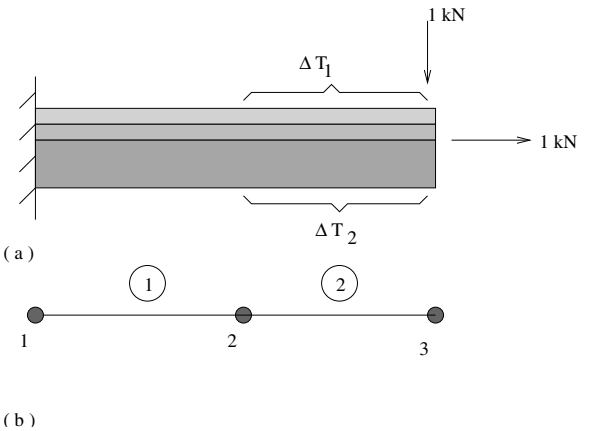

Fig. 5.20. Beam model in thermoelastic study (a) the load and boundary conditions (b) the SFE discretization

It is important to note that in the mechanical loading case only two loads are acting at the tip of the beam, one in the axial direction, another in the transverse direction. However, in the thermo-mechanical case, other than these two loads, there are eight extra concentrated loads. Four of them act at the tip of the beam (node 3) and are of the same sign as the mechanical loads and thus reinforce them. The rest of the loads act at the mid-point of the beam (node 2) in the opposite direction of the loads at the tip. Thus, while the tip loads induce positive velocity, central loads induce negative velocity. The waves generated from these loadings are further reflected at the fixed end and change their sign. All these activities are visible in the responses measured at the tip of the beam and shown in Figure 5.21. In all the subfigures, the solid line denotes the response due to pure mechanical loading and the broken line denotes the response due to thermo-mechanical loading.

Figure 5.21 shows the variation of the axial, contractional and the transverse velocity for the two different loadings. For both mechanical and thermo-mechanical responses, there is negative velocity at around 400 μs, which is the reflected wave generated at the fixed end from the tip load. The effect of the central load is seen in the form of negative velocity at around 200 μs, which travels only 0.5 m to reach the tip of the beam. Reflection of this wave (from the fixed end) travels 1.5 m and is visible in the form of positive velocity at around 300 μs. In comparison, the wave generated at the tip travels 2.0 m and hence arrives late. Also, it can be seen that the presence of the ther-

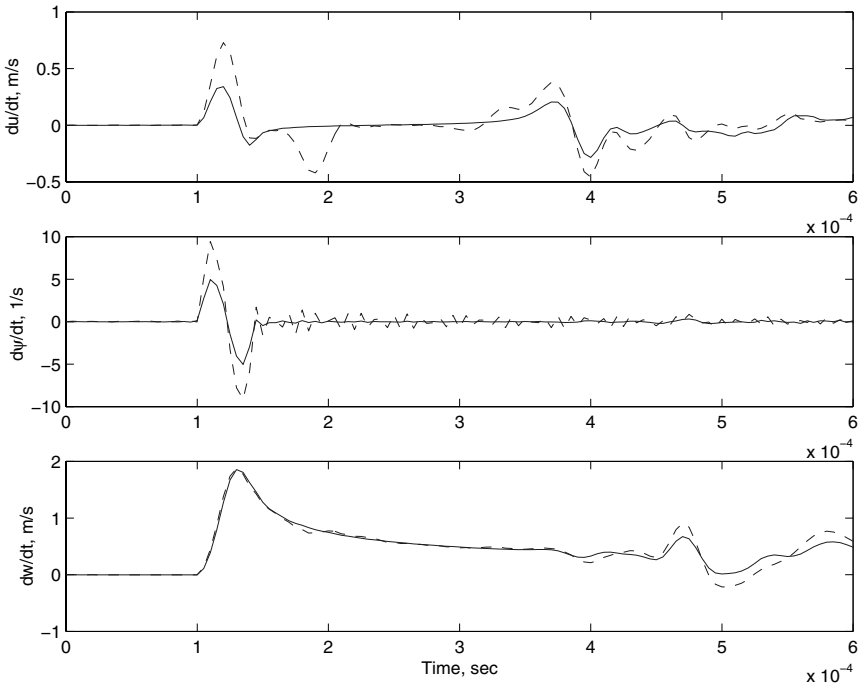

Fig. 5.21. Axial, contractional and transverse velocity histories at the tip of the beam: solid line - pure mechanical loading, dashed line - thermo-mechanical loading

mal field greatly magnifies the pure mechanical response, which depends upon the specified temperature rise. The ratio of the maximum axial velocity for thermo-mechanical loading and the maximum axial velocity for mechanical loading is 2.14, which indicates the major contribution of the thermal field.

In the variation of the contractional velocity, the thermo-mechanical response shows considerable dispersiveness compared to the mechanical response. The ratio of the maximum amplitudes in this case is 1.9, which again shows the strong effect of the thermal field.

For the variation of the transverse velocity, as opposed to the previous cases, the response due to the mechanical loading is of the same order as the thermo-mechanical load response. This is because the moment generated due to the thermal load is of very small magnitude compared to the transverse mechanical load and the axial load has little bearing on the transverse response.

On the whole it can be said that the effect of the thermal field is predominant over the axial and contractional modes, which again justifies the need for considering the HMT for thermomechanical analysis as opposed to the FSDT.

5.4 Length-wise Graded Beam: FSDT

In the previous formulation for FSDT elements, the material properties are assumed constant over the length of the beam, which may not always be the case. In this section, we extend the previous formulation for lengthwise graded beam, which brings out several new features of the inhomogeneous wave. In this formulation, the non-zero stresses are related to the non-zero strains by

$$\{\sigma\} = \begin{Bmatrix} \sigma_{xx} \\ \tau_{xz} \end{Bmatrix} = f(x) \begin{bmatrix} \bar{Q}_{11}(z) & 0 \\ 0 & \bar{Q}_{55}(z) \end{bmatrix} \begin{Bmatrix} \epsilon_{xx} \\ \gamma_{xz} \end{Bmatrix} = f(x)[Q]\{\epsilon\}\,, \tag{5.49}$$

where $f(x)$ denotes the x dependency of the inhomogeneity, which in general can be any function. Similarly, density of the material is also assumed to vary in both x and z direction as

$$\rho(x,z) = \rho_\circ(z)s(x)\,. \tag{5.50}$$

The governing equations in terms of the unknown displacement field are

$$(f(x)A_{11}u_{,x} - f(x)B_{11}\phi_{,x}\,)_{,x} - I_\circ s(x)\ddot{u} + I_1 s(x)\ddot{\phi} = 0\,, \tag{5.51}$$

$$-(f(x)B_{11}u_{,x} - f(x)D_{11}\phi_{,x}\,)_{,x} + f(x)A_{55}\,(w_{,x} - \phi) - I_2 s(x)\ddot{\phi} + I_1 s(x)\ddot{u} = 0\,, \tag{5.52}$$

$$(f(x)A_{55}\,(w_{,x} - \phi))_{,x} - I_\circ s(x)\ddot{w} = 0\,, \tag{5.53}$$

and the three associated force boundary conditions are

$$f(x)(A_{11}u_{,x} - B_{11}\phi_{,x}\,) = N_x\,, \tag{5.54}$$

$$f(x)A_{55}\,(w_{,x} - \phi) = V_x\,,\ -f(x)B_{11}u_{,x} + f(x)D_{11}\phi_{,x} = M_x\,, \tag{5.55}$$

where N_x, V_x and M_x are the applied nodal axial force, shear force and bending moments, respectively. The stiffness coefficients and the mass moments are as defined before.

The governing PDEs, Equations (5.51)–(5.53), are not solvable readily for arbitrary $f(x)$ and $s(x)$ and some assumption on their forms is necessary before proceeding further. In this formulation, the exponential variation is assumed for both functions, *i.e.,*

$$f(x) = e^{\alpha x}\,, \quad s(x) = e^{\beta x}\,, \tag{5.56}$$

where α and β are the inhomogeneous parameters, which control the gradation. They may or may not be equal to each other. However, when they are equal the governing PDEs are exactly solvable as they become equations with constant coefficients. When $\beta \neq \alpha$, some approximation is necessary to keep the equations in the same constant coefficient form.

Substituting Equation (5.56) in Equations (5.51)–(5.53), the new set of governing PDEs are

$$A_{11}(\alpha u_{,x} + u_{,xx}) - B_{11}(\alpha\phi_{,x} + \phi_{,xx}) - I_\circ\gamma\ddot{u} + I_1\gamma\ddot{\phi} = 0\,, \tag{5.57}$$

$$-B_{11}(\alpha u_{,x} + u_{,xx}) + D_{11}(\alpha\phi_{,x} + \phi_{,xx}) + A_{55}(w_{,x} - \phi) - I_2\gamma\ddot{\phi} + I_1\gamma\ddot{u} = 0\,, \tag{5.58}$$

$$A_{55}(\alpha(w_{,x} - \phi) + w_{,xx} - \phi_{,x}) - I_\circ\gamma\ddot{w} = 0\,, \tag{5.59}$$

where $\gamma = e^{(\beta-\alpha)x}$. When $\alpha = \beta$, $\gamma = 1$ and the equations are exactly solvable in the frequency domain. When $\alpha \neq \beta$, γ can be evaluated approximately at some representative point in the element, x_c, as $\gamma = e^{(\beta-\alpha)x_c}$, thus rendering the equations once again solvable exactly.

5.4.1 Spectral Finite Element Formulation

For the element formulation, the new set of governing equations, Equations (5.57)–(5.59) will be considered. The wave matrix ($N_v = 3, p = 2$) with $\ell^2 = k^2 + jk\alpha$ becomes,

$$[W] = \begin{bmatrix} A_{11}\ell^2 - I_\circ\gamma\omega_n^2 & 0 & -B_{11}\ell^2 + I_1\gamma\omega_n^2 \\ -B_{11}\ell^2 + I_1\gamma\omega_n^2 & jA_{55}k & D_{11}\ell^2 + A_{55} - I_2\gamma\omega_n^2 \\ 0 & A_{55}\ell^2 - I_\circ\gamma\omega_n^2 & -A_{55}(jk - \alpha) \end{bmatrix}, \tag{5.60}$$

which yields the spectrum relation as

$$Q_1k^6 + Q_2k^5 + Q_3k^4 + Q_4k^3 + Q_5k^2 + Q_6k + Q_7 = 0\,. \tag{5.61}$$

Variation of these roots with ω_n is discussed in the next section for a particular material. The coefficients $Q_1 - Q_7$ are

$$\begin{aligned} Q_1 &= A_{11}D_{11}A_{55} - B_{11}^2A_{55}\,, \\ Q_2 &= 3jA_{11}\alpha D_{11}A_{55} - 3jB_{11}^2\alpha A_{55}\,, \end{aligned}$$

$$\begin{aligned} Q_3 = {} & -3A_{11}D_{11}\alpha^2A_{55} - A_{11}D_{11}I_\circ\gamma\omega^2 + 2B_{11}I_1\gamma\omega^2A_{55} \\ & - I_\circ\gamma\omega^2D_{11}A_{55} + 3B_{11}^2\alpha^2A_{55} - A_{11}\gamma I_2\omega^2A_{55} + \\ & + B_{11}^2I_\circ\gamma\omega^2\,, \end{aligned}$$

$$\begin{aligned} Q_4 = {} & 2jB_{11}^2\alpha I_\circ\gamma\omega^2 - 2jI_\circ\gamma\omega^2D_{11}\alpha A_{55} + jB_{11}^2\alpha^3A_{55} \\ & + 4jB_{11}\alpha I_1\gamma\omega^2A_{55} - jA_{11}\alpha^3D_{11}A_{55} \\ & - 2jA_{11}\alpha D_{11}I_\circ\gamma\omega^2 - 2jA_{11}\alpha\gamma I_2\omega^2A_{55}\,, \end{aligned}$$

$$\begin{aligned} Q_5 = {} & -I_1^2\gamma^2\omega^4A_{55} - A_{11}A_{55}I_\circ\gamma\omega^2 + I_\circ^2\gamma^2\omega^4D_{11} \\ & + A_{11}\alpha^2D_{11}I_\circ\gamma\omega^2 - 2B_{11}\alpha^2I_1\gamma\omega^2A_{55} + I_\circ\gamma^2\omega^4I_2A_{55} \\ & + A_{11}\gamma^2I_2\omega^4I_\circ - 2B_{11}I_1\gamma^2\omega^4I_\circ + I_\circ\gamma\omega^2D_{11}\alpha^2A_{55} \\ & - B_{11}^2\alpha^2I_\circ\gamma\omega^2 + A_{11}\alpha^2\gamma I_2\omega^2A_{55}\,, \end{aligned}$$

$$Q_6 = -2jB_{11}\alpha I_1\gamma^2\omega^4 I_\circ - jI_1^2\gamma^2\omega^4 A_{55}\alpha + jA_{11}\alpha\gamma^2 I_2\omega^4 I_\circ + jI_\circ\gamma^2\omega^4 I_2 A_{55}\alpha + jI_\circ^2\gamma^2\omega^4 D_{11}\alpha - jA_{11}\alpha A_{55}I_\circ\gamma\omega^2\,,$$

$$Q_7 = -I_\circ^2\gamma^3\omega^6 I_2 + I_1^2\gamma^3\omega^6 I_\circ + I_\circ^2\gamma^2\omega^4 A_{55}\,.$$

The spectrum relation is solved using the companion matrix method described earlier. The properties of the wavenumbers and the group velocities are discussed in detail in the next section.

5.4.2 Effect of Gradation on the Spectrum and Dispersion Relation

A steel beam with the following material properties is considered: Young's modulus $E = 210$ GPa, shear modulus $G = 80.76$ GPa, Poisson's ratio $\nu = 0.3$ and density $\rho = 7800$ kg/m^3. The beam has 0.1 m width and 0.1 m thickness. The beam is considered homogeneous in the thickness direction and inhomogeneous in the longitudinal direction. The inhomogeneous parameters α and β (with $\beta = \alpha$) are varied from 0 to 30 in four steps.

Figure 5.22 shows the spectrum relation of the beam for different values of the α and β. In the figure, k_a, k_b and k_s denote the axial, bending and shear wavenumbers, respectively. The wavenumbers plotted on the negative side of the ordinate denote the imaginary part of the wavenumbers. For $\alpha = 0 = \beta$, the beam is homogeneous and the wavenumbers are exactly the solutions of the spectrum equation known previously (see [9]). This variation has been known for a long time and more on this can be found for isotropic material (see [9]), depth-wise inhomogeneous material (Section 5.2) and anisotropic material [39]. There is one property of the wavenumbers, where attention was not focused before. That is, the wavenumbers do not possess non-zero real and imaginary parts, simultaneously. However, the situation changes dramatically, when nonzero values are assigned to α (and β). As the figure suggests, with increasing magnitude of α (as indicated by the arrows), cut-off frequencies appear for all the modes. The wavenumbers simultaneously possess both nonzero real and imaginary parts, which implies attenuation of the wave magnitude while it propagates. At high frequencies, the real parts of the wavenumbers converge to their homogeneous counterpart, whereas, the imaginary parts take the value $\alpha/2$. Also it is evident that the effect of α is more pronounced in the axial mode as shown by comparatively large shifts of the axial cut-off frequency.

The dispersion relation is plotted in Figure 5.23 where axial, bending and shear modes are denoted as C_a, C_b and C_s, respectively. For a given frequency, the presence of positive group speed indicates propagation of that particular mode. As the figure suggests, for $\alpha = 0$, axial and bending modes propagate, whereas the shear mode propagates only when the frequency exceeds the cut-off frequency, before which it is non-existant. However, non-zero α (and β) introduces cut-off frequencies in axial and bending modes, which means, if

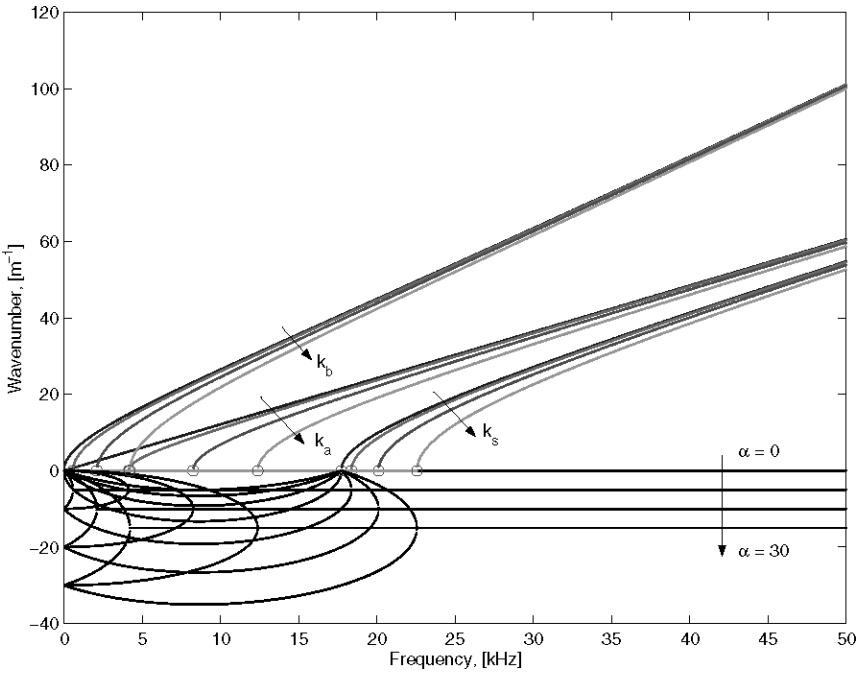

Fig. 5.22. Spectrum relation : k_a, k_b and k_s denote axial, bending and shear wavenumber, respectively (α increases in the direction of arrows and $\beta = \alpha$)

the highest frequency content of the loading is less than the lowest cut-off frequency (given by the bending mode) there will be no response in the structure, *i.e.,* gradation of materials will act as a high-pass filter.

5.4.3 Effect of Gradation on the Cut-off Frequencies

Since the propagating modes appear only when the load frequency exceeds the lowest cut-off frequency, variation of the latter with FGM parameters is important for response prediction. As opposed to the earlier relatively simple cases (FSDT and HMT), explicit forms of the cut-off frequencies cannot be obtained from the spectrum relation. This is because, in this case the cut-off frequency cannot be obtained by substituting $k = 0$ in the spectrum relation and solving for ω. To solve for the cut-off frequencies, we note that they are the frequencies where the imaginary wavenumbers take the value $-\alpha/2$. Hence, following the two steps described below, the equation governing the cut-off frequencies can be obtained. The steps are: first, substitute $k = k_r + jk_i$ in the spectrum relation and then substitute zero for k_r, thus obtaining the governing equation for the imaginary part of the wavenumbers. Next, substitute $k_i = -\alpha/2$ and arrange the equation in descending powers of ω_n. The equation can be written as

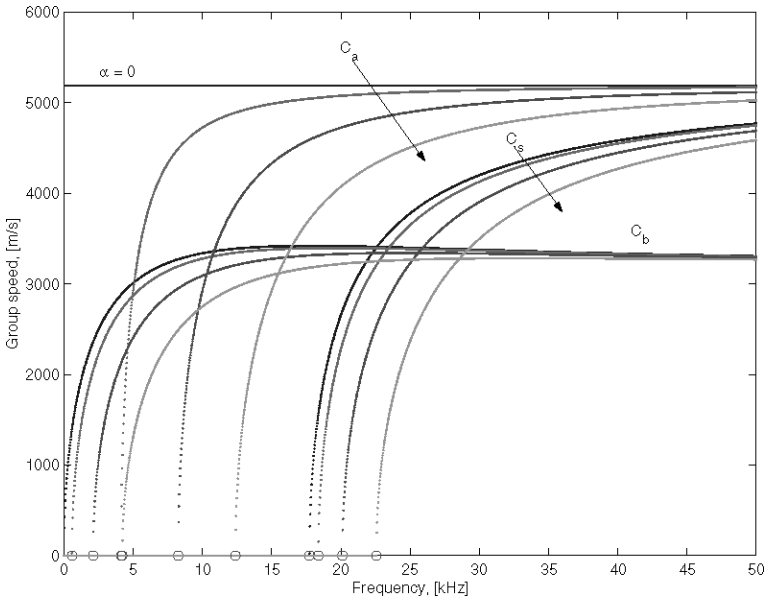

Fig. 5.23. Dispersion relation : C_a, C_b and C_s denote axial, bending and shear group speeds, respectively (α increases in the direction of arrows and $\beta = \alpha$)

$$A_1\omega_n^6 + A_2\omega_n^4 + A_3\omega_n^2 + A_4 = 0\,, \tag{5.62}$$

where the A_i are complex valued and contain material properties and α as parameters. Thus, for a fixed base material (steel in this case), the cut-off frequencies can be varied by varying α, and the required response can be obtained. In this way, mode selection for a particular load frequency as well as complete blocking is possible by tuning the inhomogeneous parameter.

To see the variation of the cut-off frequencies with α, we solve Equation (5.62), for a range of values of α and plotted in Figure 5.24. As is shown in the figure, for $\alpha = 0$, there is only one cut-off frequency (which belongs to the shear mode). For non-zero α, the axial and bending modes also have cut-off frequencies. All these frequencies vary in a non-linear fashion for low α values and at higher values they are fairly linear with α. The gradient, $\partial\omega_c/\partial\alpha$ is maximum for axial mode and gradually the axial cut-off frequency reaches the shear cut-off frequency. The bending mode cut-off frequency has the lowest value for a given α and is least affected by gradation (in terms of the gradient).

From Figure 5.24, certain conclusions can be drawn. For a given single frequency excitation, the gradation can be used to obtain the desired modal response from the structure. Let us consider a (modulated pulse) loading with a center frequency of 30 kHz. Then, for $\alpha < \alpha_1$, all the modes will participate in the response, as is shown in the figure. For $\alpha_1 < \alpha < \alpha_2$, only axial and bending modes will participate and for $\alpha_2 < \alpha < \alpha_3$, the response will be

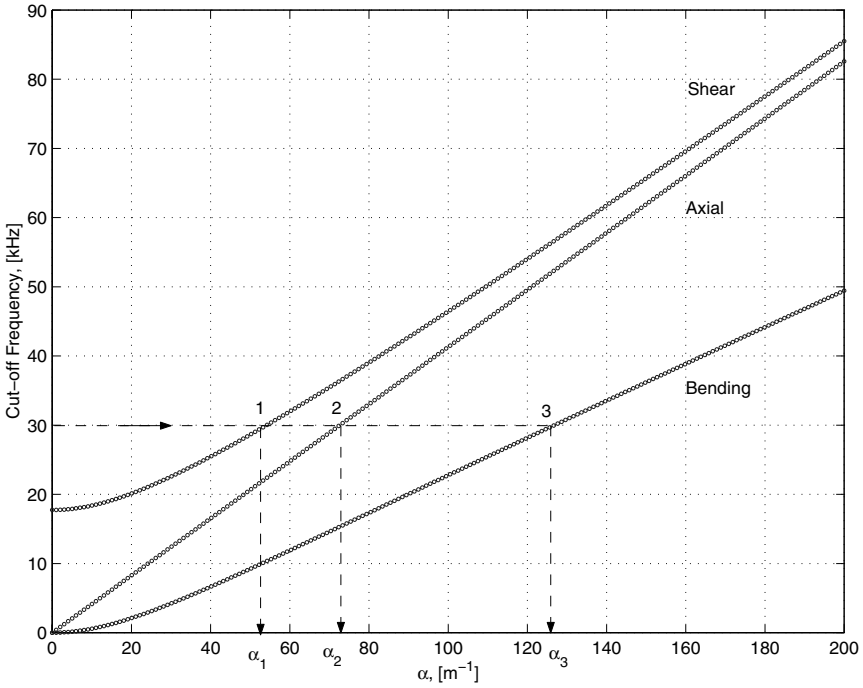

Fig. 5.24. Variation of cut-off frequencies with α ($\beta = \alpha$)

due to the bending mode only. If α is increased beyond α_3, there will be no response in the structure as all the modes are effectively blocked (damped out). Thus, gradation can be used effectively for selecting Lamb wave modes.

Once we have the spectrum relation the SFEs are formed following the same steps as outlined earlier.

5.5 Numerical Examples

In this section, numerical experiments are performed to demonstrate the effect of length-wise gradation. The effect of the inhomogeneity on the mechanical response is studied by suitably varying the inhomogeneous parameters α and β. Finally, the smoothing effect of graded material is studied by applying it to stress waves.

5.5.1 Effect of the Inhomogeneity

To study the effect of α and β, two different sets of these parameters are taken to model the inhomogeneity. In the first set, β is always equal to α and α is varied from 0.5 to 2.0 in four steps. The same cantilever beam as

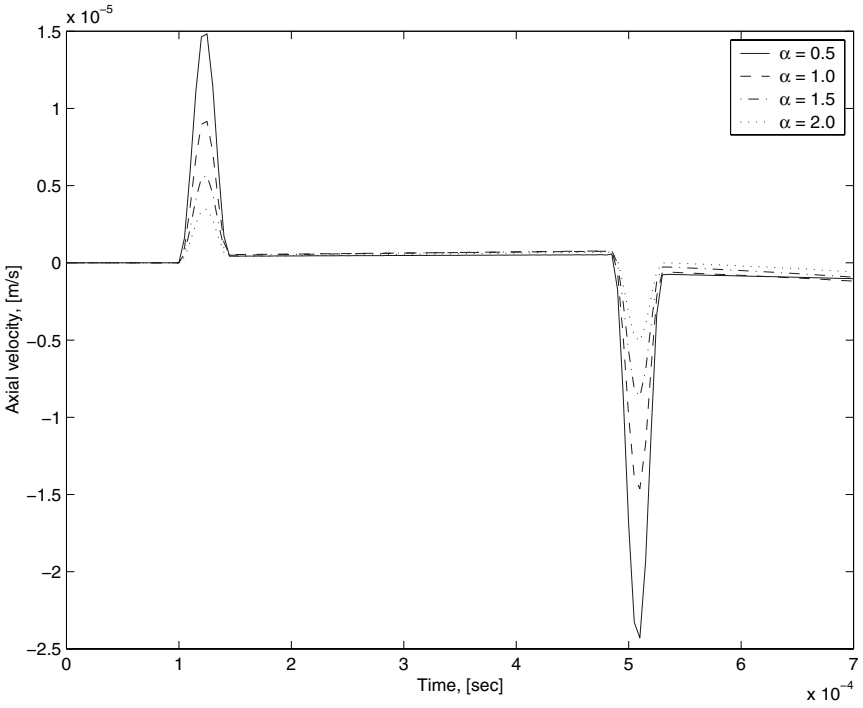

Fig. 5.25. Variation of axial velocity with α ($\beta = \alpha$)

in the previous example is also taken here along with the same axial and transverse tip loading. The axial and transverse velocities at the tip of the beam are measured and plotted in Figure. 5.25 and 5.26, respectively. Figure 5.25 shows the variation of the axial velocity for different α (hence, β) values. The figure suggests that, the incident and reflected wave amplitudes decrease with increasing α. The rate at which the velocity decreases is given by the quantity $\partial u_{max}/\partial\alpha$, which is different for different α and is computed for discrete values of the α chosen. They are -0.1135, -0.0701 and -0.0433 (all are in 10^{-04} m^2/s), for $\alpha = 1.0, 1.5$ and 2.0, respectively. Thus the effect of inhomogeneity in reducing amplitude is dominant in the initial phase and later these effects decrease. However, there is no change in the wave speed, as suggested by the same arrival time of the reflected pulse. This is because of the equal magnitude of the inhomogeneous parameters. The same features are visible in Figure 5.26, which shows the variation of the transverse velocities for different α values. Even here, the magnitude decreases with increase in α, keeping the bending wave speed constant in each case. However, the rate $\partial w_{max}/\partial\alpha$ is higher in this case given by -0.9757, -0.5950 and -0.3628 (in 10^{-04} m^2/s), for $\alpha = 1.0, 1.5$ and 2.0, respectively. Thus inhomogeneity has a

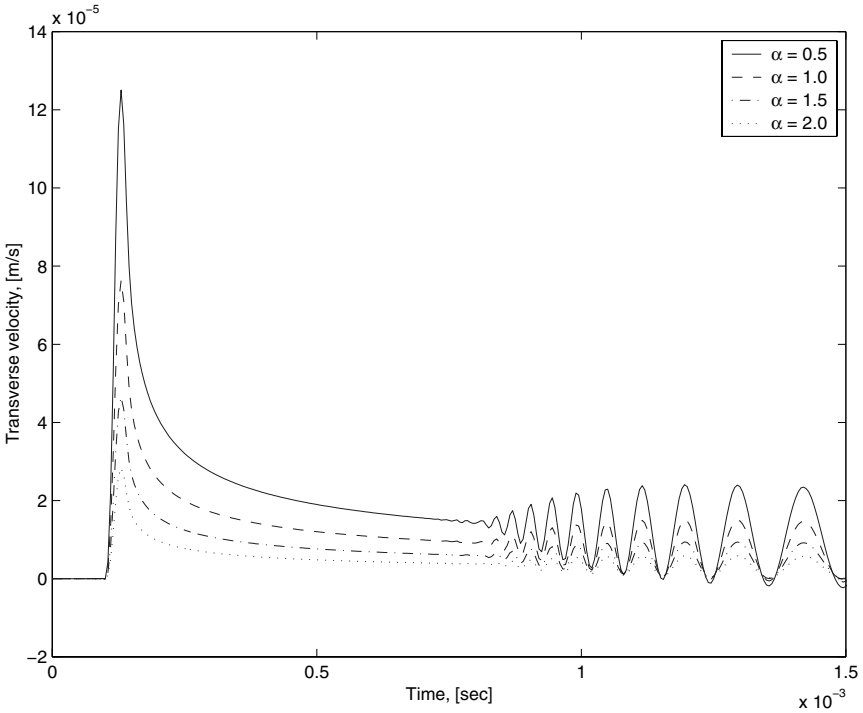

Fig. 5.26. Variation of transverse velocity with α ($\beta = \alpha$)

greater effect over the transverse velocity when it comes to the reduction of amplitude.

In the second set, α is fixed at 1.0 and β is varied from 0.9 to 1.2 in four steps. Figure 5.27 shows the variation of the axial velocities for different β values. As the figure suggests, there is no change in the magnitude of the incident pulse with varying β. However, with increasing β, both the magnitude of the reflected pulse and the axial speed decrease, as is evident in the late arrival of the reflected pulses. As α is fixed, the contribution from the modulus to the wave speed is constant.

However, with increasing β, the inertial contribution increases and hence the decrement of the wave speeds. Also, it can be concluded that the incident wave magnitude has very little bearing on the inertia of the beam, compared to the variation of the reflected wave.

In Figure 5.28, the transverse velocity histories are plotted. For clarity, they are separated into two pairs. The same traits of the axial velocity histories are also present here. There is no change in the magnitude of the incident pulse but the appearance of the reflections from the boundary is delayed with increasing β.

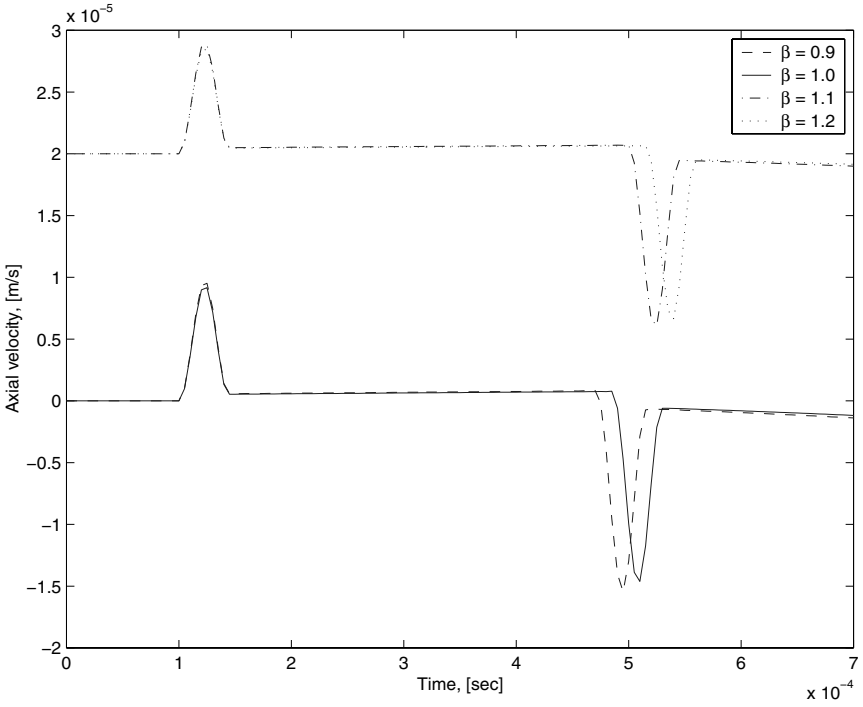

Fig. 5.27. Variation of axial velocity with β ($\alpha = 1.0$), shifted for clarity

Overall, this example shows the individual effect of the inhomogeneous parameters and the use of inhomogeneous parameters as a way of controlling the response of a structure by controlling the gradation.

5.5.2 Elimination of the Reflection from Material Boundary

As demonstrated using a rod waveguide, the advantages of using FGM are shown in this example by eliminating reflections in the stress waves originating at a bi-material interface.

In Section 5.1.2, the use of a FGM layer in eliminating reflections due to a material interface was demonstrated for a bi-material rod. We demonstrate the same here for a bi-material beam. Two cantilever beams are considered for this purpose, having the same geometry as the previous examples ($L = 1.0$ m, $b = 0.1$ m and $h = 0.1$ m). There are two different materials. One is steel and the other is aluminum, with material properties as given before. Two different material distributions in the beams are shown in Figure 5.29. In the bi-material beam, from the fixed end to the midpoint of the beam, the material is steel and the rest is aluminum. Thus the material boundary is located at the mid-point of the beam. In the second beam, half of the steel material is

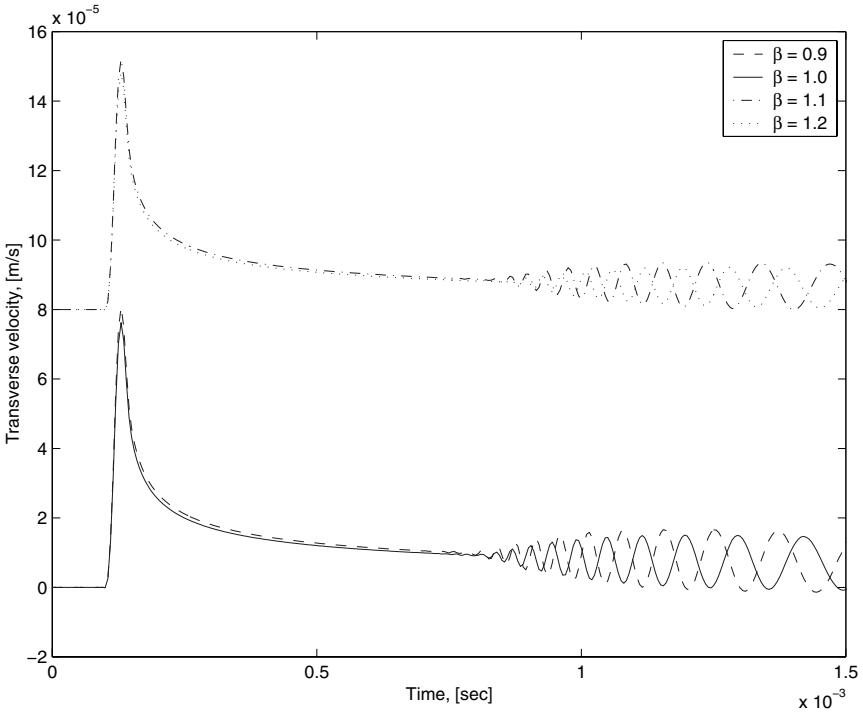

Fig. 5.28. Variation of axial velocity with β ($\alpha = 1.0$), shifted for clarity

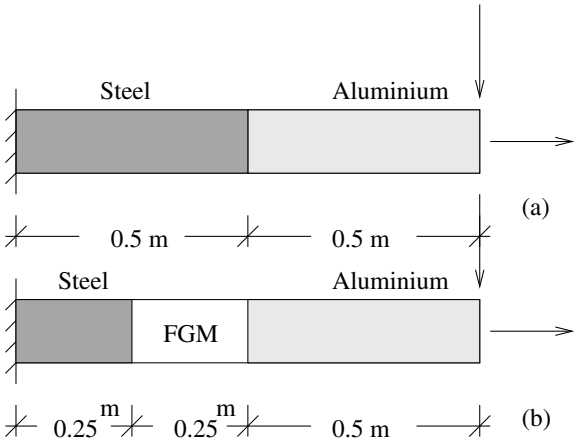

Fig. 5.29. Cantilever beam models in example 3, (a) bi-material beam, (b) bi-material beam with graded interface

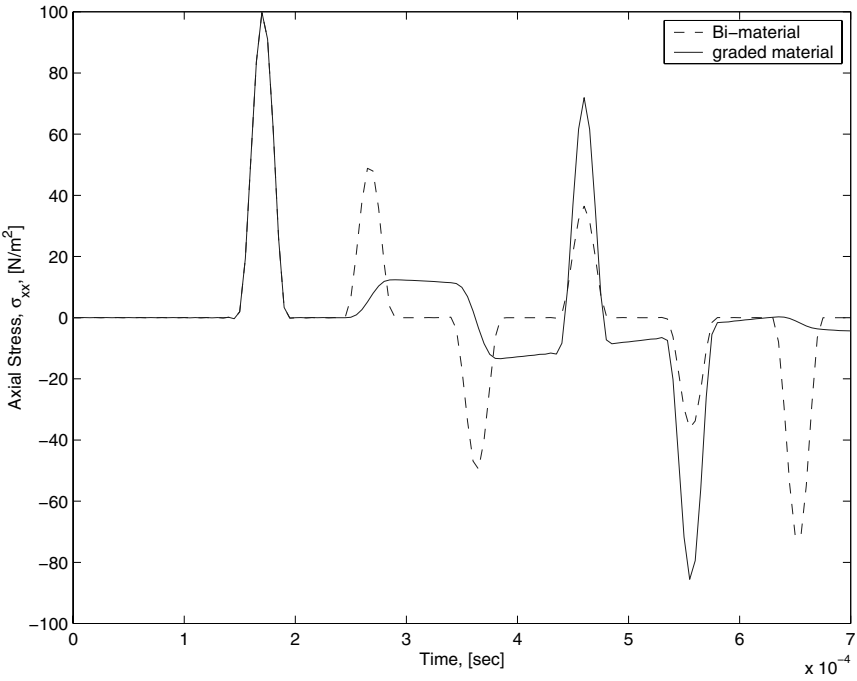

Fig. 5.30. Smoothing of axial stress

replaced by a graded material, which has steel properties at the left end and aluminum properties at the right end. Thus the inhomogeneous parameters, α and β in this case take the value of -4.3944 and -4.2435, respectively. The beams are impacted at the tip by an axial and transverse load of 1.0 N. The axial and shear stresses are measured at the mid-point of the aluminum region, *i.e.,* 0.25 m away from the free end of the beam.

Figure 5.30 shows the variation in axial stress for both beams. As is evident from the figure, the bi-material beam (in the absence of gradation) shows two extra reflections at around 250 μs and 350 μs, other than the reflection from the fixed end (at 450 μs). The magnitude of this reflected pulse is around 50% of the original incident pulse. However, the magnitude of the physical boundary reflected pulse is increased by almost 100%, which is a disadvantage incurred by the gradation. As a possible explanation, it can be stated that the energy of the suppressed waveform at the material interface is transmitted to the physical boundary and thus enhances the amplitude of the reflected pulse. However, by the elimination of the extra reflections, the structures are subjected to fewer tension–compression cycles. Figure 5.31 shows the variation in shear stress, which shows clearly the suppressed peaks from scattering at the material interfaces. In general, the stress history is reasonably smoothed in the presence of graded materials. Also, it is to be noted that in all cases,

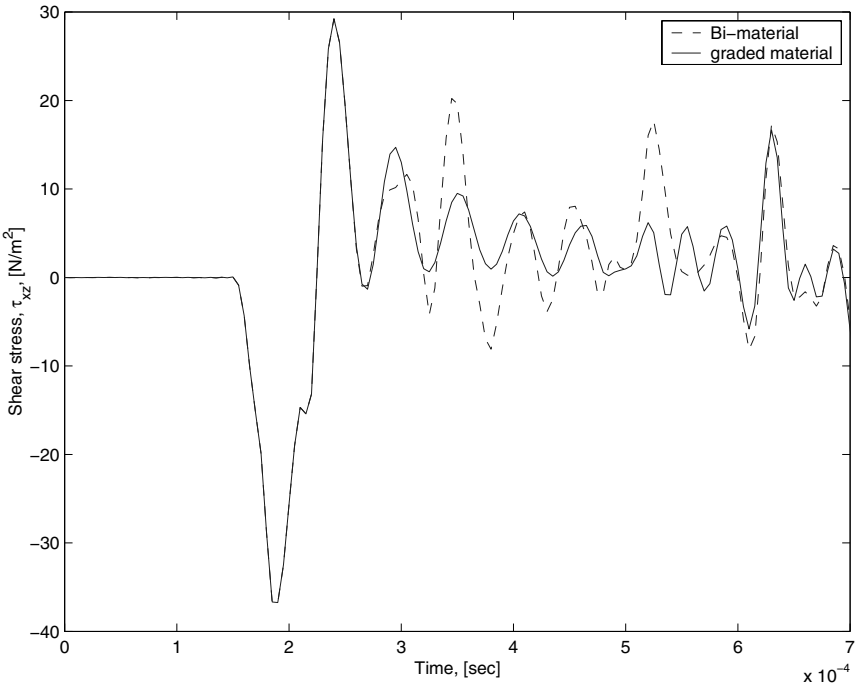

Fig. 5.31. Smoothing of shear stress

the incident waves are unchanged. This is because the gradation is effective only after the stress wave passes through the material.

So far, several SFE models have been developed for wave propagation analysis in inhomogeneous 1-D waveguides. In all higher order SFE formulations, the companion matrix method was used to compute the wavenumbers and the SVD method was used to compute the wave amplitudes. The idea of approximate SFE is introduced in the formulation of inhomogeneous rod and length-wise graded FSDT SFEs. The elements are meant for both FGM and composite materials, where the the depth-wise integrated stiffness parameters take care of the anisotropy or inhomogeneity (during integration). It has been found that the presence of a FGM layer in structures results in significant difference in the response from its parent material beams (steel and ceramic for example) due to the presence of coupled stiffness and inertial parameters. Inclusion of FGM has proven to be an effective way to smooth stress jumps in bi-material beams.

Two significant features that result from the introduction of the Poisson's contraction in the model are the extra propagating (contraction) mode and the increased dispersiveness of the axial wave. These two features were elegantly captured by the SFEs. Now, the question one needs to answer is when are the higher order effects (specially Poisson's contraction effects) significant. Two

main factors that determine the need for Poisson's contraction in the models are the load spectrum and the cut-off frequency of the contractional mode. The cut-off frequency is, in turn, dependent on the depth of the beam. The higher the depth, the lower the cut-off frequency. If the frequency band of the input signal supersedes the cut-off frequency, Poisson's contraction effect will be significant. In an attempt to quantify this idea, closed form expressions for the cut-off frequencies are given. Effect of contraction on the spectrum and the dispersion relation in comparison to the FSDT, is also shown in the study.

The length-wise graded shear flexible beam improves the modeling of inhomogeneous structures over the previously developed shear flexible SFE. In this case, the inhomogeneity is considered both in the direction of wave propagation (as considered in the rod element formulation) and normal to it. This is the most general case of inhomogeneity. It is shown that the desired response can be obtained, in particular, modes of Lamb waves can be chosen by suitably varying the gradation. Further, either the wave amplitude or the speed can be varied, alone, by fixing one parameter and varying the other. One advantage of gradation is the minimization or complete elimination of reflections from the material interfaces. This aspect is clearly demonstrated through a numerical example.

6

Wave Propagation in Two-dimensional Anisotropic Structures

Layered media are encountered in various natural (soil, wood, tissue, *etc.*) and artificial (bi-material, fibre reinforced composite, graded materials *etc.*) structural systems. Composite structural components are made up of a stack of layers (called ply or lamina) to form a laminate. These classes of materials can be both anisotropic and inhomogeneous. Further, these systems are required to resist harsh environments, such as impact load, high temperature load, *etc.* in their lifetime. Hence, analysis of these layered systems for such loading is important and requires critical attention.

The analysis of layered media is traditionally carried over in transfer matrix form where the displacements and stresses of one interface are related to the other interface by a system matrix. This matrix is assembled for more than one layer and the resulting system needs to be solved after imposing the boundary conditions. The SFEM, applied to 2-D layered media is not vastly different from the transfer matrix based method. However, the stiffness matrix form along with the exact representation of the layer makes it more efficient for modeling multiple layers and analyzing high frequency impact loading.

As discussed before, SFE for layered media was formulated using a solution obtained by the method of potentials, which is applicable only to isotropic materials. For anisotropic and inhomogeneous media, among the available methodologies, the Partial Wave Technique (PWT) is a suitable option. In this chapter, SFEs are formed using this method, where the SVD method (described in 1-D waveguide formulation) is utilized to obtain the wave amplitudes, which is essential for constructing the partial waves. In the PWT based method of Lamb wave analysis, once the partial waves are found, the wave coefficients are made to satisfy the prescribed boundary conditions, *i.e.,* two non-zero tractions specified at the top and bottom of the layer. In our case, the formulation is slightly different, as no specific problem oriented boundary conditions are imposed. Thus a system matrix is established, which relates the tractions at the interface to the interfacial displacements. This generalization enables the use of the system matrix as a finite element dynamic stiffness matrix, although formulated in the frequency/wavenumber domain.

These matrices can be assembled to model different layers of different ply-orientation or inhomogeneity, which obviates the necessity for cumbersome computation associated with multilayer analysis (*e.g.,* see [102]). The only shortcoming of the method is that each spectral layer element (SLE) can accommodate only one fiber angle, thus for different ply-stacking sequences the number of elements will be at least equal to the number of different ply-angles in the stacking.

One advantage of the present formulation is the ease in capturing the Lamb wave [23] propagation in anisotropic/inhomogeneous plate. By definition, the Lamb waves are guided waves propagating in a domain bounded by two parallel traction-free surfaces. The importance of Lamb waves in NDE applications lies in its ability to inspect large areas at a time by propagating long distances without attenuation. Hence, these waves find immense application in structural health monitoring. Historically, the dispersion relation (phase velocity frequency relation) for anisotropic materials was given first by Solie and Auld [103], where PWT were used. However, the relation was obtained for a (001)-cut copper plate. Subsequent investigations on modeling aspects of Lamb waves were carried out by several researchers [21]. Finite element modeling of Lamb waves was performed by Verdict *et al.* [104]. On the basis of discrete layer theory and a multiple integral transform an analytical-numerical approach is given by Veidt *et al.* [105]. A coupled FE-normal mode expansion method is given by Moulin *et al.*, [106]. Similarly a boundary element normal mode expansion method is given by Zhao and Rose [107]. The present formulation by virtue of a frequency wavenumber domain representation of solution is an inexpensive way of constructing the Lamb wave modes as well as predicting time domain signals.

6.1 Two-dimensional Initial Boundary Value Problem

It is assumed that there is no heat conduction in and out of the system, the displacements are small, material is homogeneous and anisotropic and the domain is 2-D Euclidean space. The general elastodynamic equation of motion for 3-D is given by

$$\sigma_{ij,j} = \rho(x_1, x_2, x_3)\ddot{u}_i\,, \quad \sigma_{ij} = C_{ijkl}(x_1, x_2, x_3)\epsilon_{kl}\,, \quad \epsilon_{ij} = (u_{i,j} + u_{j,i})/2\,, \tag{6.1}$$

where comma (,) and dot ($\dot{}$) denote partial differentiation with respect to the spatial variables and time, respectively.

For a 2-D model with orthotropic material construction, the complexity of the above equation can be further reduced by the following assumptions. The non-zero displacements are $u_1 = u$ and $u_3 = w$ in the direction $x_1 = x$ and $x_3 = z$, respectively (see Figure 6.1). Then the non-zero strains are related to these displacements by

$$\epsilon_{xx} = u_x\,, \quad \epsilon_{zz} = w_z\,, \quad \epsilon_{xz} = u_z + w_x\,. \tag{6.2}$$

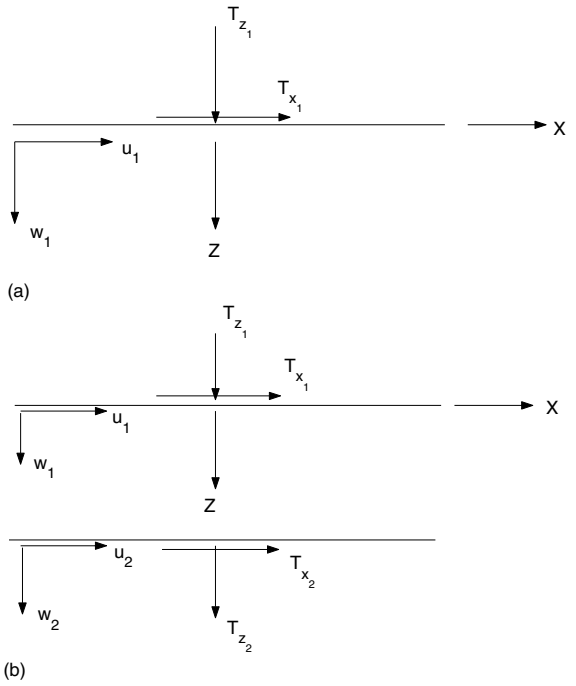

Fig. 6.1. Sign conventions of (a) throw-off spectral element (b) layer element

The non-zero stresses are then related to the strains by the relation

$$\sigma_{xx} = Q_{11}\epsilon_{xx} + Q_{13}\epsilon_{zz}\,,\ \sigma_{zz} = Q_{13}\epsilon_{xx} + Q_{33}\epsilon_{zz}\,,\ \sigma_{xz} = Q_{55}\epsilon_{xz}\,, \tag{6.3}$$

where Q_{ij} are the stiffness coefficients, which depend on the ply layup, its orientation and the z coordinate of the layer. Substituting Equation (6.3) in Equation (6.1) and imposing the assumptions, the elastodynamic equation for 2-D homogeneous orthotropic media is given by

$$\begin{aligned} Q_{11}u_{xx} + (Q_{13} + Q_{55})w_{xz} + Q_{55}u_{zz} &= \rho\ddot{u}\,, \\ Q_{55}w_{xx} + (Q_{13} + Q_{55})u_{xz} + Q_{33}w_{zz} &= \rho\ddot{w}\,. \end{aligned} \tag{6.4}$$

As mentioned in Chapter 3, here, we will attempt to reduce the governing PDEs to a set of ODEs. For this, we need to remove two variables from the system and introduce two new parameters instead. To achieve this, we will take the Fourier transform in time and the Fourier series in space. With this assumption, the spectral form of the displacement field becomes

$$u(x,z,t) = \sum_{n=1}^{N-1}\sum_{m=1}^{M-1} \hat{u}(z,\eta_m,\omega_n) \left\{ \begin{matrix} \sin(\eta_m x) \\ \cos(\eta_m x) \end{matrix} \right\} e^{-j\omega_n t}\,, \tag{6.5}$$

$$w(x,z,t) = \sum_{n=1}^{N-1} \sum_{m=1}^{M-1} \hat{w}(z,\eta_m,\omega_n) \left\{ \begin{matrix} \cos(\eta_m x) \\ \sin(\eta_m x) \end{matrix} \right\} e^{-j\omega_n t}\,, \tag{6.6}$$

where ω_n is the discrete angular frequency and η_m is the discrete horizontal wavenumber. As the assumed field suggests, for $M \to \infty$, the model will have infinite extent in the positive and negative X direction, although the domain is finite in the Z direction, *i.e.,* it will be a layered structure. In particular, the domain can be written as $\Omega = [-\infty, +\infty] \times [0, L]$, where L is the thickness of the layer. The boundaries of any layer will be specified by a fixed value of z. The X dependency of the displacement field (sine or cosine) will be determined based upon the loading pattern. In all subsequent formulation and computation, a symmetric load pattern will be considered, *i.e.,* $\sin(\eta_m x)$ for u and $\cos(\eta_m x)$ for w. The real computational domain is $\Omega_c = [-X_L/2, +X_L/2] \times [0, L]$, where X_L is the X window length. Discrete values of η_m depend upon X_L and the number of mode shapes (M) chosen.

This displacement field reduces the governing equations to a set of ODEs

$$\mathbf{A}\hat{\mathbf{u}}'' + \mathbf{B}\hat{\mathbf{u}}' + \mathbf{C}\hat{\mathbf{u}} = \mathbf{0}\,, \quad \hat{\mathbf{u}} = \{\hat{u}\ \hat{w}\}\,, \tag{6.7}$$

where prime denotes differentiation with respect to z. The matrices $\mathbf{A}$, $\mathbf{B}$ and $\mathbf{C}$ are

$$\mathbf{A} = \begin{bmatrix} Q_{55} & 0 \\ 0 & Q_{33} \end{bmatrix}, \mathbf{B} = \begin{bmatrix} 0 & -(Q_{13}+Q_{55})\eta_m \\ (Q_{13}+Q_{55})\eta_m & 0 \end{bmatrix}, \tag{6.8}$$

$$\mathbf{C} = \begin{bmatrix} -\eta_m^2 Q_{11} + \rho\omega_n^2 & 0 \\ 0 & -\eta_m^2 Q_{55} + \rho\omega_n^2 \end{bmatrix}. \tag{6.9}$$

The associated boundary conditions are the specifications of the stresses σ_{zz} and σ_{xz} at the layer interfaces. From Equation (6.3), the stresses are related to the unknowns by

$$\hat{\mathbf{s}} = \mathbf{D}\hat{\mathbf{u}}' + \mathbf{E}\hat{\mathbf{u}}\,, \hat{\mathbf{s}} = \{\sigma_{zz}\ \sigma_{xz}\}\,, \quad \mathbf{D} = \begin{bmatrix} 0 & Q_{33} \\ Q_{55} & 0 \end{bmatrix}, \quad \mathbf{E} = \begin{bmatrix} \eta_m Q_{13} & 0 \\ 0 & -\eta_m Q_{55} \end{bmatrix}. \tag{6.10}$$

The original boundary value problem (BVP) reduces to finding $\hat{\mathbf{u}}$, which satisfies Equation (6.7) for all $z \in \Omega_c$, and the specification of $\hat{\mathbf{u}}$ or $\hat{\mathbf{s}}$ at $z = 0$ or $z = L$. Once the solution is obtained for different values of z in the frequency-wavenumber domain ($Z - \eta - \omega$ domain, for given values of ω_n and η_m), the summation over η_m will bring the solution back to the $Z - X - \omega$ domain and the inverse FFT will bring the solution back to time domain, *i.e., $Z - X - t$* domain.

The solutions to these ODEs are of the form $u_\circ e^{-jkz}$ and $w_\circ e^{-jkz}$, which yields the PEP

$$\mathbf{W}\{\mathbf{u}_\circ\} = \mathbf{0}\ \,, \mathbf{W} = -k^2\mathbf{A} - jk\mathbf{B} + \mathbf{C}\,, \{\mathbf{u}_\circ\} = \{u_\circ\ w_\circ\}\,, \tag{6.11}$$

where $\mathbf{W}$ is the wave matrix given by

$$\mathbf{W} = \begin{bmatrix} -k^2 Q_{55} - \eta_m^2 Q_{11} + \rho\omega_n^2 & jk\eta_m(Q_{13} + Q_{55}) \\ -jk\eta_m(Q_{13} + Q_{55}) & -k^2 Q_{33} - \eta_m^2 Q_{55} + \rho\omega_n^2 \end{bmatrix} . \tag{6.12}$$

The singularity condition of $\mathbf{W}$ yields the following equation for determining the spectrum relation

$$\begin{aligned} Q_{33}Q_{55}k^4 + \{(Q_{11}Q_{33} - 2Q_{13}Q_{55} - Q_{13}^2)\eta_m^2 - \rho\omega_n^2(Q_{33} + Q_{55})\}k^2 \\ + \{Q_{11}Q_{55}\eta_m^4 - \rho\omega_n^2\eta_m^2(Q_{11} + Q_{55}) + \rho^2\omega_n^4\} = 0 . \end{aligned} \tag{6.13}$$

It is to be noted that for each value of η_m and ω_n, there are four values of k, denoted by $k_{lmn}, l = 1, \ldots, 4$, which will be obtained by solving Equation (6.13). Explicit solution of the wavenumber k is $k_{lnm} = \pm\sqrt{-b \pm \sqrt{b^2 - 4ac}}$, where a, b and c are the coefficients of k^4, k^2 and k^0, respectively, in Equation (6.13).

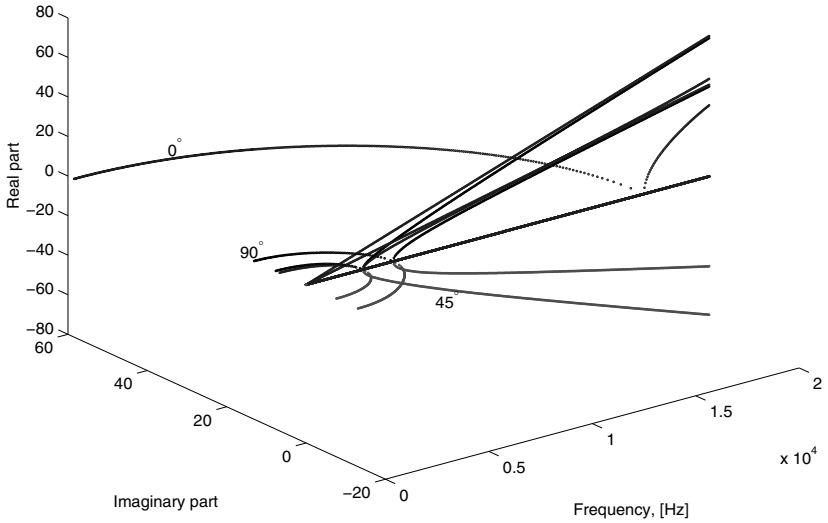

Fig. 6.2. Variation of wavenumber with ω_n ($\eta_m = 10$)

There are certain properties of the wavenumbers which will be explored now. As can be seen from Equation 6.13, for $\eta_m = 0$, the equation is readily solvable to give the roots $\pm\omega\sqrt{\rho/Q_{33}}$ and $\pm\omega\sqrt{\rho/Q_{55}}$. Since none of the ρ, Q_{33} or Q_{55} can be negative or zero, these roots are always real and linear with ω. When η_m is not zero, k becomes zero for ω satisfying

$$\begin{aligned} Q_{11}Q_{55}\eta_m^4 - \rho\omega_n^2\eta_m^2(Q_{11} + Q_{55}) + \rho^2\omega_n^4 = 0 \\ i.e., \quad (Q_{11}\eta_m^2 - \rho\omega^2)(Q_{55}\eta_m^2 - \rho\omega^2) = 0 \\ i.e., \quad \omega = \eta_m\sqrt{Q_{11}/\rho}\,, \quad \eta_m\sqrt{Q_{55}/\rho}\,, \end{aligned} \tag{6.14}$$

which are the cut-off frequencies. For frequencies lower than the cut-off frequencies, the roots are imaginary and non-propagating and above these frequencies, the roots are real and propagating. For isotropic materials the cut-off frequencies are given by $c_p\eta$ and $c_s\eta$ [108]. The current expressions for the cut-off frequencies are also reducible to that of isotropic materials if we identify Q_{11} and Q_{55} with $\lambda + 2\mu$ and μ, respectively, where λ and μ are the Lame parameters. If we identify the QP wave with Q_{33} (or Q_{11}) and the QSV wave with Q_{55}, then as the cut-off frequencies suggest, for the same value of η_m, it is the QSV wave that becomes propagating first, since $Q_{11} > Q_{55}$. In Figure 6.2, the wavenumbers are plotted for three different ply-angles, 0°, 45° and 90°. For all the ply-angles, Q_{33} and Q_{55} are assumed 9.69 GPa and 4.13 GPa, respectively. For Q_{11} and Q_{13}, the following values are assumed. For 0°, $Q_{11} = 146.3$ GPa and $Q_{13} = 2.98$ GPa, for 45°, $Q_{11} = 44.62$ GPa and $Q_{13} = 1.62$ GPa and for 90°, $Q_{11} = 9.69$ GPa and $Q_{13} = 2.54$ GPa. In Figure 6.2, the imaginary part of the wavenumbers is plotted in the horizontal plane and the real part in the vertical plane. Further, the imaginary part of the wavenumbers for 0° and 90° are plotted in the positive side, whereas for 45° it is plotted in the negative side, for distinction. Two different η_m values are considered. The linear variation of the real part of the wavenumbers are for $\eta_m = 0$ and rest of the plots are for $\eta_m = 10$. As discussed previously, the slope of the linear portion depends upon Q_{33} and Q_{55} and as they are equal for all ply-angles, this part is common for all ply-angles. The difference comes in the imaginary part and the cut-off frequencies. Two different cut-off frequencies are seen in the figure for each ply-angle, where the largest value is for 0° ply-angle because of the large Q_{11} value. Further, the shear cut-off frequency is the same for all ply-angles as Q_{55} is equal in all the cases.

Once, the required wavenumbers k are obtained, for which the wave matrix $\mathbf{W}$ is singular, the solution $\mathbf{u}_\circ$ at frequency ω_n and wavenumber η_m is

$$u_{nm} = R_{11}C_1e^{-jk_1x} + R_{12}C_2e^{-jk_2x} + R_{13}C_3e^{-jk_3x} + R_{14}C_4e^{-jk_4x}\,, \quad (6.15)$$

$$w_{nm} = R_{21}C_1e^{-jk_1x} + R_{22}C_2e^{-jk_2x} + R_{23}C_3e^{-jk_3x} + R_{24}C_4e^{-jk_4x}\,, \quad (6.16)$$

where R_{ij} are the amplitude coefficients to be determined and are called wave amplitudes. As outlined before, following the method of SVD, R_{ij} are obtained from the wave matrix $\mathbf{W}$ evaluated at wavenumber k_i.

6.2 Spectral Element for Doubly Bounded Media

Once the four wavenumbers and wave amplitudes are known, the four partial waves can be constructed and the displacement field can be written as a linear combination of the partial waves. Each partial wave is given by

$$\mathbf{a}_i = \left\{ \begin{array}{c} u_i \\ w_i \end{array} \right\} = \left\{ \begin{array}{c} R_{1i} \\ R_{2i} \end{array} \right\} e^{-jk_iz} \left\{ \begin{array}{c} \sin(\eta_m x) \\ \cos(\eta_m x) \end{array} \right\} e^{-j\omega_n t}\,, \quad i = 1 \ldots 4\,, \quad (6.17)$$

and the total solution is

$$\mathbf{u} = \sum_{i=1}^{4} C_i \mathbf{a}_i \,. \tag{6.18}$$

6.2.1 Finite Layer Element (FLE)

Once the solutions of u and w are obtained in the form of Equations (6.15) and (6.16) for each value of ω_n and η_m, the same procedure as outlined in the 1-D element formulation is employed to obtain the element dynamic stiffness matrix at ω_n and η_m. Thus, the nodal displacements are related to the unknown constants by

$$\{u_{1nm}\ v_{1nm}\ u_{2nm}\ v_{2nm}\}^T = [\mathbf{T}_{1nm}]\{C_1\ \ C_2\ \ C_3\ \ C_4\}^T \,, \tag{6.19}$$

i.e.,

$$\{\hat{\mathbf{u}}\}_{nm} = [\mathbf{T}_1]_{nm}\{\mathbf{C}\}_{nm} \,. \tag{6.20}$$

Using Equation (6.10), nodal tractions are related to the constants by

$$\{\hat{\mathbf{t}}\}_{nm} = [\mathbf{T}_2]_{nm}\{\mathbf{C}\}_{nm} \,, \quad \{\hat{\mathbf{t}}\}_{nm} = \{\sigma_{zz1}\,, \sigma_{xz1}\,, \sigma_{zz2}\,, \sigma_{xz2}\} \,, \tag{6.21}$$

where inhomogeneity of the material is utilized while evaluating the tractions at the nodes.

Explicit forms of $\mathbf{T}_{2nm}$ and $\mathbf{T}_{1nm}$ are

$$\mathbf{T}_1 = \begin{bmatrix} R_{11} & R_{12} & R_{13} & R_{14} \\ R_{21} & R_{22} & R_{23} & R_{24} \\ R_{11}e^{(-jk_1L)} & R_{12}e^{(-jk_2L)} & R_{13}e^{(+jk_1L)} & R_{14}e^{(+jk_2L)} \\ R_{21}e^{(-jk_1L)} & R_{22}e^{(-jk_2L)} & R_{23}e^{(+jk_1L)} & R_{24}e^{(+jk_2L)} \end{bmatrix} \,, \tag{6.22}$$

$$\begin{aligned} T_2(1,p) &= -Q_{55}(-jR_{1p}k_p - \eta R_{2p}) \,, \\ T_2(2,p) &= jQ_{33}R_{2p}k_p - Q_{13}\eta R_{1p} \,, \\ T_2(3,p) &= Q_{55}(-jR_{1p}k_p - \eta R_{2p})e^{(-jk_pL)} \\ T_2(4,p) &= \{-jQ_{33}R_{2p}k_p + Q_{13}\eta R_{1p}\}e^{(-jk_pL)} \,, \end{aligned}$$

where p ranges from 1 to 4.

Thus, the dynamic stiffness matrix becomes

$$[\hat{\mathbf{K}}]_{nm} = [\mathbf{T}_2]_{nm}[\mathbf{T}_1]^{-1}_{nm} \,, \tag{6.23}$$

which is of size 4×4 having ω_n and η_m as parameters. This matrix represents the dynamics of an entire layer of any length L at frequency ω_n and horizontal wavenumber η_m. Consequently, this small matrix acts as a substitute for the global stiffness matrix of FE modeling, whose size, depending upon the thickness of the layer, will be many orders larger than the SLE size.

6.2.2 Infinite Layer Element (ILE)

This is the 2-D counter part of the 1-D throw-off element. The element is formulated by considering only the forward moving components, which means no reflection will come back from the boundary. This element acts as a conduit to throw away energy from the system and is very effective in modeling the infinite domain in the Z direction. This element is also used to impose absorbing boundary conditions or to introduce maximum damping in the structure. The element has only one edge where the displacements are to be measured and tractions are to be specified. The displacement field for this element (at ω_n and η_m) is

$$u_{nm} = R_{11}C_{1nm}e^{-jk_1z} + R_{12}C_{2nm}e^{-jk_2z}\,, \tag{6.24}$$

$$w_{nm} = R_{21}C_{1nm}e^{-jk_1z} + R_{22}C_{2nm}e^{-jk_2z}\,, \tag{6.25}$$

where it is assumed that k_1 and k_2 have positive real parts. Following the same procedure as before, displacement at node 1 can be related to the constants $C_i, i = 1, 2$ as

$$\{\hat{\mathbf{u}}\}_{nm} = [\mathbf{T}_1]_{nm}\{\mathbf{C}\}_{nm}\,. \tag{6.26}$$

Similarly, tractions at node 1 can be related to the constants as

$$\{t_{x1}\ t_{y1}\}^T_{nm} = [\mathbf{T}_2]_{nm}\{C_{1nm}\ C_{2nm}\}^T\,, \quad i.e., \quad \{\hat{\mathbf{t}}\}_{nm} = [\mathbf{T}_2]_{nm}\{\mathbf{C}\}_{nm}\,. \tag{6.27}$$

Explicit forms of the matrix $\mathbf{T}_1$ and $\mathbf{T}_2$ are

$$\mathbf{T}_{1(ILE)} = \mathbf{T}_{1(FLE)}(1:2, 1:2)\,, \quad \mathbf{T}_{2(ILE)} = \mathbf{T}_{2(FLE)}(1:2, 1:2)\,. \tag{6.28}$$

The dynamic stiffness for the homogeneous infinite half space becomes

$$[\hat{\mathbf{K}}]_{nm} = [\mathbf{T}_2]_{nm}[\mathbf{T}_1]^{-1}_{nm}\,, \tag{6.29}$$

which is a 2×2 complex matrix.

6.2.3 Expressions for Stresses and Strains

From the displacement field (Equations (6.15) and (6.16)), the strain–displacement and stress–strain relations, the matrix of strain nodal displacement relation and the stress nodal displacement relation can be established as

$$\epsilon = \mathbf{B}{\mathbf{T}_1}^{-1}\hat{\mathbf{u}}\,, \quad \sigma = \mathbf{Q}\mathbf{B}{\mathbf{T}_1}^{-1}\hat{\mathbf{u}}\,, \epsilon = \{\epsilon_{xx}, \epsilon_{zz}, \epsilon_{xz}\}\,, \sigma = \{\sigma_{xx}, \sigma_{zz}, \sigma_{xz}\}\,, \tag{6.30}$$

where the elements of $\mathbf{B}$ (size $3\times$ 4) are described in terms of the wave amplitude matrix $\mathbf{R}$ as

$$\begin{aligned} B(1,p) &= R_{1p}\eta e^{-jk_pz}\,, \quad B(2,p) = -jR_{2p}k_pe^{-jk_pz}\,, \\ B(3,p) &= -(jR_{1p}k_p + R_{2p}\eta)e^{-jk_pz}\,, p = 1, \ldots, 4\,. \end{aligned} \tag{6.31}$$

Here z is the point of strain measurement. The elasticity matrix $\mathbf{Q}$ is

$$\mathbf{Q} = \begin{bmatrix} Q_{11} & Q_{13} & 0 \\ Q_{13} & Q_{33} & 0 \\ 0 & 0 & Q_{55} \end{bmatrix} . \tag{6.32}$$

6.2.4 Prescription of Boundary Conditions

Essential boundary conditions are prescribed in the usual way as is done in FE methods, where the nodal displacements are arrested or released depending upon the nature of the boundary conditions. The applied tractions are prescribed at the nodes. It is assumed that the loading function (for symmetric loading) can be written as

$$F(x,z,t) = \delta(z - z_j) \left(\sum_{m=1}^{M} a_m cos(\eta_m x) \right) \left(\sum_{n=0}^{N-1} \hat{f}_n e^{(-j\omega_n t)} \right) , \tag{6.33}$$

where δ denotes the Dirac delta function, z_j is the Z coordinate of the point where the load is applied and the z dependency is fixed by suitably choosing the node where the load is prescribed. No variation of load along the Z direction is allowed in this analysis. $\hat{f}_n$ are the Fourier transform coefficients of the time dependent part of the load, which are computed by FFT, and a_m are the Fourier series coefficients of the x dependent part of the load.

There are two summations involved in the solution and two associated windows, one in time T and the other in space X_L. The discrete frequencies ω_n and the discrete horizontal wavenumber η_m are related to these windows by the number of data points N and M chosen in each summation, *i.e.,*

$$\omega_n = 2n\pi/T = 2n\pi/(N\Delta t) , \quad \eta_m = 2(m-1)\pi/X_L = 2(m-1)\pi/(M\Delta x) , \tag{6.34}$$

where Δt and Δx are the temporal and spatial sample rate, respectively.

6.2.5 Determination of Lamb Wave Modes

As defined earlier, the Lamb waves are guided waves (see Figure 6.3), propagating in a free plate and the two lateral guiding surfaces are traction free. There are two main approaches to the analysis of Lamb waves. The first one is the method of potentials. In this method, Helmholtz decomposition of the displacement field is obtained and the governing equations are uncoupled and written in terms of the potentials. Solutions are sought for these potentials, which contain four arbitrary constants. The displacement field and the stresses are expressed in terms of the potentials and the imposition of traction-free upper and lower surfaces generates the necessary condition for finding the unknown constants and the dispersion equation (see [102]). The advantage of this method is that the symmetric and anti-symmetric modes can be isolated

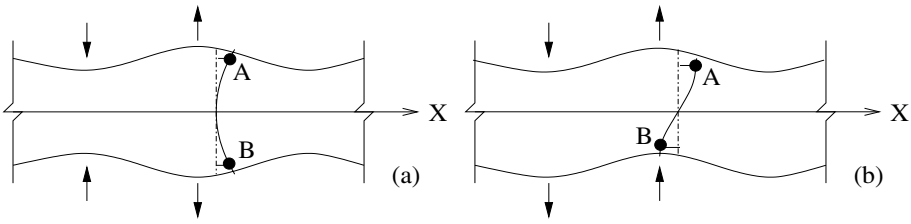

Fig. 6.3. (a) Symmetric Lamb wave propagation; (b) anti-symmetric Lamb wave propagation

during formulation (see Figure 6.3(a),(b)). However, the method is applicable only to the isotropic waveguides.

The second approach is based on the PWT, which is discussed below in detail. In the SLE formulation, there are two summations in the solutions. The outer one is over the discrete frequencies and the inner one is over the discrete horizontal wavenumbers. Each partial wave of Equation (6.18) satisfies the governing PDEs (Equation (6.4)) and the coefficients C_i as a whole satisfy any prescribed boundary conditions. As long as the prescribed natural boundary conditions are non-homogeneous, no restriction upon the horizontal wavenumber η is imposed and that leads to a double summation solution of the displacement field. However, that is not the case for traction-free boundary conditions on the two surfaces, which are the necessary condition for generating Lamb waves. The governing discrete equation for a finite layer (Equation (6.23)) in this case becomes

$$[\hat{\mathbf{K}}(\eta_m, \omega_n)]_{nm}\{\hat{\mathbf{u}}\}_{nm} = 0\,, \tag{6.35}$$

and we are interested in a non-trivial $\mathbf{u}$. Hence, the stiffness matrix $\hat{\mathbf{K}}$ must be singular, *i.e.,* $det(\hat{\mathbf{K}}(\eta_m, \omega_n)) = 0$, which gives the required relation between η_m and ω_n. Since, ω_n is made to vary independently, the above relation must be solved for η_m to render the stiffness matrix singular, *i.e.,* η_m cannot vary independently. More precisely, for each value of ω_n there is a set of values of horizontal wavenumber η_m (one for each mode) and for each value of ω_n and η_m there are four vertical wavenumbers k_{nm}. The difference in this case is in the value of η_m, which is to be solved for, as opposed to its expression in Equation (6.34) and M is the number of Lamb modes considered rather than Fourier modes. Now, for each set of $(\omega_n, \eta_m, k_{nml}), l = 1, \ldots, 4$, $\hat{\mathbf{K}}$ will be singular and $C_l, l = 1, \ldots, 4$ will be in the null space of $\hat{\mathbf{K}}$. Now using Equation (6.18), the total solution can be constructed. Following normal practice, the traction-free boundary conditions (*i.e.,* $\sigma_{zz}, \sigma_{xz} = 0$) are prescribed at $z = \mp h/2$. Using Equation (6.30), the governing equation for C_i and η_m becomes

$$[\mathbf{W}_2(\eta_m, \omega_n)]\{\mathbf{C}\}_{nm} = \mathbf{0}\,, \mathbf{C} = \{C_1, C_2, C_3, C_4\}\,, \tag{6.36}$$

where $\mathbf{W}_2$ is another form of the stiffness matrix $\hat{\mathbf{K}}$ and is given by

$$W_2(1,p) = (Q_{11\circ}R(1,p)\eta - jQ_{13\circ}R(2,p)k_p)e^{jk_ph/2}\,,$$
$$W_2(2,p) = (Q_{11\circ}R(1,p)\eta - jQ_{13\circ}R(2,p)k_p)e^{-jk_ph/2}\,,$$
$$W_2(3,p) = Q_{55\circ}(-R(1,p)k_p + jR(2,p)\eta)e^{jk_ph/2}\,,$$
$$W_2(4,p) = Q_{55\circ}(-R(1,p)k_p + jR(2,p)\eta)e^{-jk_ph/2}\,.$$

The dispersion relation is $det\{\mathbf{W}_2\} = 0$, which will yield $\eta_m(\omega_n)$ and the phase speed for Lamb waves c_{nm} will be given by ω_n/η_m. Once the values of η_m are known for the desired number of modes, the elements of $\mathbf{C}_{nm}$ are obtained by the technique of SVD as described earlier to find the elements of $\mathbf{R}$. Summing over all the Lamb modes, the solution for each frequency is obtained.

6.3 Numerical Examples

The developed spectral element is validated first to establish its accuracy and efficiency with respect to conventional 2-D FE solutions. Subsequently, propagation of lamb waves through layered media is studied for different ply-angles.

6.3.1 Propagation of Surface and Interface Waves

Wave propagation in an asymmetrically stacked composite layer is studied in this section and the results are compared with 2-D FE solutions. The material used is GFRP composite whose material properties were defined earlier. The ply-sequence considered is $[0^\circ_{10}/90^\circ_{10}/0^\circ_{10}]$, where each lamina is 0.01 m thick. This large thickness is chosen to differentiate between the incident and the reflected pulse, although any layer thickness can be chosen. The layered system is impacted by a high frequency loading, as shown in Figure 6.4, where the bottom of the layer is fixed. The time history of the high frequency load along with its spectrum is shown in Figure 5.3.

The load is applied at the center of the top layer first in the Z direction, which generates primarily QP waves, and then in the X direction, which generates primarily QSV waves. The response of the structure is measured at several locations along the surface and interfaces. For FE analysis, the layer is modeled with 3600, three-noded plane-strain FEs. In comparison, there are only three FLEs in the spectral model. The FE model results in a global system matrix of size 3656×126, whereas, the spectral model results in a global system matrix (dynamic stiffness matrix) of size 6×6. While solving via FE analysis, Newmark's time integration is adopted with a time increment of 1 μs. For the spectral analysis, the load is sampled at 48.83 Hz with 2048 (N in Equation (6.33)) FFT points. Further, for the spatial variation, 32 Fourier series coefficients (M in Equation (6.33)) are considered. For the concentrated load, all the a_m are equal to $2/X_L$, where X_L is the window length in the X

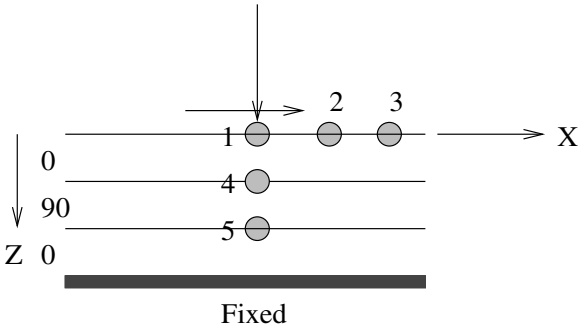

Fig. 6.4. Layer model for verification

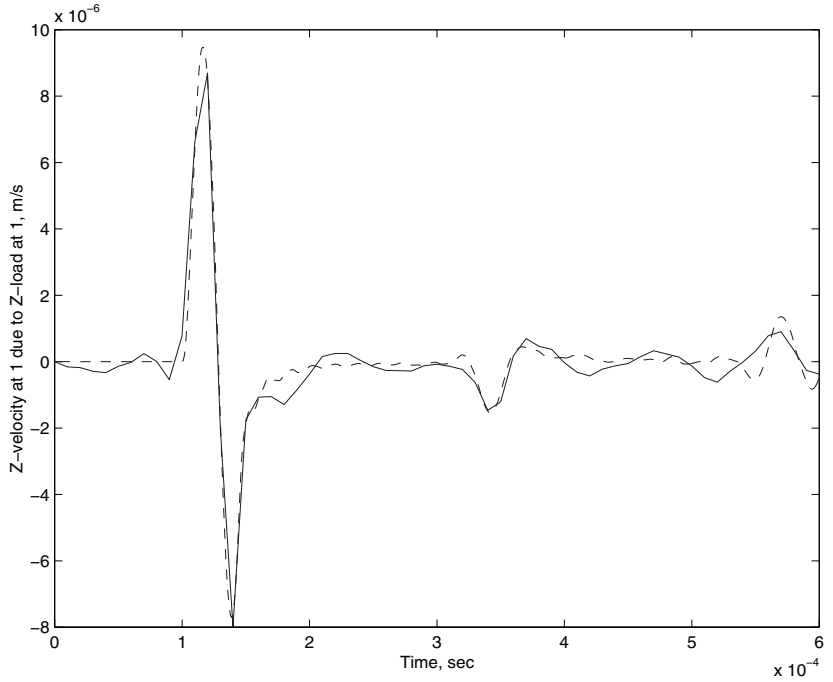

Fig. 6.5. QP wave at the surface (point 1); solid line SE, dashed line 2-D FE

direction, here taken as 1.0 m, as per the FE model. Since, the time domain response is real, the computation of displacements (or velocities) needs to be carried out only upto the Nyquist frequency. Hence, the global stiffness matrix needs to be inverted 1024×32 times. This computational requirement is many orders smaller than the requirement of the FE analysis. Further, a typical simulation in FE takes 110 s of CPU time, whereas, a SE run takes 14 s on a Compaq Alpha Server ES40 with DEC compiler.

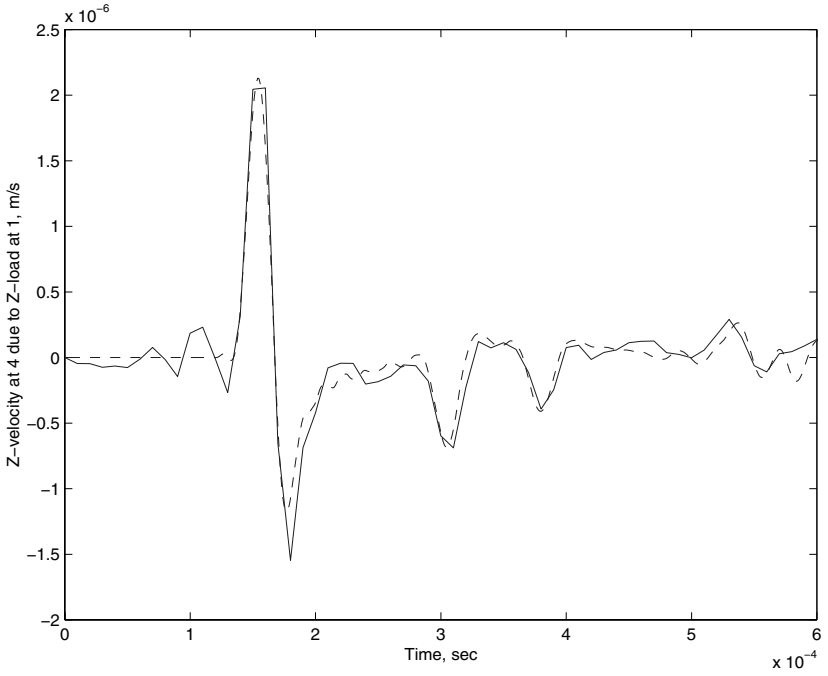

Fig. 6.6. QP wave at the interface (point 4), solid line SE, dashed line 2-D FE

Before discussing the velocity histories, a few points need to be considered. When a velocity wave encounters a stiffer zone, the reflected wave has equal magnitude and opposite sign to that of the incident wave. As opposed to that, when the wave encounters a zone of comparatively lower stiffness, the reflected wave has equal amplitude and the same sign as that of the incident wave. These phenomena are best visible in the reflections from the fixed end (infinite stiffness) and the free end (zero stiffness) of a structure. However, reflected waves are also generated at the interfaces of laminates because of the mismatch in the impedance. In the present model, propagation is considered in the direction of ply-stacking and there is a nominal change in stiffness in that direction, due to the change in laminae angle. Hence, the magnitude of the reflected waves from the interface will not be large enough to be visible, in comparison to the boundary generated waves. Thus whatever reflections are present in the velocity or stress history are solely due to reflections from the boundary.

For the load applied in the Z direction at point 1, the Z directional velocity $\dot{w}$, is measured at points marked 1, 4, and 5 (see Figure 6.4). The velocity history of these nodes are plotted in Figures. 6.5–6.7. In Figure 6.5, the peak at 100 μs is the direct effect of the load. For this kind of loading, the propagating wave is essentially a QP wave. In this case, the inverted peak at around

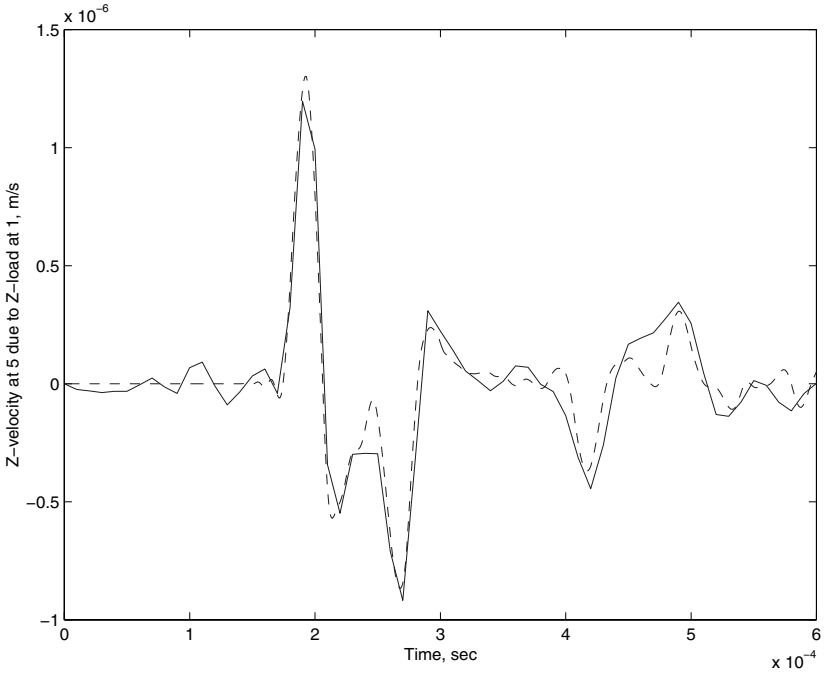

Fig. 6.7. QP wave at the interface (point 5), solid line SE, dashed line 2-D FE

3.2×10^{-4} s is the reflection from the fixed end, *i.e.,* at $z = 0.3$ m. Again at the fixed end, the wave is inverted and shows up at around 5.4×10^{-4} s. This figure also shows the excellent agreement between the FE and SLE responses.

Next, the $\dot{w}$ history at the first interface ($z = 0.1$ m, point marked 4) is plotted in Figure 6.6. The response in this case does not start at 100 μs as before, but at 130 μs. This is due to the time taken for propagation in the first layer, *i.e.,* 0° laminate. Subsequent reflections at around 2.9×10^{-4} s and 3.6×10^{-4} s are due to the reflections from the fixed edge ($z = 0.3$ m) and free edge ($z = 0.0\ m$), respectively. Further, the peak at around 5.0×10^{-4} s is the second reflection from the fixed edge.

For the $\dot{w}$ history measured at the second interface ($z = 0.2$ m, point marked 5) and the response is plotted in Figure 6.7 the main peak comes down to 1.67×10^{-4} s because of the large travel distance. The QP wave velocity at 90° laminate is less than that in the 0° laminate and hence the increase (above 1.6×10^{-4}) in propagation time. There are reflections from the fixed end (inverted peak at around 2.46×10^{-4} s), reflections from the free end (inverted peak at 4.0×10^{-4} s) and second reflections from the fixed end (peak at around 4.7×10^{-4} s). The SLE captures these reflections quite well, and except for the last reflection, the response matches satisfactorily with the FE response.

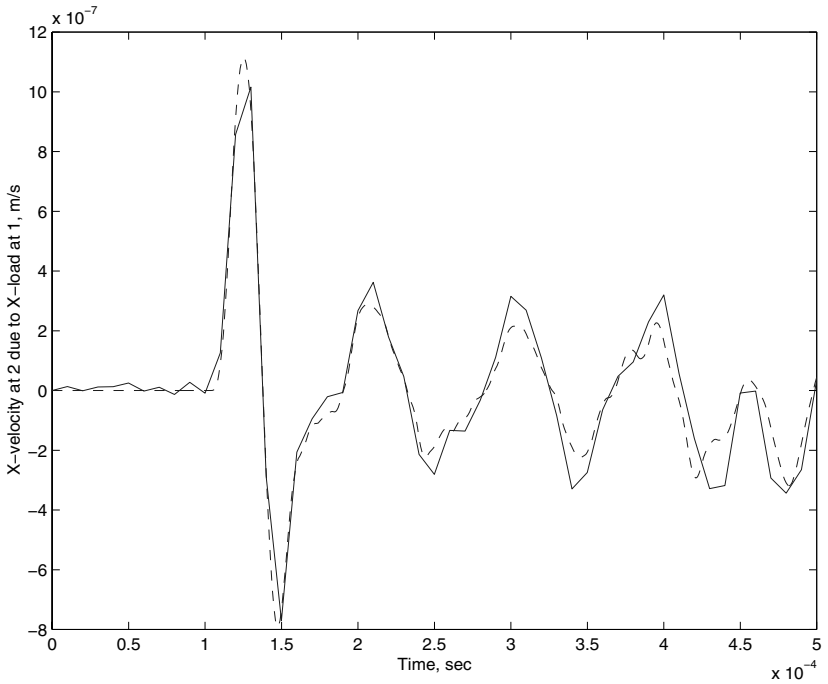

Fig. 6.8. QSV wave at the surface (point 2); solid line - SE, dashed line - 2-D FE

Next, the same load is applied at point 1 in the X direction. For this load, primarily QSV waves are generated. There will be no wave at the impact point and the X directional velocity $\dot{u}$ is measured at the surface points 2 and 3 and plotted in Figures 6.8 and 6.9, respectively. In both cases, several reflections from the fixed ends are visible. As before, good agreement between the FE and the SLE responses can be observed. These responses establish the developed SLE in terms of accuracy, efficiency and cheap cost of computation.

6.3.2 Propagation of Lamb Wave

An angle-ply lamina of 2 mm thickness is considered for the Lamb wave propagation study. Analysis is performed for three different fiber directions, 0°, 45° and 90°. Material properties of the composite are as taken before.

The dispersion relation (relation between $c_p = \omega/\eta$ and ω) is usually left in the form of a determinant equal to zero because of its complexity. Hence, solution of this kind of implicit equation requires special treatment. The solution in particular is multi-valued, unbounded and complex (although the real part is of interest). One way to solve these equations is to appeal to the strategies of non-linear optimization, which are based on non-linear least square methods. There are several choices of algorithms, like the trust-region dogleg method,

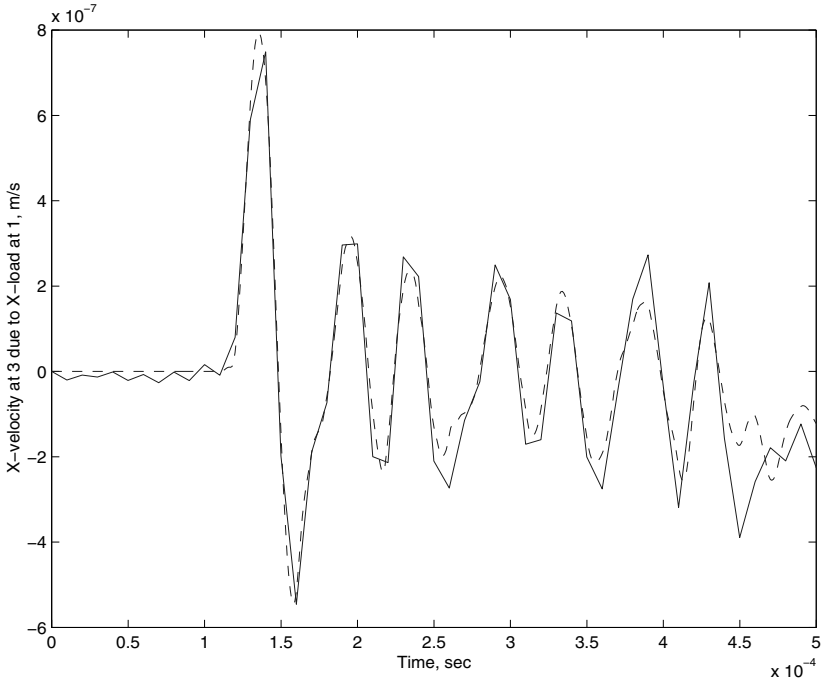

Fig. 6.9. QSV wave at the surface (point 5); solid line - SE, dashed line - 2-D FE

Gauss Newton method with a line search, or Levenberg Merquardt method with line search. Here, the MATLAB function $fsolve$ is used and for the default option for medium scale optimization, the trust-region dogleg method is adopted, which is a variant of Powell's dogleg method [109].

Apart from the choice of algorithm there are other subtle issues in root capturing for the solution of wavenumbers as the solutions are complicated in nature. Moreover, except the first one or two modes, all the other roots escape to infinity at low frequency. For isotropic materials, these cut-off frequencies are known *a priori*. However, no expressions can be found for anisotropic materials and generally, the modes (solutions) should be tracked backwards, *i.e.,* from the high frequency to the low frequency region. In general two strategies are essential to capture all the modes within a given frequency band. Initially, the whole region should be scanned for different values of the initial guess, where the initial guess should remain constant for the whole frequency range. These sweeps open up all the modes in that region, although they are not completely traced. Subsequently, each individual mode should be followed to the end of the domain or to a pre-set high value of the solution. For this case, the initial guess should be changed for each frequency to the solution of the previous frequency step. Also, sometimes it is necessary to reduce the frequency step in the vicinity of high mode gradients. Once the Lamb modes

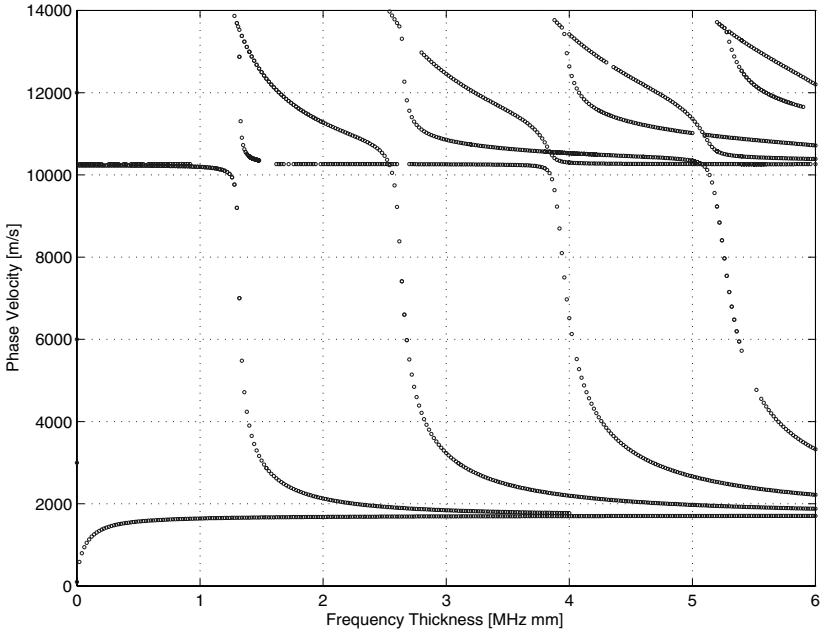

Fig. 6.10. Lamb wave modes for 0° ply-angle

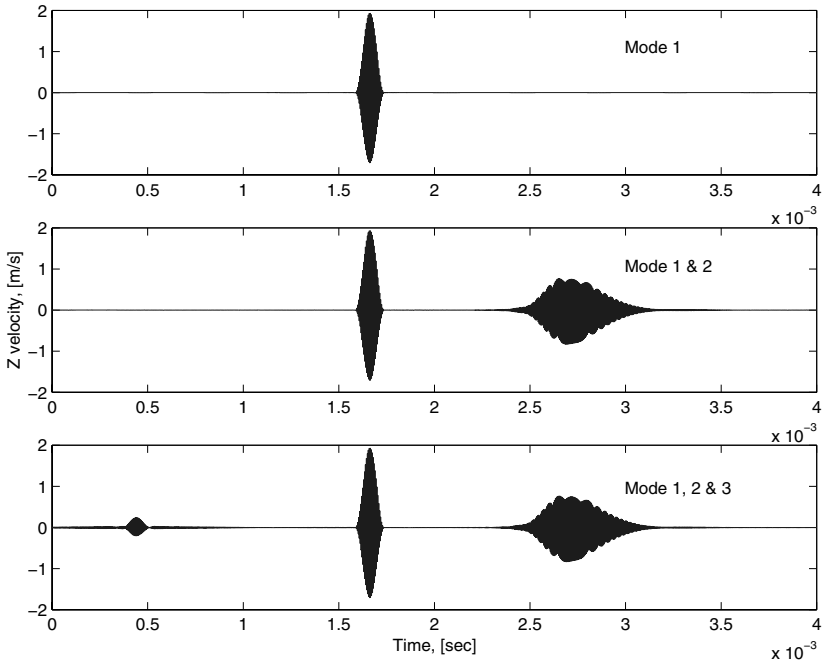

Fig. 6.11. Lamb Wave propagation for 0° ply-angle, $L = 320h$

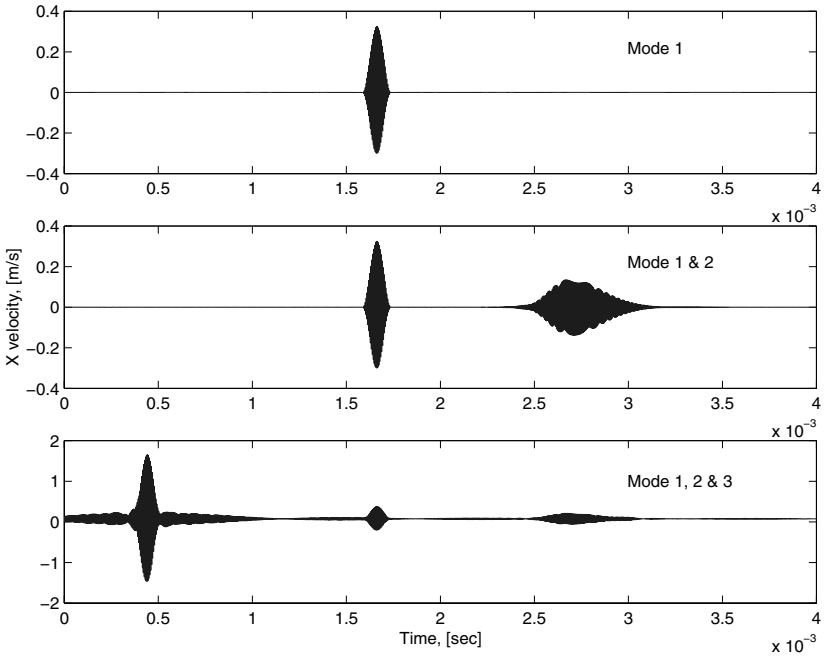

Fig. 6.12. Lamb Wave propagation for 0° ply-angle, $L = 320h$

are generated they are fed back into the frequency loop to produce the frequency domain solution of the Lamb wave propagation, which through IFFT produces the time domain signal. As the Lamb modes are generated first, they need to be stored separately. To this end data are collected from the generated modes at several discrete points over the whole frequency range. Next, a cubic spline interpolation is performed for a very fine frequency step within the same range. While generating the time domain data, interpolation is performed from these finely graded data to get the phase speed (hence, η).

To get the time history of the propagating Lamb waves a modulated pulse of 200 kHz center frequency is applied at one end of an infinite plate and X and Z velocities are measured for a propagating distance of $320h$, where h is the thickness of the plate. While studying the time domain representation, the thickness of the plate is taken as 10 mm, which amounts to a frequency-thickness value of 2. This increased thickness is taken because for this value, at least three modes will be excited in all the cases, as shown by their respective dispersion curves (Figures 6.10, 6.13 and 6.16).

In all the dispersion plots of the Lamb modes, the abscissa is given in terms of frequency times the thickness. Figure 6.10 shows the first 10 Lamb modes for fiber angle 0°. As is seen in the figure, the first anti-symmetric mode (Mode 1) converges to a value of 1719 m/s in a range of 1 MHz-mm, where all the other modes converge. In analogy to the isotropic case, this is the velocity

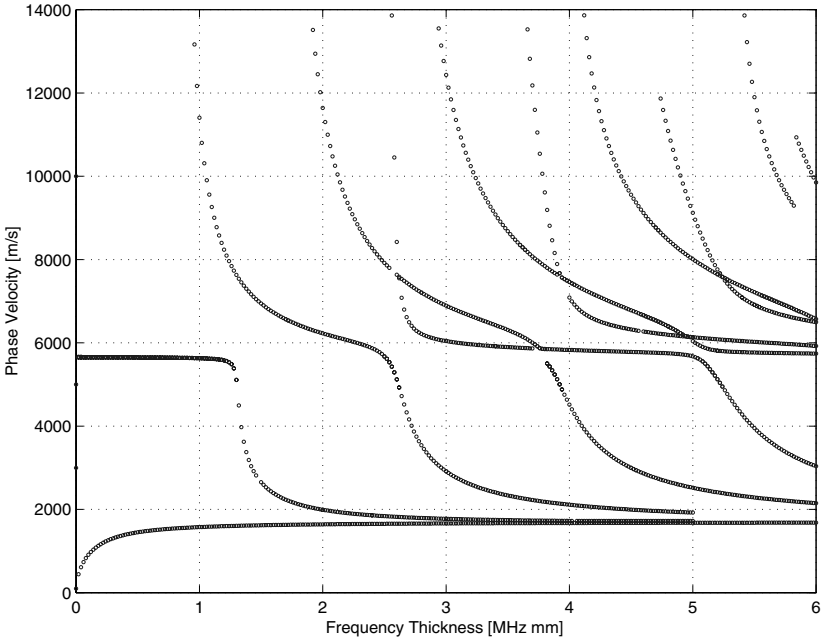

Fig. 6.13. Lamb wave modes for 45° ply angle

of the Rayleigh surface waves in 0° fiber laminae. The first symmetric mode (Mode 2) starts above 10000 m/s and drops suddenly at around 1.3 MHz-mm to converge to 1719 m/s, before which it has fairly constant value. All the other higher order modes escape to infinity at various points in the frequency range. Also the symmetric and the anti-symmetric pair of each mode escape almost at the same frequency.

Propagation of these modes are plotted in Figure 6.11 and 6.12 for the first three modes ($a_\circ, s_\circ$ and a_1), here referred to as Mode 1, 2 and 3 respectively. In Figure 6.11, the Z velocity history is plotted, whereas in Figure 6.12 the X velocity history is plotted. The figures readily show the different propagating modes, each corresponds to one blob. It is to be noted that, the wave propagation velocity is given by the group speed (and not the phase speed). Hence, Figure 6.10 will not help us to predict the appearances of different modes. However, as Figure 6.11 and 6.12 suggest, mode 2 has a lower group speed than mode 1 and mode 3 has a group speed much higher than both mode 1 and 2. One difference in the $\dot{u}$ and $\dot{w}$ history can be observed. For $\dot{u}$, the higher mode generates velocity of comparatively less magnitude, whereas, for $\dot{w}$, the magnitude is highest.

Next the fiber angle is changed to 45° and the Lamb modes are plotted in Figure 6.13. Here, the phase velocity of Mode 1 ($a_\circ$) is lower than the previous values for 0° (1690 m/s). Also, the initial phase velocity of Mode 2 ($s_\circ$) has

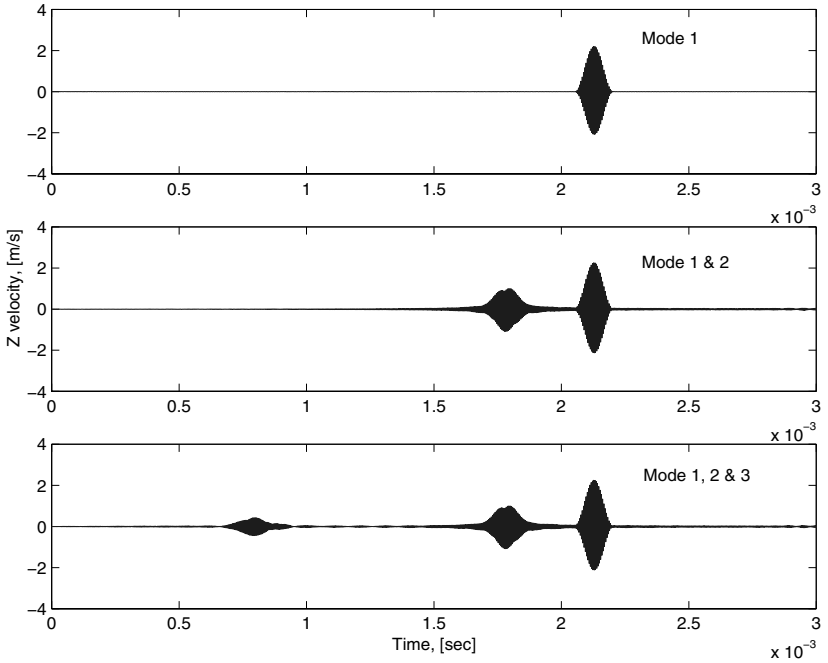

Fig. 6.14. Lamb wave propagation for 45° ply angle, $L = 320h$

come down to less than 6000 m/s in comparison to its 0° counterpart (10000 m/s). Further, the cut-off frequencies of all the higher modes are smaller than in the previous case. Also there are considerable differences in these cut-off frequencies for each pair of symmetric and anti-symmetric modes, which is absent in the 0° case. Also the number of modes is increased to 11 from 10 in the previous case. The time domain representations of the propagating waves are shown in Figures 6.14 and 6.15. In this case, however, the second mode has higher group velocity than the first mode and the third mode has the highest group speed.

Finally, the fiber angle is changed to 90° and the resulting dispersion relation is plotted in Figure 6.16. The shifting of the modes to the left of the figure continues as the number of modes is increased to 12. Further, the first symmetric mode has come down to 2600 m/s and the first anti-symmetric mode is reduced to a converged speed of 1510 m/s. For these modes the propagating Lamb wave is plotted in Figure 6.17 and 6.18 for $\dot{u}$ and $\dot{w}$, respectively. As the figures suggest, mode 2 again has lower group speed compared to mode 1 and mode 3 has higher speed than both mode 1 and 2. However, the difference between the mode 3 group speed and mode 2 group speed is not much, as opposed to the previous cases.

The study of Lamb wave propagation reveals some important effects of ply-angle. It is observed that the increase in the ply-angle increases the number

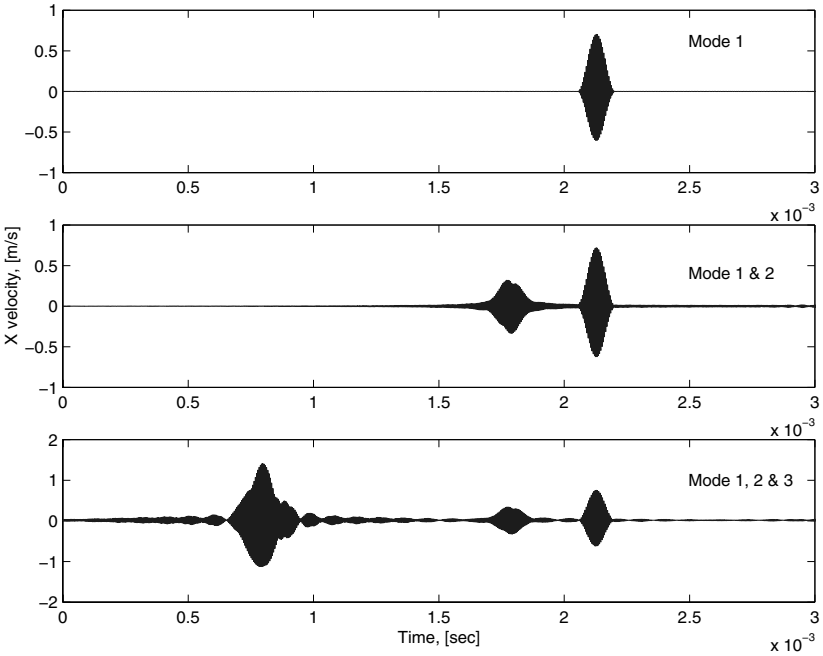

Fig. 6.15. Lamb wave propagation for 45° ply angle, $L = 320h$

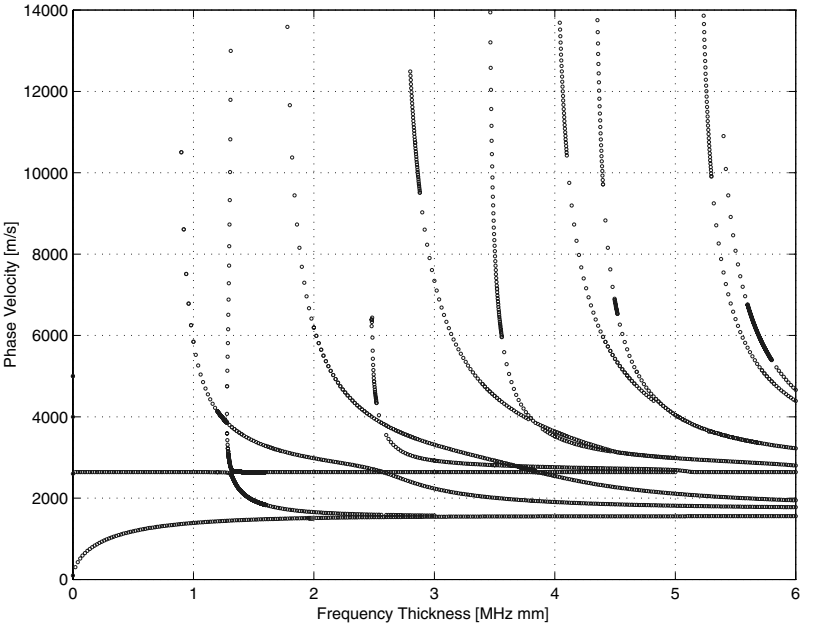

Fig. 6.16. Lamb wave modes for 90° ply-angle

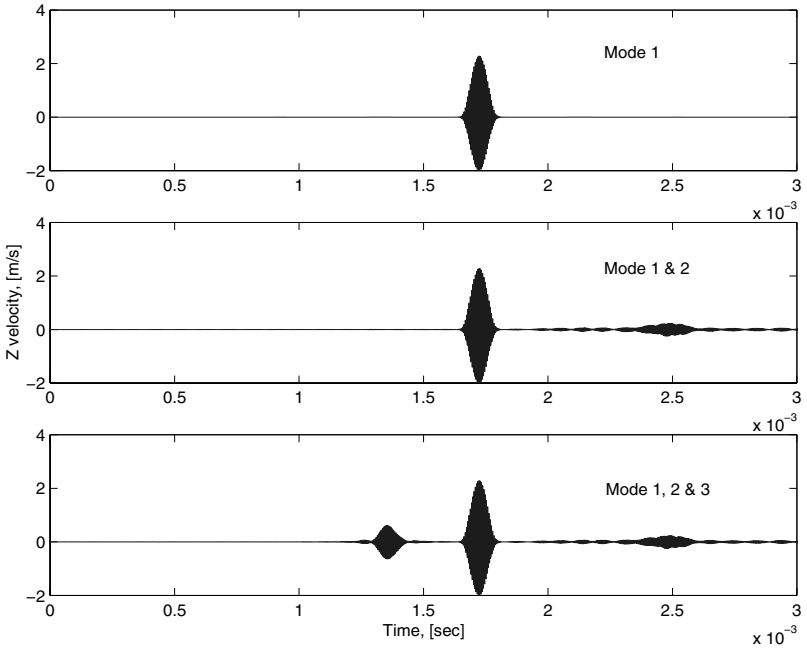

Fig. 6.17. Lamb wave propagation for 90° ply-angle, $L = 320h$

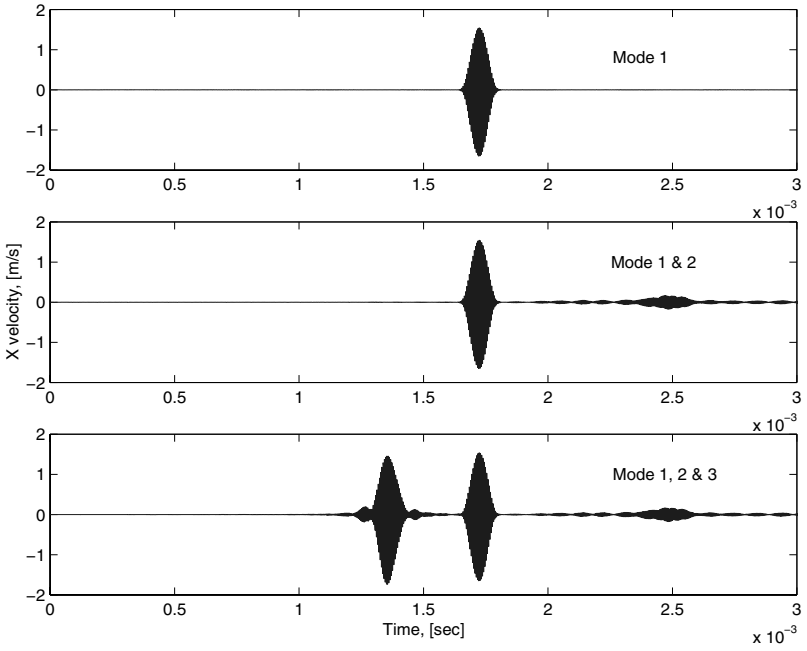

Fig. 6.18. Lamb wave propagation for 90° ply-angle, $L = 320h$

of active modes within a defined frequency range and reduces the cut-off frequencies and the phase speeds of a particular mode. Moreover, the difference in the cut-off frequencies increases with increasing ply-angle.

This chapter discusses the development and application of a SFE to analyze wave propagation in a layered anisotropic media. The element captures the response of the layered system to impact loading quite efficiently compared to the conventional FE modeling. Propagation of surface and interface waves are also shown in a layered structure. Further, Lamb modes are computed for a composite laminate for different ply-orientation and the effect of different modes on the time domain response is investigated.

7

Wave Propagation in Two-dimensional Inhomogeneous Structures

In the previous chapter we discussed the development of SFE and wave propagation aspects of layered homogeneous anisotropic media. In this chapter, inhomogeneous (isotropic or anisotropic) layered media are studied using a different set of SFEs.

As discussed before, inhomogeneous media like FGM generate wave equations with spatially dependent coefficients. The SLE for inhomogeneous material takes into account exponential material property variation in the direction of wave propagation. The element is a generalization of the beam element developed in Section 5.4. In general, the modulus and density vary in different ways and thus at least two parameters are necessary for complete description of the variation. The proposed SLE is exact when the same parameter describes the moduli and density variation, much like the beam element. However, even if a second parameter is introduced for density variation, the element works quite satisfactorily (for small variation), although an approximate dispersion relation is obtained. However, the approximate wavenumbers bring all the features of the inhomogeneous wave [24] as both real and imaginary parts are simultaneously non-zero (which cause simultaneous propagation and attenuation of the wave).

Along with the development of SFE for elastic analysis, SFE for thermoelastic analysis under dynamic theory is also formulated for both anisotropic and inhomogeneous material. For these elements, temperature is an extra degree of freedom.

7.1 SLE Formulation: Inhomogeneous Media

For the inhomogeneous layer, the general elastodynamic equation (Equation (6.1)) is simplified for 2-D media, with principal motions in the X-Z plane (see Figure 6.1), with the assumption that the material properties vary only in the Z direction. Then the non-zero stresses are related to the strains by the relation

$$\sigma_{xx} = Q_{11}(z)\epsilon_{xx} + Q_{13}(z)\epsilon_{zz}\,,\ \sigma_{zz} = Q_{13}(z)\epsilon_{xx} + Q_{33}(z)\epsilon_{zz}\,,\ \sigma_{xz} = Q_{55}(z)\epsilon_{xz}\,, \tag{7.1}$$

where Q_{ij} are the stiffness coefficients, which depend on the ply-layup, its orientation and z coordinate of the layer. Substituting Equation (7.1) in Equation (6.1), the elastodynamic equations for a 2-D inhomogeneous orthotropic media are

$$\begin{aligned} Q_{11}u_{xx} + (Q_{13} + Q_{55})w_{xz} + Q_{55}u_{zz} + Q'_{55}(u_z + w_x) &= \rho(z)\ddot{u}\,, \\ Q_{55}w_{xx} + (Q_{13} + Q_{55})u_{xz} + Q_{33}w_{zz} + Q'_{13}u_x + Q'_{33}w_z &= \rho(z)\ddot{w}\,, \end{aligned} \tag{7.2}$$

where prime denotes differentiation with respect to z. The displacement field is assumed in the same way as taken for the anisotropic material (Equations (6.5) and (6.6)).

Following the same procedure used in the last chapter, a set of ODEs is obtained (see Equation (6.7)), where the matrices $\mathbf{A}$, $\mathbf{B}$ and $\mathbf{C}$ (all functions of z) are given by

$$\mathbf{A} = \begin{bmatrix} Q_{55}(z) & 0 \\ 0 & Q_{33}(z) \end{bmatrix}, \mathbf{B} = \begin{bmatrix} Q'_{55}(z) & -(Q_{13}(z) + Q_{55}(z))\eta_m \\ (Q_{13}(z) + Q_{55}(z))\eta_m & Q'_{33}(z) \end{bmatrix}, \tag{7.3}$$

$$\mathbf{C} = \begin{bmatrix} -\eta_m^2 Q_{11}(z) + \rho(z)\omega_n^2 & -Q'_{55}(z)\eta_m \\ Q'_{13}(z)\eta_m & -\eta_m^2 Q_{55}(z) + \rho(z)\omega_n^2 \end{bmatrix}. \tag{7.4}$$

Thus the effect of inhomogeneity manifests in terms of the diagonal terms in $\mathbf{B}$ and the off-diagonal terms in $\mathbf{C}$, which are zero for homogeneous material. The associated boundary conditions are the specifications of stresses σ_{zz} and σ_{xz} at the layer interfaces. From Equation (6.3), stresses are related to the unknowns in the same way as Equation (6.10), where

$$\hat{\mathbf{s}} = \mathbf{D}\hat{\mathbf{u}}' + \mathbf{E}\hat{\mathbf{u}}\,, \hat{\mathbf{s}} = \{\sigma_{zz}\ \sigma_{xz}\}\,, \quad \mathbf{D} = \begin{bmatrix} 0 & Q_{33} \\ Q_{55} & 0 \end{bmatrix}, \quad \mathbf{E} = \begin{bmatrix} \eta_m Q_{13} & 0 \\ 0 & -\eta_m Q_{55} \end{bmatrix}, \tag{7.5}$$

where $\mathbf{D}$ and $\mathbf{E}$ are also functions of z. Any kind of inhomogeneity can be tackled in this formulation, provided the BVP is solved numerically. However, there is a special case for which the BVP is exactly solvable, and this is taken up next.

7.1.1 Exact Formulation

Let us assume that the material property variation is exponential, *i.e.,*

$$Q_{ij}(z) = Q_{ij\circ}e^{\alpha z}\,, \quad \rho(z) = \rho_\circ e^{\beta z}\,, \tag{7.6}$$

where $Q_{ij\circ}$ and $\rho_\circ$ are constant properties of the background homogeneous material. Substituting Equation (7.6) in Equations (7.3) and (7.4) we get

$$\mathbf{A} = \begin{bmatrix} Q_{55\circ} & 0 \\ 0 & Q_{33\circ} \end{bmatrix} e^{\alpha z}, \mathbf{B} = \begin{bmatrix} \alpha Q_{55\circ} & -(Q_{13\circ} + Q_{55\circ})\eta_m \\ (Q_{13\circ} + Q_{55\circ})\eta_m & \alpha Q_{33\circ} \end{bmatrix} e^{\alpha z}, \tag{7.7}$$

$$\mathbf{C} = \begin{bmatrix} -\eta_m^2 Q_{11\circ} + \rho_\circ \omega_n^2 \gamma & -\alpha Q_{55\circ}\eta_m \\ \alpha Q_{13\circ}\eta_m & -\eta_m^2 Q_{55\circ} + \rho_\circ \omega_n^2 \gamma \end{bmatrix} e^{\alpha z}, \quad \gamma = e^{(\beta-\alpha)z}. \tag{7.8}$$

Substituting Equations (7.7) and (7.8) in Equation (7.2) and cancelling the $e^{\alpha z}$ term, another equation is obtained in which the elements of the matrices $\mathbf{A}$ and $\mathbf{B}$ are constant, but the elements of $\mathbf{C}$ have z dependency in terms of γ. If β is equal to α then $\gamma = 1$ and all the matrices become constant with respect to z. Then the solutions are in the form of $u_\circ e^{-jkz}$ and $w_\circ e^{-jkz}$, where $u_\circ$, $w_\circ$ and k, the vertical (Z direction) wavenumbers, are the unknowns.

However, for the more general case $\beta \neq \alpha$, we can proceed in the same way and can naively assume that the e^{jkz} type of solution is still possible (as assumed in rod formulation, Section 5.1), which will yield an approximate solution. Since, the z dependency needs to be avoided, γ can be evaluated at some point within the domain and can be used as a representative value for γ. Here, γ is evaluated at $z = L/2$. Substituting these solutions in Equation (7.2) for the matrices given by Equations (7.7) and (7.8), the problem becomes one of finding non-trivial $u_\circ$, $w_\circ$ from the equation

$$\mathbf{W}\{\mathbf{u}_\circ\} = \mathbf{0} \ , \mathbf{W} = -k^2\mathbf{A} - jk\mathbf{B} + \mathbf{C}, \{\mathbf{u}_\circ\} = \{u_\circ \ w_\circ\}, \tag{7.9}$$

where $\mathbf{W}$ is the wave matrix. Thus, in the 2-D layered media, $N_v = 2$ and the order of the PEP $p = 2$, which yields four eigenvalues (wavenumbers). The wave matrix in explicit form is

$$\begin{bmatrix} -k^2 Q_{55\circ} - \eta_m^2 Q_{11\circ} + \rho_\circ \omega_n^2 \gamma - jkQ_{55\circ}\alpha & jk\eta_m(Q_{13\circ} + Q_{55\circ}) - Q_{55\circ}\alpha\eta_m \\ -jk\eta_m(Q_{13\circ} + Q_{55\circ}) + Q_{13\circ}\alpha\eta_m & -k^2 Q_{33\circ} - \eta_m^2 Q_{55\circ} + \rho_\circ \omega_n^2 \gamma - jkQ_{33\circ}\alpha \end{bmatrix}. \tag{7.10}$$

The singularity condition of $\mathbf{W}$ yields

$$\begin{aligned} & Q_{33\circ}Q_{55\circ}k^4 + 2jQ_{55\circ}Q_{33\circ}k^3 \\ & + \{(Q_{11\circ}Q_{33\circ} - 2Q_{13\circ}Q_{55\circ} - Q_{13\circ}^2)\eta_m^2 \\ & - \rho_\circ\omega_n^2(Q_{33} + Q_{55})\gamma - Q_{55\circ}Q_{33\circ}\alpha^2\}k^2 \\ & + \{j\alpha(Q_{11\circ}Q_{33\circ} - 2Q_{13\circ}Q_{55\circ} - Q_{13\circ}^2)\eta_m^2 - j\alpha\rho_\circ\omega_n^2(Q_{33\circ} + Q_{55\circ})\gamma\}k \\ & + \{Q_{55\circ}Q_{13\circ}\alpha^2\eta_m^2 + Q_{11\circ}Q_{55\circ}\eta_m^4 \\ & - \rho_\circ\omega_n^2\eta_m^2(Q_{11\circ} + Q_{55\circ})\gamma + \rho_\circ^2\omega_n^4\gamma^2\} = 0, \end{aligned} \tag{7.11, 7.12}$$

which is the required spectrum relation. It is to be noted that for each value of η_m and ω_n, there are four values of k, denoted by $k_{lmn}, l = 1, \ldots, 4$, which will be obtained by solving the spectrum relation.

There are several extra features of this spectrum relation compared to its homogeneous material counterpart (Equation (6.13)). First of all, the coefficient of k^3 and k are non-zero and complex, which means the roots are not complex conjugate to each other, as opposed to the homogeneous case. This

implies that the notion of the forward and backward moving wave is somewhat blurred in this case. However, this notion, which is effective for element formulation can be retained by looking at the signs of the real part only. Thus, a wavenumber with a positive real part denotes a forward propagating wave and a negative real part denotes a backward propagating wave, although their imaginary parts may have any sign.

Secondly, in the case of homogeneous material, the roots are either totally real or totally complex, *i.e.,* at no value of ω_n or η_m do the wavenumbers possess both real and imaginary (non-trivial) parts. However, in the present situation this kind of solution is quite natural because of the existence of non-zero coefficients for k^3 and k. For the same reason, the notion of the cut-off frequency is also absent. However, one can find the cut-off frequencies by setting the constant part in Equation (7.12) equal to zero, *i.e.,*

$$\rho_\circ^2\omega_n^4\gamma^2 - \rho_\circ\omega_n^2\eta_m^2(Q_{11\circ} + Q_{55\circ})\gamma + Q_{55\circ}Q_{13\circ}\alpha^2\eta_m^2 + Q_{11\circ}Q_{55\circ}\eta_m^4 = 0, \tag{7.13}$$

and the ω that satisfies this relation will be called the cut-off frequency. Thus both the ideas of forward (or backward) propagating wave and the cut-off frequency need to be modified in the inhomogeneous case.

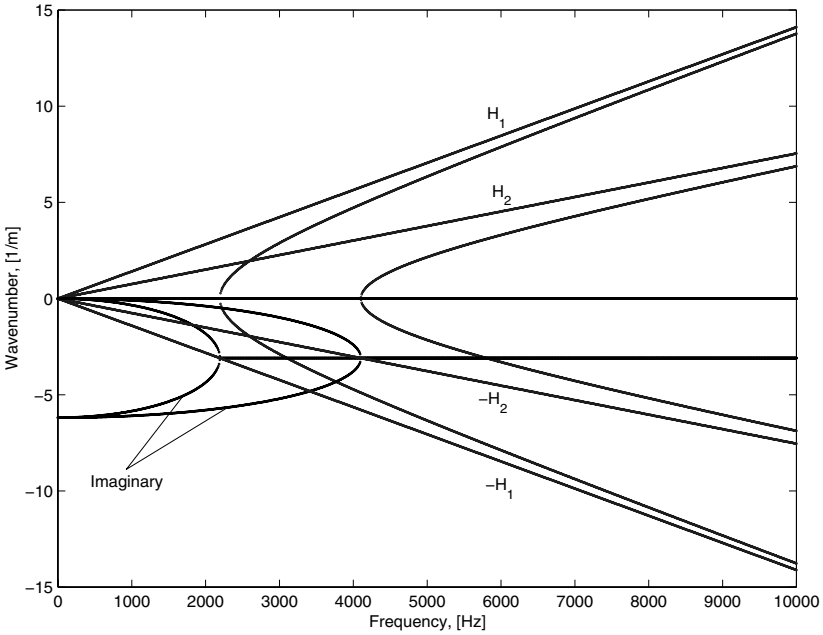

Fig. 7.1. Variation of wavenumber with ω_n and $\eta_m = 0$ (RH_j - real homogeneous)

The behavior of the roots will be more clearly visible if a particular material is considered and the spectrum relation is solved for its material properties. For this purpose, the layer is assumed to be of 0.1 m thickness, and the material properties vary from steel to ceramic. The material properties of steel are taken as follows: Young's modulus $E = 210$ GPa, poisson's ratio $\nu = 0.3$ and density $\rho = 7800$ kg/m^3. Similarly, for ceramic, $E = 390$ GPa, $\nu = 0.3$ and $\rho = 3950$ kg/m^3. For these material properties and exponential variation, inhomogeneous parameters, α and β become 6.19 m^{-1} and -6.80 m^{-1}, respectively.

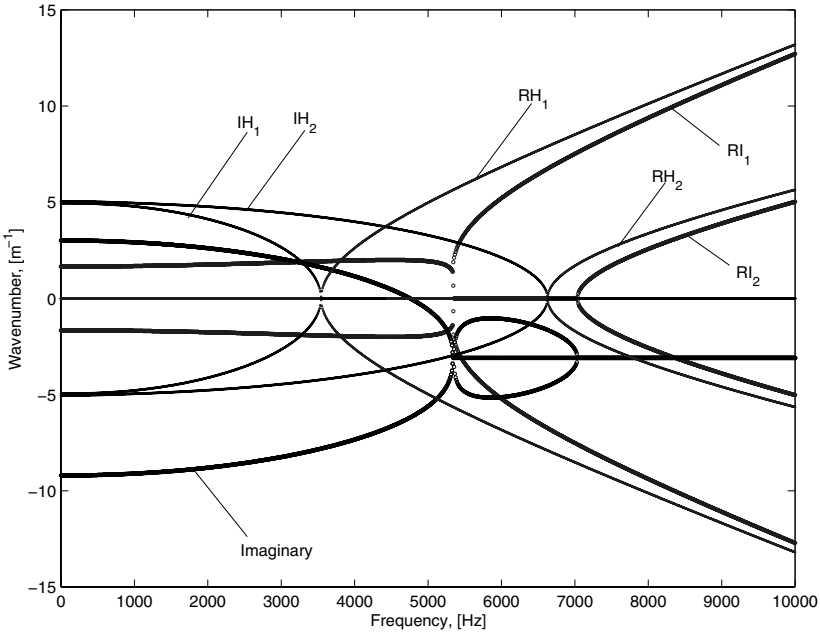

Fig. 7.2. Variation of wavenumber with ω_n and $\eta_m = 5$ (RH_j - real homogeneous, IH_j - imaginary homogeneous, RI_j - real inhomogeneous)

Figure 7.1 shows the variation of the wavenumbers with ω, for $\eta_m = 0$. Both homogeneous (marked by $\pm H_1$ and $\pm H_2$) and inhomogeneous cases are considered. For the background homogeneous (steel) material, the wavenumbers are linearly varying with ω (they are actually given by $\pm\omega\sqrt{\rho/Q_{33}}$ and $\pm\omega_n\sqrt{\rho/Q_{55}}$) as is shown in the figure. Also, the roots are symmetric about $k = 0$ and real. Compared to them, the wavenumbers of inhomogeneous materials simultaneously possess both real and imaginary parts. The real parts are symmetric about $k = 0$ and the imaginary parts are symmetric about $k = -3.158$. At higher frequencies, along with the propagating real parts there is a constant imaginary part of this magnitude, which will be respon-

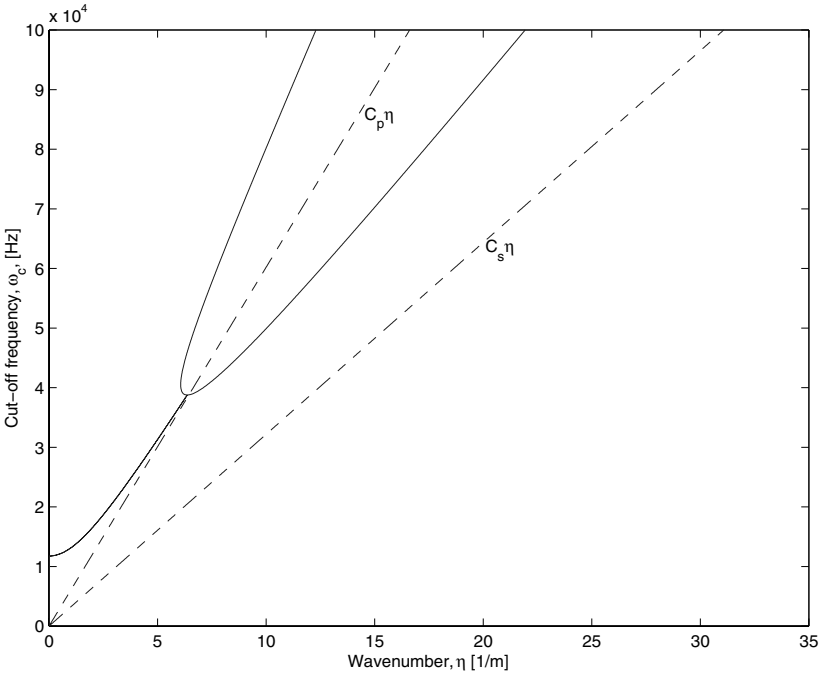

Fig. 7.3. Variation of cut-off frequency, solid line - homogeneous material, dashed line - inhomogeneous material

sible for attenuation of wave amplitudes. For non-zero η_m, the wavenumbers are plotted in Figure 7.2. Also the wavenumbers corresponding to the homogeneous material are plotted in the same figure and their real and imaginary parts are marked by RH_i and IH_i, respectively. The symmetricity of the roots (about $k = 0$) is evident here. Further, the cut-off frequencies can be identified clearly, before which the roots are imaginary. However, the behavior is considerably different in the inhomogeneous case. Here again, real and imaginary parts coexist. Further, the real and imaginary parts are symmetric about the previous values, *i.e.,* $k = 0$ and $k = -3.158$, respectively. Both the figures suggest that, at higher frequencies, the roots become closer to their homogeneous counterpart, along with an imaginary part of constant magnitude. In the homogeneous case, the cut-off frequencies are approximately at 3548 Hz and 6613 Hz, as shown in the figure. Also, it is seen that there is no frequency where both the real and the imaginary parts are zero in the inhomogeneous case. The reason for the absence of this frequency in the inhomogeneous case can be explained with the help of Figure 7.3. The figure shows the variation of ω with η, where any point on the curve satisfies Equation (7.13). For the homogeneous case, the cut-off frequencies are $c_p\eta$ and $c_s\eta$ and are shown by the two dashed straight lines. However, for inhomogeneous material, the figure

suggests that once $\eta \neq 0$, there is no cut-off frequency before 11.7 kHz, and that is the reason for the absence of zero wavenumber for $\eta = 5$. Moreover, for the homogeneous case, at any η, there are always two cut-off frequencies. However, for inhomogeneous material, upto around 40 kHz, there is only one cut-off frequency and afterwards, the bifurcation leads to the appearance of another.

The element formulation is carried out in the same way as shown for the anisotropic layer, with the wavenumbers computed above. The matrices $\mathbf{T}_1$ for the finite (Equation (6.22)) and infinite layer (Equation (6.28)) remains the same in this case. However, $\mathbf{T}_2$ (Equation (6.23)) differs as it takes into account the spatial variation of the elastic moduli.

7.2 Numerical Examples

The developed spectral element for exponential material property variation is used to study the stress wave propagation through layered media. In particular, attention is given to the stress smoothing effect of FGM. Subsequently, the propagation of Lamb waves through inhomogeneous waveguides is studied.

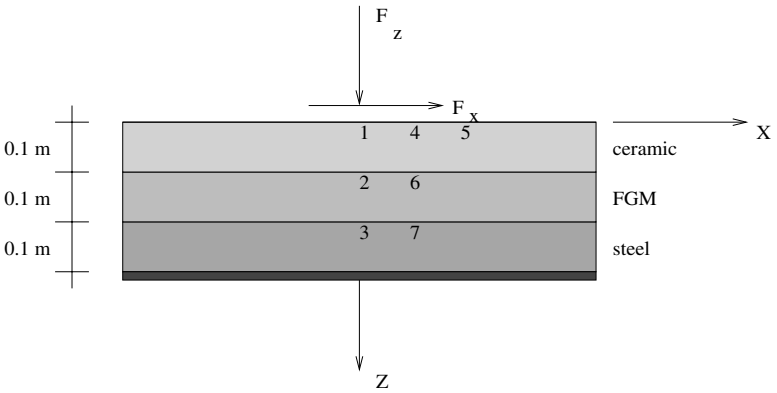

Fig. 7.4. Layer model for verification

7.2.1 Propagation of Stress Waves

In this section, the formulated element is employed to study the stress wave propagation in a layered media. In particular, inter-layer normal (σ_{zz}) and shear (σ_{xz}) stresses are of great concern as they are the root cause of failure in a layered structure. The layered system shown in Figure 7.4 is considered in this study. Tractions are specified in both the X and Z direction, where the same broadband load history (Figure 5.3) is applied.

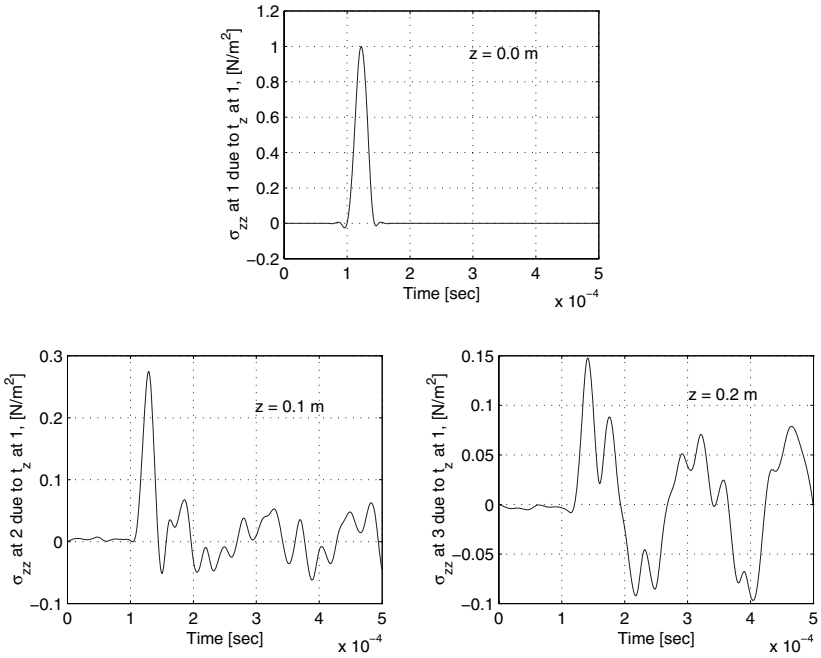

Fig. 7.5. Stress wave propagation , σ_{zz} due to t_z

First, traction is applied in the Z direction and normal stress σ_{zz} is measured at points 1, 2 and 3 (Figure 7.4). The normalized (with respect to the maximum magnitude in each case) measured stresses are shown in Figure 7.5. As is seen in the figure, at the surface the stress history profile is exactly the same as the applied traction, which is expected. However, at the interfaces the initial peak appears after a certain interval of time due to the finite propagation speed. Further, multiple reflections are visible at the interfaces, which results in both tensile and compressive stresses. For the stress wave measured at the second interface, the first positive peak is the reflection from the fixed end and the subsequent negative peak is the reflection from the free end. It is important to note that the normal stress at a FGM-metal interface is half of that at the ceramic-FGM interface and this attenuation of stresses can be attained with the use of FGM.

The shear stresses generated at the interfaces due to this load are plotted in the right two subplots of Figure 7.6. No shear stress is generated at the top surface and at the interfaces their magnitude is very much less than the normal stresses.

Next, the load is applied in the X direction and the shear stresses at the surface and interfaces are measured at an X coordinate of 0.1 m and plotted in Figure 7.7. As usual, the surface stress wave is the same as the applied stress, whereas, the main interface wave peaks are of opposite sign. Further,

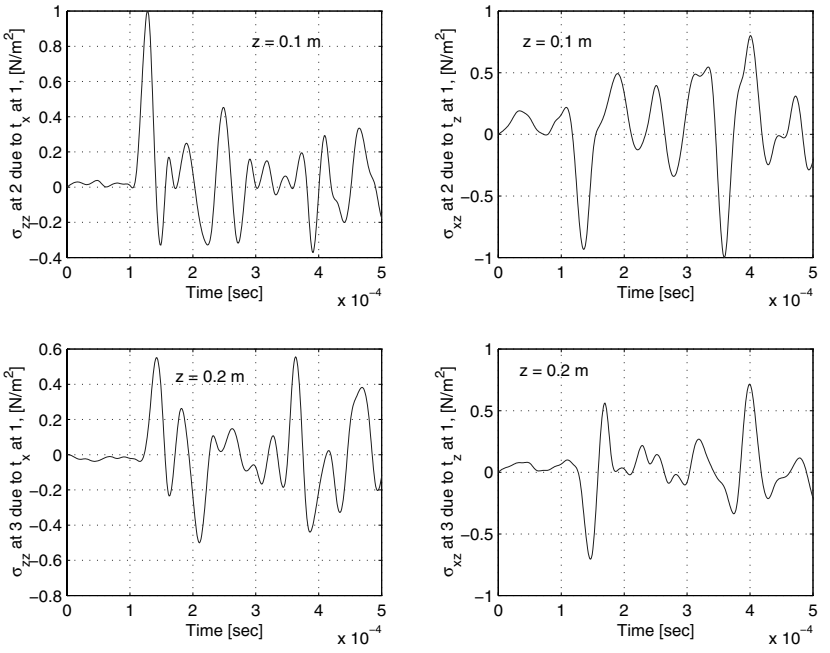

Fig. 7.6. Stress wave propagation, σ_{xz} due to t_z and σ_{zz} due to t_x

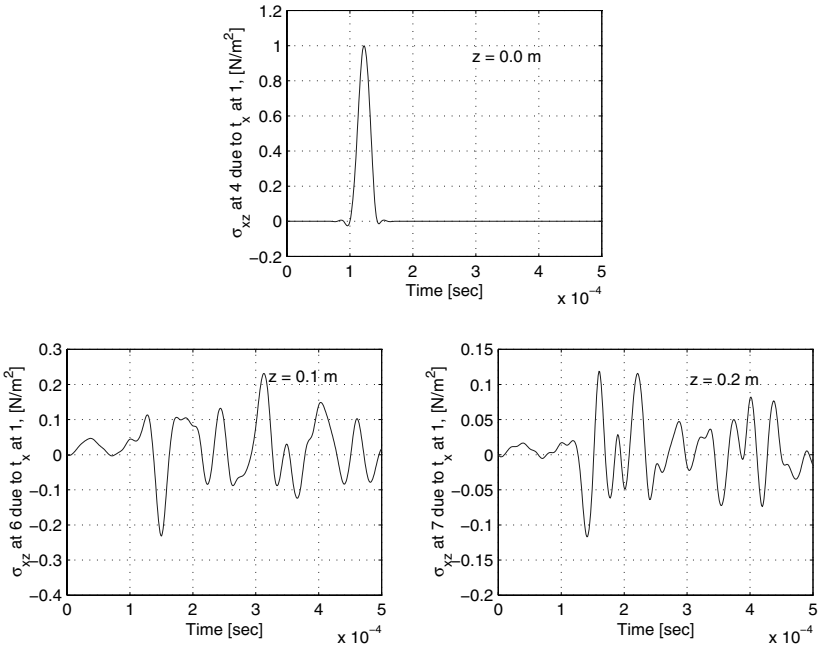

Fig. 7.7. Stress wave propagation, σ_{xz} due to t_x

the reflections from the fixed and free ends follow the same trend as the normal stress. The normal stresses generated at the interfaces due to this traction are plotted in the left two subplots of Figure 7.6. Again several reversals of stresses are visible, particularly for the second interface.

The above example shows the general stress pattern that exists in a layered media for applied normal and shear tractions and the effect of boundaries on these stresses. In particular, the boundaries generate stress waves, which may be as strong as the original pulse (especially for the shear stresses). Further, if the energy is trapped in a layer, these stress waves may cause severe damage in the absence of a suitable dissipation mechanism.

7.2.2 Propagation of Lamb Waves

A layer of 2 mm thickness is considered initially to generate the Lamb wave modes. Analysis is performed for both homogeneous and inhomogeneous materials. The background homogeneous material is taken as steel, whose material properties are as assumed before. To model the FGM layer, the inhomogeneous parameters α and β are set at 2000 m^{-1} and -2000 m^{-1}, respectively. The dispersion relation (relation between $c_p = \omega/\eta$ and ω) is obtained using the procedure outlined in the anisotropic layer case.

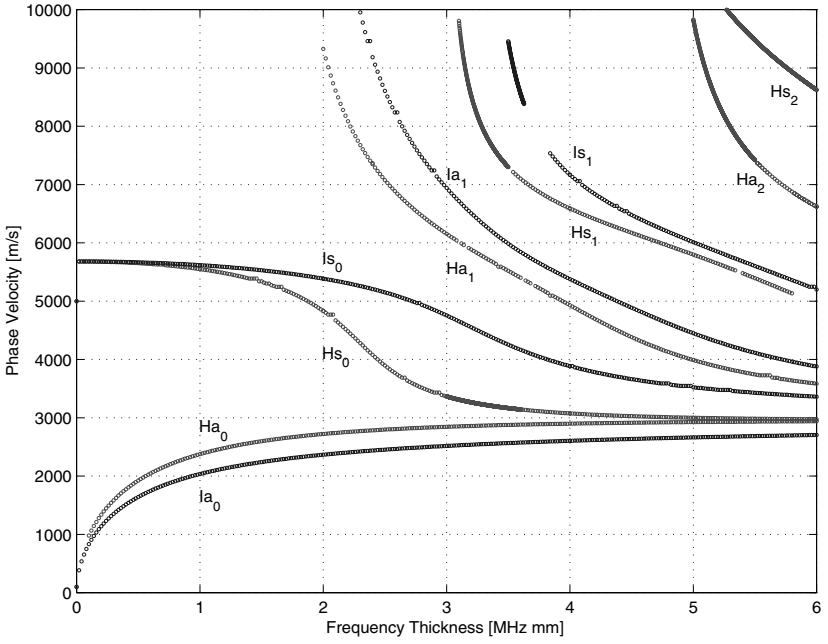

Fig. 7.8. Lamb wave modes for homogeneous and inhomogeneous plate, Ha_0, Hs_0 *etc.* are the homogeneous material modes and Is_0, Is_1 *etc.* are the inhomogeneous material modes

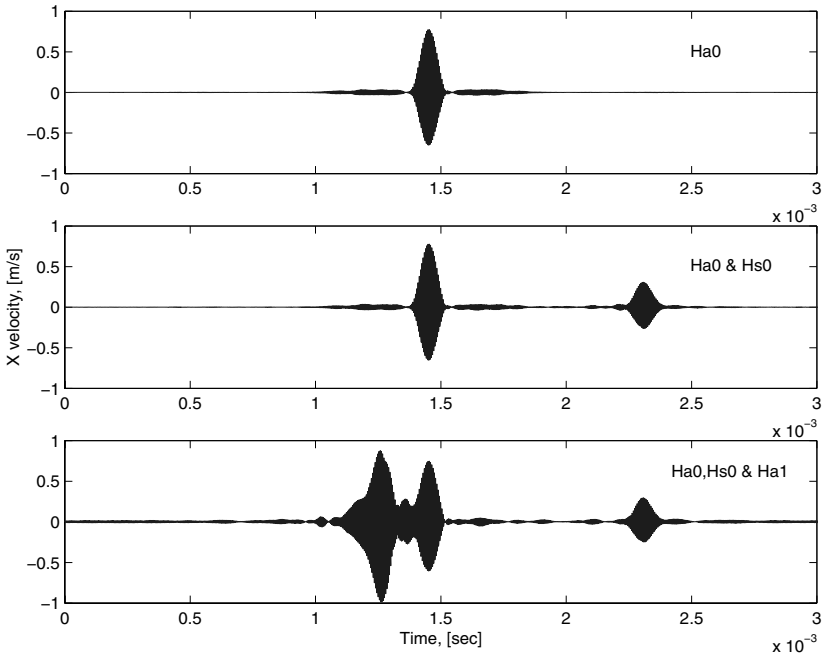

Fig. 7.9. Lamb wave propagation for homogeneous layer: $L = 320h$, $Ha0$, $Hs0$ and $Ha1$ are the homogeneous material modes

To get the time history of the propagating Lamb waves, as in the anisotropic case, a modulated pulse of 200 kHz center frequency ω_c, is applied at one end of an infinite plate and the X and Z velocities are measured for a propagating distance of $320h$, where h is the thickness of the plate. Here h is taken as 12.5 mm, which amounts to a frequency-thickness ($\omega_c h$) value of 2.5. This thickness will excite three modes for both homogeneous and inhomogeneous material, as is shown in the dispersion curve (Figure 7.8). Thus it is $\omega_c h$ that controls the magnitude of the phase speed and the same value can be attained for different h by suitably changing the ω_c. Similarly, for inhomogeneous material with exponential variation, it is the product of α or β with h (denoted αh or βh) that matters and not the individual value of α, β or h. Hence, for a new value of $h = 2$ mm, α should be changed to $(2000 \times 2)/12.5$, *i.e.,* 320 m^{-1} and β to -320 m^{-1}.

In all the plots of the Lamb modes the abscissa is given in terms of $\omega_c h$ and the plots are valid for $\alpha h = 4$ and $\beta h = -4$. Figure 7.8 shows the first six Lamb modes for steel (marked Ha_0, Hs_0, *etc.*) and the first four modes for FGM (marked Is_0, Is_1 *etc.*). For steel, as the figure suggests, first antisymmetric mode (Ha_0) and first symmetric mode (Hs_0) converge to a value of 3000 m/s at a value of 5 MHz-mm, where all the other modes converge at various later values of $\omega_c h$. This is the velocity of the Rayleigh surface waves

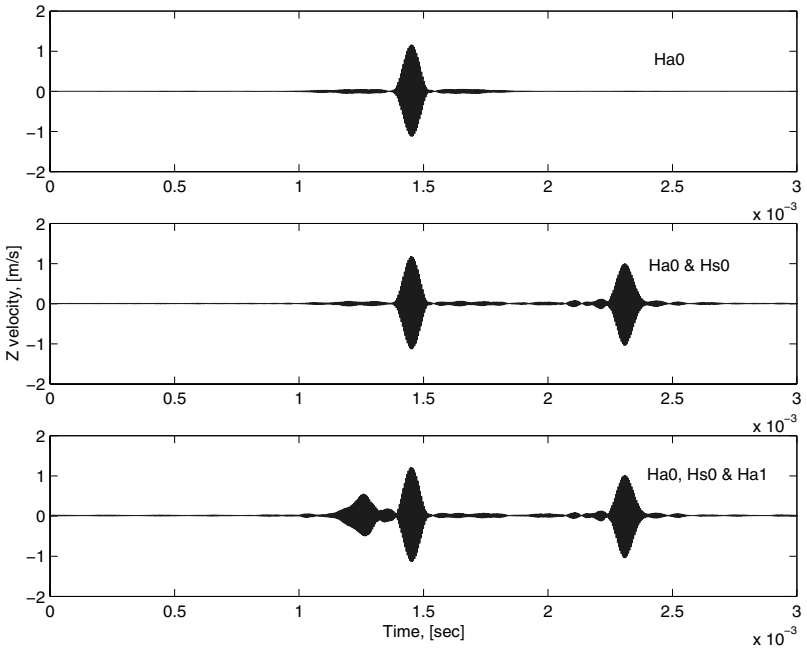

Fig. 7.10. Lamb wave propagation for homogeneous layer: $L = 320h$, $Ha0$, $Hs0$ and $Ha1$ are the homogeneous material modes

(c_R). The Hs_0 starts at about 5800 m/s and drops gradually to the value of c_R. All the other higher order modes escape to infinity at various points of $\omega_c h$ and the corresponding frequencies are the cut-off frequencies. However, the symmetric and anti-symmetric pair of each mode escape at different $\omega_c h$.

In comparison, for FGM, Ia_0 always has lower phase speed than Hs_0, although for all the other modes, starting from Is_0, phase speed is higher than the corresponding phase speed of the homogeneous material. However, the slopes at any point in the modes differ widely from their homogeneous counterpart, which suggests wide variation in the group speed and correspondingly in the order of the appearance of different propagating modes. It can be noted that, for FGM, c_R is smaller than the steel c_R, which implies that the disturbance propagates slowly in the FGM surface, compared to the metal surface. Moreover, the cut-off frequencies are also greater than that of steel, which implies, for a given frequency range, fewer modes will propagate in FGM than that in steel, which may be advantageous if properly utilized.

Propagation of these modes for steel are plotted in Figure 7.9 (X velocity $\dot{u}$) and 7.10 (Z velocity $\dot{w}$) for first three modes ($a_\circ, s_\circ$ and a_1). Similarly, the modes of FGM are plotted in Figures 7.11 ($\dot{u}$) and 7.12 ($\dot{w}$). The figures readily show the different propagating modes, each corresponds to one blob. As Figure 7.9 and 7.10 suggest, for steel, mode s_0 has a lower c_g than mode a_0

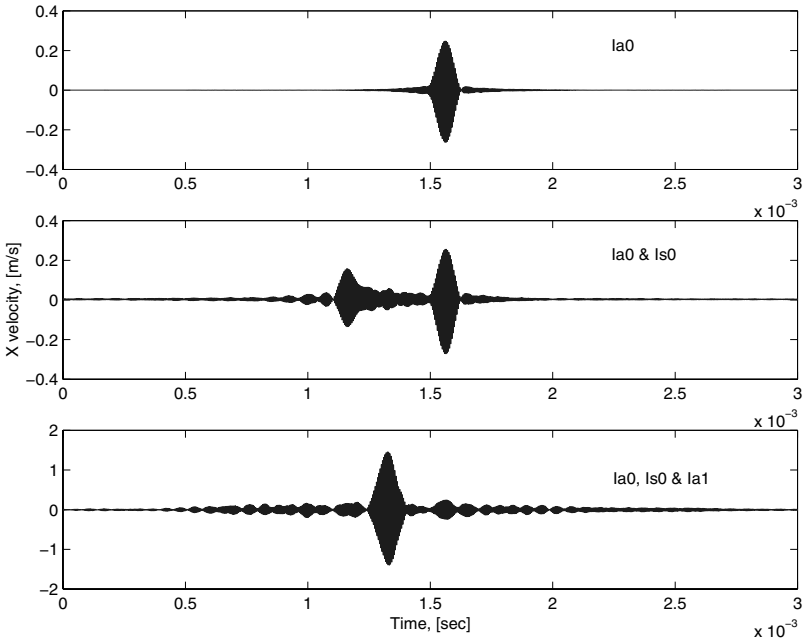

Fig. 7.11. Lamb wave propagation for inhomogeneous layer: $L = 320h$, $Ia0$, $Is0$ and $Ia1$ are the inhomogeneous material modes

and mode a_1 has a c_g higher than both mode a_0 and mode s_0. One difference in the $\dot{u}$ and $\dot{w}$ history can be observed. In $\dot{u}$, mode a_1 generates the velocity of highest magnitude, whereas, for $\dot{w}$, the magnitude is lowest for mode a_1. In comparison, in FGM, mode s_0 has higher c_g than mode a_0, although mode a_1 has a c_g in between mode a_0 and s_0. Moreover, mode a_1 has the highest velocity for both $\dot{u}$ and $\dot{w}$.

If the modes of FGM and steel are compared, it can be seen that the c_g of mode Ia_0 is lower than that of mode Ha_0, as shown by the appearance of the first mode after and before 1.5 ms. There is a drastic difference in the c_g of Hs_0 and Is_0, which totally changes the order of the modes for metal and FGM. However, the c_g of the mode Ia_1 is lower than that of mode Ha_1 by a small amount. Thus the order of the appearance of the modes can be altogether different in FGM (from the background homogeneous material), and mode selection or cancellation is possible. For example, if an FGM is prepared with the current values of α and β and a time window is chosen below 2 ms (depending upon the geometry of the structure), mode s_0 can be captured, which is not possible in the homogeneous case.

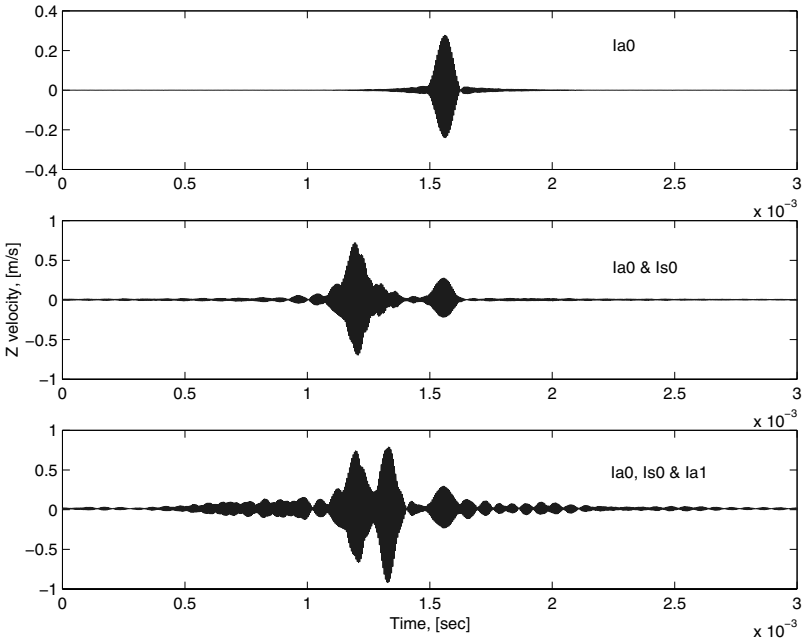

Fig. 7.12. Lamb wave propagation for inhomogeneous layer: $L = 320h$, $Ia0$, $Is0$ and $Ia1$ are the inhomogeneous material modes

7.3 SLE Formulation: Thermoelastic Analysis

In the subsequent derivations, C_{ijkl}, β_{ij} and K_{ij} denote the elements of the elasticity, thermoelasticity and heat conductivity tensor, respectively, whereas, σ_{ij} and ϵ_{ij} denote the components of the stress and strain tensor, respectively. Also, T, $T_\circ$ and η denote material temperature, ambient temperature and temperature rise, $T - T_\circ$, respectively.

The governing equation for a linear coupled dynamic thermoelasticity when applied to inhomogeneous anisotropic material, in the absence of body force and heat source, takes the form

$$\sigma_{ij,j} = \rho \ddot{u}_i \,, \quad \sigma_{ij} = C_{ijkl}\epsilon_{kl} - \beta_{ij}(\eta - t_1\dot{\eta}) \,, \tag{7.14}$$

$$\rho C_e(\dot{\eta} + t_2\ddot{\eta}) + T_\circ\beta_{ij}(\dot{\epsilon}_{ij} + \tau_\circ\ddot{\epsilon}_{ij}) - (K_{ij}\eta_{,j})_{,i} = 0 \,, \quad i,j = 1,3 \,, \tag{7.15}$$

where u_i are the components of the displacement field. The ρ and C_e denote density and thermal capacity, respectively. The t_1, t_2 are the first and second thermal relaxation parameters for the Green–Lindsay (GL) model and $\tau_\circ$ is the thermal relaxation time for the Lord–Shulman (LS) model. Equations (7.14) and (7.15) encompass both the GL and the LS model. To convert to the GL model, $\tau_\circ$ should be set to zero, whereas, to convert to the LS model, $t_1 = 0$ and $t_2 = \tau_\circ$ should be enforced.

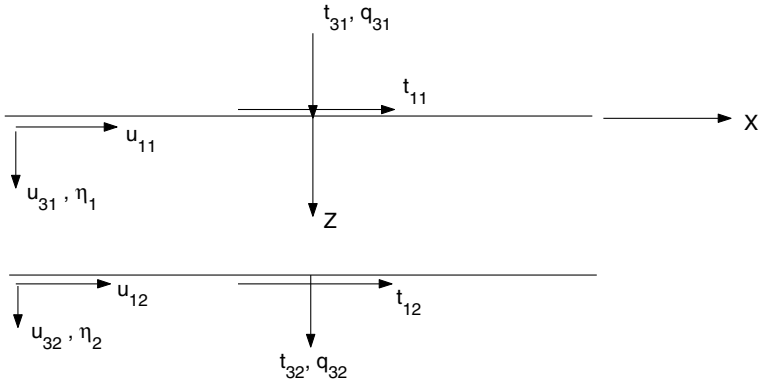

Fig. 7.13. Layer element and associated dof

7.3.1 Inhomogeneous Anisotropic Material

The governing equation for linear coupled dynamic thermoelasticity when applied to an anisotropic and inhomogeneous material and 2-D geometry is obtained from Equations (7.14) and Equations (7.15) by imposing the following assumptions. It is assumed that all the variables are functions of only $x_1 = x$ and $x_3 = z$ and $u_2 = 0$. Under these conditions Equation (7.14) becomes

$$\begin{aligned} Q_{11}u_{xx} + Q_{13}w_{xz} + Q_{55}(u_{zz} + w_{xz}) + Q'_{55}(u_z + w_x) \\ -\beta_{11}\eta_x + t_1\beta_{11}\dot{\eta}_x = \rho\ddot{u} \\ Q_{13}u_{xz} + Q_{33}w_{zz} + Q_{55}(u_{xz} + w_{xx}) + Q'_{13}u_x + Q'_{33}w_z \\ -\beta_{33}\eta_z - \beta'_{33}\eta + t_1\beta_{33}\dot{\eta}_z + t_1\beta'_{33}\dot{\eta} = \rho\ddot{w}\,. \end{aligned} \quad (7.16)$$

Similarly, the heat conduction equation (Equation (7.15)) becomes

$$\begin{aligned} \rho C_e(t_2\ddot{\eta} + \dot{\eta}) + T_\circ\beta_{11}(\dot{u}_x + \tau_\circ\ddot{u}_x) + T_\circ\beta_{33}(\dot{w}_x + \tau_\circ\ddot{w}_z) - \\ K_{11}\eta_{xx} - K_{33}\eta_{zz} - K'_{33}\eta_z = 0\,, \end{aligned} \quad (7.17)$$

The essential boundary conditions associated with these equations are the specifications of u, w or η. The natural boundary conditions are the specifications of the surface tractions (t_x or t_z) and heat flow rate q_x or q_z in the frequency domain. The tractions are specified as

$$t_x = \sigma_{xx}n_x + \sigma_{xz}n_z\,, t_x = \sigma_{xz}n_x + \sigma_{zz}n_z\,, \quad (7.18)$$

whereas, from the generalized relation

$$q_i = -K_{ij}\eta_{,j} - \tau_\circ\dot{q}_i\,, \quad (7.19)$$

the heat flow rate in the frequency domain becomes

$$q_x = -\psi K_{11}\eta_{,x} n_x\,, \quad q_z = -\psi K_{33}\eta_{,z} n_z\,, \psi = (1 + j\tau_\circ\omega_n)^{-1}\,. \tag{7.20}$$

The displacement and the thermal field are assumed to be a synthesis of the frequency and wavenumbers, both horizontal and vertical, as

$$\left\{\begin{array}{c} u(x,z,t) \\ w(x,z,t) \\ \eta(x,z,t) \end{array}\right\} = \sum_{n=0}^{N-1}\sum_{m=1}^{M} \left\{\begin{array}{c} \hat{u}(z,\eta_m,\omega_n) \\ \hat{w}(z,\eta_m,\omega_n) \\ \hat{\eta}(z,\eta_m,\omega_n) \end{array}\right\} e^{-j(\eta_m x - \omega_n t)}\,, \tag{7.21}$$

where ω_n is the discrete angular frequency, η_m is the discrete horizontal wavenumber.

To get the expressions for $\hat{u}(z)$, $\hat{w}(z)$ and $\hat{\eta}(z)$, Equation (7.21) needs to be substituted in Equations (7.16) and (7.17), which results in three ODEs for $\hat{u}(z)$, $\hat{w}(z)$ and $\hat{\eta}(z)$, where ω_n and η_m will be present as parameters. The equation in matrix–vector notation is

$$\mathbf{A}\hat{\mathbf{u}}'' + \mathbf{B}\hat{\mathbf{u}}' + \mathbf{C}\hat{\mathbf{u}} = \mathbf{0}\,, \quad \hat{\mathbf{u}} = \{\hat{u}\ \hat{w}\ \hat{\eta}\}\,. \tag{7.22}$$

The matrices $\mathbf{A}$, $\mathbf{B}$ and $\mathbf{C}$ (all functions of z) are

$$\mathbf{A} = \begin{bmatrix} Q_{55} & 0 & 0 \\ 0 & Q_{33} & 0 \\ 0 & 0 & -K_{33} \end{bmatrix}, \tag{7.23}$$

$$\mathbf{B} = \begin{bmatrix} Q'_{55} & -j(Q_{13}+Q_{55})\eta_m & 0 \\ -j(Q_{13}+Q_{55})\eta_m & Q'_{33} & \beta_{33}(jt_1\omega_n - 1) \\ 0 & \beta_{33}T_\circ\omega_n(j - \tau_\circ\omega_n) & -K'_{33} \end{bmatrix}, \tag{7.24}$$

$$\mathbf{C} = \begin{bmatrix} -\eta_m^2 Q_{11} + \rho\omega_n^2 & -jQ'_{55}\eta_m & \beta_{11}\eta_m(j + t_1\omega_n) \\ -jQ'_{13}\eta_m & -\eta_m^2 Q_{55} + \rho\omega_n^2 & \beta'_{33}(jt_1\omega_n - 1) \\ T_\circ\omega_n\eta_m\beta_{11}(1 + j\tau_\circ\omega_n) & 0 & -\rho C_e\omega_n^2 t_2 + k_{11}\eta_m^2 + j\rho C_e\omega_n \end{bmatrix}. \tag{7.25}$$

Here again, the effect of inhomogeneity manifests in terms of diagonal terms in $\mathbf{B}$ and off-diagonal terms in $\mathbf{C}$, which are zero for homogeneous material. The associated boundary conditions are the specifications of stresses σ_{zz} and σ_{xz} and the heat flux at the layer interfaces, which are related to the unknowns as

$$\hat{\mathbf{s}} = \mathbf{D}\hat{\mathbf{u}}' + \mathbf{E}\hat{\mathbf{u}}\,, \hat{\mathbf{s}} = \{\sigma_{zz}\ \sigma_{xz}\ q_z\}\,, \tag{7.26}$$

where,

$$\mathbf{D} = \begin{bmatrix} 0 & Q_{33} & 0 \\ Q_{55} & 0 & 0 \\ 0 & 0 & -K_{33} \end{bmatrix}, \quad \mathbf{E} = \begin{bmatrix} -j\eta_m Q_{13} & 0 & \beta_{33}(jt_1\omega_n - 1) \\ 0 & -j\eta_m Q_{55} & 0 \\ 0 & 0 & 0 \end{bmatrix}, \tag{7.27}$$

and the matrices are functions of z. The BVP reduces to finding $\hat{\mathbf{u}}$, which satisfies Equation (7.22) for all $z \in \Omega_c$ and the specification of $\hat{\mathbf{u}}$ or $\hat{\mathbf{s}}$ at $z = 0$ or $z = L$. Once the solution is obtained for different values of z in

the frequency–wavenumber domain, the time domain solution is obtained by following the same procedure as outlined earlier.

Any kind of inhomogeneity can be tackled in this formulation if the BVP is solved numerically. However, as we have seen before, there is a special case for which the BVP is exactly solvable, and this is taken up next.

Exact Formulation

Let us assume that the material property variation is exponential, *i.e.,*

$$[Q_{ij}(z), K_{ij}(z), \beta_{ij}(z) = [Q_{ij\circ}, K_{ij\circ}, \beta_{ij\circ}]e^{\alpha z}\,, \quad \rho(z) = \rho_\circ e^{\beta z}\,, \tag{7.28}$$

where $Q_{ij\circ}$, $K_{ij\circ}$, $\beta_{ij\circ}$ and $\rho_\circ$ are constants. Substituting Equation (7.28) in Equations (7.24) and (7.25) we get

$$\mathbf{A} = \begin{bmatrix} Q_{55\circ} & 0 & 0 \\ 0 & Q_{33\circ} & 0 \\ 0 & 0 & -K_{33\circ} \end{bmatrix} e^{\alpha z}\,, \tag{7.29}$$

$$\mathbf{B} = \begin{bmatrix} \alpha Q_{55\circ} & -j(Q_{13\circ} + Q_{55\circ})\eta_m & 0 \\ -j(Q_{13\circ} + Q_{55\circ})\eta_m & \alpha Q_{33\circ} & \beta_{33}(jt_1\omega_n - 1) \\ 0 & \beta_{33}T_\circ\omega_n(j - \tau_\circ\omega_n) & -\alpha K_{33\circ} \end{bmatrix} e^{\alpha z} \tag{7.30}$$

$$\mathbf{C} = \begin{bmatrix} -\eta_m^2 Q_{11\circ} + \rho_\circ\omega_n^2\gamma & -j\alpha Q_{55\circ}\eta_m & \beta_{11}\eta_m(j + t_1\omega_n) \\ -j\alpha Q_{13\circ}\eta_m & -\eta_m^2 Q_{55\circ} + \rho_\circ\omega_n^2\gamma & \alpha\beta_{33\circ}(jt_1\omega_n - 1) \\ T_\circ\omega_n\eta_m\beta_{11}(1 + j\tau_\circ\omega_n) & 0 & -\rho C_e\omega_n^2 t_2\gamma + k_{11}\eta_m^2 + j\rho C_e\omega_n\gamma \end{bmatrix}, \tag{7.31}$$

where $\gamma = e^{(\beta-\alpha)z}$ and the elements of $\mathbf{C}$ are to be multiplied by $\exp(\alpha z)$. Substituting Equations (7.29), (7.30) and (7.31) in Equation (7.22) and cancelling the $e^{\alpha z}$ term, another equation is obtained in which the matrices $\mathbf{A}$ and $\mathbf{B}$ are of constant coefficients, but $\mathbf{C}$ has a z dependency in terms of γ. If β is equal to α then $\gamma = 1$ and all the matrices become constants. Then the solutions are in the form of $u_\circ e^{-jkz}$, $w_\circ e^{-jkz}$ and $\eta_\circ e^{-jkz}$, where $u_\circ$, $w_\circ$, $\eta_\circ$ and k, the vertical (Z direction) wavenumbers, are unknowns.

However, for the more general case $\beta \neq \alpha$, we again assume that the e^{jkz} type of solution is still possible, which will yield an approximate solution. The γ is again evaluated at $z = L/2$. Substituting these solutions in Equation (7.22) for the matrices given by Equations (7.29), (7.30) and (7.31), the problem becomes one of finding nontrivial $u_\circ$, $w_\circ$, $\eta_\circ$ from the equation

$$\mathbf{W}\{\mathbf{u}_\circ\} = \mathbf{0}\ \ , \mathbf{W} = -k^2\mathbf{A} - jk\mathbf{B} + \mathbf{C}\,, \{\mathbf{u}_\circ\} = \{u_\circ\ w_\circ\ \eta_\circ\}\,, \tag{7.32}$$

where $\mathbf{W}$ is the wave matrix. Elements of $\mathbf{W}$ are

$$W_{11} = -k^2 Q_{55} - \eta_m^2 Q_{11} + \rho\omega_n^2 - jk\alpha Q_{55}$$
$$W_{12} = -k\eta_m(Q_{13} + Q_{55}) - j\eta_m\alpha Q_{55}$$

$$
\begin{aligned}
W_{13} &= \beta_{11}\eta_m(j + t_1\omega_n) \\
W_{21} &= -k\eta_m(Q_{13} + Q_{55}) - j\eta_m\alpha Q_{13} \\
W_{22} &= -k^2 Q_{33} - \eta_m^2 Q_{55} + \rho\omega_n^2\gamma - jk\alpha Q_{33} \\
W_{23} &= -jk\beta_{33}(jt_1\omega_n - 1) - \alpha\beta_{33}(1 - jt_1\omega_n) \\
W_{31} &= T_\circ\eta_m\omega_n\beta_{11}(1 + j\tau_\circ\omega_n) \\
W_{32} &= -jkT_\circ\omega_n\beta_{33}(j - \tau_\circ\omega_n) \\
W_{33} &= k^2 K_{33} + \eta_m^2 K_{11} + \rho C_e\omega_n(j - t_2\omega_n) + jk\alpha K_{33}\,.
\end{aligned} \tag{7.33}
$$

Thus, in this case, $N_v = 3$ and $p = 2$, *i.e.,* there are six wavenumbers which are the roots of the characteristics equation, *i.e.,* the spectrum relation (obtained from the singularity condition of $\mathbf{W}$)

$$
C_1 k^6 + C_2 k^5 + C_3 k^4 + C_4 k^3 + C_5 k^2 + C_6 k + C_7 = 0\,, \tag{7.34}
$$

where $C_i = C_i(\omega_n, \eta_m,\ etc.)$. Explicit forms of the coefficients C_i are omitted here as they are too lengthy. It is to be noted that for each value of η_m and ω_n, there are six values of k, denoted by $k_{lmn}, l = 1, \ldots, 6$, which will be obtained by solving the spectrum relation.

7.3.2 Discussion on the Properties of Wavenumbers

The coefficients in Equation (7.34) are complex (except C_1) and thus the roots are not complex conjugate to each other. Further, the expression governing the cut-off frequencies (given by $C_7 = 0$), is not in simple enough form to make quick estimations. In this situation, it is necessary to study the wavenumbers and the cut-off frequency variation numerically for a particular material. A GFRP composite layer is considered with the following material properties:

$$
\begin{array}{cccc}
E_1 = 144.4\text{ GPa}, & E_3 = 9.632\text{ GPa}, & \nu_{13} = 0.3\,, & \nu_{23} = 0.02\,, \\
G_{13} = 4.12\text{ GPa}\,, & \rho = 1389\text{kg/m}^3\,, & \alpha_{11} = 6.36 \times 10^{-6}\,, & \alpha_{33} = 32.6 \times 10^{-6}\,, \\
K_{11} = 204 \times 10^5\text{W/m}^2\,, & K_{33} = K_{11}\,, & T_\circ = 300K\,, & \tau_\circ = 0\,, \\
t_1 = 0.5 \times 10^{-6}\text{s}\,, & t_2 = t_1\,, & C_e = 940\,. &
\end{array} \tag{7.35}
$$

It is to be noted that we have taken a rather unrealistic value for K_{11} (and K_{33} in turn). This is to bring the thermal wavenumber to the same order as that of the mechanical wavenumber. However, the actual value is only 204 and consequently, the actual value of the wavenumber is approximately $100\sqrt{10}$ times the computed value. The material is made inhomogeneous by setting the gradation parameters, α and β equal to 100. For comparison, the homogeneous anisotropic case is also considered side by side. In the subsequent plots of wavenumber variation, R and I in the superscript denote real and imaginary part, respectively.

Figure 7.14 shows the wavenumber variation for $\eta_m = 0$. In the figure, k_1 and k_2 denote the elastic modes and k_3 is the thermal mode. The left subplot indicates the homogeneous case, where the right one indicates the

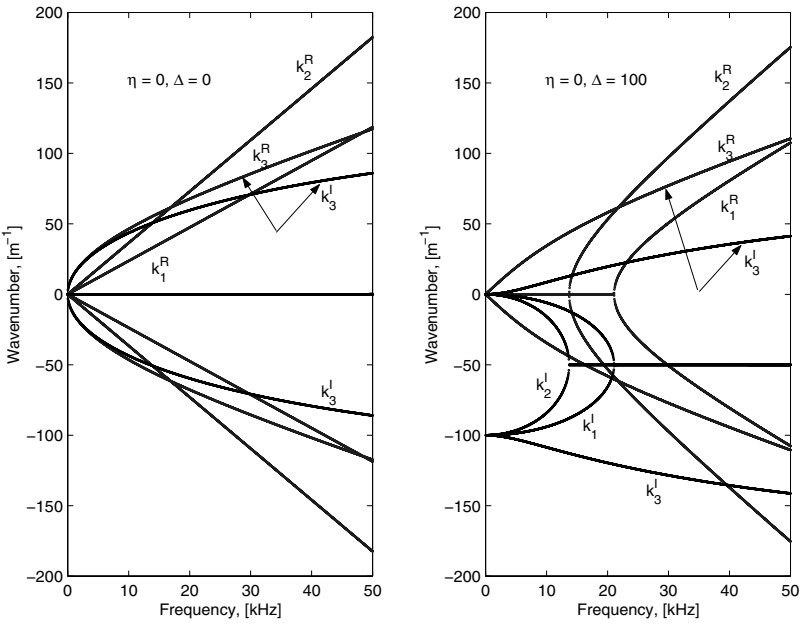

Fig. 7.14. Variation of wavenumber with ω_n, $\eta_m = 0$, $\theta = 0^\circ$

graded material (Δ denotes both α and β). The arrows show the thermal wavenumbers, which are scaled down by changing the values of K_{ii}. As the figure suggests, the effect of the inhomogeneity is dominant in the mechanical wavenumbers, where even at $\eta_m = 0$, cut-off frequencies appear, similar to the inhomogeneous layer wavenumbers, shown previously. The thermal wavenumbers are least affected due to this gradation. It is to be noted that, all the imaginary components of the wavenumbers are symmetric about -50 m^{-1}, which is exactly $-\Delta/2$.

Figure 7.15 shows the variation in the wavenumbers for $\eta_m = 10$ m^{-1}. A similar trend to the previous figure can be seen here. The thermal wavenumber is not susceptible to gradation at all, whereas, the mechanical wavenumbers develop higher cut-off frequencies (at around 3 kHz (k_2) and 16 kHz (k_1)) compared to the homogeneous wavenumbers. All the modes have non-zero imaginary part at higher frequencies, which enables the modulation of wave magnitude while propagating. As in the previous cases, the imaginary parts of the wavenumbers are symmetric about $-\Delta/2$.

It is to be noted that the earlier definition of cut-off frequency is not valid here, since the wavenumbers are not purely real or imaginary. The governing equation for cut-off frequencies is given by $C_7 = 0$, which in expanded form is

$$c_1\omega^6 + c_2\omega^5 + c_3\omega^4 + c_4\omega^3 + c_5\omega^2 + c_6\omega + c_7 = 0\,. \tag{7.36}$$

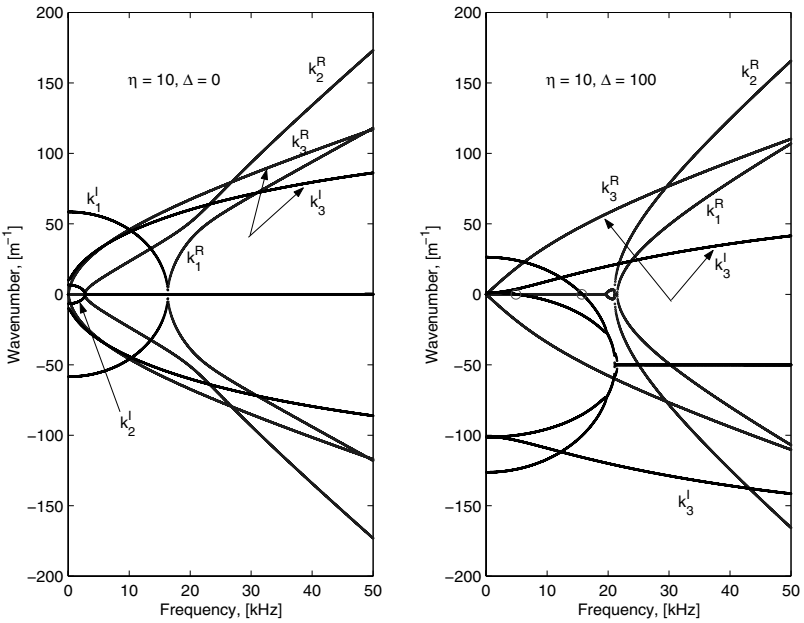

Fig. 7.15. Variation of wavenumber with ω_n, $\eta_m = 10$, $\theta = 0^\circ$

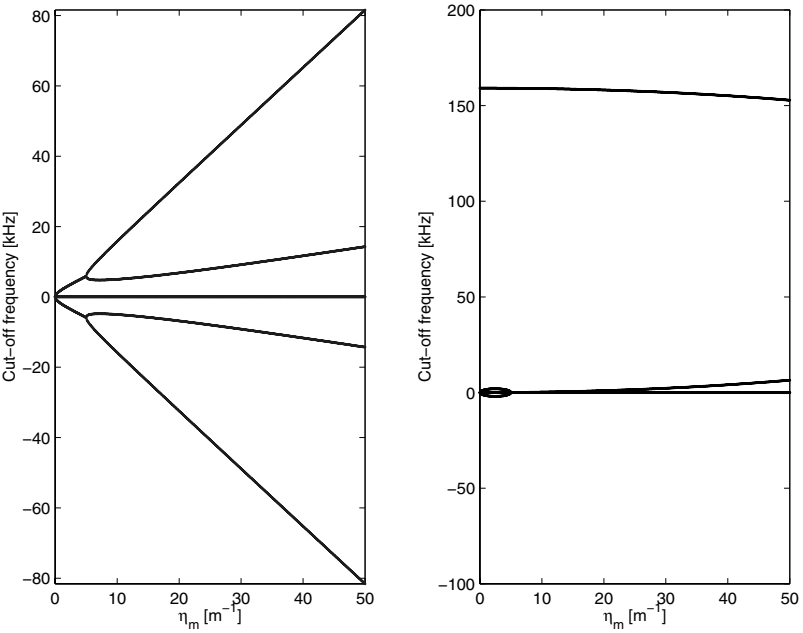

Fig. 7.16. Variation of cut-off frequencies with η_m, $\theta = 0^\circ$

As the equation suggests there are six roots of ω, which may be complex, since the coefficients c_i are complex. However, it is only the real positive roots that are of physical significance. This is because the $k-\omega$ space that is considered in the analysis contains only positive real ω. The explicit forms of the coefficients are

$$
\begin{aligned}
c_1 &= -\rho^3 C_e t_2 \,, \\
c_2 &= j\rho^3 C_e - jT_\circ \tau_\circ \eta_m^2 \beta_{11}^2 t_1 \rho \,, \\
c_3 &= T_\circ \tau_\circ \eta_m^2 \beta_{11}^2 \rho + \rho^2 Q_{55} \eta_m^2 C_e t_2 + \rho^2 k_{11} \eta_m^2 + Q_{11} \eta_m^2 \rho^2 C_e t_2 - T_\circ \eta_m^2 \beta_{11}^2 t_1 \rho \,, \\
c_4 &= -jQ_{11} \eta_m^2 \rho^2 C_e - j\rho^2 Q_{55} \eta_m^2 C_e - jT_\circ \eta_m^2 \beta_{11}^2 \rho + jT_\circ \tau_\circ \eta_m^4 \beta_{11}^2 t_1 Q_{55} \\
&\quad + jT_\circ \tau_\circ \eta_m^2 \beta_{11} \alpha^2 Q_{55} \beta_{33} t_1 \,, \\
c_5 &= -Q_{11} \eta_m^4 Q_{55} \rho C_e t_2 - Q_{11} \eta_m^4 \rho K_{11} - \rho Q_{55} \eta_m^4 K_{11} - T_\circ \tau_\circ \eta_m^4 \beta_{11}^2 Q_{55} \\
&\quad + T_\circ \eta_m^4 \beta_{11}^2 t_1 Q_{55} + T_\circ \tau_\circ \eta_m^2 \beta_{11} \alpha^2 Q_{55} \beta_{33} + T_\circ \eta_m^2 \beta_{11} \alpha^2 Q_{55} \beta_{33} t_1 \\
&\quad - \alpha^2 Q_{13} \eta_m^2 Q_{55} \rho C_e t_2 \,, \\
c_6 &= jT_\circ \eta_m^4 \beta_{11}^2 Q_{55} + jQ_{11} \eta_m^4 Q_{55} \rho C_e + jT_\circ \eta_m^2 \beta_{11} \alpha^2 Q_{55} \beta_{33} \\
&\quad + j\alpha^2 Q_{13} \eta_m^2 Q_{55} \rho C_e \,, \\
c_7 &= Q_{11} \eta_m^6 Q_{55} K_{11} + \alpha^2 Q_{13} \eta_m^4 Q_{55} K_{11} \,.
\end{aligned}
\tag{7.37}
$$

As the expressions suggest, c_2, c_4 and c_6 are essentially imaginary and the remaining coefficients are real. The presence of these imaginary coefficients renders the cut-off frequency imaginary, which is of no physical significance. The real and imaginary parts of the cut-off frequencies are shown in Figure 7.16. As seen in the figure, initially there is only one cut-off frequency and another one appears when $\eta_m \geq 6$. At these frequencies the absolute value of the wavenumber is zero. For example, at $\eta_m = 10$, the non-zero values of the real cut-off frequencies are 4.9 and 15.7 kHz. These points are shown as circles in Figure 7.15. It is evident that at this frequency both the real and the imaginary part of the pertinent wavenumber are zero. The real cut-off frequencies (after discarding the negative roots) correspond to the elastic modes. The remaining two roots are imaginary and they signify the presence of a propagating thermal mode at all frequencies. Further, the real roots vary in a non-linear fashion with η_m.

Once, the required wavenumbers k are obtained, for which the wave matrix $\mathbf{W}$ is singular, $\mathbf{u}_\circ$ is written as before

$$
\{\mathbf{u}_\circ\}_{nm} = [\mathbf{R}]_{3\times 6} [\mathbf{\Lambda}]_{6\times 6} \{\mathbf{a}\}_{6\times 1} \,, \tag{7.38}
$$

where the matrices are as described previously. Following the SVD method $\mathbf{R}$ is obtained.

7.3.3 Finite Layer Element (FLE)

Using Equation (7.38) for each value of ω_n and η_m, the nodal variables are related to the constants A_i as

$$\{u_{1nm}\ v_{1nm}\ \Theta_{1nm}\ u_{2nm}\ v_{2nm}\ \Theta_{2nm}\}^T = [\mathbf{T}_{1nm}]\{A_1\ \ A_2\ \ A_3\ \ A_4\ A_5\ A_6\}^T\,, \tag{7.39}$$

i.e.,

$$\{\hat{\mathbf{u}}\}_{nm} = [\mathbf{T}_1]_{nm}\{\mathbf{A}\}_{nm}\,. \tag{7.40}$$

The matrix $\mathbf{T}_{1nm}$ consists of the elements of $\mathbf{R}_{nm}$ suitably multiplied by $e^{-jk_{inm}L}$, $i = 1, \ldots, 6$, and its explicit form is given by

$$\begin{aligned} &T_1(p,q) = R(p,q)\,,\ p = 1\ldots 3\,, q = 1, \ldots, 6\,,\\ &T_1(p,q) = R(p-3,q)e^{-jk_qL}\,,\ p = 4, \ldots, 6\,, q = 1, \ldots, 6\,. \end{aligned} \tag{7.41}$$

Similarly, the nodal traction and heat flux vectors are related to the unknown constants by the relation

$$\{\hat{\mathbf{t}}\}_{nm} = [\mathbf{T}_2]_{nm}\{\mathbf{A}\}_{nm}\,, \tag{7.42}$$

where the elements of $\mathbf{T}_{2nm}$ are given by

$$\begin{aligned} T_2(1,p) &= jQ_{55\circ}(R_{1p}k_p + \eta R_{2p})\,,\\ T_2(2,p) &= jQ_{33\circ}R_{2p}k_p + jQ_{13\circ}\eta R_{1p}\psi_2\beta_{33}\,,\\ T_2(3,p) &= -j\psi_1 R_{3p}k_p K_{33\circ}\,,\\ T_2(4,p) &= -jQ_{55\circ}e^{\alpha L}(R_{1p}k_p + \eta R_{2p})e^{(-jk_pL)}\,,\\ T_2(5,p) &= \{-jQ_{33\circ}R_{2p}k_p - jQ_{13\circ}\eta R_{1p} - R_{3p}\psi_2\beta_{33\circ}\}e^{(-jk_pL+\alpha L)}\,,\\ T_2(6,p) &= j\psi_1 R_{3p}k_p K_{33\circ}e^{(-jk_pL+\alpha L)}\,. \end{aligned} \tag{7.43}$$

Thus, the 6×6 element dynamic stiffness matrix is obtained as

$$[\hat{\mathbf{K}}]_{nm} = [\mathbf{T}_2]_{nm}[\mathbf{T}_1]^{-1}_{nm}\,. \tag{7.44}$$

7.3.4 Infinite Layer Element (ILE)

Following the same procedure as defined, nodal variables of node 1 can be related to the constants by

$$\{\hat{\mathbf{u}}\}_{nm} = [\mathbf{T}_1]_{nm}\{\mathbf{A}\}_{nm}\,. \tag{7.45}$$

Similarly, the tractions and the heat flux at node 1 can be related to the constants by

$$\{t_{x1}\ t_{z1}\ q_{z1}\}^T_{nm} = [\mathbf{T}_2]_{nm}\{A_{1nm}\ A_{2nm}\ A_{3nm}\}^T\,, \textit{i.e.,}\ \{\hat{\mathbf{t}}\}_{nm} = [\mathbf{T}_2]_{nm}\{\mathbf{A}\}_{nm}\,. \tag{7.46}$$

Explicit forms of the matrix $\mathbf{T}_1$ and $\mathbf{T}_2$ are

$$\mathbf{T}_{1(ILE)} = \mathbf{T}_{1(FLE)}(1:3, 1:3)\,, \quad \mathbf{T}_{2(ILE)} = \mathbf{T}_{2(FLE)}(1:3, 1:3)\,. \tag{7.47}$$

The tractions at node 1 can be related to the displacements at node 1 to obtain the dynamic stiffness matrix as

$$\{\hat{\mathbf{t}}\}_{nm} = [\mathbf{T}_2]_{nm}[\mathbf{T}_1]^{-1}_{nm}\{\hat{\mathbf{u}}\} = [\hat{\mathbf{K}}]_{nm}\{\hat{\mathbf{u}}\}_{nm}\,, \tag{7.48}$$

where $\hat{\mathbf{K}}_{nm}$ is the (3×3) element stiffness matrix.

7.3.5 Homogeneous Anisotropic Material

It is to be noted that one can deduce the dynamic stiffness matrix from Equations (7.44) and (7.48) by substituting $\alpha = 0 = \beta$ and $\gamma = 1$.

7.4 Numerical Examples

Most of the examples covered in this section are for homogeneous anisotropic material, as gradation has very little effect on the thermal response. We first study the effect of different parameters on the response of a layered structure. Simultaneously, the developed spectral element is validated to establish its accuracy and efficiency with respect to the conventional purely elastic 2-D FE solutions. Also the responses of a generally stacked laminate structure are analysed for thermal flux and mechanical pulse loading. Next, the stress wave propagation through layered anisotropic media is studied. Subsequently, mechanical and thermal wave propagation due to specified temperature shock is analyzed. Finally, the effect of gradation on mechanical and thermal response is demonstrated.

7.4.1 Effect of the Relaxation Parameters - Symmetric Ply-layup

Wave propagation in a symmetrically stacked composite layer is studied in this section and the results of pure elastic analyses are compared with 2-D FE solutions. The layers are made up of GFRP composites whose material properties are as assumed previously in the example involving wavenumber computation. The ply sequence considered is $[0^\circ_{10}]$, where each lamina is 1 mm thick. The bottom of the layered system is assumed fixed. The objective is to validate the present element, show its efficiency and study the effect of t_1 and t_2 on the response. It is expected that the effect of these parameters will be more pronounced at higher frequencies. For this reason, the same pulse loading as in previous examples is considered (Figure 5.3).

First, the layered system is impacted in the Z direction, at the center of the top surface ($z = 0$), as is shown in Figure 7.17. This kind of loading primarily generates QP waves. The response of the structure, in terms of the velocity in the Z direction, is measured at the same location. The FE analysis is carried out for this loading and geometry, where the effect of thermoelasticity is neglected. For FE analysis, the layer is modeled with 1200, 3-noded plane-strain FEs. In comparison, there is only one FLE in the spectral model. The FE model results in a global system matrix of size 1215×42, whereas, the spectral model results in a global system matrix (dynamic stiffness matrix) of size 3×3. While solving via FE analysis, Newmark's time integration is adopted with a time step of 1 μs. For spectral analysis, the load is sampled at 48.83 Hz with 2048 (N in Equation 6.33) FFT points. Further, for spatial variation, 32 Fourier series coefficients (M in Equation 6.33) are considered.

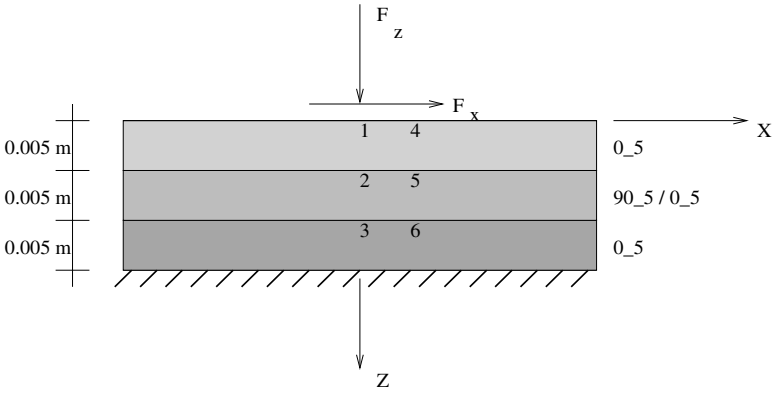

Fig. 7.17. Layered structure for symmetric/asymmetric ply orientation

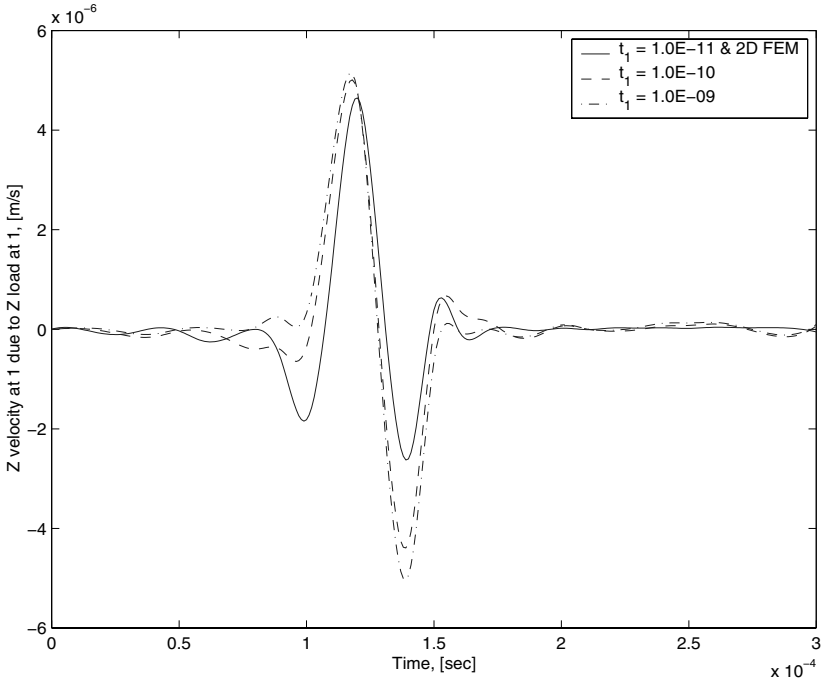

Fig. 7.18. Effect of t_1 on mechanical response, $t_2 = 0$ in GL model

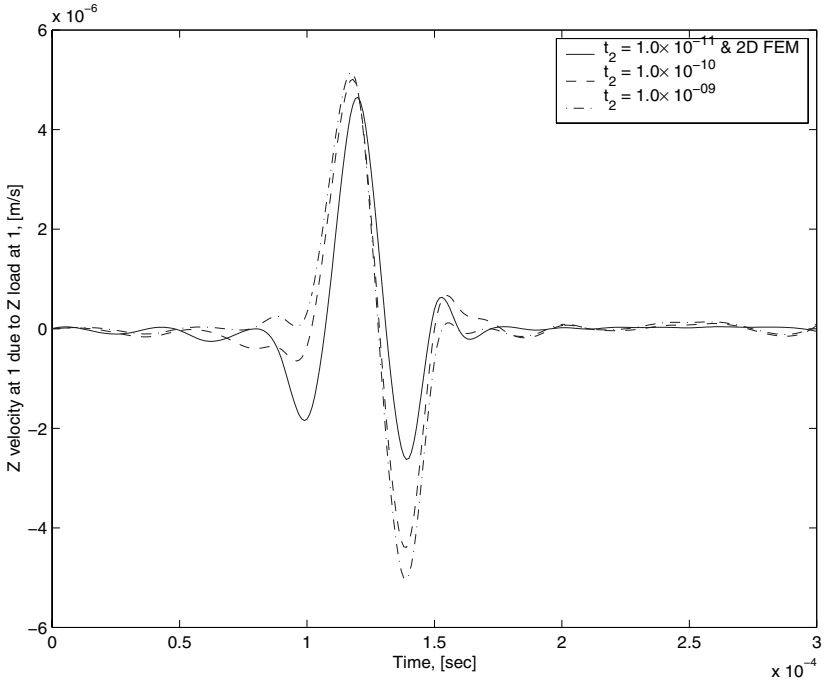

Fig. 7.19. Effect of t_2 on mechanical response, $t_1 = 0$ in GL model

First, the GL model is taken for which $\tau_\circ = 0$, although t_1 and t_2 are non-zero. The simulation is carried out for three values of t_1, keeping $t_2 = 0$. Then, t_2 is varied keeping t_1 fixed at zero. These results are plotted in Figure 7.18 and 7.19, respectively. Figure 7.18 shows the variation in mechanical responses for different values of t_1. As the figure suggests, increase in t_1 decreases the impedance of the structure as the magnitudes of both the initial velocity and subsequent reflection increase. Also, for the case of $t_1 = 1.0 \times 10^{-11}$, the effect of thermo-elastic coupling is not so strong and the response matches exactly with the FE analysis result. Similar variation of the mechanical responses can be observed for the variation of t_2 (shown in Figure 7.19). It is interesting to note that for the values of t_1 and t_2 outside the range taken in this analysis, the response is insensitive to the parametric change. Thus the effect is strongly felt only within this region of variation, *i.e.,* $t_i = 1.0 \times 10^{-11}$ to $t_i = 1.0 \times 10^{-09}$ s.

Although the effect of t_1 and t_2 can be felt strongly in the GL model, the one-parameter LS model (only $\tau_\circ$) shows no sensitivity to the variation. For the previously applied low frequency loading, the LS model shows negligible variation and hence is not shown graphically. Quantitatively it can be said that, for a variation of $\tau_\circ$ from 10^{-06} to 10^{-09}, only 0.12% difference is observed in the maximum response. It is important to note that the effect of the

thermal relaxation parameters on the mechanical wavenumbers may be negligible, although they may have a significant effect on the thermal wavenumber and speeds. However, the responses (both mechanical and thermal) are predominantly built on the mechanical wavenumbers and that is the reason for their lack of sensitivity.

For the same symmetric ply-layup and loading (Figure 5.3), applied at the same location as before, the Z velocity, $\dot{w}$ is measured at the surface and the two interfaces, points marked by 1, 2 and 3, respectively, whose Z coordinates are 0.0 m, 0.005 m and 0.01 m. The measured responses are plotted in Figure 7.20. As shown in the figure, a small attenuation is visible, which is due to the presence of the thermal field. Further, the shift in the appearance of each waveform is due to the small time taken for propagation over a distance of 5 mm.

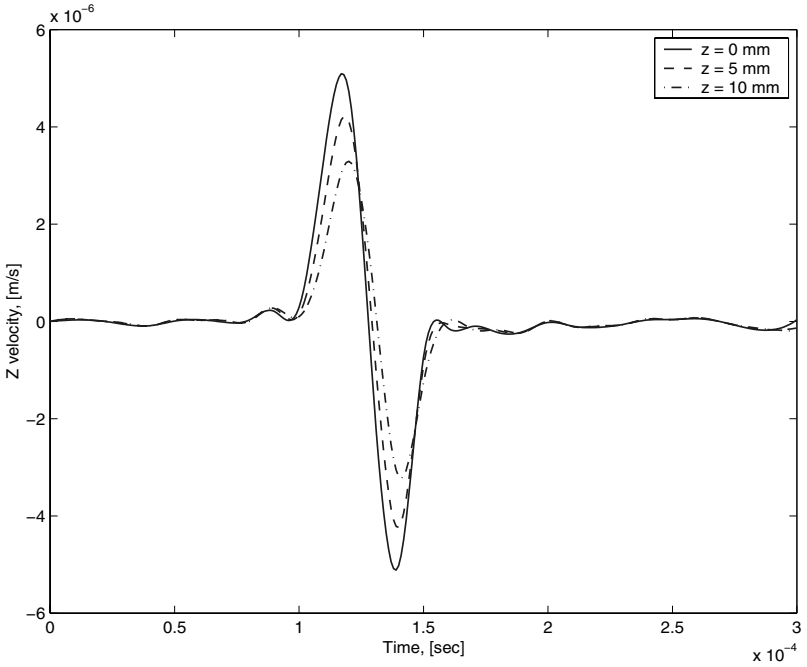

Fig. 7.20. Surface and interfacial waves, $\dot{w}$, due to mechanical loading

7.4.2 Interfacial Waves: Thermal and Mechanical Loading

Next, we consider an asymmetric ply-layup ($[0^\circ_5/90^\circ_5/0^\circ_5]$, see Figure 7.17) where the lamina thickness is kept the same as before. The material is GFRP, whose properties are specified in Section 7.3.2. The high frequency load is

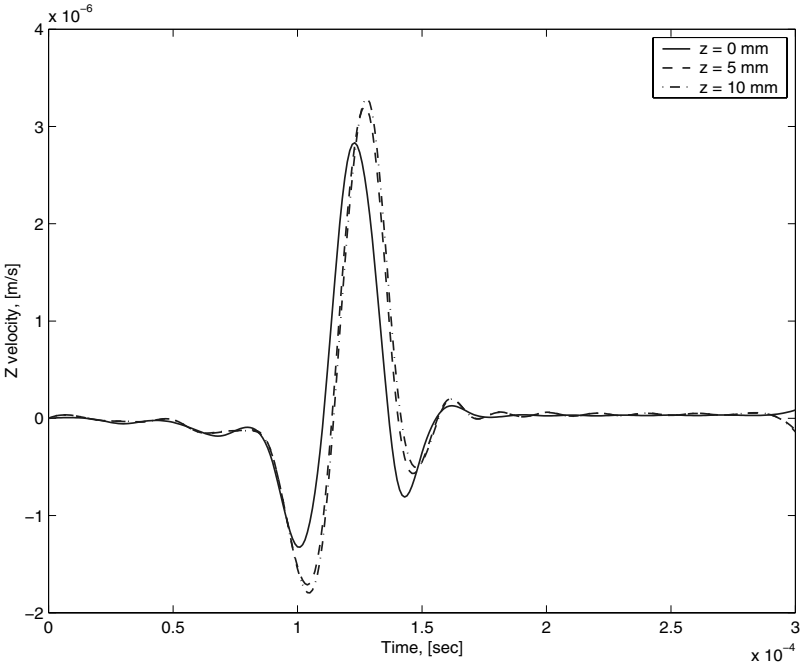

Fig. 7.21. Surface and interfacial waves, $\dot{w}$, due to mechanical loading, asymmetric ply-stacking

again applied at the mid-point of the top surface (point 1) and $\dot{w}$ is measured at the surface (point 1) and the two interfaces (points marked by 2 and 3) and plotted in Figure 7.21. The figure reveals that there are two significant differences in the waveforms compared to the symmetric ply case. First, there is no tangible difference in the amplitudes of the two interfacial waves and second, their magnitudes are larger than the surface wave magnitude, which is an artefact of the coupled thermo-elastic field. Also, the asymmetry gives rise to dispersion, which is not so dominant in the symmetric ply-stacking layer.

Overall, this example shows the propagation of surface and interfacial waves in composite layers triggered due to both mechanical and thermal loading.

7.4.3 Propagation of Stress Waves

In this section, the formulated element is employed to study stress wave propagation in layered media. The same layered system as the previous example is taken in this study for both symmetric and asymmetric ply-orientations. Tractions are specified in both X and Z directions, where the previous load history (Figure 5.3) is applied. In this study the GL model is used and to find

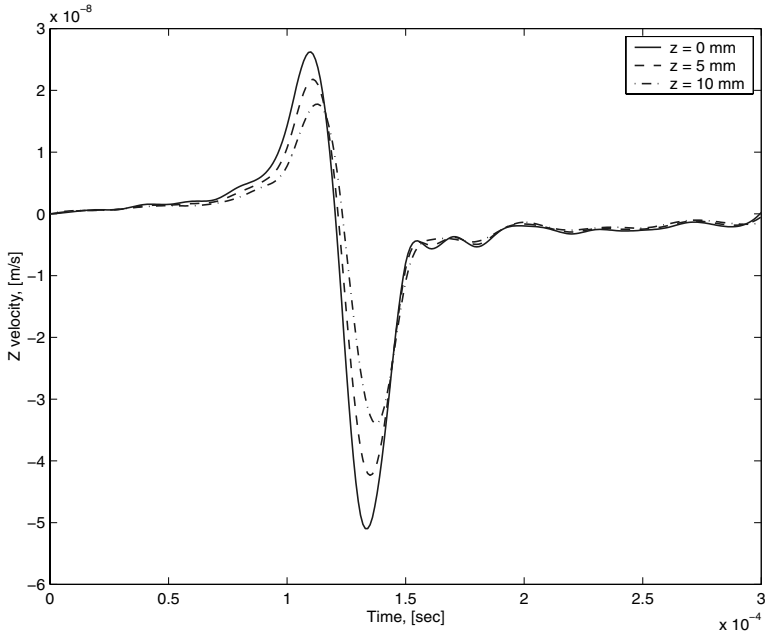

Fig. 7.22. Surface and interfacial waves, $\dot{w}$, due to thermal loading, symmetric ply-stacking

the effect of the thermal relaxation parameters, two sets of data are considered. In the first set, t_1 and t_2 are assumed to be 10^{-06} and 10^{-12}, whereas, in the second set t_1 and t_2 are taken as zero. In all the subsequent figures showing variation of stresses, the left subplots represent the first set and the right subplots represent the second set.

First, traction is applied in the Z direction at point 1, and the normal stress σ_{zz} is measured at the surface and two interfaces. The normalized stresses (with respect to the surface stress of set 1) are shown in Figures 7.23 and 7.24, for symmetric and asymmetric lay-up, respectively. As is seen in the figure, at the surface the stress history profile is exactly the same as the applied traction, which is expected. However, at the interfaces, the peak appears after a certain interval of time, which is not discernible in symmetric ply-layup although clearly visible in asymmetric ply-layup. This time lag is due to the finite propagation speed, which is lower in 90° lamina. Further, multiple reflections are visible at the interfaces, which result in both tensile and compressive stresses. These stresses will be responsible for delamination or matrix cracking, if they exceed the allowable limit. The effect of t_1 and t_2 can be seen in the reduction of the peak interfacial stresses and magnification of the reflected interfacial stresses. However, the surface stresses remain unaffected. Thus classical thermo-elastic analysis overestimates the peak interfacial stresses and underestimates the reflected interfacial stresses.

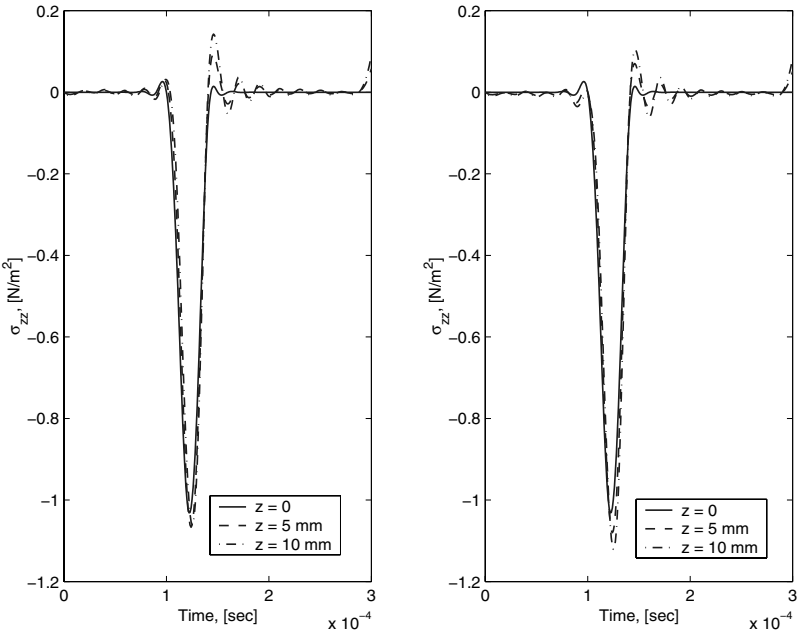

Fig. 7.23. Surface and interfacial stresses, σ_{zz}, due to t_z, symmetric ply-stacking

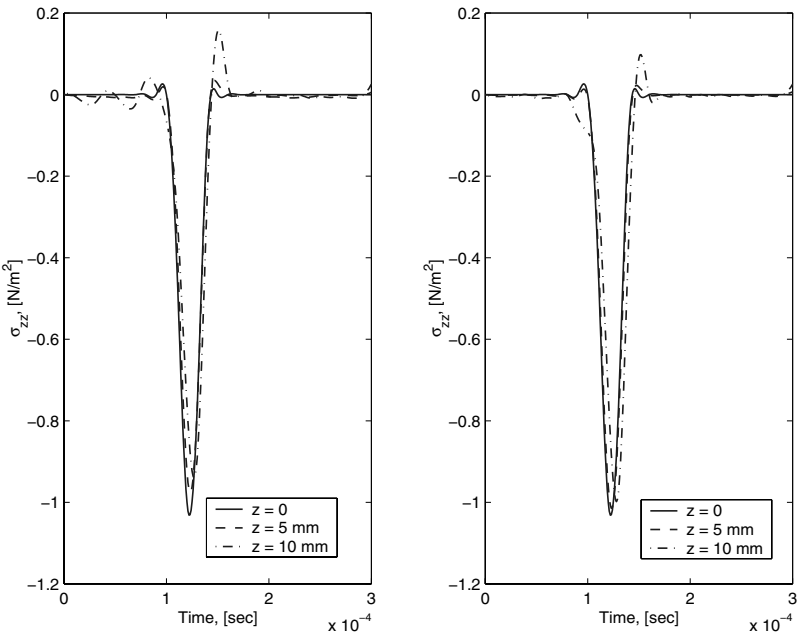

Fig. 7.24. Surface and interfacial stresses, σ_{zz}, due to t_z, asymmetric ply-stacking

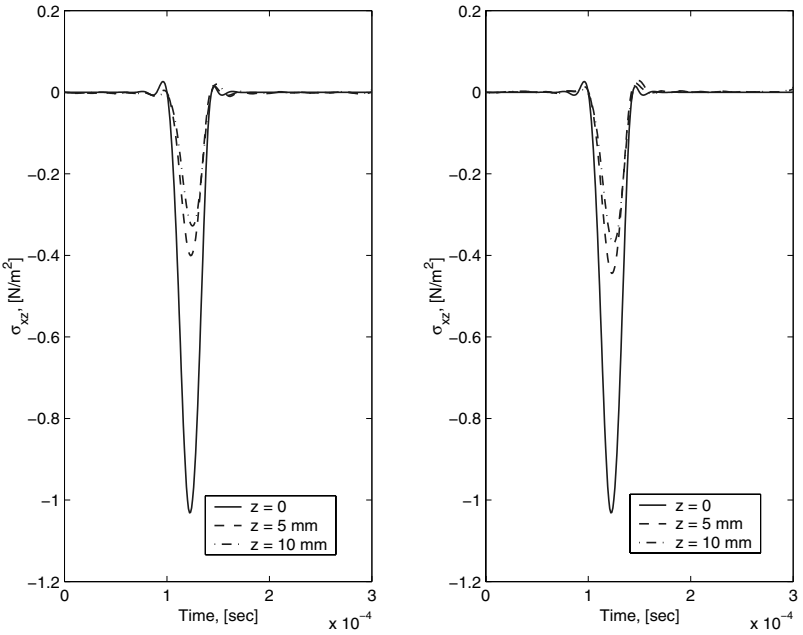

Fig. 7.25. Surface and interfacial stresses, σ_{xz}, due to t_x, symmetric ply-stacking

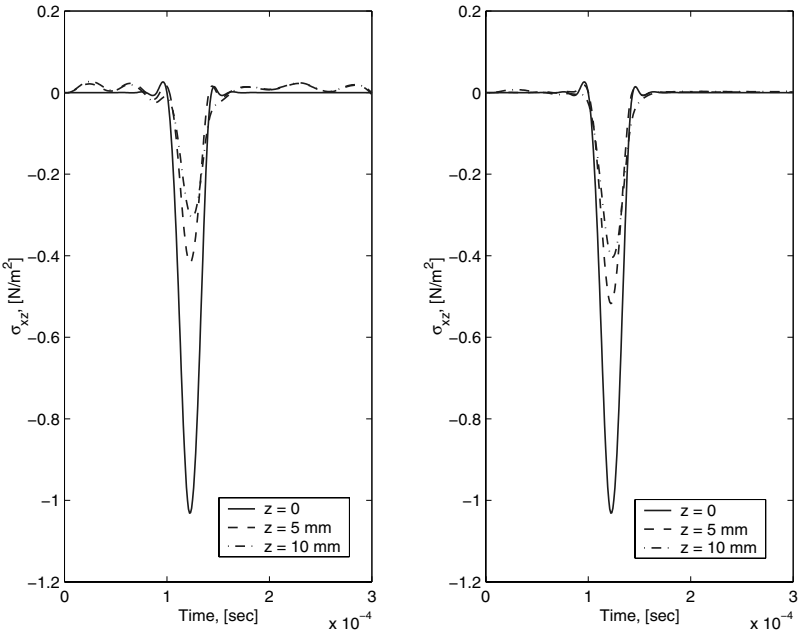

Fig. 7.26. Surface and interfacial stresses, σ_{xz}, due to t_x, asymmetric ply-stacking

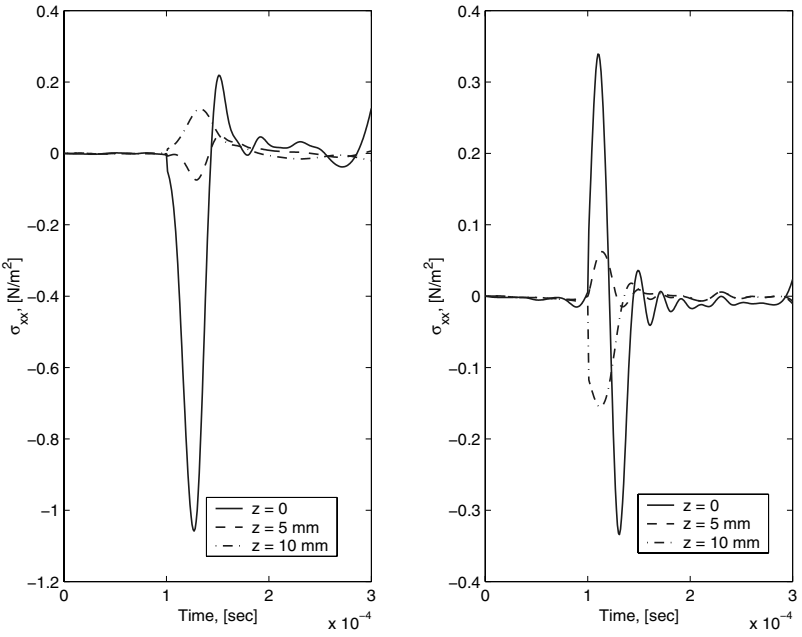

Fig. 7.27. Surface and interfacial stresses, σ_{xx}, due to t_x, symmetric ply-stacking

Next, the load is applied in the X direction at point 1 and shear stress (τ_{xz}) is measured at the surface and interfaces at an X coordinate of 0.01 m (points marked by 4, 5 and 6, respectively). Variation of the shear stresses are shown in Figures 7.25 and 7.26. As usual, the surface stress waves are the same as the applied stress. However, dispersion occurs at the interfaces, which is more visible in the asymmetric layup. As observed previously, the presence of non-zero t_1 and t_2 does not affect the surface stress profile. However, they decrease the maximum magnitude of the interfacial stress waves in both symmetric and asymmetric lay-up. This difference in magnitude is larger in the asymmetric case. This overestimation of the shear stress (by the classical thermo-elastic theory) may become crucial for high thermal environment, where accurate prediction and economy in design are essential.

Finally, for t_x, variation of σ_{xx} is plotted in Figures 7.27 and 7.28. As the figures suggest, remarkable changes can be observed in stress distribution in the presence of non-zero t_1 and t_2. Here the surface stresses are also affected, which was not the case in the previous example. It is evident that for non-zero t_1 and t_2, the top surface is in compression and the second interface is in tension. However, for zero t_1 and t_2, the stress state is completely reversed and the reversal of the surface stress is visible, which is observed in both symmetric and asymmetric cases. In the asymmetric case, in addition, the magnitude of the second interfacial stress is larger than that of the symmetric case. Further, the effect of these parameters is larger in the asymmetric lay-

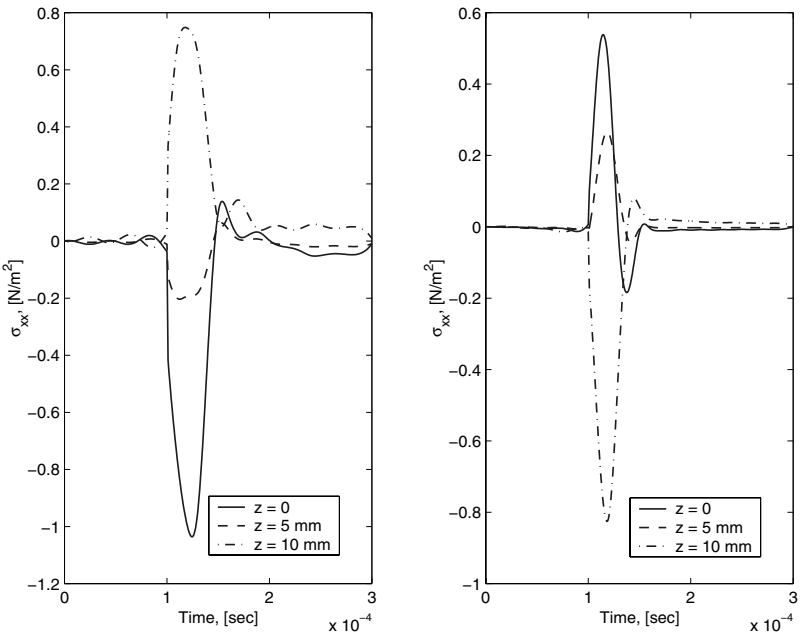

Fig. 7.28. Surface and interfacial stresses, σ_{xx}, due to t_x, asymmetric ply-stacking

up. The smoothing of the stresses at the surface, due to the presence of time parameters is beneficial for the structure.

7.4.4 Propagation of Thermal Waves

In this example, the propagation of thermal and mechanical waves due to temperature burst is investigated. The same layered structure (Figure 7.17) of previous examples is considered with symmetric ply-orientation. Temperature is specified at the top of the layer at point 1, whose time dependency is in the form of the previously applied loading (Figure 5.3). The Z velocity $\dot{w}$ and temperature T are measured at the surface and at the first interface (points 1 and 2, respectively). Figure 7.29 shows the variation of $\dot{w}$ (left subplot) and temperature (right subplot). As the magnitude of the velocity history suggests, the effect of the thermal shock is negligible on the mechanical field and is mostly compressive. The velocity profile of the interface shows discernible shift in time, which is due to comparatively low mechanical group speed.

As expected, the surface temperature history is exactly the same as the load history of Figure 5.3. However, the temperature at the interface has negligible magnitude compared to the surface temperature, although the pattern remains the same. Thus, the localized nature of the temperature field in space and time is again ascertained.

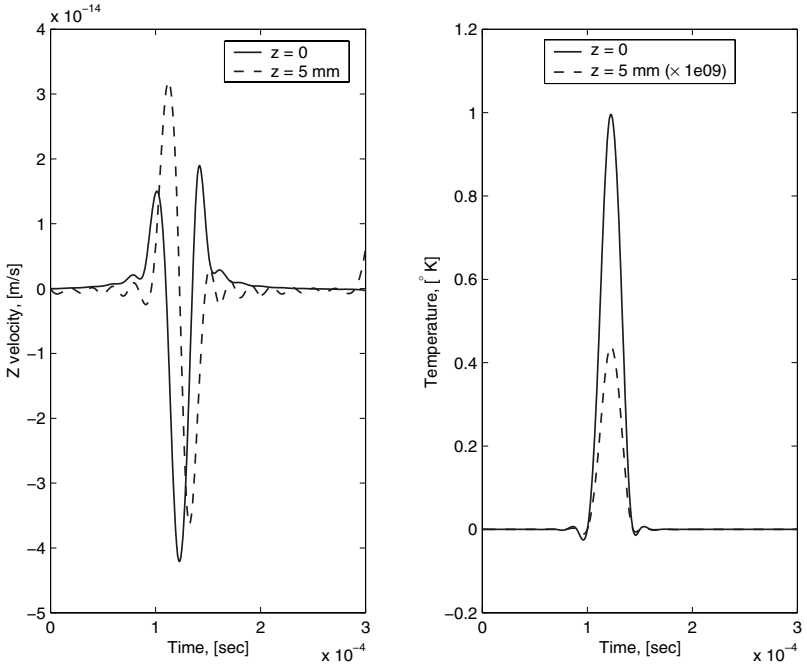

Fig. 7.29. Surface and interfacial mechanical waves due to thermal shock, symmetric ply-stacking

7.4.5 Effect of Inhomogeneity

In this section the effect of inhomogeneity on the thermal and mechanical waves due to thermal excitation is studied. A GFRP laminate of 10 mm thickness is chosen for this purpose. The top layer is subjected to a concentrated heat flux of unit amplitude and the bottom layer is fixed and the temperature is maintained at zero. Thermal and mechanical responses are measured at the surface. The layer is graded in the z direction exponentially, where α and β are set at 800. Figure 7.30 shows the variation of temperature (normalized with respect to the maximum value) measured at the point of impact. The figure shows that inhomogeneity has nominal effect on the incident pulse, whereas the decaying is marginally affected by the gradation.

Figure 7.31 shows the variation of transverse velocity, which reveals that the gradation has a significant effect on the response, where the peak amplitude is decreased by about 10%. Thus, for this thin layer, gradation has greater influence on the mechanical wave than the thermal wave.

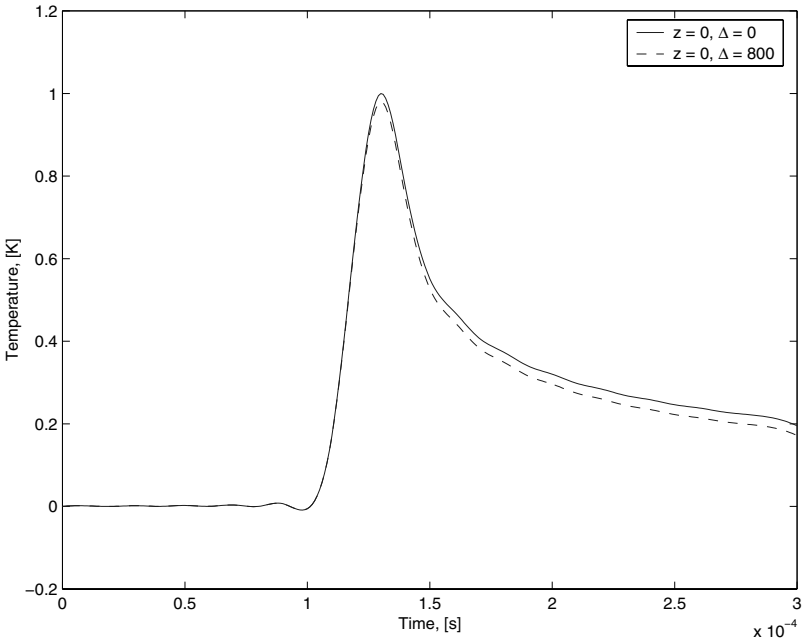

Fig. 7.30. Temperature profile at the surface and inside the layer

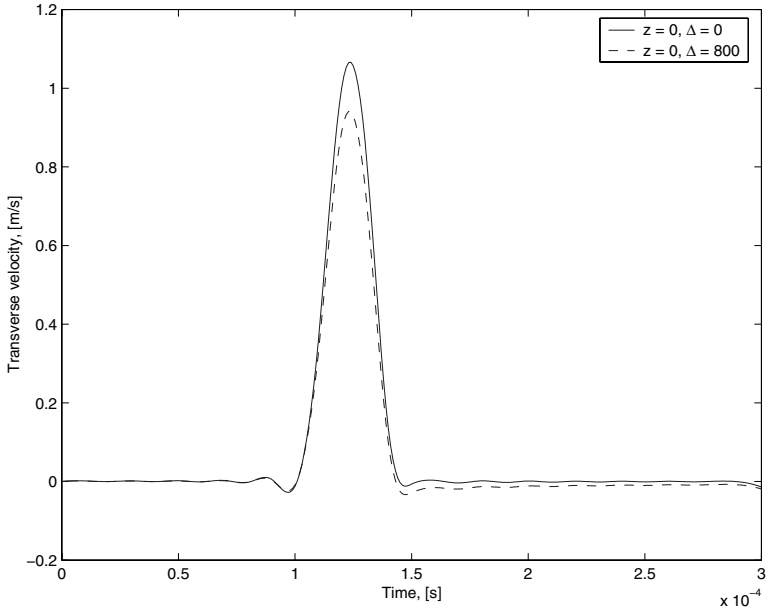

Fig. 7.31. Transverse velocity $\dot{w}$, at the surface and inside the layer

7.5 Wave Motion in Anisotropic and Inhomogeneous Plate

Although, there is a wealth of literature on the development of a composite plate element, there are few reports on the transient dynamic analysis in general and wave propagation analysis in particular. A few related works on the numerical modeling of the impact behavior of composite materials published so far are given here, but the list is in no way exhaustive. The modeling of particulate-loaded composite material is reported by Arias *et al.* [110], where a new model is implemented in a code, which validates experimental results. Closed form solutions for peak load and response due to small mass impact is given in [111], where the analysis is based on the Hertzian contact. The response of laminated composite plate under low velocity impact is studied by performing experiments and the result is validated by commercial software packages [112]. Similar experiments are conducted on glass/epoxy laminated composite plates for low velocity impact in [113]. The dynamic response of laminated composite plate is obtained by the strip element method, where the effect of rotary inertia is included [114]. Using effective laminate stiffness, an analytical model for wave propagation in multi-directional composite is proposed in [115]. Analysis of symmetric laminate to obtain the nature of impact response is done in [116]. Lee *et al.* [117] analyzed a composite folded plate structure, where third-order plate theory (TPT) was used. There are other studies on wave propagation in laminates due to low-velocity impact, mostly carried out by Mal and Lih [118], [119], [120], [121] and [122]. Further, wave propagation in composite laminate for antiplane loading was studied by Ma and Huang [123], where closed form expressions were found for displacements and stresses.

The spectral plate element (SPE) was developed by Doyle [9] for isotropic materials, where the in-plane and out of plane motions are not coupled and hence can be analyzed separately. For out-of-plane motion, Doyle formulated a wavenumber transform solution where the only unknown variable $w(x, y, t)$ was assumed to be given by

$$w(x, y, t) = \sum_{n} \sum_{m} \tilde{w}_{nm} \exp(-j\eta_m y) \exp(-j\omega_n t)\,. \tag{7.49}$$

This displacement field generated the stiffness matrix for flexural motion, which is subsequently augmented to the stiffness matrix of the in-plane motion. This plate element was used to model folded plate structures [124], which was also implemented in parallel computers (see [125] and [126]). Recently, this plate formulation for isotropic material has been extended to model cracked plate [127]. In this chapter, we extend the capability of the spectral formulation for anisotropic and inhomogeneous plate structures.

In the formulation of the SPE for in-plane motion, *i.e.,* SLEs developed in Section 7.1, the wavenumbers are computed by the method of companion matrix and then the singular value decomposition (SVD) method is employed to

compute the wave amplitudes. Although this method is quite efficient, as the previous elements demonstrate, formulation of the companion matrix proves to be cumbersome and prone to human error, especially when the system size is large, as is typical for plates and shells. Thus there is a need to automate the whole procedure for finding the wavenumbers and wave amplitudes. In this chapter, we use the concept of latent roots and right latent eigenvector of the system matrix (the wave matrix) to compute the wavenumber and the amplitude ratio matrix and the whole problem is posed as a PEP, as discussed before. As algorithms are available now for solving any PEP, even when it is not regular, the method is implemented in the spectral element formulation and tested for its performance in terms of speed and accuracy. Thus, significant changes are made in the element level stiffness matrix formulation, which sets the path for the formulation of other higher order spectral elements, like higher order plates and shells.

In this book, formulations are presented only for anisotropic materials. However, the extension to FGM is straightforward as is shown in the beam elements development. Since, the material properties are assumed to be graded only in the direction normal to the direction of wave propagation, the gradation does not affect the governing equations. Only the depth-wise integrated properties change and they are evaluated using the gradation rule chosen to model the FGM.

The next section deals with the SPE formulation for CLPT. The spectrum relations are analyzed in detail for both anisotropic and inhomogeneous plates. Subsequently, the variation of cut-off frequency with wavenumber is investigated. Next, the details of the element formulations are presented. The developed plate elements are employed to study wave propagation in a plate with ply-drop and to capture the first symmetric and anti-symmetric Lamb waves.

7.5.1 SPE Formulation: CLPT

According to the CLPT, the displacement field is

$$\begin{aligned} U(x,y,z,t) &= u(x,y,t) - z\partial w/\partial x\,, \\ V(x,y,z,t) &= v(x,y,t) - z\partial w/\partial y\,, \\ W(x,y,z,t) &= w(x,y,t)\,, \end{aligned}$$

where, u, v and w are the displacement components of the reference plane in the X, Y and Z directions, respectively and z is measured downward positive (see Figure 7.32).

The associated non-zero strains are

$$\left\{\begin{array}{c}\epsilon_{xx}\\ \epsilon_{yy}\\ \epsilon_{xy}\end{array}\right\} = \left\{\begin{array}{c}\partial u/\partial x\\ \partial v/\partial y\\ \partial u/\partial y + \partial v/\partial x\end{array}\right\} + \left\{\begin{array}{c}-z\partial^2 w/\partial x^2\\ -z\partial^2 w/\partial y^2\\ -2z\partial^2 w/\partial x\partial y\end{array}\right\} = \{\epsilon_\circ\} + \{\epsilon_1\}\,, \quad (7.50)$$

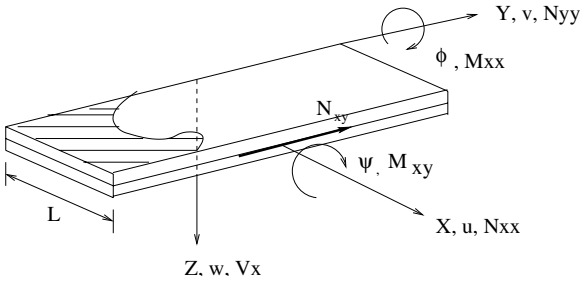

Fig. 7.32. Displacements and stress resultants of the spectral plate element (CLPT and FLPT): for CLPT $\phi = \partial w/\partial x$ and ψ is absent

where ϵ_{xx} and ϵ_{yy} are the normal strains in the X and the Y directions, respectively and ϵ_{xy} is the in-plane shear strain. The corresponding normal and shear stresses are related to these strains by the relation

$$\begin{Bmatrix} \sigma_{xx} \\ \sigma_{yy} \\ \sigma_{xy} \end{Bmatrix} = \begin{bmatrix} \bar{Q}_{11} & \bar{Q}_{12} & 0 \\ \bar{Q}_{12} & \bar{Q}_{22} & 0 \\ 0 & 0 & \bar{Q}_{66} \end{bmatrix} \begin{Bmatrix} \epsilon_{xx} \\ \epsilon_{yy} \\ \epsilon_{xy} \end{Bmatrix}, \tag{7.51}$$

where $\bar{Q}_{ij}$ are the elements of the anisotropic constitutive matrix. The expressions for $\bar{Q}_{ij}$ in terms of the elastic constants and ply-angles are given in [50]. The force resultants are defined in terms of these stresses as

$$\begin{Bmatrix} N_{xx} \\ N_{yy} \\ N_{xy} \end{Bmatrix} = \int_A \begin{Bmatrix} \sigma_{xx} \\ \sigma_{yy} \\ \sigma_{xy} \end{Bmatrix} dA \,, \begin{Bmatrix} M_{xx} \\ M_{yy} \\ M_{xy} \end{Bmatrix} = \int_A z \begin{Bmatrix} \sigma_{xx} \\ \sigma_{yy} \\ \sigma_{xy} \end{Bmatrix} dA \,. \tag{7.52}$$

Substituting Equations (7.51) and (7.50) in Equation (7.52), the relation between the force resultants and the displacement field is obtained as

$$\begin{Bmatrix} N_{xx} \\ N_{yy} \\ N_{xy} \end{Bmatrix} = \begin{bmatrix} A_{11} & A_{12} & 0 \\ A_{12} & A_{22} & 0 \\ 0 & 0 & A_{66} \end{bmatrix} \{\epsilon_\circ\} + \begin{bmatrix} B_{11} & B_{12} & 0 \\ B_{12} & B_{22} & 0 \\ 0 & 0 & B_{66} \end{bmatrix} \{\epsilon_1\}, \tag{7.53}$$

$$\begin{Bmatrix} M_{xx} \\ M_{yy} \\ M_{xy} \end{Bmatrix} = \begin{bmatrix} B_{11} & B_{12} & 0 \\ B_{12} & B_{22} & 0 \\ 0 & 0 & B_{66} \end{bmatrix} \{\epsilon_\circ\} + \begin{bmatrix} D_{11} & D_{12} & 0 \\ D_{12} & D_{22} & 0 \\ 0 & 0 & D_{66} \end{bmatrix} \{\epsilon_1\}, \tag{7.54}$$

where the elements A_{ij}, B_{ij} and D_{ij} are defined as

$$[A_{ij}\,, B_{ij}\,, D_{ij}] = \int_A \bar{Q}_{ij}[1\,, z\,, z^2]\, dz\,. \tag{7.55}$$

Note that the above expression is valid for FGM also, where $\bar{Q}_{ij}$ will be a function of z (power or exponential law [128]) instead of being constant, as in the anisotropic case.

The kinetic energy (K) and the potential energy (P) are defined in terms of the displacement field and stresses as

$$K = (1/2)\int_V \rho(\dot{U}^2 + \dot{V}^2 + \dot{W}^2)\, dV\,, \tag{7.56}$$

$$P = (1/2)\int_V (\sigma_{xx}\epsilon_{xx} + \sigma_{yy}\epsilon_{yy} + \sigma_{xy}\epsilon_{xy})\, dV\,. \tag{7.57}$$

Applying Hamilton's principle, the governing equations can be written in terms of these force resultants as

$$\partial N_{xx}/\partial x + \partial N_{xy}/\partial y = I_\circ \ddot{u} - I_1 \partial \ddot{w}/\partial x\,, \tag{7.58}$$

$$\partial N_{xy}/\partial x + \partial N_{yy}/\partial y = I_\circ \ddot{v} - I_1 \partial \ddot{w}/\partial y\,, \tag{7.59}$$

$$\begin{aligned}\partial^2 M_{xx}/\partial xx + 2\partial^2 M_{xy}/\partial xy + \partial^2 M_{yy}/\partial yy = I_\circ \ddot{w} - I_2(\partial^2 \ddot{w}/\partial xx + \partial^2 \ddot{w}/\partial yy)\\ + I_1(\partial \dot{u}/\partial x + \partial \dot{v}/\partial y)\,,\end{aligned} \tag{7.60}$$

where the mass moments are defined as

$$[I_\circ\,, I_1\,, I_2] = \int_A \rho[1\,, z\,, z^2]\, dz\,. \tag{7.61}$$

For FGM, $I_\circ\,, I_1$ and I_2 can be evaluated using the same expression, where the only change is $\rho = \rho(z)$.

The governing equations can be further expanded in terms of the displacement components. However, because of their complexity, they are not given here and can be found in [50]. The associated boundary conditions are

$$\bar{N}_{xx} = N_{xx}n_x + N_{xy}n_y\,, \quad \bar{N}_{yy} = N_{xy}n_x + N_{yy}n_y\,, \tag{7.62}$$

$$\bar{M}_{xx} = -M_{xx}n_x - M_{xy}n_y\,, \tag{7.63}$$

$$\begin{aligned}\bar{V}_x = (\partial M_{xx}/\partial x + 2\partial M_{xy}/\partial y - I_1\ddot{u} + I_2\partial \ddot{w}/\partial x)n_x\\ + (\partial M_{xy}/\partial x + 2\partial M_{yy}/\partial y - I_1\ddot{v} + I_2\partial \ddot{w}/\partial y)n_y\,,\end{aligned} \tag{7.64}$$

where $\bar{N}_{xx}$ and $\bar{N}_{yy}$ are the applied normal forces in the X and Y direction, $\bar{M}_{xx}$ and $\bar{M}_{yy}$ are the applied moments about the Y and X axes and $\bar{V}_x$ is the applied shear force in the Z direction.

The SPE formulation begins by assuming the same kind of solution for the displacement field as taken for the layer element formulation, *i.e.,* time harmonic waves are sought and the Fourier series is employed in the Y direction. Thus,

$$u(x,y,t) = \sum_{n=0}^{N-1}\sum_{m=1}^{M} \hat{u}(x) \left\{ \begin{matrix} \cos(\eta_m y) \\ \sin(\eta_m y) \end{matrix} \right\} e^{-j\omega_n t}\,, \tag{7.65}$$

$$v(x,y,t) = \sum_{n=0}^{N-1} \sum_{m=1}^{M} \hat{v}(x) \left\{ \begin{matrix} \sin(\eta_m y) \\ \cos(\eta_m y) \end{matrix} \right\} e^{-j\omega_n t}\,, \tag{7.66}$$

$$w(x,y,t) = \sum_{n=0}^{N-1} \sum_{m=1}^{M} \hat{w}(x) \left\{ \begin{matrix} \cos(\eta_m y) \\ \sin(\eta_m y) \end{matrix} \right\} e^{-j\omega_n t}\,, \tag{7.67}$$

where again the cosine or sine dependency is chosen based on the symmetry or anti-symmetry of the applied load about the X axis.

Substituting Equations (7.65)–(7.67) in Equations (7.58)–(7.60), a set of ODEs is obtained for the unknowns $\hat{u}(x)$, $\hat{v}(x)$ and $\hat{w}(x)$. Since these ODEs have constant coefficients, their solutions can be written as $\tilde{u}e^{-jkx}$, $\tilde{v}e^{-jkx}$ and $\tilde{w}e^{-jkx}$, where k is the wavenumber in the X direction, yet to be determined and $\tilde{u}$, $\tilde{v}$ and $\tilde{w}$ are the unknown constants. Substituting these assumed forms in the set of ODEs, a PEP is posed to find $(\mathbf{v}, k)$, such that,

$$\mathbf{\Psi}(k)\mathbf{v} = (k^4\mathbf{A}_4 + k^3\mathbf{A}_3 + k^2\mathbf{A}_2 + k\mathbf{A}_1 + \mathbf{A}_0)\mathbf{v} = 0\,, \quad \mathbf{v} \neq 0\,, \tag{7.68}$$

where $\mathbf{A}_i \in \mathbf{C}^{3\times 3}$, k is an eigenvalue and $\mathbf{v}$ is the corresponding right eigenvector. The matrices $\mathbf{A}_i$ are

$$\mathbf{A}_0 = \begin{bmatrix} -A_{66}\eta_m^2 + I_\circ\omega_n^2 & 0 & 0 \\ 0 & -A_{22}\eta_m^2 + I_\circ\omega_n^2 & -B_{22}\eta_m^3 + I_1\omega_n^2\eta_m \\ 0 & -B_{22}\eta_m^3 + I_1\omega_n^2\eta_m & -D_{22}\eta_m^4 + I_\circ\omega_n^2 + I_2\omega_n^2\eta_m^2 \end{bmatrix}, \tag{7.69}$$

$$\mathbf{A}_1 = \begin{bmatrix} 0 & -j\eta_m(A_{12}+A_{66}) & -j\eta_m^2(B_{12}+2B_{66}) + jI_1\omega_n^2 \\ j\eta_m(A_{12}+A_{66}) & 0 & 0 \\ j\eta_m^2(B_{12}+2B_{66}) - jI_1\omega_n^2 & 0 & 0 \end{bmatrix}, \tag{7.70}$$

$$\mathbf{A}_2 = \begin{bmatrix} -A_{11} & 0 & 0 \\ 0 & -A_{66} & -\eta_m(B_{12}+2B_{66}) \\ 0 & -\eta_m(B_{12}+2B_{66}) & -\eta_m^2(2D_{12}+4D_{66}) + I_2\omega_n^2 \end{bmatrix}, \tag{7.71}$$

$$\mathbf{A}_3 = \begin{bmatrix} 0 & 0 & -jB_{11} \\ 0 & 0 & 0 \\ jB_{11} & 0 & 0 \end{bmatrix}, \tag{7.72}$$

$$\mathbf{A}_4 = \begin{bmatrix} 0 & 0 & 0 \\ 0 & 0 & 0 \\ 0 & 0 & -D_{11} \end{bmatrix}. \tag{7.73}$$

It can be noticed that $\mathbf{A}_4$ is singular, thus the lambda matrix $\mathbf{\Psi}(k)$ is not regular [41] and admits infinite eigenvalues [129].

The PEP is solved by the methods described before. In this case, the spectrum relation is a quartic polynomial of $m = k^2$,

$$p(m) = m^4 + C_1m^3 + C_2m^2 + C_3m + C_4\,, \quad C_i \in \mathbf{C}\,, \tag{7.74}$$

which generates a companion matrix of order 4. In both the methods of wavenumber computation described earlier, an eigenvalue solver is employed, where for the QZ algorithm the cost of computation is $\sim 30n^3$ and extra $\sim 16n^3$ for eigenvector computation (n is the order of the matrix). Since, the order of the companion matrix in the second method is three times that of the first method, the cost is 27 times more, which is significant as this computation is to be performed $N \times M$ times. Further, since $\mathbf{\Psi}(k)$ is not regular, there are infinite eigenvalues and caution should be exercised in rejecting those roots. However, the second method is advantageous because it obviates the necessity for obtaining the lengthy expressions for C_i in Equation (7.74).

In the subsequent computation, both the methods are investigated for their effectiveness. It is found that for a single computation, the companion matrix method takes 0.03 s of CPU time, 0.0661 s of real time and 6991 floating point operations ($flops$), whereas, the linearized PEP method takes 0.02 s of CPU time, 0.0686 s of real time and 276735 $flops$, where all the computations are performed in a SUN Solaris workstation. Thus, the second method is faster than the companion matrix method although significantly more $flops$ are involved. In the companion matrix method, although the expressions for C_i are manageable, they are not given here because of their complexity.

7.5.2 Computation of Wavenumber: Anisotropic Plate

The polynomial governing the wavenumbers (Equation (7.74)) is solved by considering a graphite–epoxy (AS/3501) plate of 10 mm thickness with the material properties given in Equation (7.35). Two different ply-stacking sequences are considered, one symmetric $[0_{10}]$ and the other asymmetric $[0_5/90_5]$. The Y wavenumber, η_m is fixed at 50 for all the wavenumber computations. The real and imaginary part of the wavenumbers are shown in Figures 7.33 and 7.34, respectively. The points in the abscissa marked 1, 2 and 3 denote the cut-off frequencies and they are at 3, 13.7 and 21 kHz. Two roots are equal before point 1, and they are denoted by $k_{1,2}$. Thus, before point 1, there are only four non-zero real roots ($\pm k_{1,2}$) and eight non-zero imaginary roots ($\pm k_{1,2}$, $\pm k_3$ and $\pm k_4$). After point 1, one of the $k_{1,2}$ becomes pure real and another one becomes pure imaginary and there is only an imaginary root at high frequency. These roots correspond to the bending mode, w. It can be further noticed that before point 1, these wavenumbers ($k_{1,2}$) simultaneously possess both real and imaginary parts, which implies these modes are attenuated while propagating. Thus, there exist inhomogeneous waves in anisotropic composite plate [24]. The points marked 2 and 3 are the two cut-off frequencies, since the roots k_3 and k_4 become real at this point from their imaginary values. These roots correspond to the inplane motion, *i.e.,* u and v displacements.

Next, the asymmetric ply-sequence is considered (Figures 7.35 and 7.36), for which the wavenumber pattern remains qualitatively the same. The cut-off frequencies are at 5.3, 13.8 and 60 kHz, where the first one corresponds to the

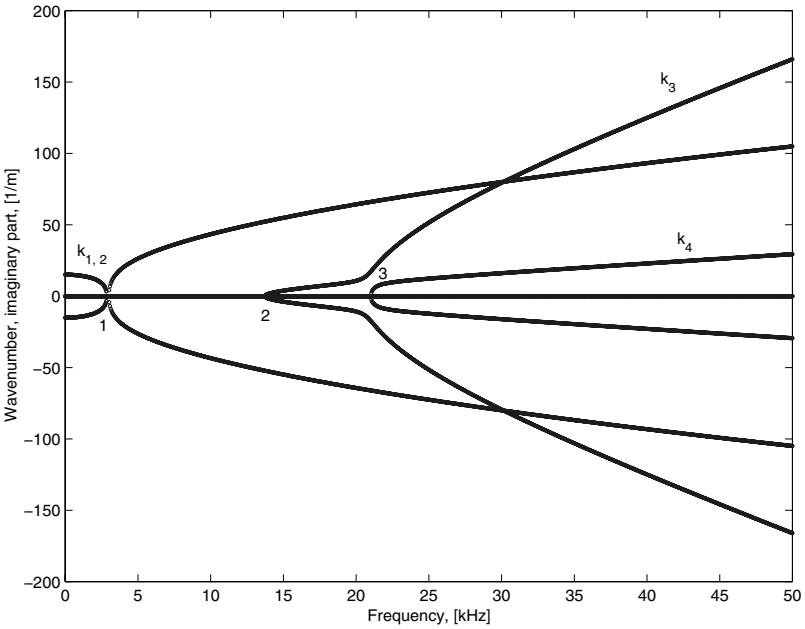

Fig. 7.33. Real part of wavenumbers, symmetric sequence

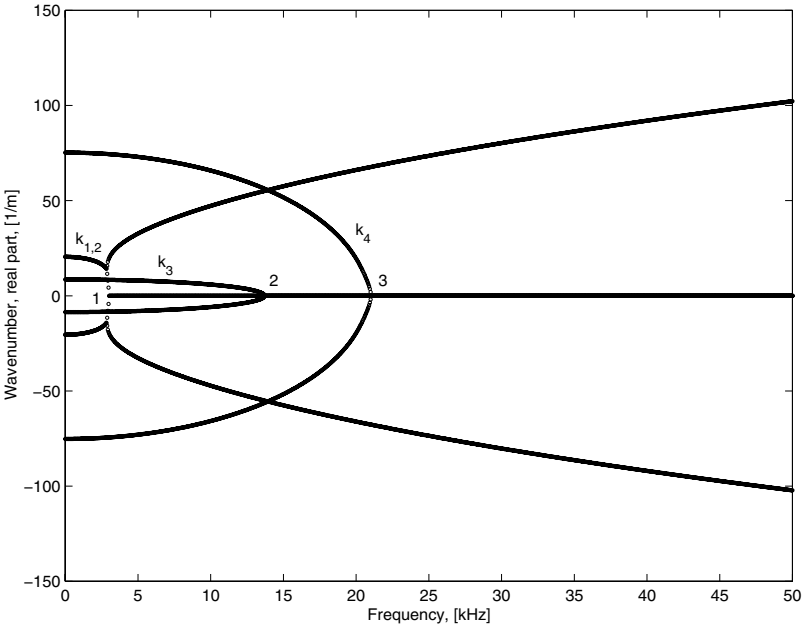

Fig. 7.34. Imaginary part of wavenumbers, symmetric sequence

bending mode and the last two correspond to the inplane motion. In comparison to symmetric ply-stacking, it can be said that the first and the third cut-off frequencies are of higher magnitude than their symmetric counterparts and the rate of increment is higher in the third cut-off frequency. Further, the magnitudes of all wavenumbers are increased. Significantly, at higher frequency, the third wavenumber k_3 has lower magnitude than the bending wavenumbers (one of $k_{1,2}$) as opposed to the symmetric case. Similar trends are visible in the imaginary part of the wavenumbers, where the magnitude is higher in all cases (almost double) than the imaginary wavenumbers of the symmetric sequence. Thus attenuation of the propagating modes is comparatively higher in the asymmetric case.

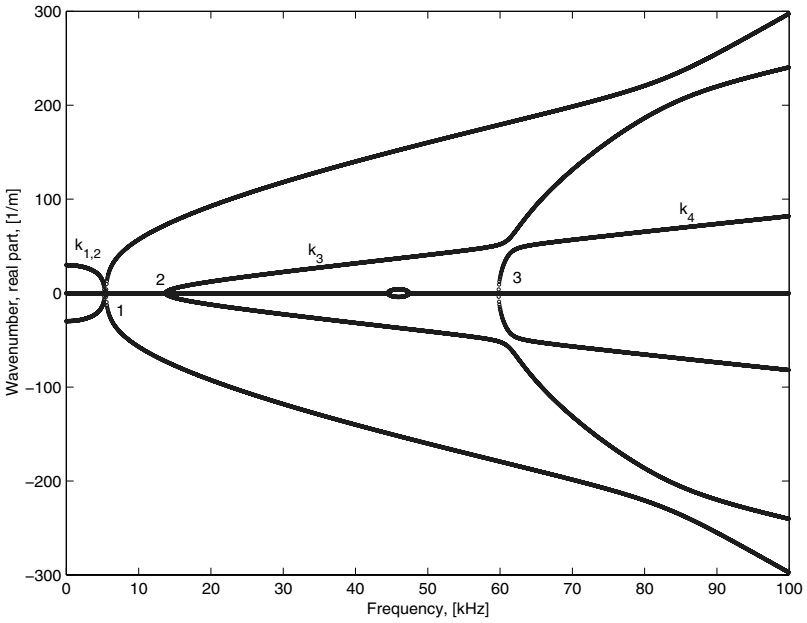

Fig. 7.35. Real part of wavenumbers, asymmetric sequence

The cut-off frequencies can be obtained from Equation (7.74) by letting $k = 0$ and solving for ω_n. The governing equation for the cut-off frequency becomes

$$a_0\omega_n^6 + a_1\omega_n^4 + a_2\omega_n^2 + a_3 = 0\,, \tag{7.75}$$

where a_i are material property and wavenumber η_m dependent coefficients given as

$$a_0 = I_\circ^2 I_2 \eta^2 + I_\circ^3 - I_\circ I_1^2 I_2\,, \tag{7.76}$$

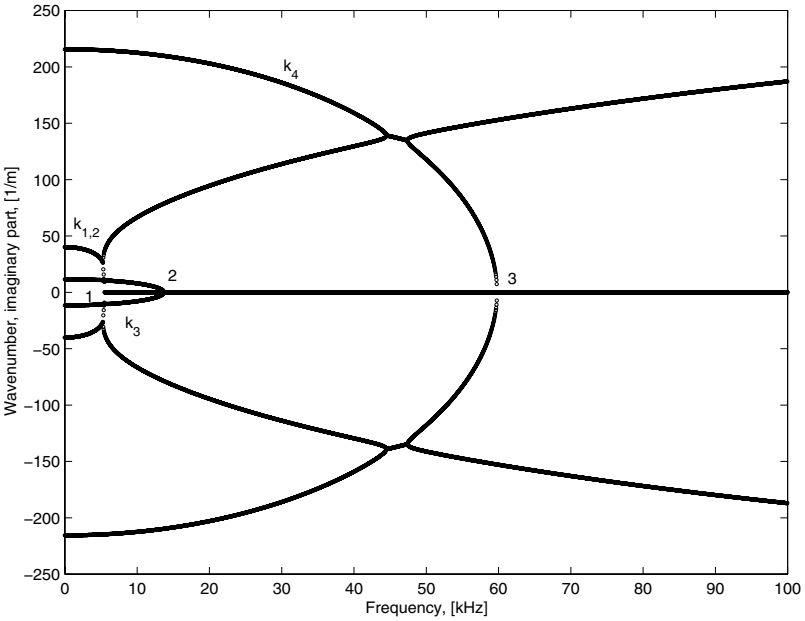

Fig. 7.36. Imaginary part of wavenumbers, asymmetric sequence

$$a_1 = -I_\circ^2 D_{22}\eta^4 - I_\circ^2(A_{22}+A_{66})\eta^2 - I_\circ I_2\eta^4(A_{66}+A_{22}) + A_{66}\eta^4 I_1^2 + 2I_\circ B_{22}\eta_4 I_1\,, \tag{7.77}$$

$$\begin{aligned} a_2 = &-I_\circ B_{22}^2\eta^6 + A_{66}\eta^4 A_{22} I_\circ + A_{66}\eta^6 I_\circ D_{22} - 2A_{66}\eta^6 B_{22} I_1 \\ &+ I_\circ A_{22}\eta^6 D_{22} + A_{66}\eta^6 A_{22} I_2\,, \end{aligned} \tag{7.78}$$

$$a_3 = A_{66}\eta^8(-A_{22}D_{22} + B_{22}^2)\,. \tag{7.79}$$

When Equation (7.75) is solved for different η_m, the variation of the cut-off frequencies with η_m can be obtained. This variation is given in Figure 7.37. As is shown in the figure, variation of the cut-off frequency for the bending mode $\omega_{1,2}$ follows a non-linear pattern, whereas the other two increase linearly. Although not evident from this figure, close inspection will reveal that the pattern for ω_3 is the same for both symmetric and asymmetric cases. Since it is the magnitude of A_{12} that has not changed with ply-angle, it can be concluded that ω_3 is proportional to the ratio of $\sqrt{A_{12}/\rho}$. Further, there is no variation in $\omega_{1,2}$ for changing ply-stacking, whereas, for ω_4, the effect is maximum. Thus, with the help of this figure, the location of the points 1, 2 and 3 in Figures 7.33- 7.36 can be explained.

7.5.3 Computation of Wavenumber: Inhomogeneous Plate

The polynomial governing the wavenumbers (*i.e.,* Equation (7.74)) is solved by considering a steel FGM ceramic plate with the following material properties.

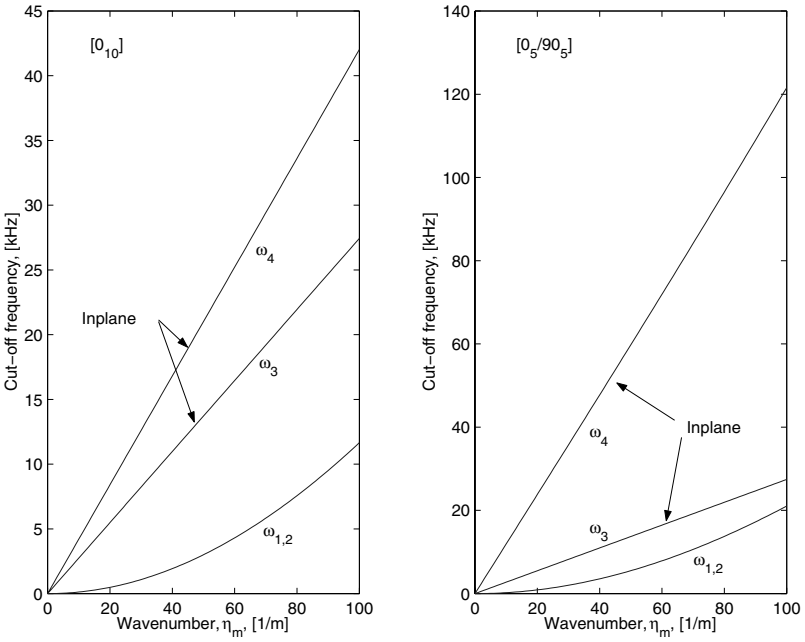

Fig. 7.37. Variation of cut-off frequency with η_m

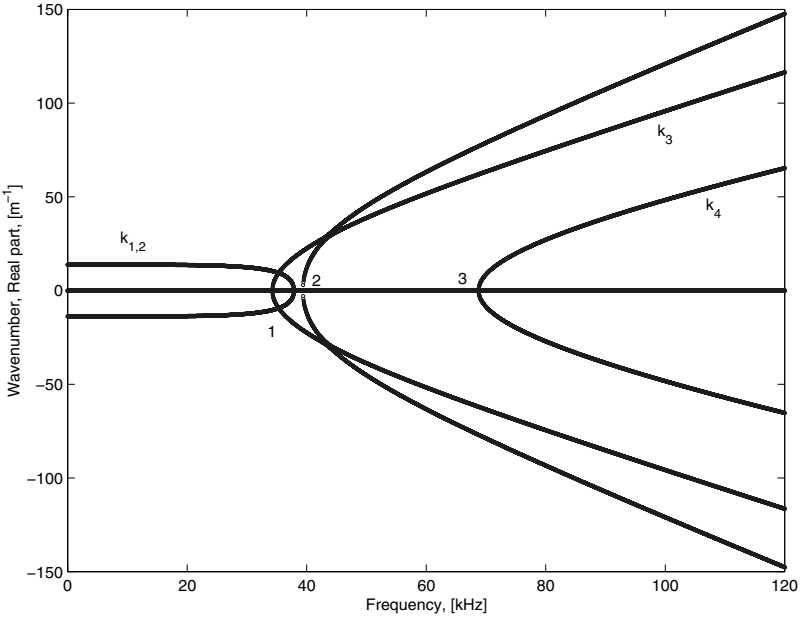

Fig. 7.38. Real part of the wavenumbers

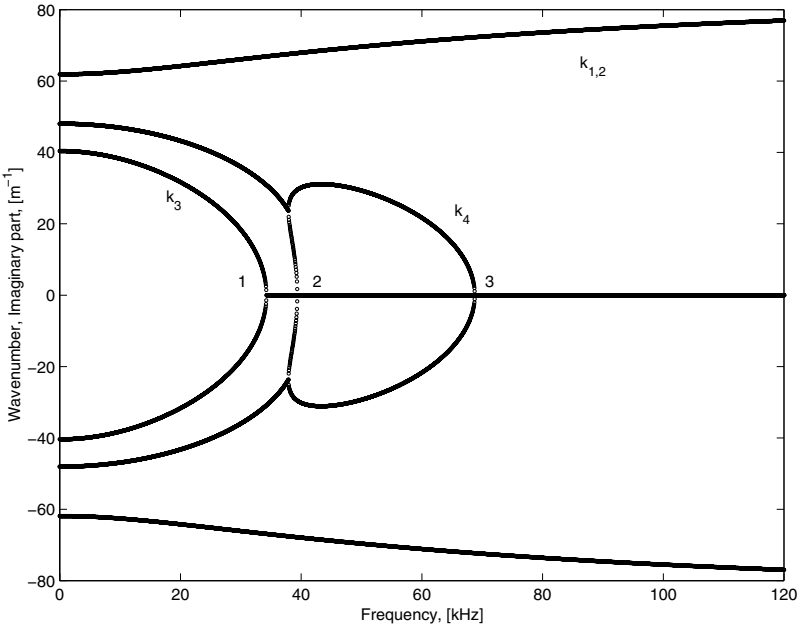

Fig. 7.39. Imaginary part of the wavenumbers

$$E_s = 210.0 \text{ GPa}\,,\ E_c = 390.00 \text{ GPa}\,,\ G_s = 80.0 \text{ GPa}\,,\ G_c = 137.0 \text{ GPa}\,,$$
$$\rho_s = 7800 \text{ kg/m}^3,\ \rho_c = 3950.0 \text{ kg/m}^3,\ h_s = 0.01\text{m} = h,\quad h_c = 0.03\text{m}\,, \tag{7.80}$$

where the subscript s and c denote steel and ceramic, respectively. and h is the thickness of the FGM layer. This depth-wise distribution of materials results in non-zero B_{ij} and I_1.

The Y wavenumber, η_m is fixed at 50 for all the wavenumber computation. The real and imaginary parts of the wavenumbers are shown in Figures 7.38 and 7.39, respectively. The points in the abscissa marked 1, 2 and 3 denote the frequencies where the real wavenumbers become imaginary and vice versa. These frequencies are called the cut-off frequencies and they are at 34.1, 39.17 and 69.12 kHz. Two roots are equal before point 1, and are denoted $k_{1,2}$. Thus, before point 1, there are only four non-zero real roots ($\pm k_{1,2}$) and eight non-zero imaginary roots ($\pm k_{1,2}$, $\pm k_3$ and $\pm k_4$). After point 2, one of the $k_{1,2}$ becomes pure real and another one becomes pure imaginary and is the only imaginary root at high frequency. These roots correspond to the bending mode, w. It can be further noticed that before point 1, these wavenumbers ($k_{1,2}$) simultaneously possess both real and imaginary parts, which implies these modes are attenuated while propagating. Thus, there exists an inhomogeneous wave in FGM plate, which is also found in composite plate. The points marked 1 and 3 are the two cut-off frequencies, where the roots k_3 and

k_4 become real from their imaginary values. These roots correspond to the inplane motion, *i.e.,* u and v displacements.

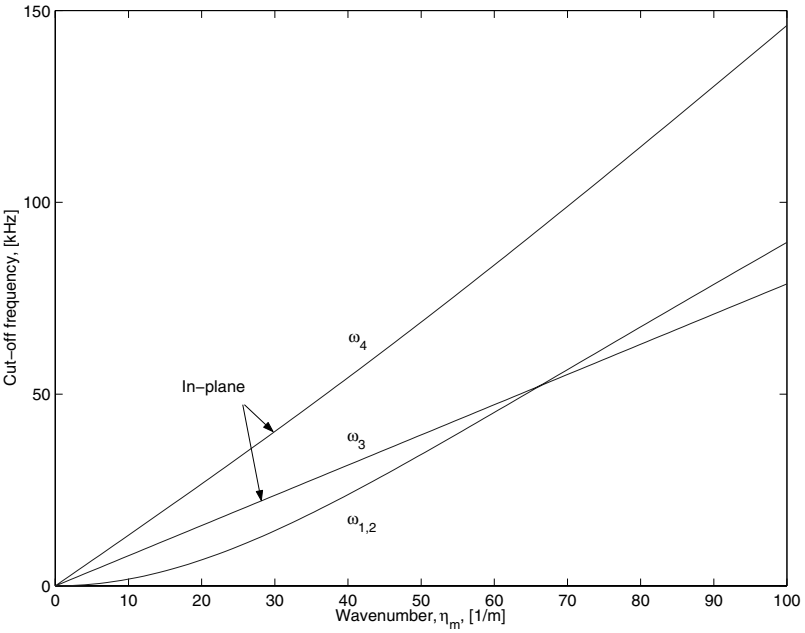

Fig. 7.40. Variation of cut-off frequency with η_m

As in the anisotropic case, the cut-off frequencies can be obtained from Equation (7.74) by letting $k = 0$ and solving for ω_n. The governing equation for the cut-off frequency becomes

$$a_0\omega_n^6 + a_1\omega_n^4 + a_2\omega_n^2 + a_3 = 0\,, \tag{7.81}$$

where a_i are material property and wavenumber η_m dependent coefficients. When Equation (7.81) is solved for different η_m, the variation of the cut-off frequencies with η_m can be obtained. This variation is given in Figure 7.40. As is shown in the figure, variation of the cut-off frequency for the bending mode, $\omega_{1,2}$, follows a non-linear pattern, whereas, the other two are linear. At higher values of η_m, this frequency exceeds the in-plane cut-off frequency, ω_3. Thus, with the help of this figure, the location of the points 1, 2 and 3 in Figures 7.38 and 7.39 can be explained.

Once, the wavenumbers are known, computation of the wave amplitudes are performed either by the SVD technique or by the method of linearized PEP. The wavenumbers and wave amplitudes are essential for the SPE formulation, which is taken up next. Two different elements are formulated in

this study, one with a semi-bounded geometry and the other one with a half-space geometry.

7.5.4 The Finite Plate Element

The geometry of the semi-bounded plate element is shown in Figure 7.32. It has four dof per node, three displacements in three coordinate directions and one rotational dof about the Y axis. Thus, there are a total of eight dofs per element, which are the unknowns. The displacement at any x coordinate of the plate (in the frequency wavenumber domain) can be written as a linear combination of all its solution given by

$$\tilde{\mathbf{u}} = \sum_{i=1}^{8} a_i \phi_i e^{-jk_i x}\,, \tilde{\mathbf{u}} = \{\tilde{u}, \tilde{v}, \tilde{w}\}^T\,, \phi_i \in \mathbf{C}^{3\times 1}\,, \tag{7.82}$$

where ϕ_i are the columns of the wave matrix. The a_i are the unknown constants, which must be expressed in terms of the nodal variables. This step can be viewed as transformation from the generalized coordinate to the physical coordinate. To do so, let us write the displacement field in a matrix vector multiplication form as

$$\{\tilde{\mathbf{u}}\} = \begin{Bmatrix} \hat{u}(x,\omega_n) \\ \hat{v}(x,\omega_n) \\ \hat{w}(x,\omega_n) \end{Bmatrix} = \begin{bmatrix} \phi_{11} \ldots \phi_{18} \\ \phi_{21} \ldots \phi_{28} \\ \phi_{31} \ldots \phi_{38} \end{bmatrix} \begin{bmatrix} e^{-jk_1 x} & 0 & \ldots & 0 \\ 0 & e^{-jk_2 x} & \ldots & 0 \\ \vdots & \ddots & \ddots & \vdots \\ 0 & \ldots & \ldots & e^{-jk_8 x} \end{bmatrix} \{\mathbf{a}\}\,, \tag{7.83}$$

where $k_{p+4} = -k_p\,, (p = 1, \ldots, 4)$ and the elements of ϕ_i are written as $\phi_{pi}\,, (p = 1, \ldots, 3)$. In concise notation the above equation becomes

$$\{\tilde{\mathbf{u}}\}_{n,m} = [\mathbf{\Phi}]_{n,m}[\mathbf{\Lambda}(x)]_{n,m}\{\mathbf{a}\}_{n,m}\,, \tag{7.84}$$

where n, m is introduced in the subscript to remind us that all these expressions are evaluated at a particular value of ω_n and η_m. $[\mathbf{\Lambda}(x)]_{nm}$ is a diagonal matrix of order 8×8 whose ith element is $e^{-jk_i x}$. $[\mathbf{\Phi}]_{n,m}$ $(= [\phi_1 \cdots \phi_8])$ is the wave amplitude matrix. $\mathbf{a}_{n,m}$ is the vector of eight unknown constants to be determined. These unknown constants are expressed in terms of the nodal displacements by evaluating Equation (7.84) at the two nodes, *i.e.,* at $x = 0$ and $x = L$. In doing so, we get

$$\{\hat{\mathbf{u}}\}_{n,m} = \begin{Bmatrix} \tilde{\mathbf{u}}_1 \\ \tilde{\mathbf{u}}_2 \end{Bmatrix}_n = [\mathbf{T}_1]_{n,m}\{\mathbf{a}\}_{n,m}\,, \quad \tilde{\mathbf{u}}_i = \{u_i\,, v_i\,, w_i\,, (\partial w/\partial x)_i\} \tag{7.85}$$

where $\tilde{\mathbf{u}}_1$ and $\tilde{\mathbf{u}}_2$ are the nodal displacements of node 1 and node 2, respectively. The elements of $[\mathbf{T}_1]_{n,m}$ are

$$
\begin{aligned}
T_1(m,n) &= \Phi(m,n)\,, \quad m = 1,\ldots,3\,, n = 1,\ldots,8\\
T_1(m,n) &= -jk_p\Phi(m-4,p)e^{-jk_nL}\,, \quad m = 5,\ldots,7\,, n = 1,\ldots,8\\
T_1(4,n) &= -jk_n\Phi(3,n)\,, \quad n = 1,\ldots,8\\
T_1(8,n) &= -jk_n\Phi(7,n)\,, \quad n = 1,\ldots,8\,.
\end{aligned}
$$

Before advancing further, it is to be noted that the element has edges parallel to the Y axis, hence at the plate boundary $n_x = \pm 1$ and $n_y = 0$. These relations are to be utilized in the force-displacement relation. Using the force boundary conditions Equations (7.62)–(7.64), the force vector $\{\mathbf{f}\}_{nm} = \{\bar{N}_{xx}\ ,\ \bar{N}_{yy}\ ,\ \bar{V}_x\ ,\ \bar{M}_{xx}\}_{n,m}$ can be written in terms of the unknown constants $\{\mathbf{a}\}_{\mathbf{n},\mathbf{m}}$ as $\{\mathbf{f}\}_{n,m} = [\mathbf{P}]_{n,m}\{\mathbf{a}\}_{\mathbf{n},\mathbf{m}}$. When the force vector is evaluated at node 1 and node 2, (substituting $n_x = \pm 1$) nodal force vectors are obtained and can be related to $\{\mathbf{a}\}_{n,m}$ by

$$
\{\hat{\mathbf{f}}\}_{n,m} = \begin{Bmatrix} \tilde{\mathbf{f}}_1 \\ \tilde{\mathbf{f}}_2 \end{Bmatrix}_{n,m} = \begin{bmatrix} \mathbf{P}(0) \\ \mathbf{P}(L) \end{bmatrix}_{n,m} \{\mathbf{a}\}_{n,m} = [\mathbf{T}_2]_{n,m}\{\mathbf{a}\}_{n,m}\,. \tag{7.86}
$$

Equations (7.85) and (7.86) together yield the relation between the nodal force and nodal displacement vector at frequency ω_n and wavenumber η_m as

$$
\{\hat{\mathbf{f}}\}_{n,m} = [\mathbf{T}_2]_{n,m}[\mathbf{T}_1]^{-1}_{n,m}\{\hat{\mathbf{u}}\}_{n,m} = [\mathbf{K}]_{n,m}\{\hat{\mathbf{u}}\}_{n,m}\,, \tag{7.87}
$$

where $[K]_{n,m}$ is the dynamic stiffness matrix at frequency ω_n and wavenumber η_m of order 8×8. The explicit form of the matrix $[\mathbf{T}_2]_{n,m}$ $(n = 1,\ldots,8)$ is

$$
\begin{aligned}
T_2(1,n) &= jk_nA_{11}\Phi(1,n) - \eta A_{12}\Phi(2,n) - k_n^2B_{11}\Phi(3,n) - \eta^2B_{12}\Phi(3,n)\,,\\
T_2(2,n) &= \eta A_{66}\Phi(1,n) + jk_nA_{66}\Phi(2,n) + 2jB_{66}k_n\eta\Phi(3,n)\,,\\
T_2(3,n) &= k_n^2B_{11}\Phi(1,n) + jB_{12}k_n\eta\Phi(2,n) + jk_n^3D_{11}\Phi(3,n) + jD_{12}k_n\eta^2\Phi(3,n)\\
&\quad + 2\eta^2B_{66}\Phi(1,n) + 2jk_n\eta B_{66}\Phi(2,n) + 4jk_n\eta^2D_{66}\Phi(3,n)\,,\\
T_2(4,n) &= -jk_nB_{11}\Phi(1,n) + \eta B_{12}\Phi(2,n) + k_n^2D_{11}\Phi(3,n) + \eta^2D_{12}\Phi(3,n)\,,\\
T_2(m,n) &= -T_2(m-4,n)e^{-jk_nL}\,, m = 5,\ldots,8\,.
\end{aligned}
$$

7.5.5 Semi-infinite or Throw-off Plate Element

For the infinite domain element, only the forward propagating modes are considered. The displacement field (at frequency ω_n and wavenumber η_m) becomes

$$
\{\tilde{\mathbf{u}}\}_{n,m} = \sum_{m=1}^{4} \phi_m e^{-jk_mx}a_m = [\mathbf{\Phi}]_{n,m}[\mathbf{\Lambda}(x)]_{n,m}\{\mathbf{a}\}_{n,m}\,, \tag{7.88}
$$

where $[\mathbf{\Phi}]_{n,m}$ and $[\mathbf{\Lambda}(x)]_{n,m}$ is now of order 4×4. The $\{\mathbf{a}\}_{n,m}$ is a vector of four unknown constants. Evaluating the above expression at node 1 $(x = 0)$,

the nodal displacements are related to these constants through the matrix $[\mathbf{T}_1]_{n,m}$ as

$$\{\hat{\mathbf{u}}\}_{n,m} = \{\tilde{\mathbf{u}}_1\}_{n,m} = [\mathbf{\Phi}]_{n,m}[\mathbf{\Lambda}(0)]_{n,m}\{\mathbf{a}\}_{n,m} = [\mathbf{T}_1]_{n,m}\{\mathbf{a}\}_{n,m}\,, \tag{7.89}$$

where $[\mathbf{T}_1]_{n,m}$ is now a matrix of dimension 4×4. Similarly, the nodal forces at node 1 can be related to the unknown constants as

$$\{\hat{\mathbf{f}}\}_{n,m} = \{\tilde{\mathbf{f}}_1\}_{n,m} = [\mathbf{P}(0)]_n\{\mathbf{a}\}_{n,m} = [\mathbf{T}_2]_{n,m}\{\mathbf{a}\}_{n,m}\,. \tag{7.90}$$

Using Equations (7.89) and (7.90), nodal forces at node 1 are related to the nodal displacements at node 1 as

$$\{\hat{\mathbf{f}}\}_{n,m} = [\mathbf{T}_2]_{n,m}[\mathbf{T}_1]^{-1}_{n,m}\{\hat{\mathbf{u}}\}_{n,m} = [\mathbf{K}]_{n,m}\{\hat{\mathbf{u}}\}_{n,m}\,, \tag{7.91}$$

where $[\mathbf{K}]_{n,m}$ is the element dynamic stiffness matrix of dimension 4×4 at frequency ω_n and wavenumber η_m. The $[\mathbf{T}_1]_{n,m}$ and $[\mathbf{T}_2]_{n,m}$ are the first 4×4 truncated part of the matrices $[\mathbf{T}_1]_{n,m}$ and $[\mathbf{T}_2]_{n,m}$ of the finite plate element.

7.6 Numerical Examples

The developed spectral element is employed to analyze a plate with ply-drop to show the efficiency of the present element in modelling complex and computationally expensive structures. Next, Lamb wave propagation in anisotropic plate is captured and the effect of axial-flexural coupling on the Lamb wave is demonstrated.

7.6.1 Wave Propagation in Plate with Ply-drop

Beam structures with ply-drop are analyzed in Chapter 4. However, in the present example, we consider the 2-D state of the stress. The aim here is to see how an extra dimension can alter the response of the structure. The present SPE can model this kind of structure easily and thus the analysis of ply-dropped plate subjected to impulse loading is quite viable. To this end the plate configuration shown in Figure 7.41 is considered. The plate is made up of GFRP composites and is 3.0 m long in the Y direction and 0.9 m in the X direction. It is fixed at one end and free at the other edge. The material properties are as taken before and each lamina is 1.0 mm thick. The plate is divided into three regions along the X direction. From the fixed end to 0.3 m, there are 10 layers in the plate. For the next 0.3 m, the plate has eight laminas and the last 0.3 m has six laminas. The plate is modeled with three finite SPEs (CLPT), which result in a system size of 12×12.

The plate is impacted at the mid-point of the free end by a concentrated load whose time dependency is the same as taken previously, *i.e.,* as given in Figure 5.3. The load is first applied in the X direction and the X velocity

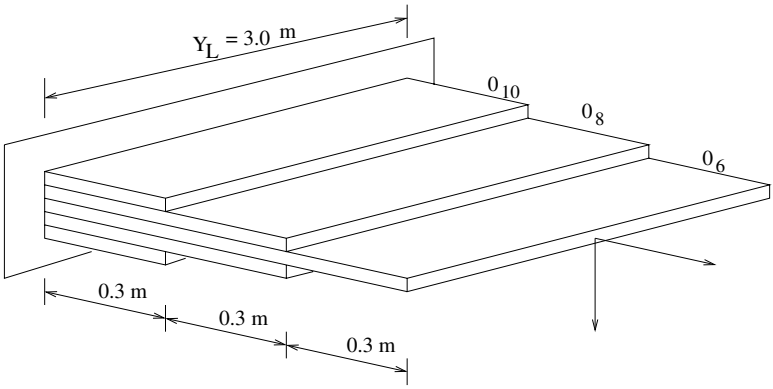

Fig. 7.41. Plate with ply-drop

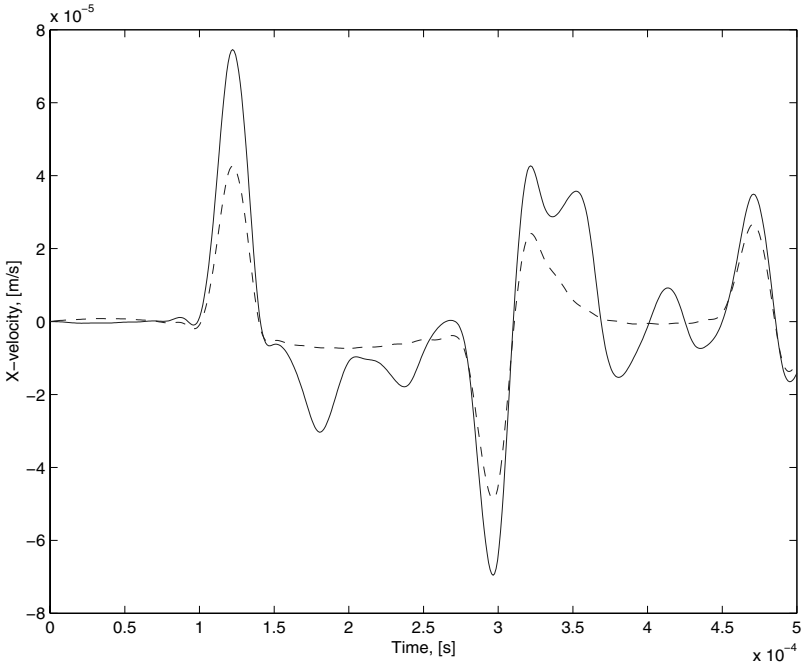

Fig. 7.42. Variation of axial velocity: solid line – ply-drop, dashed line – uniform plate

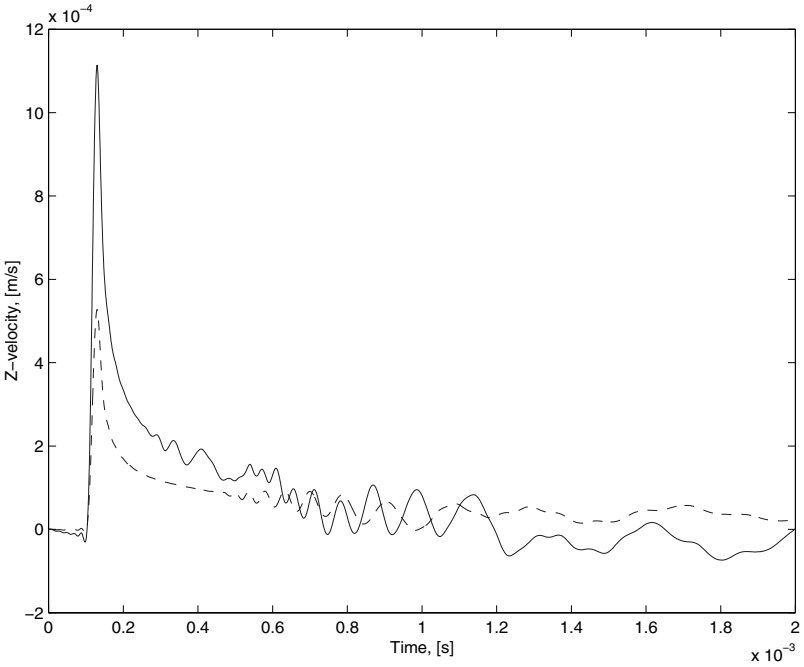

Fig. 7.43. Variation of transverse velocity: solid line – ply-drop, dashed line – uniform plate

is measured at the impact point. The measured velocity history is plotted in Figure 7.42. The same structure is also analyzed for uniform ply-stacking (10 layers) and the result is superimposed in the same figure. It is evident from the figure that ply-drop affects the stiffness of the plate considerably, as there is an increment in the maximum amplitude of about 90%. This reduction of stiffness is also visible in the reflection from the boundary. The reflection from the boundary appears at the same instance in both the cases, which indicates that there is not much alteration in the group speed due to the ply-drop. However, there are two extra reflections (inverted peaks at around 175 μs and 240 μs) in the response from the ply-drop plate before the arrival of the boundary reflection, which originate at the ply-drop junctions due to the mismatch in impedance.

Next, the plate is impacted at the same point in the Z direction and the Z velocity is measured at the same point(Figure 7.43). Simultaneously, the response of the uniform plate is also plotted in the same figure. As noticed before, there is considerable difference in the peak amplitudes (almost a factor of 2), which follows the same pattern of axial velocity history. The extra reflections originated at the interfaces are also visible (starting at around 250 μs), which are not present in the uniform plate response. However, there is no deviation in the arrival time of the boundary reflection, which denotes

the closeness of the bending group speed in both cases. Overall, this example shows the efficiency of the present element in modeling structures with discontinuity and bringing out the essential dynamic characteristics.

7.6.2 Propagation of Lamb waves

The final example is the propagation of Lamb waves in a GFRP plate with the same material properties as taken before. The propagating distance is taken as 2.0 m and to get rid of the boundary reflections, two throw-off SPEs are used. In between, the finite plate is modeled with four SPEs, which together with the throw-off elements generate a system size of $[16 \times 16]$. Lamb waves are generated in this plate by applying a tone burst signal with center frequency of 50 kHz and a bandwidth of 20 kHz. Three lamina sequences are considered, one symmetric, $[0_{10}]$, and two asymmetric, $[0_5/45_5]$ and $[0_5/90_5]$.

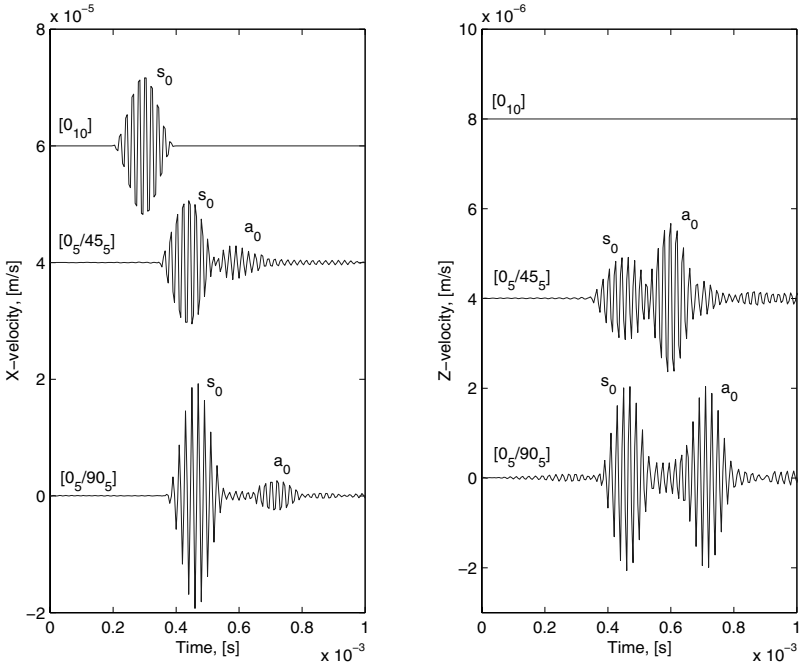

Fig. 7.44. Lamb wave due to X load, profiles are shifted for clarity

First the load is applied in the X direction and both the X and the Z velocity histories are plotted in Figure 7.44. The figure shows that the first symmetric (s_0) and anti-symmetric (a_0) modes are captured by the plate element. This is expected, since the plate element used for modeling is based on the CLPT. For the symmetric laminate, there is no axial–flexural coupling and

the X velocity history shows only the axial mode (s_0). However, for increasing coupling, the bending mode, a_0, appears in the X velocity history, as is shown in the left subfigure. The figure also shows the relative movement of the modes, which clearly shows that the Lamb wave speed is maximum for $[0_{10}]$ sequence and minimum for $[0_5/90_5]$ sequence, for both s_0 and a_0 modes. The change in the s_0 mode speed is more between the $[0_{10}]$ and $[0_5/45_5]$ case, compared to the change between the $[0_5/45_5]$ and $[0_5/90_5]$ case. For transverse velocity history (plotted in the right subfigure), as expected, there is no response for symmetric ply-sequence (since there is no coupling). However, for asymmetric lay-up, both bending and stretching modes are present. Further, variation of the group speed for the a_0 mode (shown by the movement of the a_0 blobs) is easily detectable for varying asymmetry.

Next the load is applied in the Z direction and both the X and the Z velocity histories are plotted in Figure 7.45. The left subfigure shows the variation of the X velocity. Again in this case, symmetric laminate generates no axial response, which starts only for asymmetric ply-sequences. As the figure suggests, for asymmetric lay-up, energy is concentrated more in the s_0 mode (higher amplitude). Also, the group speed variation is nominal for the s_0 mode, whereas, detectable variation can be observed for the a_0 mode. The right subfigure shows the variation of the Z velocity. As is seen in the figure, symmetric laminates are devoid of the s_0 mode, which shows up only for the asymmetric ply-stacking. The wave energy is now concentrated more in the bending mode (a_0), as the relatively large amplitude suggests. This example shows the possible application of the present SPE for modeling and simulation of Lamb wave propagation in composite laminate.

In summary, a set of spectral elements are developed to analyze wave propagation in layered media. The elements cover anisotropic and inhomogeneous materials for both purely elastic and thermoelastic analysis for high frequency mechanical loading or thermal shock. These elements capture the essential response of layered systems to impact loading quite accurately and efficiently compared to conventional FE analysis. Stress state within a multilayered system reveals trapping of energy and multiple reversal of stresses, which may prove fatal to the safety of the structure. Lamb wave modes are also computed for inhomogeneous material and the effect of gradation on the time domain response is investigated. It is shown that for inhomogeneous material, the behavior can be totally different from the background homogeneous material and the order of the appearance of different modes may differ. Thus, mode selection can be performed by suitably varying the gradation. Moreover, inhomogeneity increases the cut-off frequency of the Lamb modes and thus the number of active modes within a given frequency range decreases with the increasing gradation.

The SFEs developed to analyze generalized thermoelastic wave propagation in anisotropic and inhomogeneous layered media can accommodate both the GL and LS theory. Numerical examples using these elements reveal that the relaxation parameters of the GL model have considerable effect on the

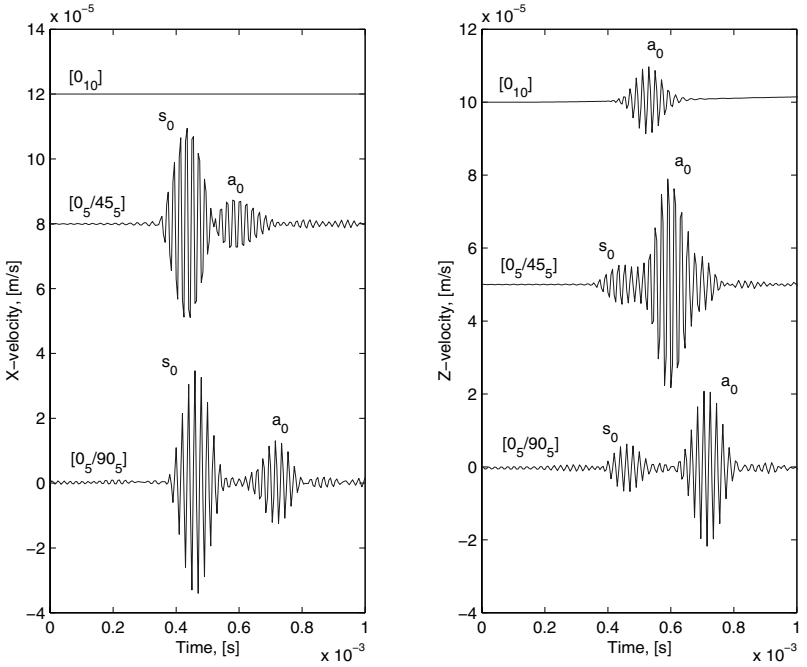

Fig. 7.45. Lamb wave due to Z load, profiles are shifted for clarity

mechanical and thermal responses, unlike the single parameter LS model. At higher frequencies, a coupled thermoelastic solution is necessary as the thermal field alters the mechanical field considerably. Studies of the surface and interface waves in thermoelastic media reveal that the thermal wave propagation is highly localized in time and space as it quickly attains a steady state value. Effects of the time parameters remain predominant as long as the wave contribution to the thermal field remains substantial. It is also found that the classical thermoelasticity overestimates the stress field as the presence of non-zero relaxation parameters decrease their magnitude considerably.

Spectral plate elements are developed by exactly solving the governing partial differential equations of CLPT in the frequency wavenumber domain. The elements are formulated using robust algorithms of SVD and PEP, which minimize human intervention and reduce the possibility of human error. The variation of the wavenumbers is obtained, which reveals the inhomogeneous nature of the propagating waves. The element efficiently captures the wave solution of layered anisotropic plate subjected to impact loading. The cost of computation is many orders less than any conventional FE analysis. The plate element is used to model complex structures like plates with ply-drop, where the responses capture the essential features of the propagating wave in bounded media. Further, Lamb waves are captured and variation of the first symmetric and anti-symmetric modes with laminae sequence is demonstrated.

8

Solution of Inverse Problems: Source and System Identification

The aim of the present chapter is to use the formulated spectral elements of the previous chapters to solve some difficult practical problems of great industrial significance. To start with, one important application of the spectral formulation is in solving inverse problems, *e.g.,* source identification and parameter estimation. Because of the frequency domain formulation of spectral elements, where the input and output responses are algebraically connected through the transfer function, force (external disturbance) reconstruction can be performed with relative ease compared to any FE based methods. Similarly, material property identification by a classical optimization based method, which requires multiple evaluation of the objective function (in this case spectral solution), is computationally feasible because of small spectral system sizes. The SLE developed in Section 6.1 is used in the following example to reconstruct the applied broadband force. Similarly, the SLE developed in Section 7.1 for inhomogeneous layered media is used to identify background homogeneous material properties and inhomogeneous parameters.

8.1 Force Identification

There are many forces (some of which are high frequency excitations) to which structures are frequently subjected throughout their lifetime and which initiate damage and crack growth in these materials. Identification of these forces is thus an important issue in the health monitoring aspect of these structures. It is one of the fundamental inverse problems.

Several reports are available in the literature on force reconstruction from measured responses in both time and frequency domain methods. Stevens [130] has presented an overview of the force identification process for the case of linear vibration systems. Hillary and Ewins [131] investigated the problems of sinusoidal load identification in a cantilever beam and the determination of impact forces acting on aircraft turbine blades with a least-square method. Ory *et al.* [132] used the William's method [133] with a time integration scheme

to identify the shock loading applied on a beam. Bateman *et al.* [134] presented two force reconstruction techniques, *i.e.,* sum of weighted acceleration and deconvolution, to evaluate the impact test for a nuclear transportation cask. Michaels and Pao [135] presented a deconvolution method, which was applied to determine the orientation and time dependent amplitude of the input force from the transient response of a plate. Recently, Huang [136] used an algorithm based on the conjugate gradient method to estimate the unknown external forces in the inverse non-linear force vibration problems. Ma *et al.* [137] presented an inverse method based on Kalman filter and recursive least square method to estimate impulsive loads on lumped mass structural systems. They applied this method to a beam structural system [138] to estimate sinusoidal forces. Chang and Sun [139], Yen and Wu [140], [141], and Wu *et al.* [142] used time domain methods to determine transverse impact force on composite laminate. Recently, some regularization methods are presented by Jacquelin *et al.* [143] to recover an experimental force. Yu and Chan [144] used frequency domain methods to identify moving force on bridges. Liu *et al.* [145] used a hybrid numerical method to identify transient loads in composite laminates. The convenience and versatility of SFE in conjunction with experimental data are demonstrated earlier to predict force history in a mono-material beam [146], bi-material beam [147], isotropic plates [148], orthotropic plates [149], isotropic layered media [150].

There are many instances where the cost of a prototype or difficulty in obtaining a suitable physical model for impact testing precludes any experimental evaluation and numerical simulation becomes the only option for parameter estimation. Also, several difficulties are associated with wave propagation experiments performed over finite length models in terms of noise and boundary reflections. For accurate force prediction, a complete trace of the measured signal is required. The experimentally generated signal is required to be truncated at some point. Choosing the point of truncation requires critical consideration since valuable information may be lost in premature truncation. For a dispersive system, in particular, caution should be exercised in the selection of these truncation points as the wave response will not die down completely within the chosen time window. In this work, FE responses were taken as surrogate experimental results. Since experimental outputs are always truncated at some point depending upon the constraints of the set-up, data acquisition system and other facilities, the FE response should be taken such that it simulates closely the experimental results. When this truncated response is given as input to the SFE solver, the force data can be reconstructed by performing the inverse analysis. The same idea is used in this work to identify the applied impact force from the FE responses.

8.1.1 Force Reconstruction from Truncated Response

The basic idea of force identification in frequency domain analysis is presented below. Since the whole spectral formulation is in the frequency/wavenumber

domain, the response is related to the input through the transfer function as

$$\tilde{Y}(\omega_n, \eta_m) = \tilde{H}(\omega_n, \eta_m)\tilde{X}(\omega_n, \eta_m)\,, \tag{8.1}$$

where $\tilde{X}(\omega_n, \eta_m)$ is the transformation of the input (say, load), $\tilde{Y}(\omega_n, \eta_m)$ is the transform of the output (typically, velocity, strain, *etc.*), and $\tilde{H}(\omega_n, \eta_m)$ is the system transfer function. Now, input force can be obtained easily by dividing the transform of the response by the transfer function, that is,

$$\tilde{X}(\omega_n, \eta_m) = \tilde{Y}(\omega_n, \eta_m)/\tilde{H}(\omega_n, \eta_m)\,. \tag{8.2}$$

Thus, if the response is known at some point, then the disturbance that caused it can be computed. This is one of the distinct advantages of the spectral approach in its ability to solve inverse problems.

In general, $\tilde{Y}(\omega_n, \eta_m)$ will be experimental data, typically the transform of the strain history [150]. In this work, FE analysis output is taken as a replacement for experimental output and when this response is fed into the spectral solver, the applied force can be reconstructed. It is to be noted that the present model is a second-order system, where in most cases the waves are non-dispersive in nature. The tracking of reflection is quite simple in such systems.

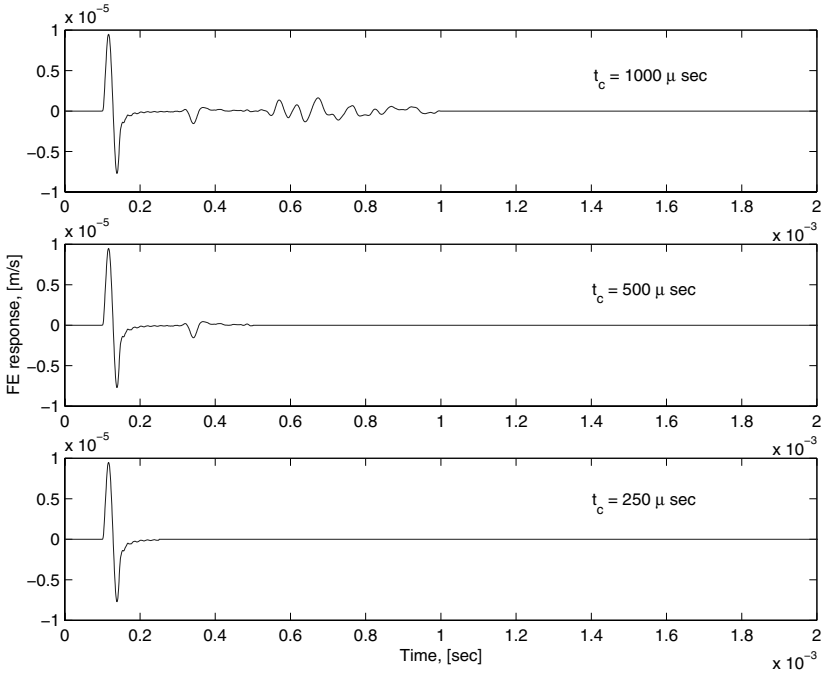

Fig. 8.1. FE response truncated at several points

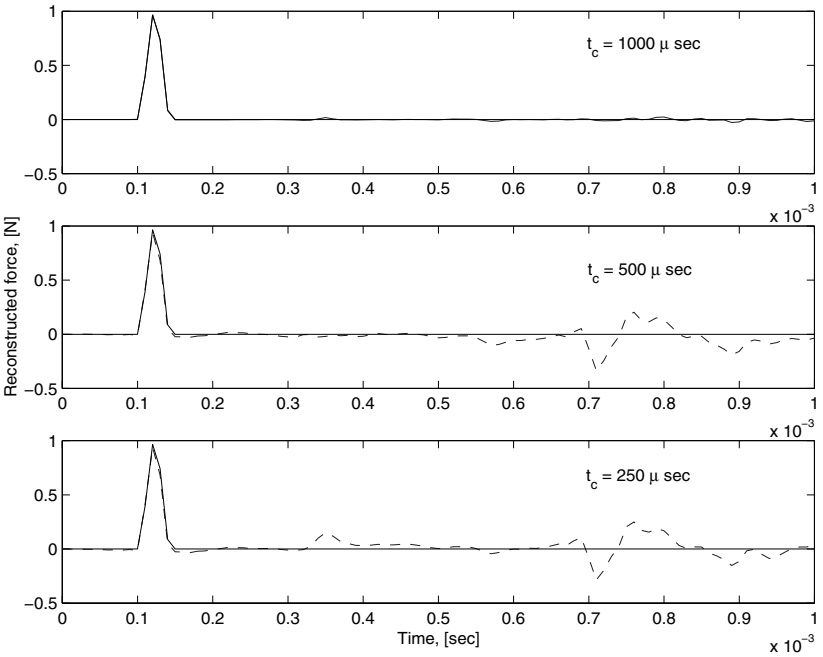

Fig. 8.2. Reconstructed force history for several truncated responses, solid line – original force history, dashed line – reconstructed force history

The anisotropic layered system in the verification study (Section 6.3.1) is taken here and the same load (Figure 5.3) is applied at point 1. The FE signal taken as a substitute for experimental output is the response of Figure 6.5, shown as a dashed line. This FE signal is truncated at three different times (t_c), 1000, 500 and 250 μs. The truncated responses are shown in Figure 8.1. When these responses are given as input to the spectral solver, force history comes as an output. These histories are plotted in Figure 8.2 for the three different cut-off points. As is seen in the figure, for the truncation time of 1000 μs, the reconstructed force history matches almost exactly with the original force history. The second and third truncated signals (t_c = 500 and 250 μs, respectively) also generate the initial form of the load history quite accurately. However, the second truncated signal registers an inverted peak at around 700 μs and the third signal shows another extra peak at around 350 μs, which are not present in the original history. These responses arise because of the removal of the later part of the FE response. Thus, the peak at 700 μs arises due to the removal of the second and subsequent reflections from the fixed end and the peak at 350 μs is due to the removal of the first reflection from the fixed end. Hence, if it is known that there is only one impact load and only the duration and magnitude of that load is desired, FE response (or the experiment output) can be truncated at any point after the

main peak. This exercise further demonstrates the inherent efficiency of the spectral formulation in source reconstruction.

8.2 Material Property Identification

Estimation of the material parameters belongs to the category of parameter identification and is very important in aircraft industries from an aging point of view. Moreover, for existing structures, all the experiments involved in the estimation procedure must be some kind of non-destructive testing. There are few works reported in the literature that deal with the estimation of material properties through judicious use of the experimentally obtained structural response and the response of the mathematical model of the structure. These methods belong to the more general class of solution techniques called Mixed Numerical/Experimental Technique (MNET). Methods belonging to this class differ among themselves in the data that are chosen for comparison and in the method of updating the design variables. For example, Sol *et al.* [151] dealt with the eigenvalues and eigenmodes of the structures and an error functional was constructed and minimized. Kim *et al.* [152] estimated the heat capacity of composites by adopting the same approach, where the error functional was the sum of the squared differences of measured and computed temperature. However, all of them used the same numerical technique, *i.e.,* non-linear optimization with constraints, which falls in the category of classical optimization.

The technique adopted here for estimating the material properties is named the Pulse Propagation Technique (PPT). Here, the structure will be subjected to pulse loading at some point and its response will be measured at another point. This response will be recorded and compared with the response of the numerical model of the structure. Initially, the numerical model of the structure will not be accurate enough to produce the experimentally measured response exactly. The squared difference in the two responses represents the cost function, which needs to be minimized, where the design variables are the material properties. Thus the problem of estimating the unknown material parameters becomes a problem of non-linear optimization, since the cost function is dependent upon the material constants in a non-linear fashion. The method of non-linear optimization requires computation of the structural response a great number of times, which means heavy computation cost if the structure is modeled by FEs. In this situation, the SLE model of the structure is most suitable as a single spectral element can replace thousands of FEs. In this way, spectral formulation is tailor-made for material property estimation by non-linear optimization. This concept was successfully utilized by Al-Khoury *et al.* ([153], [154]) for isotropic multi-layer systems, where the pavement layer moduli and thickness were estimated. The SLE developed there was based on Helmholtz decomposition and hence was applicable only to isotropic homogeneous materials.

There is no existing work that relates the classical optimization technique to material property estimation for graded materials. The existing small amount of literature has dealt with this problem by non-classical methods of optimization. Nakamura *et al.* [155] used a Kalman filter technique along with instrumented micro-indentation to estimate FGM through-thickness compositional variation and a rule-of-mixture parameter that defines effective properties of FGM. Han *et al.* [156] used a genetic algorithm (GA) to estimate material properties of FGM, where a layer element was used which accommodates quadratic material property variation. Liu *et al.* [157] used a neural network along with a layer element and combined Genetic algorithm and nonlinear least square method [158] to estimate material properties. In the next section, the SLE developed in Section 7.1 is used to estimate the elastic properties and inhomogeneous parameters of a graded layer structure.

8.2.1 Estimation of Material Properties: Inhomogeneous Layer

Estimation of the material properties through PPT requires a non-linear least square formulation where the statement of the problem is

$$\min_{q} \sum_{1}^{M} e_i(q)^2 \,, \quad q \in \mathbf{R}^N \,, \tag{8.3}$$

i.e., a function $e : \mathbf{R}^N \rightarrow \mathbf{R}^M$ is to be minimized in a least square sense. The function is defined as the difference between the experimentally measured response (*e.g.,* velocity or voltage) and the numerically obtained response.

In the present case, N is the number of design variables for which estimations will be obtained. M is the number of experimental data items which is twice the number of sensor points (real and imaginary parts), where the response of the structure is recorded. The recorded signal will be transformed into the frequency domain and optimization will be performed at each frequency step.

The layered structure shown in Figure 7.4 and the load applied to it (Figure 5.3) are considered to verify the above method. The response ($\dot{w}$) is measured at node 1 and this response is used for all the parametric estimation, hence, M=2 in this case (the real and imaginary part). As the method demands that N should be $\leq M$, at most two variables can be estimated simultaneously. In this study, the elastic moduli, density and the inhomogeneous parameters are all estimated individually and in one case α and β are estimated simultaneously. The optimization is performed with box-constraints, *i.e.,* lower and upper bounds are specified for all the variables. The optimization is performed by the MATLAB function *lsqnonlin*, where the Levenberg–Merquardt algorithm is used. The tolerances in residue and function values are set at 1.0×10^{-09} for all estimations. The variables are estimated for 100 frequency points, which cover up to 4 kHz.

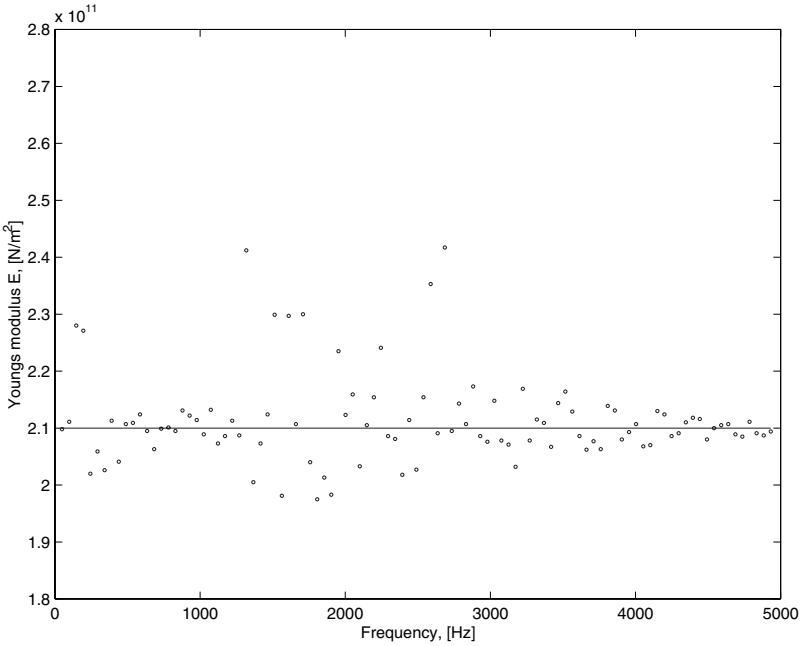

Fig. 8.3. Estimation of the Young's modulus $E_\circ$

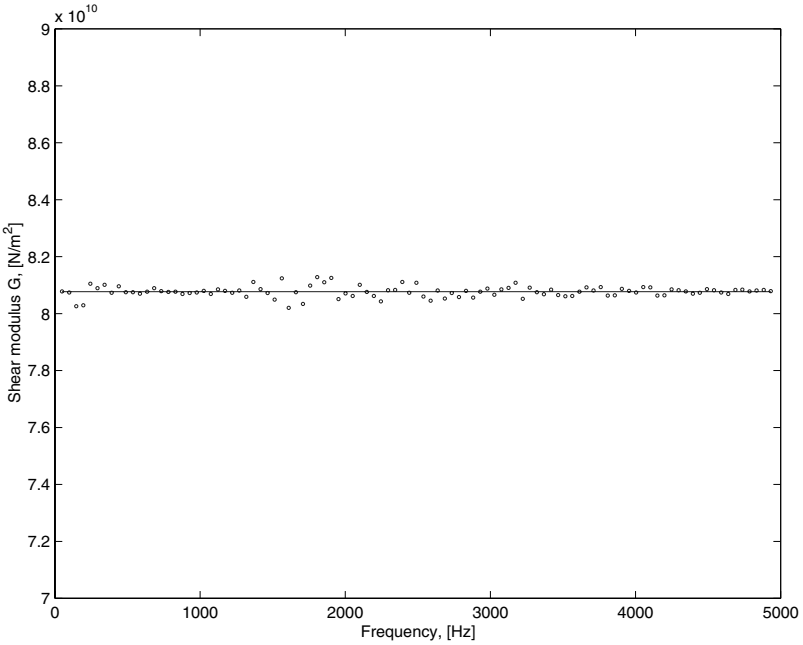

Fig. 8.4. Estimation of the shear modulus $G_\circ$

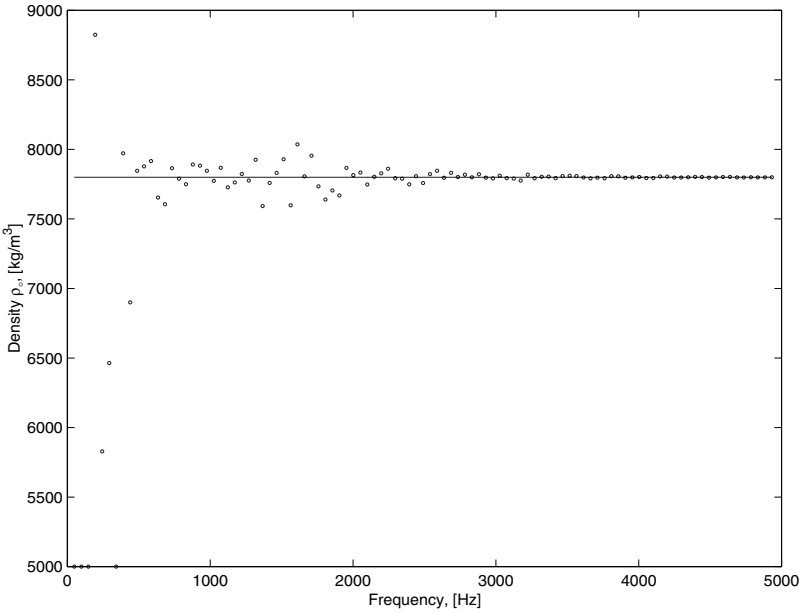

Fig. 8.5. Estimation of density $\rho_\circ$

Figure 8.3 shows the estimation of the Young's modulus of the background homogeneous material, *i.e.,* steel, whose actual value is 210 GPa. It can be seen that, except for a few points (no more than 10% of the total number), the estimated values are quite close to the exact value, which is shown by the firm line. Similarly, estimation of the shear modulus $G_\circ$ is shown in Figure 8.4 and as the figure suggests, the convergence is far better in this case (the exact value is 80.76 GPa, as shown by the firm line). The estimation of density $\rho_\circ$ (exact value is 7800 kg/m^3) shows a different trend. Initially, for low frequencies the effect of inertia is not so dominant and this is reflected in the poor estimation for $\omega < 2$ kHz. However, for higher ω, the estimation is quite close to the exact value. Finally, the inhomogeneous parameters are estimated, first individually (shown in the upper two subplots of Figure 8.6) and next simultaneously (lower two subplots of Figure 8.6). As the figure suggests, estimation of α is comparatively better than that for β, which may be due to the approximate nature of the treatment of β. Since, β is associated with inertia, initially its estimation is very poor (like density). Also it can be noticed that the estimation becomes poor (nominally for α and considerably for β) if both parameters are considered simultaneously. However, at higher frequencies the estimated values become quite close to the exact values.

Two applications of the developed SLEs are discussed in this chapter. First, the solution of the inverse problems of source identification, and second, material parameter estimation. The anisotropic SLE is used to regener-

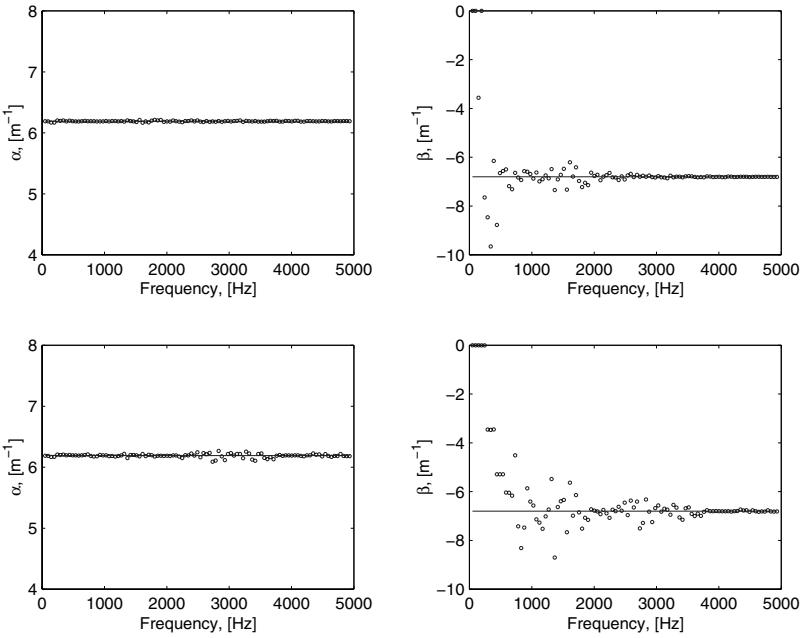

Fig. 8.6. Estimation of inhomogeneous parameters, α and β

ate a broadband pulse load from the measured truncated response, which is straightforward in SFEM because of its frequency domain based formulation. The effect of the truncation point is demonstrated and it is shown that for modeling pulse loading, most of the measured response history is redundant. Next, the inhomogeneous layer element is used to estimate inhomogeneous material properties. The estimation is carried out by posing the inverse problem as non-linear optimization in the frequency domain. It is shown that satisfactory convergence can be achieved by this method. The small system size of SLE is fully utilized in this method.

The next important inverse problem of great practical value is Structural Health Monitoring (SHM), where the presence and location of damage in a composite structure need to be determined. Since, SHM is a high frequency activity (requires probing force with high frequency content), SFEM is an ideal candidate as a modeling tool. The use of SFEM for SHM applications is discussed in great detail in the next two chapters.

9

Application of SFEM to SHM: Simplified Damage Models

Structural Health Monitoring (SHM) is a class of inverse problem wherein the state of structures requires to be determined using a predefined input and the measured output(s). In composite structures, delamination is the common type of failure. If the size of the delamination is very small, it results in negligible loss of stiffness and hence lower vibrational modes will be least affected. Hence, SHM studies require high frequency content inputs (loads) and SFEM provides a very efficient mathematical model for this purpose. The main requirements of SHM are simplified damage models and efficient damage detection studies. While the former is addressed in this chapter, the later is dealt with in the next chapter. In this chapter, various simplified damage models for single and multiple delaminations, fiber breakage, surface breaking cracks and degraded zones are formulated. Numerical examples are provided to show the wave scattering due to a crack front.

9.1 Various Damage Identification Techniques

Composite structures provide opportunities for weight reduction, tailoring the material, integrating control surfaces in the form of embedded transducers, *etc.*, which are not possible with conventional metallic structures. Since very few such high-importance composite structures have completed significant number of years of design life, the damage tolerance of these structures is yet to be explored. Unlike the design of metal structures, this information has not been incorporated into the design process. Therefore, a potential barrier at present is that the composite structures can have internal defects that are difficult to detect but need frequent monitoring to assess their vulnerability. Although, matrix cracking, fiber breakage, fiber debonding, *etc.* initiate the damage that occurs in laminated composites, inter-laminar cracking or delamination is most important and can grow, thus reducing the life of the structure. This is because, in contrast to their in-plane properties, transverse tensile and inter-laminar shear strengths are quite low. Standard

non-destructive techniques (NDT) such as ultrasonic, fractographic, thermographic or tomographic imaging techniques require that the vicinity of the damage is known *a priori* and that the portion being inspected is readily accessible [10]. These limitations make them very expensive for damage detection in aircraft or spacecraft structures, which are large and also need frequent inspection. Therefore an in-service global/local damage detection (health monitoring) system is essential, which, with built-in transducers, can frequently monitor the integrity of the structure and determine the location and extent of damage. To meet this requirement, one needs a highly efficient computing tool that can simulate the response of damaged structures with minimum human interaction. Here, the word "efficient" emphasizes reduced modeling complexity, computation time and constraints on the memory requirement in the on-board computer. Also, issues related to signal processing are expected to play a significant role.

9.1.1 Techniques for Modeling Delamination

Delaminations in composites are usually modeled using beams, plates or shells with appropriate kinematics. The technique used in [159] to model a through-width delamination subdivides the beam into a delamination region (sublaminates) and two integral regions (base laminates) on either side of the delamination region. Each of these sublaminates and base laminates is modeled as a Euler beam and the whole structure is solved satisfying the global boundary conditions. For one-dimensional beam elements, additional axial forces give rise to a net resultant internal bending moment, which creates differential stretching of the sublaminates above and below the plane of delamination. The assumption made in [159] is that the axial forces in these sublaminates are equal and opposite (*i.e.,* if one is under compression, the other is under tension by the same amount). This does not hold when the delamination is not at the mid-plane or the ply-stacking is not balanced. Therefore this imbalance gives rise to an axial load in the defect-free segments. The model used in [160] to study the effect of delamination on natural frequency is also based on engineering beam theory. However, this model uses 2-D beam elements and therefore eliminates the shortcoming discussed above. It also includes the effect of contact between the delaminated surfaces and can allow independent extensional and bending stiffness.

In [161] two different types of finite elements are considered for the healthy and delaminated elements. For the healthy elements, all the lamina are assumed to have the same transverse and longitudinal displacements at a typical cross-section, but each lamina can rotate by a different amount from the others depending on its material and geometrical properties. This is also called the "layer-wise constant shear kinematics". The delaminated element has the same transverse and axial displacement at both ends of the element. Only the rotation is different along the element length of each lamina. In the same direction Reference [162] used layer-wise plate theory for modeling delamina-

tion in plates where delaminations were simulated by step discontinuity at the interfaces.

Modeling performed in [163] assumes opening and closing action at the region of delamination. Here it is considered that after delamination, partially intact matrix and fibers still fill the delamination gap. The contact effect between the delaminated sublaminates is modeled as a distributed non-linear soft spring between them. The spring is assumed non-linear because when the delamination opens beyond some small amplitude constraints, the spring effect becomes zero; on the other hand, when the vibration mode does not tend to open the delamination, the delaminated sublaminates have the same flexural displacements and slopes. This non-linear spring is then simplified to a combination of a few linear springs. Such modeling provides better representation of the practical problem. In many mechanical components under fatigue loading, such delamination can grow, leaving non-linear modes in vibration characteristics. Related measurements in a metal beam with a fatigue crack can be found in [164]. Williams [133] proposed a generalized theory of delaminated plates using a global/local variational approach. This theory uses unique coupling between the global and local displacement fields in two different length scales and is a generalization of the earlier proposed theories based on "layer-wise constant shear kinematics".

However, these global/local analyses are based on a semi-analytic approach and are difficult to incorporate for transient dynamic and wave-based diagnostic problems as focused on in the present chapter. From the reported work discussed above, it can be seen that a more versatile approach suitable for automated modeling of delamination for dynamic problems is required. This chapter addresses related modeling issues considering 1-D waveguides without the effect of contact non-linearity. For this purpose, we will use the 1-D waveguide models formulated in earlier chapters as the basic building block for efficient modeling and analysis of delamination.

9.1.2 Modeling Issues in Structural Health Monitoring

The presence of delamination or any other modes of damage changes the structural dynamic characteristics and can be traced in natural frequencies, mode shapes, phase, dynamic strain and stress wave patterns, *etc.* Significant research has been reported on the effect of delamination on natural frequencies and mode shapes and strategies have been developed to identify the location of delamination using changes in these modal parameters [160], [161], [165], [166], [167].

Tracy and Pardoen [160] found that if the delamination is in a region of mode shape where the shear force is very high, there will be considerable degradation in natural frequency, which is otherwise not significant. Hence, by studying the mode shapes and the corresponding natural frequencies, an estimation of the location of delamination can be made. Lakshminarayana

and Jebaraj [168] used the first four bending and torsional modes and corresponding changes in natural frequencies to estimate the location of a crack in a beam. It is reported that if the crack is located at the peak/trough positions of the strain mode shapes, then percentage change in the frequency would be higher for the corresponding modes. It is also found that if the crack is located at the nodal points of the strain mode shapes, then the percentage change in the frequency values would be lower for the corresponding modes.

Schulz *et al.* [169] used *damage force* to identify the elements having damage. The method suggested by them requires the system matrix (dynamic stiffness matrix) of the healthy structure to be stored at each frequency. Displacements measured at each node for the damaged structure along with the stored system matrix can be used here to identify the elements with damage. This method is independent of the excitation force, which can be uniform, random or uncorrelated. However, it requires measurements at a large number of points on the structure to locate the damage with moderate accuracy. The system size becomes exponentially large, requiring a large storage space.

Not much work has been reported in the area of damage identification using stress wave propagation compared to that with vibration and modal analysis and testing. The reason may primarily be attributed to (1) the limitations of available finite element analysis in solving wave propagation problem in large structures, and (2) difficulty in modeling a finite complicated domain using semi-analytic methods (such as the transfer function method, spectral analysis, wavelet analysis *etc.*).

9.2 Modeling Wave Scattering due to Multiple Delaminations and Inclusions

Extensive tailorablity of fiber reinforced laminated composite and thin film type layered structures has led to the present-day state of the art in smart structures and micro-electromechanical systems (MEMS). Such structures are potential candidates for specific and complex applications due to their multifunctionality. From the viewpoint of the mechanical performance, very high stiffness-to-weight ratio is one of the well exploited functionalities. There are also special structural designs of interest, where the effect of stiffness coupling is used for flextensional and shear induced actuation and shape [170]. Also, for smart structural applications, laminated composite structures can be designed as the host structures with a diverse range of micro-sensors and actuators and even have the entire electronics [171] embedded in them. In recent times, many other applications of laminated composite materials have appeared, such as active control of sound [172], which are of less structural importance and are fabricated to meet multi-physics requirements in MEMS devices, integrated circuits operating in extreme environments.

Delamination and debonding of devices embedded in laminated composite structures is one crucial damage mode [163], [173], [174]. When such an inte-

grated heterogeneous system is exposed to highly transient dynamic or fatigue loading, for example in the flexbeam of helicopter rotor-blades [175], multiple waves in the low to high frequency ranges are generated. At minute interfaces between heterogeneous stiffness and mass systems, considerable change in the nearfield effects may occur due to the scattering of waves. One crucial outcome of such phenomena is the development of dynamic stress intensity at the delaminations tips [3]. This may enhance the formation of delamination in locations of severe stress discontinuities. Modern composite structures with several embedded microdevices need special treatment based on simulation at the design stage. Further, for operational composite structures, health monitoring becomes an important issue due to the high cost of obtaining test data and its post-processing to identify the delaminated or debonded configurations in interior locations. To address such issues in the context of structural health monitoring systems, wave based diagnostics and related modeling complexities have been discussed [176], [177], [175], [178], [179], [180]. Several defects and composite material aging changes the characteristic structural behavior. Also, non-ideal boundaries and finite geometry make model based prediction difficult to match with test data. To alleviate such difficulties, one may seek most of the numerical analysis data to be in the form of digital signals. In this chapter, we take the advantages of FFT coupled with SFEM developed in the previous chapters to solve wave propagation and its interaction with delaminations and debonding of strip inclusions embedded inside laminated composite.

In most real life situations, it is observed that one or more delaminations across the thickness of the laminated structure produce membrane flexural torsional coupling. Therefore, even in the presence of only in-plane or torsional loading, flexural waves are generated, which are dispersive in nature. As the total thickness increases, additional shear waves and then higher order antisymmetric and symmetric Lamb wave modes become dominant with wave speeds exceeding the in-plane wave speed. This implies that the modeling of delaminated configurations in conventional FE analysis to capture the propagating stress waves requires a very fine mesh. Also, the delamination tips may need further mesh refinement, which makes an efficient analysis of the global behavior very difficult.

On the other hand, in modeling approaches based on wave propagation, it is possible to identify the presence of damage using certain simplified assumptions, such as equivalent material degradation [178] at the crack or delamination interface. Such a model incurs changes in the speeds of different wave modes (longitudinal, flexural, shear) and hence the wavenumbers associated with those modes. In another approach [177], [175], a set of scattering matrices are derived based on the reflection and transmission of incident waves at structural boundaries; the phase change due to the presence of damage at different frequencies can be used to quantify the damage. However, here one needs a sensor and an actuator confining the damage, and then use of a controller to cancel the resonances and anti-resonances due to structural

boundaries through a dereverberated transfer function (DTF). Also, in the above approach, a detailed model of delamination or debonding and hence the scattering of coupled waves at and inside the damage cannot be incorporated. Further, these analytical models are limited by the possibility of algebraic manipulation in closed form, which is often very cumbersome when dealing with axial–flexural shear coupled wave propagation in composite structures. Since, most of the analytical formulations available in the literature are based on isotropic material configuration with a symmetrically placed single damage model, a general framework needs to be explored considering multiple delaminations and debonding of inclusions.

In a continuum mechanics formulation for damage or inclusion, one can use a mixed variational formulation in the local model to capture the localized stress field accurately. An assumed stress field for the local damage region and assumed displacement for the global region can generally be used [181]. Here, one can consider an appropriate damage-dependent constitutive model [182] based on the continuum damage mechanics for the local region, and an equivalent fiber matrix mixture constitutive model [50] for the global region. However, such a detailed model is computationally intensive in the context of structural health monitoring and identification of damage using model based prediction and diagnostic wave propagation. In such problems, the available simplified distributed parameter approach is to neglect the relative rotation of the damaged and healthy sections (in the case of beams and plates) and treat the structures with Euler–Bernoulli (beams) and Kirchhoff (plates) type kinematics. Such models have been verified experimentally in [175] in the context of wave propagation in delaminated isotropic helicopter flexbeams, and in [163] in the context of natural frequency change in a first-order shear deformable composite beam with delamination and the associated contact non-linearity in the low frequency dynamics. Also, such a simplified model can be found useful while modeling advanced composite with stitching [183] and various other types of material interfaces. Considering axial–flexural shear coupled wave propagation in composite beams (see Chapter 4), a spectral element for delaminated beams has been developed that will be discussed in this chapter. In this formulation based on SFEM, the exact dynamics of the internal debonded sublaminates are also taken into account. This formulation then condenses out the FE nodal information of the internal waveguides, and hence allows one to replace a healthy composite beam segment with this spectral element where delamination exists. Although the reported models, *e.g.,* [163], [180], use constant rotation of the interface between the damaged and healthy segment, they are not capable of capturing the differential rotation of individual debonded sublaminates at their interfacial cross-section with the base laminates. This is also an important effect to consider for thickness-wise multiple delaminations or other forms of damage and inclusion. This restriction due to constant shear kinematics can be eliminated using the approach reported in [162], where the layer-wise kinematics allows individual sublaminates to rotate by different amounts. A similar approach has been used in

[184], where the formulation uses a penalty function to impose appropriate constraints at the interface between the base laminates and the multiple sublaminates. In [185] and [186] the interface is assumed to translate and rotate in a rigid-body mode. Thus, the normal plane is assumed continuous across the base laminate thickness and is hence not affected by the stress discontinuity in the two delaminated faces at the tip due to Mode-I and Mode-II stable delaminations. However, this assumption may not be adequate, since strong coupling between the displacement components may exist in the case of asymmetric ply-stacking, asymmetry among the sublaminates (due to inclusions of different material) and discontinuity in the stiffness and inertia due to foreign inclusions such as MEMS devices and integrated electronics.

In the present chapter, we extend the above concept to model the individual sublaminates or strip inclusions. SFEMs developed in earlier chapters are used to model the individual sublaminates, base laminates and strip inclusions. A layer-wise constant shear kinematics is then imposed at the interfaces of sublaminates and base laminates. Equilibrium of the discretized system is obtained using the multi-point constraints (MPC) in the Fourier domain associated with the nodal displacement components and the force components at these interfaces. This allows us to model small local rotations of the individual sublaminates and the base laminates at the interface in an average sense. Also, the model is a general one, where the length-wise multiple delaminations of debonding between strip inclusions can be modeled easily. Another advantage of the proposed model is that both the frequency domain changes in phase and amplitude of scattered waves in the presence of delaminations or strip inclusions as well as the time domain change in the response, can be computed efficiently with the help of FFT [187].

9.3 Spectral Element with Embedded Delamination

The location of the nodes of the spectral elements for a delaminated beam is shown in Figure 9.1. In the absence of delamination, one spectral element between node 1 and node 2 is sufficient for analysis. The presence of delamination when treated as a structural discontinuity by neglecting the effect of stress singularity at the delamination tip, increases the number of elements from one to four. Six more nodes are introduced to model individual base laminates and sublaminates. For the sublaminate-elements (elements 3 and 4) the nodes are located at the mid-plane of the sublaminates and element lengths are equal to the length of the delamination.

The kinematic assumption for the interface of base laminate and sublaminates is that the cross-section remains straight, *i.e.,* the slope is continuous and constant at the interface. Under this assumption, one can obtain the following equations:

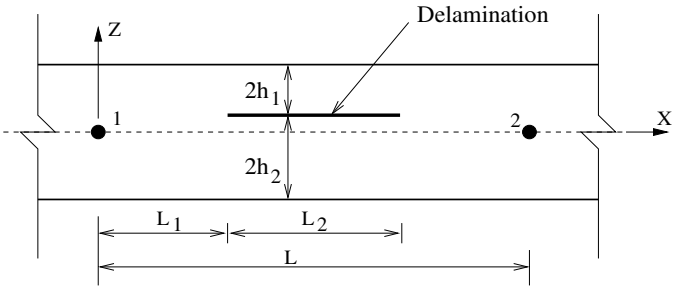

Fig. 9.1. Delamination configuration

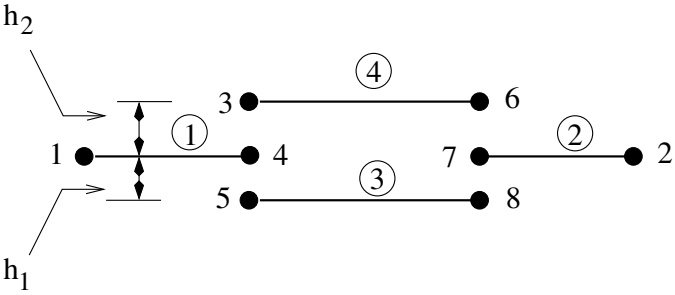

Fig. 9.2. Representation of the base laminates and sublaminates by spectral elements

$$\hat{\mathbf{u}}_{\mathbf{3}} = \begin{Bmatrix} \hat{u}_3^0 \\ \hat{\omega}_3 \\ \hat{\phi}_3 \end{Bmatrix} = \begin{Bmatrix} \hat{u}_4^0 + h_2\hat{\phi}_4 \\ \hat{\omega}_4 \\ \hat{\phi}_4 \end{Bmatrix} = \mathbf{S_1}\hat{\mathbf{u}}_{\mathbf{4}} \,, \tag{9.1}$$

$$\hat{\mathbf{u}}_{\mathbf{5}} = \begin{Bmatrix} \hat{u}_5^0 \\ \hat{\omega}_5 \\ \hat{\phi}_5 \end{Bmatrix} = \begin{Bmatrix} \hat{u}_4^0 - h_1\hat{\phi}_4 \\ \hat{\omega}_4 \\ \hat{\phi}_4 \end{Bmatrix} = \mathbf{S_2}\hat{\mathbf{u}}_{\mathbf{4}} \,; \tag{9.2}$$

and similarly,

$$\hat{\mathbf{u}}_{\mathbf{6}} = \mathbf{S_1}\hat{\mathbf{u}}_{\mathbf{7}} \,, \quad \hat{\mathbf{u}}_{\mathbf{8}} = \mathbf{S_2}\hat{\mathbf{u}}_{\mathbf{7}} \,. \tag{9.3}$$

Here all the vectors are marked with overhead hat to indicate that the variables are discretized in the frequency domain. Using these we can map the displacements at sublaminate element nodes 3, 5 (on the left interface) and 6, 8 (on the right interface) in terms of displacements of base laminate nodes 4 (on the left interface) and 7 (on the right interface), respectively (see Figure 9.2). $\mathbf{S_1}$ and $\mathbf{S_2}$ are the 3×3 transformation matrices given by

$$\mathbf{S_1} = \begin{bmatrix} 1 & 0 & h_2 \\ 0 & 1 & 0 \\ 0 & 0 & 1 \end{bmatrix} \,, \quad \mathbf{S_2} = \begin{bmatrix} 1 & 0 & -h_1 \\ 0 & 1 & 0 \\ 0 & 0 & 1 \end{bmatrix} . \tag{9.4}$$

From the equilibrium of the left interface AB (Figure 9.3), we can draw the

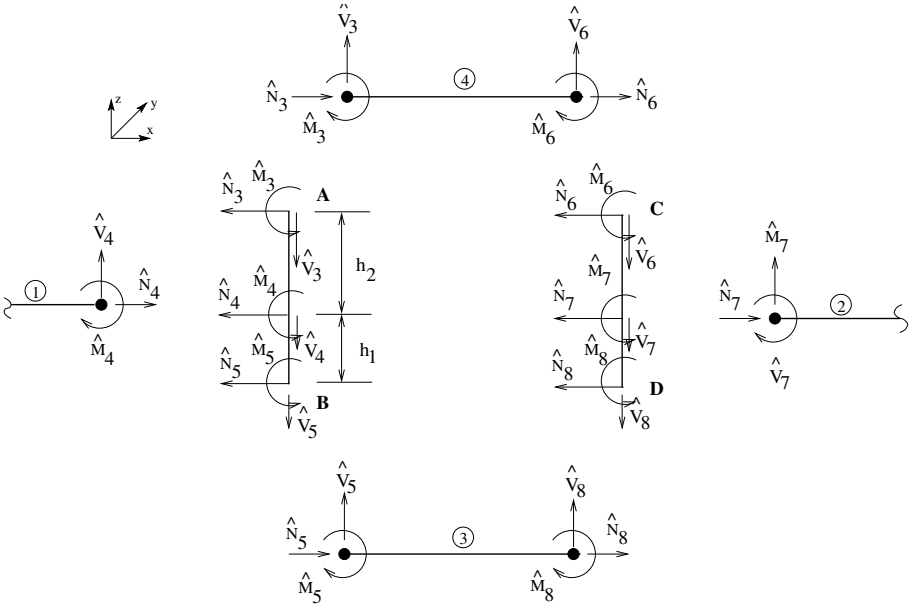

Fig. 9.3. Force balance at the interface between base laminate and sublaminate elements

following force balance equation

$$\begin{Bmatrix} \hat{N}_4 \\ \hat{V}_4 \\ \hat{M}_4 \end{Bmatrix} + \begin{Bmatrix} \hat{N}_3 \\ \hat{V}_3 \\ \hat{M}_3 \end{Bmatrix} + \begin{Bmatrix} 0 \\ 0 \\ h_2\hat{N}_3 \end{Bmatrix} + \begin{Bmatrix} \hat{N}_5 \\ \hat{V}_5 \\ \hat{M}_5 \end{Bmatrix} + \begin{Bmatrix} 0 \\ 0 \\ -h_1\hat{N}_5 \end{Bmatrix} = \begin{Bmatrix} 0 \\ 0 \\ 0 \end{Bmatrix} , \quad (9.5)$$

which, in matrix form can be written as

$$\hat{\mathbf{f}}_\mathbf{4} + {\mathbf{S}_\mathbf{1}}^T\hat{\mathbf{f}}_\mathbf{3} + {\mathbf{S}_\mathbf{2}}^T\hat{\mathbf{f}}_\mathbf{5} = \mathbf{0} . \quad (9.6)$$

Similarly, from the equilibrium of the right interface CD, we can get

$$\hat{\mathbf{f}}_\mathbf{7} + {\mathbf{S}_\mathbf{1}}^T\hat{\mathbf{f}}_\mathbf{6} + {\mathbf{S}_\mathbf{2}}^T\hat{\mathbf{f}}_\mathbf{8} = \mathbf{0} . \quad (9.7)$$

The element equilibrium equation for the jth element ($j = 1, 2$ for base laminates, $j = 3, 4$ for sublaminates) with nodes p and q can be written as

$$\hat{\mathbf{K}}^{(j)}_{(6\times6)} \begin{Bmatrix} \hat{\mathbf{u}}_\mathbf{p} \\ \hat{\mathbf{u}}_\mathbf{q} \end{Bmatrix} = \begin{Bmatrix} \hat{\mathbf{f}}_\mathbf{p} \\ \hat{\mathbf{f}}_\mathbf{q} \end{Bmatrix} . \quad (9.8)$$

This equation can be rewritten using 3×3 submatrices of the stiffness matrix as

$$\begin{bmatrix} \hat{\mathbf{K}}^{(j)}_{\mathbf{11}} & \hat{\mathbf{K}}^{(j)}_{\mathbf{12}} \\ \hat{\mathbf{K}}^{(j)}_{\mathbf{21}} & \hat{\mathbf{K}}^{(j)}_{\mathbf{22}} \end{bmatrix}_{(6\times6)} \begin{Bmatrix} \hat{\mathbf{u}}_\mathbf{p} \\ \hat{\mathbf{u}}_\mathbf{q} \end{Bmatrix} = \begin{Bmatrix} \hat{\mathbf{f}}_\mathbf{p} \\ \hat{\mathbf{f}}_\mathbf{q} \end{Bmatrix} . \quad (9.9)$$

The above equation for the local element 1 can be written as

$$\begin{bmatrix} \hat{\mathbf{K}}_{\mathbf{11}}^{(1)} & \hat{\mathbf{K}}_{\mathbf{12}}^{(1)} \\ \hat{\mathbf{K}}_{\mathbf{21}}^{(1)} & \hat{\mathbf{K}}_{\mathbf{22}}^{(1)} \end{bmatrix}_{(6\times 6)} \begin{Bmatrix} \hat{\mathbf{u}}_{\mathbf{1}} \\ \hat{\mathbf{u}}_{\mathbf{4}} \end{Bmatrix} = \begin{Bmatrix} \hat{\mathbf{f}}_{\mathbf{1}} \\ \hat{\mathbf{f}}_{\mathbf{4}} \end{Bmatrix} . \tag{9.10}$$

For the local element 2,

$$\begin{bmatrix} \hat{\mathbf{K}}_{\mathbf{11}}^{(2)} & \hat{\mathbf{K}}_{\mathbf{12}}^{(2)} \\ \hat{\mathbf{K}}_{\mathbf{21}}^{(2)} & \hat{\mathbf{K}}_{\mathbf{22}}^{(2)} \end{bmatrix}_{(6\times 6)} \begin{Bmatrix} \hat{\mathbf{u}}_{\mathbf{7}} \\ \hat{\mathbf{u}}_{\mathbf{2}} \end{Bmatrix} = \begin{Bmatrix} \hat{\mathbf{f}}_{\mathbf{7}} \\ \hat{\mathbf{f}}_{\mathbf{2}} \end{Bmatrix} . \tag{9.11}$$

For the local element 3,

$$\begin{bmatrix} \hat{\mathbf{K}}_{\mathbf{11}}^{(3)} & \hat{\mathbf{K}}_{\mathbf{12}}^{(3)} \\ \hat{\mathbf{K}}_{\mathbf{21}}^{(3)} & \hat{\mathbf{K}}_{\mathbf{22}}^{(3)} \end{bmatrix}_{(6\times 6)} \begin{Bmatrix} \hat{\mathbf{u}}_{\mathbf{5}} \\ \hat{\mathbf{u}}_{\mathbf{8}} \end{Bmatrix} = \begin{Bmatrix} \hat{\mathbf{f}}_{\mathbf{5}} \\ \hat{\mathbf{f}}_{\mathbf{8}} \end{Bmatrix} . \tag{9.12}$$

Expressing $\hat{\mathbf{u}}_{\mathbf{5}}$ and $\hat{\mathbf{u}}_{\mathbf{8}}$ in terms of $\hat{\mathbf{u}}_{\mathbf{4}}$ and $\hat{\mathbf{u}}_{\mathbf{7}}$ respectively (Equations (9.2) and (9.3)) and premultiplying both sides by ${\mathbf{S}_{\mathbf{2}}}^T$, we get

$$\begin{bmatrix} {\mathbf{S}_{\mathbf{2}}}^T \hat{\mathbf{K}}_{\mathbf{11}}^{(3)} \mathbf{S}_{\mathbf{2}} & {\mathbf{S}_{\mathbf{2}}}^T \hat{\mathbf{K}}_{\mathbf{12}}^{(3)} \mathbf{S}_{\mathbf{2}} \\ {\mathbf{S}_{\mathbf{2}}}^T \hat{\mathbf{K}}_{\mathbf{21}}^{(3)} \mathbf{S}_{\mathbf{2}} & {\mathbf{S}_{\mathbf{2}}}^T \hat{\mathbf{K}}_{\mathbf{22}}^{(3)} \mathbf{S}_{\mathbf{2}} \end{bmatrix}_{(6\times 6)} \begin{Bmatrix} \hat{\mathbf{u}}_{\mathbf{4}} \\ \hat{\mathbf{u}}_{\mathbf{7}} \end{Bmatrix} = \begin{Bmatrix} {\mathbf{S}_{\mathbf{2}}}^T \hat{\mathbf{f}}_{\mathbf{5}} \\ {\mathbf{S}_{\mathbf{2}}}^T \hat{\mathbf{f}}_{\mathbf{8}} \end{Bmatrix} . \tag{9.13}$$

For the local element 4,

$$\begin{bmatrix} \hat{\mathbf{K}}_{\mathbf{11}}^{(4)} & \hat{\mathbf{K}}_{\mathbf{12}}^{(4)} \\ \hat{\mathbf{K}}_{\mathbf{21}}^{(4)} & \hat{\mathbf{K}}_{\mathbf{22}}^{(4)} \end{bmatrix}_{(6\times 6)} \begin{Bmatrix} \hat{\mathbf{u}}_{\mathbf{3}} \\ \hat{\mathbf{u}}_{\mathbf{6}} \end{Bmatrix} = \begin{Bmatrix} \hat{\mathbf{f}}_{\mathbf{3}} \\ \hat{\mathbf{f}}_{\mathbf{6}} \end{Bmatrix} . \tag{9.14}$$

Similarly expressing $\hat{\mathbf{u}}_{\mathbf{3}}$ and $\hat{\mathbf{u}}_{\mathbf{6}}$ in terms of $\hat{\mathbf{u}}_{\mathbf{4}}$ and $\hat{\mathbf{u}}_{\mathbf{7}}$ respectively (Equations (9.1)–(9.3)) and premultiplying both sides by ${\mathbf{S}_{\mathbf{1}}}^T$, we get

$$\begin{bmatrix} {\mathbf{S}_{\mathbf{1}}}^T \hat{\mathbf{K}}_{\mathbf{11}}^{(4)} \mathbf{S}_{\mathbf{1}} & {\mathbf{S}_{\mathbf{1}}}^T \hat{\mathbf{K}}_{\mathbf{12}}^{(4)} \mathbf{S}_{\mathbf{1}} \\ {\mathbf{S}_{\mathbf{1}}}^T \hat{\mathbf{K}}_{\mathbf{21}}^{(4)} \mathbf{S}_{\mathbf{1}} & {\mathbf{S}_{\mathbf{1}}}^T \hat{\mathbf{K}}_{\mathbf{22}}^{(4)} \mathbf{S}_{\mathbf{1}} \end{bmatrix}_{(6\times 6)} \begin{Bmatrix} \hat{\mathbf{u}}_{\mathbf{4}} \\ \hat{\mathbf{u}}_{\mathbf{7}} \end{Bmatrix} = \begin{Bmatrix} {\mathbf{S}_{\mathbf{1}}}^T \hat{\mathbf{f}}_{\mathbf{3}} \\ {\mathbf{S}_{\mathbf{1}}}^T \hat{\mathbf{f}}_{\mathbf{6}} \end{Bmatrix} . \tag{9.15}$$

After assembly of the above equations for the four local elements (two base laminates and two sublaminates) and subsequent use of Equations (9.6) and (9.7) yield the following form

$$\hat{\hat{\mathbf{K}}} \begin{Bmatrix} \hat{\mathbf{u}}_{\mathbf{1}} \\ \hat{\mathbf{u}}_{\mathbf{4}} \\ \hat{\mathbf{u}}_{\mathbf{7}} \\ \hat{\mathbf{u}}_{\mathbf{2}} \end{Bmatrix} = \begin{Bmatrix} \hat{\mathbf{f}}_{\mathbf{1}} \\ \mathbf{0} \\ \mathbf{0} \\ \hat{\mathbf{f}}_{\mathbf{2}} \end{Bmatrix} , \tag{9.16}$$

where $\hat{\hat{\mathbf{K}}}$ is

$$\begin{bmatrix} \hat{\mathbf{K}}_{\mathbf{11}}^{(1)} & \hat{\mathbf{K}}_{\mathbf{12}}^{(1)} & \mathbf{0} & \mathbf{0} \\ \hat{\mathbf{K}}_{\mathbf{21}}^{(1)} & \hat{\mathbf{K}}_{\mathbf{22}}^{(1)} + \mathbf{S_1}^T\hat{\mathbf{K}}_{\mathbf{11}}^{(4)}\mathbf{S_1} + \mathbf{S_2}^T\hat{\mathbf{K}}_{\mathbf{11}}^{(3)}\mathbf{S_2} & \mathbf{S_1}^T\hat{\mathbf{K}}_{\mathbf{12}}^{(4)}\mathbf{S_1} + \mathbf{S_2}^T\hat{\mathbf{K}}_{\mathbf{12}}^{(3)}\mathbf{S_2} & \mathbf{0} \\ \mathbf{0} & \mathbf{S_1}^T\hat{\mathbf{K}}_{\mathbf{21}}^{(4)}\mathbf{S_1} + \mathbf{S_2}^T\hat{\mathbf{K}}_{\mathbf{21}}^{(3)}\mathbf{S_2} & \mathbf{S_1}^T\hat{\mathbf{K}}_{\mathbf{22}}^{(4)}\mathbf{S_1} + \mathbf{S_2}^T\hat{\mathbf{K}}_{\mathbf{22}}^{(3)}\mathbf{S_2} + \hat{\mathbf{K}}_{\mathbf{11}}^{(2)} & \hat{\mathbf{K}}_{\mathbf{12}}^{(2)} \\ \mathbf{0} & \mathbf{0} & \hat{\mathbf{K}}_{\mathbf{21}}^{(2)} & \hat{\mathbf{K}}_{\mathbf{22}}^{(2)} \end{bmatrix}.$$

On condensation of the dof at the internal nodes 4 and 7, the final form of the equilibrium equation is obtained as

$$\hat{\bar{\mathbf{K}}}_{(6\times6)} \begin{Bmatrix} \hat{\mathbf{u}}_{\mathbf{1}} \\ \hat{\mathbf{u}}_{\mathbf{2}} \end{Bmatrix} = \begin{Bmatrix} \hat{\mathbf{f}}_{\mathbf{1}} \\ \hat{\mathbf{f}}_{\mathbf{2}} \end{Bmatrix}, \tag{9.17}$$

where $\hat{\bar{\mathbf{K}}}$ is the reconstructed stiffness matrix for the *spectral element with embedded delamination*. Now, one only needs to replace the usual spectral element with this spectral element wherever a possible delamination may exist in composite beams and frame structures, keeping the original nodes unaltered. Hence, it is evident that insertion of this element on a modular approach is suitable for faster modeling and accurate prediction of delaminations in composite beams and frames with partial measurement of sensor signals. This is one of the requirements for online SHM.

9.3.1 Modeling Distributed Contact Between Delaminated Surfaces

In the above formulation we have not considered the effect of distributed contact between the delaminated surfaces, at the top from the sublaminate (4) and at the bottom from the sublaminate (3) (Figure 9.4). Although the spectral element is developed to study the interaction of diagnostic waves with the delamination and its effect captured at the distant measurement points, the objective in this section is to incorporate the additional effect due to a linearly distributed contact at the delaminated zones comprising the grain boundary of the matrix phase and the chopped fibers. In the present study, this is modeled as a viscoelastic layer between the delaminated surfaces. This model not only includes the effect of interfacial frictional slip under Mode-II fracture but also can be used as a linearized model to restrict the interpenetration and frictional contact under Mode-I fracture. However, more complex models considering a non-linear spring to restrict the occurrence of the incompatible modes due to interpenetration can be developed. Such aspects have been studied semi-analytically in [163].

Figure 9.4 shows the delaminated zone between two delaminated surfaces. Let us consider the distributed spring constants K_x and K_z and the distributed viscous damping coefficients C_x and C_z. The spectral amplitude of the distributed contact force vectors $\hat{\mathbf{\Gamma}}_t$ acting on the top surface of sublaminate (3) and $\hat{\mathbf{\Gamma}}_b$ acting on the bottom surface sublaminate (4) and consisting of longitudinal force along x, transverse force along z and moment about y due to relative motion between the top and bottom surfaces can be expressed as

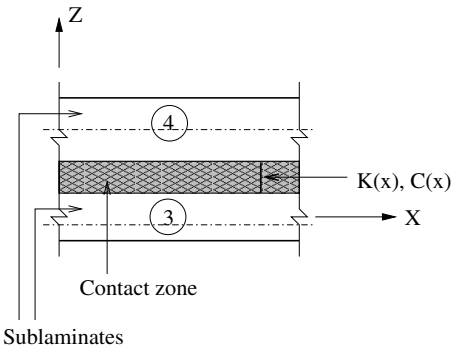

Fig. 9.4. Distributed contact idealized through distributed linear spring **K** and distributed linear viscous damper **C** between the delaminated surfaces. The waveguides (4) and (3) represents the top and bottom sublaminates respectively as shown in Figure 9.1

$$\hat{\mathbf{\Gamma}}_t = \begin{bmatrix} K_x + i\omega_n C_x & 0 \\ 0 & K_z + i\omega_n C_z \\ z_{bt}(K_x + i\omega_n C_x) & 0 \end{bmatrix} \begin{Bmatrix} \hat{u}_b - \hat{u}_t \\ \hat{w}_b - \hat{w}_t \end{Bmatrix} = \mathbf{K}^* \left(\hat{\mathbf{u}}_b - \hat{\mathbf{u}}_t \right) \ , \quad (9.18)$$

$$\hat{\mathbf{\Gamma}}_b = -\hat{\mathbf{\Gamma}}_t \ , \quad (9.19)$$

where the subscripts t and b respectively indicate the quantities associated with the top surface of the sublaminate (3) and the bottom surface of the sublaminate (4). In Equation (9.18), z_{bt} is the depth of separation between the delaminated surfaces. Considering the displacement field according to the Timoshenko beam theory in Equation (4.21), the top surface displacement vector $\hat{\mathbf{u}}_t$ for sublaminate (3) can be expressed as

$$\hat{\mathbf{u}}_t = \begin{Bmatrix} \hat{u}_t \\ \hat{w}_t \end{Bmatrix} = \begin{bmatrix} 1 & 0 & z_t^{(3)} \\ 0 & 1 & 0 \end{bmatrix} \hat{\mathbf{u}}(x, \omega_n)^{(3)} = \bar{\mathbf{S}}_1 \hat{\mathbf{u}}(x, \omega_n)^{(3)} \quad (9.20)$$

and similarly, the bottom surface displacement vector $\hat{\mathbf{u}}_b$ for sublaminate (4) can be expressed as

$$\hat{\mathbf{u}}_b = \begin{Bmatrix} \hat{u}_b \\ \hat{w}_b \end{Bmatrix} = \begin{bmatrix} 1 & 0 & z_b^{(4)} \\ 0 & 1 & 0 \end{bmatrix} \hat{\mathbf{u}}(x, \omega_n)^{(4)} = \bar{\mathbf{S}}_2 \hat{\mathbf{u}}(x, \omega_n)^{(4)} \quad (9.21)$$

where $z_t^{(3)}$ denotes the depth of the top surface measured from the local reference plane of the sublaminate (3) and $z_b^{(4)}$ denotes the depth of the bottom surface measured from the local reference plane of the sublaminate (4). Using the generic displacement vector $\hat{\mathbf{u}}(x, \omega_n)^{(3)}$ and $\hat{\mathbf{u}}(x, \omega_n)^{(4)}$ in terms of the spectral element shape function matrices and nodal displacement vectors a consistent nodal force vector can be formed. Thus, for sublaminate (3), the consistent nodal force vector is $\hat{\mathbf{f}}^{e^{(3)}} = \int_0^L \hat{\aleph}^{e^{T^{(3)}}} \hat{\mathbf{\Gamma}}_t dx$.

9.4 Numerical Studies on Wave Scattering due to Single Delamination in Composite Beam

The response obtained using the spectral element for delamination is first compared with the standard 2-D constant strain FEM results. Next, the element is used to study wave scattering in delaminated composite beams of various configurations. While comparing the response from the spectral element model and the FEM, the delaminated surfaces are left free, and hence they behave as free surfaces without any mechanism to restrict interpenetration. However, such simplification allows relative slip between the two delaminated surfaces under linear approximation and are seldom treated in pure Mode-II loading of a cracked elastic continuum. Under Mode-II loading, only shear transfer can occur between the base laminates and the sublaminates. In such a case, interpenetration of the delaminated surfaces causing incompatible modes does not occur. However, the following FEM analysis helps us clarify such behavior in detail.

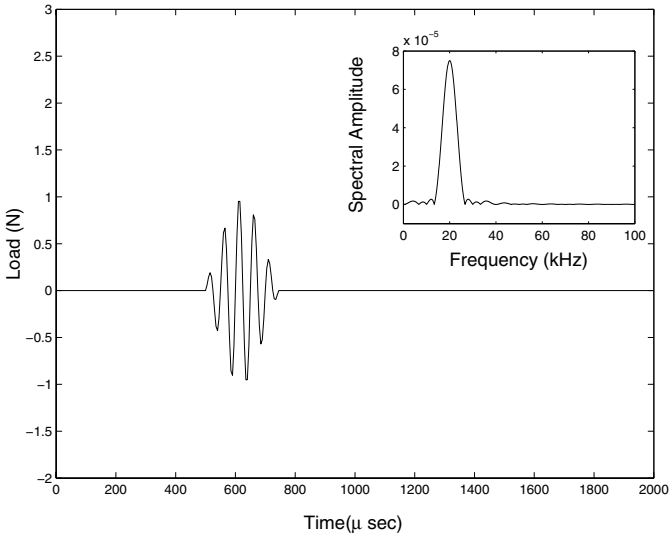

Fig. 9.5. Single frequency tone-burst sinusoidal pulse modulated at 20 kHz using trapezoidal window. The spectral amplitude $\hat{f}$ over the frequency axis is shown inset

9.4.1 Comparison with 2-D FEM

A graphite–epoxy cantilever beam of length 800 mm and having a cross-sectional area 16 mm thickness × 10 mm width is considered for this study. A 50 mm mid-plane delamination is introduced at a distance 400 mm from

the root of the beam. Modeling is done using one single spectral element with 4096 FFT sampling points ($\Delta\omega = 48.828$ Hz). In FE analysis, a fine mesh consisting of 2560 constant strain triangular elements is used. Here the element size is comparable with the wavelength of the applied excitation. Plane-stress condition in the vertical XZ plane is used. A single frequency pulse modulated at 20 kHz (Figure 9.5) is applied transversely at the tip cross-section.

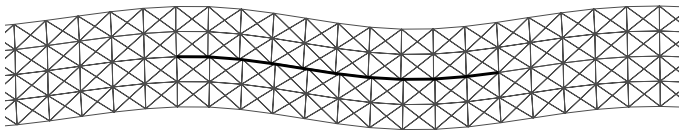

Fig. 9.6. Snapshot of the deformed FE mesh taken at the region of the delamination at $t = 0.84$ ms. The nodal displacements are magnified 10^5 times

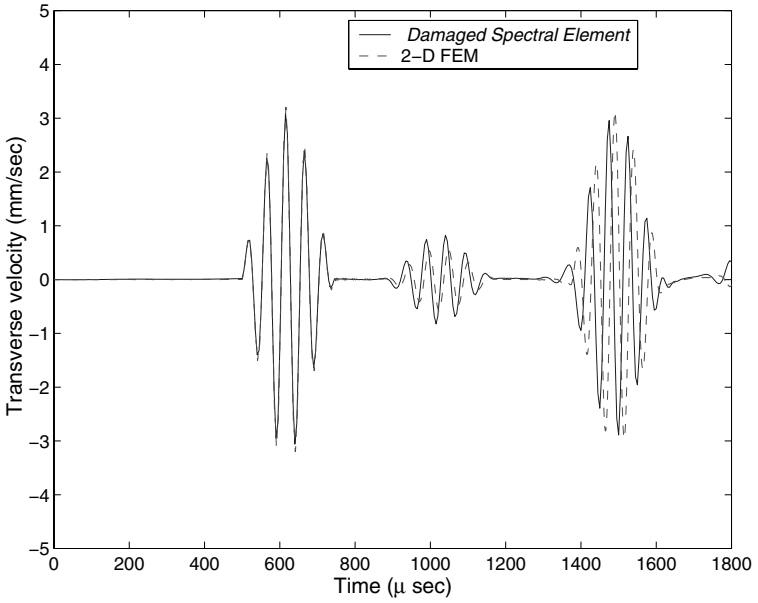

Fig. 9.7. Comparison of the transverse velocity $\dot{w}$ history computed at the tip of the cantilever using spectral element and 2-D constant strain triangular FEM

A snapshot of the deformed FE mesh at 0.84 ms having maximum slip between the delaminated surfaces at the mid-length of the delamination is shown in Figure 9.6. Nodal displacements have been magnified 10^5 times for ease of viewing. The cross-sections of the beam at vertical interfaces between sub-laminates and base laminates can be seen to be straight even in this deformed

state. This justifies the assumption made regarding the rotational continuity (Equations (9.1)–(9.3)) of the base laminate and sublaminate waveguide nodes at the interfaces during construction of the spectral element. Also it can be seen from Figure 9.6 that there is no interpenetration of the sublaminates and the deformation at the delaminated surfaces is primarily in-plane. For this reason, while considering the same type of Mode-II loading as considered here, the spectral element without the contribution of distributed contact is used in the rest of the numerical simulations. Plots of $\dot{w}$ at the mid-node of the tip cross-section predicted by the spectral element and 2-D FE analysis are shown in Figure 9.7. The first blob appearing in the time history is the incident wave. The next smaller one is the reflection generated by the delamination, which acts as a structural discontinuity; the last one is the reflected wave from the root of the beam. The incident wave matches well with the FEM results. However little difference in phase can be noticed in the reflected waves.

9.4.2 Identification of Delamination Location from Scattered Wave

To identify the location of delamination from the wave scattering wave, a graphite–epoxy $[0]_{10}$ cantilever beam of length $L = 2\,\text{m}$ having a cross-sectional area 10 mm × 10 mm is considered (Figure 9.8). A mid-plane delamination of size 20 mm is introduced at a distance $L_1 = 1.2$ m from the free end. A modulated sinusoidal pulse (Figure 9.5) is applied transversely at the free end *i.e.,* node 2 of the single spectral element used in the analysis. The flexural group speed $c_g = d\omega_n/dk_j = 2\sqrt[4]{D_{11}\omega_n^2/I_0}$, being a function of frequency is dispersive in nature. Therefore to locate a delamination with distinct arrival time of reflected waves from the delamination tip, one has to use a single frequency tone-burst signal that propagates non-dispersively. Use of such a signal in structural health monitoring experiments can be found in [188], [189].

The transverse velocity at node 2 (Figure 9.8) is plotted for both healthy and delaminated configurations. For the healthy case, the immediate incident wave and the reflected wave from the fixed end can be seen in Figure 9.9. For the delaminated case, one more reflection arrives from the delamination

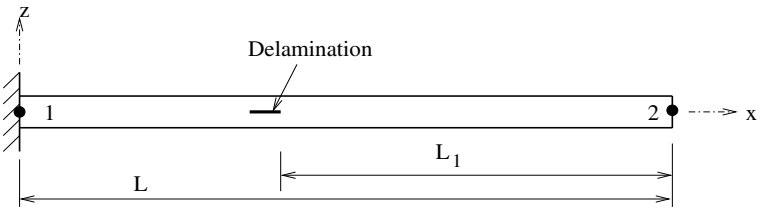

Fig. 9.8. Configuration of a cantilever beam with mid-plane delamination ($L = 2$ m, $L_1 = 1.2$ m)

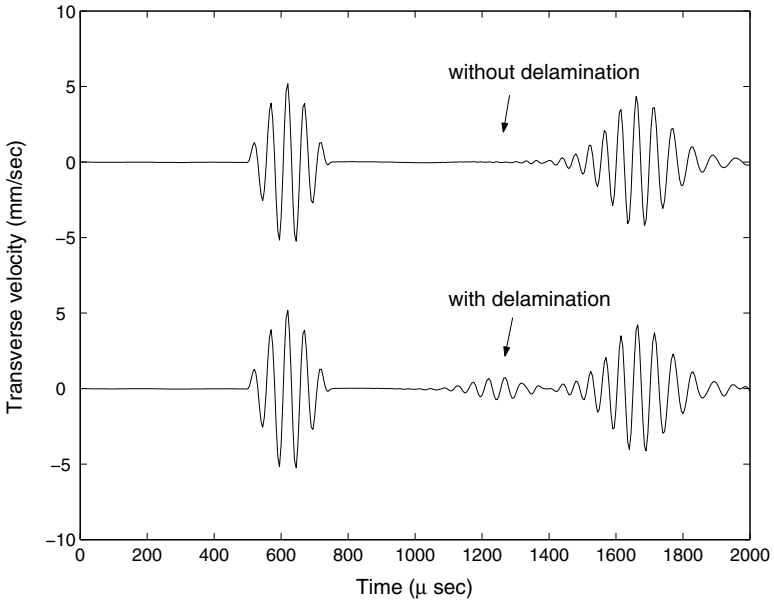

Fig. 9.9. Transverse velocity $\dot{w}$ at the cantilever tip due to modulated sine pulse transversely applied at the same location

tip. The group speed of the flexural wave (c_g) is 3850 m/s. It should take $2L/c_g \approx 1040\,\mu$s for the reflection from the root to arrive at the tip. For the reflection generated at the delamination tip this should be $2L_1/c_g \approx 625\,\mu$s. These values are found to match very closely the results shown in Figure 9.9. For the same transversely applied load, the rotational velocity history at the free end shows reflections of the same nature (Figure 9.10) and at the same time.

9.4.3 Effect of Delamination at Ply-drops

Next, we consider a delamination in the region of ply-drops in a cantilever beam. In a health monitoring application, detection of such a delamination near ply-drops, composite joints or other structural discontinuities is essential at an early stage. If the delamination length is small, the same modeling strategy as used above can be assumed to be valid here. A cantilever beam with the same material properties as used in the previous illustration and with ply-drops (Figure 9.11) is considered. The model has five plies dropped from the top, out of 15 plies on the fixed end side of the cantilever. A 20 mm long delamination is considered at the location of the ply-drops. Only two spectral elements are used in the model. Transverse velocity histories at the free end are plotted in Figure 9.12. For the healthy case, two reflections can be seen; first, one from the ply-drop due to a sudden change in the thickness, and the

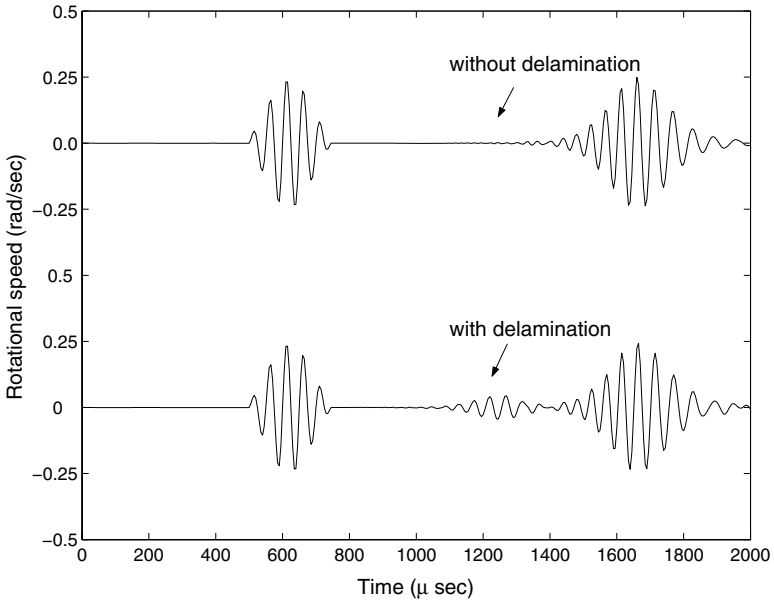

Fig. 9.10. Rotational velocity $\dot{\phi}$ at the cantilever tip due to modulated sine pulse transversely applied at the same location

second one from the fixed end of the beam. For the second case with delamination, the reflection from the ply-drop region is seen to be intensified showing a distinct blob. In actual measurement, one can use a second transducer pair to generate the incident pulse and to measure the reflected pulse both on the fixed-end side of the beam. Thus, by measuring the reflected waves on both sides of the delamination, it is possible to predict the length of the delamination very accurately. Also, the reference structural database can be updated in the presence of any local material degradation by correlating the measured signal and simulated signal using the present spectral element model.

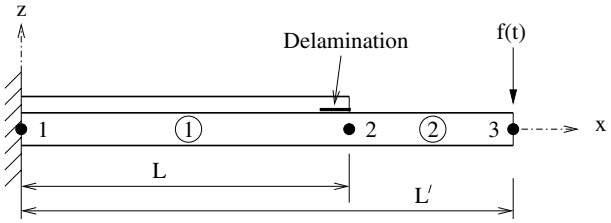

Fig. 9.11. Configuration of the cantilever beam showing a delamination in the region of ply-drops. $L = 1\,\mathrm{m}$, $L' = 1.5\,\mathrm{m}$

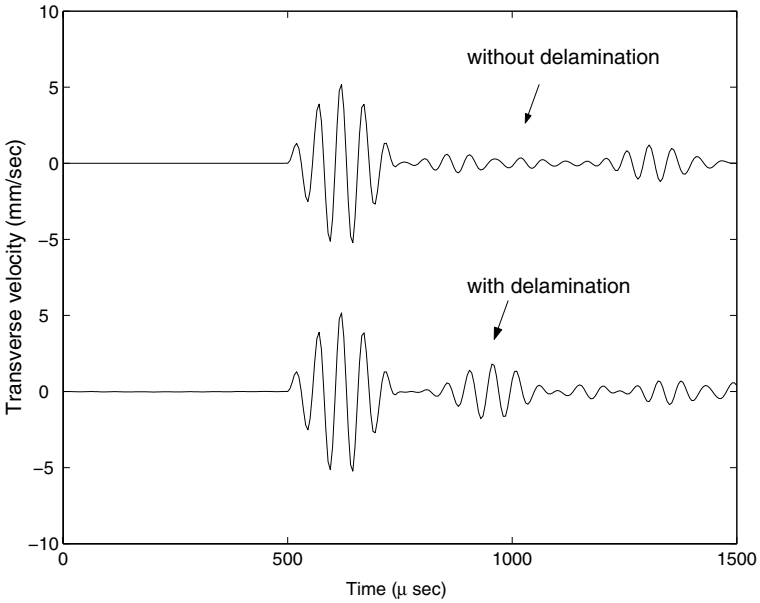

Fig. 9.12. Transverse velocity $\dot{w}$ at the free end due to modulated sine pulse applied transversely at the free end of the cantilever beam with ply-drops

9.4.4 Sensitivity of the Delaminated Configuration

To study the effects of variation in location, depth and length of delamination on reflected and transmitted waves, an infinitely long beam is taken (Figure 9.13). The beam boundaries are assumed to be at infinity to exclude unwanted boundary reflections that can distort the actual scattered wave at the delamination tip. In our model, throw-off spectral elements are connected to both the ends of a spectral element of length $L = 1.2\,\mathrm{m}$.

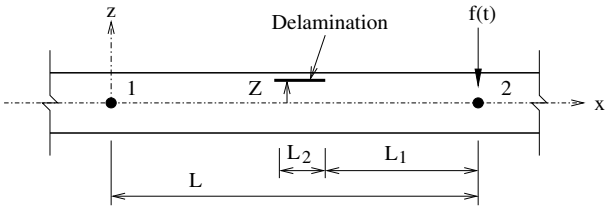

Fig. 9.13. An infinite beam considered for sensitivity analysis of delamination location (L_1), depth (Z) and length (L_2). Distance between the nodes, $L = 2\,\mathrm{m}$

Effect of Location Variation

A mid-plane delamination ($Z = 0$ in Figure 9.13) of length 20 mm is considered, to observe the effect of location variation. The distance of the right delamination-tip from node 2 (*i.e.,* L_1) is varied from 0.13 m to 1.08 m. Modulated sine pulse (Figure 9.5) is applied at node 2 in the transverse direction and the transverse velocities at node 2 and at node 1 are computed for varying location of the delamination. Response at node 2, which shows an immediate incident wave and reflected wave, is plotted in Figure 9.14. Response at node 1, which shows an immediate transmitted wave, is plotted in Figure 9.15. A linear relationship of the arrival time of the reflected wave with the location of delamination is clear from the plot in Figure 9.14. Therefore, measurement of the reflected wave can provide a good estimate of the location of the delamination. However there is no appreciable variation in the case of the transmitted wave (Figure 9.15).

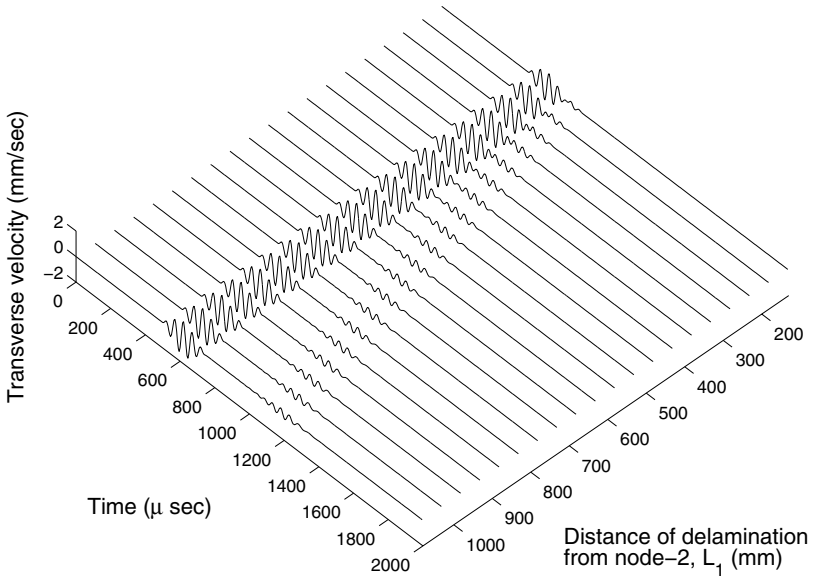

Fig. 9.14. Transverse velocity $\dot{w}$ computed at node 2 for different locations (L_1) of the delamination

Effect of Depth Variation

To study the effect of delamination depth (Z) variation on the reflected wave, a 20 mm long delamination (shown in Figure 9.13) is considered. The delamination depth is varied from −9 mm to +9 mm in steps of 1 mm from the

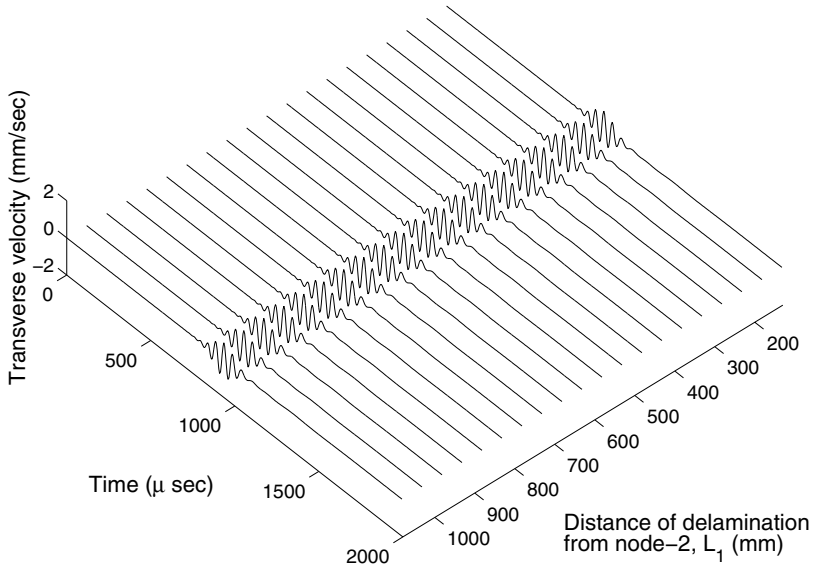

Fig. 9.15. Transverse velocity $\dot{w}$ computed at node 1 for different locations (L_1) of the delamination

mid-plane of the beam. Transverse velocity at node 2 is computed for a transversely applied pulse (Figure 9.5) at the same point. The plot in Figure 9.16 shows only the arrival of the reflected wave from the delamination tip for different Z. A non-linear relationship between the amplitude of the reflected wave and the depth of delamination can be noticed. The variations are symmetric about the mid-plane, which can be attributed to the dominance of the term z^3 in the flexural response. The strongest reflection occurs for a delamination at the mid-plane and its intensity reduces as the delamination moves away from the mid-plane. This can be explained by the fact that the highest change in stiffness occurs when the delamination is at the mid-plane.

Effect of Length Variation

Keeping the right tip of the delamination at a fixed distance $L_1 = 0.6\,\mathrm{m}$ from node 2 (see Figure 9.13), delamination length L_2 is varied from 20 mm to 215 mm with an increment of 5 mm at every step. The transverse velocity is plotted in Figure 9.17 for the same modulated sine pulse (Figure 9.5) transversely applied at node 2. Variation in the amplitude of the reflected wave from the delamination tip due to variation in the delamination length is found to be periodic in nature. It diminishes near those values of the delamination lengths that are multiples of half the group wavelength λ_g. The group speed for the symmetric sublaminates is calculated as $c_g = 2724\,\mathrm{m/s}$. Now,

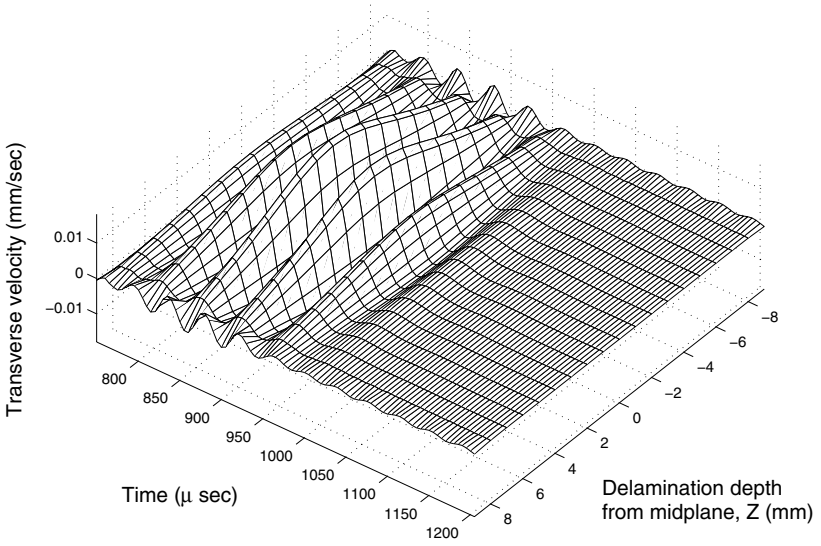

Fig. 9.16. Transverse velocity $\dot{w}$ history showing the reflected wave for different depths (Z) of delamination

considering the frequency of excitation $\nu = 20$ kHz, we compute the group wavelength as

$$\lambda_g = c_g/\nu \approx 136\,\text{mm}. \tag{9.22}$$

The reason for this periodicity of $\lambda_g/2$ can be attributed to the cancellation or amplification of scattered waves from two delamination tips. For those lengths of delamination which are near multiples of $\lambda_g/2$, the reflection generated by one delamination tip is attenuated by the reflection generated by the other tip, being out of phase. Complete cancellation of the reflection is not possible because of some unavoidable dispersiveness of the scattered wave.

9.5 A Sublaminate-wise Constant Shear Kinematics Model for Multiple Delaminations and Strip Inclusions

While modeling the delaminations in composite structures, spatial discretization becomes difficult with standard finite elements. Generally available finite element packages use plate-bending elements or degenerated shell elements, which cannot be used in the interfacial regions where more than one sublaminate form the base laminate. Moreover, due to the significant difference in the order of the thickness and planar dimensions, planar or solid elements, when used at the interfaces, yield enormous system size. In addition, there is

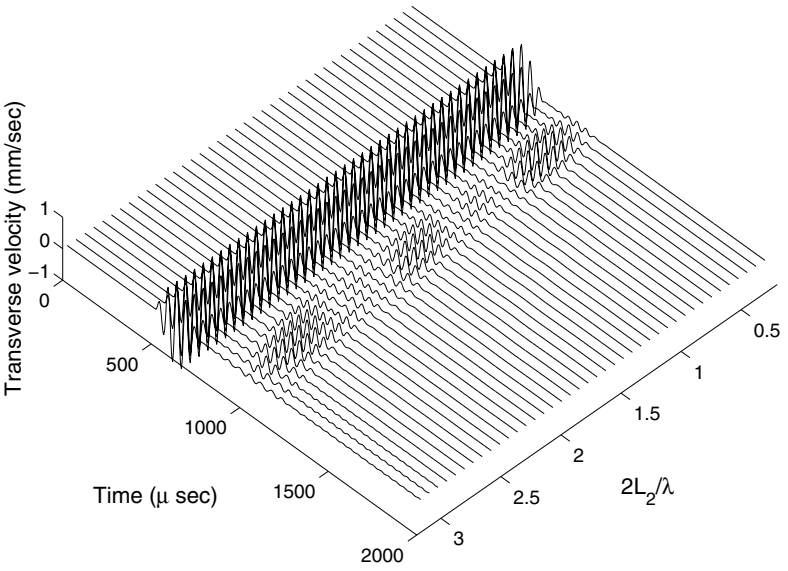

Fig. 9.17. Transverse velocity $\dot{w}$ history computed at node 2 for different lengths (L_2) of delamination

always high computational cost to handle such a large system size to capture highly transient pulse propagation. Use of a high frequency modulated pulse has been found efficient as in the wave-based diagnostics in smart SHM. In the present study, a systematic derivation is presented to model the interfaces between the base laminate and multiple sublaminates in a general form. When one of the intermediate sublaminates are of different material configuration, it can be treated as a strip inclusion. The idea is to capture the wave transmission and scattering at these delamination tips or at the interfaces between the inclusions and the host materials using a diagnostic signal. The SFEM discussed in Chapter 4 is used as the basic building block for the spectral interface model.

In this section, our main objective is to construct and solve a set of constrained equations in the Fourier domain (consistent with the framework of SFEM) for multiple delaminations and inclusions by allowing discontinuity in the rotation θ_y of the cross-sectional plane between two sublaminates above and below delaminations. The delaminated configuration is shown in Figure 9.18. This also allows a particular sublaminate made of different materials to be treated as strip inclusion debonded from the host materials. For simplicity, we assume that the dynamics of the delaminations or slip between the inclusion and host materials is governed by Mode-II fracture process, excluding any effect of Mode-I fracture (opening and closing of delaminations causing interpenetration and incompatibility in the z direction).

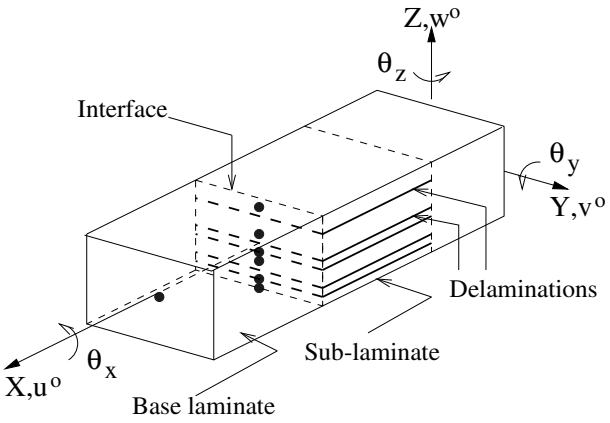

Fig. 9.18. Schematic diagram showing multiple through-width delaminations in a laminated composite beam

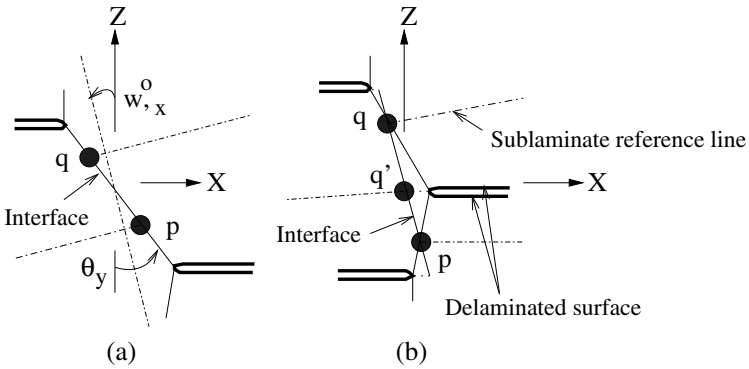

Fig. 9.19. Interfacial nodes taking part in constrained kinematics of base laminate and sublaminates or debonded strip inclusions with (b) or without (a) a third delaminated surface

The formulation is generalized by considering two cases as shown in Figure 9.19. In case (a) (Figure 9.19(a)), two consecutive nodes p and q are considered on the interface, which connect two elements on opposite sides of the interface. Since, there is no delamination between node p and node q, in-plane displacements and rotation of normal planes at these nodes can be constrained as

$$u_p^o + z_{pq}\theta_{y_p} = u_q^o \,, \quad \theta_{y_p} = \theta_{y_q} \,, \tag{9.23a}$$

where z_{pq} is the distance along the z direction between the node p and node q. In case (b) (Figure 9.19(b)), a single delamination is considered between node p and node q, which are on the same face on the interface. Each of these nodes belongs to the element representing one of the sublaminate above or below the delamination. Node q' on the other side of the interface belongs to

the element representing the base laminate. Since, under the assumption of sublaminate-wise constant shear, the normal plane passing through node q' has to rotate in a rigid body mode, the discontinuous plane passing through node p and node q must rotate in a constrained manner. Such constraint can be imposed as follows. The interface in the region including node p and node q' is already defined in Equation (9.23a) representing the case (a). Now, one needs to construct the constrained equations for interfacing the node p and node q. This can be expressed as

$$u_p^o + z_{p_t}\theta_{y_p} = u_q^o + z_{q_b}\theta_{y_q} \tag{9.23b}$$

where z_{pt} is the depth of the top surface of the sublaminate containing node p and measured from the corresponding element local reference line. Similarly, z_{qb} is the depth of the bottom surface of the sublaminate containing node q and measured from the corresponding element local reference line. For all other nodal displacement components associated with the node p and node q, the equations for constraints can be written as

$$v_p^o = v_q^o \ , \ w_p^o = w_q^o \ , \quad \theta_{xp} = \theta_{xq} \ , \ \theta_{zp} = \theta_{zq} \ . \tag{9.23c}$$

Implementation of the above displacement constraints can be automated to model multiple delaminations or inclusions across the thickness as well as for different variations of such configuration at various locations along the length of a beam. Equations (9.23a)–(9.23c) can be assembled at the global level with appropriate transformation to form the MPC equation in the nodal displacement vector. Let us consider Equation (9.23a) obtained in case (a) along with Equation (9.23c). We can write these six equations in matrix form as

$$\begin{bmatrix} 1 & 0 & 0 & 0 & z_{pq} & 0 & -1 & 0 & 0 & 0 & 0 & 0 \\ 0 & 1 & 0 & 0 & 0 & 0 & 0 & -1 & 0 & 0 & 0 & 0 \\ 0 & 0 & 1 & 0 & 0 & 0 & 0 & 0 & -1 & 0 & 0 & 0 \\ 0 & 0 & 0 & 1 & 0 & 0 & 0 & 0 & 0 & -1 & 0 & 0 \\ 0 & 0 & 0 & 0 & 1 & 0 & 0 & 0 & 0 & 0 & -1 & 0 \\ 0 & 0 & 0 & 0 & 0 & 1 & 0 & 0 & 0 & 0 & 0 & -1 \end{bmatrix} \begin{Bmatrix} \hat{u}_p^o \\ \vdots \\ \hat{\theta}_{zp} \\ \hat{u}_q^o \\ \vdots \\ \hat{\theta}_{zq} \end{Bmatrix} = \mathbf{0} \ . \tag{9.24a}$$

Now, for example, if the node numbering is p, $p+1$ and q, $q+1$ for the two elements connected to the interface, then Equation (9.24a) can be rewritten as

$$\left[\begin{array}{cc|cc} & \mathbf{C_{u1}} & & \mathbf{C_{u2}} \\ & \mathbf{0} & & \mathbf{0} \end{array}\right] \begin{Bmatrix} \mathbf{T}^T\hat{\mathbf{u}}_p^{\mathrm{g}} \\ \mathbf{T}^T\hat{\mathbf{u}}_q^{\mathrm{g}} \end{Bmatrix} = \mathbf{0} \tag{9.24b}$$

where $\mathbf{C_{u1}}$ and $\mathbf{C_{u2}}$ are the two 6×6 submatrices in Equation (9.24a). A similar form is also obtained for interface in case (b). Finally, all these equations of displacement constraints can be assembled to form a single matrix equation at the global level, which is given by

$$\mathbf{C_u}\hat{\mathbf{u}}^g = \mathbf{0}\,. \tag{9.24c}$$

Next, the equilibrium of the nodal forces at each interface is to be established. This is obtained as

$$\sum_p \mathbf{S'}_p^T \hat{\mathbf{f}}_p^{\mathrm{e}} = \hat{\mathbf{f}}\,, \tag{9.25a}$$

where the summation sign stands for all the nodes in a particular cross-section. $\hat{\mathbf{f}}$ is the applied load vector at the interface under consideration. For an element with nodes numbered p, $p+1$ and the node p on the interface,

$$\mathbf{S'}_p = \left[\begin{array}{cccccc|c} 1 & 0 & 0 & 0 & h_p & 0 & \\ 0 & 1 & 0 & 0 & 0 & 0 & \\ 0 & 0 & 1 & 0 & 0 & 0 & \\ 0 & 0 & 0 & 1 & 0 & 0 & \mathbf{0} \\ 0 & 0 & 0 & 0 & 1 & 0 & \\ 0 & 0 & 0 & 0 & 0 & 1 & \end{array}\right] \tag{9.25b}$$

h_p is the distance of the node p in the z direction measured from the bottom surface of the beam. Equation (9.25b) can be rewritten in terms of the element nodal displacement vector at the global level as

$$\sum_p \mathbf{S'}_p \mathbf{T}^T \hat{\mathbf{K}}_p^{\mathrm{e}} \mathbf{T} \hat{\mathbf{u}}_p^{\mathrm{g}} = \mathbf{T}^T \hat{\mathbf{f}}^{\mathrm{g}}\,. \tag{9.25c}$$

Equation (9.25c) can be assembled to form a single matrix equation involving force constraints at the global level, which is given by

$$\mathbf{C_f}\hat{\mathbf{u}}^{\mathrm{g}} = \mathbf{f'}\,. \tag{9.25d}$$

Now, we use two diagonal matrices of penalty parameters $\alpha_{\mathbf{u}}$ and $\alpha_{\mathbf{f}}$ to impose displacement constraints in Equation (9.24c) and force constraints in Equation (9.25d) to minimize the stationary potential

$$\hat{\prod} = \frac{1}{2}\hat{\mathbf{u}}^{\mathrm{g}^T}\hat{\mathbf{K}}^{\mathrm{g}}\hat{\mathbf{u}}^{\mathrm{g}} - \hat{\mathbf{u}}^{\mathrm{g}^T}\hat{\mathbf{f}}^{\mathrm{g}} + \frac{1}{2}\left(\mathbf{C_u}\hat{\mathbf{u}}^g\right)^T \alpha_{\mathbf{u}} \left(\mathbf{C_u}\hat{\mathbf{u}}^g\right)$$
$$+\frac{1}{2}\left(\mathbf{C_f}\hat{\mathbf{u}}^g - \mathbf{f'}\right)^T \alpha_{\mathbf{u}} \left(\mathbf{C_f}\hat{\mathbf{u}}^g - \mathbf{f'}\right) \tag{9.26}$$

in the frequency domain for each ω_n. Minimizing the above potential with respect to the global displacement vector $\hat{\mathbf{u}}^{\mathrm{g}}$, we get the spectral finite element equilibrium equation

$$\left(\hat{\mathbf{K}}^{\mathrm{g}} + \mathbf{C_u}^T \alpha_{\mathbf{u}} \mathbf{C_u} + \mathbf{C_f}^T \alpha_{\mathbf{f}} \mathbf{C_f}\right) \hat{\mathbf{u}}^{\mathrm{g}} = \hat{\mathbf{f}}^{\mathrm{g}} + \mathbf{C_f}^T \alpha_{\mathbf{f}} \mathbf{f'}\,. \tag{9.27}$$

Note that the constraint equations (Equations (9.24c) and (9.25d)) involve dissimilar dofs, whose motion is governed by the stiffness coefficients $\mathbf{A_{jl}}$ and inertial coefficients $\mathbf{M}$, which are of varying order. Therefore, use of penalty

parameters α_u and α_f consistent with the associated dofs to achieve sufficient numerical accuracy [190] is important. Note the order of the values in the additional entries in the updated dynamic stiffness matrix in Equation (9.27), that is

$$O\left(\mathbf{C_u}^T\mathbf{C_u}\right) \approx (-6, 0)\ , \quad O\left(\mathbf{C_f}^T\mathbf{C_f}\right) \approx O\left(min\left(\hat{k}^{e^2}_{jj}\right), max\left(\hat{k}^{e^2}_{jj}\right)\right)\ , \tag{9.28}$$

because in $\mathbf{C_u}$, the entries are either 1 or z_{pq} (depth of composite beam sub-laminates are typically in the order of millimeters). These lead to

$$\alpha_{u\,jj} = \left|\hat{k}^{e}_{jj}\right| \times 10^9\ , \quad \alpha_{f\,jj} = \left|\hat{k}^{e^{-1}}_{jj}\right| \times 10^3 \tag{9.29}$$

as a convenient choice of the penalty parameters while solving the constrained system in Equation (9.27).

9.6 Spectral Elements with Embedded Transverse Crack

9.6.1 Element-internal Discretization and Kinematic Assumptions

Configuration of the spectral element with embedded transverse crack and the element-internal discretization details are shown in Figure 9.20. In the absence of any crack, a single spectral element between node 1 and node 2 (Figure 9.20(a)) is sufficient to capture the exact dynamics of the shear deformable composite beam, which has been described in Section 4.4.4. Let us consider a transverse crack in a beam that requires explicit definition by three additional parameters. These three parameters are (1) the span-wise location of the transverse crack ($x = L_1 + \Delta L/2$ as shown in Figure 9.20(a), L_1 and ΔL will be defined later), (2) the thickness-wise location of the bottom crack-tip ($z = d_1$), (3) the thickness-wise location of the top crack-tip ($z = d_2$, $h = d_2 - d_1$ is the crack depth). We assume that the transverse crack is a through-width crack (along the y direction) which allows the modeling to be accomplished using one-dimensional waveguides. The element-internal discretization as shown in Figure 9.20(b) produces six internal waveguides numbered (1) to (6). For all these elements, a total of ten additional nodes apart from the node 1 and node 2 will appear in the formulation, and the dofs associated with them will be condensed out systematically. As a result, a simple two-node element can be used to model the transverse crack in a metallic or composite beam, where faster and repeated analysis with acceptable accuracy will be of prime importance for damage identification studies and various SHM applications in conjunction with a wave-based diagnostic signal.

Since the main objective behind using such a model is to improve upon the various available approximate models based on equivalent flexibility, empirical crack-functions *etc.*, it is essential for the proposed element-internal

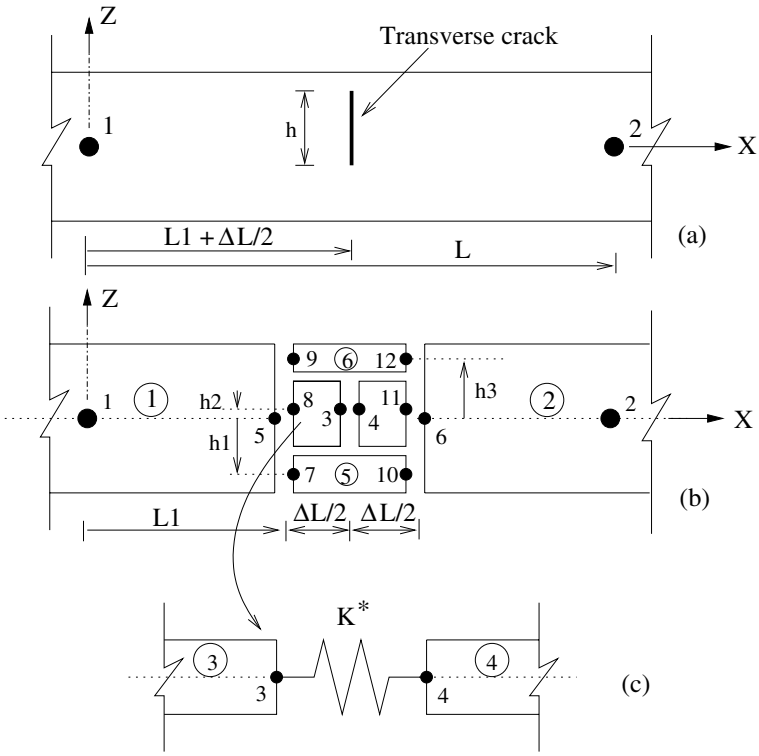

Fig. 9.20. Schematic diagram of the transverse crack configuration. (a) The 2-node spectral element configuration with embedded transverse crack. (b) Element internal discretization through the two base laminates (waveguides (1) and (2)), two continuous sublaminates (waveguides (5) at the bottom and (6) at the top) and two discontinuous sublaminates (waveguides (3) and (4)) to represent the crack. Locations of the internal element nodes $3-12$ are shown which are later condensed out. (c) Use of linear viscoelastic contact model between the crack surfaces

discretization technique (Figure 9.20) that any spurious scattering effect be avoided. It can be seen in Figure 9.20 that the elements (3) and (4) are expected to behave as hanging elements, especially when their lengths become longer. This can be avoided in two ways. Either a bound on the length of the elements (3) and (4) in terms of the incident wavelength should be imposed or appropriate constraints on the top and bottom surfaces of elements (3) and (4) should be imposed while choosing longer lengths.

Calculations for implementing both options are presented below. A bound on the length of the hanging elements is imposed for comparison with standard finite element results and other numerical simulations. The constrained equations for unbounded length of the hanging elements are formulated after the basic element formulation.

We consider equal lengths of hanging laminates denoted by $\Delta L/2$ as shown in Figure 9.20(b). For any arbitrary dynamic excitation involving multiple harmonics, the bound on the length of the hanging laminates is imposed in terms of the smallest group wavelength, which is given by

$$\Delta L < \text{Min}\,(\lambda_g)\ , \quad \lambda_g = c_g/\nu\ , \tag{9.30}$$

where c_g is the group wave velocity defined as $c_g = d\omega/dk$, k is the wavenumber, $\nu = \omega/2\pi$ is the excitation frequency. As the frequency increases, the group wavelength λ_g decreases. Note that λ_g is the same as the wavelength $\lambda = c/\nu$ for single frequency excitation (c the phase velocity), but is different from λ for a band-limited excitation about a central frequency. Considering the arrival of the waves through the uncracked base laminates, Equation (9.30) can now can be used to eliminate any spurious scattering of wave in an approximate manner.

The kinematic assumption adopted in the present formulation is that the cross-sectional interfaces between the base laminate, the sublaminates and the hanging laminates remain straight, *i.e.,* the slope is continuous and constant at these interfaces. Under this assumption, one can relate the nodal dofs at the interfaces as follows:

$$\hat{\mathbf{u}}_{\mathbf{7}} = \begin{Bmatrix} \hat{u}_7^o \\ \hat{\omega}_7 \\ \hat{\phi}_7 \end{Bmatrix} = \begin{Bmatrix} \hat{u}_5^o + h_1\hat{\phi}_5 \\ \hat{\omega}_5 \\ \hat{\phi}_5 \end{Bmatrix} = \mathbf{S_1}\hat{\mathbf{u}}_{\mathbf{5}}\ , \tag{9.31}$$

$$\hat{\mathbf{u}}_{\mathbf{8}} = \begin{Bmatrix} \hat{u}_8^o \\ \hat{\omega}_8 \\ \hat{\phi}_8 \end{Bmatrix} = \begin{Bmatrix} \hat{u}_5^o + h_2\hat{\phi}_5 \\ \hat{\omega}_5 \\ \hat{\phi}_5 \end{Bmatrix} = \mathbf{S_2}\hat{\mathbf{u}}_{\mathbf{5}}\ , \tag{9.32}$$

$$\hat{\mathbf{u}}_{\mathbf{9}} = \begin{Bmatrix} \hat{u}_9^0 \\ \hat{\omega}_9 \\ \hat{\phi}_9 \end{Bmatrix} = \begin{Bmatrix} \hat{u}_5^0 + h_3\hat{\phi}_5 \\ \hat{\omega}_5 \\ \hat{\phi}_5 \end{Bmatrix} = \mathbf{S_3}\hat{\mathbf{u}}_{\mathbf{5}}\ , \tag{9.33}$$

and similarly,

$$\hat{\mathbf{u}}_{\mathbf{10}} = \mathbf{S_1}\hat{\mathbf{u}}_{\mathbf{6}}\ , \quad \hat{\mathbf{u}}_{\mathbf{11}} = \mathbf{S_2}\hat{\mathbf{u}}_{\mathbf{6}}\ , \quad \hat{\mathbf{u}}_{\mathbf{12}} = \mathbf{S_3}\hat{\mathbf{u}}_{\mathbf{6}}\ , \tag{9.34}$$

where

$$\mathbf{S_1} = \begin{bmatrix} 1 & 0 & h_1 \\ 0 & 1 & 0 \\ 0 & 0 & 1 \end{bmatrix}\ , \quad \mathbf{S_2} = \begin{bmatrix} 1 & 0 & h_2 \\ 0 & 1 & 0 \\ 0 & 0 & 1 \end{bmatrix}\ , \quad \mathbf{S_3} = \begin{bmatrix} 1 & 0 & h_3 \\ 0 & 1 & 0 \\ 0 & 0 & 1 \end{bmatrix}\ . \tag{9.35}$$

Interface Equilibrium of Forces

Considering the left interface between the base laminate and sublaminates (Figure 9.20), the equilibrium of the associated nodal forces can be written as

$$\left\{\begin{array}{c}\hat{N}_5\\ \hat{V}_5\\ \hat{M}_5\end{array}\right\}+\left\{\begin{array}{c}\hat{N}_7\\ \hat{V}_7\\ \hat{M}_7+h_1\hat{N}_7\end{array}\right\}+\left\{\begin{array}{c}\hat{N}_8\\ \hat{V}_8\\ \hat{M}_8+h_2\hat{N}_8\end{array}\right\}+\left\{\begin{array}{c}\hat{N}_9\\ \hat{V}_9\\ \hat{M}_9+h_3\hat{N}_9\end{array}\right\}=\left\{\begin{array}{c}0\\ 0\\ 0\end{array}\right\}, \tag{9.36}$$

which, in matrix form and with the help of Equation (9.35), can be expressed as

$$\hat{\mathbf{f}}_{\mathbf{5}}+{\mathbf{S}_{\mathbf{1}}}^T\hat{\mathbf{f}}_{\mathbf{7}}+{\mathbf{S}_{\mathbf{2}}}^T\hat{\mathbf{f}}_{\mathbf{8}}+{\mathbf{S}_{\mathbf{3}}}^T\hat{\mathbf{f}}_{\mathbf{9}}=\mathbf{0}\,. \tag{9.37}$$

Similarly, considering the right interface between the base laminate and sublaminates (Figure 9.20), the equilibrium of the associated nodal forces can be expressed as

$$\hat{\mathbf{f}}_{\mathbf{6}}+{\mathbf{S}_{\mathbf{1}}}^T\hat{\mathbf{f}}_{\mathbf{10}}+{\mathbf{S}_{\mathbf{2}}}^T\hat{\mathbf{f}}_{\mathbf{11}}+{\mathbf{S}_{\mathbf{3}}}^T\hat{\mathbf{f}}_{\mathbf{12}}=\mathbf{0}\,. \tag{9.38}$$

At the crack surface,

$$\hat{\mathbf{f}}_{\mathbf{3}}+\hat{\mathbf{f}}_{\mathbf{4}}=\mathbf{0}\,, \tag{9.39}$$

and under the assumption of no contact between the crack surfaces, $\hat{\mathbf{f}}_{\mathbf{3}}=\mathbf{0}$ and $\hat{\mathbf{f}}_{\mathbf{4}}=\mathbf{0}$. The effect of contact between the crack surfaces will be dealt with as a separate case later.

Assembly of the Element-internal Waveguides

The element equilibrium equation for the jth element-internal waveguide ($j=1,2$ for base laminates, $j=5,6$ for sublaminates and $j=3,4$ for hanging laminates as shown in Figure 9.20) with nodes p and q can be expressed generically as

$$\left[\begin{array}{cc}\hat{\mathbf{K}}_{\mathbf{11}}^{(j)} & \hat{\mathbf{K}}_{\mathbf{12}}^{(j)}\\ \hat{\mathbf{K}}_{\mathbf{21}}^{(j)} & \hat{\mathbf{K}}_{\mathbf{22}}^{(j)}\end{array}\right]_{(6\times6)}\left\{\begin{array}{c}\hat{\mathbf{u}}_{\mathbf{p}}\\ \hat{\mathbf{u}}_{\mathbf{q}}\end{array}\right\}=\left\{\begin{array}{c}\hat{\mathbf{f}}_{\mathbf{p}}\\ \hat{\mathbf{f}}_{\mathbf{q}}\end{array}\right\}. \tag{9.40}$$

The above equation, for the internal element (1) is

$$\left[\begin{array}{cc}\hat{\mathbf{K}}_{\mathbf{11}}^{(1)} & \hat{\mathbf{K}}_{\mathbf{12}}^{(1)}\\ \hat{\mathbf{K}}_{\mathbf{21}}^{(1)} & \hat{\mathbf{K}}_{\mathbf{22}}^{(1)}\end{array}\right]_{(6\times6)}\left\{\begin{array}{c}\hat{\mathbf{u}}_{\mathbf{1}}\\ \hat{\mathbf{u}}_{\mathbf{5}}\end{array}\right\}=\left\{\begin{array}{c}\hat{\mathbf{f}}_{\mathbf{1}}\\ \hat{\mathbf{f}}_{\mathbf{5}}\end{array}\right\}, \tag{9.41}$$

or for the internal element (2),

$$\left[\begin{array}{cc}\hat{\mathbf{K}}_{\mathbf{11}}^{(2)} & \hat{\mathbf{K}}_{\mathbf{12}}^{(2)}\\ \hat{\mathbf{K}}_{\mathbf{21}}^{(2)} & \hat{\mathbf{K}}_{\mathbf{22}}^{(2)}\end{array}\right]_{(6\times6)}\left\{\begin{array}{c}\hat{\mathbf{u}}_{\mathbf{6}}\\ \hat{\mathbf{u}}_{\mathbf{2}}\end{array}\right\}=\left\{\begin{array}{c}\hat{\mathbf{f}}_{\mathbf{6}}\\ \hat{\mathbf{f}}_{\mathbf{2}}\end{array}\right\}, \tag{9.42}$$

Similarly, for the internal element (3), we have

$$\left[\begin{array}{cc}\hat{\mathbf{K}}_{\mathbf{11}}^{(3)} & \hat{\mathbf{K}}_{\mathbf{12}}^{(3)}\\ \hat{\mathbf{K}}_{\mathbf{21}}^{(3)} & \hat{\mathbf{K}}_{\mathbf{22}}^{(3)}\end{array}\right]_{(6\times6)}\left\{\begin{array}{c}\hat{\mathbf{u}}_{\mathbf{8}}\\ \hat{\mathbf{u}}_{\mathbf{3}}\end{array}\right\}=\left\{\begin{array}{c}\hat{\mathbf{f}}_{\mathbf{8}}\\ \hat{\mathbf{f}}_{\mathbf{3}}\end{array}\right\}. \tag{9.43}$$

Expressing $\hat{\mathbf{u}}_{\mathbf{8}}$ in terms of $\hat{\mathbf{u}}_{\mathbf{5}}$ with the help of Equation (9.32) and premultiplying both sides of Equation (9.43) by ${\mathbf{S}_{\mathbf{2}}}^T$, we get

$$\begin{bmatrix} \mathbf{S_2}^T\hat{\mathbf{K}}_{\mathbf{11}}^{(3)}\mathbf{S_2} & \mathbf{S_2}^T\hat{\mathbf{K}}_{\mathbf{12}}^{(3)} \\ \mathbf{S_2}^T\hat{\mathbf{K}}_{\mathbf{21}}^{(3)}\mathbf{S_2} & \mathbf{S_2}^T\hat{\mathbf{K}}_{\mathbf{22}}^{(3)} \end{bmatrix}_{(6\times6)} \begin{Bmatrix} \hat{\mathbf{u}}_{\mathbf{5}} \\ \hat{\mathbf{u}}_{\mathbf{3}} \end{Bmatrix} = \begin{Bmatrix} \mathbf{S_2}^T\hat{\mathbf{f}}_{\mathbf{8}} \\ \mathbf{S_2}^T\hat{\mathbf{f}}_{\mathbf{3}} \end{Bmatrix} . \tag{9.44}$$

The equilibrium equation for the internal element (4) is

$$\begin{bmatrix} \hat{\mathbf{K}}_{\mathbf{11}}^{(4)} & \hat{\mathbf{K}}_{\mathbf{12}}^{(4)} \\ \hat{\mathbf{K}}_{\mathbf{21}}^{(4)} & \hat{\mathbf{K}}_{\mathbf{22}}^{(4)} \end{bmatrix}_{(6\times6)} \begin{Bmatrix} \hat{\mathbf{u}}_{\mathbf{4}} \\ \hat{\mathbf{u}}_{\mathbf{11}} \end{Bmatrix} = \begin{Bmatrix} \hat{\mathbf{f}}_{\mathbf{4}} \\ \hat{\mathbf{f}}_{\mathbf{11}} \end{Bmatrix} . \tag{9.45}$$

Expressing $\hat{\mathbf{u}}_{\mathbf{11}}$ in terms of $\hat{\mathbf{u}}_{\mathbf{6}}$ with the help of Equation (9.34) and premultiplying both sides of Equation (9.45) by $\mathbf{S_2}^T$, we get

$$\begin{bmatrix} \mathbf{S_2}^T\hat{\mathbf{K}}_{\mathbf{11}}^{(4)} & \mathbf{S_2}^T\hat{\mathbf{K}}_{\mathbf{12}}^{(4)}\mathbf{S_2} \\ \mathbf{S_2}^T\hat{\mathbf{K}}_{\mathbf{21}}^{(4)} & \mathbf{S_2}^T\hat{\mathbf{K}}_{\mathbf{22}}^{(4)}\mathbf{S_2} \end{bmatrix}_{(6\times6)} \begin{Bmatrix} \hat{\mathbf{u}}_{\mathbf{4}} \\ \hat{\mathbf{u}}_{\mathbf{6}} \end{Bmatrix} = \begin{Bmatrix} \mathbf{S_2}^T\hat{\mathbf{f}}_{\mathbf{4}} \\ \mathbf{S_2}^T\hat{\mathbf{f}}_{\mathbf{11}} \end{Bmatrix} . \tag{9.46}$$

The element equilibrium equation for the internal element (5) is

$$\begin{bmatrix} \hat{\mathbf{K}}_{\mathbf{11}}^{(5)} & \hat{\mathbf{K}}_{\mathbf{12}}^{(5)} \\ \hat{\mathbf{K}}_{\mathbf{21}}^{(5)} & \hat{\mathbf{K}}_{\mathbf{22}}^{(5)} \end{bmatrix}_{(6\times6)} \begin{Bmatrix} \hat{\mathbf{u}}_{\mathbf{7}} \\ \hat{\mathbf{u}}_{\mathbf{10}} \end{Bmatrix} = \begin{Bmatrix} \hat{\mathbf{f}}_{\mathbf{7}} \\ \hat{\mathbf{f}}_{\mathbf{10}} \end{Bmatrix} . \tag{9.47}$$

Expressing $\hat{\mathbf{u}}_{\mathbf{7}}$ and $\hat{\mathbf{u}}_{\mathbf{10}}$ in terms of $\hat{\mathbf{u}}_{\mathbf{5}}$ and $\hat{\mathbf{u}}_{\mathbf{6}}$ respectively with the help of Equations (9.31)–(9.34) and premultiplying both sides of Equation (9.47) by $\mathbf{S_1}^T$, we get

$$\begin{bmatrix} \mathbf{S_1}^T\hat{\mathbf{K}}_{\mathbf{11}}^{(5)}\mathbf{S_1} & \mathbf{S_1}^T\hat{\mathbf{K}}_{\mathbf{12}}^{(5)}\mathbf{S_1} \\ \mathbf{S_1}^T\hat{\mathbf{K}}_{\mathbf{21}}^{(5)}\mathbf{S_1} & \mathbf{S_1}^T\hat{\mathbf{K}}_{\mathbf{22}}^{(5)}\mathbf{S_1} \end{bmatrix}_{(6\times6)} \begin{Bmatrix} \hat{\mathbf{u}}_{\mathbf{5}} \\ \hat{\mathbf{u}}_{\mathbf{5}} \end{Bmatrix} = \begin{Bmatrix} \mathbf{S_1}^T\hat{\mathbf{f}}_{\mathbf{7}} \\ \mathbf{S_1}^T\hat{\mathbf{f}}_{\mathbf{10}} \end{Bmatrix} . \tag{9.48}$$

The element equilibrium equation for the internal element (6) is

$$\begin{bmatrix} \hat{\mathbf{K}}_{\mathbf{11}}^{(6)} & \hat{\mathbf{K}}_{\mathbf{12}}^{(6)} \\ \hat{\mathbf{K}}_{\mathbf{21}}^{(6)} & \hat{\mathbf{K}}_{\mathbf{22}}^{(6)} \end{bmatrix}_{(6\times6)} \begin{Bmatrix} \hat{\mathbf{u}}_{\mathbf{9}} \\ \hat{\mathbf{u}}_{\mathbf{12}} \end{Bmatrix} = \begin{Bmatrix} \hat{\mathbf{f}}_{\mathbf{9}} \\ \hat{\mathbf{f}}_{\mathbf{12}} \end{Bmatrix} . \tag{9.49}$$

Expressing $\hat{\mathbf{u}}_{\mathbf{9}}$ and $\hat{\mathbf{u}}_{\mathbf{12}}$ in terms of $\hat{\mathbf{u}}_{\mathbf{5}}$ and $\hat{\mathbf{u}}_{\mathbf{6}}$ respectively with the help of Equations (9.33) and (9.34) and premultiplying both sides of Equation (9.49) by $\mathbf{S_3}^T$, we get

$$\begin{bmatrix} \mathbf{S_3}^T\hat{\mathbf{K}}_{\mathbf{11}}^{(6)}\mathbf{S_3} & \mathbf{S_3}^T\hat{\mathbf{K}}_{\mathbf{12}}^{(6)}\mathbf{S_3} \\ \mathbf{S_3}^T\hat{\mathbf{K}}_{\mathbf{21}}^{(6)}\mathbf{S_3} & \mathbf{S_3}^T\hat{\mathbf{K}}_{\mathbf{22}}^{(6)}\mathbf{S_3} \end{bmatrix}_{(6\times6)} \begin{Bmatrix} \hat{\mathbf{u}}_{\mathbf{5}} \\ \hat{\mathbf{u}}_{\mathbf{6}} \end{Bmatrix} = \begin{Bmatrix} \mathbf{S_3}^T\hat{\mathbf{f}}_{\mathbf{9}} \\ \mathbf{S_3}^T\hat{\mathbf{f}}_{\mathbf{12}} \end{Bmatrix} . \tag{9.50}$$

9.6.2 Modeling Dynamic Contact Between Crack Surfaces

Although the present SFE with embedded transverse crack has been developed to study the interaction of diagnostic waves with the crack and its effect captured at distant measurement locations, the effect of dynamic frictional contact and viscosity due to the polymer matrix grain boundary and broken fiber

fragments in the composite can also be modeled. Similar models for delamination can be found in [163, 180]. However, a more complex model includes a non-linear spring to restrict the occurrence of incompatible opening-closing modes due to inter-penetration. This development will not be attempted here. Figure 9.20(c) shows the transverse crack surfaces and the associated hanging laminates (3) and (4). The motion of the crack surfaces is approximated through the motion of node 3 and node 4. Let us assume that the distributed spring and viscoelastic contact force along the crack surfaces can be lumped on node 3 and node 4 as

$$\begin{Bmatrix} \hat{\mathbf{f}}_3 \\ \hat{\mathbf{f}}_4 \end{Bmatrix} = \begin{bmatrix} \hat{\mathbf{K}}^* & -\hat{\mathbf{K}}^* \\ -\hat{\mathbf{K}}^* & \hat{\mathbf{K}}^* \end{bmatrix}_{(6\times 6)} \begin{Bmatrix} \hat{\mathbf{u}}_4 \\ \hat{\mathbf{u}}_3 \end{Bmatrix} , \tag{9.51}$$

where

$$\hat{\mathbf{K}}^* = \begin{bmatrix} (K_u + i\omega C_u) & 0 & 0 \\ 0 & (K_w + i\omega C_w) & 0 \\ 0 & 0 & (K_\phi + i\omega C_\phi) \end{bmatrix} , \tag{9.52}$$

K_u, K_w, K_ϕ are the spring stiffnesses and C_u, C_w and C_ϕ are the viscous damping coefficients associated with relative longitudinal displacement, transverse displacement and rotation between node 3 and node 4.

After assembling the element equilibrium equations for the six internal elements (Equations (9.41)–(9.49)) and subsequently using Equations (9.37)–(9.39) and Equation (9.51), we get

$$\begin{bmatrix} \mathbf{K}_{11} & \mathbf{K}_{12} & \mathbf{0} & \mathbf{0} & \mathbf{0} & \mathbf{0} \\ \mathbf{K}_{21} & \mathbf{K}_{22} & \mathbf{K}_{23} & \mathbf{0} & \mathbf{K}_{25} & \mathbf{0} \\ \mathbf{0} & \mathbf{K}_{32} & \mathbf{K}_{33} & \mathbf{K}_{34} & \mathbf{0} & \mathbf{0} \\ \mathbf{0} & \mathbf{0} & \mathbf{K}_{43} & \mathbf{K}_{44} & \mathbf{K}_{45} & \mathbf{0} \\ \mathbf{0} & \mathbf{K}_{52} & \mathbf{0} & \mathbf{K}_{54} & \mathbf{K}_{55} & \mathbf{K}_{56} \\ \mathbf{0} & \mathbf{0} & \mathbf{0} & \mathbf{0} & \mathbf{K}_{65} & \mathbf{K}_{66} \end{bmatrix}_{(18\times 18)} \begin{Bmatrix} \hat{\mathbf{u}}_1 \\ \hat{\mathbf{u}}_5 \\ \hat{\mathbf{u}}_3 \\ \hat{\mathbf{u}}_4 \\ \hat{\mathbf{u}}_6 \\ \hat{\mathbf{u}}_2 \end{Bmatrix} = \begin{Bmatrix} \hat{\mathbf{f}}_1 \\ \mathbf{0} \\ \mathbf{0} \\ \mathbf{0} \\ \mathbf{0} \\ \hat{\mathbf{f}}_2 \end{Bmatrix} , \tag{9.53}$$

where

$$\mathbf{K_{11}} = \hat{\mathbf{K}}^{(1)}_{\mathbf{11}} , \quad \mathbf{K_{12}} = \hat{\mathbf{K}}^{(1)}_{\mathbf{12}} , \quad \mathbf{K_{21}} = \hat{\mathbf{K}}^{(1)}_{\mathbf{21}} ,$$

$$\mathbf{K_{22}} = \hat{\mathbf{K}}^{(1)}_{\mathbf{22}} + \mathbf{S_1}^T \hat{\mathbf{K}}^{(5)}_{\mathbf{11}} \mathbf{S_1} + \mathbf{S_2}^T \hat{\mathbf{K}}^{(3)}_{\mathbf{11}} \mathbf{S_2} + \mathbf{S_3}^T \hat{\mathbf{K}}^{(6)}_{\mathbf{11}} \mathbf{S_3} ,$$

$$\mathbf{K_{23}} = \mathbf{S_2}^T \hat{\mathbf{K}}^{(3)}_{\mathbf{12}} , \quad \mathbf{K_{25}} = \mathbf{S_1}^T \hat{\mathbf{K}}^{(5)}_{\mathbf{12}} \mathbf{S_1} + \mathbf{S_3}^T \hat{\mathbf{K}}^{(6)}_{\mathbf{12}} \mathbf{S_3} , \quad \mathbf{K_{32}} = \hat{\mathbf{K}}^{(3)}_{\mathbf{21}} \mathbf{S_1} ,$$

$$\mathbf{K_{33}} = \hat{\mathbf{K}}^{(3)}_{\mathbf{22}} + \mathbf{S_2}^T \mathbf{K}^* , \quad \mathbf{K_{34}} = -\mathbf{S_2}^T \mathbf{K}^* , \quad \mathbf{K_{43}} = -\mathbf{S_2}^T \mathbf{K}^* ,$$

$$\mathbf{K_{44}} = \hat{\mathbf{K}}^{(4)}_{\mathbf{11}} + \mathbf{S_2}^T \mathbf{K}^* , \quad \mathbf{K_{45}} = \hat{\mathbf{K}}^{(4)}_{\mathbf{12}} \mathbf{S_2} ,$$

$$\mathbf{K_{52}} = \mathbf{S_1}^T \hat{\mathbf{K}}^{(5)}_{\mathbf{21}} \mathbf{S_1} + \mathbf{S_3}^T \hat{\mathbf{K}}^{(6)}_{\mathbf{21}} \mathbf{S_3} , \quad \mathbf{K_{54}} = \mathbf{S_2}^T \hat{\mathbf{K}}^{(4)}_{\mathbf{21}} ,$$

$$\mathbf{K_{55}} = \hat{\mathbf{K}}^{(2)}_{\mathbf{11}} + \mathbf{S_1}^T \hat{\mathbf{K}}^{(5)}_{\mathbf{22}} \mathbf{S_1} + \mathbf{S_2}^T \hat{\mathbf{K}}^{(4)}_{\mathbf{22}} \mathbf{S_2} + \mathbf{S_3}^T \hat{\mathbf{K}}^{(6)}_{\mathbf{22}} \mathbf{S_3} , \quad \mathbf{K_{56}} = \hat{\mathbf{K}}^{(2)}_{\mathbf{12}} ,$$

$$\mathbf{K_{65}} = \hat{\mathbf{K}}^{(2)}_{\mathbf{21}} , \quad \mathbf{K_{66}} = \hat{\mathbf{K}}^{(2)}_{\mathbf{22}} .$$

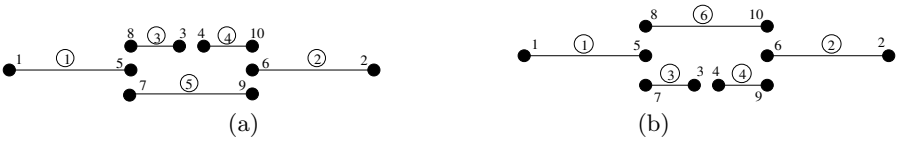

Fig. 9.21. Representation of the base laminates, sublaminates and hanging laminates by spectral elements for (a) top surface-breaking crack and (b) bottom surface-breaking crack

9.6.3 Modeling Surface-breaking Cracks

The surface-breaking cracks can be considered in the same framework as formulated above. Figure 9.21(a) and (b) show the internal elements for the top and bottom surface-breaking cracks respectively. The only differences in these cases compared to the embedded transverse crack is that here the number of elements and nodes representing the top sublaminates (element (6)) and bottom sublaminates (element 5) (in Figure 9.20(b) are absent. Therefore, by removing these element equilibrium equations while assembling, one can obtain the modified form of Equation (9.53) for the top and bottom surface-breaking cracks.

Super-element Level Condensation

We first condense out the dofs at the crack surfaces (*i.e.* node 3 and node 4), which reduces Equation (9.53) to

$$\begin{bmatrix} \bar{\mathbf{K}}_{11} & \bar{\mathbf{K}}_{12} & \mathbf{0} & \mathbf{0} \\ \bar{\mathbf{K}}_{21} & \bar{\mathbf{K}}_{22} & \bar{\mathbf{K}}_{23} & \mathbf{0} \\ \mathbf{0} & \bar{\mathbf{K}}_{32} & \bar{\mathbf{K}}_{33} & \bar{\mathbf{K}}_{34} \\ \mathbf{0} & \mathbf{0} & \bar{\mathbf{K}}_{43} & \bar{\mathbf{K}}_{44} \end{bmatrix}_{(12\times 12)} \begin{Bmatrix} \hat{\mathbf{u}}_1 \\ \hat{\mathbf{u}}_5 \\ \hat{\mathbf{u}}_6 \\ \hat{\mathbf{u}}_2 \end{Bmatrix} = \begin{Bmatrix} \hat{\mathbf{f}}_1 \\ \mathbf{0} \\ \mathbf{0} \\ \hat{\mathbf{f}}_2 \end{Bmatrix} , \tag{9.54}$$

where

$$\bar{\mathbf{K}}_{11} = \mathbf{K}_{11} , \quad \bar{\mathbf{K}}_{12} = \mathbf{K}_{12} , \quad \bar{\mathbf{K}}_{21} = \mathbf{K}_{21} , \quad \bar{\mathbf{K}}_{22} = \mathbf{K}_{22} + \mathbf{K}_{23}\mathbf{K}^*_{35} ,$$

$$\bar{\mathbf{K}}_{23} = \mathbf{K}_{25} + \mathbf{K}_{23}\mathbf{K}^*_{36} , \quad \bar{\mathbf{K}}_{32} = \mathbf{K}_{52} + \mathbf{K}_{54}\mathbf{K}^*_{45} ,$$

$$\bar{\mathbf{K}}_{33} = \mathbf{K}_{55} + \mathbf{K}_{54}\mathbf{K}^*_{46} , \quad \bar{\mathbf{K}}_{34} = \mathbf{K}_{56} , \quad \bar{\mathbf{K}}_{43} = \mathbf{K}_{65} ,$$

$$\bar{\mathbf{K}}_{44} = \mathbf{K}_{66} , \quad \mathbf{K}^*_{45} = (\mathbf{K}_{44} - \mathbf{K}_{43}{\mathbf{K}_{33}}^{-1}\mathbf{K}_{34})^{-1}\mathbf{K}_{43}{\mathbf{K}_{33}}^{-1}\mathbf{K}_{32} ,$$

$$\mathbf{K}^*_{46} = -(\mathbf{K}_{44} - \mathbf{K}_{43}{\mathbf{K}_{33}}^{-1}\mathbf{K}_{34})^{-1}\mathbf{K}_{45} ,$$

$${\mathbf{K}_{35}}^* = -({\mathbf{K}_{33}}^{-1}\mathbf{K}_{32} + {\mathbf{K}_{33}}^{-1}\mathbf{K}_{34}{\mathbf{K}_{45}}^*) , \quad \mathbf{K}^*_{36} = -{\mathbf{K}_{33}}^{-1}\mathbf{K}_{34}{\mathbf{K}_{46}}^* .$$

In the second step, we condense out the dofs at node 5 and node 6, which yields the final form of the equilibrium equation representing a two-node element with embedded transverse crack, and can be expressed as

$$\begin{bmatrix} \hat{\mathbf{K}}_{11} & \hat{\mathbf{K}}_{12} \\ \hat{\mathbf{K}}\mathbf{i}_{21} & \hat{\mathbf{K}}_{22} \end{bmatrix}_{(6\times 6)} \begin{Bmatrix} \hat{\mathbf{u}}_1 \\ \hat{\mathbf{u}}_2 \end{Bmatrix} = \begin{Bmatrix} \hat{\mathbf{f}}_1 \\ \hat{\mathbf{f}}_2 \end{Bmatrix} , \tag{9.55}$$

where

$$\hat{\mathbf{K}}_{11} = \mathbf{K}_{11} + \mathbf{K}_{12}\mathbf{K}^*_{51} , \quad \hat{\mathbf{K}}_{12} = \mathbf{K}_{12}\mathbf{K}^*_{52} , \quad \hat{\mathbf{K}}_{21} = \mathbf{K}_{43}\mathbf{K}^*_{61} ,$$

$$\hat{\mathbf{K}}_{22} = \mathbf{K}_{44} + \mathbf{K}_{43}\mathbf{K}^*_{62} , \quad \mathbf{K}^*_{61} = (\mathbf{K}_{33} - \mathbf{K}_{32}\mathbf{K}^{-1}_{22}\mathbf{K}_{23})^{-1}\mathbf{K}_{32}\mathbf{K}^{-1}_{22}\mathbf{K}_{21} ,$$

$$\mathbf{K}^*_{62} = -(\mathbf{K}_{33} - \mathbf{K}_{32}\mathbf{K}^{-1}_{22}\mathbf{K}_{23})^{-1}\mathbf{K}_{34} ,$$

$$\mathbf{K}^*_{51} = -(\mathbf{K}^{-1}_{22}\mathbf{K}_{21} + \mathbf{K}^{-1}_{22}\mathbf{K}_{23}\mathbf{K}^*_{61}) , \quad \mathbf{K}^*_{52} = -\mathbf{K}^{-1}_{22}\mathbf{K}_{23}\mathbf{K}^*_{62} .$$

Now, again one only needs to replace the spectral element for the healthy beam with this spectral element wherever the presence of a transverse crack is to be accounted for. To emphasize the novel use of this element for applications in SHM, its numerical performance is compared with standard plane-stress finite element simulations in Section 9.7.1. Before proceeding further with the numerical studies, the constrained formulation to accommodate longer hanging laminates (3) and (4) by enforcing displacement continuities, which is an alternative option to Equation (9.30), is discussed below.

9.6.4 Distributed Constraints at the Interfaces Between Sublaminates and Hanging Laminates

For longer lengths of sublaminates (5) and (6) and intermediate hanging laminates (3) and (4) shown in Figure 9.20(b), especially when $\Delta L > Min(\lambda_g)$ as discussed in the context of Equation (9.30), interfacial slip and other discontinuities at the horizontal interfaces between the hanging laminates and the top and bottom sublaminates may become significant for certain wave interactions and need to be restricted. This requires displacement continuity between the surface displacements of a hanging laminate and the neighboring sublaminate, which can be expressed as

$$\hat{\mathbf{u}}(x)^{(j)}_t = \hat{\mathbf{u}}(x)^{(l)}_b , \tag{9.56}$$

where the superscripts (j) and (l) indicates the element numbers and the subscripts t and b indicate the top or bottom surface respectively. While modeling delamination along with fiber fracture, such constraints can be removed. It can be seen from Figure 9.20(a) that there are four such horizontal interfaces where constraints need to be imposed otherwise. Considering element (5) and element (3), Equation (9.56) can be expanded using the generic field variables as

$$\begin{bmatrix} 1 & 0 & z^{(5)}_t \\ 0 & 1 & 0 \\ 0 & 0 & 1 \end{bmatrix} \begin{Bmatrix} \hat{u}^o \\ \hat{\omega} \\ \hat{\phi} \end{Bmatrix}^{(5)} = \begin{bmatrix} 1 & 0 & z^{(3)}_b \\ 0 & 1 & 0 \\ 0 & 0 & 1 \end{bmatrix} \begin{Bmatrix} \hat{u}^o \\ \hat{\omega} \\ \hat{\phi} \end{Bmatrix}^{(3)} . \tag{9.57}$$

Further, using element shape functions in Equation (9.57), we get

$$\mathbf{H}_t^{(5)} \aleph(x,\omega_n)^{(5)} \hat{\mathbf{u}}^{(5)} = \mathbf{H}_b^{(3)} \aleph(x,\omega_n)^{(3)} \hat{\mathbf{u}}^{(3)} \,. \tag{9.58}$$

Similarly for the other three interfaces, the constraints are

$$\mathbf{H}_t^{(5)} \aleph(x,\omega_n)^{(5)} \hat{\mathbf{u}}^{(5)} = \mathbf{H}_b^{(4)} \aleph(x,\omega_n)^{(4)} \hat{\mathbf{u}}^{(4)} \,, \tag{9.59}$$

$$\mathbf{H}_t^{(3)} \aleph(x,\omega_n)^{(3)} \hat{\mathbf{u}}^{(3)} = \mathbf{H}_b^{(6)} \aleph(x,\omega_n)^{(6)} \hat{\mathbf{u}}^{(6)} \,, \tag{9.60}$$

$$\mathbf{H}_t^{(4)} \aleph(x,\omega_n)^{(4)} \hat{\mathbf{u}}^{(4)} = \mathbf{H}_b^{(6)} \aleph(x,\omega_n)^{(6)} \hat{\mathbf{u}}^{(6)} \,. \tag{9.61}$$

The nodal displacement vectors $\hat{\mathbf{u}}^{(5)^T} = \{\hat{\mathbf{u}}_{\mathbf{8}}^T \; \hat{\mathbf{u}}_{\mathbf{3}}^T\}$ and $\hat{\mathbf{u}}^{(4)^T} = \{\hat{\mathbf{u}}_{\mathbf{4}}^T \; \hat{\mathbf{u}}_{\mathbf{11}}^T\}$ can now be transformed using Equation (9.53) in the above Equations (9.58)–(9.61) and the internal nodes can be condensed out systematically. To illustrate further, let us consider the constraint for the first interface as given by Equation (9.58), which can be rewritten after transformation as

$$\begin{bmatrix} \bar{\mathbf{C}}_{\mathbf{11}} \; \bar{\mathbf{C}}_{\mathbf{12}} \\ \bar{\mathbf{C}}_{\mathbf{21}} \; \bar{\mathbf{C}}_{\mathbf{22}} \end{bmatrix}_{(6\times 6)} \begin{Bmatrix} \hat{\mathbf{u}}_{\mathbf{5}} \\ \hat{\mathbf{u}}_{\mathbf{6}} \end{Bmatrix} = \begin{Bmatrix} \mathbf{0} \\ \mathbf{0} \end{Bmatrix} \,. \tag{9.62}$$

Since in Equation (9.62), $\hat{\mathbf{u}}_{\mathbf{5}}$ and $\hat{\mathbf{u}}_{\mathbf{6}}$ are the internal nodal vectors, they are mapped onto node 1 and node 2. This second step with the help of Equation (9.54), gives

$$\begin{bmatrix} \mathbf{C}_{11} \; \mathbf{C}_{12} \\ \mathbf{C}_{21} \; \mathbf{C}_{22} \end{bmatrix}_{(6\times 6)} \begin{Bmatrix} \hat{\mathbf{u}}_{\mathbf{1}} \\ \hat{\mathbf{u}}_{\mathbf{2}} \end{Bmatrix} = \begin{Bmatrix} \mathbf{0} \\ \mathbf{0} \end{Bmatrix} \quad \Rightarrow \mathbf{C}(x,\omega_n)^{(1)} \hat{\mathbf{u}}^e = \mathbf{0} \,. \tag{9.63}$$

Similar constraints for the other three horizontal interfaces can be obtained in the same way, where $\mathbf{C}(x,\omega_n)^{(j)}$, $j = 1, \cdots, 4$ are the matrices of coefficients associated with the multi-point constraints mapped on the dofs of the two-node element with embedded transverse crack. Introducing a diagonal matrix of penalty parameters α and minimizing the potential in the frequency domain [191], the updated dynamic stiffness matrix for the element with embedded transverse crack incorporating unbounded length of the internal hanging laminates can be expressed as

$$\hat{\bar{\mathbf{K}}}_U = \hat{\bar{\mathbf{K}}} + \hat{\bar{\mathbf{K}}}_C \,, \tag{9.64}$$

where

$$\begin{aligned} \hat{\bar{\mathbf{K}}}_C = & \int_0^{\Delta L/2} \left(\mathbf{C}^{(1)^T} \alpha \mathbf{C}^{(1)} + \mathbf{C}^{(3)^T} \alpha \mathbf{C}^{(3)} \right) dx \\ & + \int_{\Delta L/2}^{\Delta L} \left(\mathbf{C}^{(2)^T} \alpha \mathbf{C}^{(2)} + \mathbf{C}^{(4)^T} \alpha \mathbf{C}^{(4)} \right) dx \,. \end{aligned} \tag{9.65}$$

9.7 Numerical Simulations

The modular approach towards addition of a new element in the library of SFEs involves only three additional input parameters to model a transverse crack. These additional inputs are span-wise location of the crack ($L_1+\Delta L/2$), and depth-wise location of the top and bottom crack-tips (d_1, d_2). Although, the effect of crack-tip singularity is not included in the local analysis, it is essential to validate the performance of the proposed element for wave-based diagnostics and SHM applications, where most damage models are approximated by springs or equivalent change in the constitutive model for faster analysis. In the following section, response of a unidirectional composite cantilever beam with mid-span surface-breaking fiber fracture to a high frequency pulse loading is simulated using the developed SFE and the response is compared with a detailed 2-D FE model.

9.7.1 Comparison with 2-D FEM

A uni-directional graphite–epoxy cantilever beam of length 800 mm and having a cross-section 16 mm (thickness) × 10 mm (width) is considered for this study. An 8 mm deep top surface-breaking crack is introduced at mid-span of the beam. The same pulse loading as in previous examples (Figure 5.3) is applied at the tip of the cantilever beam in the transverse direction. SFE analysis is carried out using a single SFE with embedded crack. In all numerical simulations, the length of the hanging laminates $\Delta L/2$ is chosen using Equation (9.30). 16384 FFT sampling points ($\Delta\omega = 12.2070$ Hz) are used for the forward and inverse transform of the loading and response, respectively. In the detailed FE analysis, the fine mesh consists of 5120 constant strain triangular elements under plane-stress conditions in the $X - Z$ plane. Newmark time integration with time step $\Delta t = 1\mu$s is used. Here the element size is comparable with the wavelength of the applied excitation. The pulse load is applied consistently in the transverse direction at the tip cross-section of the FE model.

Figure 9.22 shows the plots of $\dot{w}$ history at the mid-node of the tip cross-section predicted by SFE and detail 2-D FE analysis. After the incident pulse, the effect of the crack due to wave scattering at around $0.55 - 0.6$ ms can be seen. The peak amplitude of the velocity history and its arrival time matches very well with the 2-D FE prediction. However, a small additional peak before the main peak amplitude can be seen, which is due to several approximations made in the proposed modeling compared to the actual local crack-tip behavior. Indeed, the overall trend of the response predicted by the proposed spectral element can be seen as reliable, in terms of the arrival time of the broadband wave scattered from the crack, as well as the associated peak amplitude in the signal. Another important aspect we need to mention in this context is that the inter-penetration of the crack surfaces of the breathing crack in the detailed 2-D FE analysis (in the absence of contact elements) was

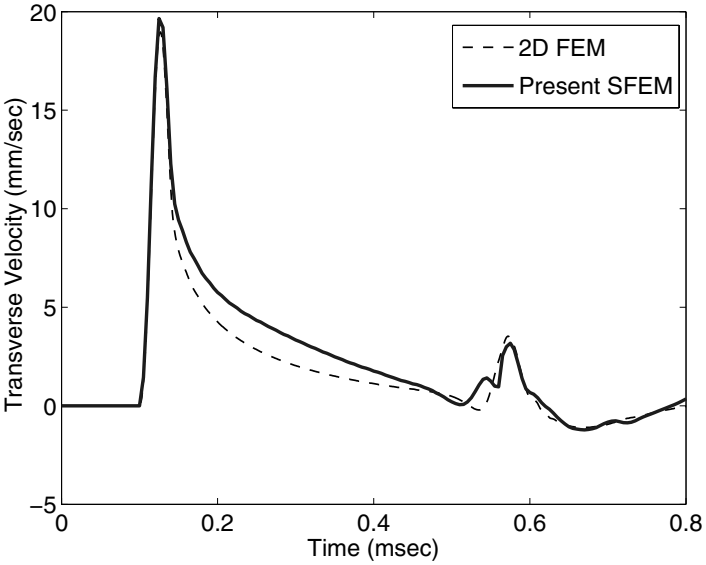

Fig. 9.22. Comparison of the transverse velocity $\dot{w}$ history at the mid-plane of the tip of the cantilever beam predicted by the single spectral element and detailed 2-D FE models under high frequency pulse loading (Figure 5.3)

found to occur much beyond the time window shown in Figure 9.22 and had neglible amplitude (relative displacement between the crack surfaces). Hence this can be considered less significant for transient wave-based diagnostics. However, long duration monitoring under sustained loading and associated incremental crack-growth related study need further strategy for FE model-based identification of frequency dependent dynamic contact forces, which can be used then in the present spectral element for more accurate analysis.

9.7.2 Identification of Crack Location from Scattered Wave

To identify the location of a crack from the scattered wave through numerical simulation, the same graphite–epoxy cantilever beam as considered earlier is used. Compared to the 8 mm deep surface-breaking crack in Figure 9.22, Figure 9.23 shows the $\dot{w}$ history at the cantilever tip of the beam with a mid-span 8 mm deep embedded crack introduced symmetrically across the thickness. From the group speed of the flexural wave the time of arrival of the flexural wave is estimated and is shown by $*$ on Figure 9.23. Although the time of arrival is the same for both the surface-breaking crack and embedded crack, which is obvious, a smaller blob visible at 0.58 ms is due to the presence of the embedded crack.

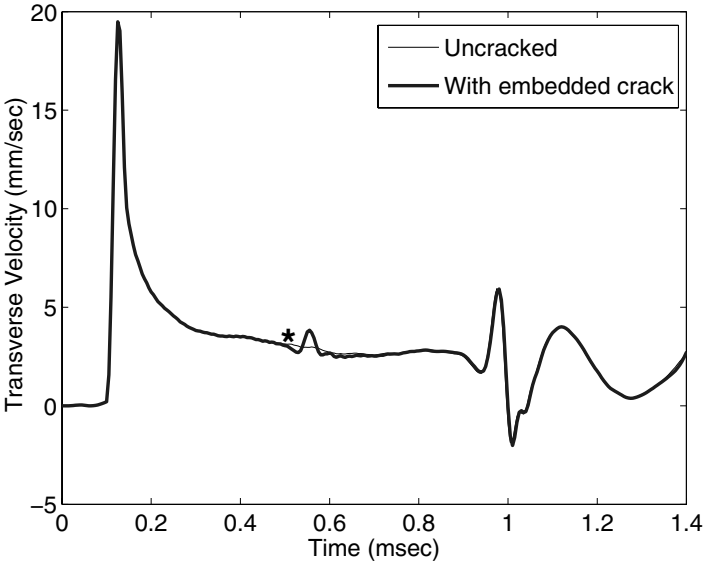

Fig. 9.23. Transverse velocity $\dot{w}$ history at the cantilever tip due to a high frequency pulse (Figure 5.3) applied at the cantilever tip in the transverse direction for a mid-span 8 mm deep embedded crack placed symmetrically across the beam thickness. $*$ shows the analytical estimate of the arrival time of the reflected wave from the crack

Next we consider a sinusoidal pulse modulated at 20 kHz as shown in Figure 9.5 for wave-based interrogation of the cracked beam. Such a pulse will contain maximum energy within a very small frequency band and the peak energy will be at the frequency at which it is modulated.

Using this modulated pulse applied at the cantilever tip in the transverse direction, the transverse velocity $\dot{w}$ at the cantilever tip is simulated. Figure 9.24 shows the response for a mid-span 8 mm deep top surface-breaking crack.

Figure 9.25 shows the response for a mid-span 8 mm deep embedded crack. Analytical estimate of the arrival time ($t = 2l/c_g$, $c_g = 1944.59$ m/s) of the reflected pulse is shown in the figures by $*$. The simulated arrival time is found to match very closely with the analytical estimates. It can be seen from Figures 9.24 and 9.25 that the reflected wave amplitude from the embedded crack is slightly higher than those due to the surface-breaking crack of the same depth and same load.

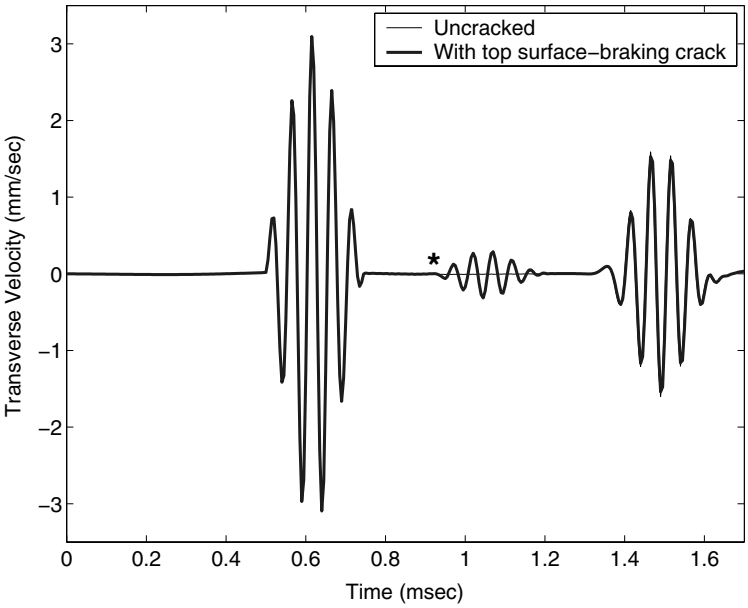

Fig. 9.24. Transverse velocity $\dot{w}$ at the cantilever tip due to modulated sine pulse transversely applied at the tip of the cantilever with a mid-span 8 mm deep top surface-breaking crack

9.7.3 Sensitivity of the Crack Configuration

Numerical simulations with varying crack depth and contact stiffnesses of the crack surfaces produce no visible fluctuation in the scattered waves from the embedded crack under the present loading in the flexural shear mode. However, the surface-breaking crack with variation in the crack depth and contact stiffnesses of the crack surfaces shows significant changes in the scattered waves, which are plotted in Figure 9.26 and 9.27, respectively. As the crack depth becomes more than half the beam thickness (16 mm), additional peaks after the first reflection can be seen in Figure 9.26. In Figure 9.27, the contact stiffness between the crack surfaces is varied using a stiffness factor β, where only the surface-normal contact stiffness is considered and is assumed to be $K^* = \beta Q_{11}$. Apart from the main reflected wave from the crack at around 1 ms, which indicates the crack location, Figure 9.27 shows small amplitude of additional scattering for contact stiffness smaller than Q_{11}, and significant amplitude additional scattering for contact stiffness more than Q_{11}, which can be considered as a stiff inclusion. In the present one-dimensional model, the higher order Lamb wave modes, especially the thickness stretching mode, are not accounted for. From the simulations, it appears that for identification of the crack configuration completely, especially the crack depth and thickness-wise location, a higher-order Lamb wave model based on high

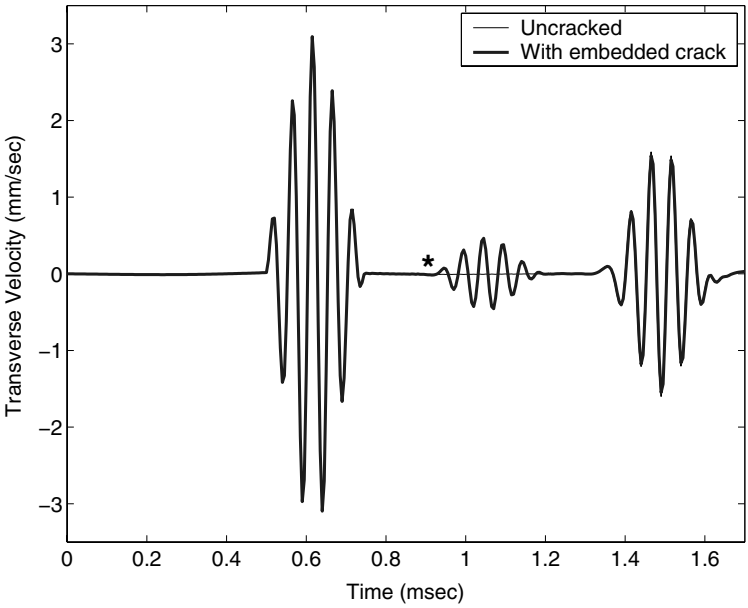

Fig. 9.25. Transverse velocity $\dot{w}$ at the cantilever tip due to modulated sine pulse transversely applied at the tip of the cantilever with a mid-span 8 mm deep embedded crack

frequency excitation in flexural shear thickness stretching modes may be necessary. Such data can be used to develop efficient soft computing tools for crack identification.

9.8 Spectral Finite Element Model for Damage Estimation

Spectral analysis and associated numerical techniques for studying wave interaction with material interfaces are particularly suitable for damage diagnostics. In the same way as in interrogation strategies using acoustic devices, computational simulation techniques based on spectral analysis can be efficiently integrated in SHM software. The potential of such strategies is reported in [192], [193].

The basic steps in developing the SFEM for the degraded laminated composite beam are as follows. Considering a general ply-stacking sequence (unbalanced), the axial–flexural–shear coupled wave equation for a first-order shear deformable beam is formed. The spectral element for coupled wave propagation in such a beam involves two nodes at the end of the element and a standard finite element assembly. The frequency response as well as temporal response can be obtained in this approach under any general dynamic loading.

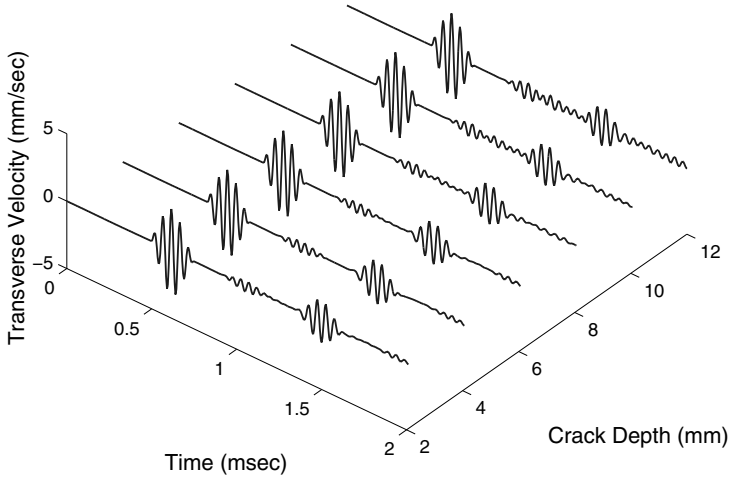

Fig. 9.26. Transverse velocity $\dot{w}$ at the cantilever tip due to modulated sine pulse transversely applied at the tip of the cantilever with a top surface-breaking crack of varying depth. No contact between the surfaces is assumed

For characteristic wave propagation in such a beam, the high frequency limit is imposed by the unmodeled kinematics that may cause higher Lamb wave modes (first symmetric stretching mode and higher, and third anti-symmetric stretching mode and higher). Hence, the bandwidth of any attached acoustic device needs to be operated within the above limits. In the present model, one such spectral element with degraded ply properties is considered. We represent the degraded laminate constitutive property under plane-stress or plane-strain condition by

$$\begin{Bmatrix} \sigma_{xx} \\ \sigma_{zz} \\ \tau_{xz} \end{Bmatrix} = \begin{bmatrix} \alpha_{11}Q_{11} & \alpha_{13}Q_{13} & 0 \\ \alpha_{13}Q_{13} & \alpha_{33}Q_{33} & 0 \\ 0 & 0 & \alpha_{55}Q_{55} \end{bmatrix} \begin{Bmatrix} \varepsilon_{xx} \\ \varepsilon_{zz} \\ \gamma_{xz} \end{Bmatrix}, \tag{9.66}$$

where z is the laminate thickness direction and x is the longitudinal direction (0° fiber direction). α_{ij} are degradation factors, which are unity for healthy laminates.

The element nodal dofs are condensed after the assembly of two undamaged elements on both sides of the damaged zone. Finally, it is possible to describe the damage configuration just by prescribing three sets of parameters: (1) the degradation factors (α_{ij}) describing the damaged laminate (Equation (9.66)); (2) the approximate span-wise location of one of the interface between the undamaged and damaged zone; and (3) the length of the dam-

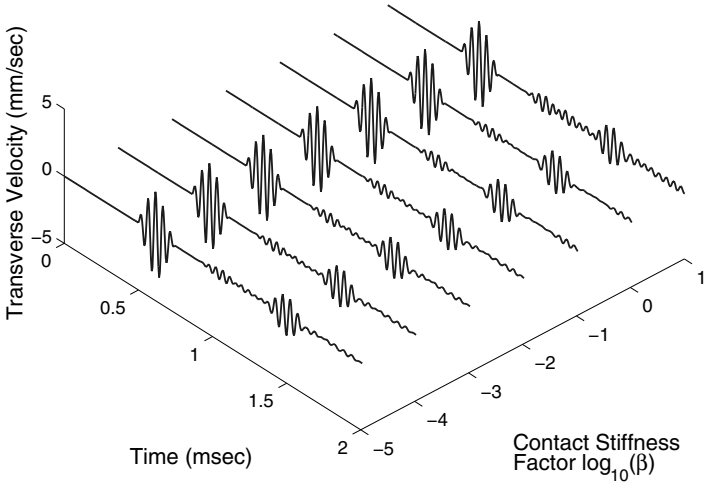

Fig. 9.27. Transverse velocity $\dot{w}$ at the cantilever tip due to modulated sine pulse transversely applied at the tip of the cantilever with a top surface-breaking crack with varying contact stiffnesses ($K^* = \beta Q_{11}$). Crack depth is 8 mm

aged zone. Considering a similar assembly technique, models for delamination and a large transverse crack can be found in [194, 195].

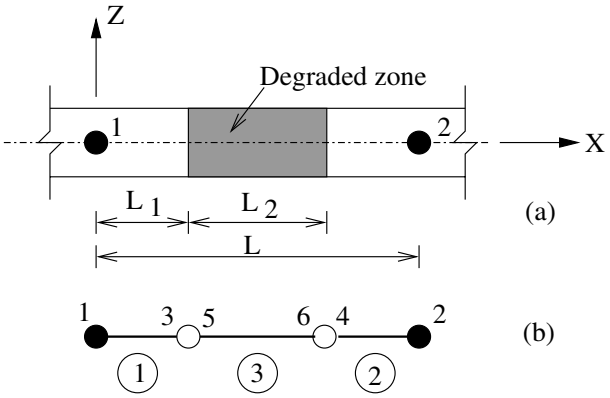

Fig. 9.28. (a) Composite beam segment with degraded zone of size L_2. The whole segment is represented by the end nodes 1 and 2 of the spectral element. (b) Element local configuration showing the internal element numbers (1), (2) and (3) by circles and the associated nodes 1–3, 2–4, and 5–6

9.8.1 Spectral Element with Embedded Degraded Zone

The location of the two nodes of spectral elements with an embedded degraded zone in a beam is shown in Figure 9.28(a). In the absence of degradation, one spectral element between node 1 and node 2 is sufficient for analysis. The presence of degradation, when treated as a structural discontinuity by neglecting the effect of stress singularity at the delamination tip, increases the number of elements from one to three as shown in Figure 9.28(b). Four more nodes are introduced to model the degraded zone (element (3)) and the surrounding undamaged zones (elements (1) and (2)). In a practical situation, it may so happen that the matrix crack density in laminates may decrease with some gradation from the damaged zone. In such a case, the elements (1) and (3) can be used with such graded laminate properties, based on the same constitutive model as discussed in Equation (9.66).

The kinematic assumption of continuity of displacements and rotations at the internal element nodes 3,5 and 4,6 leads to

$$\hat{\mathbf{u}}_{\mathbf{5}} = \left\{ \hat{u}_5^0 \; \hat{\omega}_5 \; \hat{\phi}_5 \right\}^T = \hat{\mathbf{u}}_{\mathbf{3}} \; , \quad \hat{\mathbf{u}}_{\mathbf{6}} = \left\{ \hat{u}_6^0 \; \hat{\omega}_6 \; \hat{\phi}_6 \right\}^T = \hat{\mathbf{u}}_{\mathbf{4}} \; . \tag{9.67}$$

From equilibrium of the nodal forces and moments at the left interface (between nodes 3 and 5) and at the right interfaces (between nodes 4 and 6), we get respectively

$$\hat{\mathbf{f}}_{\mathbf{3}} + \hat{\mathbf{f}}_{\mathbf{5}} = \mathbf{0} \; , \quad \hat{\mathbf{f}}_{\mathbf{4}} + \hat{\mathbf{f}}_{\mathbf{6}} = \mathbf{0} \; . \tag{9.68}$$

The element equilibrium equation for the jth internal element ($j = 1, 2, 3$) with nodes p and q can be written as

$$\begin{bmatrix} \hat{\mathbf{K}}_{\mathbf{11}}^{(j)} & \hat{\mathbf{K}}_{\mathbf{12}}^{(j)} \\ \hat{\mathbf{K}}_{\mathbf{21}}^{(j)} & \hat{\mathbf{K}}_{\mathbf{22}}^{(j)} \end{bmatrix}_{(6\times 6)} \begin{Bmatrix} \hat{\mathbf{u}}_{\mathbf{p}} \\ \hat{\mathbf{u}}_{\mathbf{q}} \end{Bmatrix} = \begin{Bmatrix} \hat{\mathbf{f}}_{\mathbf{p}} \\ \hat{\mathbf{f}}_{\mathbf{q}} \end{Bmatrix} \; . \tag{9.69}$$

Assembling Equation (9.69) for the three internal elements (1), (2) and (3), we get

$$\begin{bmatrix} \hat{\mathbf{K}}_{\mathbf{11}}^{(1)} & \hat{\mathbf{K}}_{\mathbf{12}}^{(1)} & \mathbf{0} & \mathbf{0} \\ \hat{\mathbf{K}}_{\mathbf{21}}^{(1)} & \hat{\mathbf{K}}_{\mathbf{22}}^{(1)} + \hat{\mathbf{K}}_{\mathbf{11}}^{(2)} & \hat{\mathbf{K}}_{\mathbf{12}}^{(2)} & \mathbf{0} \\ \mathbf{0} & \hat{\mathbf{K}}_{\mathbf{21}}^{(2)} & \hat{\mathbf{K}}_{\mathbf{22}}^{(2)} + \hat{\mathbf{K}}_{\mathbf{11}}^{(3)} & \hat{\mathbf{K}}_{\mathbf{12}}^{(3)} \\ \mathbf{0} & \mathbf{0} & \hat{\mathbf{K}}_{\mathbf{21}}^{(3)} & \hat{\mathbf{K}}_{\mathbf{22}}^{(3)} \end{bmatrix}_{(12\times 12)} \begin{Bmatrix} \hat{\mathbf{u}}_{\mathbf{1}} \\ \hat{\mathbf{u}}_{\mathbf{3}} \\ \hat{\mathbf{u}}_{\mathbf{4}} \\ \hat{\mathbf{u}}_{\mathbf{2}} \end{Bmatrix} = \begin{Bmatrix} \hat{\mathbf{f}}_{\mathbf{1}} \\ \mathbf{0} \\ \mathbf{0} \\ \hat{\mathbf{f}}_{\mathbf{2}} \end{Bmatrix} \; . \tag{9.70}$$

On condensation of the dofs at the internal nodes 3 and 4 and assuming no load is applied to the damaged zone, Equation (9.70) becomes

$$\hat{\mathbf{K}}_{(6\times 6)} \begin{Bmatrix} \hat{\mathbf{u}}_{\mathbf{1}} \\ \hat{\mathbf{u}}_{\mathbf{2}} \end{Bmatrix} = \begin{Bmatrix} \hat{\mathbf{f}}_{\mathbf{1}} \\ \hat{\mathbf{f}}_{\mathbf{2}} \end{Bmatrix} \; , \tag{9.71}$$

where the submatrices of the new dynamic stiffness matrix $\hat{\mathbf{K}}$ are defined as

$$\hat{\mathbf{K}}_{\mathbf{11}} = \hat{\mathbf{K}}_{\mathbf{11}}^{(1)} - \hat{\mathbf{K}}_{\mathbf{12}}^{(1)} \left(\hat{\mathbf{K}}_{\mathbf{22}}^{(1)} + \hat{\mathbf{K}}_{\mathbf{11}}^{(2)} \right)^{-1} \mathbf{X_2} \,, \tag{9.72}$$

$$\hat{\mathbf{K}}_{\mathbf{12}} = \hat{\mathbf{K}}_{\mathbf{12}}^{(1)} \left(\hat{\mathbf{K}}_{\mathbf{22}}^{(1)} + \hat{\mathbf{K}}_{\mathbf{11}}^{(2)} \right)^{-1} \hat{\mathbf{K}}_{\mathbf{12}}^{(2)} {\mathbf{X_1}}^{-1} \hat{\mathbf{K}}_{\mathbf{12}}^{(3)} \,, \tag{9.73}$$

$$\hat{\mathbf{K}}_{\mathbf{21}} = \hat{\mathbf{K}}_{\mathbf{21}}^{(3)} {\mathbf{X_1}}^{-1} \hat{\mathbf{K}}_{\mathbf{21}}^{(2)} \left(\hat{\mathbf{K}}_{\mathbf{22}}^{(1)} + \hat{\mathbf{K}}_{\mathbf{11}}^{(2)} \right)^{-1} \hat{\mathbf{K}}_{\mathbf{21}}^{(1)} \tag{9.74}$$

$$\hat{\mathbf{K}}_{\mathbf{22}} = \hat{\mathbf{K}}_{\mathbf{22}}^{(3)} - \hat{\mathbf{K}}_{\mathbf{21}}^{(3)} {\mathbf{X_1}}^{-1} \hat{\mathbf{K}}_{\mathbf{12}}^{(3)} \,, \tag{9.75}$$

$$\mathbf{X_1} = \left(\hat{\mathbf{K}}_{\mathbf{22}}^{(2)} + \hat{\mathbf{K}}_{\mathbf{11}}^{(3)} \right) - \hat{\mathbf{K}}_{\mathbf{21}}^{(2)} \left(\hat{\mathbf{K}}_{\mathbf{22}}^{(1)} + \hat{\mathbf{K}}_{\mathbf{11}}^{(2)} \right)^{-1} \hat{\mathbf{K}}_{\mathbf{12}}^{(2)} \,, \tag{9.76}$$

$$\mathbf{X_2} = \hat{\mathbf{K}}_{\mathbf{21}}^{(1)} + \hat{\mathbf{K}}_{\mathbf{12}}^{(2)} {\mathbf{X_1}}^{-1} \hat{\mathbf{K}}_{\mathbf{21}}^{(2)} \left(\hat{\mathbf{K}}_{\mathbf{22}}^{(1)} + \hat{\mathbf{K}}_{\mathbf{11}}^{(2)} \right)^{-1} \hat{\mathbf{K}}_{\mathbf{21}}^{(1)} \,. \tag{9.77}$$

Equation (9.71) is the equilibrium equation for the spectral element with embedded degraded zone, where only the dofs at the end nodes 1,2 need to be used while forming the global system of a damaged structure.

9.9 Numerical Simulations

To simulate the effect of stiffness degradation on the diagnostic signal, a graphite–epoxy cantilever beam of length 0.8 m, thickness 16 mm and width 10 mm is considered. All the plies are assumed to be of equal thickness with stacking sequence $(0_{40}/90_{80}/0_{40})$. A 20 mm long degraded zone is introduced at 0.3 mm from the fixed end of the beam. The finite element model of the beam consists of a single damaged spectral element under plane stress conditions in the $X-Z$ plane (Figure 9.28). It is assumed that all the 90° plies are degraded with the same factor, α_{11} (Equation (9.66)) in the longitudinal mode. In the transverse and shear modes, the plies are assumed to be undamaged. In a practical situation, however, the transverse and shear moduli will also have degradation but their effect on the damaged structural response under flexural wave excitation (as in the present case) will be negligible compared to that due to degradation in the longitudinal elastic modulus. A sinusoidal pulse modulated at 20 kHz (shown in Figure 9.5) is applied in the transverse direction (parallel to the Z-axis) at the tip. 2048 FFT sampling points are used in the analysis. Transverse velocity histories at the tip of the beam due to the variation in degradation of cross-ply are shown in Figure 9.29. As seen in this figure, the first pulse appearing at $0.5 - 0.75$ ms is the incident wave. The next smaller pulses seen at higher degradation (smaller values of α_{11}) are reflections from the two ends of the degraded zone. Here we assume that the plies were degraded uniformly within the degraded zone. To study the effect of the length of the degraded zone, we consider the same cantilever beam with one of the interfaces fixed at 0.4 m from the tip. The length of the degraded zone is varied by moving the other interface towards the fixed end from 0.1 m to 0.4 m. The last case represents one half of the beam on the fixed end side

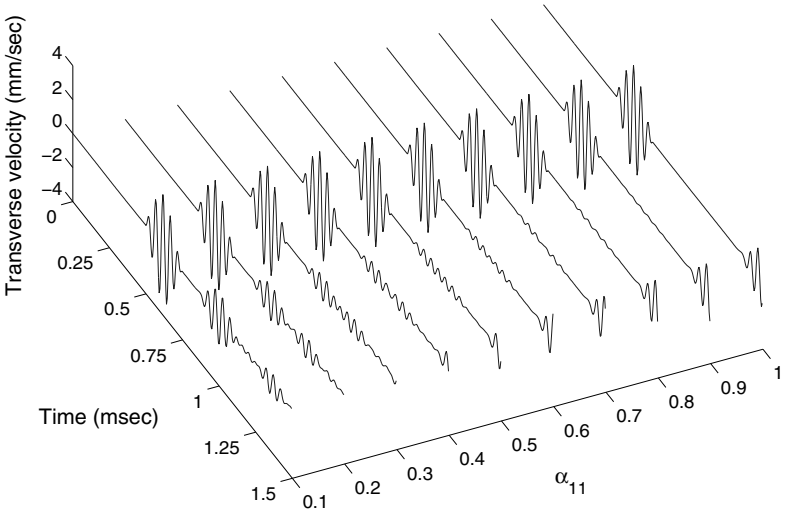

Fig. 9.29. Transverse velocity history due to variation in the degradation factor α_{11} using a narrow-band diagnostic signal (Figure 9.5). Length of the degraded zone is 20 mm

of the beam as degraded. The variation of the transverse velocity histories at the tip of the beam with the variation of the size of the degraded zone is shown in Figure 9.30 for $\alpha_{11} = 0.2$. From the figure it can be seen that for a smaller size degraded zone with higher degradation (smaller values of α), both reflections from the two interfaces are easily detectable.

In the above numerical simulations, a narrow-band modulated pulse is used as diagnostic signal, which is typically generated using inter-digital transducers (IDTs) for SHM. In order to study the difference between the response of the damage due to degradation in the effective ply properties and that due to large delamination or transverse cracks in ply groups, we consider three different damage configurations as shown in Figure 9.32. The models for delamination and the transverse crack are formulated in Section 9.3 and 9.5, respectively. Figure 9.33 shows the transverse velocity histories at the tip of the beam for these three types of damage configuration with a broadband pulse applied at the tip. The peaks R_1, R_2 and R_3 indicate reflections from the front interface (for transverse crack only one discontinuity), reflections from the second interface (towards the fixed-end side) and reflections from the fixed end of the beam, respectively. Although, the interrogating signal generates multiple waves at different characteristic dispersions, and hence are expected to contain the maximum amount of information it is possible to

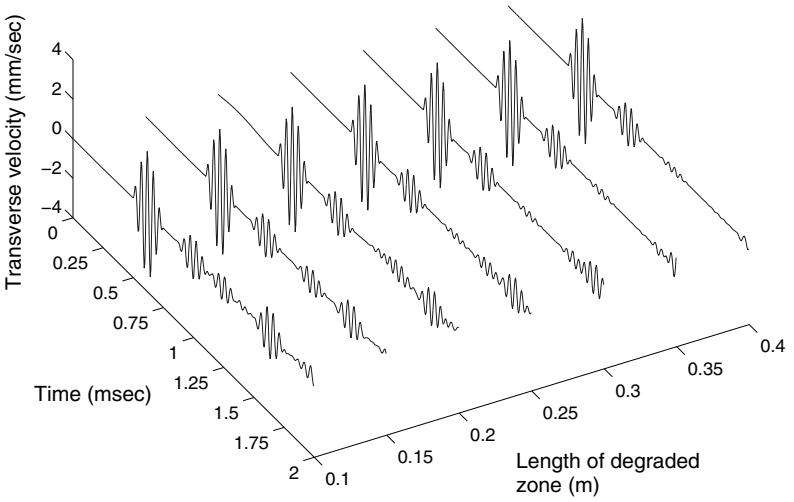

Fig. 9.30. Transverse velocity histories due to variation in the length of the degraded zone with narrow-band diagnostic signal (Figure 9.5). Degradation factor $\alpha_{11} = 0.2$

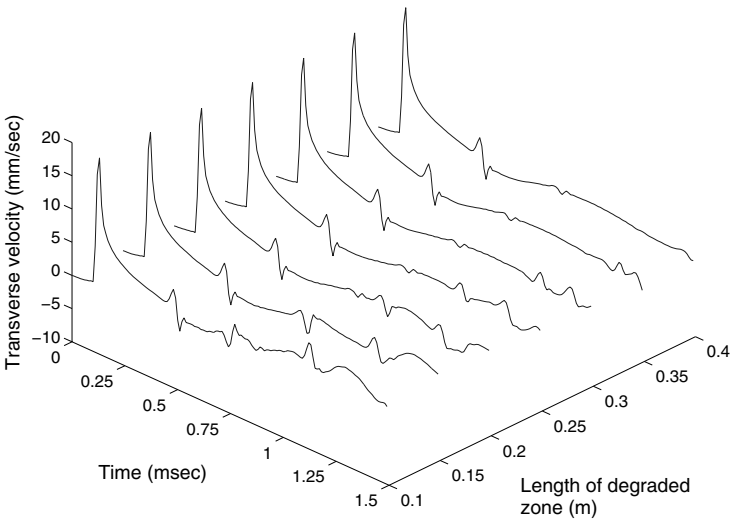

Fig. 9.31. Transverse velocity histories due to variation in the length of the degraded zone with broadband diagnostic signal (Fig. 5.3). Degradation factor $\alpha_{11} = 0.2$

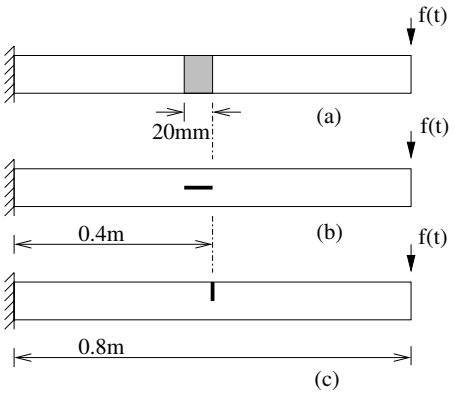

Fig. 9.32. Different damage configurations considered for comparative diagnostic response. (a) Stiffness degradation of length 20 mm, degradation factor $\alpha_{11} = 0.2$; (b) delamination of length 20 mm; and (c) transverse crack of depth 4 mm

extract from the damaged zone, the simple temporal signal in comparison with a base-line signal (as in Figure 9.33) is not of much help except some correlation with the approximate location of the damage. Therefore, it appears important that certain appropriate estimation techniques involving the statistical nature of the broadband spectral data be developed, where both the model-generated data (as often generated by using different semi-analytic wave analysis techniques, standard FEM and the present SFEM) as well as the on-line measured data can be used. Towards this development, a neural network model suited to handling broadband spectral data through SFEM is developed. This is discussed in [196].

This chapter gives a complete overview of the applications of spectral finite element modeling and analysis to structural health monitoring of composite beam type structures. The chapter goes into the details of novel modeling, analysis and damage diagnostic techniques using SFEMs. These are summarized item-wise in the paragraphs to follow.

Spectral element for delaminated beams
A spectral element to model the wave scattering in a composite beam with delamination is presented. Complete description of the delamination by inputting just three quantities (local coordinates of delamination tip and delamination length) wherever the delamination is to be inserted, and compact matrix computation shows the usefulness of the element. Excellent performance of the element is observed when comparing the response with 2-D FE analysis. Also, cross-checks are performed to identify the location of delamination by wave scattering modeled with the proposed element. Sensitivity of the global structural response due to variation in the delamination location, depth and length is investigated. Interestingly, a periodicity of half the group

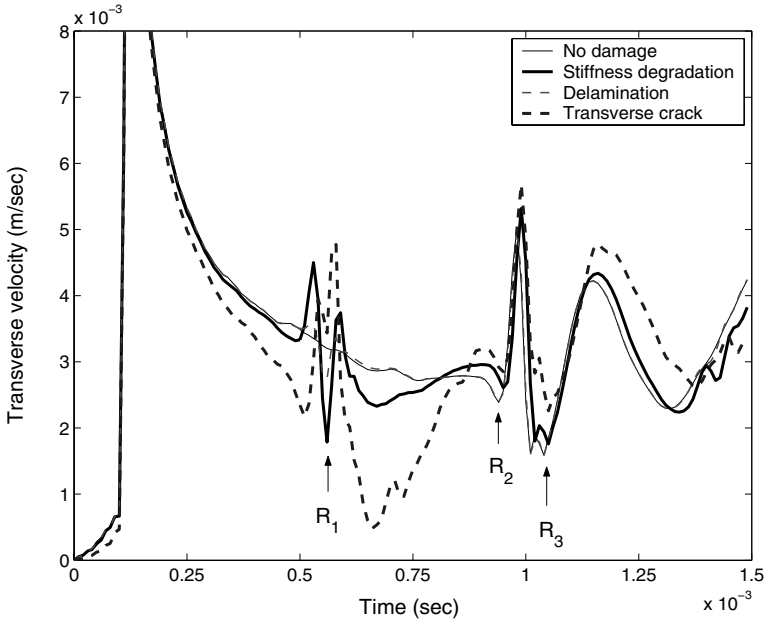

Fig. 9.33. Transverse velocity histories showing a comparison of the response of the cantilever beam with three different damage configurations (Figure 9.32) with broadband pulse

wavelength in the length of delamination is found to amplify the amplitude of the wave reflection from the near delamination tip. More detailed modeling of this aspect may be important for future developments. While developing the FFT based efficient spectral finite element model, potential use of scattered wave measurement to off-line and on-line structural health monitoring software has been kept as the immediate goal. For validation of the measured signal, this spectral element for delamination can be inserted in the finite element model based on the known configuration of single or multiple delaminations. Also, for the construction of an accurate reference structural model of any aging skeletal component, and for frequency domain identification of multiple delaminations in composite beams and frames, any number of such spectral elements can be inserted in the finite element model easily, keeping the system size reasonable.

Spectral element transversely cracked beams

A simplified spectral element model for transverse cracks is formulated using simplified beam kinematics for the twin purpose of studying wave scattering from the crack as well as using it for damage diagnostics. The beam kinematics in this case gives rise to a hanging interface, which is modelled using distributed springs. The beam kinematics is changed a little to incorporate

modeling of surface-breaking cracks. A number of parametric studies are performed to show the nature of scattering from the crack face. Comparisons of results with FEM show good agreement.

Spectral element for degraded regions
The formulation of this element is very similar to the previous two cases except that the constitutive models in the degraded zone are perturbed using a degradation parameter. Even here, a number of parametric studies were conducted to determine the extent of wave scattering as a function of the degradation parameters and the degraded zone length. One can observe that through the beam kinematics spectral model, synergy is brought about in handling different types of damage.

10

Application of SFEM to SHM: Efficient Damage Detection Techniques

In this chapter the damage model derived in Chapter 9 will be used to develop numerical algorithms for damage detection studies. This chapter will present four such algorithms, namely, spectral power flow, the damage force indicator, genetic algorithms and the artificial neural network (ANN).

10.1 Strategies for Identification of Damage in Composites

With the increasing use of composites as structural materials in aerospace and other industries, there is a growing need for identification of delamination and other modes of damage as part of the structural health monitoring and structural integrity evaluation. Several methods based on vibration characteristics for structural health monitoring have been reviewed in [10]. In more recent times in this direction, new sophisticated strategies for damage identification using modal parameters have been studied extensively [197], [198], [199], [200], [167]. Since modal parameters depend on the material property and geometry, the change in natural frequencies, mode shape curvature *etc.* can be used to locate damage in structures without knowing the excitation force when linear analysis is adequate. Lim and Kashangaki [201] located damage in space truss structures by computing Euclidian distances between the measured mode shapes and the best achievable eigenvectors. The best achievable eigenvectors are the projection of the measured mode shapes onto the subspace defined by the refined analytical model of structure and measured frequencies. Liu [202] used direct minimization of residue in the eigenequation for identification and damage detection in trusses using modal data. Manning [203] used active member transfer function data in conjunction with an ANN to detect damage in structures. It relies on training a neural network using active member transfer function pole/zero information to classify damaged structural measurements and predicts the degree of damage in a structure. The active members (transducers) that are already present in the

controlled structure can be utilized for this purpose (input and output for interrogation). However, modal methods are not very sensitive to the small size delaminations which are of practical interest, and can be very cumbersome as well as computationally expensive when implementing in practice for on-line health monitoring. In most methods based on modal parameters, it is assumed that the modes under consideration are affected by damage. As pointed out in [200] the change in individual natural frequencies due to slight damage may become insignificant and may fall within measurement error. In practical situations, this can considerably reduce the effectiveness of the prediction. With a view to alleviating such difficulty, results of broadband analysis using the spectral element for delaminated beams are discussed in this chapter.

Wave propagation analysis has been used extensively in non-destructive techniques (NDT). However, in the context of intelligent health monitoring tasks, there are several possibilities that such wave propagation analysis can be employed along with certain emphasis on efficient modeling and signal processing aspects. Zhang *et al.* [204] used broadband excitation and frequency domain measurement using remotely placed transducers and transmittance function to interrogate damage in beams. Valdes and Soutis [188] investigated how low frequency Lamb waves can be used to detect delaminations in thick composite plates. In their experiment with surface mounted piezoelectric transducers, artificially induced delamination of the order of 1 cm^2 was identified from reflections generated at the damaged region. Feasibility studies on diagnostic Lamb waves using active transducer elements have been carried out by Lin and Yuan [205].

Doyle [176] used the spectral element method for a metallic beam along with experimental data and a genetic algorithm to identify the location and size of a transverse crack in a beam. Spectral analysis using strip elements for wave scattering in composite plates and cylinders with crack has been carried out in [206], [64], [207], [192]. In these studies based on the strip element method, the characteristic wave equation is solved in wavenumber space (k-space). The spectral amplitudes are derived from a series approximation of Green's function that involves computation of eigenvalues and right and left eigenvectors. On the other hand, in SFEM, the characteristic coupled wave equations are solved in k-space, but the spectral amplitudes are computed in terms of coupled wave coefficients and by solving the finite element system at each FFT sampling frequency point (typically $512 - 8192$ points) irrespective of eigenvalues over a broad frequency band. This makes SFEM computationally much faster than other methods. Keeping this advantage of SFEM in mind, in this study, we use the spectral element for delaminated beams for model based identification and sensitivity studies of single and multiple delaminations in composite beams. The studies reported in this chapter also show the possibility of using similar elements for automated modeling and efficient software development for on-line structural health monitoring. In addition, there are many inherent features in spectral analysis such as identification of damping (which was discussed in Chapter 3), handling inverse problems

for force identification [208], [209] model update and digital signal processing. These can be implemented easily within the proposed framework for use in conjunction with on-line measurement.

In this chapter, the spectral element for a delaminated beam is used to evaluate a damage force indicator derived from the healthy structural model and the nodal force spectrum for the damaged structure. As a process of interrogation in structural health monitoring, this damage force indicator can be obtained by post-processing the measured data. This strategy was proposed by Schulz *et al.* [169] where the healthy structural model was constructed using standard finite elements. However, when using a standard finite element mesh, one needs to have force measurements at these finite element nodes. This requires several sensors to be placed at the locations of the finite element nodes. When force measurements are not possible directly, the same can be identified by solving the inverse problem [210] using other signals. Apart from the fact that such an inverse identification task can efficiently be handled by spectral analysis [208], the greatest advantage in using the spectral element for a delaminated beam in the structural model is that a uniform beam with a single delamination anywhere inside the beam needs only two end-nodes. The beam can be of any length with any type of boundary condition that can be linearized. Hence, the maximum requirement in this case is only four measurement points (top and bottom surfaces at each of the two nodes). This can be useful in reducing the hardware to a great extent. Lee and Shin [211] studied the effect of random noise on a damage indicator based on the spectral element method, which shows that reliability of the prediction can be very high even in the case of a maximum noise-to-signal ratio of nearly 10%. With such improvement, on-line health monitoring of large composite framed structures becomes much easier.

Genetic algorithms (GAs) are powerful and widely applicable stochastic search and optimization algorithms based on the principle of natural selection and genetic evolution [212], [213]. Because of their wide applicability and versatility, they are receiving increasing attention for solving engineering optimization problems, *e.g.,* structural design [214], [215], [216], [217], [218], parameter estimation [219], optimal control in smart structures [220], [221], [222] and damage detection [223], [224]. The conventional calculus based search technique uses the gradient of the function to find local minima or maxima. These search techniques are problem dependent and can work well for simple and smooth functions. Practical problems in mechanics (like we are trying to solve here) are very complex having a finite number of discontinuities, and hence gradient-based search methods cannot handle such problems efficiently. On the contrary, the main advantage of GAs lies in their robustness in handling non-smooth problems. In other words, the global optimum configuration can be captured without getting locked on to local ones. Another principal advantage is that GAs can handle most objective functional spaces with or without constraints that represent the required physics of the problem.

In solid mechanics and elastodynamics, the complexity of the damage identification problem has led many researchers to adopt GAs. Doyle [209] developed a genetic algorithm for determining the location of structural impact. Stavroulakis [210] used GA as a soft computing tool for the identification of cracks using a boundary element method. Mares and Surace [223] applied GAs with the residual force method for the identification of damage in elastic solids. The residual force method is based on conventional modal analysis and is derived from the stiffness matrix of the damaged structure. The experimental results have been simulated by adding random noise to natural frequencies and mode shapes. Friswell *et al.* [224] used natural frequencies as the measuring parameter in the objective functions. In this study a search was performed to locate an element with damage in a system of very few elements. Modeling of damage was done in an ad hoc manner by using stiffness reduction. Therefore the achievements of the search cannot be seen as very significant one since *a priori* knowledge regarding which modes are affected due to the existence of damage, are are not available. This particular aspect of the global structural model-independent identification process in smart structural health monitoring will play an important role in further developments of software and systems. The present study is focused on developing automated SFE estimation in the frequency domain integrated with GA specially tailored for a fast and efficient damage identification strategy.

Damage identification is essentially an inverse problem, wherein the damage needs to be detected using the measured input and output signals and previously updated system parameters. The best way to handle the identification task is to start with a transfer function or FRF and construct certain measures to estimate the state of damage. Conventional techniques such as time domain FEM are extremely difficult to apply for such problems due to the enormous computational cost to obtain a transfer function. Frequency domain analysis is ideally suited to such problems since FRFs are a direct by-product of the approach.

Modeling wave scattering in delaminated composite beams by a spectral element was derived in the last chapter. The results produced show that wave scattering can be used very effectively for detecting delamination, its location or extent in composite structures. However, to study the basic behavior of wave scattering due to the presence of a delamination, either semi-infinite or very long beam segments were considered in the above studies, thus eliminating the effects of boundary reflections. On the contrary, real life structures are of finite lengths. This allows the presence of many boundary reflections when broadband or single frequency tone-burst signals are introduced to interrogate the damage configuration. Therefore it becomes difficult to distinguish the scattered waveform due to delamination from temporal signals. Also, in model based predictions using the spectral element, it has been observed that final observation and identification processes using temporal responses need an enormous number of data-points to give sufficient resolution in frequency domain filtering, noise elimination and waveform reconstruction. Therefore, for

a better identification procedure, it appears more attractive to use frequency domain information directly [176]. It is also more realistic in the context of on-line measurements since sensors are required (as long as the signal is sensitive to delamination configurations) [180]. However, the frequency domain response is difficult to correlate directly with the delamination configuration. This problem becomes more complex in the presence of multiple delaminations (of unknown number). The *damage force indicator* [180], [169], which uses the frequency spectrum of displacement vectors, can be experienced best in a system with very few elements, if accurately modeled. Hence, it can be effectively used for identifying the damage zone modeled by a long spectral element for a delaminated beam with a pair of transducers placed at the two boundary-nodes of the beam. However, to locate delamination more precisely inside the zone (without increasing the number of transducers), the need for a second level of local identification strategy arises. Therefore to identify delamination from the frequency domain response for finite short beams of practical interest, we need to depend on some optimizing techniques like GAs. Aided by the fast and accurate computation power of the spectral element, GAs can extract the delamination configuration from remotely measured responses.

At the end of this chapter, we attempt to exploit the concept behind GA and Multi-layer Perceptron (MLP) to predict the damage configuration and parameters for a built-in, model based strategy for smart structural health monitoring. The known parameters are only the healthy structural configuration (mass, stiffness and damping matrices updated from previous phases of monitoring), sensor measurements, actuation load and environmental load. In the present context, one can think of various damage configurations. Here we restrict the complexity to a known number of delaminations. Typically, each configuration results in a solution-space in the same way as the individual population of living species performs with their genetic inheritance in the living world. Therefore, we consider this similarity to develop an automated procedure to decide what possible damage configuration(s) might have produced the observed fluctuation in the measured signals. An MLP feedforward neural network is trained using an error back propagation gradient descent algorithm to deal with a broadband spectral data as a diagnostic signal for the estimation of damage parameters.

10.2 Spectral Power Flow

The spectral power [225]

$$\hat{P} = \frac{1}{2}\hat{\mathbf{f}}^T \left[i\omega_n \hat{\mathbf{u}}\right]^* \tag{10.1}$$

is defined as the product of force vector and complex conjugate of the velocity vector at a material point. These quantities can easily be computed by post-processing the spectral element nodal results.

10.2.1 Properties of Spectral Power

(1) Real part of the spectral power is space invariant
Let us consider the coupled wave propagation involving u°, w° and θ_y. Lateral motion and torsional motion are excluded to reduce the level of algebraic manipulation. Expanding Equation (10.1) after substituting for $\hat{\mathbf{f}}$ and $\hat{\mathbf{u}}$, we have

$$\hat{P} = -\frac{1}{2} i\omega_n \left[\left(A_{1111}\hat{u}_{,x} + A_{1113}\hat{\theta}_{y,x} \right) \hat{u}^* + A_{5511} \left(\hat{w}_{,x} + \phi \right) \hat{w}^* \right.$$
$$\left. + \left(A_{1113}\hat{u}_{,x} + A_{1133}\hat{\theta}_{y,x} \right) \hat{\theta}_y^* \right] . \tag{10.2a}$$

Differentiating with respect to x and simplifying using the wave equations in u°, w° and θ_y, we get

$$\frac{\partial \hat{P}}{\partial x} = -\frac{1}{2} i\omega_n \left[-\omega_n^2 M_{11} \left(\hat{u}^o \hat{u}^{o*} + \hat{w}^o \hat{w}^{o*} \right) + A_{1111} \hat{u}^o{}_{,x}\, \hat{u}^{o*}{}_{,x} + A_{5511} \hat{w}^o{}_{,x}\, \hat{w}^{o*}{}_{,x} \right.$$
$$+ \left(A_{5511} - \omega_n^2 M_{33} \right) \hat{\theta}_y \hat{\theta}_y^* + A_{1133} \hat{\theta}_{y,x}\, \hat{\theta}^*{}_{,x} - \omega_n^2 M_{13} \left(\hat{\theta}_y \hat{u}^{o*} + \hat{u} \hat{\theta}_y^* \right)$$
$$\left. + A_{5511} \left(\hat{\theta}_y \hat{w}^{o*}{}_{,x} + \hat{\theta}_y^* \hat{w}^o{}_{,x} \right) + A_{1113} \left(\hat{\theta}_{y,x}\, \hat{u}^{o*}{}_{,x} + \hat{\theta}^*{}_{y,x}\, \hat{u}^o{}_{,x} \right) \right] . \tag{10.2b}$$

Note that in Equation (10.2b), the right-hand side is purely an imaginary quantity. Therefore, by equating the real part and imaginary part of the spectral power $\hat{P} = \hat{P}_R + i\hat{P}_I$, we get

$$\frac{\partial \hat{P}_R}{\partial x} = 0 . \tag{10.2c}$$

That is the real part of the power is space invariant.
(2) Real part of the spectral power indicates the amount of energy trapped in a structural member
Using Equation (10.2a), it can be shown that for a purely longitudinal wave

$$\hat{u}^o = \tilde{u}_1 e^{-ik_1 x} + \tilde{u}_2 e^{-ik_1 (L-x)} , \tag{10.3a}$$

where k_1 is the longitudinal wavenumber, the real part of the spectral power

$$\hat{P}_R = \frac{1}{2} \omega_n k_1 A_{1111} \left[-\tilde{u}_1 \tilde{u}_1^* + \tilde{u}_2 \tilde{u}_2^* \right] \tag{10.3b}$$

is a stationary quantity and vanishes when

$$|\tilde{u}_1| = |\tilde{u}_2| , \tag{10.3c}$$

that is when the forward and backward propagating waves are of the same amplitude. This necessitates the two longitudinal forces ($\hat{N}_{x1}$ and $\hat{N}_{x2}$) at the boundaries either being equal and opposite in sign and hence self-equilibrating

or such that the wave coefficients $\tilde{u}_1$ and $\tilde{u}_2$ are with relative phase $\phi_1 - \phi_2$ given by

$$e^{i(\phi_1-\phi_2)} = \frac{\hat{N}_{x2} - \hat{N}_{x1}e^{ik_1L}}{\hat{N}_{x2}e^{ik_1L} - \hat{N}_{x1}} \,. \tag{10.3d}$$

Similar conclusions can be drawn from the purely transverse flexural waves

$$\hat{w}^o = \tilde{u}_9 e^{-ik_9x} + \tilde{u}_{10}e^{-ik_9(L-x)} + \tilde{u}_{11}e^{-k_9x} + \tilde{u}_{12}e^{-k_9(L-x)} \,, \tag{10.3e}$$

$$\begin{aligned}\hat{\theta}_y = {} & R_{5,9}\tilde{u}_9 e^{-ik_9x} + R_{5,10}\tilde{u}_{10}e^{-ik_9(L-x)} + R_{5,11}\tilde{u}_{11}e^{-k_9x} \\ & + R_{5,12}\tilde{u}_{12}e^{-k_9(L-x)} \,,\end{aligned} \tag{10.3f}$$

$$\begin{aligned}\hat{P}_R = {} & \frac{1}{2}\omega_n k_9 \left[-\left(A_{5511} + A_{1133}R_{5,9}R^*_{5,9}\right)\tilde{u}_9\tilde{u}^*_9 \right. \\ & \left. + \left(A_{5511} + A_{1133}R_{5,10}R^*_{5,9}\right)\tilde{u}_{10}\tilde{u}^*_{10} \right] \,.\end{aligned} \tag{10.3g}$$

From Equation (10.3g), it is clear that the real part of the spectral power is stationary and vanishes when

$$|R_{5,9}\tilde{u}_9| = |R_{5,10}\tilde{u}_{10}| \tag{10.3h}$$

that is when the forward and backward propagating wave components in transverse as well as rotational motions are of the same amplitude, since $R_{5,9} = -R_{5,10}$ and $R_{5,11} = -R_{5,12}$. This can happen when the pair of boundary forces (transverse shear forces and moments) are self-equilibrating in nature or they are of the same amplitude and generate a relative phase between the forward and backward propagating wave coefficients similar to that in Equation (10.3d). In addition, note that in the real part of the spectral power, there is no contribution of the evanescent wave component.

(3) The imaginary part of the spectral power carries the phase information

Here we illustrate the traveling nature of the power wave. Let us consider longitudinal wave propagation (Equation (10.3a)). Using Equation (10.1), the imaginary part of the spectral power is obtained as

$$\hat{P}_I = \tilde{P}_1 e^{-i2k_1x} - \tilde{P}^*_1 e^{i2k_1x} \tag{10.4a}$$

where the power wave coefficients $\tilde{P}_1$ and $-\tilde{P}^*_1$ (* indicates complex conjugation) associated with the forward and backward traveling power wave components are given by

$$\tilde{P}_1 = \frac{1}{2}i\omega_n k_1 A_{1111}\tilde{u}_1\tilde{u}^*_2 e^{ik_1L} \,. \tag{10.4b}$$

Therefore, if there is no change in the geometry and material properties between the two boundary nodes, the traveling wave causes flow of power, which has equal amplitudes in the forward and backward propagating power waves as seen in Equation (10.4a).

10.2.2 Measurement of Wave Scattering due to Delaminations and Inclusions Using Spectral Power

From the earlier discussions, it is quite clear that any structural discontinuity inside a structural member creates scattered waves by changing the wave coefficients by a certain factor called the "scattering coefficient". This, in turn, causes changes in energy transmission and hence, power flow. To study the effect of delaminations and strip inclusions on the scattered waves, we consider two nodal points (1 and 2) along the beam x-axis with associated spectral power $\hat{P}_1$ and $\hat{P}_2$ on the two sides of the delaminations or inclusions. Then we construct a measure of the scattered power as

$$\Delta = \sum_{n=n1}^{n2} \frac{\left|\hat{P}(\omega_n)_h - \hat{P}(\omega_n)_d\right|}{\left|\hat{P}(\omega_n)_h\right|} \tag{10.5}$$

where $\hat{P}(\omega_n)_h$ and $\hat{P}(\omega_n)_d$ are, respectively, the scattered power $\hat{P}_1 - \hat{P}_2$ for the healthy structure and the structure with discontinuities. We denote the power measure in Equation (10.5) over the frequency band $n = [n_1, n_2]$. In the numerical simulations, we estimate the effect of delaminations and inclusions using three frequency bands: low ($\omega_n = 1$ Hz $-$ 1 kHz), medium ($\omega_n = 1$ kHz $-$ 10 kHz) and high ($\omega_n = 10$ kHz $-$ 100 kHz).

10.3 Power Flow Studies on Wave Scattering due to Delaminations and Strip Inclusion in Composite Beam

10.3.1 Wave Scattering due to Single Delamination

A graphite–epoxy unidirectional [0°] composite cantilever beam with single mid-plane delamination is considered as shown in Figure 10.1. The objective here is to estimate the effect of wave scattering from the delamination tip due to different sizes L_d of the mid-plane delamination. A broadband load of duration 50 μs and dominant frequency content upto 40 kHz as shown in Figure 4.5 is applied at the tip of the cantilever. Two measurement nodes 1 and 2 shown in Figure 10.1 are used to compute the scattered power Δ (Equation (10.5) at the low frequency, medium frequency and high frequency bands. For delamination lengths $L_d = 1$ cm and 5 cm, the spectra of scattered power are plotted in Figure 10.2 over a frequency range of 100 kHz. Greater scattering due to the 5 cm long delamination can be seen in this plot. Next, the feasibility of using the scattered power to characterize the severity of the delamination configuration is studied. For this purpose, the delamination length L_d is varied from 1 cm to 10 cm in steps of 0.5 cm. The scattered power in low frequency, medium frequency and high frequency bands is plotted in Figure 10.3. From this plot it is clear that small delaminations did not

influence the energy transmission in low frequency and medium frequency bands. For increasing length of delamination, the order of scattered power increases almost linearly over the medium frequency band. Although the plot shows sudden jumps in the order of scattered power in the medium and high frequency bands, the mean levels have steady increases for increasing size of delamination.

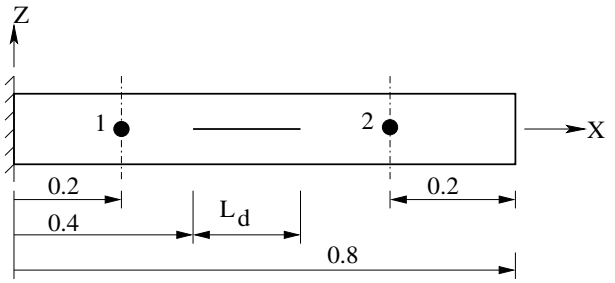

Fig. 10.1. A cantilever beam with single mid-plane delamination of length L_d. Nodal locations 1 and 2 for estimation of spectral power are shown. All dimensions are in metres

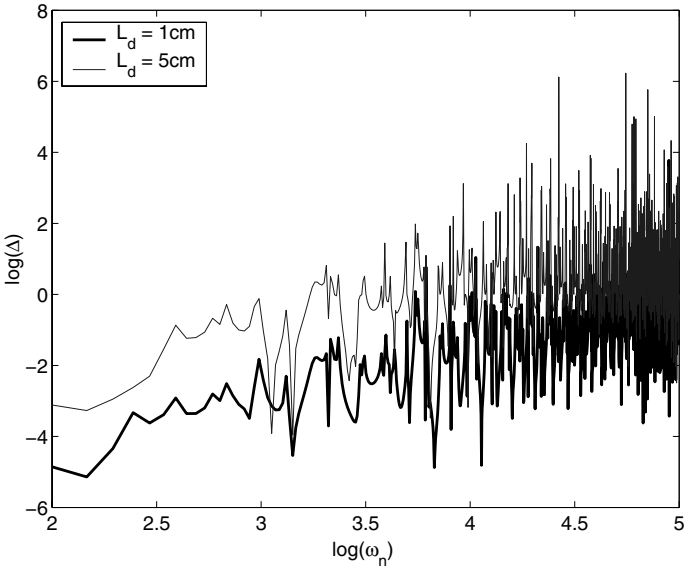

Fig. 10.2. Spectrum of scattered power due to delaminations of length 1 cm and 5 cm

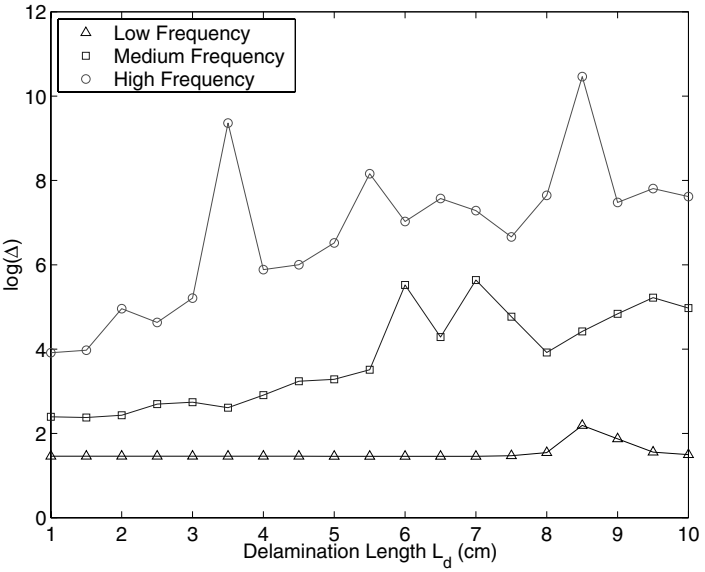

Fig. 10.3. Scattered power in low frequency (1 Hz–1 kHz), medium frequency (1 kHz–10 kHz) and high frequency (10 kHz–100 kHz) bands for varying length of single delamination

10.3.2 Wave Scattering due to Length-wise Multiple Delaminations

Here we consider length-wise multiple delaminations in the same graphite–epoxy cantilever beam as considered earlier. Figure 10.4 shows the beam with three mid-plane delaminations of the same length. The broadband transverse load (Figure 4.5) is applied at the cantilever tip. The location of the measurement nodes 1 and 2 used to compute the scattered power measure Δ are shown in Figure 10.4. In the numerical simulations, we consider three different cases containing one, two and three delaminations from the left side, respectively. Figure 10.5 shows the spectrum of scattered power due to one delamination and three delamination over the high frequency band. Very little difference in the spectra can be seen in the plots. Figure 10.6 shows a comparison of the three cases in low frequency, medium frequency and high frequency bands. It can be seen from this plot that increasing the number of mid-plane delaminations of the size considered in the simulation is less likely to alter the power flow significantly in the low frequency band. Change in the order of scattered power in the medium frequency band linearly increases with increasing number of delaminations, whereas a significant change is seen over the high frequency band.

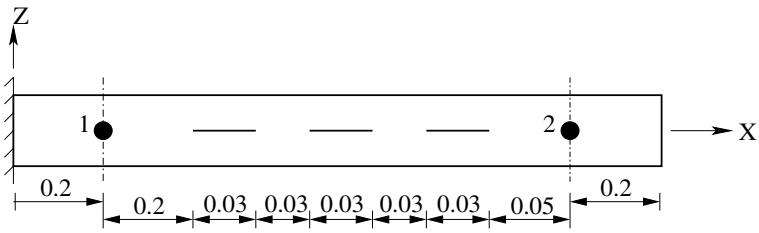

Fig. 10.4. A cantilever beam with length-wise multiple delaminations. Nodal locations 1 and 2 for estimation of spectral power are shown

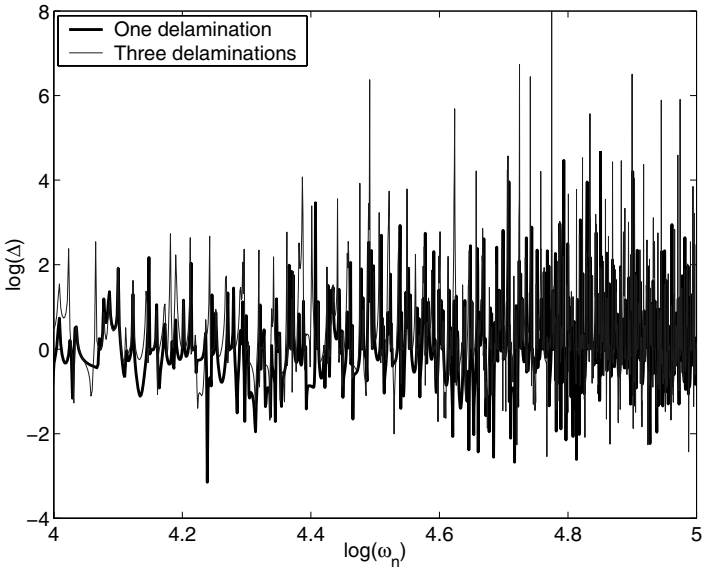

Fig. 10.5. Spectrum of scattered power over the high frequency band due to length-wise increasing number of delaminations

10.3.3 Wave Scattering due to Depth-wise Multiple Delaminations

Impact type loading on laminated composite structures may often cause depth-wise multiple delamination growing from the face opposite to the loading face. That is, at the bottommost interlaminar region. The size of delamination can be expected to be larger due to the higher interlaminar stress gradient. When such damage occurs, it is essential to monitor the load carrying capacity of the damaged structures, possibly using diagnostic wave measurements. Figure 10.7 shows a configuration with three delaminations with progressively increasing size towards the bottom face of the unidirectional graphite–epoxy composite cantilever beam as considered in the earlier studies. In the numerical simulations we consider three cases, one, two and three delaminations from the bottom face, respectively. The location of measurement nodes 1 and 2 for

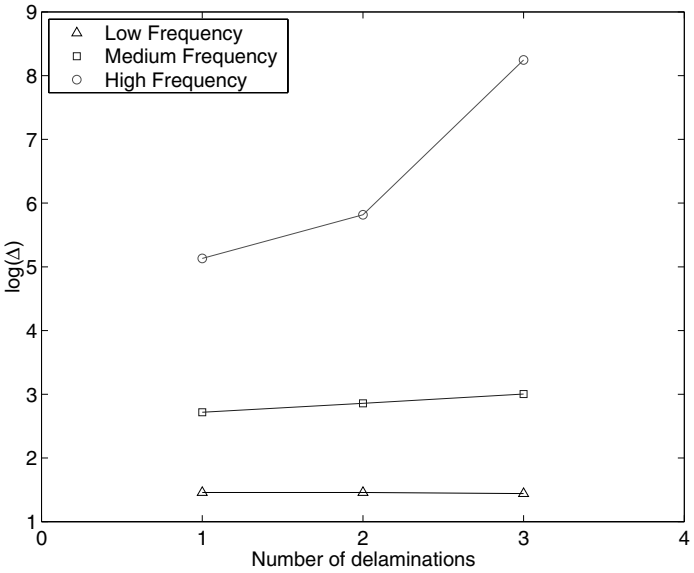

Fig. 10.6. Scattered power at low frequency (1 Hz − 1 kHz), medium frequency (1 kHz − 10 kHz) and high frequency (10 kHz − 100 kHz) bands for length-wise increasing number of delaminations.

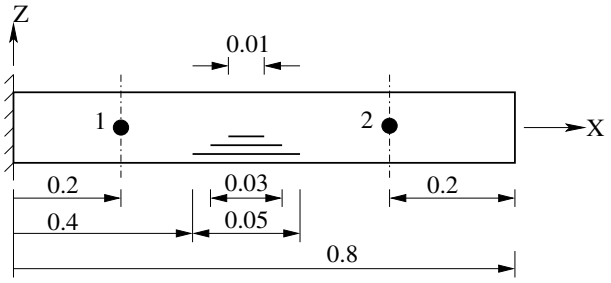

Fig. 10.7. A cantilever beam with depth-wise multiple delaminations. Location of the nodes 1 and 2 for estimation of spectral power is shown. All dimensions are in meters

computation of the scattered power in shown in Figure 10.7. Figure 10.8 shows plots of the scattered power measure in the low frequency, medium frequency and high frequency bands. It can be seen that in the medium frequency band, the configuration with three delaminations creates less scattering than the configuration with two bottommost delaminations, which makes direct correlation difficult. This can be attributed to the shift in the peaks as well as the appearance of several additional peaks (Figure 10.9) due to modification in structural discontinuities, as was observed in the context of variation of delamination length (Figure 10.3). However, the high frequency band pro-

vides good correlation for an increasing number of delaminations, as seen in Figure 10.8.

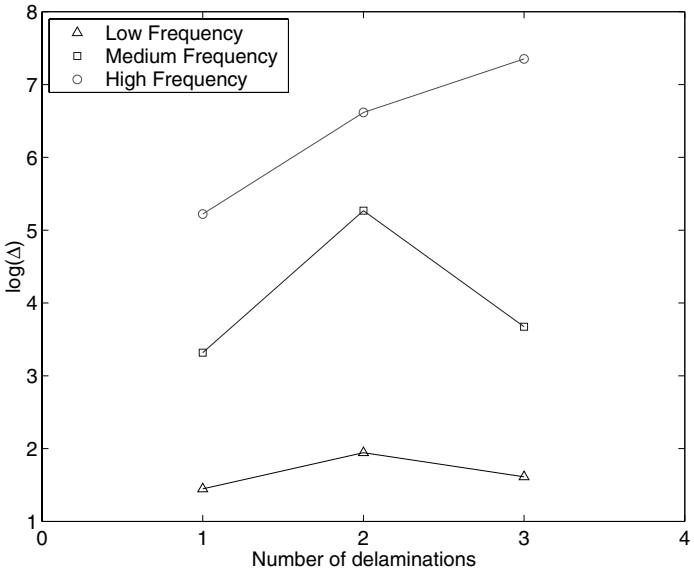

Fig. 10.8. Scattered power at low frequency (1 Hz − 1 kHz), medium frequency (1 kHz − 10 kHz) and high frequency (10 kHz − 100 kHz) bands for depth-wise increasing number of delaminations

10.4 Wave Scattering due to Strip Inclusion

10.4.1 Power Flow in a Semi-infinite Strip Inclusion with Bounded Media: Effect of Change in the Material Properties

In this section, we study the effect of strip inclusion in laminated composite beams. Modeling of such an inclusion and the associated wave scattering effect is simplified using the constrained interfaces at the end of the strip inclusions and hence by considering it as a debonded sublaminate with different material properties and bounded in viscoelastic medium, as discussed in the context of SFEM.

In laminated composite, the healthy interlaminar region and the delaminated surfaces are exposed to friction contact due to the presence of loose fibers and matrix grain boundaries. Similarly, any foreign material system such as electronic chips, MEMS devices, embedded sensors and actuators, *etc.,* also experience dislocation from the host structures through the surrounding

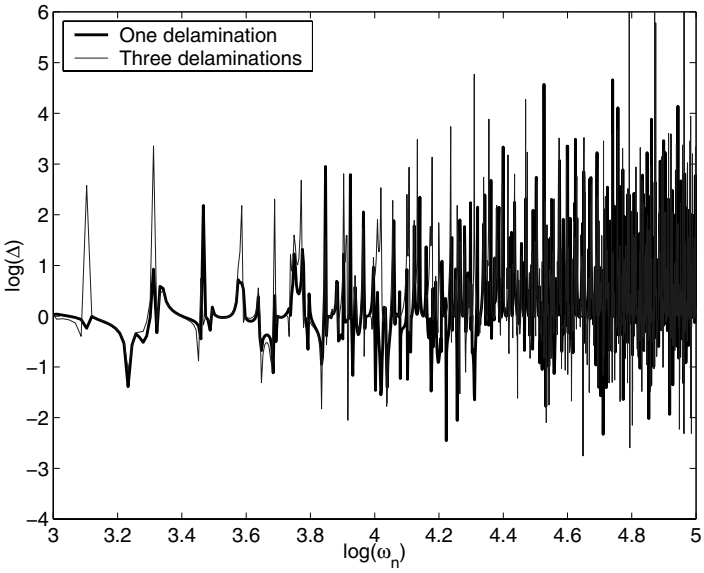

Fig. 10.9. Spectrum of scattered power in the medium frequency and high frequency bands due to depth-wise increasing number of delaminations

interfaces. Although, the model presented in this section accounts for the viscoelastic behavior of such dislocations, only the effects of friction contact (distributed spring stiffness K_x and K_z) are considered in the following simulations. Propagation of longitudinal and flexural waves in the presence of such distributed spring stiffness are studied first. For this purpose, a semi-infinite unidirectional graphite–epoxy sublaminate constrained by distributed spring stiffness K_x and K_z at the top and bottom surfaces is considered as shown in Figure 10.10. The base laminate A (thickness 16 mm), the top and bottom sublaminates B and C (thickness 6 mm each), the strip inclusion D (thickness 4 mm) and the distributed media E (of negligible thickness at the interlaminar region) modeled using spring stiffness (K_x, K_z) are shown in the figure. Reflection and transmission of waves propagating through the base laminate A occur at the vertical interface. The transmitted waves when propagate through the strip inclusion D interact with the distributed spring in longitudinal and transverse motion. To study this behavior, we apply a broadband load (shown in Figure 4.5) longitudinally at the left end of D, which is semi-infinite at the other end.

Figure 10.11 shows the propagation of longitudinal waves as they travel from the interface at the left end to the right end. $K_x = 1 \times 10^7$ N/m and $k_j \rightarrow k_j(1 - i\eta)$, $\eta = 1 \times 10^{-3}$ are used. Note the non-dispersive nature of the longitudinal wave after incidence (the initial peak). At increasing distance from the interface, this effect dies down. For varying spring stiffness K_x, the spectral power $\hat{P}$ (given in Equation (10.1)) at $x = 0.4$ m away from the left

end is plotted in Figure 10.12. It can be seen from the plots that for increasing values of K_x, additional peaks appear in low frequency to high frequency bands. Interestingly, the number of peaks is greater for the imaginary part of the spectral power than the real part of the spectral power. This can be attributed to the fact that all the incident energy is transmitted from the left end to the right end, apart from the small amount of spatial loss due to the presence of the damping factor η in the wavenumber. Hence the power level, which is governed by the real part, remains almost unchanged. The significant change appears in the imaginary part of the spectral power, which carries the phase information.

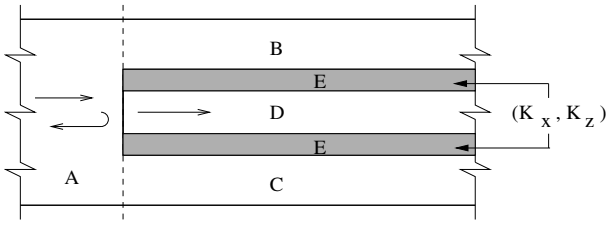

Fig. 10.10. Strip inclusion bounded in distributed spring in a laminated composite semi-infinite beam

Next the same broadband load (Figure 4.5) is applied in the transverse direction at the left end of D. The propagation of flexural waves is shown in Figure 10.13. The incident wave amplitude changes due to the dispersive nature of the flexural and shear modes, which is unaltered by the distributed spring stiffness K_z. However, at a later time, additional waves of smaller amplitude and low phase modulation appear, which are otherwise absent when $K_z = 0$. For different orders of magnitude of K_z, the spectral power at $x = 0.1\,\mathrm{m}$ away from the left end is plotted in Figure 10.14. Unlike the case of longitudinal waves in Figure 10.12, here the power flow is almost unaltered for K_z up to $1 \times 10^7\,\mathrm{N/m}$. It can be observed that for $K_z = 1 \times 10^9\,\mathrm{N/m}$, the real part of the spectral power is decreased for load frequencies above 50 kHz, and additional peaks appear in the imaginary part of the spectral power. Such an effect can be attributed to very high spring stiffness, which actually tends to form a few stop-bands by blocking the energy transmission at low and medium frequencies.

10.4.2 Effect of Change in the Material Properties of a Strip Inclusion

To study the effect of changes in material properties, especially stiffness of the strip inclusion, the same graphite–epoxy unidirectional cantilever beam with a 5 cm long and 4 mm thick strip inclusion is considered as shown in

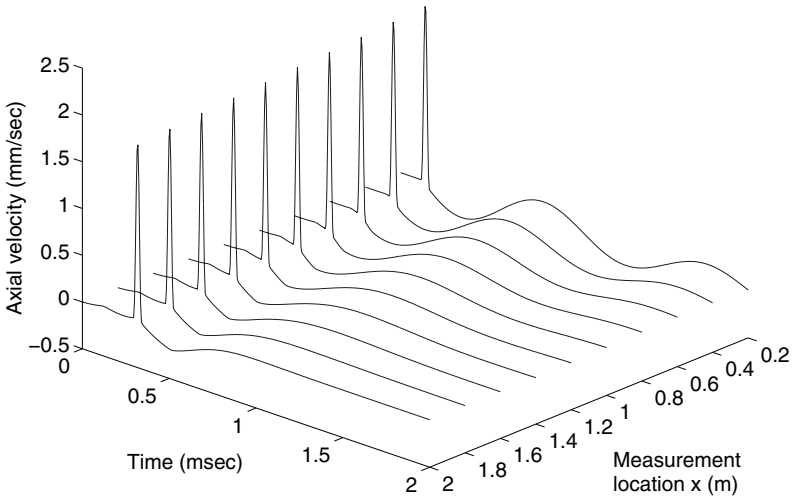

Fig. 10.11. Propagation of longitudinal wave in a graphite–epoxy unidirectional composite semi-infinite beam bounded in distributed uniform spring stiffness $K_x = 1 \times 10^7$ N/m at the top and bottom surfaces

Figure 10.15. Similar analysis can be applied while monitoring the health of the composite beam structures with degraded material properties at sublaminate level. For an assumed change or degradation in the elastic moduli of

$$\bar{\mathbf{C}}' = \alpha \bar{\mathbf{C}} \tag{10.6}$$

where, $\bar{\mathbf{C}}'$ is the modified elasticity matrix for the composite, $\bar{\mathbf{C}}$ is the original elasticity matrix and α is a matrix of degradation factors for simplicity. In such a case, the wavenumbers k_j for the sublaminate waveguides with degraded material properties also change. Hence, the amount of scattering at the interfaces as well as the propagation of individual wave components in individual waveguides also change. In the present numerical simulations, we assume $K_x = 0$ and $K_z = 0$ and α is assumed same (scalar) for all the elastic moduli. Figure 10.16 shows plots of the scattered power measured in the low, medium and high frequency bands for varying α. From the results, direct correlation becomes difficult, especially in the medium and high frequency bands. In the low frequency band, however, significant order change in the scattered power for $\alpha = 0.4$ can be seen for which the scattered power is plotted over the frequency axis in Figure 10.17 in comparison with $\alpha = 0.9$. The spectrum shows significant change in the peaks at low frequency, which produced a high level of scattering for $\alpha = 0.4$. Similar inference can also be drawn from the appearance of peaks in the medium and high frequency bands for $\alpha = 0.5$.

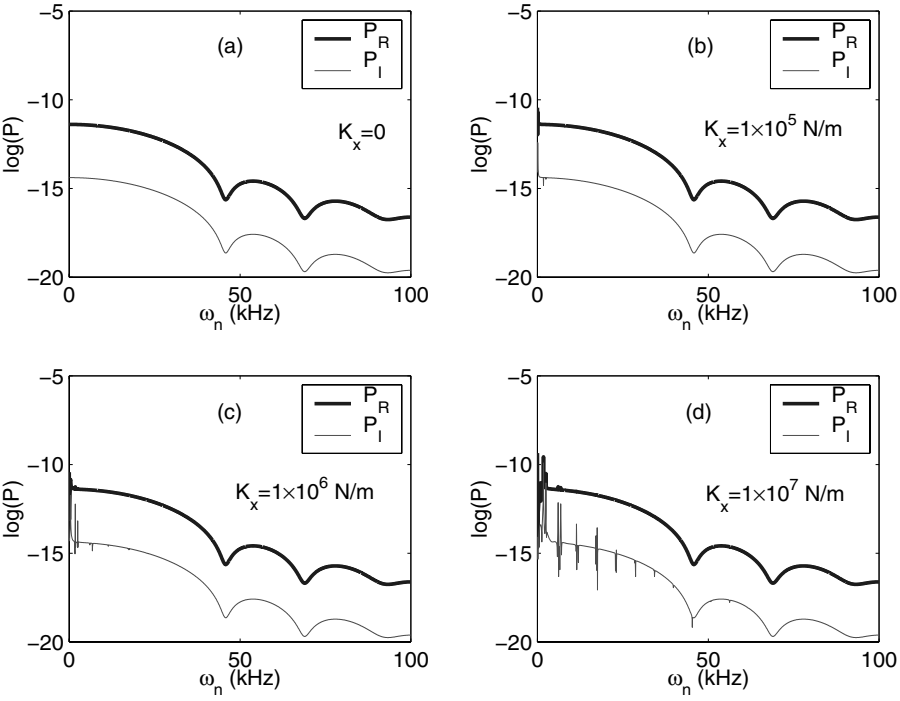

Fig. 10.12. Change in spectral power due to variation in distributed spring stiffness K_x in propagation of longitudinal wave in graphite–epoxy unidirectional composite semi-infinite beam bounded in distributed uniform spring stiffness. Measurement location is $x = 0.4$ m

The presence of wave scattered from the fixed and free ends of the cantilever also interact with the scattered waves from the interface alone and amplify the amplitude of the waves trapped between the two interfaces, the fixed and free ends of the cantilever. These higher wave amplitudes contribute to the higher level of scattered power compared to any single or multiple delaminations (in Figures 10.3, 10.6 and 10.8) as can be seen in Figure 10.16.

10.5 Damage Force Indicator for SFEM

The concept of damage force has been used in [165] to derive a damage indicator for detecting the elements having flaws. The dynamic stiffness matrix of the reference healthy structure along with the nodal displacements of the damaged structure are required to find which elements contain damage. This technique bounds the damage location within the region of the sensing points. Keeping the objective of on-line health monitoring in mind, a similar strategy is implemented here. But the basic difference is that the finite element sys-

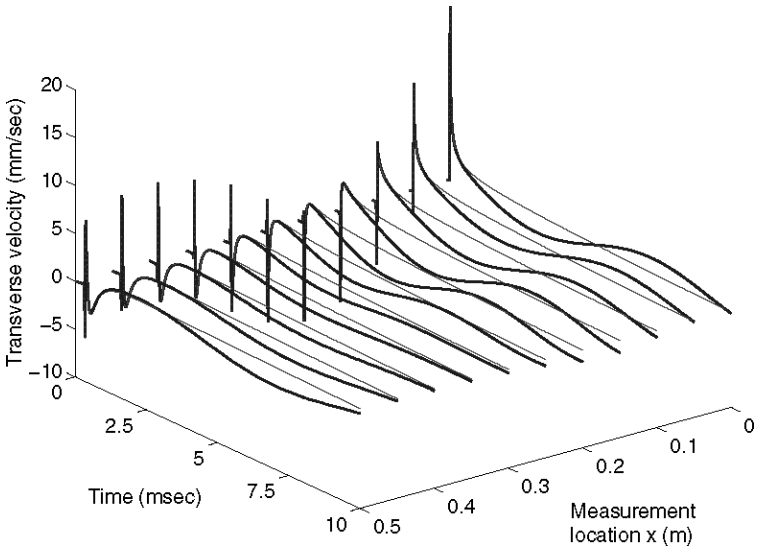

Fig. 10.13. Propagation of flexural wave in a graphite–epoxy unidirectional composite semi-infinite beam bounded in distributed uniform spring stiffness $K_z = 1 \times 10^5$ N/m (shown with thick solid lines) at the top and bottom surfaces. The solid lines show the responses for $K_z = 0$

tem is constructed entirely in the frequency domain under the framework of SFEM. And one advantage is that a much lower number of sensors are sufficient, since the number of measurements complying with SFEM dof is many orders smaller than that required when using conventional FEM. The only limiting factor when using fewer sensors is that the measured signal must be reliable enough to differentiate the effect of wave scattering in the presence of slight damage along with the effect of damping. For polymer composite, this is an important issue because a sensor placed too far from the damage location may not be able to capture the measurable fluctuations when damage is present.

The global dynamic stiffness matrix of the healthy structure $\hat{\mathbf{K}}_h(\omega_n)$ at each FFT sampling frequency ω_n is obtained using a standard finite element assembly for all spectral elements. The spectral amplitude of global displacement vector $\hat{\mathbf{u}}$ consists of axial displacement $\hat{u}^o$, transverse displacement $\hat{w}$ and rotation $\hat{\phi}$ at each node. Now, the damage force vector is defined as

$$\Delta\hat{\mathbf{f}} = \hat{\mathbf{K}}_h \hat{\mathbf{u}}_d - \hat{\mathbf{f}}_d \tag{10.7}$$

where the subscript h denotes healthy structure and d denotes for delaminated structure. If delamination occurs, the vector $\Delta\hat{\mathbf{f}}$ will have non-zero entries only at the dofs connected to the elements with damage. The above expression requires the excitation force ($\hat{\mathbf{f}}_d$) or the internal forces at the nodes

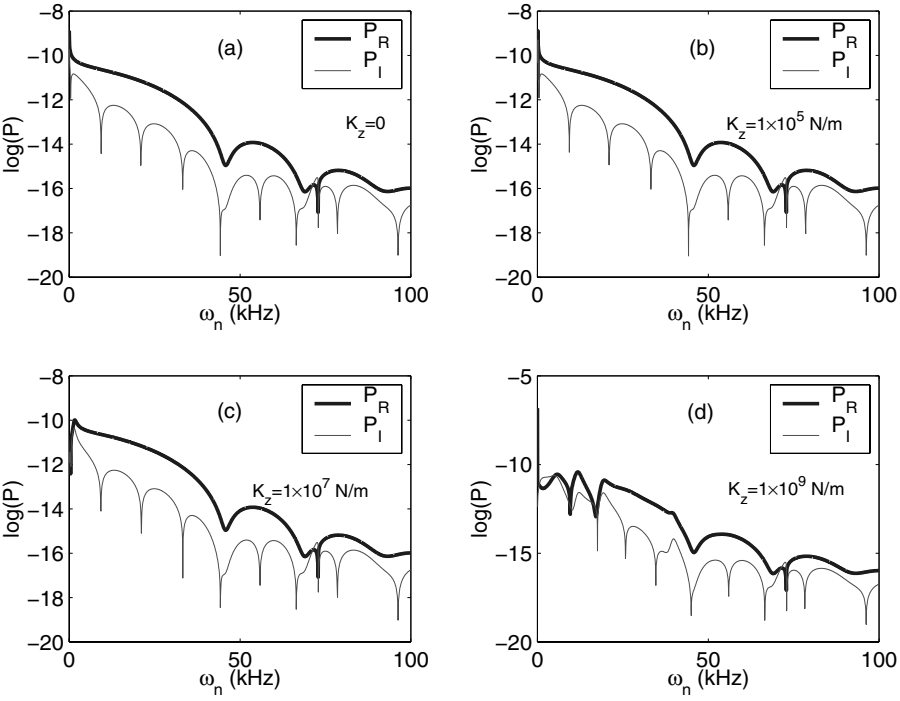

Fig. 10.14. Change in spectral power due to variation in distributed spring stiffness K_z in propagation of flexural wave in graphite–epoxy unidirectional composite semi-infinite beam bounded in distributed uniform spring stiffness. Measurement location is $x = 0.1$ m

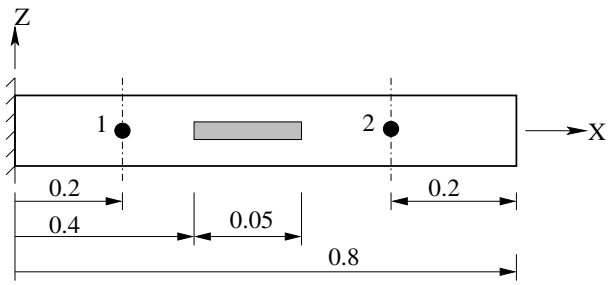

Fig. 10.15. A graphite–epoxy cantilever beam with a strip inclusion. Location of the nodes 1 and 2 for estimation of spectral power is shown. All dimensions are in metres

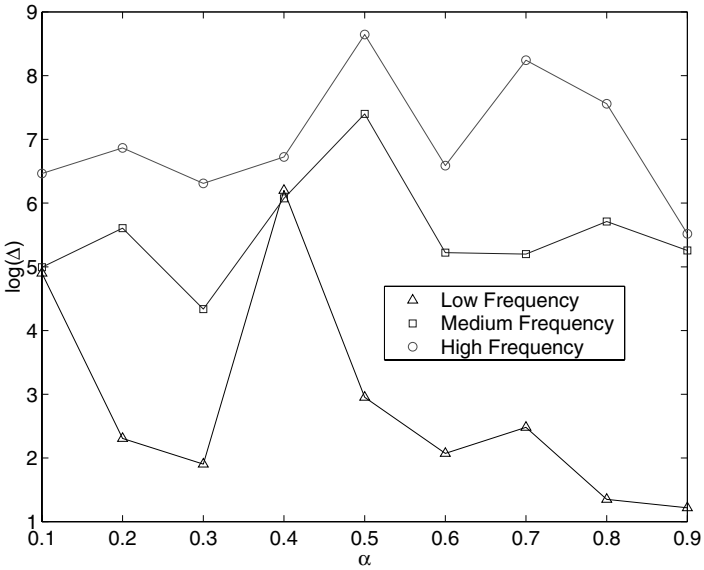

Fig. 10.16. Scattered power at low frequency (1 Hz − 1 kHz), medium frequency (1 kHz − 10 kHz) and high frequency (10 kHz − 100 kHz) bands for different material stiffness of a strip inclusion

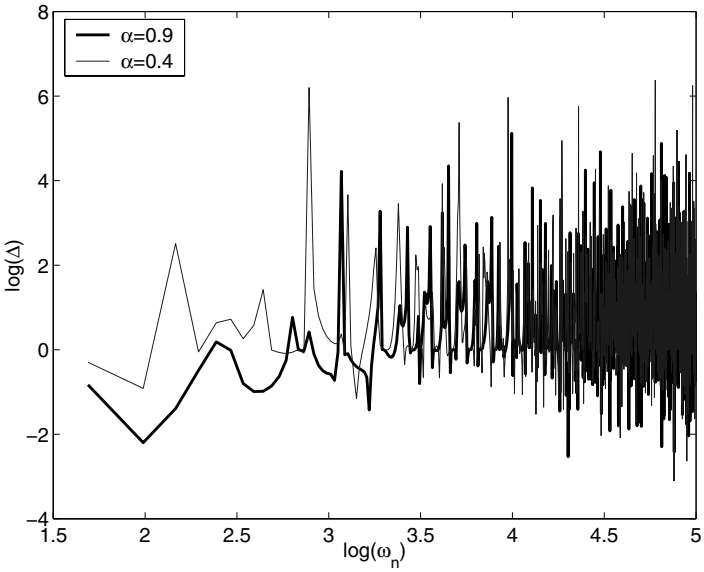

Fig. 10.17. Spectrum of scattered power due to 10% ($\alpha = 0.9$) and 60% ($\alpha = 0.4$) degradation in the material stiffness

to be known. Direct measurement of this requires force sensors and may not always be feasible [165]. The damage indicator proposed by Schulz [165] overcomes this limitation by computing the damage force directly as $\hat{\mathbf{K}}_h \hat{\mathbf{u}}_d$. In this section, the same expression is used assuming the vector $\hat{\mathbf{f}}_d$ is unknown in the simulation. However, in SFEM, the inverse problem can be solved to obtain $\hat{\mathbf{f}}_d$ from other types of signal measurement such as displacements, strains or their rates. For delamination identification, we already have the spectral element for delamination that can be inserted in the healthy structure by comparing some indicator from experimentally obtained and post-processed signals. For this purpose, a combined force vector $\hat{\mathbf{r}}(\omega_n)$ is considered

$$\hat{\mathbf{r}}(\omega_n) = \Delta\hat{\mathbf{f}} + \hat{\mathbf{f}}_d = \hat{\mathbf{K}}_h \hat{\mathbf{u}}_d \,. \tag{10.8}$$

Multiplying $\hat{\mathbf{r}}$ by transpose of its complex conjugate $\hat{\mathbf{r}}^*$, we get one $(m \times m)$ square matrix $\hat{\mathbf{R}}(\omega_n)$:

$$\hat{\mathbf{R}}(\omega_n) = \hat{\mathbf{r}}\hat{\mathbf{r}}^* \tag{10.9}$$

where m is the total number of dofs in the model. Now, if the delamination is expected in the ith element, the existing element can be replaced by the spectral element for delamination. There will be non-zero diagonal entries in $\hat{\mathbf{R}}(\omega_n)$ corresponding to the dofs associated with the ith element. The rest of the diagonal entries will be zero. The magnitude of these non-zero diagonal entries will depend on the applied load, and the configuration of delamination. Summing up the absolute values of the diagonal entries in $\hat{\mathbf{R}}(\omega_n)$ over all frequency steps $n = 1, \cdots, N$ (N = Nyquist frequency in FFT), a damage force indicator vector $\mathbf{d}$ of length m is obtained as

$$d_i = \sum_{\omega_n} |\hat{R}_{ii}| \,, \quad i \in [1,\, m] \,, \quad n = 1, \ldots, N \,. \tag{10.10}$$

10.6 Numerical Simulation of Global Identification Process in Delaminated Composite Beams Using the Damage Force Indicator

This section deals with numerical simulations showing the efficient use of the spectral element for a delaminated beam in the identification process. Also, the effect of delamination configuration on the damage indicator is investigated. During real-life health monitoring, similar results may be expected if accurate measurements and signal conditioning can be performed.

10.6.1 Effect of Single Delamination

One infinite graphite–epoxy beam of 10 mm × 10 mm cross-section is considered as shown in Figure 10.18. Eight SFEs of equal length (100 mm) are assumed between two throw-off elements at the ends. $\hat{\mathbf{K}}_h$ is stored for each FFT

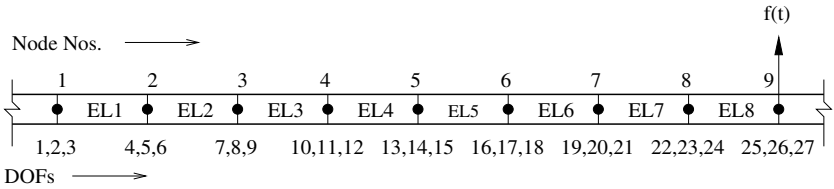

Fig. 10.18. An infinite beam considered to study the identification of delaminations using a damage force indicator

sampling frequency. A broadband load (Figure 4.5) is applied in transverse direction (dof-26) on the right node of the 8th element. Each time one mid-plane delamination of length 20 mm is introduced (Figure 10.19(a)) in one of these elements and $\hat{\mathbf{u}}_d$ is computed. The damage force indicator $\mathbf{d}$ is computed for each of these delamination configurations using Equations (10.7)–(10.10) and plotted in Figure 10.20. Peaks at the dofs associated with the delaminated elements can be seen in the bar-plots. All the entries in $\mathbf{d}$ are normalized with respect to Max($\mathbf{d}$), separately for transverse and rotational dofs. It is also found that $\mathbf{d}$ is in decreasing order from the point of application of load. This is because of attenuation and gradual dissipation of energy in a slightly damped system. Some small non-zero amplitudes of $\mathbf{d}$ can be noticed at the dof of the applied load ($i = 26$) for all cases. This appears because the applied load was not eliminated from the dof while computing $\mathbf{d}$, presuming it to be an unknown in a practical problem (see Equation (10.8)).

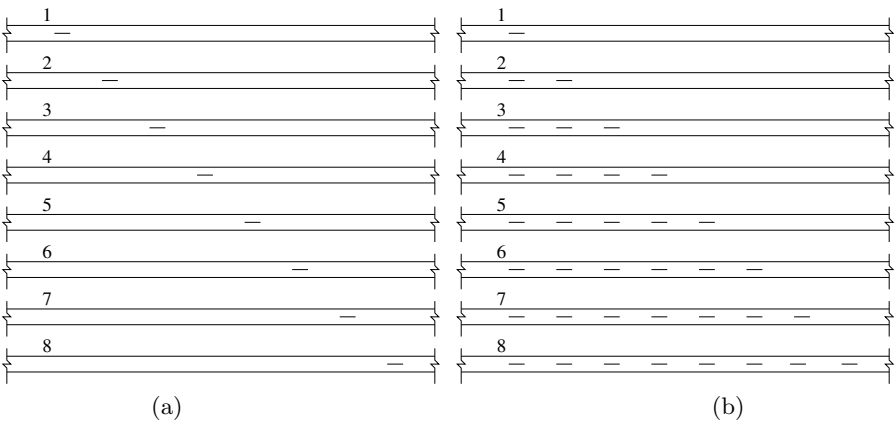

Fig. 10.19. Different configurations considered for the infinite beam with delamination; (a) with single delamination and (b) with multiple delaminations

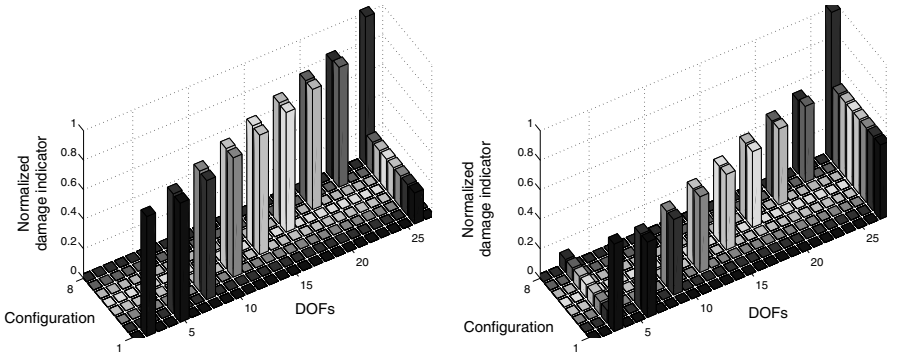

Fig. 10.20. Normalized damage force indicator **d** for (a) transverse and (b) rotational dofs for different configurations (varying location of a single delamination shown in Figure 10.19(a)) modeled using single spectral element for delamination

10.6.2 Effect of Multiple Delaminations

For the same infinite beam and applied load as considered in the last example (Figure 10.18), multiple delaminations are introduced progressively, *i.e.,* first in element 1, then simultaneously in element 1 and element 2 and so on (see Figure 10.19(b)). For these varying configuration, normalized **d** is plotted in Figure 10.21. Normalization is done with respect to the maximum of **d**

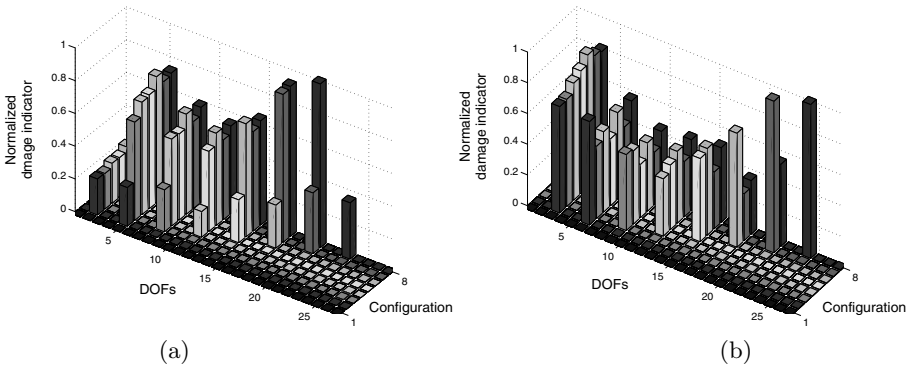

Fig. 10.21. Normalized damage force indicator **d** for (a) transverse and (b) rotational dofs for different configurations (varying number of delaminations shown in Figure 10.19(b)) modeled using one spectral element for each delamination

among all the delaminated configurations. But, due to this normalization, no peaks for the first configuration are visible. The peaks are also not in any ordered magnitude as in the previous study. This can be attributed to the

interference between the reflected waves generated by different delamination tips. Computation time to obtain **d** is plotted in Figure 10.22. This shows cubic polynomial time complexity [226] of computation for increasing numbers of delaminations. Therefore with this same identification strategy and further development of spectral elements for plates and shells, a real-scale structural health monitoring task appears tractable.

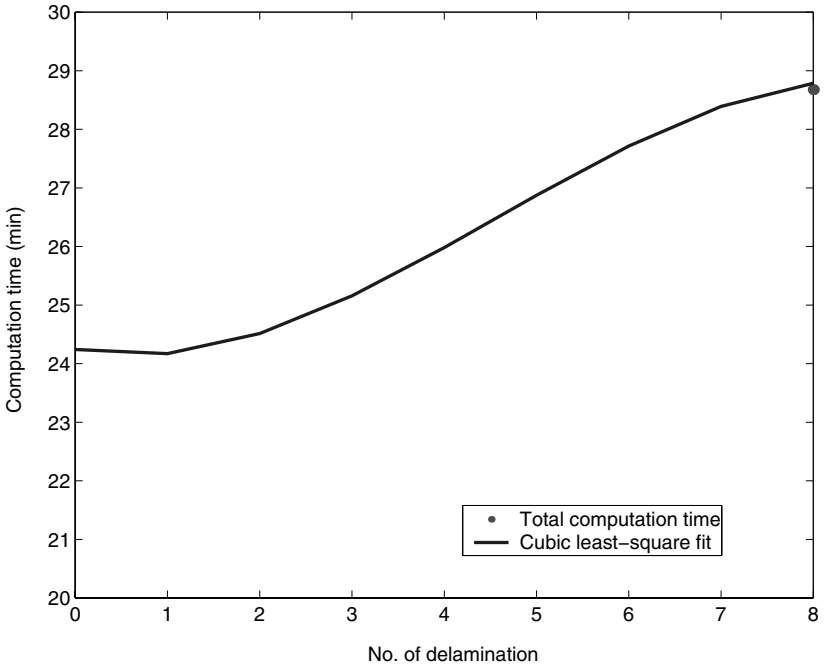

Fig. 10.22. Computation time for damage force indicator in the case of an increasing number of delaminations (shown in Figure 10.19(b))

10.6.3 Sensitivity of Damage Force Indicator due to Variation in Delamination Size

The aim of the following studies is to determine whether the damage force indicator can also quantify the intensity of the delamination. For this purpose, a 2 m long spectral element for delamination with throw-off elements connected to both ends is considered (Figure 10.23). The width of the beam is kept fixed at 10 mm, while the beam thickness is varied from 10 mm to 20 mm in uniform steps of 2 mm. For each different beam thickness, the length of mid-plane delamination is varied from 10 mm to 100 mm in uniform steps of 5 mm in both directions equally about the center. Component of **d** for the

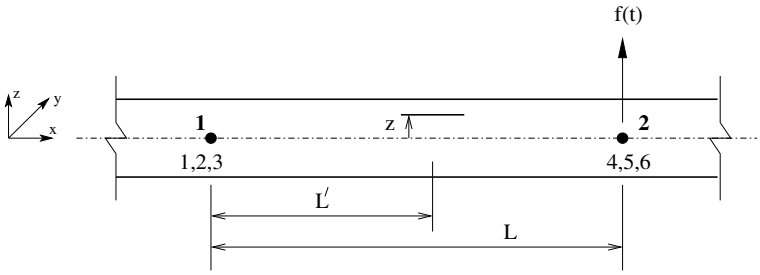

Fig. 10.23. Infinite beam with single delamination for sensitivity analysis of delamination parameters on damage force indicator. The node numbers (in bold letters) and the dofs are shown

transverse and rotational dofs at node 2 (*i.e.,* d_5 and d_6) are computed for all of these configurations and are plotted in Figures 10.24 and 10.25. Exponential increments in $\mathbf{d}$ with the delamination length are observed for the transverse case. This shows that with increasing delamination length, change in the dynamic response increases exponentially. However, the variation with beam thickness for a fixed size of delamination is not monotonous. For the rotational dofs, these fluctuations are more pronounced. The transverse damage force indicator is a minimum for a delamination length of 10 mm when the beam thickness is 20 mm; and maximum when they are 100 mm and 16 mm, respectively. Next, the real part of the dynamic stiffness component $\hat{\hat{K}}^{\mathrm{e}}_{22}$ (transverse motion at left node 1) for the delamination configuration corresponding to the minimum and maximum of $\mathbf{d}$ are plotted over the frequency axis in Figures 10.26 and 10.27. Similar plots of $\hat{K}_{33}$ (rotational motion at left node 1) are shown in Figures 10.28 and 10.29. The plots clearly show considerable deviation in the stiffness component between delaminated and healthy configurations when the damage force indicator reaches its maximum value. Changes in the locations of poles and zeros in the frequency spectrum are the effect of structural discontinuity at the delamination tips. It can be observed in Figures 10.26, 10.27, 10.28 and 10.29 that delaminations of length 10 mm are less likely to alter the dynamic stiffness in the low frequency range and therefore low frequency modal methods may fail to capture the effect of damage, unless broadband estimation is carried out.

10.6.4 Sensitivity of Damage Force Indicator due to Variation in Delamination Depth

For the same element length and different beam thicknesses considered in the previous study, the location of the delamination along thickness was varied from $z = -3\,\mathrm{mm}$ to $z = +3\,\mathrm{mm}$. Delamination length was kept fixed at 20 mm. Damage force indicators in transverse and rotational dofs are plotted respectively in Figures 10.30 and 10.31.

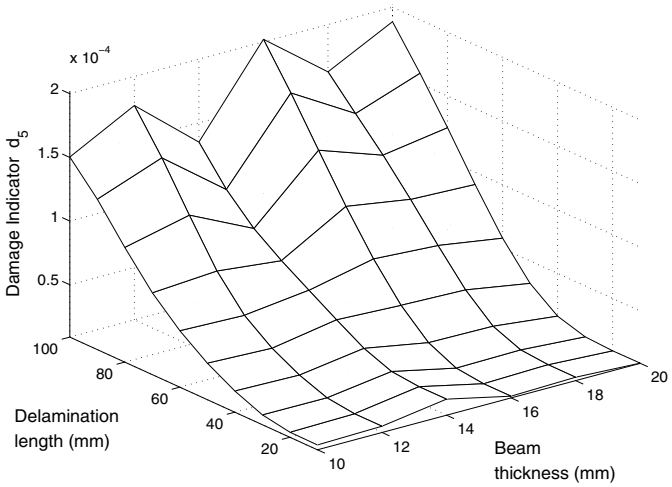

Fig. 10.24. Damage force indicator for transverse dofs at node 2 (Figure 10.23) for different lengths of single delamination ($z = 0$) and various beam thicknesses. Delamination length is varied from its center, left and right simultaneously by equal amounts

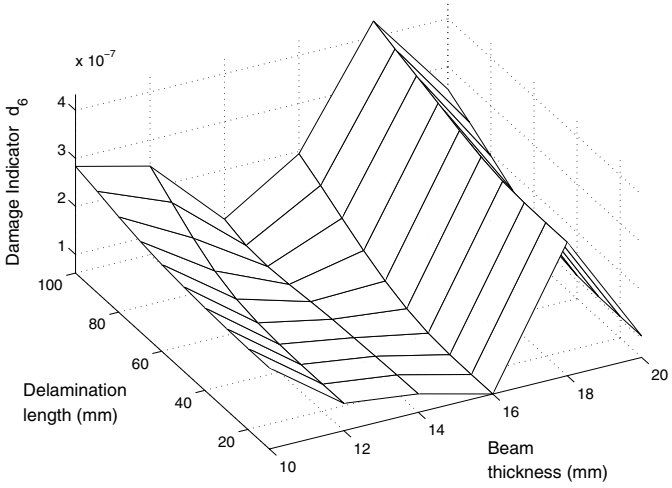

Fig. 10.25. Damage force indicator for rotational dofs at node 2 (Figure 10.23) for different lengths of single delamination ($z = 0$) and various beam thicknesses. Delamination length is varied from its center, left and right simultaneously by equal amounts

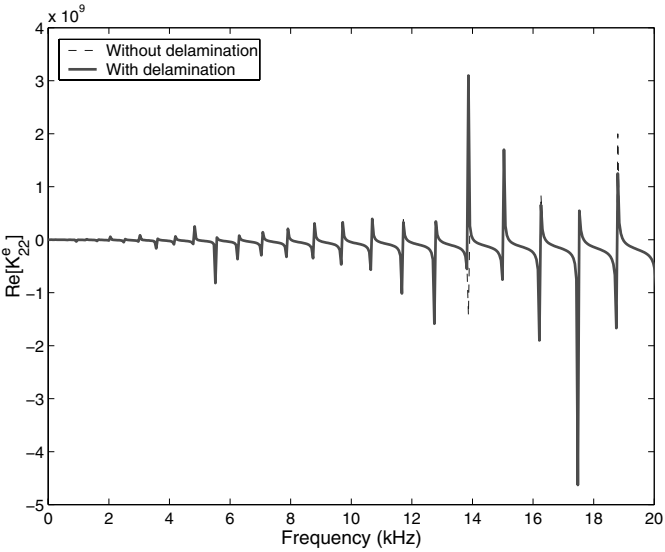

Fig. 10.26. Real part of dynamic stiffness component $\hat{\hat{K}}^{\mathrm{e}}_{22}$ for minimum ($z = 0$, delamination length = 10 mm, beam thickness = 16 mm) damage force indicator in transverse dof (Figure 10.24)

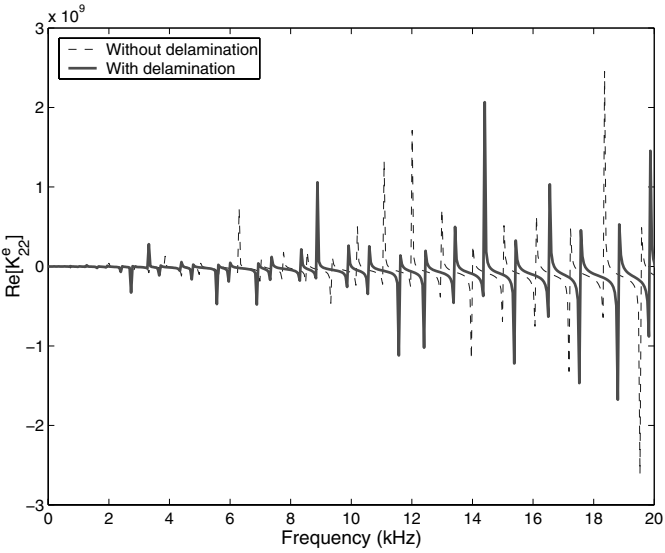

Fig. 10.27. Real part of dynamic stiffness component $\hat{\hat{K}}^{\mathrm{e}}_{22}$ for maximum ($z = 0$, delamination length = 100 mm, beam thickness = 16 mm) damage force indicator in transverse dof (Figure 10.24)

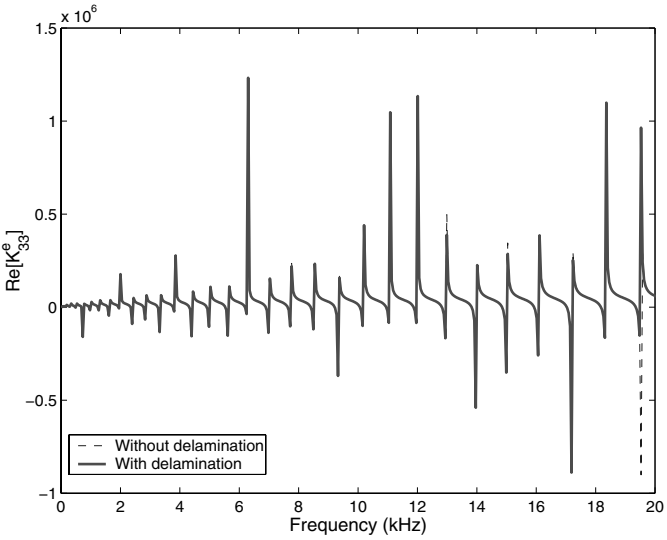

Fig. 10.28. Real part of dynamic stiffness component $\hat{\hat{K}}^{\mathrm{e}}_{33}$ for minimum ($z = 0$, delamination length = 10 mm, beam thickness = 18 mm) damage force indicator in rotational dof (Figure 10.25)

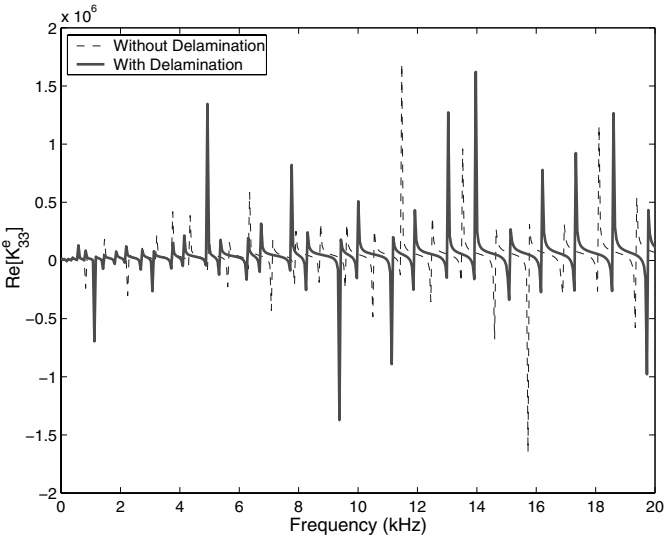

Fig. 10.29. Real part of dynamic stiffness component $\hat{\hat{K}}^{\mathrm{e}}_{33}$ for maximum ($z = 0$, delamination length = 100 mm, beam thickness = 18 mm) damage force indicator in rotational dof (Figure 10.25)

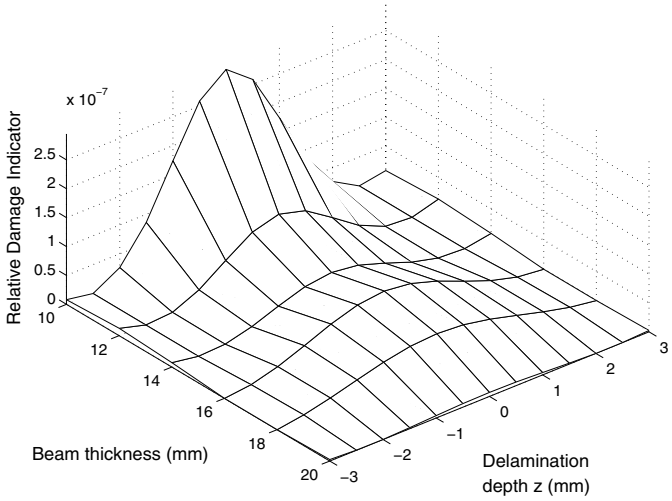

Fig. 10.30. Relative damage force indicator for transverse dofs at node 2 (Figure 10.23) for different depth (z) of single delamination of length 20 mm for various beam thicknesses

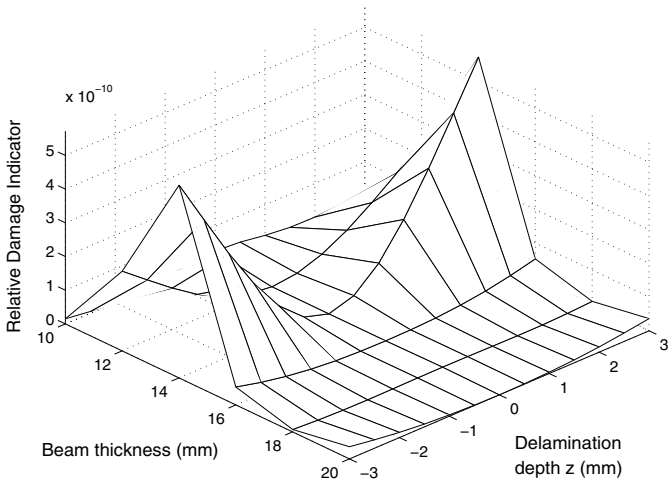

Fig. 10.31. Relative damage force indicator for rotational dofs at node 2 (Figure 10.23) for different depth (z) of single delamination of length 20 mm for various beam thicknesses

Due to significant scale variation in the damage force indicator with change in beam thickness, the magnitudes are plotted relative to Min($\mathbf{d}$) (separately for transverse and rotational dofs) for corresponding beam thicknesses. With variation in the delamination depth, a non-linear relationship symmetric about the mid-plane ($z = 0$) is observed in Figures 10.30 and 10.31. In the case of the transverse dof (Figure 10.30), the depth for which the minima occurs (zero value in the plot for some beam thicknesses), is different for different beam thickness. However, they are always maximum for a mid-plane delamination. In the case of the rotational dof (Figure 10.31), the maxima does not always occur for a mid-plane delamination. From these plots, it can be concluded that for thin beams, the effect of mid-plane delamination can be captured with maximum reliability. Whereas, for asymmetrically delaminated beams, predictions are much easier for moderate thicknesses. However, the dynamic stiffness components $\hat{\hat{K}}^{\mathrm{e}}_{22}$ plotted in Figures 10.32 and 10.33 corresponding to the minimum and maximum of $\mathbf{d}$ and $\hat{\hat{K}}^{\mathrm{e}}_{33}$ in Figures 10.34 and 10.34 show minor differences from the undelaminated beam. This shows that strategies based on modal analysis may not be very effective for predicting the depth-wise location of delaminations.

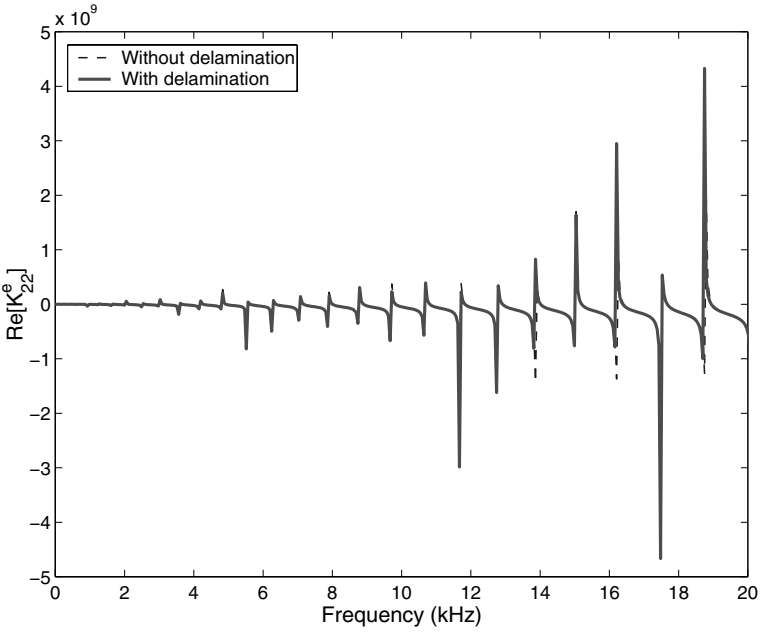

Fig. 10.32. Real part of dynamic stiffness component $\hat{\hat{K}}^{\mathrm{e}}_{22}$ for minimum damage force indicator in transverse dof (Figure 10.30). Magnitudes are plotted relative to Min($\mathbf{d}$) for corresponding beam thicknesses

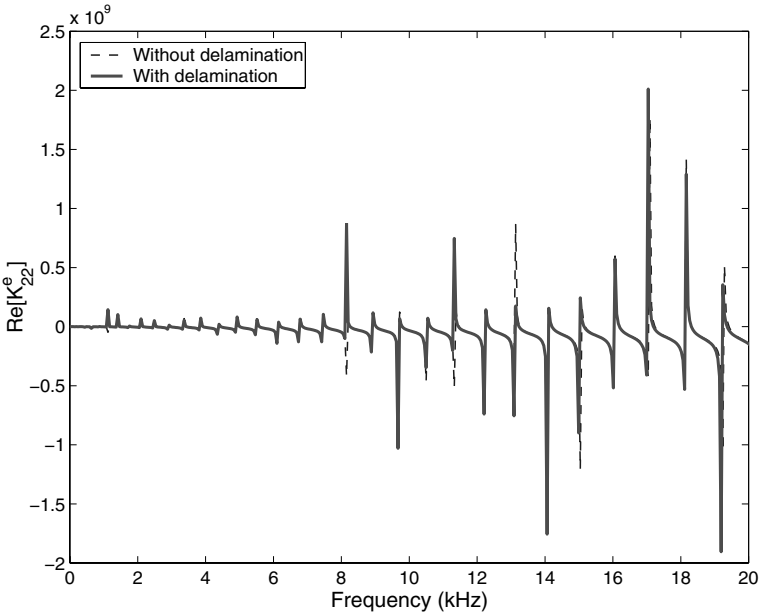

Fig. 10.33. Real part of dynamic stiffness component $\hat{\hat{K}}^{\mathrm{e}}_{22}$ for maximum damage force indicator in transverse dof (Figure 10.30). Magnitudes are plotted relative to Min(**d**) for corresponding beam thicknesses

10.7 Genetic Algorithm (GA) for Delamination Identification

In an identification strategy, one may possibly locate the delaminations and their sizes by extremizing certain norms constructed from experimentally obtained data and model data for delaminations of unknown location and size. Standard terminologies and the basic framework of GA can be found in [212] and are not discussed in this section. Coello and Christiansen [218] discussed various strategies in genetic operations proposed by various researchers in the context of multi-objective GA. An overview of GA derived in the present study is schematically presented in Figure 10.36.

Two major features here are (1) selection from an enlarged sampling space, consisting of parent and offspring pools, and (2) prohibition of duplicate chromosomes in the early generations using constraints and instructions for punishment and killing of abnormal offspring. At this stage, it is necessary to correlate some of the standard terminologies used in GA as follows.

- **Chromosome** – The damage configuration in coded form
- **Genes** – The individual parameters or variables representing the damage configuration

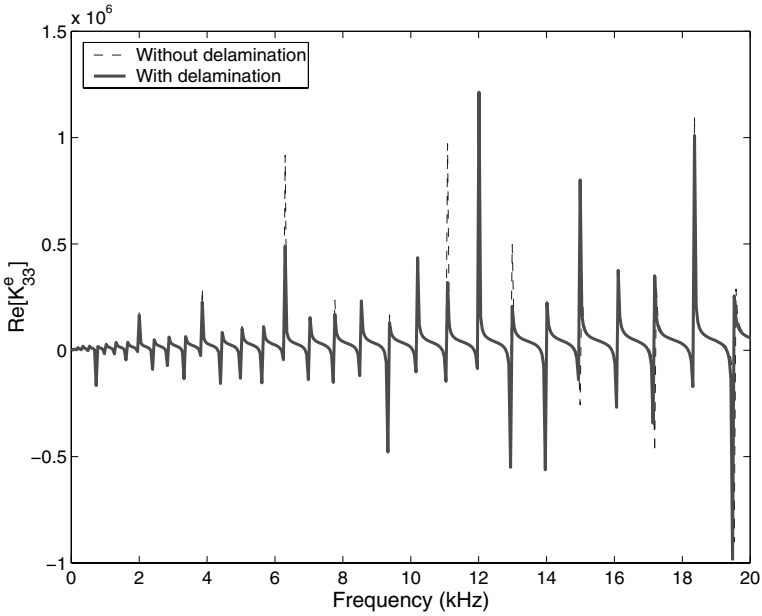

Fig. 10.34. Real part of dynamic stiffness component $\hat{\bar{K}}_{33}$ for minimum damage force indicator in rotational dof (Figure 10.31). Magnitudes are plotted relative to Min(**d**) for corresponding beam thicknesses

- **Phenotype** – Decoded solution or the possible damaged configuration of the structure
- **Genotype** – Encoded solution or the set of values of the variables in binary string in our problem, that represents the damaged structure when decoded

10.7.1 Objective Functions in GA for Delamination Identification

Performance of a GA largely depends upon the objective function. With a smooth function or a function with few local extrema, GAs converge more rapidly than a function with a large number of ups and downs. In this section, we first examine the behavior of different possible objective functions. Two physical parameters, namely the displacement and the frequency domain power (spectral power), are tested on a cantilever beam and a fixed beam with a single delamination.

10.7.2 Displacement-based Objective Functions

Four possible displacement-based objective functions are examined. These functions J_1, J_2, J_3 and J_4 can be derived from the baseline or experimental response (generated with known configuration in the absence of actual

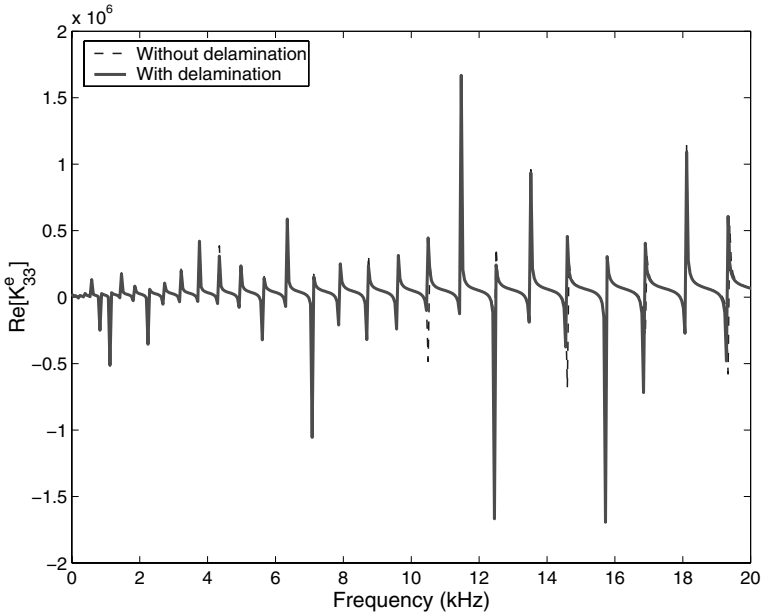

Fig. 10.35. Real part of dynamic stiffness component $\hat{\bar{K}}_{33}$ for maximum damage force indicator in rotational dof (Figure 10.31). Magnitudes are plotted relative to Min(**d**) for corresponding beam thicknesses

experimental data) with the simulated response and are expressed as

$$J_1 = \left[1 + \frac{1}{N}\sum_n \frac{\left|\hat{u}^o_{\text{comp}} - \hat{u}^o_{\text{expt}}\right|}{\left|\hat{u}^o_{\text{expt}}\right|}\right]^{-1}, \tag{10.11}$$

$$J_2 = \left[1 + \frac{1}{N}\sum_n \frac{\left|\hat{w}_{\text{comp}} - \hat{w}_{\text{expt}}\right|}{\left|\hat{w}_{\text{expt}}\right|}\right]^{-1}, \tag{10.12}$$

$$J_3 = \left[1 + \frac{1}{N}\sum_n \frac{\left|\hat{\phi}_{\text{comp}} - \hat{\phi}_{\text{expt}}\right|}{\left|\hat{\phi}_{\text{expt}}\right|}\right]^{-1}, \tag{10.13}$$

$$J_4 = \left[1 + \frac{1}{3N}\sum_n \left\{\frac{\left|\hat{u}^o_{\text{comp}} - \hat{u}^o_{\text{expt}}\right|}{\left|\hat{u}^o_{\text{expt}}\right|} + \frac{\left|\hat{w}_{\text{comp}} - \hat{w}_{\text{expt}}\right|}{\left|\hat{w}_{\text{expt}}\right|} + \frac{\left|\hat{\phi}_{\text{comp}} - \hat{\phi}_{\text{expt}}\right|}{\left|\hat{\phi}_{\text{expt}}\right|}\right\}\right]^{-1} \tag{10.14}$$

The above computations require spectral amplitudes at a spectral element node at each FFT sampling frequency (ω_n). The subscript "comp" in the above equations indicates the simulated data from SFEM. The subscript "expt" denotes baseline data. For identification using multi-node responses,

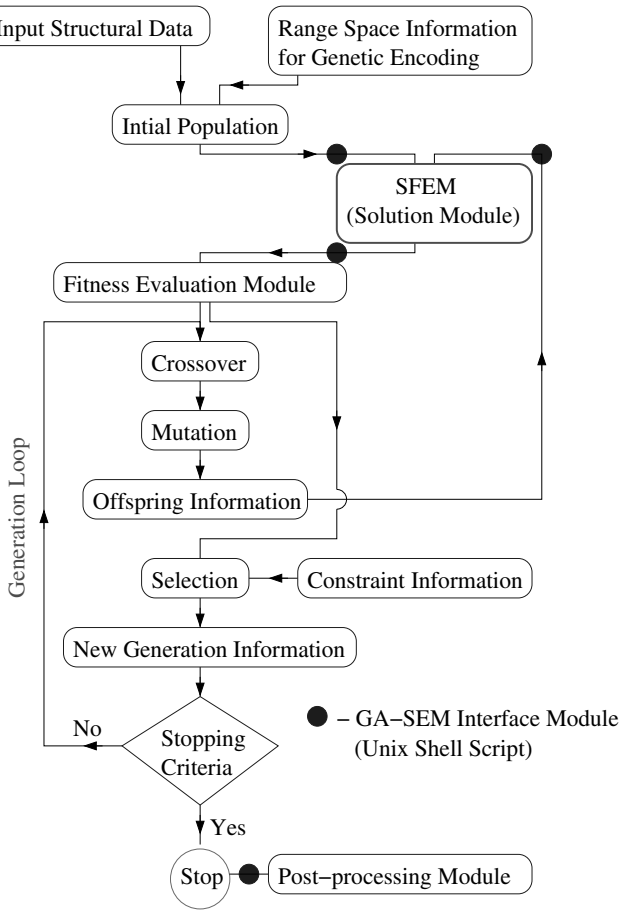

Fig. 10.36. Flowchart of genetic search

the function construction is a straightforward representation in vector form. All of these are maximizing functions and they achieve the maximum value (equal to 1) when the simulated results (hence the damage configuration) match with the experimental (filtered) data. Through genetic evolution over generations, more phenotypes (each having a particular delaminated configuration) can be expected to have maximized values of the objective function, and this convergence is estimated by the average fitness (average values of the objective function) of the population.

The configuration of the delamination in the cantilever beam and the fixed beam are shown respectively in Figures 10.37 and 10.38. A unidirectional graphite–epoxy 0^o ply-stacking sequence is used in all the case studies. The sensitivity of J with respect to each of the three delamination parameters (tip location L, delamination length and layer depth) on these functions are

studied separately, keeping the other two parameters fixed. In the study of delamination location, the reference data is generated by introducing a 20 mm mid-plane delamination at location $L = 250$ mm. Broadband transverse load (Gaussian history) is applied at node 2. The delamination location is varied from $L = 0$ to 500 mm and the corresponding objective functions are computed. For the cantilever beam, the functions are plotted in Figure 10.39 and for the fixed beam in Figure 10.40. None of these functions is smooth; all of them have many local discontinuities (poles and zeros in the spectrum). This non-smooth behavior is inherent to any elastodynamic problem. The most important feature here that one should examine is the bandwidth of the search variable (here L) around the optimum point, where function values are higher than those in neighboring regions. This bandwidth is found to be almost equal for all functions.

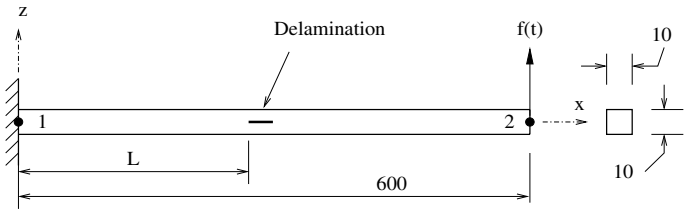

Fig. 10.37. Configurations of cantilever beams considered to examine the sensitivity of GA objective functions

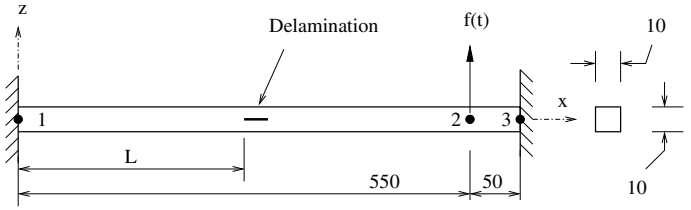

Fig. 10.38. Configurations of fixed beams considered to examine the sensitivity of GA objective functions

In the case of depth z, the function values are plotted in Figure 10.41 for the cantilever beam and in Figure 10.42 for the fixed beam. The reference response data is generated with a 20 mm long delamination at a depth $z = -3$ mm. It is interesting to note here that while using the functions based on the transverse and rotational components of the response (*i.e.,* J_2 and J_3 respectively), the maximum fitness value of 1 occurs at the actual depth location of the delamination and also at a depth which is the mirror image of the actual depth about the mid-plane (*i.e.,* $-z$). However, the other two

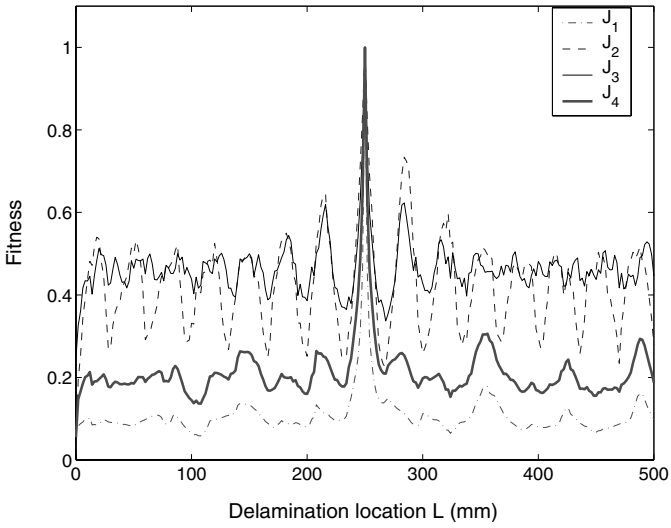

Fig. 10.39. GA objective functions J_1 to J_4 (Equations (10.11)–(10.14)) plotted with varying location of delamination for cantilever beams

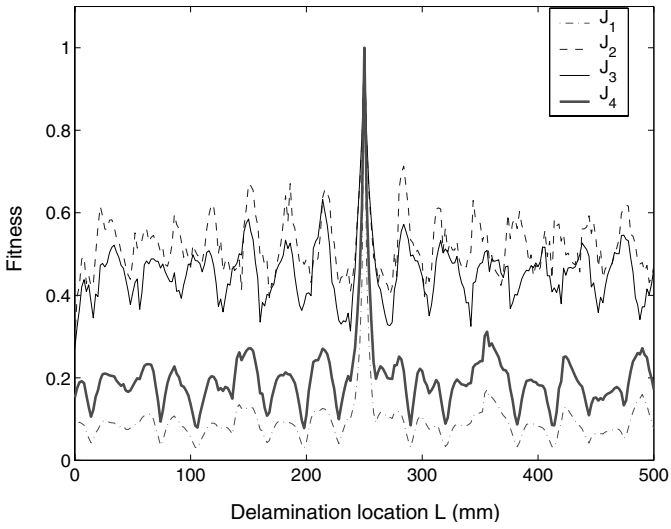

Fig. 10.40. GA objective functions J_1 to J_4 (Equations (10.11)–(10.14)) plotted with varying location of delamination for fixed beams

functions (*i.e.,* J_1 and J_4) do not behave in this way. This can be explained by the fact that the net bending stress for these two delamination configurations (one at a depth which is the mirror image of other about the mid-plane) are identical at any instant of time. The net axial stress, however, is different due to the axial–flexural coupling. In modal analysis, this type of motion is termed anti-symmetric thickness shear mode. However, compared to the earlier cases for search of L, the overall nature of the functions is found to be quite smooth. A direct conclusion that can be drawn from this study is that the function J_4 will be most suitable for identification of depth from mixed-mode wave propagation.

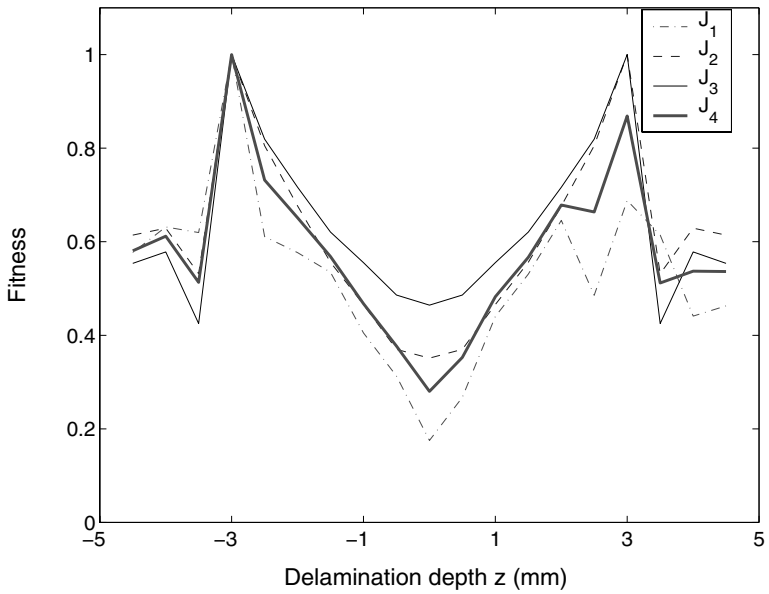

Fig. 10.41. GA objective functions J_1 to J_4 (Equations (10.11)–(10.14)) plotted with varying depth of delamination for cantilever beams

All the functions are found to be most well behaved when it comes to delamination length or size identification. The reference data is generated for a delamination of length 20 mm located at distance $L = 250$ mm from the left node and at the mid-plane of the beams. In the plots (Figure 10.43 and Figure 10.44), it can be seen that functions J_2 and J_3 overlap.

10.7.3 Power-based Objective Functions

The displacement-based objective functions studied in the previous section are quite well behaved except for the delamination location (L). Search for a better function is extended with the spectral power flow [227] expressed as

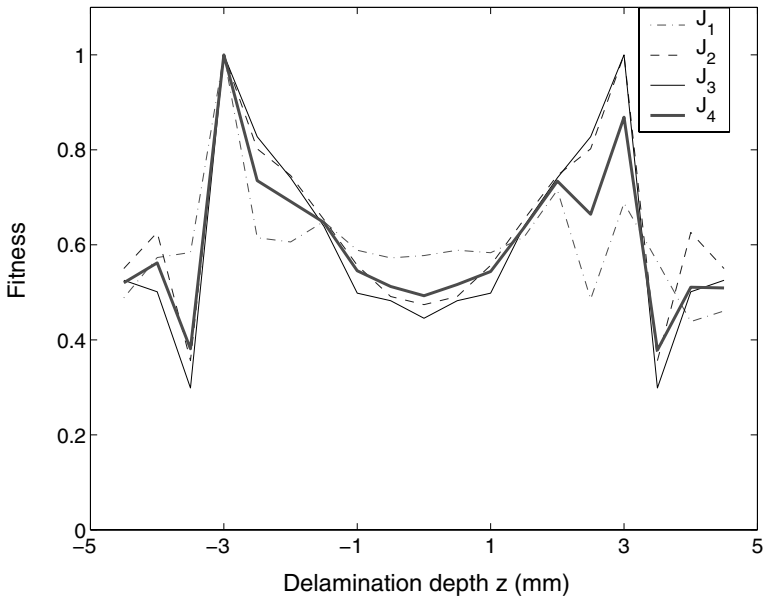

Fig. 10.42. GA objective functions J_1 to J_4 (Equations (10.11)–(10.14)) plotted with varying depth of delamination for fixed beams

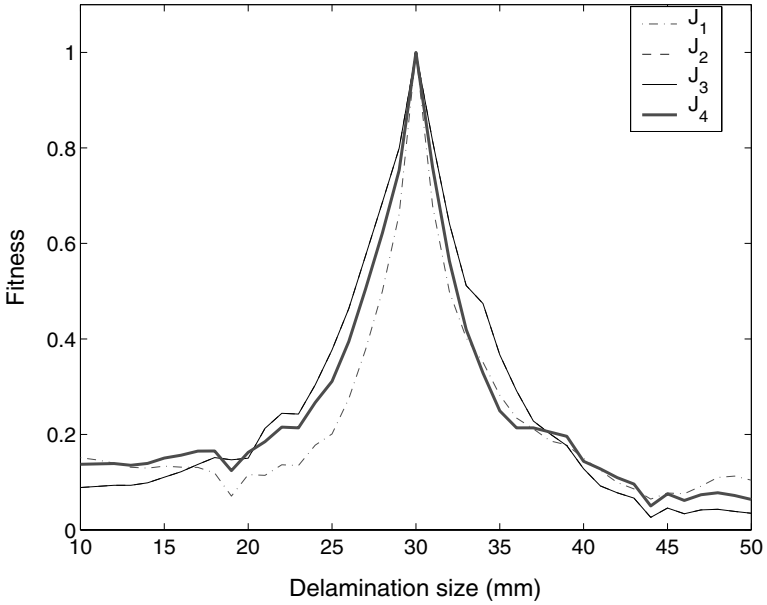

Fig. 10.43. GA objective functions J_1 to J_4 (Equations (10.11)–(10.14)) plotted with varying size of delamination for cantilever beams

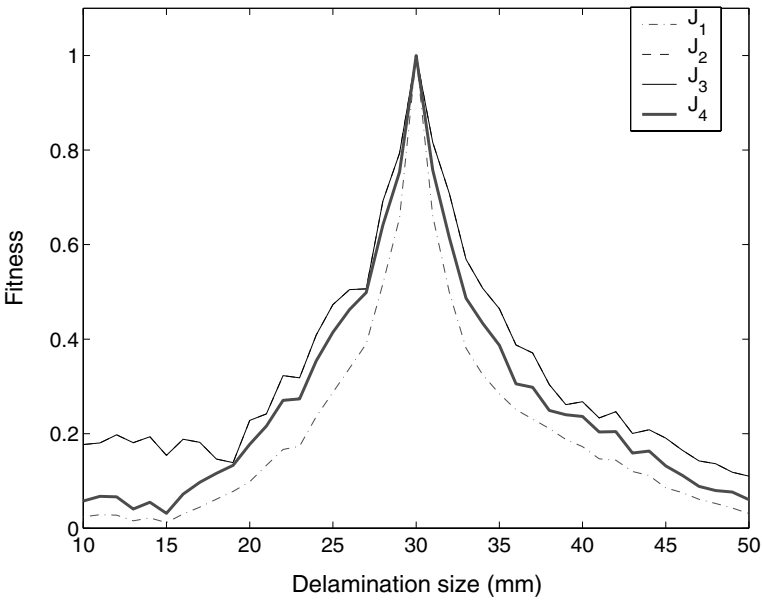

Fig. 10.44. GA objective functions J_1 to J_4 (Equations (10.11)–(10.14)) plotted with varying size of delamination for fixed beams

$$\hat{P}(x,\omega_n) = \hat{\mathbf{f}}(x,\omega_n)^T \left(i\omega_n \hat{\mathbf{u}}(x,\omega_n)\right)^* \tag{10.15}$$

where the superscript * represents the complex conjugate. The reason for choosing power as a measure is that for a non-dissipative medium, the real part of it is space invariant. The objective function based on spectral power is derived as

$$J_5 = \left[1 + \frac{1}{N}\sum_n \frac{\left|\hat{\mathbf{f}}^T_{\text{comp}} \left(i\omega_n \hat{\mathbf{u}}_{\text{comp}}\right)^* - \hat{\mathbf{f}}^T_{\text{expt}} \left(i\omega_n \hat{\mathbf{u}}_{\text{expt}}\right)^*\right|}{\left|\hat{\mathbf{f}}^T_{\text{expt}} \left(i\omega_n \hat{\mathbf{u}}_{\text{expt}}\right)^*\right|}\right]^{-1} \tag{10.16}$$

The fitness plot of the function J_5 for identification of location L is shown in Figure 10.45 in comparison with the displacement-based function J_4. However, J_5 can in no way be said to be better behaved than J_4. Also, it shows many more fluctuations compared to the other displacement-based functions. Hence, it stresses the fact that any quadratic measure as objective function (representative of the energy components in different frequency bands) will have similar drawbacks and one needs to explore further for better functional space. This can provide improved performance of GA-based identification strategies for non-smooth problems as in the present case. Other directions to improve the performance such as rank-based non-domination [228] and immune diversity [222] are less likely to ensure global optima unless better objective functions (*e.g.,* J_4 in the present case which includes the effect of axial–flexural coupling)

are used. Similar observation in the context of a benchmark problem called the Travelling Salesman Problem (TSP) can be found in [229]. In the present study, we restrict simulations to using only the objective functions discussed so far and show the performance of the proposed GA-based identification strategy in terms of the accuracy of the converged result and computational cost in the following section.

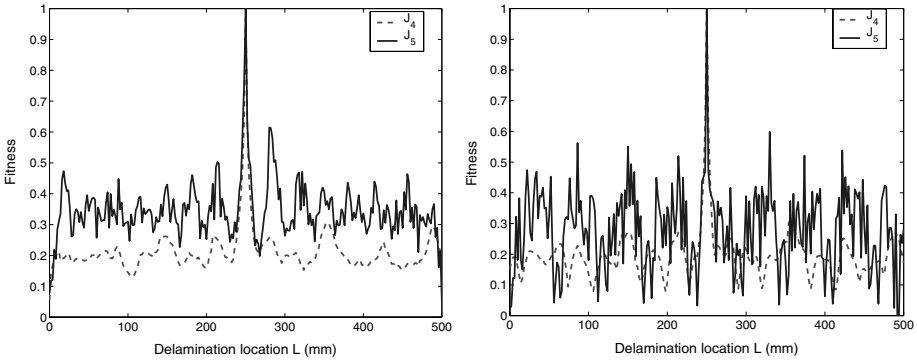

Fig. 10.45. GA objective functions J_4 and J_5 (Equations (10.14) and (10.16)) plotted with varying location of delamination for (a) cantilever and (b) fixed beams

10.8 Case Studies with a Cantilever Beam

The cantilever beam shown in Figure 10.37 is now considered for identification. Short duration Gaussian excitation having frequency content up to 40 kHz is applied at the cantilever tip in the transverse direction. First, single parameter identification is performed. Later, it is extended to two parameters and finally three-parameter identification is performed. Unless otherwise mentioned, function J_2 is considered the objective function. Although J_4 is ideal as discussed earlier, the reason for choosing J_2 is to demonstrate the efficiency of the proposed SFEM-GA strategy in terms of computational cost as well as accuracy, while using an inferior objective function. In the present work, a general purpose research code comprising several modules has been developed to implement the proposed SFEM-GA strategy and is ported on an IBM-RS/6000 high performance computer in serial mode.

10.8.1 Identification of Delamination Location

In this case study, the size and depth of delamination is assumed to be known. The reference data is generated by considering a 20 mm delamination at a

depth $z = -2$ mm. The location of delamination X from the root is identified with the following input data.

$$\begin{aligned} \text{Variable limits} &: 0 \leq X \leq 500\,\text{mm} \\ \text{Population size} &: 15 \\ \text{Crossover type} &: \text{two point} \\ \text{Selection type} &: \text{deterministic} \\ \text{Crossover rate } p_c &: 0.6 \\ \text{Mutation rate } p_m &: 0.04 \end{aligned}$$

The fitness curve is given in Figure 10.46. Location of the delamination ($X = 200\,\text{mm}$) is identified exactly. The number of generations passed is 24. In total 251 function evaluations are performed and the time required to complete this computation is only 25 min. Note that the structural analysis here must involve the dynamics up to the frequency content of the excitation signal (here 40 kHz). Such high frequency excitation is particularly useful when smaller damage zones (typically a few centimeters in most aerospace composite beams and panels) need to be detected. The plot in Figure 10.46 shows that the run reached a very good fitness value at generation 14. The total number of function evaluations up to generation 14 is 161 and the corresponding computation time is found to be 17 min. The computational cost shows many orders of improvement over the available GA-based strategies for similar problem complexity and accuracy. Similar improvement can be observed in all the other case studies presented below.

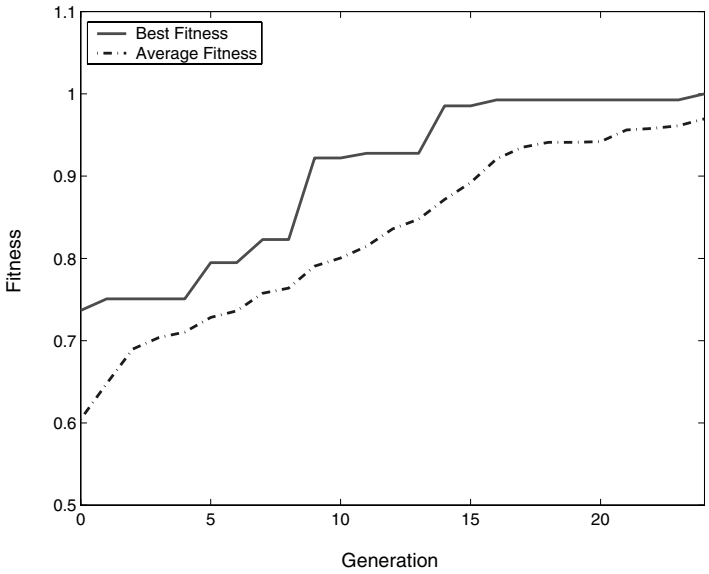

Fig. 10.46. Fitness curve of the GA run for identification of delamination location

10.8.2 Identification of Delamination Size

In this case study, the delamination size (X) is considered as the only unknown parameter. The delamination location ($L = 200\,\text{mm}$) and depth ($z = -2\,\text{mm}$) are presumed to be known parameters. The input data for the GA run is given below.

$$\begin{aligned} \text{Variable limits} &: 0 \leq X \leq 50\,\text{mm} \\ \text{Population size} &: 7 \\ \text{Crossover type} &: \text{two point} \\ \text{Selection type} &: \text{deterministic} \\ \text{Crossover rate } p_c &: 0.6 \\ \text{Mutation rate } p_m &: 0.04 \end{aligned}$$

A lower population size was considered because of the reduced complexity of the problem as discussed in the context of Figures 10.43 and 10.44. The exact size of the delamination ($X = 20\,\text{mm}$) is identified from the search. The fitness curve is given in Figure 10.47. The number of generations passed is six. A total of 25 function evaluations is performed and total computation time is only 3 min. Much better performance is found with this problem compared to location identification. This was expected as the fitness function behaves much better with variations in delamination size. The narrow bound in the variable limits is also another reason for this better convergence.

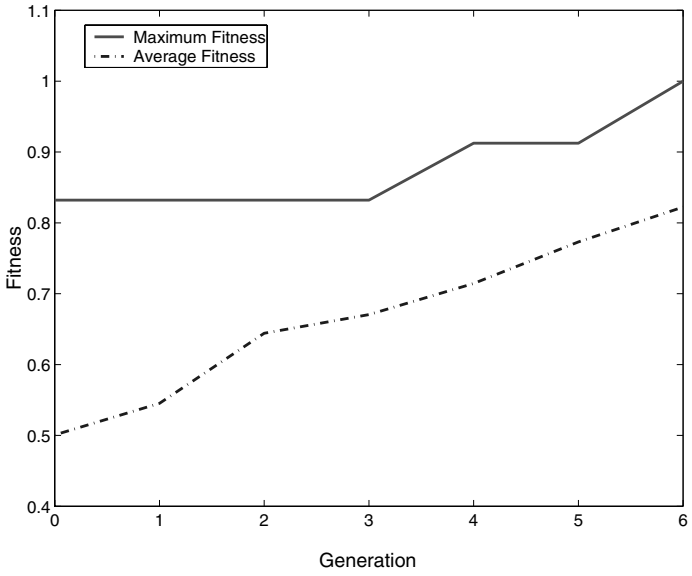

Fig. 10.47. Fitness curve of the GA run for identification of delamination size

10.8.3 Identification of Delamination Location and Size

In this case study, two variables, delamination location (X_1) and its size (X_2) are identified in a single run. The delamination depth ($z = -2\,\text{mm}$) is assumed to be the only known parameter. The input data for the GA run is shown below.

Variable limits : $0 \leq X_1 \leq 500\,\text{mm}$; $0 \leq X_2 \leq 50\,\text{mm}$
Population size : 20
Crossover type : two point
Selection type : deterministic
Crossover rate p_c : 0.6
Mutation rate p_m : 0.04

The fitness curve is given in Figure 10.48. The search results are tabulated in Table 10.1. The number of generations passed is 39. In total, 438 function evaluations are performed and the total computation time is 41 min.

Table 10.1. Results of genetic search for delamination location and size

Parameter	Actual value	Identified value
Location (X_1)	250 mm	250 mm
Size (X_2)	20 mm	19.9 mm

10.8.4 Identification of Delamination Location, Size and Depth

In this case study, all three parameters of a delamination; *i.e.,* delamination location (X_1), its size (X_2) and depth (X_3) are identified in a single GA run. Since the function J_2 is not sensitive to the delamination depth, function J_4 is used instead. The input data for the GA run is shown below.

Variable limits : $0 \leq X_1 \leq 500\,\text{mm}$; $0 \leq X_2 \leq 50\,\text{mm}$;
$-4\,\text{mm} \leq X_3 \leq +4\,\text{mm}$
Population size : 20
Crossover type : two point
Selection type : deterministic
Crossover rate p_c : 0.8
Mutation rate p_m : 0.1

The crossover and mutation rates are increased to enable better exploration of the solution space. The fitness curve over the generations is shown in Figure 10.49. The results of the search are tabulated in Table 10.2. The number of generations required for convergence is 72. A total of 660 function evaluations are performed and total computation time is 2 hr and 52 min. Total computation time is comparatively higher than the previous studies. This is because

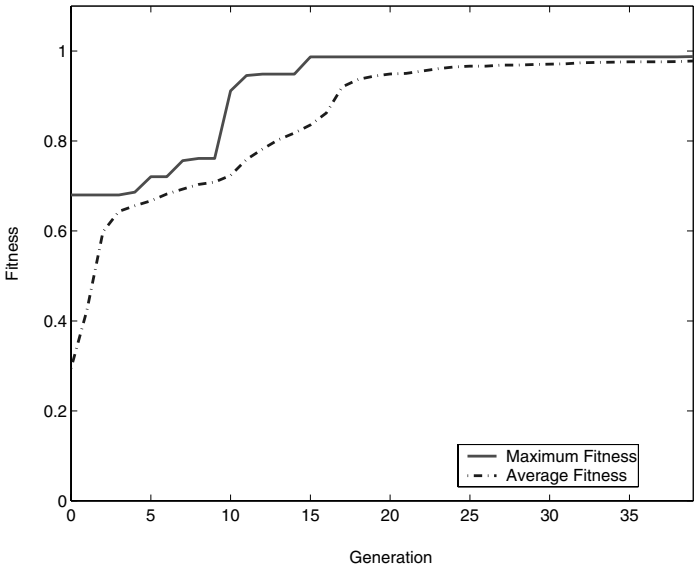

Fig. 10.48. Fitness curve of the GA run for identification of delamination location and size.

the function J_4 needs all three displacement components, which increases the computation time inside the fitness evaluation module (Figure 10.36). The net time is indeed very much attractive considering the complexity involved in the problem.

Table 10.2. Results of genetic search for delamination location, depth and size

Parameter	Actual value	Identified value
Location (X_1)	200 mm	200 mm
Size (X_2)	20 mm	20 mm
Depth (X_3)	−1 mm from mid-plane	−1 mm from mid-plane

10.8.5 Effect of Delamination Near the Boundary

In all the case studies presented so far, we have considered baseline configurations having delamination near the mid-span of the beam. Moreover, the proposed SFEM-GA based identification is oriented towards wave-based diagnostics, where most of the reported literature deals with semi-infinite models or models with artificially introduced absorbing (radiating) boundary conditions to eliminate boundary scattering. Hence, in a real-life situations, the

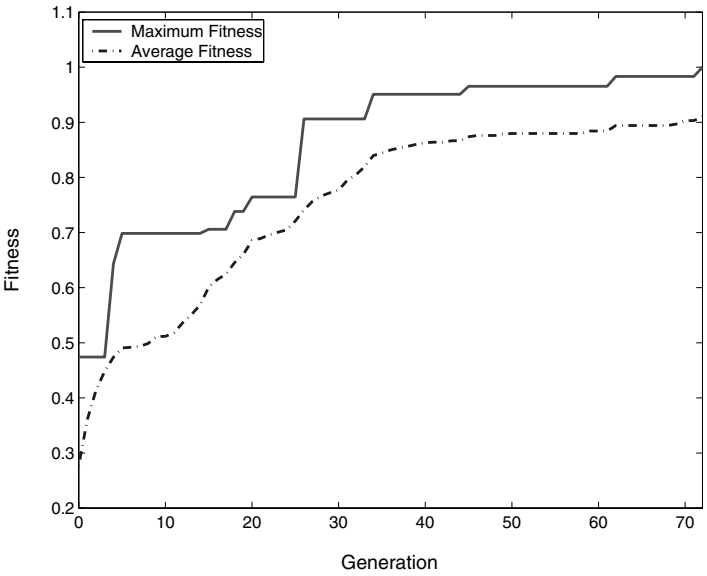

Fig. 10.49. Fitness curve of the GA run for identification of delamination location, depth and size

integrated structural health monitoring systems and identification tools based on such a strategy may perform poorly. To study the performance of the proposed SFEM-GA, the following two case studies are made by considering baseline configurations of the cantilever beam (dimensions are shown in Figure 10.37) with a 50 mm delamination at the fixed end. In the first baseline configuration, it is a mid-plane delamination. Figure 10.50 shows the plots of the objective function J_4 for three subpopulations with delamination at $z = 0$ (mid-plane), $z = -3\,\text{mm}$, $z = +3\,\text{mm}$ respectively, and with varying delamination length. In the second baseline configuration, the delamination is at $z = +3\,\text{mm}$. Figure 10.51 shows the plots of the objective function J_4 for three subpopulations with delaminations at $z = +3\,\text{mm}$, $z = 0$, $z = -3\,\text{mm}$ respectively, and with varying delamination length. Two distinct features are clear from these plots. One is the robust performance of the proposed SFEM-GA in the of presence of strong boundary scattering and delamination at the structural boundary. The second feature is that the subpopulations with $z = \pm 3\,\text{mm}$ in the first case (Figure 10.50) and the sub-populations with $z = 0, -3\,\text{mm}$ in the second case (Figure 10.51) are less likely to affect the evolution process even in the presence of high rates of mutation and crossover. This can be attributed to the efficient modeling of axial–flexural shear coupled waveguides and the property of the objective function J_4 as discussed in Section 10.7.2.

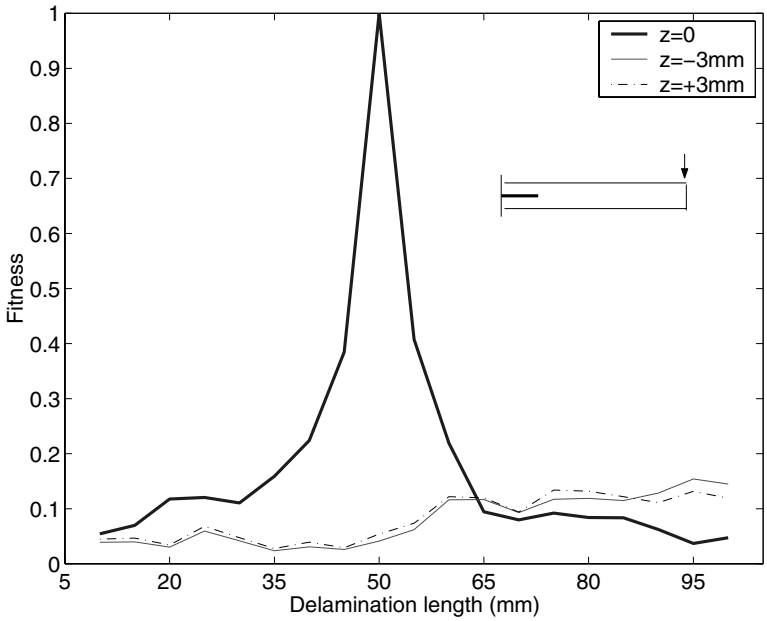

Fig. 10.50. The GA objective function J_4 (Equation (10.14)) plotted with varying length of delamination starting from the cantilever fixed end for baseline configuration of 50 mm long mid-plane delamination at the fixed end and

10.9 Neural Network Integrated with SFEM

An MLP feedforward neural network using an error back propagation (BP) algorithm is trained and tested to estimate (1) the span-wise location of the damage (L_1), (2) the approximate length of the degraded zone (L_2) and (3) the stiffness degradation factors α_{ij} for damage in the composite beam. Detailed discussion on such network models can be found in [230]. A schematic flow-chart on the use of frequency domain spectral analysis tools and model-generated data to train and test neural networks was reported in [231]. The main difference in the strategy developed here compared to that reported in [231] is that the measurement is assumed to be carried out at a single sensor location, especially for univariate data (*i.e.,* data containing the information of a single damage configuration), whereas in [231] the data from several sensor locations (as many as the number of input nodes) at a particular frequency need to be fed as inputs while using that network. In the present model, we assume that broadband spectral data is available from a single sensor measurement. In SFEM, the spectral band ranges from ω_1 to ω_N, where N is the Nyquist frequency. Hence the number of input nodes in the input layer needs to be fixed by considering the frequency resolution in the model during training. Therefore, if one needs to use the complete spectrum of the vector $\hat{\mathbf{u}}(\omega_n)_i$ (for beam it consists of $\hat{u}^o$, $\hat{w}$ and $\hat{\phi}$) at the nth sampling frequency

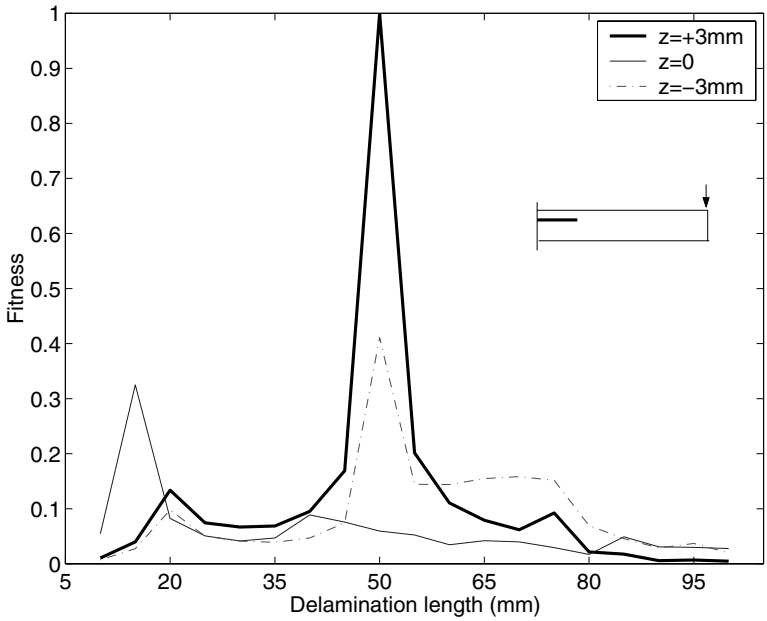

Fig. 10.51. The GA objective function J_4 (Equation (10.14)) plotted with varying length of delamination starting from the cantilever fixed end for baseline configuration of 50 mm long offset delamination ($z = +3$ mm) at the fixed end

and from the ith sensor location, then N complete sets (each containing three displacement components) of neurons in the input layer can be included. The network model is shown in Figure 10.52. Since the broadband spectral data consist of real and imaginary components at every sampling frequency, the number of neurons in the input layers is assigned as follows. First the amplitude and phase of the spectral data for each displacement component are computed at each sampling frequency. This doubles the length of the data array. Figure 10.53 shows typical spectra of amplitude and phase of transverse displacement used as the network input. The data set corresponding to the first sample (at $\omega_n = 0$) is removed as it does not contribute to the dynamic characteristics. The input data to the input layer are formed by adding one additional element of unity as input bias with the previous array.

The output from the neurons in the output layer are the damage location (L_1), the length of degraded zone (L_2) and the stiffness degradation factor α_{11} (in general a set of α_{ij} as seen in Equation (9.66) depending on the importance and reliability of the diagnostic measurement). It should be noted that for higher resolution spectral data obtained through the simulation or measurements for neural network training, the number of neurons in the input layer will increase in proportion. As a result, the number of hidden layers and the number of neurons in each of these hidden layers also must

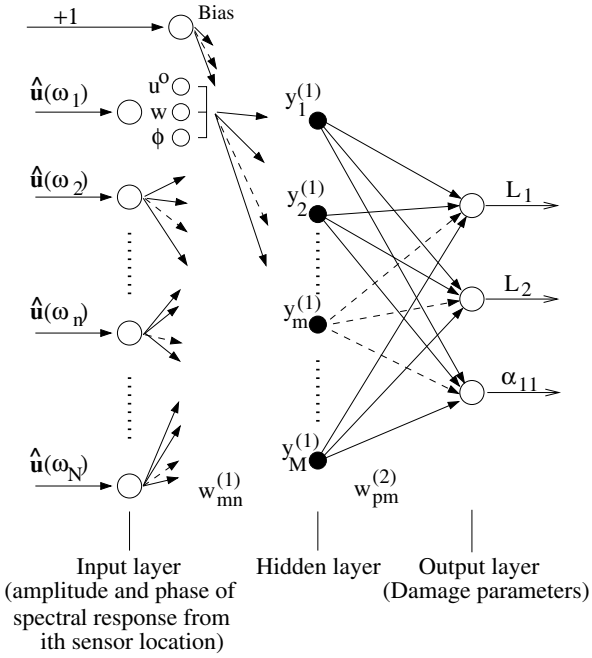

Fig. 10.52. Multi-layer perceptrons feed forward neural network for estimation of damage parameters from broadband spectral data

increase to provide optimal evolution of the information pattern to be embedded in the network. However, there is an inherent drawback to such a large network in that an excessive number of hidden layers causes slower convergence in the learning when using error back propagation. Hence, for better network performance when dealing with spectral data having low, medium or high resolution, it is essential to restrict the number of neurons in the input layers. Depending on the resolution (frequency sampling) and the extent of useful diagnostic information, any FFT spectral data set can be transformed to a data set with pre-assigned and smaller dimension but having the same bandwidth. Although we restrict our study to estimation of a single damage configuration, the model shown in Figure 10.52 can be extended to a two-dimensional network to deal with broadband spectral data from multiple sensor locations. Obviously, in such a case it would be more practical to use a number of measurement sensors in proportion to the number of damage incidents to be monitored. However, dealing with problems of such enormous complexity remains a future area of development.

The following network details are chosen for the training and performance testing. The same graphite–epoxy cantilever beam with one damage configuration (defined by the damage parameters L_1, L_2 and α_{11}) as discussed earlier is considered. One single spectral element with embedded degraded zone is used

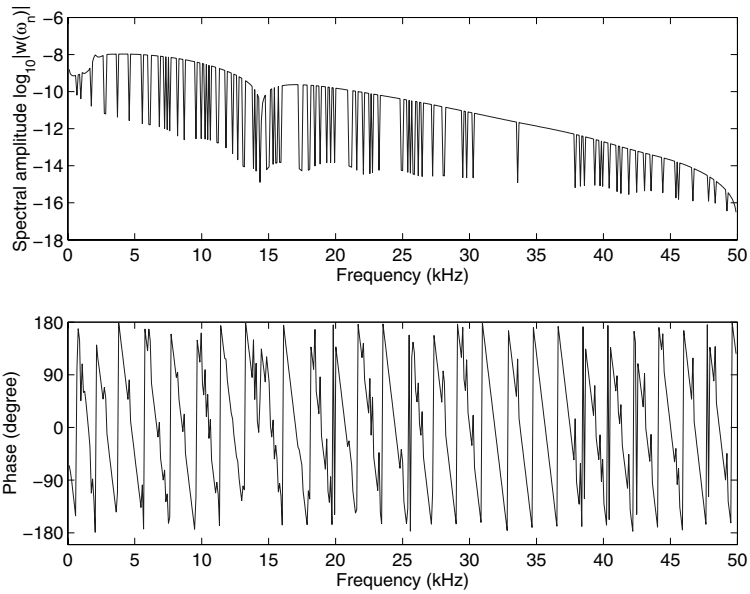

Fig. 10.53. Typical amplitude and phase spectra of transverse displacement used as the neural network input

to generate the data sets. Only the transverse displacement spectrum $\hat{w}(\omega_n)$ obtained at the tip of the cantilever is used. Training is carried out in sequential mode using S data sets. For each of these cases, the SFEM computation is performed through automated scripts by varying the damage parameters randomly. The number of neurons in the input layer is fixed at 1023 (511 neurons for amplitude, 511 neurons for phase and one neuron for bias). The amplitudes are normalized as

$$y_n^{(0)} = 1.6\left(\frac{\bar{w}_n - \mathrm{Min}[w_n,\theta_n]_S}{\mathrm{Max}[w_n,\theta_n]_S - \mathrm{Min[w_n,\theta_n]_S}}\right) - 0.8 \quad \in [-0.8, 0.8]\,, \tag{10.17}$$

$$\bar{w}_n = \log_{10}|\hat{w}(\omega_n)|\,, \qquad \theta_n = \tan^{-1}\left(\frac{\mathrm{Im}[\hat{w}(\omega_n)]}{\mathrm{Re}[\hat{w}(\omega_n)]}\right) \quad \in [0, 2\pi] \tag{10.18}$$

and the phases are normalized as

$$y_n^{(0)} = 1.6\left(\frac{\theta_n - \mathrm{Min}[w_n,\theta_n]_S}{\mathrm{Max}[w_n,\theta_n]_S - \mathrm{Min}[w_n,\theta_n]_S}\right) - 0.8 \quad \in [-0.8, 0.8]\,, \tag{10.19}$$

where $\mathrm{Max}[\,]_S$ and $\mathrm{Min}[\,]_S$ are respectively the maximum and minimum values in the S input data set. The S output data sets are also normalized in a similar way within the range $[-0.8, 0.8]$. In the present numerical study, we have only one hidden layer having 512 neurons. The synaptic weights between the neurons of the input layer and the neurons of the hidden layer are initialized as a matrix $\mathbf{w}(0)^{(1)}_{(512\times1023)}$. The synaptic weights between the neurons

of the hidden layer and the neurons of the output layer are initialized as a matrix $\mathbf{w}(0)^{(2)}_{(3\times512)}$. Both $\mathbf{w}(0)^{(1)}_{(512\times1023)}$ and $\mathbf{w}(0)^{(2)}_{(3\times512)}$ consist of normally distributed random numbers (with mean zero, variance one and standard deviation one).

Feedforward Computation

Following the standard algorithm for the feedforward MLP network [230], the input to the mth neuron in the lth layer during the rth learning step can be expressed as

$$v(r)^{(l)}_m = \sum_{n=1}^{N} w(r)^{(l)}_{mn} y(r)^{(l-1)}_n \ , \tag{10.20}$$

where $y(r)^{(l-1)}_n$ is the output of the nth neuron in the previous layer $l-1$ at the rth learning step. $w(r)^{(l)}_{mn}$ is the synaptic weight of the mth neuron in the lth layer that is fed from neuron n in layer $l-1$. In the present case $y(r)^{(0)}_n = y^{(0)}_n$ is the input spectral data in normalized form as given in Equations (10.18) and (10.19), $y^{(0)}_1 = +1$ is the bias to one neuron in the input layer. $y(r)^{(2)}_m, m = 1, 2, 3$, is the output of the three neurons in the output layer at the rth learning step, where $\mathbf{o}^{(2)} = \{L_1 \ L_2 \ \alpha_{11}\}^T$ is the expected output vector from the three neurons in the output layer. The output of the mth neuron in the lth layer through the activation function of the input to the mth neuron can be expressed as

$$y(r)^{(l)}_m = \Phi^{(l)}_m \left(v(r)^{(l)}_m \right) \ . \tag{10.21}$$

In the present case, a *bipolar sigmoidal* function

$$\Phi^{(l)}_m = \frac{1 - e^{v(r)^{(l)}_m}}{1 + e^{v(r)^{(l)}_m}} \tag{10.22}$$

is used as the activation function in all neurons in the hidden layer as well as in the output layer. The error signal at the output of the mth neuron in the output layer $l = 2$ is defined as

$$e(r)^{(l}_m) = o^{(l)}_m - y(r)^{(l)}_m \ . \tag{10.23}$$

For a total number of M neurons in the output layer, the Mean Squared Error (MSE) in the network output when training in sequential mode over S training data sets is then defined as

$$\text{MSE} = \frac{1}{2S} \sum_{m=1}^{M} \left[e(r)^{(L)}_m \right]^2 \ . \tag{10.24}$$

During supervised learning, the MSE, which is also called the training error (TE), is used as the stopping criteria over the number of epochs (number

of learning steps) when training is performed. Additional quantifications of network performance are given by the MSE during testing, which is also called the generalization error (GE), and the total error is given by

$$\text{total error} = \frac{S \times \text{TE} + S' \times \text{GE}}{(S + S')} \ , \tag{10.25}$$

where S' is the number of test data sets.

Error Back Propagation

The error in the output signal from the neuron in the output layer (given in Equation (10.23)) is back propagated using a gradient descent algorithm, where the local gradient is computed as

$$\delta(r)_m^{(l)} = \begin{cases} (e(r)_m)^{(L)} {\phi_m}^{(L)'} & \text{for neuron } m \text{ in output layer } L \\ {\phi_m}^{(l)'} \sum_n \delta(r)_n^{(l+1)} w(r)_{nm}^{(l+1)} & \text{for neuron } m \text{ in hidden layer } l \, , \end{cases} \tag{10.26}$$

where ${\phi(r)_m}^{(l)'}$ denotes differentiation with respect to the function argument defined in Equations (10.21) and (10.22). In the next epoch $r + 1$, the synaptic weights connecting layer l to layer $l + 1$ are updated according to the generalized delta rule [232] as

$$w(r+1)_{mn}^{(l)} = w(r)_{mn}^{(l)} + \Delta w(r)_{mn}^{(l)} \ , \tag{10.27}$$

$$\Delta w(r)_{mn}^{(l)} = \beta^{(l)} \Delta w(r-1)_{mn}^{l} + \eta^{(l)} \delta(r)_m^{(l)} y(r)_m^{(l-1)} \ , \tag{10.28}$$

where $\eta^{(l)}$ is the learning rate parameter and $\beta^{(l)}$ is the momentum constant for the neurons in layer l.

For optimal performance of the network, especially in the present problem where the amount of input spectral data is voluminous and highly non-smooth, it is important to choose the learning rate parameters for each of the layers carefully. After observation of the numerical performance of the network over a small number of training data sets as a trial, the learning rate parameters for the neurons in the hidden layer and output layer were fixed at $\eta^{(1)} = 0.03$ and $\eta^{(2)} = 0.03$. Without using any momentum constant ($\beta^{(l)}$=0) for additional stability, good convergence of the MSE has been achieved along with closely matching damage parameters. The numerical results are presented in the following section.

10.10 Numerical Results and Discussion

The case study performed here is with the spectrum of the transverse displacement $\hat{\mathbf{w}}(\omega_n)$ at the tip of the 0.8 m long graphite–epoxy cantilever beam with

single damage configuration subjected to the broadband pulse (Figure 4.5) applied in transverse direction at the tip. From SFE computation, spectral data having 512 sampling points up to the Nyquist frequency are taken directly into the neural network training and testing. Sampling is done at $\Delta\omega = 97.66$ Hz. No frequency scaling or dimensionality reduction is made when the data are taken for normalization. Sets of damage parameters used during generation of input data sets for training and testing are taken as combination of two different sets S_1 and S_2, where

$$\begin{aligned} S_1 : & L_1 \in [0.1 \text{ m}, 0.6 \text{ m}] \text{ in steps of } 0.1 \text{ m} \\ & L_2 \in [0.01 \text{ m}, 0.21 \text{ m}] \text{ in steps of } 0.05 \text{ m} \\ & \alpha_{11} \in [0.1, 0.9] \text{ in steps of } 0.2 \end{aligned}$$

$$\begin{aligned} S_2 : & L_1 \in [0.2 \text{ m}, 0.45 \text{ m}] \text{ in steps of } 0.05 \text{ m} \\ & L_2 \in [0.01 \text{ m}, 0.26 \text{ m}] \text{ in steps of } 0.05 \text{ m} \\ & \alpha_{11} \in [0.1, 0.85] \text{ in steps of } 0.15 \end{aligned}$$

The total number of training data sets is 316 and the total number of test data sets is 20 (randomly selected from S_1).

Table 10.3. Error-level in the network output after 600 epochs.

	L_1	L_2	α_{11}
$(\text{TE})^{1/2}$	0.0095	0.0304	0.0115
$(\text{GE})^{1/2}$	0.0224	0.0265	0.0632
$(\text{total error})^{1/2}$	0.0141	0.0100	0.0332
Maximum error	0.0412	0.0632	0.1749

Table 10.3 shows the error-level in the network output after 600 epochs. It can be seen that the error in α_{11} is highest. Although one can proceed with training the network further to obtain optimal network parameters, the network performance at the end of 600 epochs shows acceptable accuracy in estimating the damage parameters. The accuracy of these results is discussed next.

Figure 10.54(a) and (b) show the nature of neural estimation compared to the actual values of L_1 during training and testing respectively. Similar comparisons for L_2 and α are shown in Figure 10.55(a) and (b) and Figure 10.56(a) and (b) respectively. It can be seen from these figures that L_1 is estimated most accurately, except for test sample number 18. Corresponding actual damage parameters are $L_1 = 0.3$ m, $L_2 = 0.15$ m and $\alpha_{11} = 0.3$. Interestingly, $L_2 = 0.15$ m represents, comparatively, a large-size damage. But the $L_1 = 0.3$ m *i.e.,* the first interface where the waves are scattered, is sufficiently far away, hence is expected to transmit less energy through the first interface into the damaged zone. The corresponding $\alpha_{11} = 0.3$ indicates very high degradation in stiffness, so that it is obvious that only a very small

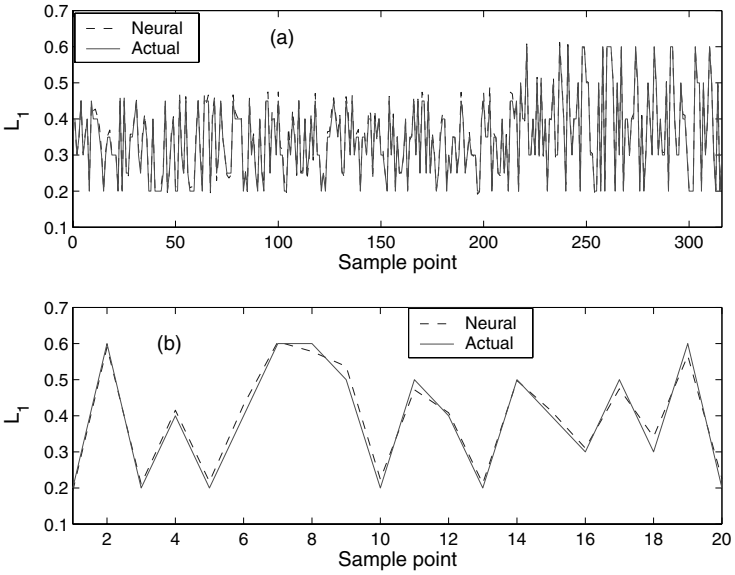

Fig. 10.54. Actual and estimated values of damage location L_1 during (a) training and (b) testing at the end of 600 epochs

amount of energy is left to scatter back from the second interface (with L_2 information) and arrive at the measurement location (cantilever tip). This is why L_2 is predicted with maximum deviation from the actual for test sample number 18. Subsequently, α_{11} is also predicted for this sample with maximum error (see Table 10.3). Table 10.3 indicates small training and testing errors, which shows the generalization capability of the network. However, the overall estimate of the damage parameters is made with acceptable accuracy.

Effect of Noise

Noise is inherent to any spectral estimation from on-line sensor signals, especially in SHM based on acoustic wave excitation. This is because of (1) features due to manufacturing defects in the structure, (2) ambient environment and interference in the sensor hardware, (3) limitations on the transducer bandwidth, and (4) other unknown sources of scattered waves which are unaccounted for in the case of finite element model-based training of the neural network. Therefore, it is important to study the effect of different levels of noise on the network, which has already been trained. To numerically simulate such a situation, random noise is added to some of the test data sets. This is done by adding noise to the amplitude and phase of the spectra separately. Only those data sets are selected for which the addition of noise does not exceed the normalization range $[-0.8, 0.8]$ for which that network has already been trained.

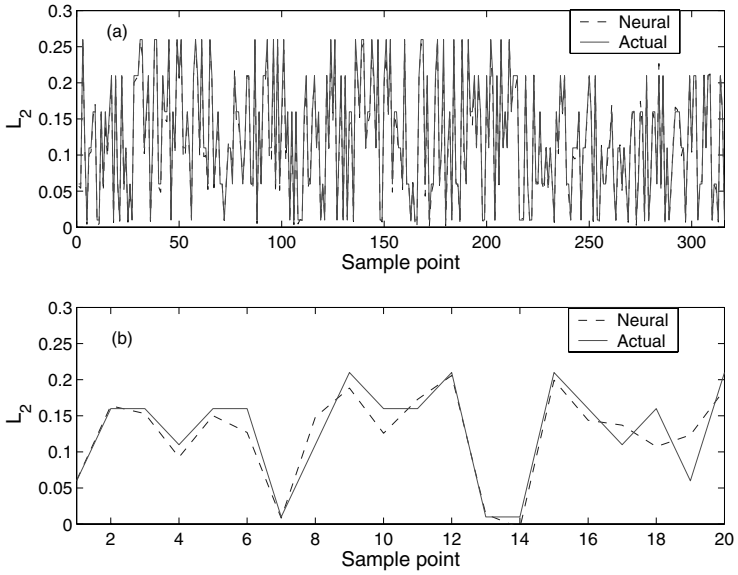

Fig. 10.55. Actual and estimated values of damage size L_2 during (a) training and (b) testing at the end of 600 epochs

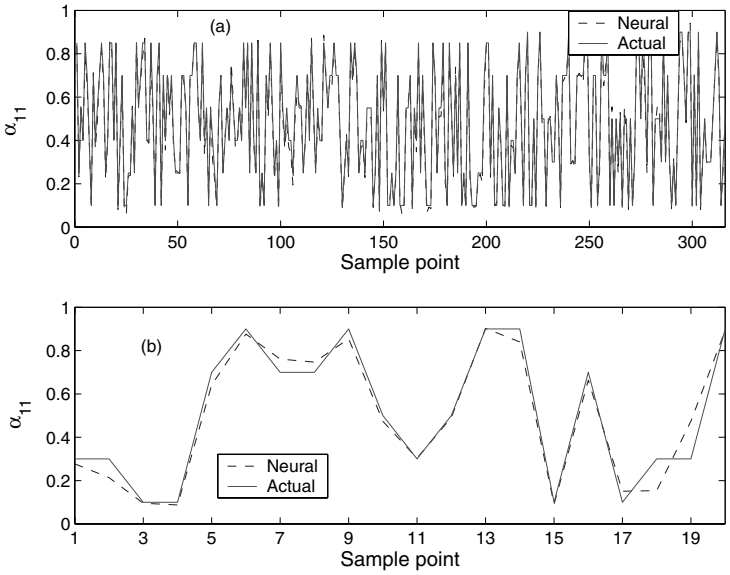

Fig. 10.56. Actual and estimated values of stiffness degradation factor α_{11} during (a) training and (b) testing at the end of 600 epochs

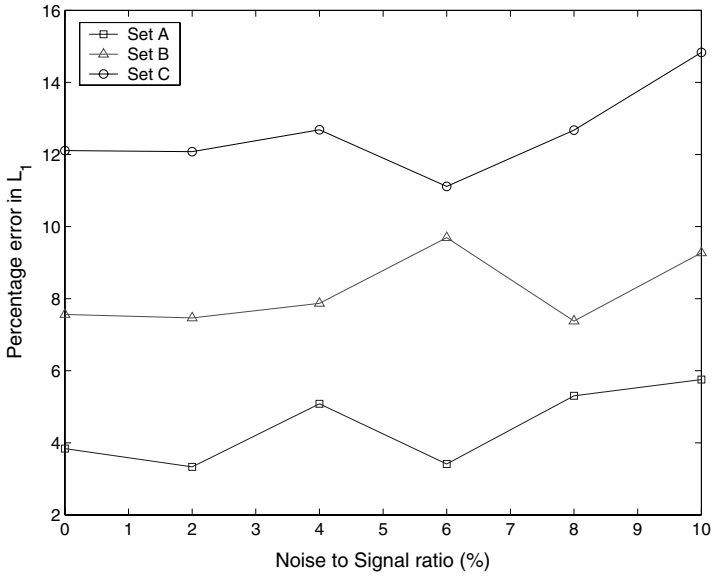

Fig. 10.57. Percentage deviation of estimated L_1 compared to the actuals when using a noisy input to the neural network during testing

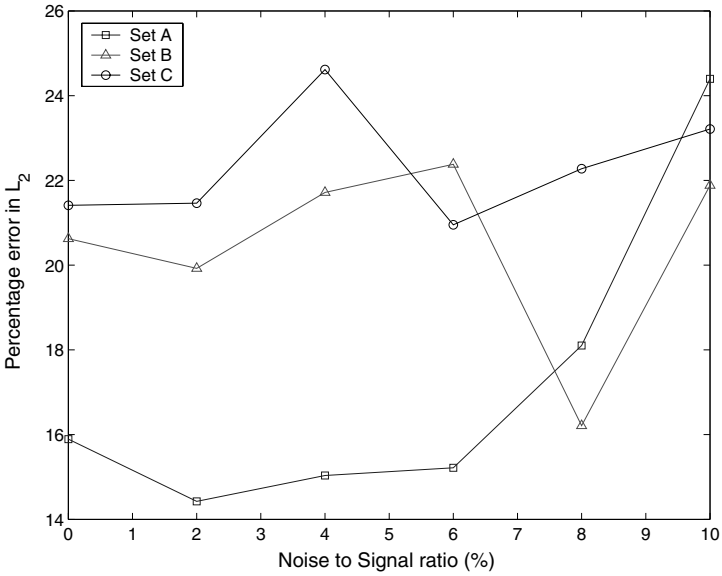

Fig. 10.58. Percentage deviation of estimated L_2 compared to the actuals when using a noisy input to the neural network during testing

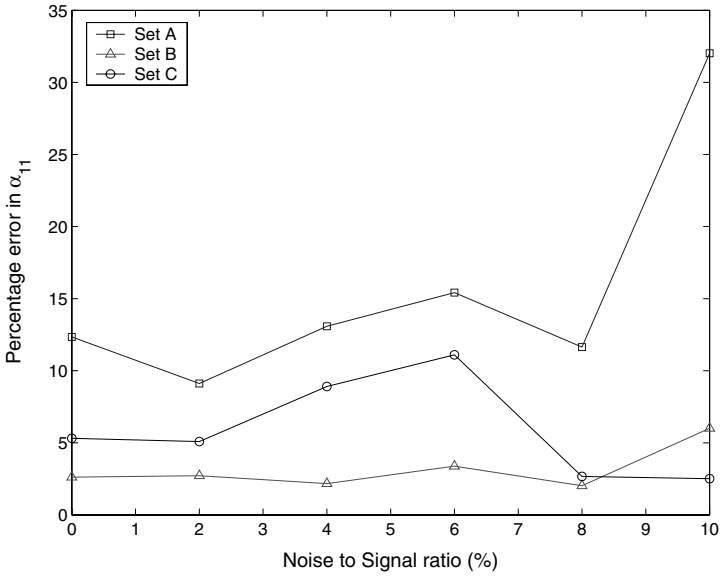

Fig. 10.59. Percentage deviation of estimated α_{11} compared to the actuals while using noisy input to the neural network during testing

Figure 10.57, 10.58 and 10.59 show the percentage deviation of the estimated L_1, L_2 and α_{11} with respect to the actual values in the presence of a noise-to-signal ratio up to 10%. In these figures, the results are shown for three different sets A, B and C of damage parameters. These three sets correspond to test sample numbers 4, 6 and 8 (see Figure 10.54 − 10.56). It can be seen from Figure 10.58 that L_2 is highly sensitive to noise, whereas Figure 10.59 shows that α_{11} is less sensitive to noise until high noise-to-signal levels are present. It can also be noted from Figure 10.56 and 10.59 that α_{11} of Set B (test sample number 6) is estimated accurately and so also is L_1 of Set B (as seen from Figure 10.54 and 10.57). On the other hand, since the estimation of L_2 of Set B is less accurate in the absence of noise (see Figure 10.55), it is further affected leading to a higher sensitivity to noise.

This chapter gives a complete overview of damage detection techniques used in the SFEM environment for structural health monitoring of composite beam structures. The chapter details novel modeling, analysis and damage diagnostic techniques using SFEMs. These are summarized item-wise in the following paragraphs.

In this chapter four different damage detection methodologies are explored. In the first approach, damage is detected by estimating the energy trapped in the structures due to broadband loading at different frequency levels. This is accomplished through the estimation of spectral power. Studies are performed for both single and multiple delaminations of different sizes and also for a beam with stripped inclusions.

The next method explored is the damage force method, wherein the damage is located using the healthy stiffness and the damaged response. This can be applied practically to any type of damage. The method is demonstrated using simulated experimental results for both single and multiple delamination detection.

A genetic algorithm integrated with spectral estimation suited to efficient identification of delamination in composite beams has also been developed. With this model-based approach, just a few transducer nodes appear sufficient for measurements in delaminated beams and connected structures. Various objective functions in GA are explored to determine the efficiency of the proposed algorithm under the SFE environment. The results show good GA performance in terms of computational efficiency compared with many other damage detection techniques.

The well-known MLP feedforward network trained using an error back propagation algorithm is used owing to its previously successful applications in damage identification problems. Its simplicity of implementation in software and hardware is exploited. The network is designed in such a way that model-generated spectral data from SFEM for training as well as on-line measurement can be accommodated easily. The performance shows acceptable accuracy for the estimated damage parameters. The study also shows that the estimated size of a degraded zone is highly sensitive to measurement noise.

11

Spectral Finite Element Method for Active Wave Control

The concept of broadband control in flexible structure has evolved over recent times. Tremendous technological success in the field of smart structures and MEMS has laid the path towards implementation of such concepts. Structures made of multi-functional composites have provided a wide range of platforms for precision sensing, distributed actuation and control related applications. Most of the mathematical frameworks behind the control systems normally use the frequency domain characteristics of the system. Since the basic foundation of SFEM is in the frequency domain, these aspects will be fully exploited in the present chapter, while developing a finite element model with integrated control algorithm for the control of a distributed flexible structure. The approach uses SFEM developed earlier to model the dynamics of the host structures. The control element, namely the sensor and the actuator, will be modeled through an active spectral finite element (ASFE). This chapter supplements Chapter 2 in giving a complete overview of the constituent models for different smart sensors/actuators. Towards the end, a case study of helicopter cabin noise reduction is presented.

11.1 Challenges in Designing Active Broadband Control Systems

Broadband control is important for many flexible structures with stringent vibration and noise level specifications and subjected to broadband loading. In most aerospace structures, such as helicopters, launch vehicles, satellites and spacecraft, many component-level vibrations contribute to the system-level noise spectrum, which is broadband. This is unlike the control requirement for steady-state vibration in machinery, where passive devices can perform efficiently. Almost all broadband control systems require active devices to augment the band-limited performance of passive devices.

In terms of high amplitudes of structural vibration and noise, gearbox transmitted noise in helicopters, launch load induced noise in launch vehicle

firing, *etc.,* fall into a category where a high-powered fatigue-tolerant active control system is the only option. Traditionally, an acoustic blanket covers many flexible parts of a helicopter fuselage, and electrohydraulic actuators are used at the gearbox fuselage interface. The concept of transmission-path treatment by providing active struts for gearbox mounts has been found suitable for active vibration/noise control (AVC)/(ANC) systems. A 10–20 dB reduction in the helicopter cabin noise spectrum within the frequency band 10 Hz − 5 kHz has been targeted [233]. Launch vehicles impart high levels of vibration to spacecraft during launch. The vibration environment is defined over several frequency bands (1) transient vibration < 80 Hz, (2) random vibration 20–2000 Hz, and (3) pyrotechnique shock 100–10000 Hz. Loads from transient vibrations define spacecraft design of primary structures such as spacecraft bus, solar panels and antenna support, instruments mounts, *etc.,* Loads from random vibrations define the design of spacecraft light structures such as antenna and solar panels, and shock loads define the design of electronic components and instruments. Spacecraft must survive the combination vibration environment. This involves broadband control and needs to be cost-effective for short launch duration [234].

On the other hand, instrument jitter during air and space-born measurements, micro-gravity isolation in satellites and spacecraft, *etc.,* fall into a category where a low-powered, lightweight but high precision active control system is required throughout the design life [235].

In the following sections, first we discuss the available strategies for vibration and wave control. Next, active material systems (piezoelectric and magnetostrictive) integrated with composite beam structure are considered. Different active composite material models are developed. The active spectral finite element model (ASFEM) is then developed for broadband control of vibration and waves in skeletal structures with generalized sensor/actuator configuration. Numerical simulations of the effect of distributed actuator dynamics and active control of wave transmission in helicopter gearbox support-struts are carried out. Optimal control strategies using frequency domain power flow are developed. Numerical simulation of the optimal broadband control of a composite beam network with piezoelectric fiber composite (PFC) actuators and point sensors for non-collocated feedback is carried out.

11.1.1 Strategies for Vibration and Wave Control

The design of smart structural systems based on the control of the first few resonant modes individually are most common in practice. For many vibration control applications, this serves as the control objective, since the modal energy is distributed over he first few resonant modes only. The basic steps in the development of such active control system models can be described as follows.

- Assume appropriate kinematics and constitutive model. For actuators or load cells mounted on the host structure, appropriate lumping of

the control force and actuator inertia can be considered. For surface-bonded or embedded layered sensors/actuators, the same kinematics as the host structure with additional constraints (*e.g.,* shear-lag to model active/passive constrained layers, discontinuous function to represent interfacial slip while handling inclusions, air-gap, *etc.,*) may be needed.

- Adopt an application-specific control scheme. For a known harmonic disturbance, the control force can be applied in the open-loop having optimal phase difference with the mechanical disturbance. The actuator force can be directly specified to add on the equivalent mechanical force vector. For unknown dynamic loading, and as required in most stable controller designs, closed-loop control schemes are adopted. The initial configuration of the error sensors, whose placements and numbers are fixed based on optimal control performance (observability and controllability), can be used for feedback or feedforward control. These error measurements are considered inputs to the controller under design. The controller output vector is used as the input electrical signal to the actuators. For off-line optimal control design based on conventional optimization techniques, the above steps are repeated at every iteration while extremizing the cost function(s). For off-line optimal control design based on soft-computing tools (*e.g.,* genetic algorithm), the solution space can be explored directly.
- Once all the system parameters (stiffness, mass, damping, electromechanical properties of sensors and actuators, sensor locations, actuator locations, actuator input, *etc.,*) for a particular configuration are available, develop the global model for the passive structure and the senor/actuator segment using analytical, finite element or boundary element techniques. In certain cases of electromechanical coupling, the system matrices can be decoupled into passive and active components. For the fully coupled electromechanical case, the analytical solution can be obtained for only a few electromechanical boundary conditions. However, for mounted actuators or load cells, this is not a problem when lumping the effect of actuator stiffness, inertia and force in the respective system matrices.
- Adopt suitable methods of system solution in temporal or modal space. When the discretized system size is large, appropriate reduced-order modeling techniques can be used. Dynamic condensation, proper orthogonal decomposition (POD) or a system equivalent reduction expansion process (SEREP), among many reduced-order modeling techniques, are found useful. Based on the formalism of the control cost function construction, a state-space model (first-order representation) is often used instead of a direct second-order representation. This is particularly suitable for conventional designs based on a quadratic regulator approach, where the state-space plant matrix, the input/output matrix along with the required weighting matrices are introduced. Peak response specifications are generally found to be linear matrix functions of the design variables, which allows them to be incorporated within the design framework without increasing the complexity of the optimization [164]. In time marching schemes

(*e.g.,* Newmark time integration), when designing the optimal control system the control cost function is minimized, including special control system features (*e.g.,* gain scheduling, feedback delay, *etc.*). When modal analysis is adopted, the modified dynamic stiffness matrix (including the contribution of sensor, controller and actuator parameters) are to be optimized so that the prescribed modes are controlled. In this approach, the control efficiency is quantified in terms of reduction in the modal amplitude level in the frequency response.

- Once the range of control system parameters, and the sensor/actuator collocation pattern are obtained, sensitivity and stability studies are carried out. Sensitivity studies are important to identify the most effective solution space of the design parameters. This also helps in visualizing the deviation in the desired response due to control uncertainty and measurement noise. With the narrowed-down solution space of the design parameters thus obtained, the loci of the roots of the characteristic system, *i.e.,* poles (resonances) and zeros (anti-resonances) of the system transfer function for varying design parameters are studied. The range of design parameters that produces a root locus on the right-half phase-plane are unstable and are avoided in the final design. A secondary objective is often in terms of control of transient disturbances, which is to minimize the transient response time of the controller.
- For a real-time automatic control system, the off-line design stages discussed above are augmented by an adaptive filter that tunes the control gains in the presence of measurement errors and uncertainty [236]. Also, there are certain drawbacks to the finite-dimensional design when used to control a distributed parameter system, such as control spillover. This is the result of insufficient modes considered in the MIMO state-space model. Although adaptive filters can augment the performance of off-line design based on a finite number of states, better modeling techniques for distributed parameter system are often advantageous. Many such recent techniques for structural vibration and waves based on the exact solution of the wave equations are available and these are the main aspect of study in the present chapter.

The most commonly used system for structural vibration control consists of active/passive tuned mass damper (TMD) devices [237], [238]. Several types of TMD devices are available in industry. Many of them consist of a combination of lumped masses, springs and viscoelastic rod/beam/solid block type structures. Also, various configurations based on electrohydraulic damping mechanisms, electrorheological (ER) fluid, magnetically controlled reaction mass and magnetic valve type damping mechanisms are available. Shape memory alloys (SMAs) have also been used in TMD for building structural control [239]. In TMD devices, the combined effect of spring, mass and passive damper is used. A single such device is capable of controlling a single mode or a few closely-spaced modes at most. On the other hand, in TMD devices with con-

strained viscoelastic layers, modes within a somewhat broader frequency band can be controlled. Multiple TMD devices can be used for multi-mode control. A general treatment of finite element computational models based on complex modes for a large structure having multiple TMD devices can be found in [240]. Optimization of the performance of TMD devices over a specified frequency band has also been reported [241].

In active devices, typically based on PZT layers/stacks, a much wider design space can be effectively used. Anderson *et al.* [242] developed a packaged flexible PZT strip with integrated electronics for active vibration control. Using these devices 5–10 % damping of a single mode within the frequency range 10–200 Hz was reported. Although conventional active/passive TMD devices find application mostly in civil engineering structural controls, active damping systems with integrated electronics are now being used extensively in aerospace applications, ranging from instrument jitter control to launch vehicle vibration isolation to spacecraft component-level and system-level stabilization [243], [242], [244], [245].

Both active/passive devices as a subsystem or active layers bonded or embedded in composite for distributed actuation require accurate modeling and analysis. Simpler structures with distributed actuator layers can be modeled using semi-numerical approaches, such as the Rayleigh–Ritz method, assumed modes method, Galerkin's method and the collocation method [246]. However, for complex configurations, a finite element method is used. For narrowband applications involving the control of a few lower modes, the solution of a finite element system in modal coordinates is computationally efficient compared to direct time integration [201]. However, in the case of displacement, velocity and acceleration feedback, in general the modified non-symmetric system matrices cause loss of orthogonality. For this reason, special care is required when using the natural modes. Also, the number of steps in matrix computation increases. Beside this, one would require a fine finite element mesh to minimize any unwanted discretization error in capturing the coupled electromechanical or magnetomechanical field. As the number of modes under consideration increases, especially in broadband applications, the computational cost becomes significantly higher.

In contrast to the modal approach for broadband control, the wave approach is based on the solution of a finite set of traveling waves. Instead of the active/passive control systems for structural vibration (standing waves) as discussed above, wave-absorbing controllers are the only viable solution for controlling disturbance propagation in flexible structures. References [247], [248] and [249] developed transfer function based models and point control forces to cancel the traveling waves in skeletal structures. The basic objective here is to completely cancel the unwanted component(s) of the original traveling waves. In a similar direction, a wave-absorbing control model for piezotransducers bonded to an isotropic beam was developed in [250].

Apart from the fact that in the available transfer function based models for wave control, which are semi-analytical in nature, and hence applicable to a

specific sensor/actuator collocation and structural boundary, the implementation of a generic closed-loop control model is not possible. In most broadband control applications, criticality of the problem can be summarized as follows. Fundamental limits on the performance of the available active control systems are found at low and high frequencies. The low frequency limit is caused by the nearfield of the secondary source corrupting the output of the error sensor [251]. In all the feedforward wave cancellation-based active control systems described in the literature [252, 253, 254, 255], this happens because the nearfield information is not inherent to the controller input. Therefore, restrictions regarding the relative placements of sensors and actuators must be made when adopting such control systems. Also, it is true that dispersive wave speed (group speed) increases with increasing frequency and hence the arrival of nearfield noise is difficult to identify in complex interconnections of structural components. Experiments on a metallic beam show that such a high frequency limit on the error signal delay increases for reduced flexural rigidity [251]. Also at the component level, this effect becomes manifold, which must be captured accurately from the integrated mechanics. As a complementary strategy, one can consider adaptive tuning of the filter to compensate the cumulative error in phase and amplitude of the actuator input signal [251], [256], [246]. However, such adaptation may always be fast enough against high frequency transient loading. In another direction, feedback control of wave transmission has been studied in [257, 258, 259]. In these studies, stabilization of the close-loop plant was carried out. This can be viewed as augmentation of the feedforward wave cancellation of incoherent noise on the error sensors by minimizing certain cost functions. Similar wave absorbing techniques using transfer function-based methods were proposed, which considered the exact solution to the wave equation in the frequency domain [248, 249, 250]. Essentially, in these studies, and also in our present approach, the main objective of the feedback control effort is the local or low-authority control (LAC) of the transmitted waves.

However, the effect of the distributed actuator dynamics related to such applications has been little studied. Although analytical in nature, and restricted to continuous cantilever beams, similar reported studies have shown the possibility of using fewer distributed actuators with strain sensors for the control of multiple waves. While mounting packaged TMD devices or integrated active layers, the original poles and zeros of the system transfer function (even under open-loop conditions) can experience significant sliding due to the added component-level dynamics [260].

Although significant development in the robustness of the control system has been reported in the literature, the effect of finite actuator dynamics in the control of distributed parameter systems still remains a core problem area from the stability point of view. Such stability problems encountered in distributed space structures were discussed in [261]. Noyer and Hanagud [262] proposed a Laplace domain model for optimal control of beam structures including actuator dynamics. In the present study, we prefer visualization

of the closed-loop responses (hence locations of poles and zeros along the frequency axis) directly, since the ASFE model proposed in this chapter is computationally more efficient than equivalent state-space or Laplace domain models.

In [263, 264] frequency domain models based on SFEM were employed for open-loop feedforward and closed-loop PID feedback control. Exact actuator dynamics and electromechanical boundary scattering were considered in these models. This enables one to analyze multiply connected beams with arbitrary geometry, and non-collocated as well as distributed sensor–actuator configurations. This concept is the basic framework of ASFEM developed in this chapter, and it accounts for the axial–flexural wave coupling due to out of plane bending actuation and the anisotropic electromagnetic properties across the beam thickness.

11.1.2 Active LAC of Structural Waves

LAC implies that the control law is based only on information from the vicinity of the actuator. Typically, collocated actuators and sensors are used for LAC, because if the actuators and the sensors are collocated and dual (their product is power) then the input-output transfer function is positive real, with an alternating pole zero structure and phase bounded by $\pm 90^\circ$ [265, 266]. If, in addition, the compensator applied to the structure is strictly positive real then the closed-loop system is guaranteed to be stable and the compensator will add damping to the structure. Also, the corresponding modeling and analysis become straightforward. Once, stability is guaranteed in LAC, it makes a perfect compliment for global or high authority control (HAC). By providing broadband increase in damping, local controller(s) make the flexible modes robust in the roll-off region and improve performance at higher frequencies, where HAC is not designed to work [258, 267].

However, a collocated sensor/actuator configuration is not the best option for LAC for two reasons. First, for control of dispersive waves at high frequencies, time delay in collocated feedback can be higher than the arrival time of wave packets. This is bound to produce phase difference and loss of coherence, and hence sensor–actuator collocation may not always be the best choice. Instead, such incoherence can be exploited to obtain the optimal control performance. Second is that a non-collocated sensor/actuator configuration may yield less power requirement for the same broadband control objective. This would require analysis of the non-collocated sensor/actuator configurations for LAC.

Although earlier studies on structural wave propagation in infinite or semi-infinite rods and beams form the basis for understanding the overall system behavior, they are not adequate for modeling complex configurations. This is because, structural boundaries and material interfaces may produce significant distortion and scattering of the original traveling waves. Consideration of the trapped energy in a structural member will be an important factor for a

control system, designed for spatially local attenuation of kinetic energy components at different frequencies. In the studies [268], [269] on finite beams, it is predicted that a single wave (axial or flexural or torsional) can be controlled completely by minimizing the power flow corresponding to the control force with the associated degree of freedom. But in many situations, considerations such as actuator dynamics and coupling between the different types of waves may require one to use multiple actuators.

In the case studies reported in this chapter, we model the control performance of axial–flexural coupled wave. The optimal performance that can be realized is also discussed. As suggested by [269], coupling between the axial and flexural waves can be modeled by an equivalent asymmetric scattering termination for one-dimensional structural members. An experimental study by [269] supporting this model reveals that control of one wave type (axial or flexural) results in standing waves in both types, if the scattered waves from terminations are not effectively controlled. Since, the exact coupling between various wave types was not studied in the available literature, it was concluded in the study [270] that the effective control of all the waves would require at least one actuator per wave type. An experimental investigation supporting this conclusion can be found in [246]. The experimental study by [233] also indicates that the coupling between axial and flexural waves will be important due to the presence of transverse dynamic loading along with the primary axial loads.

As mentioned above the control of wave transmissions is essentially local or low authority control (LAC). Therefore, a general framework to develop computational model is required, which can deal with arbitrary sensor/actuator collocation. Distributed actuator dynamics with non-collocated feedback is not tractable in the modal method. In methods based on traveling waves and transfer function matrices, a number of complicated and application-specific algebraic manipulation makes the analysis cumbersome. Further, optimization of such non-collocated sensor/actuator configuration for broadband LAC applications is a challenging task.

11.2 Externally Mounted Passive/Active Devices

Use of bulk transducer material with piezoelectric, magnetostrictive, electro-opto-mechanical and electromagnetic properties have long been exploited in the ultrasonic, ferroelectric and optical devices. For structural vibration and wave related applications, they are comparatively new in modeling, design, fabrication and range of applications. The additional issues, namely the distributed actuator dynamics, actuation bandwidth, actuator authority *etc.* are some of the important aspects which are being addressed for vibration and wave related applications. Also, issues in integration of these bulk materials with the host composite structures have provided a new dimension in design. Subsequently, accurate modeling, analysis and understanding of different ac-

tuation and sensing mechanisms play an important role in the cost-effective technology development. The most commonly used piezoelectric material is the lead zirconium titanate (PZT) with varying crystal structures [271, 272]. At present, several categories of PZT (hard and soft) are available in wafer, deposited thin-film, powder and fiber forms [273, 274]. PZT wafers (typical thickness is of the order of *milimeters* to *micrometers*) polarized with uniform surface electrodes or polarized with Interdigital Electrodes (IDEs) can be used in the surface-bonded or embedded form in a laminated composite with ply cut-outs or resin pockets. PZT powder mixed with polymer matrix and reinforcing fibers can be manufactured using appropriate curing methods in the presence of a polarizing field. Piezoelectric fibers of various shapes and binder matrix with improved conductivity can be used to manufacture the piezoelectric fiber composite (PFC). In all these active composites, the effects of residual stress, low compaction, dielectric breakdown and electrical insulation are major manufacturing issues that are intense areas of research, which will help in improving the performance of such active composite for broadband, reliable sensing and control applications. Among the magnetostrictive materials for structural sensing and actuation, Terfenol-D ($Tb_xDy_{1-x}Fe_2$) appears to be the best candidate, having a wide linear constitutive relation, small hysteresis and high actuator authority. However, for both PZT and Terfenol-D, hysteresis and a non-linear constitutive relation is common, and an appropriate DC bias electric/magnetic field is required to achieve best results. Terfenol-D in the form of rod as well as powder mixed with polymer matrix in composite [275] can be used for structural actuation.

Table 11.1. Comparison of solid state actuation materials with their bulk properties

	PZT 5H	PVDF	PMN	Terfenol-D	Nitinol
Actuation Mechanism	piezo- (31) ceramic	piezo film	electro-strictive	magneto-strictive	SMA
Max. Strain	0.13%	0.07%	0.1%	0.2%	2%-8%
Modulus (GPa)	60.6	2	64.5	29.7	28(m), 90(a)
Density (kg/m^3)	7500	1780	7800	9250	7100
Actuation Energy Density (J/kg)	6.83	0.28	4.13	6.42	252-4032
Hysteresis	10%	>10%	<1%	2%	High
Temperature Range	-20^o to 200^{o}C	Low	0^o to 40^{o}C	High	-
Bandwidth	100kHz	100kHz	100kHz	<10kHz	<5Hz

Table 11.1 shows a comparison of of the properties of bulk PZT 5H (hard), PVDF, PMN, Terfenol-D and Nitinol. PZT 5H is commonly used for high actuator authority and high dielectric breakdown voltage in structural control.

Polyvenyl difluoride (PVDF) is commonly used as a thin-film sensor. Lead magnesium niobet (PMN) falls into the category of electrostrictive material with quadratic non-linearity in the constitutive relation, and can be used for sensing and low strength actuation. Terfenol-D is commonly used in structural actuation with high actuator authority. However, excessive heating and weight due to its magnetic housing and magnetizing coil limit its wider application. Nitinol is the industrial name of nickel titanium alloy and shows the shape memory effect due to diffusionless transformation between its martensitic and austenitic microstructures. The temperature-induced transformation, which is primarily responsible for the shape-memory effect, is commonly exploited for static shape control and low-frequency vibration control. The stress-induced superelastic effect also helps providing a high passive damping feature of shape memory alloys (SMAs) in vibration and wave control applications.

For sensing and active control of vibration and waves, the frequency bandwidth of the transducer is one important parameter, which provides their operational limits in terms of frequency range of excitation. For vibration and wave sensing, any measurement at the higher end of the frequency bandwidth is likely to introduce high signal-to-noise ratio in the sensor output. On the other hand, for vibration and wave control applications, the requirement of any actuation at the higher end of the bandwidth and above may cause control spill-over. As can be seen in Table 11.1 Nitinol is suitable only for low frequency applications, whereas Terfenol-D and PZTs are suitable for medium and high frequency applications, respectively.

Apart from the piezoelectric or magnetostrictive composite, which are recent developments, packaged sensors and actuators have been commonly used in structural vibration and waves [276, 270, 277]. Figures 11.1 and 11.2 show the typical configurations of a packaged magnetostrictive rod actuator and piezoelectric stack actuator. Similar actuators have been used to control the gearbox-induced noise transmission in a helicopter cabin, as reported in [270, 233]. In such packaged transducers with housing, multi-modal control can be obtained using suitable block-force (provided by pre-stressing the core) and different directional mounts having a group of such transducers. Also, additional tuned mass can be used to provide passive damping features. However, for multi-modal control, one needs to have an adaptive feedforward or feedback algorithm and error sensors in to guide these actuators.

On the other hand, when using distributed actuators bonded or embedded in composite, one can use the active material properties and geometry as design parameters for the required distributed actuator dynamics. Crawley and Luis [278] developed an analytical model to study the strain-induced actuation due to surface bonded and embedded piezoelectric layers. Piezoelectric strain transfer assuming shear-lag through the bonding layer showed hyperbolic variation of strain as a function of the length, the thickness and the shear modulus of the bonding layer and the beam-to-piezoelectric stiffness ratio. In the same work [278], a scaling analysis was also carried out to study the effect of coupling between the piezoelectric actuator and the host beam

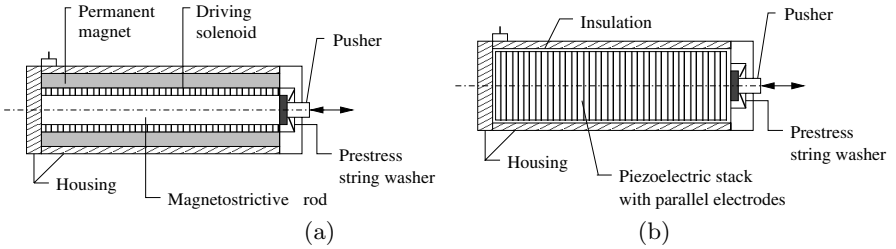

Fig. 11.1. Configuration of the packaged magnetostrictive/piezoelectric transducers. (a) Magnetostrictive rod actuator. (b) Piezoelectric stack actuator. (c) Piezoelectric stack pair

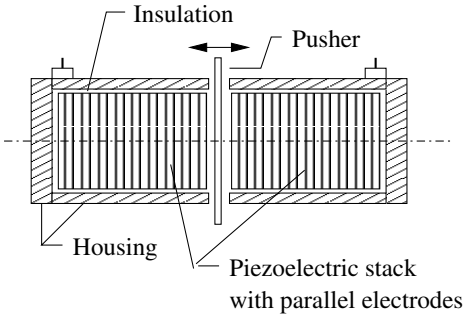

Fig. 11.2. Piezoelectric stack pair

structure. It was found that the active damping for rate feedback control of a specified mode is only dependent on the actuator material properties, when the geometry of the actuator and host beam structure is scaled by constant value. Such analysis also brings out the fact that the optimal placement of the actuator should be at the region of high average strain.

However, the application of distributed actuators for broadband structural control as opposed to single mode control is not directly amenable from this framework. Also, for wave control applications, one needs to draw a rationale between the optimal placement of actuators in terms of high average strain transfer as well as sensor collocation with maximum response sensitivity. This particular aspect of optimal broadband control is focussed on the numerical simulations presented in this chapter. Apart from the modeling issues discussed above, the residual stress developed during the manufacture of integrated actuator and additional pre-stressing arrangement needs to be designed based on specific application. For example, in [277] a packaged layered actuator with dual force/strain sensing capability was devloped for distributed actuation and control. A force/strain feedback mixing coefficient and thickness and length of the actuator layer were considered as design parameters.

A layered sensor and actuator configuration is suitable to model and analyze using elementary or shear deformable beam/plate kinematics [279, 280,

281]. Multiple sensor and actuator layers have been modeled [280] using multiple potential degrees of freedom along with a layer-wise kinematics. Cai *et al.* [172] presented a technique based on a 2-D elasticity solution for multiple piezoelectric layers. To accommodate the effect of adhesive interface between the surface bonded active layer and host beam structure, additional constrained shear layer damping has been studied in the work [282, 283, 284].

Currently a number of designs are available which use PZT ceramic fibers, magneto-elastic inclusions and conventional matrix. The coupled electromechanical field and boundary conditions at the matrix-fiber interfaces are the main aspect of micromechanical modeling in these types of multi-phase composite. In conventional fiber reinforced brittle matrix composite, the homogenization techniques based on periodic representative volume elements (RVEs) are used [285]. Treatment of additional non-linear effects such as strain softening in polymeric composites can be found in the work of Sluis *et al.* [286]. Finite element prediction of PFC properties of electroded PZT was reported in [46]. Following this development, experimental investigation for standardizing the design of PFC with IDEs for structural actuation was carried out in [274]. For model validation, uniform field models of PFCs with circular and square PZT fibers were developed. The 3-D constitutive models of bulk electromechanical properties of the constituents were homogenized. To achieve this, the boundary conditions at RVEs were imposed, which is the same as in microscopic composite. This is known as the repeating element approach, and has been used extensively in modeling. The only difficulty, which is due to non-uniformities of IDEs, were modeled assuming uniform electric field between the IDEs and this was found satisfactory in comparison with the experimental results. Also these models perform well in the linear and high frequency regime. Following the performance standardization of these PFCs as distributed actuators and sensors, the main task remains how they can be deployed for better control applications. In the particular case of transverse bending actuation [287, 273], PFCs have been found suitable. It is found that the required conformity of active fiber composite with the host structure can also be achieved due to their tailorability in choosing fiber volume fraction, orientation and electrical properties of the matrix [273, 288, 289].

Although various issues related to the fabrication, constitutive modeling, packaging and reliability, *etc.,* of PFCs have been addressed, application of such PFCs for distributed structural actuation in vibration and wave control related applications are very few [290]. Also, there are destabilizing effects of such distributed but finite actuator dynamics on the control performance, especially for non-collocated feedback, which needs to be accurately dealt with in the framework of a distributed parameter model. In the present study, we consider the effect of integration of similar PFC actuators and sensors with the host composite beam structures on their control performance as one of the key issues. We also consider the broadband actuation and sensing capability (up to kHz range) of these PFCs to develop a linear wave mechanics based structure-control interaction model.

11.3 Modeling Distributed Transducer Devices Integrated with Composite Structures

Before obtaining a distributed parameter model for an integrated active/ passive material system to be used for structural wave control applications, it is essential to incorporate the key features of these material assemblies accurately. Several literature and finite element models are at present available for carrying out detailed 2-D/3-D analysis and design for smart transducers [291], [292]. These transducers externally bonded or embedded inside the composite when acting as sensors, generate electrical signals (with the help of appropriate circuit and signal-processors) due the induced mechanical strain. On the other hand, when they are designed as actuators, they induce mechanical strain in the host structure due to the application of an electromagnetic field. In the present study, we consider only piezoelectric (*e.g.,* PZT) and magnetostrictive materials (*e.g.,* Terfenol-D) as bulk transducer materials. Modeling surface-bonded and embedded wafers or thin-film type structures as well as stacked actuators fitted in composite rod/beam segments are considered. A more complicated material system in the form of inter-digital transducers (IDEs), which are often used in MEMS, ultrasonics and surface acoustic wave (SAW) applications, are derived next. Use of piezoelectric fiber composite (PFC), which is a more recent development in distributed structural actuation technology, has introduced the possibility of using active fiber composite in various forms. Although simplified models of different PFCs based on homogenization have been developed [274], such constitutive models have not been applied to study their distributed actuation capabilities for structural wave control or SAW type applications. At the end of the following section, a uniform field model of PFCs is derived, which is studied later in the context of distributed actuator dynamics.

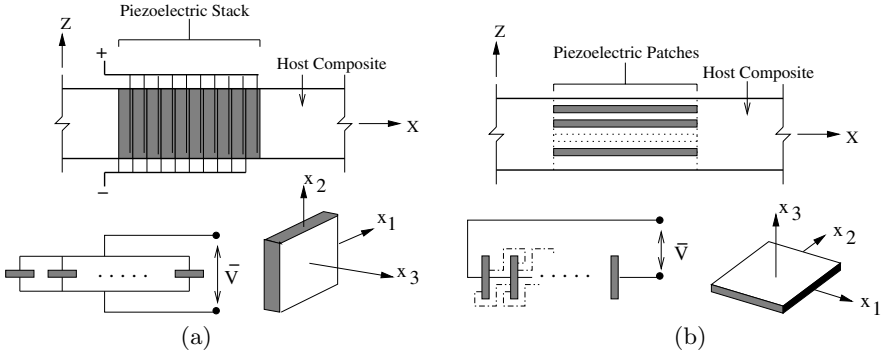

Fig. 11.3. Configuration of piezoelectric transducer integrated with host composite beams. (a) Piezoelectric stack configuration with the equivalent parallel plate capacitor model. (b) Piezoelectric patches adhesively bonded or embedded in host laminated composite and the equivalent parallel plate capacitor model

Figure. 11.3(a) and (b) show the active composite beam segments with piezostack and layers respectively. A similar configuration is also possible for Terfenol-D rod, stack and matrix patch with magnetostrictive particles. However, for Terfenol-D rod or stack, the magnetic coil assembly and housing can be modeled with appropriate additional mass and stiffness lumping. For matrix patch with magnetostrictive particles, the magnetic coil assembly can also be modeled in similar way. However, since the present work is not supported by any fabrication and experimental design, these modeling aspects are not considered. Assuming perfect bonding between the stack or layers with the electrodes and the host structures, the beam kinematics can be defined as for a Euler–Bernoulli beam or first-order shear deformable beam. For concise representation, we proceed with the constitutive model and equation of motion for the first-order shear deformable beam, and these can be reduced to the Euler–Bernoulli (thin beam) model by imposing shear deformation $\phi - w_{,x} = 0$. For sensing, we assume a single layer with output electric field $E(x,t)$ due to the mechanical strain. For actuation with layered configuration (Figure 11.3), we assume multiple layers with input electric field $E(x,t)$ in each layer. To arrive at the constitutive model, we start with the constitutive model of the bulk active materials and then reduce it to a plane stress constitutive model in the $X-Z$ plane. The derivations for piezoeletric actuators are presented in detail. The same procedure is also applicable to bulk magnetostrictive materials in rod or layered form.

11.3.1 Plane Stress Constitutive Model of Stacked and Layered Piezoelectric Composite

The constitutive model for piezoelectric composite is derived on similar lines to that done for laminated composite in Chapter 2. We shall first consider the orthotropic constitutive model of the composite lamina and the piezoelectric layers in the material coordinate system (x_1, x_2, x_3) as shown in Figure. 11.3(b). The complete three-dimensional orthotropic constitutive model [293] can be expressed as

$$\begin{Bmatrix} \sigma_{11} \\ \sigma_{22} \\ \sigma_{33} \\ \sigma_{23} \\ \sigma_{31} \\ \sigma_{12} \\ D_1 \\ D_2 \\ D_3 \end{Bmatrix} = \begin{bmatrix} C_{11}^E & C_{12}^E & C_{13}^E & 0 & 0 & 0 & 0 & 0 & -e_{31} \\ C_{12}^E & C_{22}^E & C_{23}^E & 0 & 0 & 0 & 0 & 0 & -e_{32} \\ C_{13}^E & C_{23}^E & C_{33}^E & 0 & 0 & 0 & 0 & 0 & -e_{33} \\ 0 & 0 & 0 & C_{44}^E & 0 & 0 & 0 & -e_{24} & 0 \\ 0 & 0 & 0 & 0 & C_{55}^E & 0 & -e_{15} & 0 & 0 \\ 0 & 0 & 0 & 0 & 0 & C_{66}^E & 0 & 0 & 0 \\ 0 & 0 & 0 & 0 & e_{15} & 0 & \epsilon_{11}^{\varepsilon} & 0 & 0 \\ 0 & 0 & 0 & e_{24} & 0 & 0 & 0 & \epsilon_{22}^{\varepsilon} & 0 \\ e_{31} & e_{32} & e_{33} & 0 & 0 & 0 & 0 & 0 & \epsilon_{33}^{\varepsilon} \end{bmatrix}$$

$$\times \left\{ \varepsilon_{11}\ \varepsilon_{22}\ \varepsilon_{33}\ 2\varepsilon_{23}\ 2\varepsilon_{31}\ 2\varepsilon_{12}\ E_1\ E_2\ E_3 \right\}^T , \tag{11.1}$$

where σ_{ij} and ε_{ij} are respectively the stress and strain components in the material coordinate system (x_1, x_2, x_3), which makes an angle θ with the ply coordinate system (X, Y, Z) as shown in Figure 11.3(b). For the piezoelectric layers, D_i are the components of electric displacement in the plane normal to the direction i. E_i are the components of electric field $-\nabla\varphi$ (φ being the electric potential) along the direction i. In Equation (11.1), $\mathbf{C}$ is the elasticity matrix. e_{ij} and $\epsilon_{ij}^{\varepsilon}$ respectively represent the electromechanical coupling coefficients and dielectric constants. The superscript E in C_{ij}^{E} indicates the stiffness measured under prescribed electric field E. The superscript ε associated with $\epsilon_{ij}^{\varepsilon}$ indicates the dielectric constants measured under prescribed mechanical strain ε. Under linear range of transduction, constant values of C_{ij}^{E} and $\epsilon_{ij}^{\varepsilon}$ are used for a particular grade of PZT. Transformation of the conjugate variables, *i.e.,* (σ, ε) and $(\mathbf{D}, \mathbf{E})$ from the material coordinate system (x_1, x_2, x_3) to the ply-local coordinate system (X, Y, Z) can be carried out by following [50] as

$$\begin{Bmatrix} \sigma \\ \mathbf{D} \end{Bmatrix} = \mathcal{T} \begin{bmatrix} \bar{\mathbf{C}} & -\bar{\mathbf{e}} \\ \bar{\mathbf{e}}^T & \bar{\epsilon} \end{bmatrix} \mathcal{T}^T \begin{Bmatrix} \varepsilon \\ \mathbf{E} \end{Bmatrix}, \tag{11.2}$$

where the transformation matrix $\mathcal{T}$ is of the form

$$\mathcal{T} = \begin{bmatrix} \mathcal{T}_{11} & \mathbf{0} \\ \mathbf{0} & \mathcal{T}_{22} \end{bmatrix}, \tag{11.3}$$

$$\mathcal{T}_{11} = \begin{bmatrix} \cos^2\theta & \sin^2\theta & 0 & 0 & 0 & -2\cos\theta\sin\theta \\ \sin^2\theta & \cos^2\theta & 0 & 0 & 0 & 2\cos\theta\sin\theta \\ 0 & 0 & 1 & 0 & 0 & 0 \\ 0 & 0 & 0 & \cos\theta & \sin\theta & 0 \\ 0 & 0 & 0 & -\sin\theta & \cos\theta & 0 \\ \cos\theta\sin\theta & -\cos\theta\sin\theta & 0 & 0 & 0 & \cos^2\theta - \sin^2\theta \end{bmatrix}, \tag{11.4}$$

$$\mathcal{T}_{22} = \begin{bmatrix} \cos^2\theta & \sin^2\theta & 0 \\ \sin^2\theta & \cos^2\theta & 0 \\ 0 & 0 & 1 \end{bmatrix}. \tag{11.5}$$

θ is the angle of orientation of (x_1, x_2) system with respect to (X, Y) in Figure. 11.3. The constitutive relation in the ply coordinate thus finally can be expressed as

$$\begin{Bmatrix} \sigma_{xx} \\ \sigma_{yy} \\ \sigma_{zz} \\ \tau_{yz} \\ \tau_{zx} \\ \tau_{xy} \\ D_x \\ D_y \\ D_z \end{Bmatrix} = \begin{bmatrix} \bar{C}_{11} & \bar{C}_{12} & \bar{C}_{13} & 0 & 0 & \bar{C}_{16} & 0 & 0 & -\bar{e}_{31} \\ \bar{C}_{12} & \bar{C}_{22} & \bar{C}_{23} & 0 & 0 & \bar{C}_{26} & 0 & 0 & -\bar{e}_{32} \\ \bar{C}_{13} & \bar{C}_{23} & \bar{C}_{33} & 0 & 0 & \bar{C}_{36} & 0 & 0 & -\bar{e}_{33} \\ 0 & 0 & 0 & \bar{C}_{44} & \bar{C}_{45} & 0 & -\bar{e}_{14} & -\bar{e}_{24} & 0 \\ 0 & 0 & 0 & \bar{C}_{45} & \bar{C}_{55} & 0 & -\bar{e}_{15} & -\bar{e}_{25} & 0 \\ \bar{C}_{16} & \bar{C}_{26} & \bar{C}_{36} & 0 & 0 & \bar{C}_{66} & 0 & 0 & -\bar{e}_{36} \\ 0 & 0 & 0 & \bar{e}_{14} & \bar{e}_{15} & 0 & \bar{\epsilon}_{11} & \bar{\epsilon}_{12} & 0 \\ 0 & 0 & 0 & \bar{e}_{24} & \bar{e}_{25} & 0 & \bar{\epsilon}_{12} & \bar{\epsilon}_{22} & 0 \\ \bar{e}_{31} & \bar{e}_{32} & \bar{e}_{33} & 0 & 0 & \bar{e}_{36} & 0 & 0 & \bar{\epsilon}_{33} \end{bmatrix}$$

$$\times \left\{ \varepsilon_{xx}\ \varepsilon_{yy}\ \varepsilon_{zz}\ \gamma_{yz}\ \gamma_{zx}\ \gamma_{xy}\ E_x\ E_y\ E_z \right\}^T \ , \tag{11.6}$$

where $\gamma_{yz} = 2\varepsilon_{yz}$, $\gamma_{zx} = 2\varepsilon_{zx}$, $\gamma_{xy} = 2\varepsilon_{xy}$.

Since the composite beams with embedded piezoelectric patches are considered, a plane stress condition in the vertical $X - Z$ plane (Figure 11.3) needs to be developed from the three-dimensional constitutive relation as in Equation (11.6). In addition, only the application of the electric field along the Z-axis and the corresponding surface charge in the electrodes parallel to the $X - Y$ plane associated with electric displacement D_z will be sufficient to describe the transduction for layered configuration. For piezoelectric stack configuration, this will be discussed next. Now, for the layered configuration (with parallel electrodes in the $X - Y$ plane), treatment in vertical $X - Z$ plane is equivalent to neglecting the effect of electric displacements D_x and D_y in the planes $Y - Z$ and $X - Z$ parallel to which there are no electrodes. Imposing $\sigma_{yy} = 0$, $\tau_{xy} = 0$, $\tau_{yz} = 0$, $D_x = 0$ and $D_y = 0$ in Equation (11.6) and eliminating the out-of-plane strains ε_{yy}, γ_{xy} and γ_{yz} and the electric fields E_x and E_y, the reduced form of the constitutive relation for piezoelectric layered configurations can be expressed as

$$\begin{Bmatrix} \sigma_{xx} \\ \sigma_{zz} \\ \tau_{zx} \\ D_z \end{Bmatrix} = \begin{bmatrix} \bar{Q}_{11} & \bar{Q}_{13} & 0 & -\bar{\bar{e}}_{31} \\ \bar{Q}_{13} & \bar{Q}_{33} & 0 & -\bar{\bar{e}}_{33} \\ 0 & 0 & \bar{Q}_{55} & 0 \\ \bar{\bar{e}}_{31} & \bar{\bar{e}}_{33} & 0 & \bar{\bar{\epsilon}}_{33} \end{bmatrix} \begin{Bmatrix} \varepsilon_{xx} \\ \varepsilon_{zz} \\ \gamma_{zx} \\ E_z \end{Bmatrix} , \tag{11.7}$$

where

$$\bar{Q}_{11} = \bar{C}_{11} + \frac{1}{\Delta}\left[\bar{C}_{12}(\bar{C}_{26}\bar{C}_{16} - \bar{C}_{66}\bar{C}_{12}) + \bar{C}_{16}(\bar{C}_{26}\bar{C}_{12} - \bar{C}_{22}\bar{C}_{16})\right] , \tag{11.8a}$$

$$\bar{Q}_{13} = \bar{C}_{13} + \frac{1}{\Delta}\left[\bar{C}_{12}(\bar{C}_{26}\bar{C}_{36} - \bar{C}_{66}\bar{C}_{23}) + \bar{C}_{16}(\bar{C}_{26}\bar{C}_{23} - \bar{C}_{22}\bar{C}_{36})\right] , \tag{11.8b}$$

$$\bar{Q}_{33} = \bar{C}_{33} + \frac{1}{\Delta}\left[\bar{C}_{23}(\bar{C}_{26}\bar{C}_{36} - \bar{C}_{66}\bar{C}_{23}) + \bar{C}_{36}(\bar{C}_{26}\bar{C}_{23} - \bar{C}_{22}\bar{C}_{36})\right] , \tag{11.8c}$$

$$\bar{Q}_{55} = \bar{C}_{55} - \bar{C}_{45}^2/\bar{C}_{44} , \tag{11.8d}$$

$$\bar{\bar{e}}_{31} = \bar{e}_{31} - \frac{1}{\Delta}\left[\bar{e}_{32}(\bar{C}_{12}\bar{C}_{66} - \bar{C}_{16}\bar{C}_{26}) + \bar{e}_{36}(\bar{C}_{16}\bar{C}_{22} - \bar{C}_{12}\bar{C}_{26})\right] , \tag{11.8e}$$

$$\bar{\bar{e}}_{33} = \bar{e}_{33} - \frac{1}{\Delta}\left[\bar{e}_{32}(\bar{C}_{23}\bar{C}_{66} - \bar{C}_{26}\bar{C}_{36}) + \bar{e}_{36}(\bar{C}_{22}\bar{C}_{36} - \bar{C}_{23}\bar{C}_{26})\right] , \tag{11.8f}$$

$$\bar{\bar{\epsilon}}_{33} = \bar{\epsilon}_{33} + \frac{1}{\Delta}\left[\bar{e}_{36}(\bar{C}_{22}\bar{e}_{36} - \bar{C}_{26}\bar{e}_{32}) + \bar{e}_{32}(\bar{e}_{32}\bar{C}_{66} - \bar{C}_{26}\bar{e}_{36})\right] , \tag{11.8g}$$

$$\Delta = -\bar{C}_{26}^2 + \bar{C}_{22}\bar{C}_{66} . \tag{11.8h}$$

For piezoelectric layered configuration (Figure 11.3(b)) with assumed shear deformable kinematics in the $X - Z$ plane, the required constitutive model from Equation (11.7) finally becomes

$$\begin{Bmatrix} \sigma_{xx} \\ \tau_{zx} \\ D_z \end{Bmatrix} = \begin{bmatrix} \bar{Q}_{11} & 0 & -\bar{\bar{e}}_{31} \\ 0 & \bar{Q}_{55} & 0 \\ \bar{\bar{e}}_{31} & 0 & \bar{\bar{\epsilon}}_{33} \end{bmatrix} \begin{Bmatrix} \varepsilon_{xx} \\ \gamma_{zx} \\ E_z \end{Bmatrix} . \tag{11.9}$$

The above equation also holds for passive fiber reinforced polymer matrix composite layers with $\bar{\bar{e}}_{31} = 0$ and $\bar{\bar{\epsilon}}_{33}$ almost negligible compared to the piezoelectric materials.

For piezoelectric stack configuration Figure 11.3(a), the constitutive model becomes

$$\begin{Bmatrix} \sigma_{xx} \\ \tau_{zx} \\ D_x \end{Bmatrix} = \begin{bmatrix} \bar{Q}_{33} & 0 & -\bar{\bar{e}}_{33} \\ 0 & \bar{Q}_{55} & 0 \\ \bar{\bar{e}}_{33} & 0 & \bar{\bar{\epsilon}}_{33} \end{bmatrix} \begin{Bmatrix} \varepsilon_{xx} \\ \gamma_{zx} \\ E_x \end{Bmatrix} , \tag{11.10}$$

as the actuation of the stack happens along the X direction, which is the same as the direction vector of the electric field, *i.e.,* x_3 as shown in Figure 11.3(a) having material coordinate (x_1, x_2, x_3) for the individual stack. For passive fiber reinforced polymer matrix composite, the constitutive model remains the same as discussed in the context of Equation (11.9).

11.3.2 Constitutive Model for Piezoelectric Fiber Composite (PFC)

Use of PFCs for structural actuation is discussed in Section 11.2. In the following section, we derive a constitutive model of the PFC based on shear stress transfer from active fiber to the surrounding matrix and a uniform field model of the representative volume element (RVE). Also, the frequency dependent dielectric property of the active fiber and viscoelastic properties of the polymer matrix are considered in the model. Typical configuration of the PFC actuator bonded with the host composite beam structure is shown in Figure 11.4.

The RVE of the two-phase piezoceramic matrix composite system can be described by one quadrant axisymmetric model about the x_3 axis. Here, h is the total depth of a single PFC layer, p is the uniform spacing of IDEs spanning along x_1, and b is the width of each electrode. Similar configuration with uniform square packing circular fiber and rectangular packing square fiber is also possible [274]. Before obtaining the uniform field model as reported in [274], we first consider the nature of stress transfer from the active fiber to the surrounding matrix. The objective is to obtain an equivalent constitutive model from the bulk properties of piezo fiber and matrix. This is then used in the uniform field model.

Let us consider a uniform circular fiber of length L embedded in matrix as shown in Figure 11.5. The constitutive relation for linear orthotropic piezoelectric material excluding the uncoupled shear modes, can be expressed using [293] as

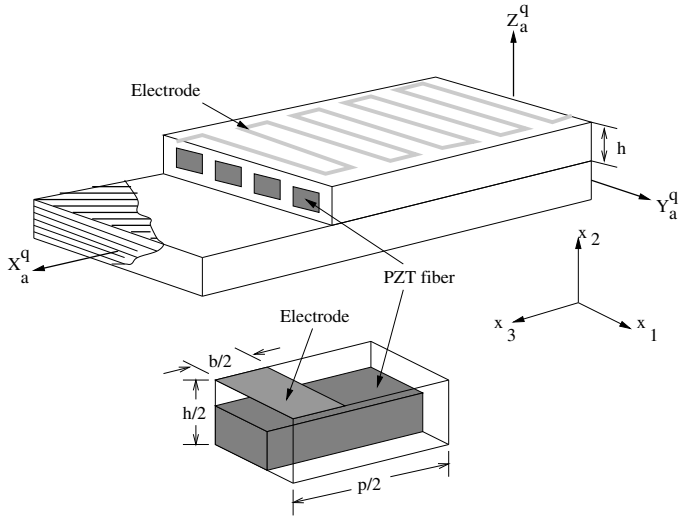

Fig. 11.4. Configuration of a square fiber PFC for distributed actuation. The RVE for rectangular packing square fiber and a segment of IDE is shown in the inset

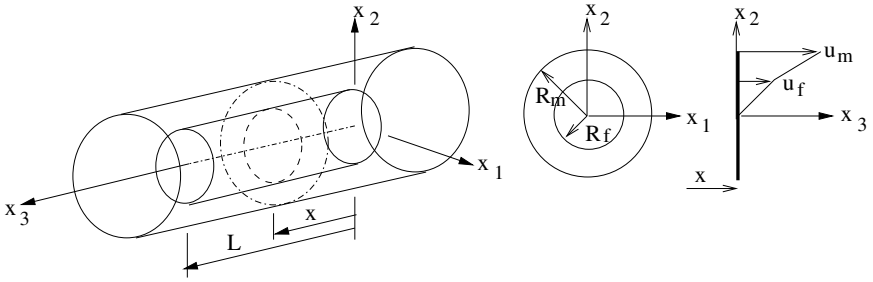

Fig. 11.5. Shear lag model of active uniform circular fiber embedded in matrix

$$\begin{Bmatrix} \sigma_{11} \\ \sigma_{22} \\ \sigma_{33} \\ D_3 \end{Bmatrix} = \begin{bmatrix} C_{11}^E & C_{12}^E & C_{13}^E & -e_{31} \\ C_{12}^E & C_{22}^E & C_{23}^E & -e_{32} \\ C_{13}^E & C_{23}^E & C_{33}^E & -e_{33} \\ e_{31} & e_{32} & e_{33} & \epsilon_{33}^{\varepsilon} \end{bmatrix} \begin{Bmatrix} \varepsilon_{11} \\ \varepsilon_{22} \\ \varepsilon_{33} \\ E_3 \end{Bmatrix} . \tag{11.11}$$

The material coordinate system is (x_1, x_2, x_3) as shown in Figure 11.5. For pure piezoceramic, $C_{11}^E = C_{22}^E$, $C_{23}^E = C_{13}^E$, $e_{32} = e_{31}$. Under dynamic actuation, the electric field consists of DC and AC components, thus

$$\mathbf{E} = \mathbf{E}_{\mathrm{DC}} + \mathbf{E}_{\mathrm{AC}} . \tag{11.12}$$

Due to the presence of the AC field with frequency ω, the dielectric will have frequency dependence. Here, a non-resonant model [274] can be used, where it is assumed that the polarization relaxation modes and the internal electromechanical resonance are outside the frequency range (typically 1 Hz to 10

kHz) of interest. In this approach, the complex dielectric of bulk piezoceramic can be expressed as

$$\epsilon^{\varepsilon} = \epsilon(1 - jd) - \frac{j}{\omega\rho} , \tag{11.13}$$

where ϵ is the real dielectric constant, d is the dielectric loss factor and ρ is the resistivity. Similarly, to include the effect of piezoelectric shunting and mechanical losses, the elastic coefficients can be replaced by their complex equivalent as

$$\mathbf{C}^{E} = \mathbf{C}(1 - j\eta_f) , \tag{11.14}$$

where $\mathbf{C}$ is the real elastic coefficient and η_f is the frequency dependent mechanical loss factor in piezoceramic fiber. A detailed characterization of the above complex properties of bulk PZT can be found in [274]. For matrix phase, all e_{ij} are zero, and their mechanical and dielectric properties are represented without superscripts. Similarly, for inactive fibers in the host structure, all e_{ij} and $\epsilon_{ij}^{\varepsilon}$ have negligible effect. The rate dependence of the viscoelastic matrix in bulk form can be included in the constitutive model as

$$\mathbf{C} = \mathbf{C}' + j\mathbf{C}'' , \tag{11.15}$$

where C' and C'' are respectively the real and imaginary components of the complex modulus and are characterized by the frequency dependent loss factor

$$\eta_m = \frac{C'}{C''} . \tag{11.16}$$

For fibers perfectly bonded in the matrix, a shear lag model accurately described the stress transfer in composite. Such a shear lag model has been used in [294] to study active fiber fragmentation in PFC. Following this model, the fiber axial load in the RVE (shown in Figure 11.5) is transferred to the fiber according the relation

$$\frac{d\sigma_{33}^{f}}{dx} = H(u_f - u_m) , \tag{11.17}$$

where σ_{33}^{f} is the stress in the fiber and is assumed constant at the cross-section located at x (Figure 11.5). u_f is the axial displacement at surface ($r = R_f$) of the fiber. u_m is the axial displacement at $r = R_m$ in the matrix and is assumed to be unaffected by the shear stress transferred from the fiber-matrix interface. In PFCs, R_m is typically taken as half of the center-to-center distance between the fibers. H is a constant for given bulk material properties and geometry of RVE. Differentiating both side of Equation (11.17) once with respect to x, we get

$$\frac{d^2\sigma_{33}^{f}}{dx^2} = H(\frac{du_f}{dx} - \frac{du_m}{dx}) . \tag{11.18}$$

du_f/dx is the axial strain in the fiber and is related to the fiber stress through the constitutive relation Equation (11.11) as

$$\sigma_{33}^{f} = C_{33}^{E} \frac{du_f}{dx} - e_{33} E_3 \ . \tag{11.19}$$

Substituting Equation (11.19) in Equation (11.18) and assuming E_3 and $\varepsilon_{33} = du_m/dx$ as constants in the RVE, we get a second-order differential equation in σ_{33}^{f} with constant coefficients, which is given by

$$\frac{d^2\sigma_{33}^{f}}{dx^2} - \frac{H}{C_{33}^{E}}\sigma_{33}^{f} - H\left(\frac{e_{33}E_3}{C_{33}^{E}} - \varepsilon_{33}\right) = 0 \ . \tag{11.20}$$

Solution of Equation (11.20) is of the form

$$\sigma_{33}^{f} = C_{33}^{E} - e_{33}E_3 + S_1 e^{\left(\sqrt{H/C_{11}^{E}}\right)x} + S_2 e^{-\left(\sqrt{H/C_{11}^{E}}\right)x} \ , \tag{11.21}$$

where S_1 and S_2 are constants of integration and depend on the stress boundary conditions at the fiber ends. To obtain explicit form for the constant H, we need to equate the fiber axial force with the transferred shear force at the fiber-matrix interface. At surface $r = R_f$, this can be written as

$$\pi R_f^2 d\sigma_{33}^{f} = -2\pi R_f \tau(R_f) dx \ , \tag{11.22}$$

where $\tau(R_f)$ is the fiber surface shear stress. The shear strain can be expressed as

$$\frac{du}{dr} = \frac{\tau(r)}{C_{55}} = \frac{R_f \tau(R_f)}{r C_{55}} \ . \tag{11.23}$$

Integrating Equation (11.23) over the region of tress transfer, *i.e.,* $r = R_f$ to $r = R_m$ and using Equations (11.17) and (11.22), we get

$$H = \frac{2C_{55}}{R_f^2 \ln\left(\frac{R_m}{R_f}\right)} \ . \tag{11.24}$$

Assuming the PFCs are bonded on the surface of the host composite (Figure 11.4) the stress boundary condition at the fiber ends ($x = 0, L$) becomes $\sigma_{33}^{f} = 0$. However, for embedded PFCs, one needs to use a dynamic stress boundary obtained from purely mechanical analysis of the host composite without embedded PFCs. This is beyond the scope of the present study and hence will not be attempted. Now, after eliminating S_1 and S_2 from Equation (11.17) by substituting the above stress boundary conditions at the fiber ends, the axial stress in the fiber can be expressed as

$$\sigma(x)_{33}^{f} = \left(C_{33}^{E}\varepsilon_{33} - e_{33}E_3\right)\psi_\sigma \ , \tag{11.25}$$

where ψ_σ is the axial stress recovery factor given by

$$\psi_\sigma = 1 - \frac{\cosh\left[\sqrt{\frac{H}{C_{33}^{E}}}\left(\frac{L}{2} - x\right)\right]}{\cosh\left(\sqrt{\frac{H}{C_{33}^{E}}}\frac{L}{2}\right)} \ . \tag{11.26}$$

The shear stress transferred to the matrix can be expressed as

$$\tau(r,x) = \left(C_{33}^{E}\varepsilon_{33} - e_{33}E_3\right)\psi_\tau \ , \tag{11.27}$$

where ψ_τ is the shear stress recovery factor given by

$$\psi_\tau = \left(\frac{R_f}{r}\right)\frac{1}{\sqrt{2\ln\left(\frac{R_m}{R_f}\right)}}\sqrt{\frac{C_{55}}{C_{33}^{E}}}\frac{\sinh\left[\sqrt{\frac{H}{C_{33}^{E}}}\left(\frac{L}{2}-x\right)\right]}{\sinh\left[\sqrt{\frac{H}{C_{33}^{E}}}\frac{L}{2}\right]} \ . \tag{11.28}$$

Effect of Stress Recovery in PFC

To obtain maximum actuator authority for prescribed bulk material properties while designing PFCs, one needs to have maximum specific actuation, given by

$$\sigma_{SA} = \frac{\int \sigma_{33}^{f} dAdx}{\int dAdx} \tag{11.29}$$

with the shear stress τ at the fiber ends below the allowable shear stress for fiber-matrix debonding. Now, for prescribed mechanical strain and electrical input (voltage or current), maximizing σ_{SA} means maximizing the axial stress recovery factor ψ_σ with respect to the fiber volume in the RVE. And to ensure that fiber fragmentation does not occur for the chosen fiber length L, the shear stress at the fiber-matrix interface at the fiber ends must be kept below the allowable shear stress ($\tau_{\max}$) for fiber-matrix debonding, *i.e.,*

$$|\tau(R_f,0)| = |\tau(R_f,L)| < \tau_{\max} \ . \tag{11.30}$$

Figures 11.6 and 11.7 show the variations in ψ_σ and ψ_τ along the length of the fiber. From Figure 11.6 it can be seen that for a specified fiber radius R_f, the order of the shear stress at the fiber-matrix interface at the fiber ends is almost constant and of the same order as the axial stress irrespective of the fiber length. On the other hand Figure. 11.7 shows that for specified fiber length, the shear stress at the fiber-matrix interface near the fiber ends can be much higher than the axial stress developed in fibers of higher radius. Note that for a particular fiber length and radius, maximum axial stress is developed over the fiber span x having $\sigma_{33}^{f} \approx 1$. Therefore, this span can be defined as the specific length of the PFC, since it is actually a measure of the distributed actuation. Also note that the specific actuation σ_{SA} in Equation (11.29) represents the same information for a specified electromechanical loading.

For a particular structural dynamic actuation and optimal control performance of PFC, the fiber length constraint has something to do with the control cost function and is problem specific. Before obtaining the optimal length of PFC actuators based on analysis of the host structure with integrated PFCs and error sensors, we need a macroscopic constitutive model, which can be used to accurately capture the microscopic behavior of PFCs. The uniform field model as discussed earlier is considered for this purpose.

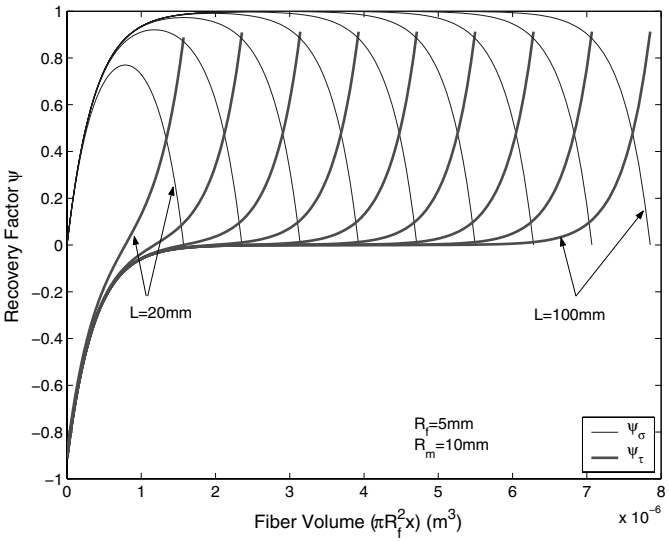

Fig. 11.6. Nature of axial and shear stress recovery in circular PZT fiber embedded in matrix for varying fiber length

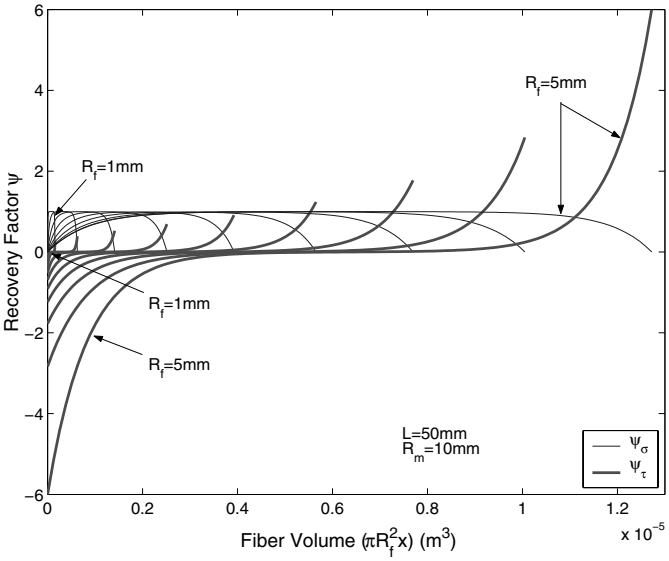

Fig. 11.7. Nature of axial and shear stress recovery in circular PZT fiber embedded in matrix for varying fiber radius.

Uniform Field Model

Although the uniform field model, in some cases, violates the compatibility and equilibrium of electrostatics, it provides a sufficiently accurate macroscopic constitutive model in the case of large material mismatches between the individual phases. The finite element predictions as well as the experimental characterization reported in [46] validates this fact. In addition, various analyses in closed form can be carried out based on this model while optimizing the actuator authority of PFCs.

Let us consider the RVE shown in the inset of Figure 11.4, which is a one quadrant fibermatrix mixture with a segment of electrode on the top surface. Figure 11.8 shows the corresponding representation of the equivalent multi-phase mixture of the RVE having fiber volume fraction $\nu_1^f \nu_2^f \nu_3^f$ through the cases A, B and C. The basic assumption here is that the electric field in the active fiber is dominated by the component E_3, although there will be dominance of component E_2 near the electrodes, which is neglected. The

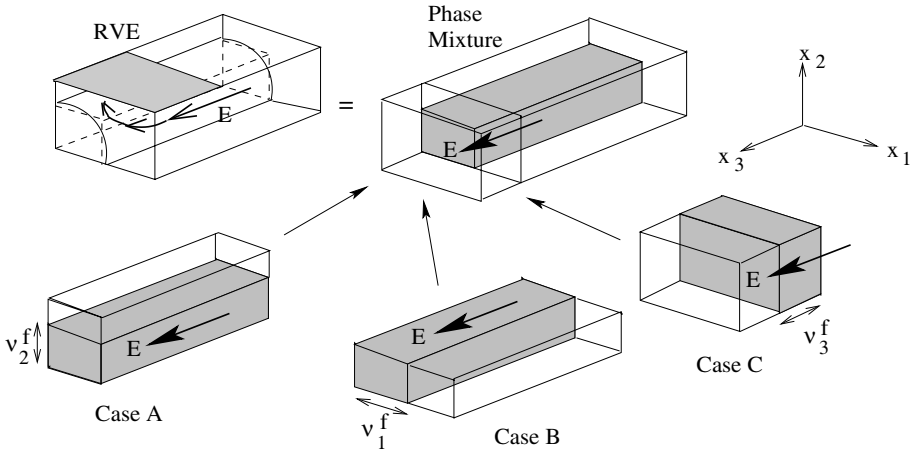

Fig. 11.8. Representative volume element (RVE) showing the uniform field model geometry. Case A, B and C represent the individual two-phase mixtures. E indicates the direction of electric field (same as the direction of the polarization vector)

complete phase mixture is obtained from the combination of the three cases. The effective properties from one case is substituted for the properties of the piezoceramic fiber phase (f) in the next case. The matrix phase is denoted by m. For each case (A, B, C), the piezoceramic phase (f) is kept fully orthotropic to accommodate the higher degree of anisotropy that a composite produces. While obtaining the mixture in the three cases sequentially, the first step is to identify the field variables which are equal in both phases. In case A, these fields are ε_{11}, σ_{22}, ε_{33} and E_3. The conjugate of these fields can be obtained by rearranging Equation (11.11) (without superscript E for matrix phase) in

the two phases as

$$\left\{\begin{array}{c}\sigma_{11}\\ \varepsilon_{22}\\ \sigma_{33}\\ D_3\end{array}\right\}_{f,m} = \mathbf{A}_{f,m}\left\{\begin{array}{c}\varepsilon_{11}\\ \sigma_{22}\\ \varepsilon_{33}\\ E_3\end{array}\right\}_{f,m} , \tag{11.31}$$

where the elements of the matrix $\mathbf{A}_{f,m}$ are functions of the bulk material properties (elastic coefficients, electromechanical coupling factors and dielectric coefficients) of the two phases. The average fields can be expressed as the linear combination (weighted with the volume fraction of the phases) of Equation (11.31) as

$$\left\{\begin{array}{c}\bar{\sigma}_{11}\\ \bar{\varepsilon}_{22}\\ \bar{\sigma}_{33}\\ \bar{D}_3\end{array}\right\} = \nu_2^f\left\{\begin{array}{c}\sigma_{11}\\ \varepsilon_{22}\\ \sigma_{33}\\ D_3\end{array}\right\}_f + \nu_2^m\left\{\begin{array}{c}\sigma_{11}\\ \varepsilon_{22}\\ \sigma_{33}\\ D_3\end{array}\right\}_m = \bar{\mathbf{A}}\left\{\begin{array}{c}\bar{\varepsilon}_{11}\\ \bar{\sigma}_{22}\\ \bar{\varepsilon}_{33}\\ \bar{E}_3\end{array}\right\} , \tag{11.32}$$

where $\bar{\mathbf{A}} = \nu_2^f\mathbf{A}_f + \nu_2^m\mathbf{A}_m$. Rearranging the average conjugate fields obtained from Equation (11.32), the equivalent constitutive model for Case A can be written as

$$\left\{\begin{array}{c}\bar{\sigma}_{11}\\ \bar{\sigma}_{22}\\ \bar{\sigma}_{33}\\ \bar{D}_3\end{array}\right\} = \left[\begin{array}{cccc}\bar{C}_{11} & \bar{C}_{12} & \bar{C}_{13} & -\bar{e}_{31}\\ \bar{C}_{12} & \bar{C}_{22} & \bar{C}_{23} & -\bar{e}_{32}\\ \bar{C}_{13} & \bar{C}_{23} & \bar{C}_{33} & -\bar{e}_{33}\\ \bar{e}_{31} & \bar{e}_{32} & \bar{e}_{33} & \bar{\epsilon}_{33}\end{array}\right]_A \left\{\begin{array}{c}\bar{\varepsilon}_{11}\\ \bar{\varepsilon}_{22}\\ \bar{\varepsilon}_{33}\\ \bar{E}_3\end{array}\right\} , \tag{11.33}$$

where

$$\bar{C}_{11} = (C_{11}^E\nu_2^f + C_{11}\nu_2^m) - \frac{1}{\Delta_1}\nu_2^f\nu_2^m(C_{12} - C_{12}^E)^2 , \tag{11.34a}$$

$$\bar{C}_{12} = \frac{1}{\Delta_1}(C_{12}^E C_{11}\nu_2^f + C_{12}C_{22}^E\nu_2^m) , \tag{11.34b}$$

$$\bar{C}_{22} = \frac{1}{\Delta_1}C_{22}^E C_{11} , \tag{11.34c}$$

$$\bar{C}_{13} = (C_{13}^E\nu_2^f + C_{12}\nu_2^m) - \frac{1}{\Delta_1}\nu_2^f\nu_2^m(C_{12} - C_{12}^E)(C_{12} - C_{23}^E) , \tag{11.34d}$$

$$\bar{C}_{23} = \frac{1}{\Delta_1}(C_{23}^E C_{11}\nu_2^f + C_{12}C_{22}^E\nu_2^m) , \tag{11.34e}$$

$$\bar{C}_{33} = (C_{33}^E\nu_2^f + C_{11}\nu_2^m) - \frac{1}{\Delta_1}\nu_2^f\nu_2^m(C_{12} - C_{23}^E)^2 , \tag{11.34f}$$

$$\bar{e}_{31} = e_{31}\nu_2^f + \frac{1}{\Delta_1}e_{32}\nu_2^f\nu_2^m(C_{12} - C_{12}^E) , \tag{11.34g}$$

$$\bar{e}_{32} = \frac{1}{\Delta_1}e_{32}\nu_2^f C_{11} , \tag{11.34h}$$

$$\bar{e}_{33} = e_{33}\nu_2^f + \frac{1}{\Delta_1} e_{32}\nu_2^f \nu_2^m (C_{12} - C_{23}^E) \,, \tag{11.34i}$$

$$\bar{\epsilon}_{33} = (\epsilon_{33}^{\varepsilon}\nu_2^f + \epsilon_{33}\nu_2^m)\frac{1}{\Delta_1} e_{32}^2 \nu_2^f \nu_2^m \,, \tag{11.34j}$$

$$\Delta_1 = C_{11}\nu_2^f + C_{22}^E \nu_2^m \,. \tag{11.34k}$$

Since the direction of the electric field (direction of polarization) is assumed to be uniform, the equivalent constitutive model in Case B is obtained by interchanging the subcripts 1 and 2 with the independent fields in both phases; *i.e.,* σ_{11}, ε_2, ε_3 and E_3. Case C accommodates the effect of the region below the electrode, where the independent field variables in both phases are ε_{11}, ε_{22}, σ_{33} and D_3. Following the same reasoning as in Equation (11.34), here we can write

$$\begin{Bmatrix} \sigma_{11} \\ \sigma_{22} \\ \varepsilon_{33} \\ E_3 \end{Bmatrix}_{f,m} = \mathbf{C}_{f,m} \begin{Bmatrix} \varepsilon_{11} \\ \varepsilon_{22} \\ \sigma_{33} \\ D_3 \end{Bmatrix}_{f,m} \,. \tag{11.35}$$

Unlike Case A and B, the macroscopic mechanical properties are dominated by the piezoceramic phase, and this is consistent with the assumption that the matrix phase does not contribute to the mechanical response in Case C. Thus the equivalent fields are

$$\bar{\sigma}_{11} = \sigma_{11}^f \,, \quad \bar{\sigma}_{22} = \sigma_{22}^f \,, \quad \bar{\varepsilon}_{33} = \varepsilon_{33}^f \tag{11.36a}$$

$$\bar{E}_3 = \nu_3^f E_3^f + \nu_3^f E_3^m \,, \tag{11.36b}$$

where the electric field strength depends on the separation of the piezoceramic phase from the electrode and the electrode geometry. Therefore, combination of Case C with Cases A and B depends on the nature of piezoceramic fiber and IDE width and spacing. Typically, for uniform packing circular/square fiber ($\nu_1^f = \nu_2^f$), the line fraction of piezoceramic phase ν_3^f is obtained as the ratio of the electric field path length from the Case A (or Case B) and the total path length between the electrode surfaces (Figure 11.4), *i.e.,*

$$\nu_3^f = \frac{p/2}{p/2 + \nu_2^m h/2} = \frac{p/h}{p/h + (1 - \nu_2^f)} \qquad (b << p) \,. \tag{11.37}$$

whereas for rectangular packing (the packing fraction X_2 can be as high as 0.92), there can be negligible separation between the piezoceramic phase and the electrodes and therefore

$$\nu_3^f = \frac{p/h}{p/h + (1 - X_2)} \qquad (b << p) \tag{11.38}$$

Also, this localized influence of electric field path on the piezoceramic phase needs to be accounted for first rather than the effect of the fields along the

fiber length. Hence, the accurate equivalent constitutive relation based on the uniform field model for rectangular packing PFC should follow the combination $C \rightarrow A \rightarrow B$, and for uniform packing PFC, the combination should be $A \rightarrow B \rightarrow C$. A detailed discussion of these issues and related procedure for experimental characterization can be found in [46]. Now for Case C, following the averaging of fields from Equations (11.36) as

$$\begin{Bmatrix} \bar{\sigma}_{11} \\ \bar{\sigma}_{22} \\ \bar{\varepsilon}_{33} \\ \bar{E}_3 \end{Bmatrix} = \begin{Bmatrix} \sigma_{11} \\ \sigma_{22} \\ \sigma_{33} \\ \nu_3^f E_3 \end{Bmatrix}_f + \begin{Bmatrix} \sigma_{11} \\ \sigma_{22} \\ \sigma_{33} \\ \nu_3^m E_3 \end{Bmatrix}_m = \bar{\mathbf{C}} \begin{Bmatrix} \bar{\varepsilon}_{11} \\ \bar{\varepsilon}_{22} \\ \bar{\sigma}_{33} \\ \bar{D}_3 \end{Bmatrix} \tag{11.39}$$

and rearranging, we get the effective constitutive model for case C as

$$\begin{Bmatrix} \bar{\sigma}_{11} \\ \bar{\sigma}_{22} \\ \bar{\sigma}_{33} \\ \bar{D}_3 \end{Bmatrix} = \begin{bmatrix} \bar{C}_{11} & \bar{C}_{12} & \bar{C}_{13} & -\bar{e}_{31} \\ \bar{C}_{12} & \bar{C}_{22} & \bar{C}_{23} & -\bar{e}_{32} \\ \bar{C}_{13} & \bar{C}_{23} & \bar{C}_{33} & -\bar{e}_{33} \\ \bar{e}_{31} & \bar{e}_{32} & \bar{e}_{33} & \bar{\epsilon}_{33} \end{bmatrix}_C \begin{Bmatrix} \bar{\varepsilon}_{11} \\ \bar{\varepsilon}_{22} \\ \bar{\varepsilon}_{33} \\ \bar{E}_3 \end{Bmatrix} , \tag{11.40}$$

where

$$\bar{C}_{jk} = C_{jk} + \frac{1}{\Delta_3} \nu_3^m e_{3j} e_{3k} , \tag{11.41a}$$

$$\bar{e}_{3j} = \frac{1}{\Delta_3} \epsilon_{33} e_{3j} , \tag{11.41b}$$

$$\bar{\epsilon}_{33} = \frac{1}{\Delta_3} \epsilon_{33} \epsilon_{33}^{\varepsilon} , \tag{11.41c}$$

$$\Delta_3 = \nu_2^f \epsilon_{33} + \nu_3^m \epsilon_{33}^{\varepsilon} . \tag{11.41d}$$

Following the sequence for combination of the three cases as discussed earlier, the effective constitutive model for the RVE is obtained as

$$\begin{Bmatrix} \sigma_{11} \\ \sigma_{22} \\ \sigma_{33} \\ \sigma_{23} \\ \sigma_{31} \\ \sigma_{12} \\ D_3 \end{Bmatrix} = \begin{bmatrix} C_{11}^{\text{eff}} & C_{12}^{\text{eff}} & C_{13}^{\text{eff}} & 0 & 0 & 0 & -e_{31}^{\text{eff}} \\ C_{12}^{\text{eff}} & C_{22}^{\text{eff}} & C_{23}^{\text{eff}} & 0 & 0 & 0 & -e_{32}^{\text{eff}} \\ C_{13}^{\text{eff}} & C_{23}^{\text{eff}} & C_{33}^{\text{eff}} & 0 & 0 & 0 & -e_{33}^{\text{eff}} \\ 0 & 0 & 0 & C_{44}^{\text{eff}} & 0 & 0 & 0 \\ 0 & 0 & 0 & 0 & C_{55}^{\text{eff}} & 0 & 0 \\ 0 & 0 & 0 & 0 & 0 & C_{66}^{\text{eff}} & 0 \\ e_{31}^{\text{eff}} & e_{32}^{\text{eff}} & e_{33}^{\text{eff}} & 0 & 0 & 0 & \epsilon_{33}^{\text{eff}} \end{bmatrix} \begin{Bmatrix} \varepsilon_{11} \\ \varepsilon_{22} \\ \varepsilon_{33} \\ \varepsilon_{23} \\ \varepsilon_{31} \\ \varepsilon_{12} \\ E_3 \end{Bmatrix} , \tag{11.42}$$

where the effective shear moduli, unlike in the uniform field model, are obtained from the phase morphology, and they can be expressed as

$$C_{kk}^{\text{eff}} = C_{kk}^m \frac{C_{kk}^f (1 + \nu^f) + C_{kk}^m (1 - \nu^f)}{C_{kk}^m (1 + \nu^f) + C_{kk}^f (1 - \nu^f)} , \quad \nu^f = \nu_1^f \nu_2^f \nu_3^f . \tag{11.43}$$

In the numerical simulations carried out in the latter part of this chapter, we use a one-dimensional model of actuation using surface bonded PFC,

where C_{33}^{eff} affects the actuator stiffness, e_{33}^{eff} affects the actuator authority and $\epsilon_{33}^{\text{eff}}$ affects the electrical energy consumption. It can be seen from Equations (11.34) (Case A) that along the length of the fiber between the IDEs, $\bar{C}_{33}$, $\bar{C}_{13}$ and $\bar{C}_{11}$ follow one-dimensional parallel rules of mixtures softened by the matrix, which reduces the transverse clamping effects on the piezoceramics. On the other hand, $\bar{C}_{22}$, $\bar{C}_{23}$ and $\bar{C}_{12}$ essentially follow the series rules of mixtures, with the latter two introducing the Poisson's effects. From Equations (11.41) (Case C), it can be seen that $\bar{C}_{11}$ is modified due to the electrical influence of the matrix phase. This additional term is the difference between the short-circuit and the open-circuit stiffness for the piezoceramic phase. When dielectric mismatch is low ($\epsilon_{33}^{\varepsilon} = \epsilon_{33}$) or the matrix fraction below the electrode is small ($\nu_3^m \to 0$), the above additional stiffening term also vanishes and a nearly short-circuit condition is realized. For more electrically isolated piezoceramic phase (open-circuit condition), the effective dielectric term is simply a series capacitor combination as seen in Equation (11.41c) and the factor of reduction by which the electric field reaches the piezoceramic phase is ϵ_{33}/Δ_3. Use of carbon filler with conventional polymer matrix has shown significant increase in the field strength under open-circuit conditions [46]. Figure. 11.9 shows the variation in the effective PFC stiffness C_{33}^{eff} in the actuator longitudinal direction for varying volume fraction of piezoceramic fiber (PZT 5H) for different stiffness mismatches (C_{33}^{E}/C_{33}). Properties of neat resin with no conductive filler are used for the matrix phase. The variation is linear for a particular stiffness mismatch and the PFC recovers the fiber stiffness at higher volume fraction of fiber. Figure 11.10 shows the variation in the effective PFC actuator authority for varying volume fraction of piezoceramic fiber for different dielectric mismatches ($\epsilon_{33}^{\varepsilon}/\epsilon_{33}$). It can be seen that for higher dielectric mismatch, only a moderate actuator authority can be obtained at very high volume fraction of fiber. For low dielectric mismatch, this is considerably higher for higher volume fraction of fiber. This can be attributed to the lower clamping effect on e_{33}^{eff} due to the dielectric of the matrix phase.

As has been discussed earlier in Section 11.3.2, the PFC actuator length constraint for specified PFC effective properties (hence specified actuator authority) for vibration and wave control will depend on the required control authority defined by the control cost function. The design issues involved in the integrated smart structural system are discussed below.

11.3.3 Design Steps for Broadband Control

Once the bulk material properties of PFC and the IDE geometry are available, one can compute the minimum specific actuation length that can sustain the allowable shear stress due to the assumed electromechanical loading as discussed in Section 11.3.2. After obtaining the effective properties of the chosen PFC actuator as discussed in Section 11.3.2 and its optimal placement, a coupled broadband analysis considering the distributed PFC actuator dynamics

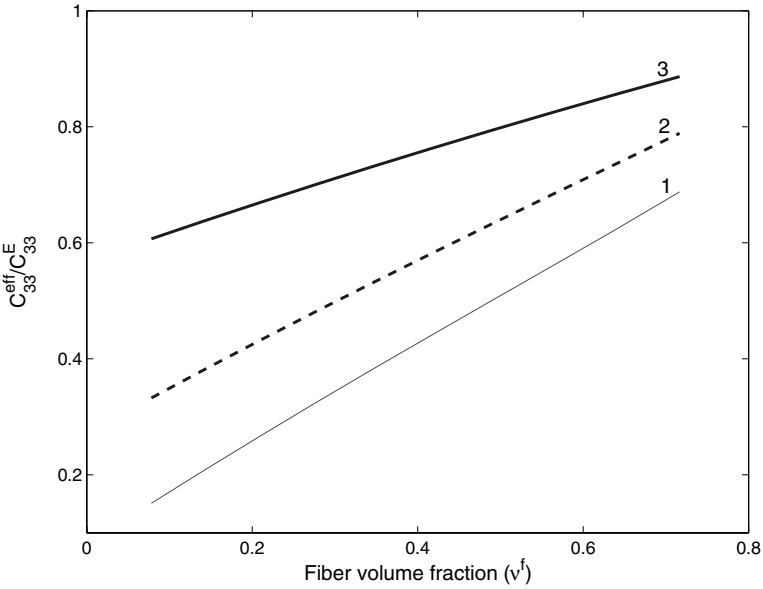

Fig. 11.9. Effective PFC properties for $b/h = 1$, $p/h = 6$. Stiffness constant for $\epsilon_{33}^{\varepsilon}/\epsilon_{33} = 500$ and ratios C_{33}^{E}/C_{33} of 7, 3.5, 1.75 for curves 1, 2, 3 respectively

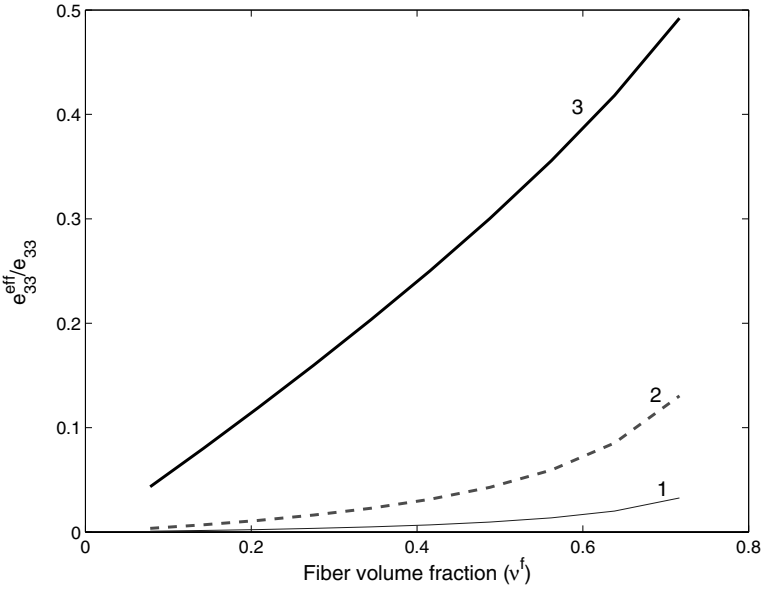

Fig. 11.10. Effective PFC properties for $b/h = 1$, $p/h = 6$. Clamped actuator authority for $C_{33}^{E}/C_{33} = 7$ and ratios $\epsilon_{33}^{\varepsilon}/\epsilon_{33}$ of 500, 100, 10 for curves 1, 2, 3 respectively

needs to be carried out. Since a closed form solution for multiple modal control over broad frequency band is not possible, optimal PFC actuator configuration (length, placement and electrical input) can be obtained by extremizing one or more cost functions over a broadband by iteration, which can be the most general strategy. However, the preliminary information regarding optimal actuator configuration for static and steady-state requirement available in closed form [278] can be used as the initial configuration for optimal control. Also, any additional constraint due to actuator electrical saturation and limited power supply can be imposed for practical applications. Figure 11.11 represents the above design steps for PFC distributed actuation for broadband structural control.

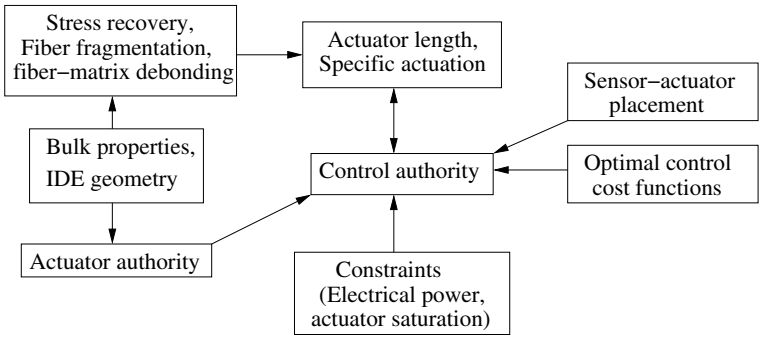

Fig. 11.11. Schematic diagram showing the design steps for PFC distributed actuation for broadband structural control

In the following sections, first we derive an ASFEM for closed-loop broadband control of vibration and waves in composite skeletal structures. The basic framework of the model is based on the SFEs presented in the earlier chapters of the book. Next the effect of distributed PFC actuator dynamics for broadband control is studied using the developed ASFEM. A case study of the active feedback control of multiple wave transmission in helicopter gearbox support-struts is carried out, which brings out the various advantages of ASFEM while dealing with various complexities related to the finite and integrated strut–actuator dynamics and non-collocated feedback control of waves. Further, to develop an efficient and model-based optimal control design methodology, an optimal spectral control scheme based power-flow is developed and integrated with the ASFEM. Performance of this scheme is analyzed using numerical simulation of a MIMO system.

11.4 Active Spectral Finite Element Model

In this model, the beam network is discretized and classified into three different classes of elements. These classes are (1) the spectral element for finite beams with mechanical and passive properties, (2) the distributed or point sensors and (3) the distributed or point actuators. A schematic diagram of a sensor–actuator element configuration is shown in Figure 11.12. Here, it

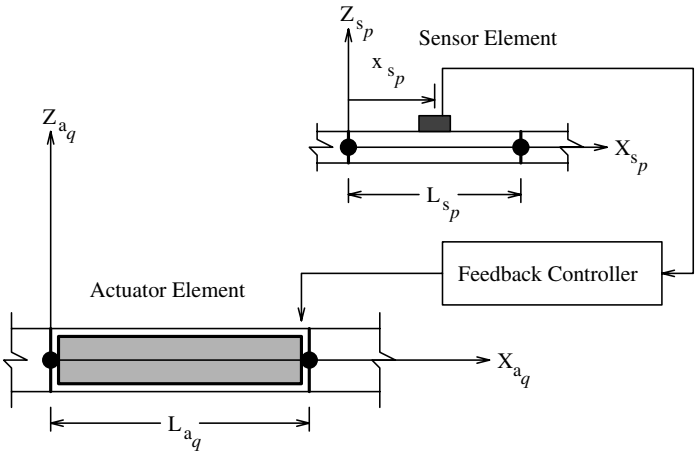

Fig. 11.12. Sensor–actuator element configuration for active spectral finite element model

is assumed that the controller output for a single actuator can be designed based on a feedback signal constructed from a group of sensors. Furthermore, in Figure 11.12, the connectivity between the pth sensor and the qth actuator is also shown, where the sensor response is measured at the local coordinate system (X_s^p, Z_s^p) and the actuation force is provided at the local coordinate system (X_a^q, Z_a^q).

11.4.1 Spectral Element for Finite Beams

The SFEM for composite beams derived in Chapters 4 and 5 can be used here to represent the dynamics. Repeating the element-level equations involving the nodal displacement vector

$$\hat{\mathbf{u}}^e = \{\hat{u}_1^o \; \hat{w}_1 \; \hat{\theta}_1 \; \hat{u}_2^o \; \hat{w}_2 \; \hat{\theta}_2\}^T \; , \tag{11.44a}$$

and the nodal force vector

$$\hat{\mathbf{f}}^e = \{\hat{N}_1 \; \hat{V}_1 \; \hat{M}_1 \; \hat{N}_2 \; \hat{V}_2 \; \hat{M}_2\}^T \; , \tag{11.44b}$$

we have

$$\hat{\mathbf{u}}(x,\omega_n) = \aleph(x,\omega_n)\hat{\mathbf{u}}^e \ , \quad \hat{\mathbf{f}}^e = \hat{\mathbf{K}}^e\hat{\mathbf{u}}^e \ , \tag{11.44c}$$

where $\aleph$ is the exact spectral element shape function matrix and $\hat{\mathbf{K}}^e$ is the exact element dynamic stiffness matrix. The transformation of the element equilibrium equation from local element coordinate system to the global coordinate system is carried out as

$$\hat{\mathbf{u}}^e = \boldsymbol{\Gamma}\hat{\mathbf{U}} \ , \quad \hat{\mathbf{f}}^e = \boldsymbol{\Gamma}\hat{\mathbf{f}} = \boldsymbol{\Gamma}^T\hat{\mathbf{K}}^e\boldsymbol{\Gamma}\hat{\mathbf{U}} \ , \tag{11.44d}$$

where $\boldsymbol{\Gamma}$ is the orthogonal coordinate transformation matrix [1].

11.4.2 Sensor Element

For illustrative purposes, a point sensor has been considered in the modeling. However, it should be noted that the formulation does allow for distributed sensors such as piezoelectric film sensors. The force balance equations for the sensor element are identical in form to Equations (11.44c) and (11.44d). Based on the response measured by a displacement sensor (s), which is located at (x_{s_p}, z_{s_p}) in the pth sensor element (denoted by subscript s_p), the actuator input spectrum can be expressed with the help of Equation (11.44c) as

$$\hat{\eta}_u(x_{s_p}, z_{s_p}, \omega_n) = (j\omega_n)^m \alpha \left[\sum_{j=1}^{6} \left(\aleph_{1j} - z_{s_p}\aleph_{3j} \right) \hat{u}_j^e \right] \ , \tag{11.45a}$$

when the longitudinal displacement is measured, and

$$\hat{\eta}_w(x_{s_p}, z_{s_p}, \omega_n) = (j\omega_n)^m \alpha \left[\sum_{j=1}^{6} \aleph_{2j}\hat{u}_j^e \right] \ , \tag{11.45b}$$

when the transverse displacement is measured. In Equation (11.45a) and (11.45b), α is the sensor sensitivity parameter and $m = 0$, 1, and 2, for displacement, velocity, and acceleration spectra, respectively. Similarly, if a strain sensor is used, one can write the actuator input spectrum as

$$\hat{\eta}_\varepsilon(x_{s_p}, z_{s_p}, \omega_n) = (j\omega_n)^m \alpha \left[\sum_{j=1}^{6} \left(\frac{\partial \aleph_{1j}}{\partial x} - z_{s_p}\frac{\partial \aleph_{3j}}{\partial x} \right) \hat{u}_j^e \right] \ . \tag{11.45c}$$

11.4.3 Actuator Element

In the formulation of ASFEM presented here, we consider the PID (proportional, integral and derivative) feedback control scheme [295]. Other types of frequency domain control schemes, such as feedforward control, can also be

implemented. Controller output in the form of current spectrum ($\hat{I}$) (or voltage spectrum $\hat{\varphi}$) for the qth actuator, and the resulting field (magnetic field $\hat{H}$ for magnetostrictive material or electric field $\hat{E}$ for piezoelectric material) can be written as

$$\hat{I} = \sum_{p} \gamma \hat{\eta} \, , \quad \hat{H} = \beta \hat{I} \, , \quad \hat{\eta} = (\hat{\eta}_u, \hat{\eta}_w, \hat{\eta}_\varepsilon) \, , \tag{11.46}$$

where $\hat{\eta}$ is given by Equation (11.45a), (11.45c). The constant γ is a scalar gain, and β is the actuator sensitivity parameter introduced to account for the actuator assembly and packaging properties (*e.g.,* the solinoid configuration for packaged Terfenol-D rod actuator [296], voltage-to-electric field conversion factor for plane-polarized PZT wafers, *etc.*). Next, after substituting for $\hat{H}$ from the magnetomechanical (or electromechanical) force boundary condition (Equation (11.56a)and(11.56b)) into Equation (11.46) and following the same procedure as used for discretizing the purely mechanical domain using SFE, the force balance equation for the qth actuator element (denoted by subscript a_q) in actuator local coordinate system can be obtained as

$$\hat{\mathbf{f}}^e_{a_q} = \hat{\mathbf{K}}^e_{a_q} \hat{\mathbf{u}}^e_{a_q} + \begin{bmatrix} A^{\text{eff}}_{33} & 0 & -B^{\text{eff}}_{33} & -A^m_{33} & 0 & B^m_{33} \end{bmatrix}^T_{a_q} \beta \gamma \hat{\eta} \, , \tag{11.47}$$

where

$$\left[A^{\text{eff}}_{33}, B^{\text{eff}}_{33}\right] = \int e^{\text{eff}}_{33}[1, z] dA \tag{11.48}$$

defines the equivalent mechanical stiffness due to effective magnetomechanical (or electromechanical) coupling coefficient e^{eff}_{33} (see Equation (11.42) for PFC) for actuation in the longitudinal mode. A similar vector with non-zero second and fifth elements in Equation (11.47) for actuation in the shear mode can also be used. After substituting $\hat{\eta}$ in terms of the sensor element shape function matrix ($\aleph$) and the corresponding nodal displacement vector ($\hat{\mathbf{u}}^e$) from Equation (11.45a)and(11.45b), the Equation (11.48) can be re-written as

$$\hat{\mathbf{f}}^e_{a_q} = \hat{\mathbf{K}}^e_{a_q} \hat{\mathbf{u}}^e_{a_q} + \hat{\mathbf{K}}^e_{a_q \leftarrow s_p} \{\hat{u}\}^e_{s_p} \, , \tag{11.49}$$

where, the notation $\hat{\mathbf{K}}^e_{a_q \leftarrow s_p}$ is introduced to represent the sensor–actuator stiffness influence matrix (SASIM). Equation (11.44d) is followed to obtain the transformation of displacements and forces at the actuator nodes from the local coordinate system to the global coordinate system. This procedure leads to the final expression for the qth actuator element with the pth feedback sensor, which is given by

$$\hat{\mathbf{f}}_{a_q} = \mathbf{\Gamma}^T_{a_q} \hat{\mathbf{K}}^e_{a_q} \mathbf{\Gamma}_{a_q} \hat{\mathbf{U}}_{a_q} + \mathbf{\Gamma}^T_{a_q} \hat{\mathbf{K}}^e_{a_q \leftarrow s_p} \mathbf{\Gamma}_{s_p} \hat{\mathbf{U}}_{s_p} \, . \tag{11.50}$$

Hence, the assembled closed-loop MIMO system with general sensor–actuator configuration in the ASFEM is obtained in the form

$$\left\{\begin{array}{c}\hat{\mathbf{f}}_{s_p}\\ \vdots\\ \hat{\mathbf{f}}_{a_q}\end{array}\right\} = \left[\begin{array}{ccc}\boldsymbol{\Gamma}_{s_p}^T\hat{\mathbf{K}}_{s_p}^e\boldsymbol{\Gamma}_{s_p} & \cdots & \mathbf{0}\\ \vdots & \ddots & \vdots\\ \boldsymbol{\Gamma}_{a_q}^T\hat{\mathbf{K}}_{a_q\leftarrow s_p}^e\boldsymbol{\Gamma}_{s_p} & \cdots & \boldsymbol{\Gamma}_{a_q}^T\hat{\mathbf{K}}_{a_q}^e\boldsymbol{\Gamma}_{a_q}\end{array}\right]\left\{\begin{array}{c}\hat{\mathbf{U}}_{s_p}\\ \vdots\\ \hat{\mathbf{U}}_{a_q}\end{array}\right\}. \tag{11.51}$$

As evident from the above derivation, restrictions are not placed on sensor and actuator locations. Also, in terms of the computational cost and broadband analysis capabilities, the proposed ASFEM is a better option compared to the conventional state-space model which is of very high order and several accuracy related problems due to error in model-order reduction, modal truncation, *etc.,* need to be addressed before they can be applied for broadband LAC. So far as the LAC is concerned, after combining the displacement (or strain) field generated by the primary disturbance (external mechanical load) and the secondary sources (actuators), one can obtain the wave coefficient vector $\tilde{\mathbf{u}}$ for a subdomain Ω of interest as

$$\tilde{\mathbf{u}}_\Omega = \hat{\mathbf{T}}_\Omega^{-1}\left[\hat{\mathbf{K}} + \hat{\mathbf{K}}(x_s)_{a\leftarrow s}\right]^{-1}\hat{\mathbf{f}}_\Omega\,. \tag{11.52}$$

At this stage, if a transfer function based concept of wave cancellation is chosen to design the controller, Equation (11.52) provides a direct way to carry out identification of the appropriate control gains for known sensor and actuator locations that will reduce certain elements of $\tilde{\mathbf{u}}_\Omega$ to zero, and hence the corresponding wave components can be controlled. However, the analytical approach to achieve this is limited by the fact that one cannot obtain an explicit expression for the dependence of local wave components on sensor and actuator locations and other control parameters for a complex problem, which may have more than one discretized subdomain. Hence, a semi-automated scheme integrated with ASFEM is chosen to analyze the spatially rediscretized system by changing sensor locations or actuator locations on an iterative basis. This is feasible because of the fast computation and small system size permitted by ASFEM.

11.4.4 Numerical Implementation

As the first step, the input time dependent forces or disturbances are decomposed into Fourier components using the forward FFT. Note that all of the element-level operations as well as the global system-level operations are carried out at each discrete frequency ω_n. Except for this basic difference, the proposed program architecture is almost identical (for an open-loop configuration) to a finite element program in terms of features such as input, assemblage, solving of the system, and the output. For a closed-loop system, we use Equation(11.51) to implement the explicit form of the global dynamic stiffness matrix at a particular frequency, which is in most cases, neither banded nor symmetric. Here, a non-symmetric sparse complex matrix inversion routine is used as part of the global system solver. After solving the closed-loop system

at each frequency, the time history of displacements, strains, stresses, *etc.,* are then post-processed using inverse FFT.

11.5 Effect of Broadband Distributed Actuator Dynamics

Here we consider a composite cantilever beam with surface-bonded PFC to study the effect of distributed actuator dynamics on broadband control of the transverse response of the cantilever tip under transverse impact type loading at the tip. Essentially the control point of interest for LAC in this case is the cantilever tip. This requires a feedback sensor to be placed at the same location. It is well known that the optimal placement of an actuator is dictated by the location of high average strain [278]. Hence, while controlling the static or first mode shape under tip loading on a cantilever beam, it is essential that the actuator be placed at the root of the cantilever beam. For velocity feedback with a collocated sensor, Crawley and Luis [278] have shown that the damping of a particular vibration mode when using surface-bonded PZT wafer, can be expressed as

$$\xi = \frac{e_{31}\gamma_{\dot{w}}}{2\hat{M}\omega_0 L_{\mathrm{B}}} \frac{\psi h_{\mathrm{B}} b}{(6+\psi)} \left[\hat{\phi}(x_2)_{,x} - \hat{\phi}(x_1)_{,x}\right] , \tag{11.53}$$

where $\gamma_{\dot{w}}$ is the velocity feedback gain, ω_0 is the natural frequency associated with the mode, M is the modal mass, L_{B} is the length of the beam, b is the width of the beam, h_b is the thickness of the beam, $\psi = (C_{\mathrm{B}} h_{\mathrm{B}})/(C_{\mathrm{PZT}} h_{\mathrm{B}})$ is the effective stiffness ratio for a PZT wafer thickness of h_{B}. $\hat{\phi}(x_2)_{,x} - \hat{\phi}(x_1)_{,x}$ is the difference between the gradients of the strain mode shape at the two ends (x_1, x_2) of the PZT actuator. With the specified actuator-to-beam length scale, the maximum modal damping of a single mode is obtained for maximum feedback gain

$$(\gamma_{\dot{w}})_{\max} = \frac{E_{\max} h_{\mathrm{PZT}}}{\omega_0 \hat{w}_{\max}} , \tag{11.54}$$

where $E_{\max}$ is the saturation electric field. Note that when the feedback sensor is placed non-collocated with the actuator, the sensor output signal will have a phase difference with the modal strain at the actuator ends and the effect can be destabilizing for a phase difference of more that 180^o. Similar consequences will also be evident when controlling more than one mode using the same configuration. For example, when controlling the second mode along with the first mode, one has to overcome the difficulty of almost zero average modal strain around the strain node (point of zero modal strain) at $x = 0.216 L_{\mathrm{B}}$. Two options are available to overcome this difficulty. One is to use segmented actuators, where one actuator located at $x < 0.216 L_{\mathrm{B}}$ must be driven 180° out of phase with a second actuator located at $x > 0.216 L_{\mathrm{B}}$. Obviously, control over a greater number of modes means more strain nodes and

hence more segmented actuators. Also, the possibility of interaction between the controlled modes and modal spillover for multiple segmented actuators becomes evident. This necessitates the requirement for an appropriate optimal control strategy. The second option for multi-modal control is to use a single actuator at the root of the cantilever beam with optimal length of actuator and frequency-weighted optimal gain while using a non-collocated sensor. Direct feedback from the control point of interest is found to be more suitable when a large number of modes over a broad frequency band are to be controlled. The fundamental behavior of this non-collocated sensor–actuator configuration for LAC resembles that of disturbance propagation in a structural network [297].

In the following numerical simulation, the sensitivity of the PFC actuator length (actuator located at the cantilever root) while using the velocity feedback from the sensor (located at the cantilever tip) is studied. The configuration is shown in Figure 11.13. The beam is of length $L = 1\,\mathrm{m}$, thick-

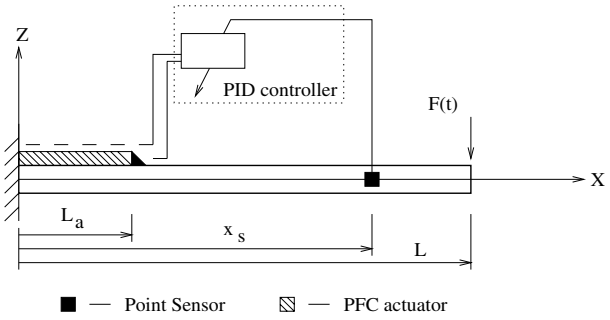

Fig. 11.13. A composite cantilever beam with surface bonded PFC actuator and non-collocated velocity feedback sensor placed at $x = x_s$ for broadband local control at the tip

ness 2 cm. AS/3501-6 graphite–epoxy material properties with ply-stacking sequence $[0_5^\circ/90_5^\circ]$ are considered. Assuming Euler–Bernoulli beam kinematics, the coupled electromechanical wave equation can be expressed as

$$\rho A\ddot{u}^o - A_{33}u^o{}_{,xx} + B_{33}w_{,xxx} + A_{33}^{\mathrm{eff}}E_{3,x} = 0\,, \tag{11.55a}$$

$$\rho A\ddot{w} - B_{33}u^o{}_{,xxx} + D_{33}w_{,xxxx} + B_{33}^{\mathrm{eff}}E_{3,xx} = 0\,. \tag{11.55b}$$

The force boundary conditions are

$$A_{33}u^o{}_{,x} - B_{33}w_{,xx} - A_{33}^{\mathrm{eff}}E_3 = N_x\,, \tag{11.56a}$$

$$B_{33}u^o{}_{,xx} - D_{33}w_{,xxx} - B_{33}^{\mathrm{eff}}E_{3,x} = V_x\,, \tag{11.56b}$$

$$-B_{33}u^o{}_{,x} + D_{33}w_{,xx} + B_{33}^{\mathrm{eff}}E_3 = M_x\,. \tag{11.56c}$$

In Equations (11.55) and (11.56), the mechanical stiffness coefficients A_{ij}, B_{ij}, D_{ij} are defined in Equation (4.29) and the electromechanical stiffness

coefficients A_{ij}^{eff} and B_{ij}^{eff} are described in Equation (11.48). One actuator element and one composite beam element (with a point sensor in it) are used in the ASFEM.

The beam is subjected to impact loading (Figure 4.5) in the transverse direction at the cantilever tip. Note that under such loading, which is likely to excite many higher order modes, the control analysis becomes challenging because of the additional axial–flexural coupling due to the unsymmetric ply-stacking sequence. Control of multiple spectral peaks in the frequency response of the transverse tip displacement is considered as the local control objective. If satisfied, this requirement will also ensure the stability of the close-loop system, as all the resonant modes will be damped and hence the poles will be moved to the left-half of the complex phase-plane. Also, the possibility of modal truncation over a sufficiently large frequency band can be eliminated. It is important to note that the waves that will travel from tip to the fixed end of the beam will be of the same order of magnitude as the incident impact. It is also necessary that the scattered axial and flexural waves from the fixed end be suppressed. This is also one reason, apart from those discussed in the context of Equations (11.53) and (11.54), for which the PFC actuator is placed adjacent to the fixed end. The sensor is assumed at $x = x_s$, which is considered near the tip for direct velocity feedback to the actuator in advance.

A non-dimensional scalar feedback gain g is derived from the feedback gain γ (Equation (11.46)) to perform the parametric study. These two quantities are related by $g = (c_o\alpha\beta)\gamma/E_o$, where E_o is a reference AC voltage and c_o is the speed of sound in air. An optimal closed-loop performance, which corresponds to $L_a = 0.25$ m, $x_s = 1.0$ m (at the tip) and $g = 3.4 \times 10^6$ is shown in Figure 11.14.

From Figure 11.14, which shows the locations of the forced resonances and anti-resonances along the frequency axis and the corresponding spectral amplitudes of transverse displacement at the tip, it can be seen that the configuration is able to suppress most of the resonant modes. Further, we study the effect of parametric variation on the amplitude level over the frequency range 0–20 kHz under consideration. First, it is assumed that the feedback gain g chosen above is optimal and is not sensitive to small variation in other parameters, such as L_a and x_s. L_a is slowly varied from 0.15 m to 0.35 m, corresponding to the velocity feedback from various sensor locations x_s moving away from the cantilever tip (Figure 11.13). The integral effect of the change in the amplitude level of the closed-loop response (transverse displacement at the tip) over the whole frequency range is evaluated using the control cost function

$$\hat{\prod} = \sum_{n=1}^{N/2} (20.0) \left[log_{10}|\hat{w}(\omega_n)^2_{open}| - log_{10}|\hat{w}(\omega_n)^2_{close}| \right] \tag{11.57}$$

In Figure 11.15, the sensitivity of $\hat{\prod}$ is shown by a two-dimensional solution space involving the actuator length L_a and sensor location x_s. This

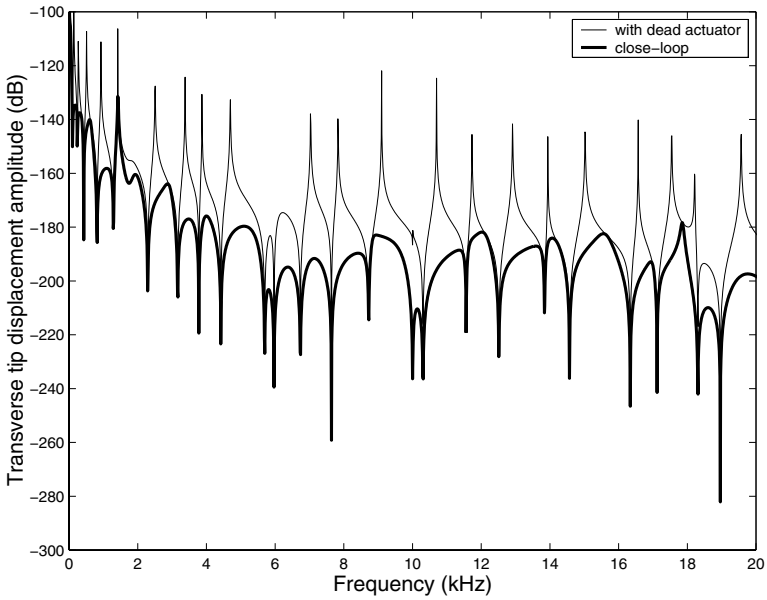

Fig. 11.14. Closed-loop transverse displacement at the cantilever tip under unit impulse excitation at the tip ($x_s/L = 1, L_a/L = 0.25$)

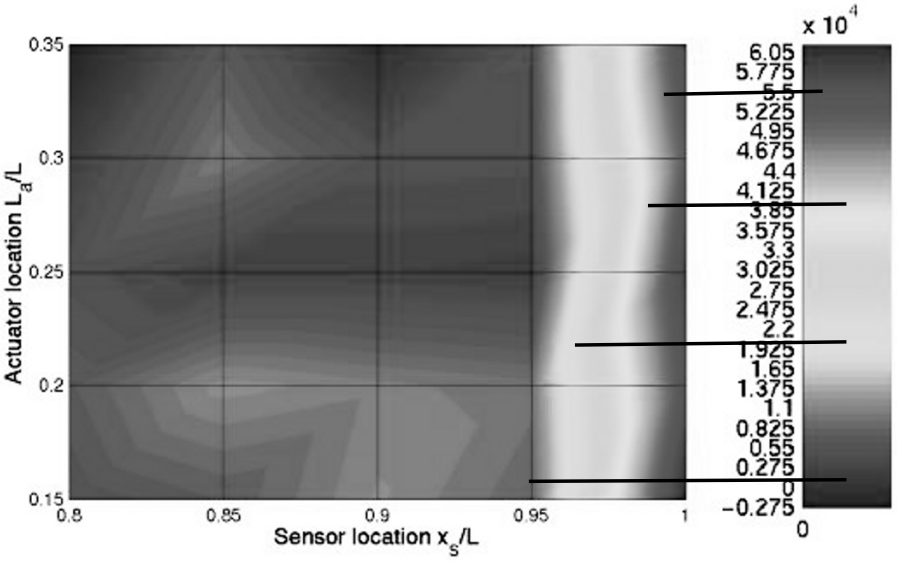

Fig. 11.15. Performance of actuator and control point interaction by variation in total amplitude level of transverse tip response

plot confirms the result of Figure 11.14 that one optimum solution exists at ($x_s/L = 1.0$, $L_a/L = 0.25$), and yields a total reduction of 6.025 dB in $\hat{\prod}$. Figure 11.15 also predicts that another solution exists at ($x_s/L = 1.0$, $L_a/L = 0.15$). It is clear from the plot that a sensor placed at less than 0.96 m never performs effectively over the significant resonant modes. Whereas, the collocated configuration at less than 0.8 m may not produce stable performance.

11.6 Active Control of Multiple Waves in Helicopter Gearbox Support Struts: Numerical Simulation Using ASFEM

In the previous section we discussed the issues and possible solutions to deal with distributed actuator dynamics for broadband control. In the present case study, we focus on the issues and possible solutions to deal with the problem of controlling multiple wave transmissions in helicopter gearbox support struts fitted with Terfenol-D packaged actuators. ASFEM is used for numerical simulation of feedback control performance and the effect of sensor–actuator configuration.

Helicopter cabin noise reduction has received considerable attention over the last two decades. With interior noise reduction, passenger comfort as well as operational ease can be improved along with the enhancement of structural fatigue life. The main rotor and gearbox mechanisms serve as the main sources (see Figure 11.16) of persistent acoustic disturbances while quick changes in gear teeth movement and aero-elastic events associated with maneuver transitions can result in transient acoustic disturbances. In many helicopters, the entire gearbox assembly is mounted on a set of vertical and inclined struts [298, 299]. The transient and persistent disturbances generated by the gearbox mechanisms as well as the main rotor are transmitted through the struts into the fuselage; this transmission is one of the main sources of structure-borne noise in a helicopter cabin. The frequency components associated with this noise are within the bandwidth extending up to 6 kHz [300, 301].

Among many approaches pursued to realize cabin noise reduction, control of waves transmitted through the noise path such as struts has been found to be viable. An early initiative in this regard is due to Westland Helicopters Ltd. During the late 1980s, they demonstrated that considerable reduction of the average vibration level can be achieved by using an Active Control of Structural Response (ACSR) system at the blade passing frequency of 17.5 Hz [298, 302]. An electrohydraulic actuator is used in this low frequency application. Recently, the application of active wave control in the gearbox support strut at high frequencies was carried out in a major group effort as part of the Reduction of Helicopter Interior Noise (RHINO) project. This project involved Westland Helicopters Ltd., Agusta, and others [270]. As reported in

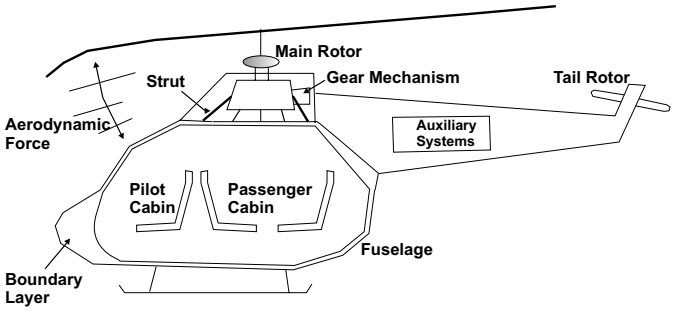

Fig. 11.16. Shematic diagram showing the sources of noise in a helicopter

this work, an actual helicopter strut was tested in a test rig under realistic loading conditions. A primary source in the form of a shaker was used to excite the system at the upstream end-plate of the strut, and a group of three secondary sources in the form of magnetostrictive actuators were mounted in parallel to the strut. The choice of the driving voltage inputs (*i.e.,* amplitudes and phases) to the actuators was based on minimizing the sum of the squared responses measured by six error sensors at the downstream end-plate. The location of the compliant ring for the secondary actuator group housing was chosen based on earlier studies on structural wave control in ducts and beams [276, 251, 303]. As reported in the study [270], an adaptive multiple actuator feedforward control scheme produced energy attenuation of up to 40 dB at the downstream interface of the strut over different discrete frequencies in the range extending to 1.25 kHz. Development of an ANC system for the S-76 helicopter by Sikorsky Aircraft Corporation has also been reported [304], [305].

Although active material integrated finite struts have been used extensively in experimental studies of full-scale systems, related analytical efforts have focused primarily on infinite struts. Pelinescu and Balachandran [233] also developed integrated mechanics models for finite struts and used them for open-loop studies of longitudinal and flexural wave transmission. In their models, the strut is treated as a homogeneous cylindrical waveguide, and the actuators are also modeled as waveguides. In a related study by Ortel and Balachandran [306], these models are used to develop closed-loop schemes for control of flexural wave transmission. Although these studies represent progress towards analytical development of an integrated active system, in order to use them for realistic configurations, the following features need to be taken into account in the modeling: (a) the effects of structural boundaries, joints, and other local discontinuities that can be important in the high-frequency range, (b) the steady-state axial and transverse loading, and (c) the coupling between longitudinal and flexural waves. In addition, the developed models need to be amenable to establishing schemes for controlling wave transmission over a broad frequency range that includes multiple spectral peaks as in

the present problem. However, models of realistic systems including the above features are not amenable to analytical solutions. Efforts in the following work have been directed towards using ASFEM to analyze and design the active strut system for optimal performance.

Apart from ASFEM, similar Fourier domain representations and transfer function concepts were developed in [247] and [307]. These transfer function based methods were later extended to adaptive control of structural waves for minimizing the transmitted power flow through one-dimensional elastic members [268, 269]. For distributed structural networks, the concept of LAC (Section 11.1.2) of traveling waves has also been developed and studied using a feedback compensator [253]. However, the aspects of distributed sensing and actuation and issues such as actuator dynamics have not been addressed in the above studies based on the transfer function concept.

From the above mentioned studies, it is noted that as complexity in the structural geometry and in applying the transfer function analysis increases, the control analysis involves extensive computations. On the other hand, the ASFEM can be efficient from a computational viewpoint due to its generalized matrix assembly procedure and easy post-processing.

11.6.1 Active Strut System

Helicopter gearbox support struts can be idealized as monolithic cylindrical shells with appropriate end sections to support bearings. As reported in [270], the ring frequency of the EH101 strut is typically 22.5 kHz. A high ring frequency is indicative of the dominance of torsional and warping modes in the overall response. Based on the disturbance frequency range, it was concluded in this study that the torsional motion is unlikely to be excited and that the resonances associated with warping motions are too high to affect the control performance significantly. Hence, for simplicity, only axial and flexural modes are considered in the model development following the analytical studies in [233].

The cylindrical strut is modeled as a beam with stiffness-equivalent solid cross-section. Terfenol-D rod-type actuators including the actuator housing are considered to be mounted on either the strut ends or on the surface with the help of rigid rings. In Chapter 4, an accurate mechanical model of a uniform cylindrical strut/tube shows that a new propagating mode (radial mode) causing strong dispersiveness in other modes appears above the cut-off frequency of 8.5 kHz. However, this cut-off can be considered very high compared to the major noise spectrum. In order to allow for dynamic boundary conditions, the strut ends are considered under dynamic reaction by the gearbox and fuselage interfaces. As noted in the study [233], this configuration is an idealization made to suit linear analysis.

In this case study, we use a feedback scheme based on the responses measured by downstream displacement or strain sensors. This model-based scheme requires accurate modeling of actuator-induced strain in the host structure to

capture the near-field effects. With a good model, it is believed that the analysis and control design effort may be carried out with a lower number of actuators than that required for a feedforward scheme.

We consider linear coupled magneto-elastic equations for the Terfenol-D rod-type actuator [296] given by

$$\varepsilon_{33} = s_{33}^{\text{eff}}\sigma_{33} + d_{33}^{\text{eff}}H_3 \ , \qquad B_3 = d_{33}^{\text{eff}}\sigma_3 + \mu_{33}^{\text{eff}}H_3 \ . \tag{11.58}$$

The significance of the notation and the corresponding units are in accordance with the IEEE Standard [308], where the direction 3 represents the axial direction of the rod shaped magnetostrictive actuator, $s_{33}^{\text{eff}} = (C_{33}^{\text{eff}})^{-1}$ is the effective compliance, $d_{33}^{m} = s_{33}^{\text{eff}} e_{33}^{\text{eff}}$ is the effective magnetostrictive constant, μ_{33}^{eff} is the effective magnetic permeability. B is the magnetic flux density normal to the rod cross-section and H_3 is the the magnetic field strength. The effective material properties can be obtained from the bulk properties of magnetostrictive materials [308]. It is assumed that a linear strain magnetic field strength $(\varepsilon - H)$ characteristic can be used to describe the actuator. This can be realized by using an appropriate DC bias magnetic field H_0. Further details can be found in [296]. The design value of H_0 needs to be determined from the analysis. If the actuator specification does not meet this required value of H_0, then, the use of more similar actuators in a group can be an option. The governing equation of motion and dynamic force-boundary equations for the magneto-elastic domain can be obtained as in Equations (11.55) and (11.56).

11.6.2 Numerical Simulations

Following the work of [233], the finite-length strut considered is a 1.0 m long hollow cylindrical aluminum strut with 7.62 cm outer diameter and 6.35 cm inner diameter. Harmonic loads are applied at the strut ends in longitudinal and transverse directions. As considered in [233], such dynamic loading represents a simplified model of high impedance gearbox reaction at one end and reaction from the bearing at the fuselage interface. A cylindrical magnetostrictive actuator with rod-shaped Terfenol-D core is chosen due to their high force capability. Such an actuator has its own housing and reaction mass [301]. These aspects can also be accurately modeled in ASFEM if the effective stiffness and mass distributions are known for packaged actuators. Based on the strut geometry considered here and the loading conditions to be considered, it is known that the longitudinal motion is expected to contribute substantially to the total kinetic energy at the fuselage interface. The main objective of numerical simulation here is to control the transmitted waves at the strut–fuselage interface. With these in mind, the first case considered below has to do with the control of longitudinal wave transmission.

Control of Longitudinal Wave Transmission

In Figure 11.17, an actuator located at the strut–fuselage interface is shown along with a point velocity feedback sensor mounted at a distance x_s from the

gearbox end of the strut. This system is described by two spectral elements, one an actuator element and the other a strut element. The results obtained in the uncontrolled and controlled cases are shown in Figure 11.18. With the actuator, the system resonances are shifted to lower frequencies and it appears that the magnitude of frequency shift increases linearly with the mode number. A non-dimensional scalar velocity feedback gain g defined as

$$g = (\alpha\beta\gamma)/(n_o I_o/c_o) \tag{11.59}$$

is used, where α and β are, respectively, the sensitivity parameters for sensor and actuator as discussed in Section 11.4. γ is the constant gain, n_o is the number of specific turns in the actuator coil, I_o is a nominal r.m.s. coil current, and c_o is the speed of sound in air. In all the numerical studies conducted here, the values of the different quantities are $\alpha = 1$, $\beta = 1$, $n_o = 1 \times 10^6\,\mathrm{m}^{-1}$, $I_o = 1\,\mathrm{A}$ r.m.s., and $c_o = 340\,\mathrm{m/s}$. The sensor is located at the strut–fuselage interface (*i.e.,* $x_s = 1.0\,\mathrm{m}$), and the parameter g for velocity feedback is increased in the range from 3.4 to 34. It is seen that the sensor–actuator collocated configuration (Figure 11.17) can be used to attain considerable displacement response attenuation throughout the frequency bandwidth of interest. Similar displacement response attenuation at targeted frequencies based on an analog feedforward scheme for the same sensor–actuator configuration was reported in [233].

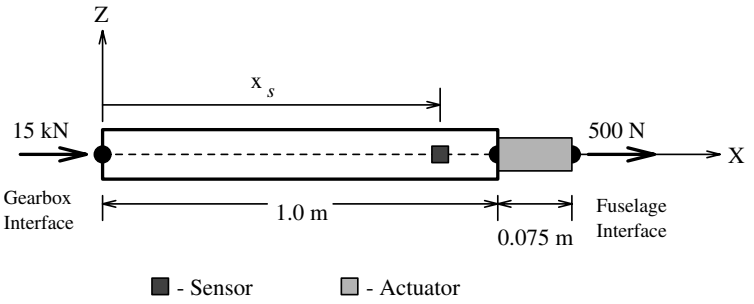

Fig. 11.17. Active strut for control of longitudinal wave transmission. Maximum amplitudes of representative multi-harmonic loading $\hat{f}_{\max}$ are shown

Since it may be difficult to place the sensor at the actuator base exactly, an alternative configuration is used wherein the sensor is placed away from the actuator base. The results obtained for the configurations $x_s = 0.9\,\mathrm{m}$ and $x_s = 0.8\,\mathrm{m}$ for $g = 17.0$ (optimal in Figure 11.18) are shown in Figure 11.19. It is observed that $x_s = 0.9\,\mathrm{m}$ may be the preferred sensor location, since for this choice, the response close to the fourth mode resonance location is completely suppressed. For the non-collocated case $x_s = 0.8\,\mathrm{m}$, although the largest suppression is at the frequency location close to the resonance of the

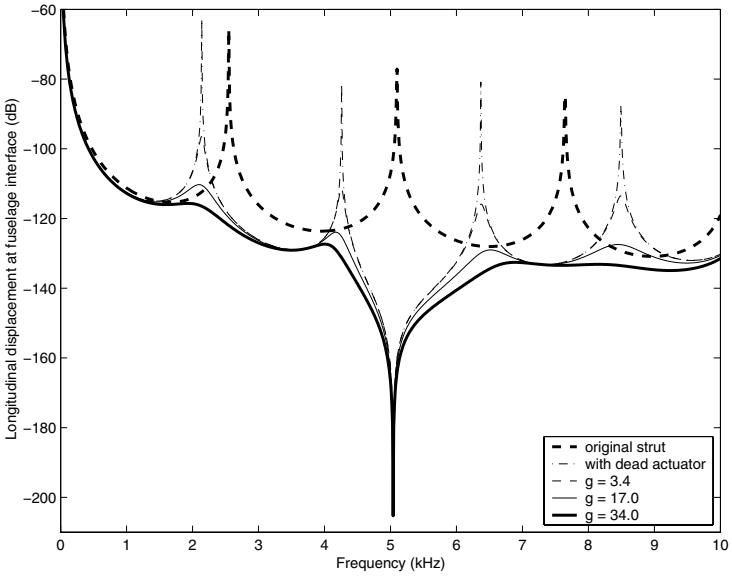

Fig. 11.18. Longitudinal displacement at strut–fuselage interface in uncontrolled cases and controlled cases with different gain values. The sensor is collocated with the actuator at strut end ($x_s = 1.0\,\mathrm{m}$)

second mode, suppression at the location close to the resonance of the fourth mode is not as good as that obtained for the case $x_s = 0.9\,\mathrm{m}$. However, in this latter case, suppression at the location near the resonance of the second mode is not as good as that obtained with $x_s = 0.8\,\mathrm{m}$.

In some designs, it may be necessary to use a group of actuators rather than one actuator to realize the required actuator force. Such actuator groups have been used in earlier work [270]. In this study, performance of three secondary magnetostrictive actuators in a group (hosted by a steel endcap) was studied in an experimental arrangement. Input to the actuators was decided based on the measurement from one error sensor located on the upstream side of the actuator. The actuators were driven in phase to control longitudinal wave transmission through a strut, and they were driven out of phase to control flexural wave transmission. To illustrate the applicability of the AS-FEM for actuator group configurations, here, the active strut illustrated in Figure 11.20(a) is considered. There are two actuators in the actuator group here, and these are represented by the spectral elements 3–5 and 4–6 in the modeling, as shown in Figure 11.20(b). Apart from these two elements, the computational model consists of four other elements, which include one sensor element (2–7) downstream of the actuators. The base ring is modeled as a rigid link (4–2–3). Next, results generated for this configuration with different actuator group locations x_a with $x_s = 0.9$ m is shown in Figure 11.21, and for different sensor locations x_s with $x_a = 0.8$ m is shown in Figure 11.22. For

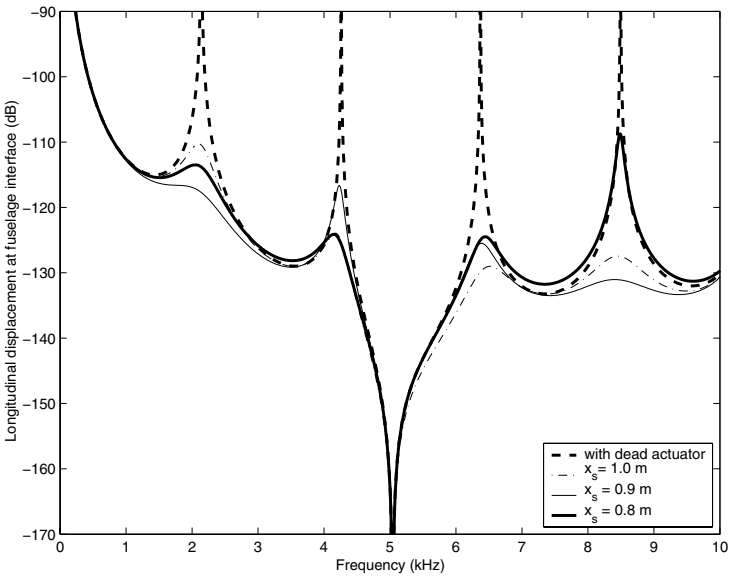

Fig. 11.19. Longitudinal displacement at strut–fuselage interface in uncontrolled case and controlled cases for different sensor locations. Control gain parameter $g = 17.0$ in all cases

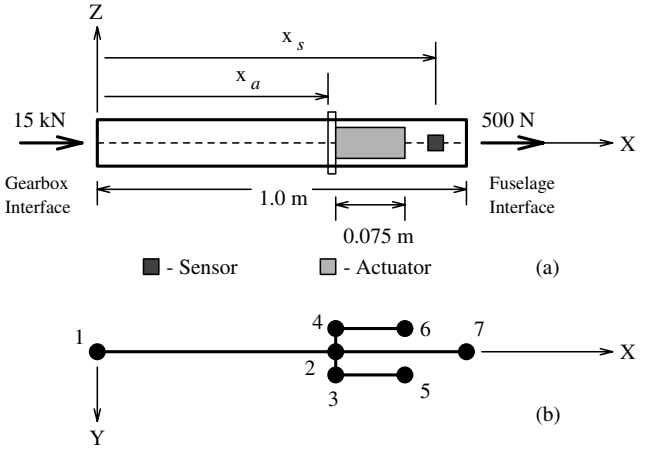

Fig. 11.20. (a) Configuration of strut with two intermediate actuators in group, for control of longitudinal wave transmission. Maximum amplitudes of representative multi-harmonic loading $\hat{f}_{\max}$ are shown. (b) Spectral element representation of actuators, sensor, strut, and base ring

each actuator, $g = 8.5$ (one half of the optimal value obtained previously for the one actuator case) and both of the actuators receive identical inputs. In all cases, attenuation at locations close to the resonance of the first mode is considerable but less than that obtained at other frequency locations. In Figures 11.21 and 11.22, a zero (anti-resonance) is introduced in the closed-loop system (other zeros lie towards infinity along the frequency axis, and fewer in number than the number of poles, meaning the system is a realizable one) at a frequency close to the resonance frequency of the second mode (or pole) of the open-loop system. Interestingly, this corresponds with the second root-locus of the open-loop system transfer function moving towards a closed-loop zero as the control effort is increased (meaning the mode is a stabilizable one).

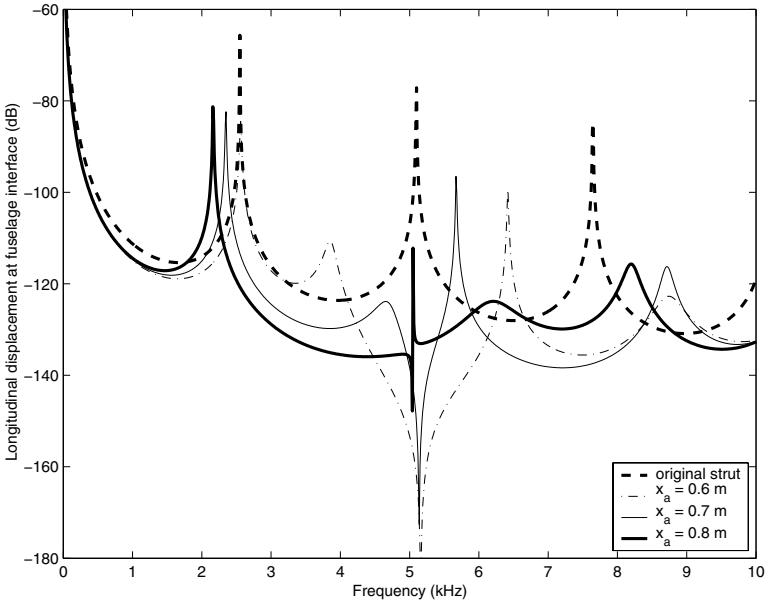

Fig. 11.21. Longitudinal displacement at strut-fuselage interface in uncontrolled case and controlled cases for different actuator group locations. Sensor location at $x_s = 0.9\,\text{m}$ in all three cases, and control gain parameter $g = 8.5$ for each actuator

Control of Flexural Wave Transmission

Figure 11.23 shows the active strut configuration for the control of flexural wave transmission. A single transverse actuator is placed at x_a as in [233], and a single point velocity feedback sensor is placed downstream of the actuator. In the study [306] and also here, it was found that the introduction of single and multiple actuators alters the resonance of the system. Mechanically,

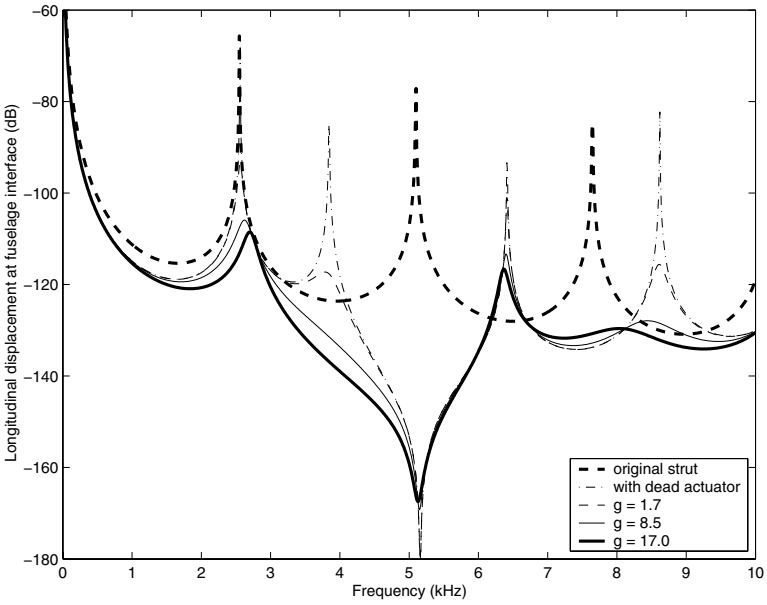

Fig. 11.22. Longitudinal displacement at strut-fuselage interface in uncontrolled case and controlled cases for actuator group location at $x_a = 0.8\,\mathrm{m}$ and sensor location at $x_s = 0.9\,\mathrm{m}$

therefore, the presence of a dead actuator may cause considerable change in the open-loop system due to the stiffness and inertia of the actuator. The spectral characteristics also suggest the presence of secondary axial–flexural coupled modes; these are due to the scattering of the incident flexural wave producing additional longitudinal waves at the strut–actuator interface. This observation indicates the need for considering the dynamics of distributed actuation in similar broadband (multiple tone) structural control problems.
In Figure 11.24, responses of the closed-loop system with different values of g are shown for $x_a = 0.6\,\mathrm{m}$, $x_s = 1.0\,\mathrm{m}$. Good attenuation is obtained at all frequency locations except for the first mode resonance close to 5 kHz. The locations of the zeros observed in the open-loop system also appear to be unchanged in the closed-loop cases. In Figure 11.25, the sensor is shifted away from the strut–fuselage interface to $x_s = 0.9\,\mathrm{m}$. The trends are similar to those seen in the context of Figure 11.24, except that a few zeros disappear. The results are suggestive of the inability to achieve response attenuation at locations close to the first resonance location of the open-loop system. This indicates the requirement for an additional damping mechanism to absorb high energy that is associated with the first mode. However, in most helicopters, such damping mechanisms already exist along with elastomeric bearings to augment the performance.

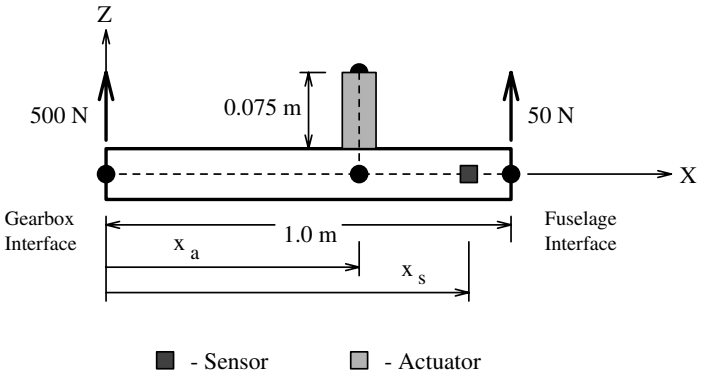

Fig. 11.23. Active strut for control of flexural wave transmission. Maximum amplitudes of representative multi-harmonic loading $\hat{f}_{\max}$ are shown

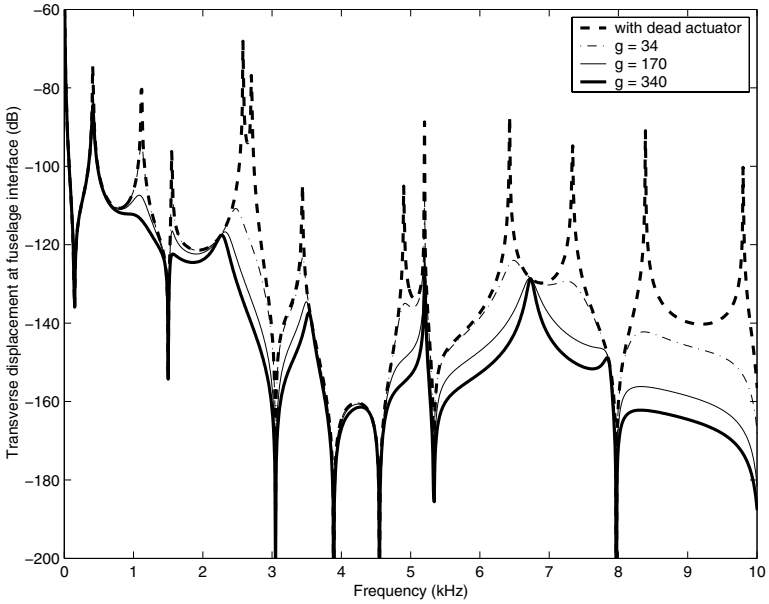

Fig. 11.24. Transverse displacement at strut–fuselage interface in uncontrolled case and controlled cases with different gain values, $x_a = 0.6\,\mathrm{m}$, $x_s = 1\,\mathrm{m}$

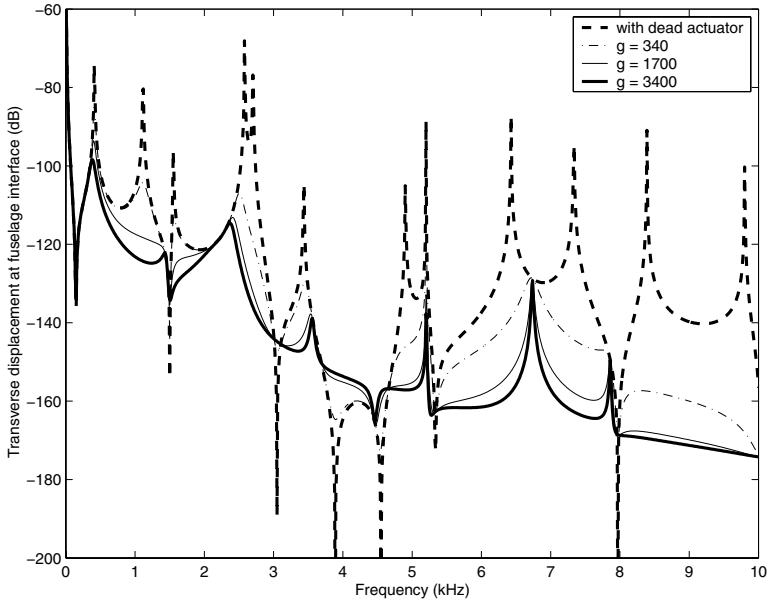

Fig. 11.25. Transverse displacement at strut–fuselage interface in uncontrolled case and controlled cases with different gain values, $x_a = 0.6\,\mathrm{m}$, $x_s = 0.9\,\mathrm{m}$

Control of Axial–Flexural Coupled Wave Transmission

One of the main objectives of the numerical study is to investigate coupled axial–flexural wave transmission. A two-actuator configuration chosen for this purpose is shown in Figure 11.26. One of these actuators is inclined at an angle θ with respect to the longitudinal axis of the strut. Control inputs to both actuators are based on a single error sensor response. Based on the results presented in the earlier subsections, sensor location is chosen to be $x_s = 0.9\,\mathrm{m}$ which is an "optimal" location for the greatest number of axial and flexural modes. Uncontrolled and controlled longitudinal displacements at the strut–fuselage interface is plotted in Figure 11.27. Overall performance of the simultaneous control of axial–flexural wave transmission is shown by the kinetic energy spectrum at the strut–fuselage interface in Figure 11.28 for varying θ. The appearance of a number of secondary axial–flexural coupled modes can be seen in these figures. It can be seen that the additional secondary modes do not contribute significantly to the axial displacement response compared to those due to the primary modes. However, this is not the case for the flexural displacement response, where the primary modal amplitudes are influenced considerably by the secondary coupled modes, leading to shifts in the locations of poles and zeros of the closed-loop system.

While constructing the closed-loop system, it is assumed that the sensor outputs corresponding to both longitudinal and transverse forced frequency

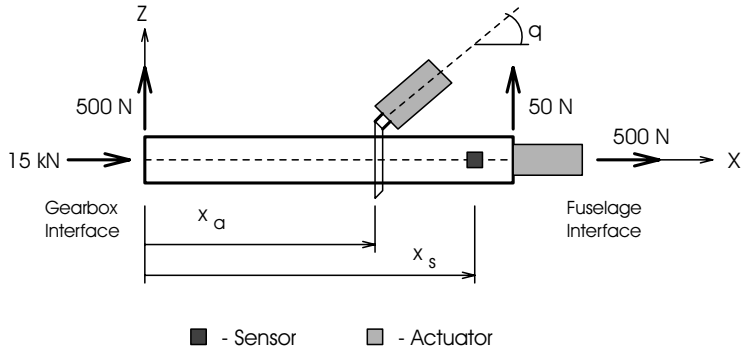

Fig. 11.26. Two-actuator configuration for control of coupled axial–flexure wave transmission. Maximum amplitudes of representative multi-harmonic loading $\hat{f}_{\max}$ are shown

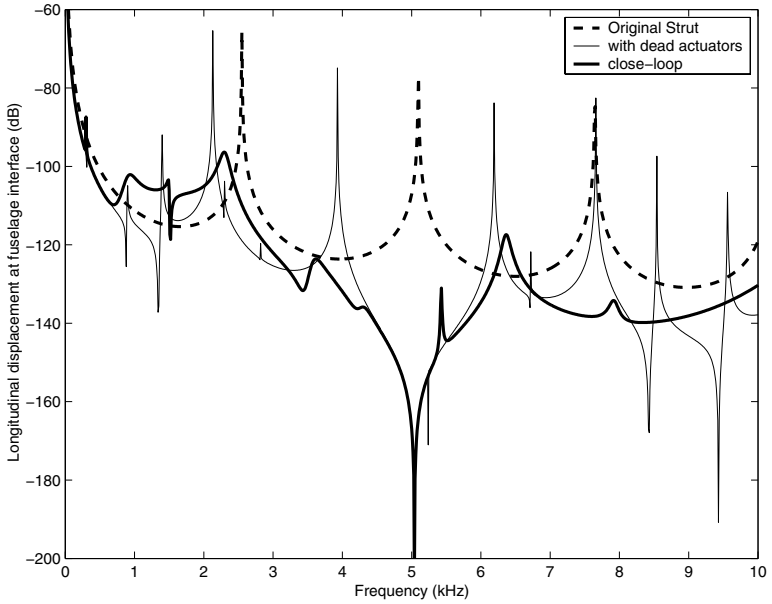

Fig. 11.27. Longitudinal displacement at the strut–fuselage interface in uncontrolled and controlled cases. Velocity feedback to each actuator is from sensor at $x_s = 0.9\,\mathrm{m}$. For the inclined actuator at $x_a = 0.6\,\mathrm{m}$, $\theta = 90^o$

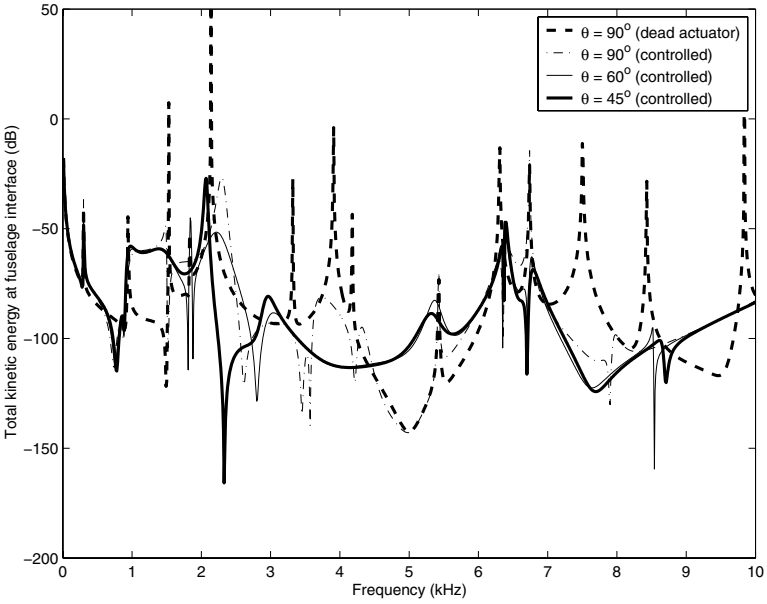

Fig. 11.28. Total kinetic energy at strut–fuselage interface in uncontrolled and controlled cases with different θ for the inclined actuator at $x_a = 0.6\,\mathrm{m}$. Velocity feedback provided to each actuator is from sensor at $x_s = 0.9\,m$

responses are available from the chosen sensor location. The longitudinal and inclined actuators are driven based on these measured longitudinal and transverse responses, respectively. Among different sets of parametric values considered for velocity feedback gains (g_u for longitudinal actuator and g_w for inclined actuator) and x_s considered earlier for control of axial and flexural waves separately, the best results are achieved for $g_u = 17.0$ and $g_w = 340$. From the results, it can be seen that with a constant gain velocity feedback scheme, an increase in the effort to control flexural waves leads to less attenuation in the longitudinal response.

Modeling efforts presented here may be used as a basis for carrying out path treatment for helicopter cabin noise. In such cases, it is of interest to know the level of energy attenuation at the spatial location of interest; here, the strut–fuselage interface. The kinetic energy has contributions from longitudinal (primary) and transverse (secondary) motions. In order to analyze the distribution of the total kinetic energy among its longitudinal and transverse components in the closed-loop system, Figure 11.29 is presented. Plots of the normalized spectrum of relative amplitudes of kinetic energy $\hat{E}_u$ (for longitudinal motions) and $\hat{E}_w$ (for transverse motions) at the strut–fuselage interface are shown in this figure. The corresponding expressions are

$$E_u = \frac{|(\hat{u}^o)^2|}{|(\hat{u}^o)^2| + |\hat{w}^2|} \ , \quad E_w = 1 - E_u \ , \tag{11.60}$$

where $\hat{u}^o$ and $\hat{w}$ are the spectral amplitudes of longitudinal and transverse displacements, respectively, at the strut–fuselage interface. From this figure, it can be said that the kinetic energy associated with the significant transverse modes is attenuated, except at frequency locations close to the first transverse resonance mode and the other three modes associated with resonances near 5.2 kHz and 6.8 kHz.

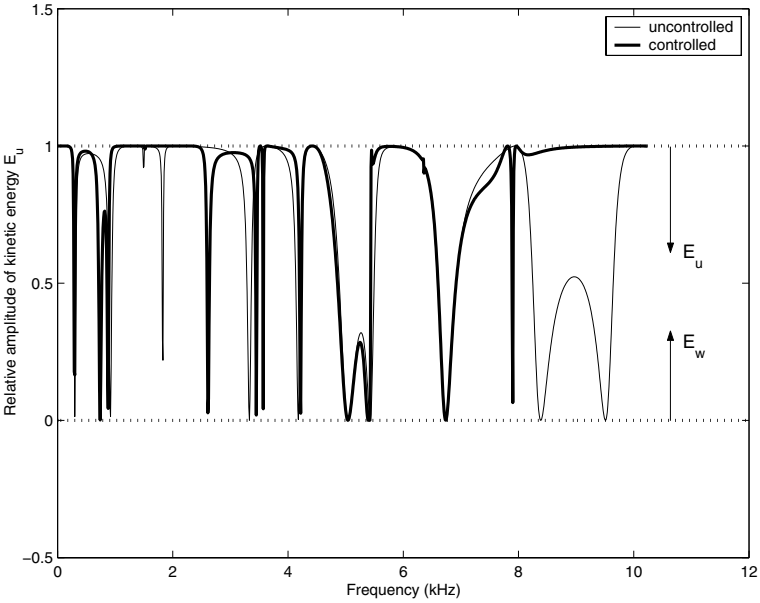

Fig. 11.29. Distribution of kinetic energy into longitudinal and transverse components at strut–fuselage interface in uncontrolled and controlled cases for $\theta = 90^o$

11.7 Optimal Control Based on ASFEM and Power Flow

In this section we propose a broadband optimal control strategy based on the ASFEM (derived in Section 11.4) and spectral power (Equation (10.1). An upper-bound to the electrical input (voltage) is used as a constraint in the optimal control.

In structural acoustics control problems, the primary concern is the sound power radiated by the structure, which forms dense modal space and is broadband in nature. On the other hand, in structural wave propagation problems

related to the present context, the broadband control performance is depicted in terms of response (displacement, velocity or acceleration) amplitude or kinetic energy level at the control points. Here, we consider the physical significance of the structural power (as in structural acoustics) in the sense that it constitutes the characteristics of both displacements and stresses generated at critical structural members [268]. In the proposed model, the frequency domain power (see Section 10.2) at the desired points (spectral element nodes) are computed as a post-processing operation on the controlled system response. In ASFEM, the power flow computation becomes very accurate and efficient, capturing all the necessary structural complexities. Hence, the amplitudes of the complex power at the spectral element node(s) close to the control point(s) are considered to construct a quadratic performance measure at each discrete frequency (FFT sampling frequency ω_n). We shall see that such a frequency domain measure can be used for frequency weighting of feedback gain, and its variation has an upper bound in terms of actuator saturation (or allowable voltage into PFC below dielectric breakdown voltage). This leads to one possibility of optimizing the feedback gain spectrum so that all the structural modes within the chosen frequency band can effectively be controlled, provided that the sensor–actuator locations and connectivities are admissible from a control system design point of view. One of the main advantage of such optimal control integrated with ASFEM is that the system size is very small. This means a frequency domain equivalent of the very high order state-space plant is already in place. But in all traditional MIMO optimal feedback based on frequency weighting through linear-quadratic (LQ) design [295], the controller order required is roughly the same as the full-order plant of the structure. Through ASFEM, we can have a very small plant, which is also accurate over a broad frequency band. Therefore the possibility of a robust and much lower order controller (compared to that in full-order state feedback) can be achieved through ASFEM and PID feedback with a group of sensors and actuators. In the present work, only the issues related to model-based structure-control estimation are discussed, which are essentially off-line. Digital controller design based on such an analysis needs further study and is a future area of research.

11.7.1 Linear Quadratic Optimal Control Using Spectral Power

As a distributed measure of the controlled structural response, we consider frequency domain power flow at the spectral element nodes which is defined as the product of the nodal force vector and conjugate of the nodal velocity vector. In matrix notation, this is expressed as

$$\hat{P}(\omega_n)^e = \hat{\mathbf{f}}^{e^T} \left(j\omega_n \hat{\mathbf{u}}^e\right)^* \ . \tag{11.61}$$

Various properties of the spectral power as a measure of disturbance propagation were discussed in Section 10.2. Considering power expression for an

element internal point (x, z), it was shown that the real part of the complex power is constant over a uniform element domain and the spatial rate of change of total power is purely imaginary, *i.e.,* $Re[\partial\hat{P}/\partial x] = 0$. This implies that the real part of complex power is the contribution from farfield disturbance transmitted through the structural joints. The imaginary part amounts to the energy trapped in the element, which is essentially the nearfield effect on the sensor. Since, we emphasize the accuracy of the feedback signal from the sensor near the control point in LAC, one possible approach is to consider the power amplitude. Here, we choose a linear quadratic performance measure $\{\mathcal{H}_{ctrl}\}$ for the closed-loop system subjected to an upper-bound $\{\mathcal{E}_{drv}\}$ of the actuator input voltages. For multiple LAC objectives the elements of the matrix measure to be achieved are expressed as

$$\mathcal{H}_{ctrl} = \frac{|\hat{P}(\omega_n)_0| - |\hat{P}(\omega_n)_m|}{|\hat{P}(\omega_n)_0|} > 0 \ , \mathcal{E}_{drv} = |\hat{E}(\omega_n)_{max}| - |\gamma(\omega_n)_m \hat{\eta}(\omega_n)_m| > 0 \ . \tag{11.62}$$

The subscripts *ctrl* and *drv* stand for the control points (for LAC) and driving points (actuator element nodes), respectively. The amplitude of $\hat{E}(\omega_n)_{max}$ represents the allowable peak voltage to the PFC actuator and the corresponding frequency range depends on the capacity of the voltage amplifier being used. It is to be noted that ω_n must be considered within the actuator bandwidth to match the numerically simulated performance. In ASFEM, all the required matrix computations for open-loop as well as closed-loop are performed at every discrete frequency ω_n. Equation (11.51) is solved for unit amplitude of the FFT signal for an external mechanical disturbance. After solving the system, the actual frequency response for displacement, force, power and controller input output transfer function are obtained by convolving with the original mechanical loading spectrum. Constrained optimization of power flow at the control points, which is governed by Equation (11.62), is performed at ω_n. As shown in Equation (11.62), frequency weighting of the feedback gain $\gamma(\omega_n)$ at ω_n for a sensor s_p is obtained by maximizing $\mathcal{H}_{ctrl}$ with constraint $\mathcal{E}_{drv} > 0$ using a non-uniform iterative scheme. Here, subscript m represents the mth iteration at a particular ω_n and subscript 0 represents the uncontrolled system. In ASFEM, the spatially discretized model is much smaller in size than other MIMO models. Taking advantage of this aspect, a semi-automated scheme is integrated with ASFEM to achieve optimal location of sensors and actuators.

11.7.2 Broadband Control of a Three-member Composite Beam Network

In the following numerical simulations, a three-member composite beam network is considered with the objective of controlling one of its nodal displacements over a frequency band of 10 kHz. The Y-shaped network is made of three AS/3501-6 graphite–epoxy composite beam members connected through a common rigid joint (node 1) as shown in Figure 11.30. The free end (node

11) of the network is subjected to impact type excitation (Figure 4.5). The local control objective is framed as the simultaneous control of horizontal displacement u as well as transverse displacement w at the common joint (node 1) of the network with the minimum number of PFC actuators of prescribed length.

From the nature of the considered structural geometry and boundary conditions, it can be said that there will be multiple scattered waves, which are axial–flexural coupled. Therefore, significant nearfield will exist at the sensors placed near node 1. However, at the initial stage of disturbance propagation, there will be only the dominant transmitted wave component arriving at node 1 from the free end side. But, at later stages of time, the effect of multiple scattering, amounting to a major part of the trapped energy in the fixed end portions, will increase. Based on this behavior, we assume four PFC actuators (each of length 0.15 m) at the locations shown in Figure 11.30.

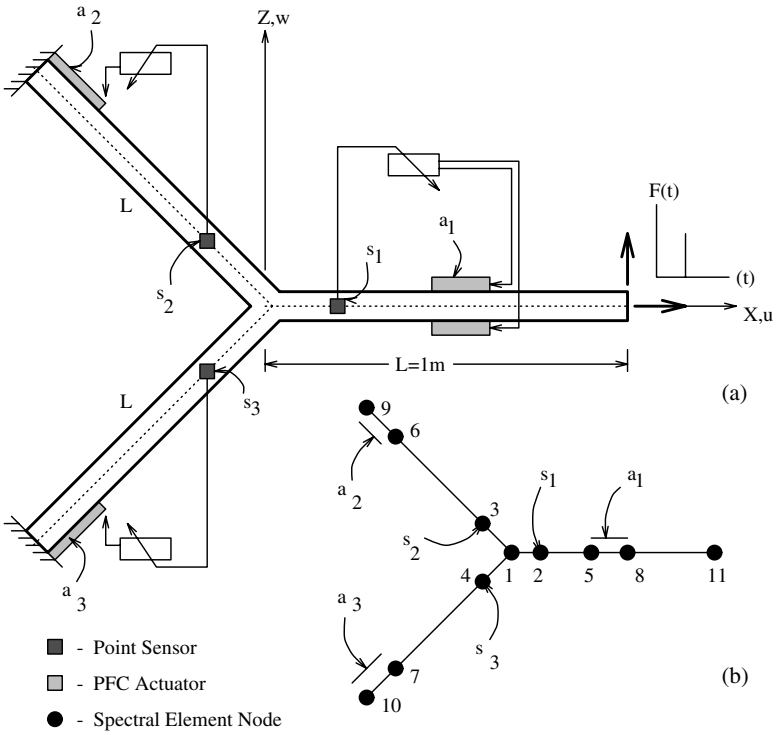

Fig. 11.30. A Three-member composite beam network with non-collocated sensor–actuator configuration to control waves at the network joint. (a) Schematic diagram of the feedback model. (b) Spectral element configuration

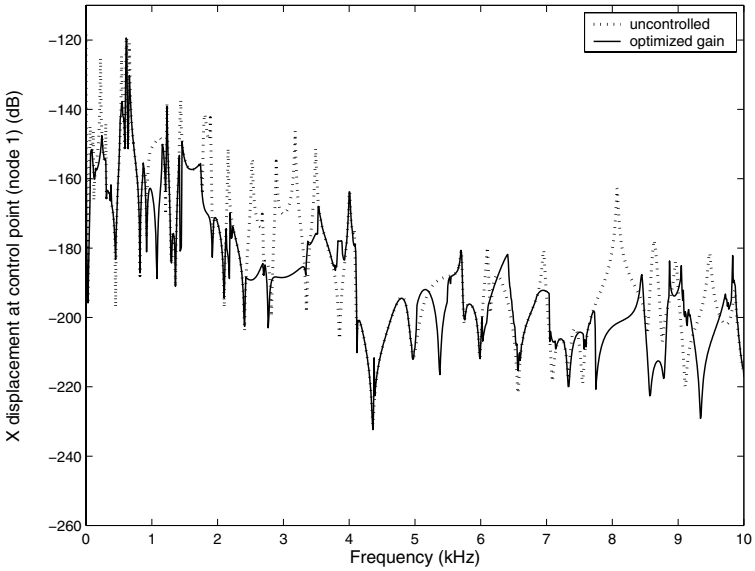

Fig. 11.31. Optimized closed-loop performance showing displacement amplitude in X direction at the control point (node 1 in Figure 11.30)

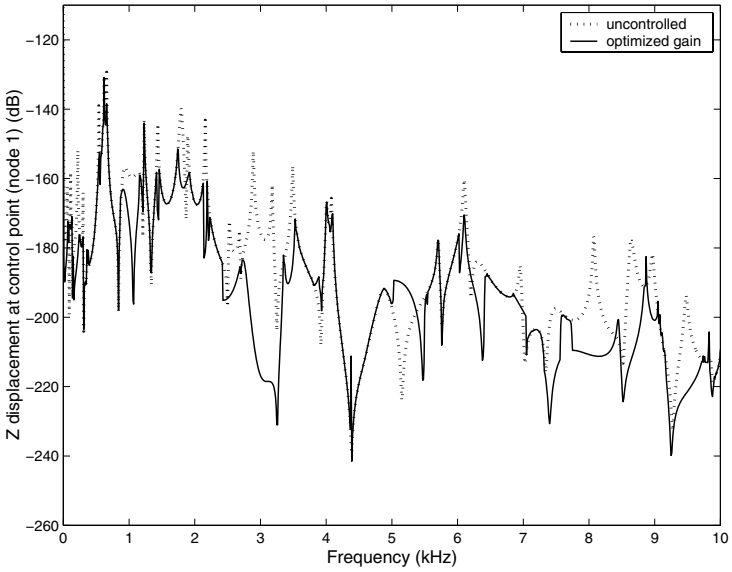

Fig. 11.32. Optimized closed-loop performance showing displacement amplitude in Z direction at the control point (node 1 in Figure 11.30)

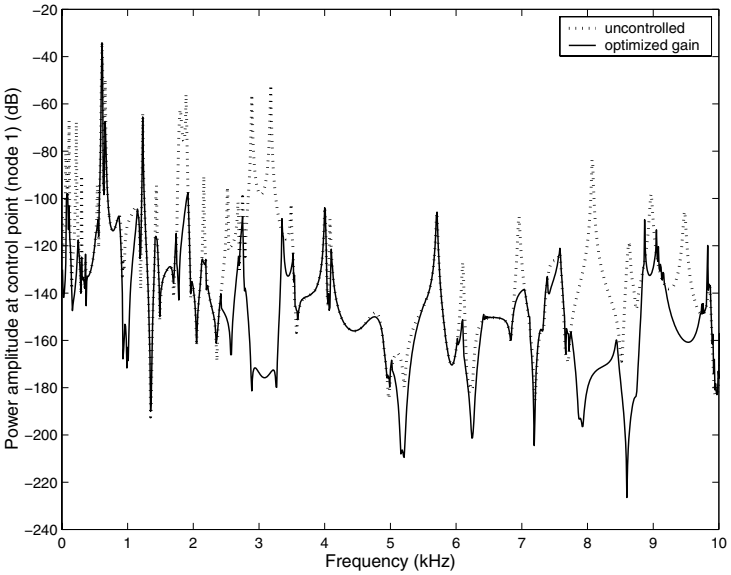

Fig. 11.33. Optimized closed-loop performance showing optimized power flow at the control point (node 1 in Figure 11.30)

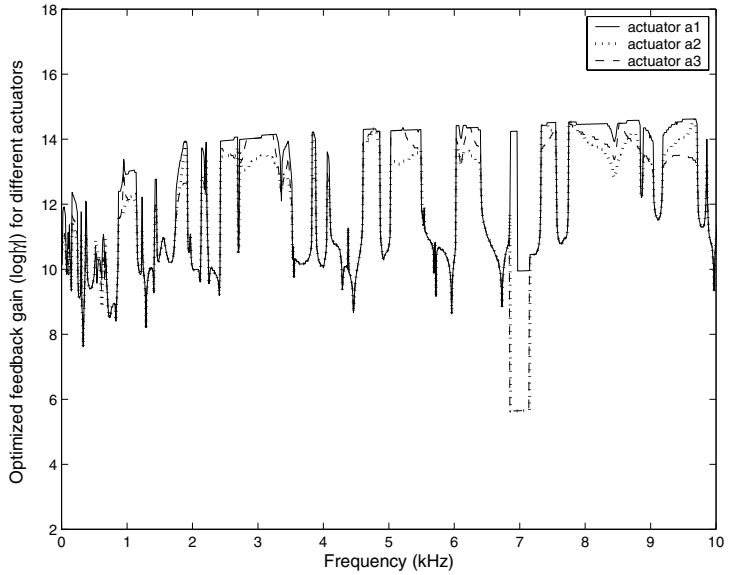

Fig. 11.34. Optimized closed-loop performance showing feedback gain spectrum for three actuators

For direct velocity feedback to these actuators, we consider three point sensors near node 1 (Figure 11.30). Sensor s_1 is used for transverse velocity ($j\omega_n\hat{w}$) feedback to the actuator pair a_1. Sensors s_2 and s_3 are used for axial velocity feedback ($j\omega_n\hat{u}$) in $\pm 135^o$ rotated coordinate systems which are local to the two inclined members. All of these three sensors are assumed at 0.1 m from node 1. The spectral element configuration of the above closed-loop system is schematically represented in Figure 11.30(b) showing the mechanical and active element nodes in SFEM. The spatially discretized system size is 27×27 including three sensor nodes and three actuator elements. Constrained optimization as discussed in Section 11.7.1 for the control point (node 1) is carried out assuming an allowable specific actuator input voltage of 9 kV/cm to each of the PFC actuators. To control the primary disturbance transmitted from node 11 towards the control point, the actuator pair a_1 is placed at 0.45 m from the control point node 1. In Figure 11.31 and 11.32 respectively, the horizontal and transverse displacements corresponding to the optimal closed-loop performance are plotted. Figure 11.33 shows the closed-loop constrained power amplitude spectrum at the control point. Frequency weighted feedback gain amplitude $\log|\gamma|$ for the three actuators is plotted in Figure 11.34. From Figures 11.31, 11.32 and 11.33, it can be seen that the controlled performance at different frequency bands over the resonant modes are similar in the power amplitude spectrum and the displacement amplitude spectrum. Therefore, optimization of the constrained power flow proves to be an effective strategy for active distributed control of structural waves. However, in both the horizontal and transverse responses, the performance near 0.6 and 4 kHz may not be satisfactory. This can be attributed to the fact that only power amplitude was optimized. Real and imaginary components of the closed-loop power (which constituted the farfield and nearfield effects, respectively, due to asynchronized phase) were not optimized separately. Therefore, the current optimization scheme has worked on an average basis by considering both the amplitude of nearfield and farfield disturbances, and not by considering the associated phase information.

This chapter is focused on the development of SFEM integrated with control algorithms for the analysis and design of MIMO control systems for structural vibration and broadband wave control applications. An overview of the problem complexity and the modeling difficulties encountered in existing modeling techniques is presented. Some of the main issues in distributed parameter control system modeling, namely the control-spillover due to insufficient modal information, stability of the LAC instead of global control, finite actuator dynamics, single actuator multi-modal control, *etc.,* are discussed. Constitutive modeling of layered piezoelectric materials surface-bonded or embedded in host composite structures are presented. Modeling of PFC based on a uniform field model is presented. Design criteria for such PFCs in surface-bonded or embedded form, which becomes an ideal candidate for distributed structural actuation, is outlined considering the structural performance, actuator authority and overall control authority of the integrated system. Next,

the ASFEM is derived considering PID feedback sensors and distributed actuators in non-collocated form. The resulting closed-loop model is shown to be a very high-dimensional one but having discretized system size as small as the total number of sensor nodes, actuator nodes and structural boundary nodes. This demonstrates the suitability of ASFEM in broadband control where many vibration modes participate in the dynamics, and a conventional state-space model needs very large system size for accurate MIMO system realization and optimal control design. Numerical simulations are carried out to study the effect of distributed actuator dynamics. A case study on the active control of multiple waves in a helicopter gearbox support strut is presented. The effect of sensor–actuator location in non-collocated feedback is studied. Also, the study shows a systematic approach towards the development of a single actuator multi-mode control system. To this end an optimal control algorithm based on ASFEM and spectral power flow is developed and implemented. Numerical simulations are presented to demonstrate the optimal control performance of a beam network with non-collocated point sensors and distributed PFC actuators.

References

1. K. J. Bathe, Finite Element Procedures, Prentice Hall, 1997.
2. S. Gopalakrishnan, A deep rod finite element for structural dynamics and wave propagation problems, International Journal for Numerical Methods in Engineering 48 (2000) 731–744.
3. A. Chakraborty, D. R. Mahapatra, S. Gopalakrishnan, Finite element analysis of free vibration and wave propagation in asymmetric composite beams with structural discontinuities, Composite Structures 55(1) (2002) 23–36.
4. A. Chakraborty, S. Gopalakrishnan, Poissonś contraction effects in a deep laminated composite beam, Mechanics of Advanced Materials and Structures 10(3) (2003) 205–225.
5. M. Mitra, S. Gopalakrishnan, M. Bhat, A new super convergent thin walled composite beam element for analysis of box beam structures, International Journal of Solids and Structures 41(5-6) (2004) 1491–1518.
6. A. Chakraborty, S. Goapalakrishnan, J. Reddy, A new beam finite element for the analysis of functionally graded materials, International Journal of Mechanical Sciences 45(3) (2003) 519–539.
7. G. Strang, G. Fix, An Analysis of Finite Element Method, Prentice Hall, NJ, USA, 1973.
8. D. Beskos, G. Narayanan, Dynamic response of frameworks by numerical laplace transform, Computer Methods in Applied Mechanics and Engineering 37 (1983) 289–307.
9. J. Doyle, Wave Propagation in Structures, Springer, New York, 1997.
10. S. Doebling, C. Farrar, M. Prime, D. Shevitz, Damage identification and health monitoring of structural and mechanical systems from changes in their vibration characteristics: A literature review, Los Alamos National Laboratory, Report LA - 13070 - MS.
11. R. Jones, Mechanics of Composite Materials, Scripta, Washington, DC, 1975.
12. S. Tsai, H. Hahn, Introduction to Composite Materials, Technomic, 1980.
13. S. Suresh, A. Mortensen, Fundamentals of Functionally Graded Materials, IOM Communications Ltd., London, 1998.
14. A. Markworth, K. Ramesh, W. P. Jr., Modelling studies applied to functionally graded materials, Journal Material Science 30 (1995) 2183–2193.
15. J. Kim, G. Paulino, Finite element evaluation of mixed mode stress intensity factors in functionally graded materials, International Journal for Numerical Methods in Engineering 53 (2002) 1903–1935.

16. C. Zhang, A. Savaidis, G. Savaidis, H. Zhu, Transient dynamic analysis of a cracked functionally graded material by a biem, Computational Material Science 26 (2003) 167–174.
17. K. Wakashima, T. Hirano, M. Niino, Space applications of advanced structural materials, ESA SP-303 97.
18. T. Nakamura, T. Wang, S. Sampath, Determination of properties of graded materials by inverse analysis and instrumented indentation, Acta Materialia 48(17) (2000) 4293–4306.
19. R. Christensen, Mechanics of Composite Materials, Wiley, 1979.
20. G. Liu, A step-by-step method of rule-of-mixture of fiber and particle-reinforced composite materials, Composite Structures 40 (1998) 313–322.
21. A. H. Nayfeh, Wave Propagation in Layered Anisotropic Media, North Holland, Amsterdam, 1995.
22. P. Boulanger, M. Hayes, Inhomogeneous plane waves in viscous fluids, Continuum Mechanics and Thermodynamics 2(1).
23. I. Viktorov, Rayleigh and Lamb Waves, Plenum Press, New York, 1967.
24. G. Caviglia, A. Morro, Inhomogeneous Waves in Solids and Fluids, World Scientific, Singapore, 1992.
25. S. Hunter, Viscoelastic Waves, Progress in Solid Mechanics, North Holland, Amsterdam, 1960.
26. F. Lockett, The reflection and refraction of waves at an interface between viscoelastic materials, Journal Mechanics and Physics of Solids 10(1) (1962) 53–64.
27. H. Cooper, Reflection and transmission of oblique plane waves at a plane interface between viscoelastic media, Journal of Acoustic Society of America 42 (1967) 1064–1069.
28. B. Poiree, Complex harmonic plane waves, Physical Acoustics (O. Leroy and M.A. Breazeale eds.), Plenum Press, New York, 1991.
29. L. M. Brekhovskikh, Waves in Layered Media, Academic Press, New York, 1960.
30. K. F. Graff, Wave Motion in Elastic Solids, Dover Publications Inc., 1991.
31. I. Sneddon, Partial Differential Equations, McGraw-Hill, New York.
32. I. Sneddon, Fourier Transforms, McGraw-Hill, New York, 1951.
33. H. Conway, M. Jakubowski, Axial impact of short cylindrical bars, Journal of Applied Mechanics 36 (1969) 809–813.
34. R. Davies, A critical study of the hopkinson pressure bar, Philosophical Transactions of the Royal Society 240 (1948) 375–457.
35. D. Hsieh, H. Kolsky, An experimental study of pulse propagation in elastic cylinders, Proceedings of the Philosophical Society 71 (1958) 608–612.
36. M. Heideman, D. Johnson, C. Burrus, Gauss and the history of the fast fourier transform, IEEE ASSP Magazine 1(4) (1984) 14–21.
37. J. Cooley, J. Tukey, An algorithm for the machine calculation of complex fourier series, Mathematical Computation 19 (1965) 297–301.
38. D. R. Mahapatra, S. Gopalakrishnan, T. S. Shankar, Spectral-element-based solution for wave propagation analysis of multiply connected unsymmetric laminated composite beams, Journal of Sound and Vibration 237(5) (2000) 819–836.
39. D. R. Mahapatra, S. Gopalakrishnan, A spectral finite element model for analysis of axial-flexural-shear coupled wave propagation in laminated composite beams, Composite Structures 59(1) (2003) 67–88.

40. P. Lancaster, Lambda Matrices and Vibrating Systems, Pergamon Press, 1966.
41. P. Lancaster, Theory of Matrices, Academic Press, 1969.
42. G. Golub, C. V. Loan, Matrix Computations, The Johns Hopkins University Press, Baltimore, 1989.
43. S. Rizzi, J. Doyle, A spectral element approach to wave motion in layered solids, Journal of Vibration and Acoustics 114 (1992) 569–577.
44. F. Moon, A critical survey of wave propagation and impact in composite materials, AMS Report NASA Lewis Research Center (1103).
45. S. Gopalakrishnan, D. R. Mahapatra, Optimal spectral control of broadband waves in smart composite beams with distributed sensor-actuator configuration, SPIE Symposium on Smart Materials and MEMS Paper 4234-12.
46. A. Bent, Piezoelectric fiber composite for structural actuation, MS Thesis Massachusetts Institute of Technology (USA).
47. S. Marur, T. Kant, Transient dynamics of laminated beams: an evaluation with a higher-order refined theory, Composite Structures 41 (1998) 1–11.
48. K. Chandrashekhara, K. Krishnamurthy, S. Roy, Free vibration of composite beams including rotary inertia and shear deformation, Composite Structures 14 (1990) 269–279.
49. A. Bhimaraddi, Computation of ply thickness of laminated beam for which Euler-Bernoulli theory is adequate, Composite Structures 29 (1994) 415–420.
50. J. N. Reddy, Mechanics of Laminated Composite Plates, CRC Press, USA, 1997.
51. S. Gopalakrishnan, M. Martin, J. Doyle, A matrix methodology for spectral analysis of wave propagation in multiple connected timoshenko beam, Journal of Sound and Vibration 158 (1992) 11–24.
52. S. Timoshenko, On the correction for shear of differential equation for transverse vibration of prismatic bars, Philosophical Magazine 41 (1968) 744–746.
53. G. Cowper, On the accuracy of timoshenko beam theory, ASCE Journal of Applied Mechanics 94 (1968) 1447–1453.
54. N. Stephen, M. Levinson, A second order beam theory, Journal of Sound and Vibration 67 (1979) 293–305.
55. F. Yuan, R. Miller, A higher order finite elements for laminated beams, Composite Structures 14 (1990) 125–150.
56. S. Marur, T. Kant, Transient analysis of laminated beams: an evaluation with higher order refined theory, Composite Structures 41 (1998) 1–11.
57. H. Abramovich, A. Livshits, Free vibration of non-symmetric cross-ply laminated composite beams, Journal of Sound and Vibration 176 (1994) 597–612.
58. R. Mindlin, G. Herrmann, A one dimensional theory of compressional waves in an elastic rod, Proceedings of First U.S. National Congress of Applied Mechanics (1950) 187–191.
59. M. Karim, M. Awal, T. Kundu, Elastic wave scattering by cracks and inclusions in plates: In-plane case, International Journal of Solids and Structures 29(19) (1992) 2355–2367.
60. S. Gopalakrishnan, J. Doyle, Wave propagation in connected waveguides of varying cross-section, Journal of Sound and Vibration 175(3) (1994) 347–363.
61. R. Langley, Application of dynamic stiffness method to the free and forced vibration of aircraft panels, Journal of Sound and Vibration 135(2) (1989) 319–331.

62. T. Caughey, M. O'Kelly, Classical normal modes in damped linear dynamic systems, Transaction of ASME, Journal of Applied Mechanics 32 (1965) 583–588.
63. S. Adhikari, Damping models for structural vibrations, PhD Thesis Cambridge University UK.
64. G. Liu, J. Achenbach, Strip element method to analyze wave scattering by cracks in anisotropic laminated plates, ASME Journal of Applied Mechanics 62 (1995) 607–613.
65. F. Tisseur, K. Meerbergen, The quadratic eigenvalue problem, SIAM Review 43(2) (2001) 235–286.
66. M. Géradin, D. Rixen, Mechanical Vibrations, John Wiley & Sons, 1997.
67. J. Woodhouse, Linear damping models for structural vibration, Journal of Sound and Vibration 215(3) (1998) 547–569.
68. H. Banks, D. Inman, On damping mechanisms in beams, Journal of Applied Mechanics 58 (1991) 716–723.
69. S. Chen, K. Liu, Z. Liu, Spectrum and stability for elastic system with global or local kelvin-voigt damping, SIAM Journal of Applied Mathematics 59(2) (1998) 651–668.
70. W. Elmore, M. Heald, Physics of Waves, Dover, New York, 1985.
71. W. Prosser, M. Gorman, J. Dorighi, Extensional and flexural waves in a thin-walled graphite/epoxy tube, Journal of Composite Materials 26(14) (1992) 418–427.
72. W. Fitcher, A theory for inflated thin-wall cylindrical beams, NASA Technical Note TN D-3466.
73. S. Gopalakrishnan, D. R. Mahapatra, Active control of structure-borne noise in helicopter cabin transmitted through gearbox support strut, Proceedings of IUTAM Symposium on Designing for Quietness 102 (Kluwer Academic Publishers).
74. I. Mirsky, G. Herrmann, Nonaxially symmetric motions of cylindrical shells, Journal of Acoustical Society of America 29 (1957) 1116–1123.
75. R. Cooper, P. Naghdi, Propagation of nonaxially symmetric waves in elastic cylindrical shells, Journal of Acoustical Society of America 29 (1957) 1365–1372.
76. J. Greenspan, Vibration of a thick-walled cylindrical shell - comparison of the exact theory with the approximate theories, Journal of Acoustical Society of America 32 (1960) 571–578.
77. J. Reddy, C. Liu, A higher-order shear deformation theory of laminated elastic shells, International Journal of Engineering Science 23 (1985) 440–447.
78. A. Leissa, J. Chang, A higher-order shear deformation theory of laminated elastic shells, International Journal of Engineering Science 23 (1996) 440–447.
79. M. Qatu, Accurate equations for laminated composite deep thick shells, International Journal of Solids and Structures 36 (1999) 1917–2941.
80. D. Gazis, Three dimensional investigation of the propagation of waves in hollow circular cylinders - I. Analytical foundation II. Numerical results, Journal of Acoustical Society of America 31 (1959) 568–578.
81. Z. Xi, G. Liu, K. Lam, H. Shang, Dispersion and characteristic surfaces of waves in laminated composite circular cylindrical shells, Journal of Acoustical Society of America 108(5) (2000) 2179–2186.

82. G. Sun, P. Bennett, F. Williams, An investigation on fundamental frequencies of laminated circular cylinders given by shear deformable finite element, Journal of Sound and Vibration 205(3) (1997) 265–273.
83. J. Reddy, Bending of laminated anisotropic shells by a shear deformable finite element, Composite Science and Technology 17 (1982) 9–24.
84. J. Reddy, Exact solutions of moderately thick shells, Journal of Engineering Mechanics Division, American Society of Civil Engineers 110 (1984) 794–809.
85. K. Chandrashekhara, Free vibrations of anisotropic laminated doubly curved shells, Computers and Structures 33 (1989) 435–440.
86. R. Langley, The modal density and mode count of thin cylindrical and curved panels, Journal of Sound and Vibration 169(1) (1994b) 43–53.
87. M. Bennett, M. Accorsi, Free wave propagation in periodically ring stiffened cylindrical shells, Journal of Sound and Vibration 171(1) (1994) 49–66.
88. J. Kaplunov, L. Kossovich, E. Nolde, Dynamics of Thin Walled Elastic Bodies, Academic Press, UK, 1998.
89. X. Wang, K. Zhang, W. Zhang, J. Chen, Theoretical solution and finite element solution for an orthotropic thick cylindrical shell under impact load, Journal of Sound and Vibration 236(1) (2000) 129–140.
90. O. Song, L. Liberescu, Structural modeling and free vibration analysis of rotating composite thin-walled beams, Journal of the American Helicopter Society October 1997 (1997) 358–369.
91. O. Rand, Fundamental closed-form solutions for solid and thin-walled composite beams including a complete out-of-plane warping model, International Journal of Solids and Structures 35(21) (1998) 2775–2793.
92. E. Armanios, A. Badir, Free vibration analysis of anisotropic thin-walled closed-section beams, AIAA Journal 33(10) (1995) 1905–1910.
93. D. Dancila, E. Armanios, The influence of coupling on the free vibration of anisotropic thin-walled closed-section beams, International Journal of Solids and Structures 35(23) (1998) 3105–3119.
94. J. Ferrero, J. Barrau, J. Segura, B. Castanie, M. Sudre, Torsion of thin-walled composite beams with midplane symmetry, Composite Structures 54(1) (2001) 111–120.
95. K. Graff, Wave Motion in Elastic Solids, Dover Publications Inc., NY, 1975.
96. D. R. Mahapatra, S. Gopalakrishnan, A spectral finite element model for analysis of axial-flexural-shear coupled wave propagation in laminated composite beams, Composite Structures 59(1) (2002) 67–88.
97. S. Gopalakrishnan, J. Doyle, Wave propagation in connected waveguides of varying cross-sections, Journal of Sound and Vibration 175(3) (1994) 347–363.
98. A. Chakraborty, S. Gopalakrishnan, Various numerical techniques for analysis of longitudinal wave propagation in inhomogeneous one-dimensional waveguides, Acta Mechanica 194 (2003) 1–27.
99. A. Chakraborty, Wave propagation in anisotropic & inhomogeneous structures, Ph.D Thesis Indian Institute of Science (2004) .
100. P. Bailey, W. Everitt, A. Zettl, The SLEIGN2 Sturm-Liouville Code Manual. URL `http://www.math.niu.edu/SL2`
101. A. Polyanin, V. Zaitsev, Handbook of Exact Solutions for Ordinary Differential Equations, CRC Press, Boca Raton, 1995.
102. J. Rose, Ultrasonic Waves in Solid Media, Cambridge University Press, 1999.
103. L. Solie, B. Auld, Elastic waves in free anisotropic plates, Journal of Acoustic Society of America 54(1) (1973) 50–65.

104. G. Verdict, P. Gien, C. Burger, Finite element study of Lamb wave interactions with holes and through thickness defects in thin metal plates, NDT & E International 29(4) (1996) 248.
105. M. Veidt, T. Liub, S. Kitipornchai, Modelling of Lamb waves in composite laminated plates excited by interdigital transducers, NDT & E International 35(7) (2002) 437–447.
106. E. Moulin, J. Assaad, C. Delebarre, S. Grondel, D. Balageas, Modeling of integrated Lamb waves generation systems using a coupled finite element normal mode expansion method, Ultrasonics 38 (2000) 522–526.
107. G. Zhao, J. Rose, Boundary element modeling for defect characterization potential in a wave guide, International Journal of Solids and Structures 40(11) (2003) 2645–2658.
108. S. Rizzi, A spectral analysis approach to wave propagation in layered solids, Ph.D. Thesis, Purdue University (1989).
109. M. Powell, A fortran subroutine for solving systems of nonlinear algebraic equations, Numerical Methods for Nonlinear Algebraic Equations P. Rabinowitz, ed., Ch.7. (1970) 115–161.
110. A. Arias, R. Zaera, J. Lopez-Puente, C. Navarro, Numerical modeling of the impact behavior of new particulate-loaded composite materials, Composite Structures 61 (2003) 151–159.
111. R. Olsson, Closed form prediction of peak load and delamination onset under small mass impact, Composite Structures 59 (2003) 341–349.
112. Z. Aslan, R. Karakuzu, B. Okutan, The response of laminated composite plates under low-velocity impact loading, Composite Structures 59 (2003) 119–127.
113. F. Mili, B. Necib, Impact behavior of cross-ply laminated composite plates under low velocities, Composite Structures 51 (2001) 237–244.
114. Y. Wang, K. Lam, G. Liu, The effect of rotary inertia on the dynamic response of laminated composite plate, Composite Structures 48 (2000) 265–273.
115. J. Lee, Plate waves in multi-directional composite laminates, Composite Structures 46 (1999) 289–297.
116. A. Christoforou, A. S. Yigit, Characterization of impact in composite plates, Composite Structures 43 (1998) 15–24.
117. S. Lee, S. Wooh, S. Yhim, Dynamic behavior of folded composite plates analyzed by the third order plate theory, International Journal of Solids and Structures 41 (2004) 1879–1892.
118. A. Mal, S. Lih, Elastodynamic response of a unidirectional composite laminate to concentrated surface loads: Part i, Journal of Applied Mechanics 59 (1992) 878–886.
119. S. Lih, A. Mal, Elastodynamic response of a unidirectional composite laminate to concentrated surface loads: Part ii., Journal of Applied Mechanics 59 (1992) 887–892.
120. S. Lih, A. Mal, On the accuracy of approximate plate theories for wave field calculation in composite laminates, Wave Motion 21 (1995) 17–34.
121. S. Lih, A. Mal, Response of multilayered composites to dynamic surface loads, Composites B 29B (1996) 633–641.
122. A. Mal, Elastic waves from localized sources in composite laminates, International Journal of Solids and Structures 39 (21-22) (2002) 5481–5494.
123. C. Ma, K. Huang, Wave propagation in layered elastic media for antiplane deformation, International Journal of Solids and Structures 32 (5) (1995) 665–678.

124. A. N. Danial, J. F. Doyle, S. A. Rizzi, Dynamic analysis of folded plate structures, Journal of Vibration and Acoustics 118 (4) (1996) 591–598.
125. A. N. Danial, J. F. Doyle, Dynamic analysis of folded plate structures on a massively parallel computer, Computers and Structures 54 (3) (1995) 521–529.
126. A. N. Danial, J. F. Doyle, Massively parallel implementation of the spectral element method for impact problems in plate structures, Computing Systems in Engineering 5 (4-6) (1994) 375–388.
127. M. Krawczuk, M. Palacz, W. Ostachowicz, Wave propagation in plate structures for crack detection, Finite Elements in Analysis and Design 40 (2004) 991–1004.
128. G. Praveen, J. Reddy, Nonlinear transient thermoelastic analysis of functionally graded ceramic-metal plates, International Journal of Solids and Structures 35(33) (1998) 4457–4476.
129. F. Tisseur, N. J. Higham, Structured pseudospectra for polynomial eigenvalue problems, with applications, SIAM Journal of Matrix Analysis and Applications 23 (1) (2001) 187–208.
130. K. Stevens, Force identification problems - an overview, Proceedings of the SEM Spring Conference, Houston, TX (1987) 14–19.
131. B. Hillary, D. Ewins, The use of strain gauges in force determination and frequency response function measurements, Proceedings of the Second IMAC Orlando, FL (1984) 627–634.
132. H. Ory, H. Glaser, D. Holzdepp, Quality of modal analysis and reconstruction of forcing function based on measured output data, Proceedings of the Fourth IMAC Los Angeles, CA (1986) 850–857.
133. D. Williams, Dynamics loads in aeroplanes under given impulsive loads with particular reference to landing and gust loads on a large flying boat, Aeronautics Research Council Tech. Report No. 2221 (1948) –.
134. V. Bateman, T. Carne, D. Gregory, S. Attaway, H. Yoshimura, Force reconstruction for impact tests, ASME, Journal of Vibration and Acoustics 113 (1991) 192–200.
135. J. Michaels, Y. Pao, The inverse source problem for an oblique force on an elastic plate, Journal of Acoustic Society of America 77 (1985) 2005–2011.
136. C. Huang, An inverse nonlinear force vibration problem of estimating the external forces in a damped system with time dependent system parameters, Journal of Sound and Vibration 242 (2001) 749–765.
137. C. Ma, P. Tuan, D. Lin, C. Liu, A study of an inverse method for the estimation of impulsive loads, International Journal of System Science 29 (1998) 663–672.
138. C. Ma, J. Chang, D. Lin, Input forces estimation of beam structures by an inverse method, Journal of Sound and Vibration 259(2) (2002) 387–407.
139. C. Chang, C. Sun, Determining transverse impact force on a composite laminate by signal deconvolution, Experimental Mechanics 29(4) (1989) 414–419.
140. C. Yen, E. Wu, On the inverse problems of rectangular plates subjected to elastic impact. Part I: method development and numerical verification, Journal of Applied Mechanics 62(3) (1995) 692–698.
141. C. Yen, E. Wu, On the inverse problems of rectangular plates subjected to elastic impact. part ii: Experimental verification and further applications, Journal of Applied Mechanics 62(3) (1995) 699–705.
142. E. Wu, J. Yeh, C. Yen, Impact on composite laminated plates: an inverse method, International Journal of Impact Engineering 15(4) (1994) 417–433.

143. E. Jacquelina, A. Bennani, P. Hamelin, Force reconstruction: analysis and regularization of a deconvolution problem, Journal of Sound and Vibration 265 (2003) 81–107.
144. L. Yu, T. Chan, Moving force identification based on the frequency-domain method, Journal of Sound and Vibration 261 (2003) 329–349.
145. G. Liu, W. Ma, X. Han, An inverse procedure for identification of loads on composite laminates, Composites Part B 33 (2002) 425–432.
146. J. Doyle, Further developments in determining the dynamic contact law, Experimental Mechanics 24 (1984) 265–270.
147. J. Doyle, Force identification from dynamic response of a bi-material beam, Experimental Mechanics 33 (1993) 64–69.
148. J. Doyle, Determining the contact force during transverse impact of plates, Experimental Mechanics 27 (1987) 68–72.
149. J. Doyle, Experimentally determining the contact force during the transverse impact of ortho-tropic plates, Journal of Sound and Vibration 118(3) (1987) 441–448.
150. S. Rizzi, J. Doyle, Force identification for impact of a layered system, Computational Aspects of Contact, Impact and Penetration (1991) 222–241.
151. H. Sol, H. Hua, J. D. Visscher, J. Vantomme, W. D. Wilde, A mixed numerical/experimental technique for the nondestructive identification of the stiffness properties of fibre reinforced composite materials, NDT & E International 30(2) (1997) 85–91.
152. S. Kim, B. Jung, H. Kim, W. Lee, Inverse estimation of thermophysical properties for anisotropic composite, Experiment in Theoretical & Fundamental Science 27 (2003) 697–704.
153. R. Al-Khoury, C. Kasbergen, A. Scarpas, J. Blaauwendraad, Spectral element technique for efficient parameter identification of layered media Part I: Forward calculation, International Journal of Solids and Structures 38 (2001) 1605–1623.
154. R. Al-Khoury, C. Kasbergen, A. Scarpas, J. Blaauwendraad, Spectral element technique for efficient parameter identification of layered media Part II: Inverse calculation, International Journal of Solids and Structures 38(48-49) (2001) 8753–8772.
155. T. Nakamura, T. Wang, S. Sampath, Determination of properties of graded materials by inverse analysis and instrumented indentation, Acta Materialia 48(17) (2000) 4293–4306.
156. X. Han, G. Liu, K. Lam, A quadratic layer element for analyzing stress waves in fgms and its application in material characterization, Journal of Sound and Vibration 236(2) (2000) 307–321.
157. G. Liu, X. Han, Y. Xu, K. Lam, Material characterization of functionally graded material by means of elastic waves and a progressive learning neural network, Composite Science and Technology 61 (2001) 1401–1411.
158. G. Liu, X. Han, K. Lam, A combined genetic algorithm and nonlinear least square method for material characterization using elastic waves, Computer Methods in Applied Mechanics and Engineering 191 (2002) 1909–1921.
159. P. Majumdar, S. Suryanarayan, Flexural vibration of beams with delamination, Journal of Sound and Vibration 25(3) (1988) 441–461.
160. J. Tracy, G. Pardoen, Effect of delamination on the natural frequencies of composite laminates, Journal of Composite Materials 23 (1989) 1200–1215.

161. R. Gadelrab, The effect of delamination on the natural frequencies of a composite beam, Journal of Sound and Vibration 197(3) (1996) 283–292.
162. E. Barbero, J. Reddy, Modeling of delamination in composite laminates using a layer-wise plate theory, International Journal of Solids and Structures 28(3) (1991) 373–388.
163. H. Luo, S. Hanagud, Dynamics of delaminated beams, International Journal of Solids and Structures 37 (2000) 1501–1519.
164. F. Léonard, J. Lanteigne, S. Lalonde, Y. Turcotte, Free-vibration behaviour of a cracked cantilever beam and crack detection, Mechanical Systems and Signal Processing 15(3) (2001) 529–548.
165. M. Schulz, A. Naser, P. Pai, J. Chung, Locating structural damage using frequency response reference functions, Journal of Intelligent Material Systems and Structures 9 (1998) 899–905.
166. Y. Zou, L. Tong, G. Steven, Vibration-based-model-dependent damage (delamination) identification and health monitoring for composite strutures - a review, Journal of Sound and Vibration 230(2) (2000) 357–378.
167. S. Chinchalkar, Determination of crack location in beams using natural frequencies, Journal of Sound and Vibration 247(3) (2001) 417–429.
168. K. Lakshminarayana, C. Jebaraj, Sensitivity analysis of local/global modal parameters for identification of a crack in a beam, Journal of Sound and Vibration 228(5) (1999) 977–994.
169. M. Schulz, A. Naser, P. Pai, J. Chung, Locating structural damage using frequency response reference functions, Journal of Intelligent Material Systems and Structures 9 (1998) 899–905.
170. S. Senthil, R. Batra, Exact solution for the cylindrical bending of laminated plates with embedded piezoelectric shear actuators, Smart Materials and Structures 10 (2001) 240–251.
171. M. Heschel, J. Kuhmann, S. Bouwstra, M. Amskov, Stacking technology for a space constrained microsystem, Journal of Intelligent Material Systems and Structures 9 (1998) 749–754.
172. C. Cai, G. Liu, K. Lam, A technique for modelling multiple piezoelectric layers, Smart Materials and Structures 10 (2001) 689–694.
173. J. Tsai, C. Guo, C. Sun, Dynamic delamination fracture toughness in unidirectional polymer composites, Composite Science and Technology 61 (2001) 87–94.
174. L. Tong, D. Sun, S. Atluri, Sensing and actuating behaviours of piezoelectric layers with debonding in smart beams, Smart Materials and Structures 10(4) (2001) 713–723.
175. A. Purekar, D. Pines, Detecting damage in non-uniform beams using the dereververated transfer function response, Smart Materials and Structures 9 (2000) 429–444.
176. J. Doyle, Detection of size and location of transverse crack in beams, Experimental Mechanics 35 (1995) 272–280.
177. K. Lakshmanan, D. Pines, Damage identification of chordwise crack size and location in uncoupled composite rotorcraft flexbeams, Journal of Intelligent Material Systems and Structures 9 (1998) 146–155.
178. G. Park, H. Cudney, D. Inman, An integrated monitoring technique using structural impedence sensors, Journal of Intelligent Material Systems and Structures 11 (2000) 448–455.

179. S. Kessler, S. Spearing, C. Soutis, Damage detection in composite materials using Lamb wave methods, Smart Materials and Structures 11 (2002) 269–278.
180. A. Nag, D. Mahapatra, S. Gopalakrishnan, Identification of delamination in a composite beam using a damaged spectral element, Structural Health Monitoring 1(1) (2002) 105–126.
181. N. Pagano, Interlaminar response of composite materials, Composite Materials Series 5 Elsevier.
182. T. Coats, C. Harris, Experimental verification of a progressive damage model for im7/5260 laminates subjected to tension-tension fatigue, Journal of Composite Materials 29(3) (1995) 280–305.
183. B. Sankar, H. Zhu, The effect of stitching on the low-velocity impact response of delaminated composite beams, Composite Science and Technology 60 (2000) 2681–2691.
184. M. Kouchakzadeh, H. Sekine, Compressive buckling analysis of rectangular composite laminates containing multiple delaminations, Composite Structures 50 (2000) 249–255.
185. J. Lee, Z. Gurdal, H. Griffin, Layer-wise approach for the bifurcation problem in laminated composites with delaminations, AIAA Journal 31(2) (1993) 331–338.
186. J. Lee, Free vibration analysis of delaminated composite beams, Computers and Structures 74 (2000) 121–129.
187. D. R. Mahapatra, S. Gopalakrishnan, B. Balachandran, Active feedback control of multiple waves in helicopter gearbox support struts, Smart Materials and Structures 10 (2001) 1046–1058.
188. S. Valdes, C. Soutis, Application of the rapid frequency sweep technique for delamination detection in composite laminates, Advanced Composite Letters 8(1) (1999) 19–23.
189. S. Valdes, C. Soutis, A structural health monitoring system for laminated composites, ASME Design Engineering Technical Conference Proc. of 18th Biennial Conference on Vibration and Noise (2001) Pittsburgh USA.
190. R. Cook, D. Malkus, M. Plesha, Concepts and Applications of Finite Element Analysis, John Wiley & Sons, 1989.
191. D. R. Mahapatra, S. Gopalakrishnan, Spectral finite element analysis of coupled wave propagation in composite beams with multiple delaminations and strip inclusions, International Journal of Solids and Structures 41 (2004) 1173–1208.
192. S. Ishak, G. Liu, H. Shang, S. Lim, Locating and sizing of delamination in composite laminates using computational and experimental methods, Composites: Part B 32 (2001) 287–298.
193. A. Nag, D. R. Mahapatra, S. Gopalakrishnan, Identification of delaminations in composite: Structural health monitoring software based on spectral estimation and hierarchical genetic algorithms, Proc. ISSS-SPIE 2002 International conference on Smart Materials Structures and Systems (2002) 675–682.
194. A. Nag, D. R. Mahapatra, S. Gopalakrishnan, T. Sankar, A spectral finite element with embedded delamination for modeling of wave scattering in composite beams, Composite Science and Techonology 63(15) (2003) 2187–2200.
195. D. Kumar, D. R. Mahapatra, S. Gopalakrishnan, A spectral finite element for wave propagation and structural diagnostic analysis of composite beam with transverse crack, Finite Elements in Analysis and Design 40(13-14) (2004) 1729–1751.

196. D. R. Mahapatra, Development of spectral finite element models for wave propagation studies, health monitoring and active control of waves in laminated composite structures, Ph.D. Thesis, (2003) 73–95.
197. C. Ratcliffe, Damage detection using a modified laplacian operator on mode shape data, Journal of Sound and Vibration 204(3) (1997) 505–517.
198. H. Lam, J. Ko, C. Wong, Localization of damaged structural connections based on experimental modal and sensitivity analysis, Journal of Sound and Vibration 210(1) (1998) 91–115.
199. C. Ratcliffe, W. Bagaria, Vibration technique for locating delamination in a composite beam, AIAA Journal 36(6) (1998) 1074–1077.
200. C. Ratcliffe, Determination of crack location in beams using natural frequencies, Journal of Sound and Vibration 247(3) (2000) 417–429.
201. T. Lim, T. Kashangaki, Structural damage detection of space truss structures using best achievable eigen vectors, AIAA Journal 32(5) (1994) 1049–1057.
202. P. Liu, Identification and damage detection of trusses using modal data, Journal of Structural Engineering 121(4) (1995) 599–607.
203. R. Manning, Structural damage detection using active members and neural networks, AIAA Journal 32(6) (1994) 1331–1333.
204. H. Zhang, M. Schulz, A. Naser, F. Ferguson, P. Pai, Structural health monitoring using transmittance functions, Mechanical Systems and Signal Processing 13(5) (1999) 765–787.
205. X. Lin, F. Yuan, Diagnostic Lamb waves in an integrated piezoelectric sensor/actuator plate: analytical and experimental studies, Smart Materials and Structures 10 (2001) 907–913.
206. G. Liu, J. Tani, T. Ohyoshi, K. Watanabe, Transient waves in anisotropic laminated plates, part 1: Theory; part 2: Application, ASME Journal of Vibration and Acoustics 113 (1991a) 230–239.
207. Z. Xi, G. Liu, K. Lam, H. Shang, A strip element method for analyzing wave scattering by a crack in a fluid-filled composite cylindrical shell, Composite Science and Technology 60 (2000) 1985–1996.
208. J. Doyle, Determining the contact force during the transverse impact of plates, Experimental Mechanics 27 (1987) 68–72.
209. J. Doyle, A genetic algorithm for determining the location of structural impacts, Experimental Mechanics 34 (1994) 37–44.
210. G. Stavroulakis, Inverse and Crack Identification Problems in Engineering Mechanics, Vol. 46 of Applied Optimization, Kluwer Academic Publishers, 2001.
211. U. Lee, J. Shin, Spectral element method: Applications to structural damage identification, Proceedings of 2002 ISSS-SPIE International Conference on Smart Materials and Systems.
212. D. Goldberg, Genetic Algorithm in Search, Optimization, and Machine Learning, Addison-Wesley Publishing Company, 1989.
213. M. Gen, R. Cheng, Genetic Algorithms and Engineering Design, John Wiley and Sons, Inc, 1997.
214. D. Goldberg, C. Kuo, Genetic algorithms in pipeline optimization, Journal of Computing in Civil Engineering 1(2) (1987) 128–41.
215. W. Jenkins, Towards structural optimization via the genetic algorithm, Computers and Structures 40(5) (1991) 1321–27.
216. A. Keane, Passive vibration control via unusual geometries: the application of genetic algorithm optimization to structural design, Journal of Sound and Vibration 185(3) (1995) 441–453.

217. K. Sivakumar, N. Iyengar, K. Deb, Optimum design of laminated composite plates with cutouts using a genetic algorithm, Composite Structures 42 (1998) 265–279.
218. C. Coello, A. Christiansen, Mutiobjective optimization of trusses using genetic algorithms, Computers and Structures 75 (2000) 647–660.
219. S. Dunn, Modified genetic algorithm for the identification of aircraft structures, Journal of Aircraft 34(2) (1997) 251–253.
220. A. Sadri, J. Wright, R. Wynne, Modelling and optimal placement of piezoelectric actuators in isotropic plates using genetic algorithms, Smart Materials and Structures 8 (1998) 490–498.
221. L. Sheng, R. Kapania, Genetic algorithms for optimization of piezoelectric actuator locations, AIAA Journal 39(9) (2000) 1818–1822.
222. F. Gao, Y. Shen, L. Li, The optimal design of piezoelectric actuator for plate vibroacoustic control using genetic algorithms with immune diversity, Smart Materials and Structures 9 (2000) 485–491.
223. C. Mares, C. Surace, An application of genetic algorithms to identify damage in elastic structures, Journal of Sound and Vibration 195(2) (1996) 195–215.
224. M. Friswell, J. Penny, S. Garvey, A combined genetic and eigen sensitivity algorithm for the location of damage in structures, Computers and Structures 69 (1998) 547–556.
225. C. Howard, S. Snyder, C. Hansen, Calculation of vibratory power transmission for use in active vibration control, Journal of Sound and Vibration 233(4) (2000) 573–585.
226. T. Cormen, C. Leiserson, R. Rivest, Introduction to Algorithms, Prentice-Hall, 1998.
227. R. Langley, Analysis of power flow in beams and frameworks using the direct dynamic stiffness method, Journal of Sound and Vibration 136(3) (1990) 439–452.
228. N. Srinivas, K. Deb, Multiobjective optimization using non-dominated sorting in genetic algorithm, Technical Report Department of Mechanical Engineering (India) (1993) Indian Institute of Technology–Kanpur.
229. J. Alander, Population size, building blocks, fitness landscape and genetic algorithm search efficiency in combinatorial optimization: An empirical study, Practical Handbook of Genetic Algorithms Complex Coding Systems (Chapter 13 (Edited by Chambers L D) CRC Press).
230. S. Haykins, Neural Networks, Pearson Education Inc., 2001.
231. Y. Xu, G. Liu, Z. Wu, X. Huang, Adaptive multilayer perceptron network for detection of cracks in anisotropic laminated plates, International Journal of Solids and Structures 38 (2001) 5625–5645.
232. D. Rumelhart, G. Hinton, R. Williams, Learning representations of back-propagation errors, Nature 323 (1986) 533–536.
233. I. Pelinescu, B. Balachandran, Analytical and experimental investigations into active control of wave transmission through gearbox struts, Proc. SPIE Smart Structures and Materials Conference on Smart Structures and Integrated Systems 3985 (2000) 76–85.
234. P. Wilke, C. Johnson, P. Grosserode, D. Sciulli, Whole-spacecraft vibration isolation for broadband attenuation, Proc. IEEE Aerospace Conference Montana (2000) March 19–25.
235. T. Anderson, Fracture Mechanics, CRC Press, 1995.

236. E. Anderson, J. How, Active vibration isolation using adaptive feedforward control, American Control Conference Albuquerque NM (Paper I-97115B).
237. M. Abe, Y. Fujino, Dynamic characterization of multiple tuned mass dampers and some design formulas, Earthquake Engineering and Structural Dynamics 23(8) (1994) 813–835.
238. M. Abe, T. Igusa, Tuned mass dampers for structures with closely spaced natural frequencies, Earthquake Engineering and Structural Dynamics 24(2) (1995) 247–261.
239. J. Inaudi, J. Kelly, Experiments on tuned mass dampers using viscoelastic, frictional and shape-memory alloy materials, Proc. First World Conference on Structural Control: International Association for Structural Control Los Angeles.
240. J. Lin, W. Zhang, D. Sun, Q. He, R. Lark, F. Williams, Precise and efficient computation of complex structures with tmd devices, Journal of Sound and Vibration 223 (5) (1999) 693–701.
241. D. Rade, V. Steffen, Optimisation of dynamic vibration absorbers over a frequency band, Mechanical Systems and Signal Processing 14(5) (2000) 679–690.
242. E. Anderson, M. Holcomb, D. Leo, A. Bogue, F. Russo, Integrated electromechanical devices for active control of vibration and sound, International Mechanical Engineering Congress and Exposition Dallas Texas (Nov 16-21).
243. E. Anderson, D. Leo, Vibroacoustic modeling of a launch vehicle payload fairing for active acoustic control, Proceedings of 3rd Turbine Engine High Cycle Fatigue Conference San Antonio (Feb 2-5).
244. B. Allen, E. Ruhl, B. Fowler, Advanced isolation design for avionics on launch vehicles, Proceedings of SPIE Smart Structures and Materials Conference San Diego CA.
245. R. Maly, P. Wilke, E. Fowler, S. Haskett, D. Sciulli, T. Meink, Espa: Eelv secondary payload adapter with whole-spacecraft isolation for primary and secondary payloads, Proc. SPIE Smart Structures and Materials Conference Newport Beach-CA.
246. R. Clark, J. Pan, C. Hansen, An experimental study of multiple wave types in elastic beams, Journal of Acoustical Society of America 89(1) (1992) 871–876.
247. A. Flotow, Disturbance propagation in structural network, Journal of Sound and Vibration 106(3) (1986) 433–450.
248. H. Fujii, T. Ohtsuka, T. Murayama, Wave-absorbing control for flexible structures with noncollocated sensors and actuators, Journal of Guidance Control and Dynamics 15(2) (1992) 431–439.
249. N. Tanaka, Y. Kikushima, Optimal vibration feedback control of an euler-bernoulli beam: Toward realization of the active sink method, Journal of Vibration and Acoustics 121 (1999) 174–182.
250. A. Koma, G. Vukovich, Vibration suppression of flexible beams with bonded piezotransducers using wave-absorbing controllers, Journal of Guidance, Control, and Dynamics 23(2) (2000) 347–354.
251. S. Elliott, L. Billet, Adaptive control of flexural waves propagating in a beam, Journal of Sound and Vibration 163 (1993) 295–310.
252. A. Roure, Self-adaptive broadband sound control system, Journal of Sound and Vibration 101 (1985) 429–441.
253. A. Flotow, Traveling wave control for large spacecraft structure, Journal of Guidance and Control 9(4) (1986) 462–468.

254. R. Mace, Active control of flexural vibrations, Journal Sound and Vibration 114 (1987) 253–270.
255. D. Pines, A. Flotow, Active control of bending waves propagation at acoustic frequencies, Journal of Sound and Vibration 142 (1990) 391–412.
256. S. Kuo, D. Morgan, Active Noise Control Systems, Wiley, New York, 1996.
257. M. Balas, Direct velocity feedback control of large space structures, Journal of Guidance and Control 2 (1979) 242–253.
258. J. Auburn, Theory of control of structures by low-authority controllers, Journal of Guidance and Control 3 (1980) 444–451.
259. W. Baumann, An adaptive feedback approach to structural vibration suppression, Journal of Sound and Vibration 205(1) (1997) 121–133.
260. K. McConnell, P. Cappa, Transducer inertia and stringer stiffness effects on frf measurements, Mechanical Systems and Signal Processing 14(4) (2000) 625–636.
261. C. Goh, T. Caughey, On the stability problem caused by finite actuator dynamics in the collocated control of large space structures, International Journal of Control 41(3) (1985) 787–802.
262. B. M. Noyer, S. Hanagud, Single actuator and multi-mode acceleration feedback control, Adaptive Structures and Material Systems 54 (1997) 227–235.
263. D. R. Mahapatra, S. Gopalakrishnan, Spectrally formulated finite element for elementary composite beam with embedded smart layers, Proceedings of the ISSS-SPIE International Conference on Smart Materials, Structures and Systems Bangalore (India) (1999) 337–342.
264. D. R. Mahapatra, S. Gopalakrishnan, T. Shankar, Spectral-element-based solutions for wave propagation analysis of multiply connected laminated composite beams, Journal of Sound and Vibration 237(5) (2000) 819–836.
265. S. Burke, J. Hubbard, J. Meyer, Colocation: design constraints for distributed and discrete transducers, Proc. 13th Biennial Conference on Mechanical Vibration and Noise 34 (1991) 75–81.
266. F. Fleming, E. Crawley, The zeroes of controlled structures: sensor/actuator attributes and structural modelling, Proc. 32nd AIAA Structures - Structural Dynamics and Materials Conference Baltimore, MD (AIAA paper 91-0984).
267. S. Hall, E. Crawley, J. How, B. Ward, Hierarchic control architecture for intelligent structures, Journal of Guidance Control and Dynamics 14(3) (1991) 503–512.
268. J. Pan, C. Hansen, Active control of total vibratory power flow in a beam i: Physical system analysis, Journal of Acoustical Society of America 89(1) (1991) 200–209.
269. P. Gardonio, S. Elliott, Active control of wave in a one-dimensional structure with scattering termination, Journal of Sound and Vibration 192 (1996) 701–730.
270. T. Sutton, S. Elliott, M. Brennan, K. Heron, D. Jessop, Active isolation of multiple structural waves on a helicopter gearbox support strut, Journal of Sound and Vibration 205(1) (1997) 81–101.
271. W. Mason, Piezoelectric Crystals and their Applications to Ultrasonics, Van Nostrand, 1950.
272. W. Cady, Piezoelectricity, Dover, 1964.
273. A. Bent, N. Hagood, J. Rodgers, Anisotropic actuation with piezoelectric composites, Journal of Intelligent Material Systems and Structures 6(3) (1995) 338–349.

274. A. Bent, Active fiber composites for structural actuation, PhD Thesis Massachusetts Institute of Technology (USA).
275. Y. Wu, Magnetostrictive particle actuator and its characterization for smart structure applications, PhD Thesis University of Maryland-UMBC.
276. P. Nelson, S. Elliott, Active Control of Sound, Academic Press, London, 1992.
277. A. Makarenko, E. Crawley, Force and strain feedback for distributed actuation, Technical Report - MIT SSL 98-10.
278. E. Crawley, J. Luis, Use of piezoelectric actuators as elements of intelligent structures, AIAA Journal 25(10) (1987) 1373–1385.
279. X. Peng, K. Lam, G. Liu, Active vibration control of composite beams with piezoelectrics: A finite element model with third order theory, Journal of Sound and Vibration 209(4) (1998) 635–650.
280. D. Sarvanos, P. Heyliger, D. Hopkins, Layerwise mechanics and finite element for the dynamic analysis of piezoelectric composite plates, International Journal of Solids and Structures 34(3) (1997) 359–378.
281. M. Krommer, On the correction of the bernoulli-euler beam theory for smart piezoelectric beams, Smart Materials and Structures 10 (2001) 668–680.
282. B. Douglas, J. Yang, Transverse compressional damping in vibratory response of elastic-viscoelastic-elastic beams, AIAA Journal 16 (1978) 925–930.
283. A. Baz, J. Ro, Vibration control of plates with active constrained layer damping, Smart Materials and Structures 5 (1996) 272–280.
284. A. Baz, Spectral finite-element modeling of the longitudinal wave propagation in rod treated with active constrained layer damping, Smart Materials and Structures 9 (2000) 372–377.
285. A. Taliercio, R. Coruzzi, Mechanical behaviour of brittle matrix composite: a homozenization approach, International Journal of Solids and Structures 36 (1999) 3591–3615.
286. O. Sluis, P. Vosbeek, P. Schreurs, H. Meijer, Homogenization of heterogeneous polymers, International Journal of Solids and Structures 36 (1999) 3193–3214.
287. N. Hagood, R. Kindel, K. Ghandhi, P. Gudenzi, Improving transverse actuation of piezoceramics using integrated surface electrodes, SPIE Proc. North American Conference on smart structures and materials (1993) 1917–25.
288. J. French, J. Weitz, R. Luke, R. Cass, Production of continuous piezoelectric ceramic fibers for smart materials and active control devices, SPIE Proc. 3044.
289. I. Sevostianov, V. Levin, M. Kachanov, On the modeling and design of piezocomposites with prescribed properties, Archive of Applied Mechanics 71 (2001) 733–747.
290. T. Mahut, A. Agbossou, J. Pastor, Dynamic analysis of piezoelectric fiber composite in an active beam using homogenization and finite element method, Journal of Intelligent Material Systems and Structures 9 (1998) 1009–1015.
291. J. Mackerle, Sensors and actuators: finite element and boundary element analyses and simulations. A bibliography (1997-1998), Finite Elements in Analysis and Design 33 (1999) 209–220.
292. A. Benjeddou, Advances in piezoelectric finite element modeling of adaptive structural elements: a survey, Computers and Structures 76 (2000) 347–363.
293. IEEE standard on piezoelectricity, IEEE Std 176-1978 The Institute of Electrical and Electronics Engineers.
294. A. Pizzochero, Residual actuation and stiffness properties of piezoelectric composites: theory and experiment, PhD Thesis Massachusetts Institute of Technology (USA).

295. B. Anderson, J. Moore, Optimal Control, Prentice Hall, Englewood Cliffs, NJ, 1990.
296. J. Butler, Application Manual for the Design of ETREMA Terfenol-D Magnetostrictive Transducers Ames IA: EDGE Technologies Incorporated.
297. D. Miller, S. Hall, A. von Flotow, Optimal control of power flow in structural junctions, Journal of Sound and Vibration 140(3) (1990) 475–497.
298. A. Staple, D. Wells, The development and testing of an active control of structural response system for the eh101 helicopter, Proceedings of the 16th European Rotorcraft Forum III.6.1.1-III.6.1.11.
299. G. Vignati, Research on helicopter interior noise: A survey on current activities in helicopter industries, 2nd Community Aeronautics RTD Conf. Luxembourg: Commission of the European Communities (1993) 493–503.
300. A. Sampath, B. Balachandran, Studies on performance functions for interior noise control, Smart Materials and Structures 6 (1997) 315–332.
301. I. Pelinescu, B. Balachandran, Analytical study of active control of wave transmission through cylindrical struts, Smart Materials and Structures 10 (2001) 121–136.
302. A. Staple, B. MacDonald, Active vibration control system, US Patent No 5-219-143.
303. M. Brennan, R. Pennington, S. Elliot, Mechanisms of noise transmission through helicopter gearbox support struts, Journal of Vibration and Acoustics 116 (1994) 548–554.
304. C. Yoerkie, J. Newington, W. Welsh, N. Haven, H. Sheehy, Helicopter active noise control system, US Patent No 5-310-137.
305. T. Millot, W. Welsh, C. Yoerkie, D. MacMartin, M. Davis, Flight test of an active gear-mesh noise control on the s-76 aircraft, 54th Annual Forum of the American Helicopter Society (Washington, DC 1998) (1998) 241–249.
306. D. Ortel, B. Balachandran, Control of flexural wave transmission through struts, Proceedings of the SPIE Smart Structures and Materials Conference on Smart Structures and Integrated Systems (Newport Beach, CA) 3668(2) (1999) 567–577.
307. D. Miller, A. von Flotow, A traveling wave approach to power flow in structural networks, Journal of Sound and Vibration 128(1) (1989) 145–162.
308. IEEE standard on magnetostrictive materials: Piezomagnetic nomenclature, IEEE Std 319-1990 The Institute of Electrical and Electronics Engineers.

Index